Imperial College London

The Influence of Fold and Salt-Wall Growth on Deepwater Sedimentary Systems in an Active Salt Mini-Basin, offshore Angola

Gemma Doughty-Jones

A dissertation submitted to the Department of Earth Science and Engineering of Imperial College London in partial fulfilment of the requirements for the degree of Doctor of Philosophy

December 2014

Declarations

I declare that this thesis

The influence of fold and salt-wall growth on deepwater sedimentary systems in an active salt mini-basin, offshore Angola

is entirely my own research carried out under the supervision of Dr. Lidia Lonergan, Dr. Michael Mayall and Dr. Stephen Dee. The research was carried out in the Department of Earth Science and Engineering at Imperial College London. All published and unpublished material used in this thesis has been given full acknowledgement. None of this work has been previously submitted to this or any other academic institution for a degree or diploma, or any other qualification.

The copyright of this thesis rests with the author and is made available under a Creative Commons Attribution Non-Commercial No Derivatives licence. Researchers are free to copy, distribute or transmit the thesis on the condition that they attribute it, that they do not use it for commercial purposes and that they do not alter, transform or build upon it. For any reuse or redistribution, researchers must make clear to others the licence terms of this work.

Gemma Doughty-Jones
PhD student
Department of Earth Science and Engineering
Imperial College London

Abstract

Interactions between deepwater sedimentary systems and growing coeval salt structures result in the development of unique morphological features. This thesis focuses on controls on the formation and development of these features in a deforming deepwater passive margin setting, offshore Angola. Using 3D seismic datasets and well data, the evolution of basin-bounding structures and infill history of a salt withdrawal mini-basin are investigated, focusing on fan lobe complexes and mass transport complexes (MTCs). Structural restoration, isopachs and sediment accumulation rate maps are used to describe the basin evolution, with rates of change of bed length of individual structures calculated using biostratigraphic data.

Early sedimentation on the slope was dominated by erosional channel complexes (33.9 - 18.26 Ma). Subsequently, salt movement and a concomitant increase in the growth rate of the basin-bounding anticlines, led to the formation of MTCs (18.26 - 8.29 Ma). Two types of MTC are examined:

1. laterally extensive deposits which thin onto structures and were sourced from the contemporaneous shelf;
2. small-scale MTCs sourced from basin-bounding structures.

As salt movement continued, the basin became largely enclosed and ponded fans developed (8.29 - 5.58 Ma). Four lobe complexes imaged in unprecedented detail are investigated, revealing systematic changes in sediment entry point, fan shape and orientation through time.

Combining observations on spatial distribution of sedimentary systems with maps showing the rate of growth of structures within the mini-basin and observations of the variations in stratal relationships through time, the following can be concluded:

- ponded fan deposition occurred during low growth rate intervals (rate of change of bed length <10 mMa^{-1}). The lobe complex shape resulted from their passive response to relict topography from preceding high rate of change of bed length periods,
- regional MTC deposits respond passively to structural growth and relict topography, being preferentially deposited in bathymetric lows, whilst
- channels and local MTCs respond actively to medium and high growth rate structures; channel pathways change in response to structures with bed length change rates >15 mMa^{-1}.

Acknowledgements

I would like to extend my heartfelt thanks to all three of my supervisors for their help, support and encouragement throughout this PhD. They have each approached the research presented in this thesis from different angles and their inputs have greatly complimented each other. Without their combined knowledge, differing insights, and complimentary mentoring styles, this work could have turned out very differently. I would like to thank Dr. Lidia Lonergan at Imperial College London for her unwavering support and infectious enthusiasm for this research which really helped me stay interested in the subject throughout and motivated me at periods when I felt my interest was flagging. Dr. Mike Mayall at BP, I would like to thank for always finding time for a chat and a catch-up in his busy schedule, our discussions have never failed to help develop my understanding of the intricate details of sedimentary systems and I wish him all the best for his upcoming retirement. I would also like to thank Dr. Steve Dee also at BP for all of the support he has provided throughout the last three and a half years, not only academically, but also logistically.

I would like to extend my gratitude to NERC who funded this project in partnership with BP. I would also like to thank those people in BP who have worked on my behalf to obtain the permissions for me to work on this, highly sensitive, seismic data. Namely Drs. Mike Mayall and Steve Dee, who also ensured that I had a desk to work at in the office at Sunbury, helped me make contact with the relevant people and made sure that I was never left on my own at lunchtime. I would like to thank everyone in the SST Team too for their support and encouragement, particularly over the last few months.

I would also like to thank my fellow PhD students in the Department of Earth Science and Engineering, both past and present, for their friendship, humour and support. My particular thanks go to Dr. Grace Cairns, Annabel Dale, Byami Jolly, Dr. Seb Turner and Dr. Antony Burnham for always being able to brighten up my day.

Lastly I would like to thank my parents Caroline and John Jones, as well as my sisters, who have constantly supported my work and provided much needed encouragement, humour and cake along the way. A very special thank you to my wonderful fiancé Matthew Doughty for without his support, his love and his Word and Excel skills this PhD would not have progressed to this stage. I am very much looking forward to celebrating together at our wedding in just a few weeks' time and hope that the rest of our lives together go more smoothly.

List of Publications

Jones, G., Mayall, M., and Lonergan, L., 2012, Contrasting depositional styles on a slope system and their control by salt tectonics: through-going channels, ponded fans, and mass transport complexes, *in*, Rosen, N.C. Weimer, P., dos Anjos, S.M.C., Henrickson, S., Marques, E., Mayall, M., Fillon, R, D'Agostino, T, Saller, A., Campion, K., Huang, T., Sarg, R. and Schroeder, F., eds, New Understanding of the Petroleum Systems of Continental Margins of the World, 32nd Annual GCSSEPM Foundation Bob. F. Perkins Conference, p. 503-533.

Contents

Chapter 1	**Introduction**	**25**
1.1	Rationale	25
1.2	Aims and Objectives	26
1.3	Thesis Outline	28
Chapter 2	**Introduction to the Study Area**	**31**
2.1	Introduction and Regional Setting	31
2.2	Regional Stratigraphic Framework	31
2.3	Regional Structural Setting	37
Chapter 3	**Principles Behind the Study: A Sedimentological Literature Review**	**45**
3.1	Introduction	45
3.2	Sedimentation Types	45
3.2.1	Mass Transport Complexes (MTCs)	45
3.2.2	Ponded Fan Systems	52
3.2.3	Channel Complex Systems	58
3.3	Regional Boundary Condition Controls on Deepwater Depositional Systems	59
3.3.1	Sediment Supply	60
3.3.2	Sedimentation Rate	61
3.3.3	Climate Change	61
3.4	Local Boundary Condition Variations – Topographical Changes	62
3.5	Summary	64
Chapter 4	**Data Sources and Methodology**	**67**
4.1	Data Sources	67
4.1.1	PSVM Survey	67
4.1.2	Regional Survey	69
4.1.3	Horizon Ages	70
4.1.4	Well Data	72
4.2	Methods	72
4.2.1	Seismic Interpretation	72

4.2.2 Seismic Attribute Analysis 73
4.2.3 Depth Conversion 75
4.2.4 Isopach Maps 76
4.2.5 Structural Restoration 78
4.2.6 Depth Conversion for 2D Move® 81
4.2.7 Decompaction for 2D Restoration 82
4.2.8 Algorithm Choice for Restorations 84
4.2.9 Strain Analysis 86
4.2.10 Errors Associated with Bed Length Change Measurements 89
4.2.11 Interpreting Bed Length Change Graphs 91
4.2.12 Stratal Growth Pattern Analysis 92
4.2.13 ArcGIS Analysis 94
Chapter 5 Structural Analysis of the Mini-Basin 97
5.1 Abstract 97
5.2 Introduction 97
5.3 Methodology 98
5.4 Regional Overview 99
5.4.1 Gravity and Magnetic Analysis 99
5.4.2 Regional Salt Setting 100
5.5 Mini-Basin Structural Setting 102
5.6 2D Reconstruction across the Mini-Basin 106
5.7 Isopach and Sediment Accumulation Analysis 109
5.8 Bed Length Change Analysis of Basin Structures 116
5.9 Bed Length Change Analysis of a Single Structure 123
5.10 Maps Showing Rate of Change of Bed Length 127
5.11 Discussion 129
5.11.1 Structural Driving Forces 129
5.11.2 Linking Bed Length Change Rates, Growth and Topography 131
5.12 Conclusions 135

Chapter 6 Mass Transport Complex Deposits Generated by, and Subsequently Influenced by, Active Salt Growth Structures 137

6.1 Abstract 137

6.2 Introduction 137

6.3 Methods 139

6.4 Structural Constraints 140

6.5 Age of MTCs 142

6.6 Local Mass Transport Systems – MTC 1 142

6.6.1 Bounding Surfaces 143

6.6.2 Internal Characteristics 147

6.7 Comparison between MTCs 1, 2 and 3 150

6.7.1 Bounding Surfaces 150

6.7.2 Internal Characteristics 153

6.7.3 Volume and Area 158

6.8 Regional Mass Transport Systems 159

6.8.1 Age and Frequency 160

6.8.2 Thickness and Extent 160

6.8.3 Internal Characteristics 163

6.8.4 Source Area and Derivation 169

6.9 Discussion 170

6.9.1 Comparison between Debris Flows and Slides 170

6.9.2 Structural Evolution and Corresponding MTC Deposits 172

6.10 Conclusions 174

Chapter 7 Development of Deepwater Ponded Fan Systems within a Mini Basin; their Characteristics and Evolution 177

7.1 Abstract 177

7.2 Introduction 178

7.3 Methodology 180

7.4 Structural Constraints 182

7.5 Stratigraphy 184

7.6 Northern Channel Complex 190
7.7 Ponded Interval Analysis 192
7.7.1 P10 – P20 193
7.7.2 P20 – P30 196
7.7.3 P30 – P40 203
7.7.4 P40– P50 211
7.8 Well Data 219
7.9 Comparison to Other Systems 220
7.9.1 Seismic Studies 220
7.9.2 Modern Seafloor Studies 223
7.9.3 Outcrop Studies 226
7.10 Discussion 229
7.10.1 Morphological Variations 229
7.10.2 Observational Scales 234
7.11 Conclusions 235
Chapter 8 Interactions between Deepwater Sedimentary Systems and Active Salt Structures 237
8.1 Abstract 237
8.2 Introduction 237
8.3 Methodology 239
8.4 Structural Controls on the Mini-Basin 239
8.5 Interactions between Active Structural Growth and Channel Complexes 242
8.5.1 Response of Channels to Structural Growth during Early Channel Interval 242
8.5.2 Response of Channels to Structural Growth during Late Channel Interval 245
8.5.3 Discussion of Channel Interactions 247
8.6 Interactions between Active Structural Growth and Mass Transport Complexes 252
8.6.1 Regional MTCs 252
8.6.2 Stratal Relationships of Regional MTCs 255
8.6.3 Local MTCs 256
8.6.4 Discussion of MTCs and their Interactions with Structural Growth 259

8.7 Interactions between Active Structural Growth and Ponded Fans 260

8.7.1 Spatial Distribution of Ponded Fan Lobe Complexes 260

8.7.2 Stratal Relationships of Ponded Fan Lobe Complexes 263

8.7.3 Summary Discussion of Ponded Fan Lobe Complexes and their Interactions with Structural Growth 266

8.8 Responses of Deepwater Slope Sedimentary Systems to Seabed Topography 267

8.8.1 Active Responses to Structural Growth 269

8.8.2 Passive Responses to Structural Growth 271

8.9 Conclusions 271

Chapter 9 Conclusions 273

9.1 Key Conclusions 273

9.1.1 Effect of Structural Growth Rate on Sedimentary Systems 276

9.1.2 How Useful is Bed Length Change Analysis? 277

9.1.3 Main Structural Drivers in the Mini-Basin Formation 278

9.1.4 Bed Length Change is a Useful Method to Assess Structural Evolution 279

9.1.5 New Details on Lobe Complex Development 279

9.1.6 Implications for Petroleum Geology 280

9.2 Future Work 281

References 283

List of Figures

Figure 1.1 Map showing the location of Block 31 (green outline) with respect to the Angolan Coast, the study area is located in the north-eastern corner of Block 31. Note the present day location of the Congo canyon to the north of the study area 27

Figure 2.1 Series of diagrams showing the palaeogeographic evolution of the region from the Cretaceous through to the Miocene (Compiled using data from Burke et al., 2003, Macdonald et al., 2003, Seranne and Anka, 2005, Scotese, 2008). 33

Figure 2.2 Stratigraphic column through the Lower Congo Basin showing the main tectonic events and sediments deposited within the basin from the Cretaceous to present day. Taken from Anderson et al. (2012). 34

Figure 2.3 A series of palaeogeographic maps showing the distribution of the coarse clastic sediments and active structures across the Lower Congo at four periods during the evolution of the margin. The dashed line separates the extensional and contractional domains and the black box represents the approximate location of the study area within the Lower Congo Basin. Modified from Anderson et al. (2012). 36

Figure 2.4 (a) Regional map showing the approximate location of the shelf slope break in the Lower Congo Basin during the Miocene, and how the shelf break has prograded relative to the Congo Fan, (b) major post-rift elements with approximate location of Block 31 outlined in green and the study area in yellow (Modified from Anderson et al., 2000). 37

Figure 2.5 Structural elements map over the entire area covered by the Lower Congo Basin highlighting allochthonous salt structures, major faults and folds as well as limits of the contractional and extensional domains on the passive margin during the Tertiary. An approximate location of the study area investigated in this thesis is shown with a black box. The map is taken from Anderson et al. (2012). 39

Figure 2.6 Overview of the regional salt tectonic providences offshore Angola, using a map and cross-sections to show variations along the margin. Blue outline on the map indicates the location of Block 31, orange shows the outline of the PSVM and the red box on Transect A shows the area of interest in this study (Modified from Marton et al., 2000, Tari et al., 1998). 41

Figure 3.1 Diagram illustrating the main structures and domains associated with mass transport complexes and the syndepositional features associate with their development. The broad white arrows indicate the direction of transport with the sections through showing the features in that area. This is taken from Richardson et al. (2011) which is in turn modified from Bull et al. (2009) and Prior et al. (1984). 48

Figure 3.2 A series of diagrams illustrating the different kinds of mass transport complexes (MTCs) and the processes associated with their initiation, as outlined by Moscardelli and Wood (2008). (a) Slope-attached MTCs whereby the sediments are derived from catastrophic failure of the upper slope area. (b) Shelf-attached MTCs where shelf-edge delta collapse sources the material for the deposits. (c) Detached MTCs associated with the collapse along the flank of a mud volcano (in the case of the study area salt diapir growth could source this type of detached MTC). (d) Detached MTC associated with over-steepening of a margin along a deepwater mini-basin, and (e) detached MTC deposit whose genesis is associated with a levee-channel complex. Image taken directly from Moscardelli and Wood (2008). 50

Figure 3.3 A comparison between MTCs defined according to the type of frontal emplacement exhibited. They have been defined as being either (a) frontally emergent whereby the material ramps up over the basal shear surface and out onto the seabed where it is able to travel a considerable distance over the unconfined seafloor or (b) frontally confined systems where the internal volume of the MTC is buttressed against the frontal ramp of the MTC and does not leave the original basal shear surface. Taken from Frey Martinez et al. (2006). 52

Figure 3.4 (a) Plan view of a typical deepwater submarine fan (from Prelat et al., 2009) showing the hierarchy of the depositional elements compared to (b) a typical fan found in the study area, note that the features can be recognised down to the lobe element scale. 53

Figure 3.5 Cartoon showing the different types of submarine fans that develop along the continental margin depending on the slope topography (Modified from Gamberi and Rovere, 2011). Vertical scale highly exaggerated; approximate horizontal scale of 200 km. 55

Figure 3.6 Cartoon showing the different methods by which ponded sediments can be deposited within a confined basin (Sinclair and Tomasso, 2002). 57

Figure 3.7 General model for the channel complex systems used throughout this thesis showing a third order channel complex system with a dominantly erosional base, several fourth order channel complexes in which axis and margin areas can be recognised and individual channels (modified from Mayall et al., (2006) and taken directly from Jones et al. (2012)). 59

Figure 3.8 Flow chart showing how intra- and extra-basinal controls can impact deepwater systems. Image taken directly from Kolla (2007). 60

Figure 4.1 Extent of the PSVM data shown using the seafloor bathymetric profile, the five wells within the study area are labelled for reference. 67

Figure 4.2 Analysis of the frequency change in the seismic data with depth; graphs show quality decreasing with depth. 68

Figure 4.3 Diagrams showing how the high-resolution seismic dataset over the PSVM area was generated with (a) showing how the primary ray (event 1) pathway taken from the source array to the target receiver compares to those ghost reflector pathways (events 2, 3, and 4) generated from the sea surface which contaminate and obscure the seismic images of the subsurface, and (b) the impact of the ghost notches on the frequency of the signal received, in this example the first notch appears at 11 Hz frequency. Images provided by J. Verhaeghe, 2014, from BP internal documents. 68

Figure 4.4 Extent of the regional dataset offshore Angola with the nine 3D surveys highlighted in green going from A to C north to south and 1 to 3 west to east, such that Block 31 (yellow) and the PSVM (orange) lie within 3D grid A1. Right-hand side shows regional bathymetry over the blocks that BP has access to and known salt in pink. 70

Figure 4.5 Diagram showing the definition of an isoproportional horizon. These were generated between mapped intervals of interest and used to produce amplitude extraction maps. 75

Figure 4.6 A series of amplitude extraction maps over the same 25 ms interval generated using three different types of algorithm: (a) a root mean squared amplitude algorithm is applied which calculates the square root of the summed amplitudes, (b) a maximum positive algorithm is applied to the same data highlighting the maximum positive amplitudes in white and negative

amplitudes in black, and (c) a maximum negative amplitude extraction where the high negative amplitudes are white and positive amplitudes black. 76

Figure 4.7 Velocity model overlaid on an inline of the PSVM data showing how the velocity varies with depth and sediment type. Velocity model used to calculate the vertical resolution and to convert horizons from time to depth. 77

Figure 4.8 Diagram showing the difference between the vertical thickness (v) and the stratigraphic thickness (s) and hence how this can improve the accuracy of the measurement of bed thickness for steeply dipping beds. 77

Figure 4.9 Percentage overestimate of bed thickness if calculated as a vertical thickness using the equation % overestimate = ((vertical thickness – stratigraphic thickness)/vertical thickness)*100 78

Figure 4.10 Diagrams illustrating the processes of restoration of a simple cross-section through flexural slip. This is based on the model that bed lengths do not change during deformation and that internal deformation occurs through layer parallel simple shear. (a) illustrating a deformed section prior to the process of (b) flexural-slip restoration, (c) shows the effect of constant bed-length thickness flexural slip model (after Klingfield et al., 1986) 80

Figure 4.11 Diagram illustrating vertical and oblique simple shear, whereby a reference horizon is restored to a specified datum and underlying beds move accordingly, thus preserving vertical thickness but changing bed length and true thickness. This is illustrated using a vertical simple shear algorithm where (a) a cross-section based on a series of lithological logs where zero elevation is sea level (s.l.), sh: shale, ss.: sandstone, ls: limestone is also shown in (b) flattened to a datum at the top of the sandstone, thus revealing an anticline within the limestone beds. As well as by oblique simple shear. Here medium weight solid lines are marker beds, dotted lines represent the shear direction and are equally spaced at an arbitrary distance, S, and the shear angle is α, (a) shows a deformed cross-section while (b) shows this same section restored using the oblique, or inclined, simple shear. Diagrams taken from 2D Move user manual. 81

Figure 4.12 A graph showing all the well data from the area surrounding the basin. This is plotted to generate the algorithm used to depth convert the seismic section which was used for the structural restoration in 2D Move®. 82

Figure 4.13 Comparisons between the patterns in stratigraphy generated by using three different restoration algorithms. 85

Figure 4.14 Diagrams illustrating the methodology used to calculate the bed length change of (A) overlapping syn-tectonic sediments and (B) onlapping syn tectonic sediments (modified from Poblet et al. (2004)). 87

Figure 4.15 Illustration showing the deformation in an experimental detachment fold train. Taken from Poblet et al. (2004) but ultimately modelled after Price and Cosgrove (1990). 90

Figure 4.16 A visual comparison between two theoretical cross-sections through anticlines and the corresponding bed length change graphs. 92

Figure 5.1 Maps over the region offshore Angola showing (a) regional gravity with a 200 km wavelength filter applied, red is high gravity and purple low and (b) regional magnetic intensity map where red is high intensity and purple is low intensity. In both maps Block 31 is outlined in grey and the study area in white. 100

Figure 5.2 Bathymetry map of the top H120 surface which highlights the main salt domains off the Angolan Passive margin. The study area is outlined in white. The section is a stylised section located slightly to the north of the basin (i.e. located almost directly north of the bathymetric map) which has similar features to those seen near to the study area. The approximate location of the study area on the passive margin is also shown, modified from Marton et al.(2000). 101

Figure 5.3 Structural elements map showing the location of the main structures in the area. Salt distribution (pink) is that seen at or near the surface at present day; black lines indicate anticlines visible in the seismic data, pink lines indicate anticlines inferred from the seismic data, red lines 1 – 4 relate to seismic sections in Figures 5.4 and 5.5. The blue crosses represent locations of the six main wells in the area. 102

Figure 5.4 Seismic sections through the basin showing (a) Line 1, selected through the length of the basin and (b) Line 2 in the north of the area. Locations of these lines are shown in Figure 5.3. Black lines show fault locations and brown line indicates the base of a slump. 104

cont. Seismic lines perpendicular to the main basin orientation, (c) Line 3 across the centre of the basin and (d) Line 4 across the south of the area and showing the normal fault. The locations of both of these lines are shown in Figure 5.3. Black lines show the location of the normal fault and brown lines indicate the possible location of slip surfaces at the base of slide deposits. 105

Figure 5.5 A structural restoration using a seismic section across the southern part of the basement (the location is seen in Figure 5.2). Two alternative basement structure models are also shown to give an indication of how basement structure could impact the original salt distribution. The white lines on the two oldest sections indicate two alternative basement models, these cuts across the known salt, but are drawn as schematic sections. 107

Figure 5.6 Isopach analysis showing how sediment thickness varies through time from (g) the H00 to H10 (33.9 Ma to 18.26 Ma) period through to (a) the H120 - seafloor period (5.04 – 0 Ma). Pink anticlines indicate inferred anticlines where horizons are obscured by recent salt growth. Note that the interval 11.86 Ma to 10.89 Ma was thought to be unreliable and as such has been omitted. 111

Figure 5.7 Sediment accumulation rate maps through the different periods of the basin evolution, corresponding to the periods seen in the isopach map in Figure 5.6. Note that again the interval 11.86 Ma to 10.89 Ma was thought to be unreliable and as such has been omitted. 112

Figure 5.8 A series of close-up seismic sections through three of the most influential structures with (a) showing Line 2 within Area A in the north of the mini-basin, (b) showing Line 5 a section through the flanks of the long-lived salt wall within Area B and (c) Line 20 north of the salt diapir within Area F on the eastern margin of the mini-basin. The location of these lines can be seen on Figure 5.9. 117

Figure 5.9 The location of the lines used in the bed length change analysis of the basin bounding structures is shown alongside the graphical analysis of the cumulative bed length change of the structures which bound the basin. The graphs are grouped according to the structural areas, the location of which are shown in the map on the left. 119

Figure 5.10 A graph showing the cumulative bed length change for all of the structures analysed within the study area. Note how all of the structures within the area, with the exception of line 17, have a broadly similar pattern of development through the history of the basin. 121

Figure 5.11 Sections at the same scale showing the variation in the cumulative bed length change and bed length change rate on (a) the margin of the basin compared to those seen at (b) towards the centre of the basin. 122

Figure 5.12 A plot showing the variation in bed length change along the length of the main structure within Area C. The area between 12 km and 16 km has been affected by salt breakthrough and hence the data is less robust than in other areas along the length of the anticline. The arrows labelled (a) – (d) link to the rate of change of bed length graphs shown in Figure 5.14. 124

Figure 5.13 Seismic section through Line 7, Structure 2, Area C. This shows the typical structure through this part of the anticline with a salt-core and sediment packages thinning towards the actively growing structure. 125

Figure 5.14 Bed length change analysis through four of the structures within measurements taken from lines which are orientated perpendicular to the anticline within Area C. 126

Figure 5.15 A series of maps showing the growth of the structures which surround the basin at time periods corresponding to those seen in the isopach maps and sediment accumulation rate maps. 128

Figure 5.16 Contrasting models of fold growth impacting on the shape and topography observed at the seafloor surface. From Poblet and Hardy (1995). 132

Figure 5.17 Diagram illustrating the development of growth strata as a record of fold kinematics developed by growth of a detachment fold by limb rotation. Modified from Shaw et al. (2005). 133

Figure 5.18 Illustration linking the impacts and effects of relative changes in growth rate of a structure and sedimentation rate. Note the passive onlap geometries in the post-growth sediments and the rotated onlap in the syn-growth sediment. Image from L. Lonergan. 134

Figure 6.1 Map showing the location of the main local MTC deposits studied in this chapter and the flow directions of these. Note that the majority of the locally sourced MTCs are derived from the structures along the western margin of the basin. The main local MTCs are highlighted using the relevant root mean squared (RMS) amplitude extractions where white indicates high amplitudes and black low amplitudes. 141

Figure 6.2 RMS amplitude extraction maps and sketch maps highlighting the main features of MTC 1 with (a) showing an RMS amplitude map extracted over a 10 ms twtt window above the base of the MTC where white indicates high amplitude and black low amplitude and (b) showing an RMS amplitude extraction through an isopachous interval between the top and the middle of the MTC where white indicates high amplitudes, red middle amplitudes and black low amplitude. The main faults are highlighted in the sketch maps where blue and red lines have been used to colour code extensional and compressional faults respectively, the outline of the base of the MTC is shown in dashed green lines on the top MTC sketch map to highlight the inferred edge of the frontal ramp. The middle of the upper half of the MTC contains a band of unclassified faults containing both normal and thrust fault. 143

Figure 6.3 Maps showing (a) the thickness of MTC 1 calculated using the stratigraphic thickness algorithm discussed in Chapter 4 applied to the top and base mapped surfaces, note the interval of thick sediment extends further into the basin on the western side of the MTC deposit, this shape is reflected in (b) a dip/azimuth map over the basal surface of MTC 1. The location of the seismic lines seen in Figure 6.4 are also shown on this dip map. 144

Figure 6.4 Seismic sections through MTC 1 showing (a) Line A, a strike section parallel to the direction of flow of the MTC and flattened on the H120 surface. This flattening simulates the topography present at the time of deposition of MTC 1, (b) Line B, an un-flattened seismic line perpendicular to the main flow direction which shows a section through the lateral margins of the MTC and how it relates to the older MTC to the west of the area. The third seismic section, (c) Line C is also an unflattened seismic section perpendicular to the flow direction but further basinwards than Line B. The location of all three of these lines is shown on Figure 6.5. 145

Figure 6.5 A close-up seismic image showing the detail within the compressional domain of MTC 1, highlighting the thrust faulting and folding within this domain. Note how the frontal ramp cuts up through the stratigraphy and the development of a series of folds and thrusts behind this ramp. 146

Figure 6.6 A close-up on the thrust faults within the compressional toe of MTC 1 with (a) showing an RMS amplitude extraction map over this toe region and a sketch map highlighting the trend of these faults on the map, note how these are slightly more obvious in the amplitude extraction map than in (b) the seismic section, where the fault traces are still visible, but slightly harder to identify. Note that both the amplitude extraction maps and the seismic sections are at the same horizontal scale. 149

Figure 6.7 Two seismic section through the second cluster of MTCs, highlight MTC 2a, 2b and 2c. (a) Line A is orientated perpendicular to the flow direction to highlight the complex nature of the lateral margins of the deposits and their interactions with topography whilst (b) Line B is orientated along strike of the MTCs parallel to the flow of the slumps The section is taken through the older portion of MTC 2a, in order to also bisect MTC 2b. 152

Figure 6.8 Top and base maps through the northern section of MTC 2a with (a) showing an amplitude extraction through a 20 ms window from the base of the MTC 2a with the main faults and structures observed within this window sketched below, and (b) a section though the top of a dip map which has been flattened on the base of MTC 2a highlighting the compressional thrust faults in the toe and clear ridges towards the centre of the MTC. 153

Figure 6.9 An RMS amplitude extraction map and corresponding sketch highlighting the main features within MTC 3 which is sourced from the eastern margin of the basin (see Figure 6.1 for the location of this deposit). Note how the faults become more closely spaced towards the toe end of the deposit and rotate to become orientated parallel to this margin. The yellow line indicates the position of the seismic sections shown in Figure 6.10. Red faults are clearly compressional, blue fault traces are clearly extensional and the green line indicates the position of the start on the frontal ramp on the basal shear surface. 154

Figure 6.10 Cross-sections through MTC 3 (a) Line A is orientated perpendicular to the flow direction of the MTC within the compressional domain and (b) Line B, a strike section parallel to the flow direction within MTC 3, with a relatively small extensional domain and a long compressional domain overlying the H110 ponded section in the west. Location of the sections are shown in Figure 6.9. 156

Figure 6.11 Comparison between three different local MTCs within the area, all shown at the same scale. MTC 2a is an amalgamation of the features seen in the extensional domain and recorded in the amplitude extraction map and the features in the compressional domain recorded in the dip map in Figure 6.7. The fault traces coloured blue are clearly extensional and those coloured red are clearly compressional thrust faults. 157

Figure 6.12 A seismic cross-section through the centre of the basin highlighting the regional MTCs and showing the change in thickness and the distribution of the regionally derived MTCs. The three main MTCs (α, β and γ) which are discussed in detail in the text are also highlighted; amplitude extractions from within these deposits are shown in Figure 6.13. 160

Figure 6.13 RMS amplitude extraction maps taken through approximately 10 ms windows towards the centre of three of the large scale MTC deposits identified in Figure 6.14. (a) shows MTC α, the oldest regional MTC investigated, located above the H20 horizon, note how clear ridges can be seen in the amplitudes here, indicating the flow direction of the deposit, (b) shows a 10 ms widow thought the centre of MTC β which does not extend as far throughout the basin, note how this MTC has a more chaotic, speckled appearance and (c) the youngest MTC, MTC γ which covers the most area within the mini-basin. All amplitude extractions show low amplitudes in black and high amplitudes in white. 162

Figure 6.14 Isopach map showing the thickness of MTC β and highlighting the interactions with the basin bounding and internal structures. Note that this does not extend as far north as the amplitude extraction shown in Figure 6.15 due to thinning of the MTC package in this area. 163

Figure 6.15 (a) A semblance map and (b) an RMS amplitude extraction map through MTC β highlighting the chaotic nature of the sediments carried within the MTC deposit. 164

Figure 6.16 An RMS amplitude extraction map through a 20 ms window within the centre of MTC β with high amplitudes shown in white, medium amplitudes shown in red and low amplitudes black. These shown smaller blocks of high amplitude within the internal matrix, a few of which are highlighted by red circles. 165

Figure 6.17 (a) An RMS amplitude extraction map highlighting the thrust fault traces within MTC γ and the location of (b) a seismic section through MTC γ flattened on the H70 surface in order to highlight the thrust faults within the regional MTC deposit in this section of the basin. The location of the amplitude extraction map is shown in Figure 6.13. 166

Figure 6.18 Two seismic sections through MTCs α and β which highlight the topography on the upper and basal surfaces of the regional MTCs and some of the key internal characteristics associated with them. 168

Figure 6.19 Bed length change graphs showing the amount of bed length change and the rate of bed length change recorded through the structures associated with the local MTCs. The red arrows indicate the period during which the respective regional MTCs were deposited whilst the light blue arrow indicate the period when the regionally MTCs were deposited throughout the basin. The line numbers are the same as those used in the study of all the structures within the basin in Chapter 5. 173

Figure 7.1 A root mean squared (RMS) amplitude extraction map through the interval between the green (P50) and the red horizons. The section is the top isopachous interval of four taken between the P40 and P50 horizons, with the P40 horizon shown in purple. Sections illustrate how the amplitude extractions identify real channels. The correlation in section (a) is not as easy to identify as the red line partially covers the amplitude event. 180

Figure 7.2 Flow diagram showing the method used to create a frequency decomposition colour blended volume. Here the three main frequencies are ascribed to a red, green or blue colour and then blended such that areas where one frequency dominated will be associated by the dominant

assigned colour and areas where the frequencies overlap will be coloured according to the diagram on the bottom left side of the figure (From McArdle and Ackers, 2012). 181

Figure 7.3 Comparison between (a) root mean square (RMS) amplitude extraction (b) lower frequency decomposition blend and (c) a higher frequency decomposition blend. Note how the different methods highlight different features from within the data. 182

Figure 7.4 Location of the ponded area with respect to the main structures within the basin. This shows the maximum extent of the ponded sediments. The high-resolution seismic data does not extend further south than the Area E label and the blue channel outlines are younger systems that cut the ponded material. Red lines indicate the locations of seismic sections referred to later in the chapter. 183

Figure 7.5 Seismic sections along the length of the normal fault from (a) a section across the central area of the fault and (b) towards the eastern fault tip. These show how the throw on the fault decreases to the east, away from the salt structure within Area C, corresponding to a decrease in the difference in thickness either side of the normal fault. Line locations are shown in the location diagram in the bottom right corner. 184

Figure 7.6 Cross-section though the ponded basin highlighting the four packages within the ponded interval, brown line indicates the western boundary of a slump within the P20 – P30 interval. Note how the basin is bound to the east and west by folded anticlinal structures which the packages onlap onto. Line location shown in Figure 7.4. 185

Figure 7.7 Cross-section along the strike of the basin. Note the younger channel cutting through the north of the basin and the change in thickness between the four packages from north to south. The top of the older ponded package is also identified. Line location is shown on Figure 7.4. 186

Figure 7.8 Section across the normal fault that cuts through the P30 – P40 unit and the P40 – P50 unit. The P30 – P40 unit almost doubles in thickness across this section of the normal fault. The second older ponded interval is clearly imaged beneath the ponded interval which is imaged here. A second younger channel is also imaged south of the normal fault which cuts through the ponded interval. Line location is shown in Figure 7.4. 187

Figure 7.9 Isopach maps showing the sediment thickness through the ponded interval. In all images the thickness ranges from 0 m (yellow) to 200 m (purple) according to the scale shown in the bottom right corner; (a) the P10 – P20 interval (oldest interval) where the sediment is thickest in a triangle spreading out from the north-east and thinning towards the south, (b) P20-P30 interval which has thicker sediment either side of the previous high in the P10 – P20 interval whereas in (c) within the P30 – P40 interval the sediment is thickest in the southeast, something which continues in (d) P50 – P40 interval where the thickest sediment is again in the east of the mini-basin. Note how the distribution of sediment within the two oldest intervals is effected by slump deposits (mass transport complexes; MTCs). 189

Figure 7.10 Cross-section through the channel complex in the north of the area. The P10 – P20 unit extends beneath the channel and, as such, was clearly active prior to the formation of this later channel complex. The edge of the channel complex is outlined in red and clearly erodes through units P10 – P20, P20 – P30 and P30 – P40. The P40 – P50 unit does not extend this far north. The line location is shown in Figure 7.4. 190

Figure 7.11 Root mean squared (RMS) amplitude extraction beneath the channel complex that cuts through the north of the area. This indicates that the channels that form the lobe complex within the P10

– P20 unit are sourced from a channel feeder system which enters the basin from the northeast and are not simply a crevasse splay feature that relate to the younger channel system in this area, a cross-section through which is shown in Figure 7.10. 191

Figure 7.12 An RMS amplitude extraction map taken from within the channel system is outlined in red and superimposed on top of an RMS amplitude extraction taken from a 20 ms Twtt window within the P10 – P20 interval beneath the younger channel system. Note how the younger channel turns to the north in this area whilst the older underlying system swings to the south (as shown by the yellow arrow). 192

Figure 7.13 Fan lobe complex imaged using a root mean squared (RMS) amplitude extraction across a variable window (maximum thickness 25 m towards centre of mini-basin) with (a) uninterpreted and (b) interpreted with the lobe complex (orange), lobes (yellow), lobe elements (red) and channels (pink) highlighted. The present day salt diapir locations are also shown in light pink along with the normal fault, active at the time of lobe complex deposition (white). 193

Figure 7.14 Isopach showing the thickness variations across the P10 – P20 unit. The edge of the slump deposits are highlighted with dashed brown lines, note how the eastern slump is related to a reduction of sediment thickness of the P10 – P20 unit in that part of the mini-basin. 194

Figure 7.15 Isoproportional RMS amplitude extraction maps from four intervals within the P10 – P20 unit. Red dashed lines show the extent of the slump deposits and rose diagrams indicate orientation of channels within each interval. 195

Figure 7.16 Isopach map showing the thickness variations across the P20 – P30 unit. It is interesting to compare the thickness patterns in this unit to that observed in the P10 – P20 unit (Figure 7.16) with thicker sediments in this unit distributed to the east and west of those in the preceding unit. 197

Figure 7.17 RMS amplitude extraction maps generated using isoproportional intervals within the P20 – P30 unit. Note how the extent of the slump deposit (dashed in red) has less impact on the channel distribution through time. Interval 1 is the oldest and interval 4 is the youngest interval within the P20 – P30 unit. 200

Figure 7.18 Annotated diagrams showing how the individual channels behave within the four intervals that comprise the P20 – P30 unit. Using these it is possible to identify periods when the lobes are stepping onto the basin and compensational stacking of the lobes which is particularly apparent in intervals 3 and 4. 202

Figure 7.19 Histogram illustrating the range of channel widths within the channels in each of the intervals within the P20 – P30 unit. These channels were systematically measured towards the branching point to ensure consistency. 203

Figure 7.20 Isopach thickness map of the P30 – P40 unit. The sediment distribution is very different to that observed in the previous unit with significantly thicker sediment identified south of the normal fault. The slump deposit is not outlined in this interval as it no longer appears to impact the thickness of the sediment. 204

Figure 7.21 RMS amplitude extraction maps from the P30 – P40 unit north of the normal fault highlighting variations in the extent of the fan lobe complex through the history of the mini-basin. Note that maps start at interval 3 as intervals 1 and 2 contain predominantly MTC material. 207

Figure 7.22 A series of sketches showing how the fan complex develops in the P30 – P40 unit. Note how the system steps away from the western edge of the basin during Interval 5. Compensational stacking at the lobe scale is also visible between intervals 3 and 4. 209

Figure 7.23 Bar chart illustrating the variety seen within the channel widths during the P30 – P40 unit with the majority of widths within the 60 to 90 m width bin in all the intervals. Interval 4 contains the highest frequency of channels overall within the P30 – P40 unit. 210

Figure 7.24 Frequency decomposition images showing channels south of the normal fault within the P30 – P40 interval with (a) an older slice compared to (b) a younger slice through the blended decomposition volume. 211

Figure 7.25 Isopach thickness for the P40 – P50 unit. Note how this unit extends south of the normal fault and the thickest sediment in the north follows a pattern mimicking the main channel systems within this interval (Figure 7.25). A younger channel complex in the south (blue line) has eroded part of the ponded sediment. 212

Figure 7.26 A series of isoproportional amplitude extractions from the P40 – P50 interval north and south of the normal fault. 214

Figure 7.27 A series of diagrams showing how the channels within the ponded fan systems vary through the history of the basin within the P40 – P50 unit. This clearly highlights the change in channel orientation and entry point south of the normal fault. 216

Figure 7.28 Width measurements recorded in the four intervals within the P40 – P50 unit, note how there is more variety within the frequency bins than in the width measurements from the other units.218

Figure 7.29 Gamma Ray analysis of two wells which intercept the ponded interval in the northwest corner of the basin. Arrows on the well logs indicate the broad changes in grain size 219

Figure 7.30 A direct comparison between (a) one of the lobe complexes seen in this area and (b) a channel and fan systems studies by Adeogba (2005) at a similar scale. 221

Figure 7.31 Comparison between the downdip propagating channels and lobe systems seen (a) within the P20 – P30 unit in this study compared to those lobes observed in (b) the Kwanza basin also offshore Angola where in an updip shift of the erosion front occurs alongside the downdip progradation of the system (Hay, 2012). 223

Figure 7.32 A comparison between (a) RMS amplitude extraction data from the P30 – P40 interval and (b) the fronds recorded by Twichell at al. (1992); shown at similar scales. 224

Figure 7.33 Comparison between the braided channel systems recorded in the Orinoco submarine fan, Barbados and those recorded in seismic data offshore Angola, (a) shows the GLORIA side-scan sonar image of the Orinoco system (Belderson et al., 1984) with a section of this further interpreted in (b) using backscatter data (modified from(Ercilla et al., 1998), note that the backscatter images show a cluster of braided channels in the west with a series of lobes in the east. (c) shows the braided system recorded within south of the normal fault within P40 – P50 interval 4, here the channels are approximately 10 times smaller than those seen on the Orinoco submarine fan system, but also occur alongside lobe features. 225

Figure 7.34 (a) Proximal channels observed in the Ross Formation by Sullivan et al. (2000, 2004) compared to (b) feeder channels on a similar scale seen within the lobe complex within P40 – P50, Interval 4. 226

Figure 7.35 Compensational stacking observed within the transitional domain observed in (a) outcrop data from the Ross Formation, County Clare by Sullivan et al. (2004) and (b) commonly within the transitional domain of the fan lobe complexes in the study area, as imaged here in P40 – P50 interval 4. The red line shows 1 km on the amplitude extraction map, showing a similar distance as illustrated in the sketch cross section. 227

Figure 7.36 Two images showing (a) an cross section through amalgamated and densely channelised lobes in an outcrop in the Karoo Basin (Prelat et al. 2009) compared to (b) an amplitude extraction map showing a similar area within the lobe complex in the P30 – P40, interval 2. 227

Figure 7.37 A comparison between (a) the layered and amalgamated sheets observed in outcrop section in the Ross formation, County Clare (image courtesy of M. Mayall) and (b) the high amplitude fringes observed towards the edges of individual lobes and lobe complexes studied here. 228

Figure 7.38 (a) conceptual model showing the distribution of hybrid beds around the fringes of a submarine fan system (modified from Kane and Pontén, 2012, Hodgson, 2009), compared to one of the intervals within this fan system (P20 – P30, interval 4) which has a series of high amplitude channel systems which bifurcate to form lobes towards the end of the system and these lobes are surrounded by high amplitude, undefined beds, postulated to be hybrid beds. 229

Figure 7.39 Sketch showing the development of the lobe complex units north of the normal fault through time illustrating the change in main sediment entry point through time with a switch from a sediment entry in the north to the entry point in the east. 230

Figure 7.40 (a) Uninterpreted RMS amplitude extraction map highlighting the main channel and lobe systems within P40 – P50, interval 4 alongside (b) an annotated image showing the main fan outlines and also highlighting the high amplitude fan fringes. White shows high amplitudes and black low amplitudes indicating sand and shale respectively, (c) shows this in comparison to the compensational stacking observed at the lobe scale in a schematic correlation panel from the Karoo Basin, South Africa, taken from Prelat et al. (2009). 231

Figure 7.41 RMS amplitude extraction map highlighting some of the detail within the P40 – P50 unit, interval 4 shown both (a) un-annotated to show all detail and (b) annotated illustrating how the confinement of a channel system between the high topography of the basin edge and the relatively high topography caused by an older fan system can impact on the characteristics of the resulting channel. 233

Figure 7.42 A series of diagrams indicating how large scale allocyclic controls (in this case a normal fault) can impact on the sediment distribution and fan lobe complex characteristics. 234

Figure 8.1 Structural elements map showing the location of the main structures in the area. Salt distribution (pink) is that seen at or near the surface at present day, black lines indicate anticlines visible in the seismic data, pink lines indicate anticlines inferred from the seismic data, green lines 3, 6, 12 and 18 relate to graphs shown in Figure 8.2. Line numbers are the same as Chapter 5. 240

Figure 8.2 A series of graphs showing the absolute bed length change (black line) and the rate of change of bed length change (grey bar chart) across four of the structures bounding the western edge of the basin. Lines located in Figure 8.1. The graphs have been sub-divided to show the dominant sedimentary packages. 241

Figure 8.3 General model for the channel complex systems in the area studied. (A) General model includes a third order channel complex system with a dominantly erosional base, several fourth-

order channel complexes in which axis and margin areas can be recognised and individual channels (modified from Mayall et al., 2006). (B) Representative seismic section through a channel complex system with the third order base interpreted. Figure from Jones et al. (2012). 242

Figure 8.4 Distribution of channel complex systems from 25 Ma to 18.26 Ma, (a) shows the channel systems within the Late Channel interval from 22.5 Ma to 18.26 Ma during which time the channel complex systems continue to deflect around Areas B and D but also deflect around Area C, divert in front of Area E, cut across the structure within Area A and divert around Area F, and (b) the Early Channel interval from 25 Ma to 22.5 Ma which shows channel complex systems deflect to the north and south around Areas B and D (the areas of greatest salt movement), divert around Area C, cut across Areas A and E and show northwards offset stacking from Area F. Both these maps highlight the channels using root mean squared (RMS) amplitude maps calculated using 50 ms Twtt window. General regional slope direction is east to west. Red coloured anticlines indicate high rates of bed length change, green indicate medium rates of bed length change, yellow indicate low rates of bed length change and black indicates where no bed length change analysis was conducted. Cross-sections Lines 3, 5, and 20 shown in Figure 8.6. 243

Figure 8.5 Typical seismic lines through four of the channel systems as they encounter actively growing structures: (a) Channel complex 1.1 cutting into the structure growing in Area E with the third-order channel base highlighted, (b), Channel complex 1.3 showing the system offsetting and cutting into the structure in Area C, (c) Channel complexes 1.3/1.4 showing offset stacking of the channel complexes away from the growing structure in Area F, and (c) Channel complex 1.6 showing multiple incisions into the growing structure in Area E. This figure is slightly modified from one published in Jones et al. (2012). 244

Figure 8.6 Three anticlines which link to form Area C presented alongside the location and maps showing the main channel complexes. Note that Channels 1.4 and 2.4 cross the structure in the northeast where the bed length change is the lowest and the lowest rates of change of bed length are observed whereas Channels 1.3 and 2.3 are deflected by the anticlines in regions where bed length change, and hence structural growth, is highest. 258

Figure 8.7 Sections through some of the key structures where channels respond to structural growth, with the Early channels deposited between the purple and yellow horizons (25 Ma to 22.5 Ma) and the Late channels between the yellow and orange horizons (22.5 Ma to 18.26 Ma). Black arrows indicate onlapping and offlapping strata and have also been shown within the interval containing regional MTCs (the orange to blue horizons deposited between 18.26 Ma and 13.25 Ma) which will be referred to in Section 8.6.1. Line locations shown in Figure 8.4. (a) shows a section through Area A on the north-western margin of the mini-basin where onlap can be observed in the packages containing the channel complexes, (b) shows a section through Area B which had consistently higher growth rates throughout the history of the mini-basin resulting in extreme folding of the sediments and the generation of local MTC deposits (outlined in brown), and (c) a seismic section taken through Area F directly to the north of the diapiric salt. 250

Figure 8.8 Maps illustrating the areal extent of two of the regional MTC deposits with anticlines coloured according to bed length change values from the whole interval from 13.25 to 18.26 Ma. (a) shows the extend of MTC α, the oldest system and (b) shows the extent of MTC γ, a younger system deposited in the mini-basin. The maps show RMS amplitude extractions taken through the centre of each of the MTC deposits using a 10 ms twtt window to highlight the main features. Red coloured anticlines indicate high rates of bed length change, green are medium

rates of bed length change, yellow are low rates of bed length change, and black are areas where no bed length change analysis was conducted. 253

Figure 8.9 Section through Area C showing details on the stratal relationships within the 18.26 Ma to 13.25 Ma interval containing the regional MTCs. Note how the younger strata overlap the structure whereas the older strata onlap. Line location shown in Figure 8.8. 255

Figure 8.10 Location and extent of a selection of local MTCs. (a) shows a series of older anticlines deposited with the interval between 8.29 Ma and 5.58 Ma (H100 to H110) whist (b) shows the MTCs deposited in the period following this between 5.54 Ma and 5.04 Ma (H100 to H120). Note how all these local MTCs are sourced from anticlines along the margin of the basin and are cover a broadly similar area. (c) highlights the higher rates of bed length change recorded in the preceding intervals. Map show RMS amplitudes extracted through windows of between 10 - 25 ms Twtt. White arrows show the direction of movement of the MTCs. Location of sections through the MTCs are labelled 1 – 3 (see Figure 8.11). 257

Figure 8.11 Sections through the local MTCs. (a) and (b) are taken through the MTC 2 complex whilst (c) shows a section through MTC 1. Extensional structures in the headwall area, with contractional structures seen towards the toe of the slides. Location of sections shown in Figure 8.10. 258

Figure 8.12 Ponded sediments deposited within the mini-basin between 8.29 Ma and 5.58 Ma are examined with (a) showing the youngest fan system feeding in from the south and extending north and south of the normal fault, (b) an older system with channels branching away from Area F, (c) a fan systems feeding into the basin from the north, (d) the youngest fan system feeding into the mini-basin from the north and trending broadly north to south along the basin axis, and (e) the rates of change of bed length from the preceding interval give an indication of the relict topography in the basin when the ponded sediments were deposited. RMS amplitude extraction maps are used over an isopachous interval with a maximum thickness of 25 ms Twtt. More detailed RMS amplitude maps are shown in Figure 8.13 and Chapter 7. 261

Figure 8.13 RMS amplitude maps calculated using 10 ms Twtt windows to illustrate the details within the deepwater ponded fan systems seen in Figure 8.12 with (a) showing a more detailed view of the second oldest fan system (seen in Figure 8.13 (c)) and (b) showing a detailed image of the youngest fan system (seen in Figure 8.12 (a)), i, ii and iii on Figure 8.13 (b) highlight some of the main details; individual channels branch towards the edge of the basin and more amalgamated channels are observed south of the normal fault. 262

Figure 8.14 Seismic sections along the western (a) and (b) eastern margins of the mini-basin; with black arrows showing some of the onlap that occurs at these locations. 264

Figure 8.15 Map showing the onlap outline for four mapable boundaries within the ponded package that existed within the basin from 8.98 Ma to 5.58 Ma (H100 – H100) with the oldest P20 horizon outlined to the youngest P50. The maximum outline of the slump deposits are also outlined on the map, the western slump is only active within the P20 – P30 unit. The location of the seismic sections shown in Figure 8.14 are also identified in red. 265

Figure 8.16 Series of conceptual models showing the response of (a) channel complexes, (b) regional MTCs (dark brown), local MTCs (light brown), and (c) ponded fan lobe complexes to the growth of the salt-cored structures in the area. 268

List of Tables

Table 3.1 The classification scheme proposed by Moscardelli and Wood (after 2008) but based on work from Dott (1963), Nardin et al. (1979) and Moscardelli et al. (2006). This definition of the main features within MTC deposits has been used throughout this chapter. Table taken from Moscardelli and Wood (2008). 47

Table 3.2 A summary table showing four of the most important issues highlighted by this literature review and the preceding discussion of the structural history of the study area in Chapter 2. The table shows how these topics will be examined further in the thesis. 65

Table 4.1 Showing how the vertical resolution varies with depth through the section. 69

Table 4.2 Vertical resolution of the regional data measured over a similar area to the PSVM with the same velocity values. 70

Table 4.3 Showing the horizon picks and ages available in the PSVM study area provided by BP. Those horizons which have been less reliably dated, with the ages interpolated between the reliably dated biostratigraphic picks are italicised. 72

Table 4.4 A series of cartoons illustrating the types of stratal relationships with structural growth. 94

Table 4.5 Two types of halokinetic sequence described by Giles and Rowan (2012) with the main characterises outlined below the images. 95

Table 6.1 Table outlining the area covered by the local MTCs discussed in this section. 158

Table 6.2 A table detailing the main characteristics of the two scales of MTC deposit examined in this chapter, note how they are for the most part very different in composition and morphology. 171

1 Introduction

1.1 Rationale

Deformation of the seafloor by structural processes such as salt diapirism, shale diapirism, faults and folds can have a major impact on both the routing of sedimentary systems and the sedimentary facies deposited within an area. Limited, or aerially restricted areas of seafloor deformation can cause channel systems entering an area to divert or deflect from their course (Cronin, 1995, Rowan and Weimer, 1998, Haughton, 2000, Mayall and Stewart, 2000, Hodgson and Haughton, 2004, Morgan, 2004, Smith, 2004, Gee and Gawthorpe, 2006, Mayall et al., 2006, Heinio and Davies, 2007, Clark and Cartwright, 2009, Cross et al., 2009, Mayall et al., 2010, Clark and Cartwright, 2011), to pond within mini-basins or other topographic lows (Winker, 1996, Prather et al., 1998, Booth et al., 2000, McGilvery and Cook, 2003, Hay, 2012) and can lead to the generation of slumps, slides and debris flows (Gawthorpe and Clemmey, 1985, Hampton et al., 1996, Beaubouef and Friedmann, 2000, Moscardelli et al., 2006, Masson et al., 2010, Mosher et al., 2010).

The effect that the deformation of the seafloor has on a sedimentary system is dependent upon the relationship between the amount of topographic relief generated by the structural growth, the timing of the deformation and the erosive power of the sediments encountering the topography (Clark and Cartwright, 2009, Mayall et al., 2010, Clark and Cartwright, 2011). If deformation of the seafloor is extensive, enclosed intra-slope basins may form and infill with ponded lobes of sand (Prather et al., 1998, Booth et al., 2000, Winker and Booth, 2000, Prather, 2003). This extensive deformation can also create instability of sediment along the flanks of growing structures which in turn leads to the formation of slumps, slides and debris flows sourced from intra-slope highs. The mass transport complexes (MTCs) generated can vary greatly in size, distance travelled from source area and erosional capacity, ranging from those which are very local in their extent with limited lateral movement of the source sediment, to large deposits covering tens of square kilometres and initiated hundreds of kilometres from the area of deposition (Hampton et al., 1996, Huvenne et al., 2002, Haflidason et al., 2004, Frey Martinez et al., 2005, Masson et al., 2006, Moscardelli et al., 2006, Posamentier and Martinsen, 2011).

Several studies have discussed the interactions between deepwater channel complexes and developing topography, focussing on the morphological variations which can be observed such as avulsions (Ferry et al., 2005b, Gee and Gawthorpe, 2006, Clark and Cartwright, 2009, Callec et al., 2010), changes in channel sinuosity (Cronin et al., 1994, Pirmez and Flood, 1995, Ferry et al., 2005b, Gee and Gawthorpe, 2006, Gee et al., 2007), and changes in the width to depth ratio of channel systems (Deptuck et al., 2003, Huyghe et al., 2004, Ferry et al., 2005a, Ferry et al., 2005b, Gee and Gawthorpe, 2006, Gee et al., 2007, Clark and Cartwright, 2009, Wood and Mize-Spansky, 2009). However, fewer studies have been carried out examining the reaction of several different types of depositional system (i.e. fan complexes and MTC deposits) to changes in topography. Likewise few studies have investigated the links between structural growth and the changes in deepwater systems in a more quantitative way. These two issues form the focus of the work presented in this thesis.

The structural growth in a salt controlled mini-basin in the contractional domain of the gravitational system on the Angolan passive margin is investigated using a novel approach whereby bed length change is calculated and mapped on the structures to record growth throughout the basin's history (Chapter 5). Two of the more under-studied sedimentary processes operating within the mini-basin, MTC deposits and fan lobe complexes, are studied in detail (Chapters 6 and 7 respectively) and the interactions between these sedimentary systems and the growing, active structures examined (Chapter 8).

1.2 Aims and Objectives

The aims of the research reported in this thesis are:

1. to develop a better understanding of the Oligocene and younger structural history of the mini-basin; constraining the rates at which structures formed through time and the spatial development of the marginal and intra-basin structures,
2. to use the data to increase understanding of the sedimentological features, in particular the ponded fan lobe complexes and MTC deposits within the mini-basin fill, and
3. to draw the results of these investigations together in order to investigate the impact that actively growing structures have on deepwater sedimentary systems.

This thesis uses a high resolution seismic dataset located within the Lower Congo Basin offshore northern Angola. The area is a subset of Block 31 comprising of the Plutão, Saturno, Vênus and Marte (PSVM) fields in the North East sector of Block 31 (Figure 1.1). It is located on the Angolan continental slope 200 km offshore, and some 400 km north west of Luanda in water depths of approximately 2000 m. Whilst the examples presented here are specific to the PSVM area it is hoped that the ideas developed will be applicable elsewhere in the Lower Congo Basin and in other basins characterised by a similar structural evolution (i.e. Gulf of Mexico). The stratigraphic interval of interest comprises the sediments deposited from the Oligocene (33.9 Ma) to the present day. The thesis examines channel complexes deposited between 25 Ma and 18.26 Ma, regional MTC deposits which dominated the basin fill from 18.26 Ma to 13.25 Ma, ponded fan lobe complexes which occurred primarily between 8.29 Ma and 5.58 Ma and local MTC deposits which occur around the time of deposition of the fan lobe complexes between 13.25 Ma and 5.04 Ma.

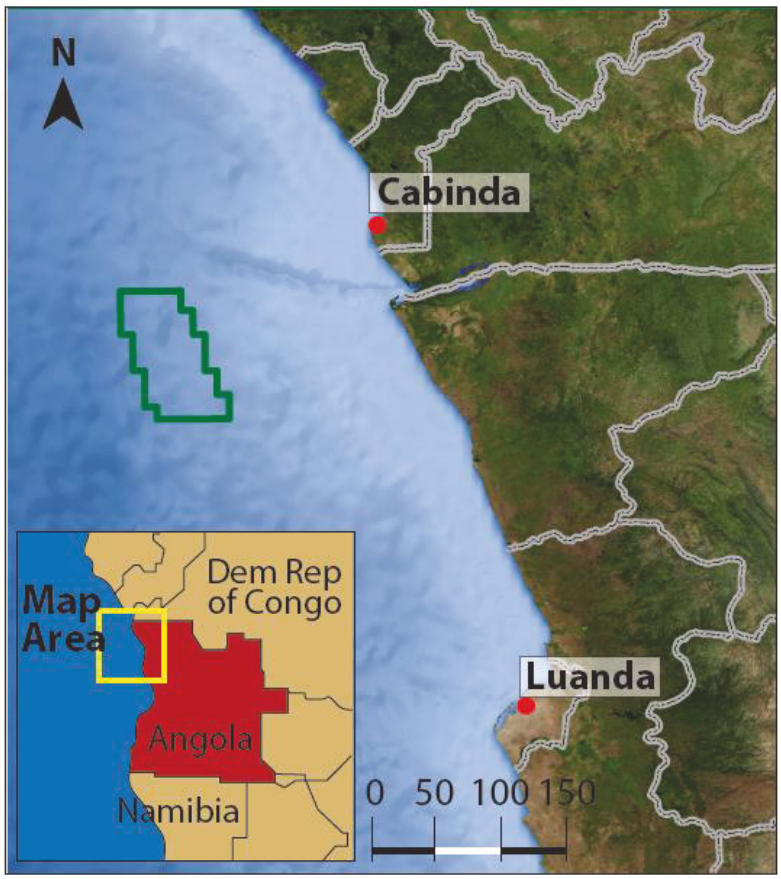


Figure 1.1 Map showing the location of Block 31 (green outline) with respect to the Angolan Coast, the study area is located in the north-eastern corner of Block 31. Note the present day location of the Congo canyon to the north of the study area.

In order to achieve the research aims outlined in the preceding paragraph, the following specific objectives were defined:

1. to map the spatial location of the main structures within the mini-basin,
2. to perform a structural reconstruction across the mini-basin,
3. to carry out isopach analysis and generate sediment accumulation maps of the main intervals within the basin fill to allow determination of the main active structures,
4. bed length change analysis of the main structures situated within and bounding the mini-basin
5. to map of the results from the bed length change analysis, then
6. to map the main local MTCs and regional MTCs adding new horizons where necessary,
7. carrying out detailed analysis of the MTCs using thickness maps and seismic attribute analysis,
8. detailed mapping of the packages within the interval containing the ponded sediment fill,
9. performing a fine-scale attribute analysis and frequency decomposition analysis to reveal the main features within these packages, and
10. documenting the response and spatial locations of the ponded fan complexes, MTC deposits and earlier channel systems with respect to the structures with the highest growth rates.

The high-resolution dataset has generated images of a resolution and quality never before recorded from subsurface fan lobe complexes. Mapping the individual channels and lobes within these systems has meant that details of their development and evolution in response to both structural changes and local bathymetric changes caused by older lobes can be documented at a level of detail only previously observed within outcrop studies. This, coupled with the novel approach to mapping the growth histories of the main structures within the mini-basin, has revealed new insights into the interaction between sedimentary systems and topography.

1.3 Thesis Outline

As previously discussed the main goal of this thesis was to apply a novel approach to the analysis of structural growth within a mini-basin to aid in understanding how sediment depositional systems react to changes in relative topography. This research spanned a range of topics including structural analysis of the mini-basin and detailed sedimentological analyses of MTC deposits and fan lobe complexes within the mini-basin fill, in order to present a thorough assessment of the impact of changes in bathymetry on the sedimentary infill of a basin. A brief overview of the arrangement of this thesis is given here.

Chapter 2 introduces the regional stratigraphic and structural setting of the mini-basin, situated within the Lower Congo Basin, offshore Angola. Particular emphasis is placed on the development of the basin from the Oligocene onwards and the variation in salt structures observed across the passive margin.

A literature review is given in **Chapter 3** which focuses on the deepwater sedimentary systems discussed in detail in the subsequent chapters of the thesis. This review has been divided into three sections, which focus on three main aspects of the work: 1) the different types of sedimentary systems deposited within the basin, reviewing work previously carried out on these sediments and outlining the terminology that will be used throughout the thesis; 2) the regional boundary conditions which should be taken into account when investigating interactions between sedimentary systems and structural growth; and 3) reviewing literature on previous work which investigates the effect of local seabed topographic change on sediment characteristics and spatial distribution in deepwater settings.

Chapter 4 summarises the datasets used in this study and outlines the key methodologies and techniques applied throughout this thesis. Particular emphasis is placed on considering the properties of the high-resolution dataset, well data and the reliability of the mapped horizons. This chapter also includes a more detailed examination of the principles behind the key structural techniques, such as restoration and bed length change analysis, which have been applied to the three dimensional seismic dataset and a full discussion of the errors associated with these techniques.

An analysis of the structural evolution of the mini-basin is presented in **Chapter 5** using a variety of different approaches to fully understand the structural history of the basin. First a restoration across the basin is presented which is used to illustrate the periods during which the main structures were active. This is complimented by a basin-wide analysis of isopach and sediment accumulations rate maps showing

sediment thickness changes within the mini-basin from 33.9 Ma to present day. These were used to identify significant structures on which bed length change analysis was performed. Bed length change analysis is carried out on twenty-one 5 km long sections across the key structures, and identifies periods of relatively high, medium and low structural growth within the mini-basin. Using these values, maps are generated which show the spatial distribution of these high, medium and low growth rate structures. These maps are used in the subsequent chapters.

Chapter 6 gives a full description of the local and regional Miocene-aged MTCs deposited within the basin. Both these systems are described in detail using a variety of attribute analysis techniques including amplitude extractions, dip maps and coherency maps. The main features associated with these two types of MTC deposit are compared and contrasted, and their relationship with the key structures is discussed in detail.

A thorough discussion of the Upper Miocene ponded facies within the mini-basin is presented in **Chapter 7**. The youngest ponded package in the mini-basin is sub-divided into four intervals each of which has been found to contain a lobe complex. Isoproportional sections of these are created and amplitude extractions applied to these sections reveal details down to the lobe element scale. These exceedingly well-imaged sections reveal changes in the deposition patterns of the lobe complexes within this interval showing large-scale changes in the sediment entry point and more local compensational stacking patterns and channel avulsions. The quality and resolution of these images is without parallel within the subsurface, allowing comparisons to be made to outcrop examples and bridging the gap between the outcrop resolution and conventional resolution seismic images.

Chapter 8 bring the strands of the analysis from Chapters 5 to 7 together in a discussion of how the depositional style of the sediments preserved within the mini-basin has changed in response to changes in the rate of growth of the coeval, adjacent salt structures. Late Oligocene and Lower Miocene channel complexes are also discussed in this chapter as they can have a more complex relationship with the structures; incising deeply into some structures and being clearly deflected by others. Maps of the spatial distribution of the main sedimentary systems are combined with maps showing the amount of bed length change on structures, and analysis of the stratal relationships in order to draw conclusions on the response of these systems to growth within the basin.

Chapter 9 contains the main conclusions from this research; clarifying the key results and relating these back to the original aims and objectives. As this research was conducted, several areas where the work could be extended were identified and those which could warrant further examination are also discussed within this chapter.

2 Introduction to the Study Area

2.1 Introduction and Regional Setting

The study area for this thesis is located within Block 31 in the Lower Congo Basin, on the Angolan continental margin (see Chapter 1, Figure 1.1). The Lower Congo Basin is one of a series of sub-basins running along the West African passive margin in the Southern Atlantic Ocean, with the Kwanza basin located to the south and the Gabon Basin to the north (Figure 2.1). These basins developed in response to rifting and subsequent passive margin subsidence along the South Atlantic margin and all contain Aptian salt which influences both the structural evolution and the distribution of depositional systems within the basins (Burke, 1996, Cramez and Jackson, 2000, Marton et al., 2000, Anderson et al., 2012, Quirk et al., 2012). Although all of these sub-basins are formed on salt, there are significant differences between them: for example the Kwanza Basin is dominated by autochthonous salt structures and has a relatively thin Oligo-Miocene sedimentary fill whereas the Lower Congo Basin has a thick Oligo-Miocene clastic section and more complicated salt tectonics.

This thesis investigates how deepwater channels, mass transport complexes and fan lobe complexes entering the basin in the Miocene interact with evolving salt structures which caused local gradient changes on the seafloor. A review of the structural and sedimentological history of the region is presented in this chapter which will provide a thorough background to the work carried out within this thesis.

2.2 Regional Stratigraphic Framework

Development of the regional palaeogeography from the early Cretaceous break-up of Gondwana to the present day is shown in Figure 2.1. The geological history of the region can be split into three major phases, each with distinctly different palaeogeographical signatures:

1. a Valanginian to Early Aptian rift sequence,
2. an early transgressive succession with the formation of the major South Atlantic salt basins, followed by the development of carbonate platforms, and finally
3. the Albian to recent passive margin phase

The sub-basins seen along the South Atlantic margin at the present day share a common origin related to the break-up of Gondwana, with rift basins forming as the continental crust thinned and Africa and South America drifted apart (Brice et al., 1982, Moore, 1988, Anderson et al., 2000, Macdonald et al., 2003). Three discrete stages of rifting ending in the Early Aptian are widely recognised with each phase generating a series of deep, under-filled transtensional depocentres. These were infilled with siliciclastic non-marine sediments comprising of fluvial and lacustrine deposits which formed within graben lakes (Figure 2.1; Karner et al., 1997, de Matos, 1999, Karner and Driscoll, 1999, Burke et al., 2003, Macdonald et al., 2003, Dupré et al., 2007).

Rifting in the Angola region is thought to have stopped by the Barremian (Karner et al., 1997, Marton et al., 2000). In the Upper Barremian, the northern part of the South Atlantic Ocean became restricted by a volcanic ridge stretching along the Walvis Ridge and Rio Grande Rise (Figure 2.1 (d)). The ridge prevented marine waters from entering the northern South Atlantic basin for 14 Ma, until the end of the Aptian, resulting in a sub-aerial basin extending from the Walvis Ridge to Cameroon. An arid climate and desert conditions prevented the formation of a permanently deep filled lake in this area. However, intermittently balance-filled lakes of varying salinity formed, possibly due to marine transgressions across the subsiding Walvis ridge (Brognon and Verrier, 1966, Burke, 1975, Burke et al., 1971, Roberts, 1975). These lakes occupied the basin to a maximum extent of one million square kilometres, encompassing the African and Brazilian shorelines, and formed the late Aptian Loeme Formation (Figures 2.1 and 2.2; Wardlaw and Nicholls, 1972, Liro and Dawson, 2000, Davison, 2007). There is still some discussion as to the water depth at which the evaporitic sequence that makes up the Loeme Formation formed (Bolli et al., 1978, Fonck et al., 1998, Jackson et al., 2000, Marton et al., 2000, Davison, 2007, Davison et al., 2012, Quirk et al., 2012). However, Fonck et al. (1998) and Davison (2007) suggest that the Angolan and Brazilian salt margins were separated by a subaerial proto mid-Atlantic ridge and therefore never formed a continuous salt basin. Estimates for the original in-situ thickness of the salt in the Lower Congo Basin range from 700 m to 1,500 m with regional gravity spreading likely to have caused local thickening downslope (Anderson et al., 2000). The volume of salt deposited also appears to decrease northwards along the Angolan margin (Figure 2.5; Marton et al., 2000).

In the Albian, marine waters overtopped the Walvis Ridge in the northern South Atlantic forming a transgressive marine system and a return to normal marine salinities (Macdonald et al., 2003). The Albian strata consist of carbonate platform rocks (Pinda Formation), shallow-marine clastic rocks and deepwater shales. Salt structures were active syn-depositionally and the carbonates often show large variations in thickness (Coward et al., 1999). Upper Cretaceous strata are composed predominantly of shallow marine clastic sedimentary rocks and their deeper water marl and shale equivalents (Figures 2.1 and 2.2). Anoxic basin conditions periodically occurred within this time period within which regional black shale intervals formed (Figure 2.2; Anderson et al., 2000).

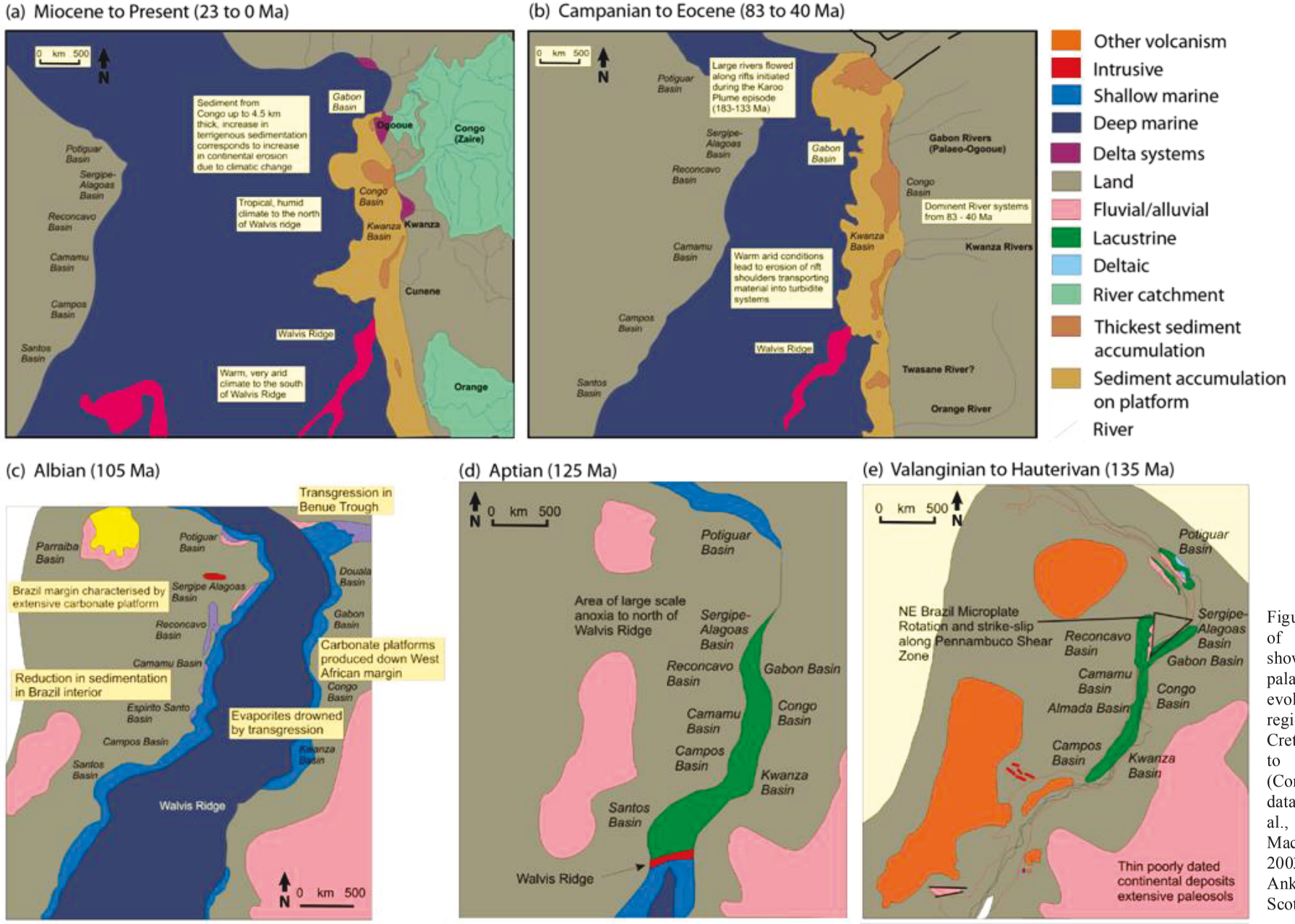


Figure 2.1 Series of diagrams showing the palaeogeographic evolution of the region from the Cretaceous through to the Miocene (Compiled using data from Burke et al., 2003, Macdonald et al., 2003, Seranne and Anka, 2005, Scotese, 2008).

A thin, condensed section of marl and shale records a period of sediment starvation in the Paleocene to Eocene (Figure 2.2; Anderson et al., 2000). The beginning of the Oligocene at 33.9 Ma marks a dramatic change in the stratigraphic history of the area; since the Rupelian large volumes of clastic sediments have been transported from the shelf edge, originating from deepwater channel systems which entered the basin south of the present day Congo Canyon, and deposited on the slope and abyssal plain (Figure 2.3; Anderson et al., 2012). This clastic system, known as the Malembo Formation, dominated the margin from then until the Pleistocene and is up to 8 km thick in some parts of the Lower Congo Basin (Coward et al., 1999, Anderson et al., 2000, Lavier et al., 2000, Valle et al., 2001, Ardill et al., 2003, Anderson et al., 2012). Anderson et al. (2012) suggest that the Malembo Formation sediments are sourced from Proterozoic Angolan shield granites and metaclasts, generating subarkose and quartzose sands carried by the Congo (Zaire) River from its large interior drainage basin onto the shelf throughout the Miocene (Figure 2.1; Bolli et al., 1978, Uchupi, 1992, Anderson et al., 2000).

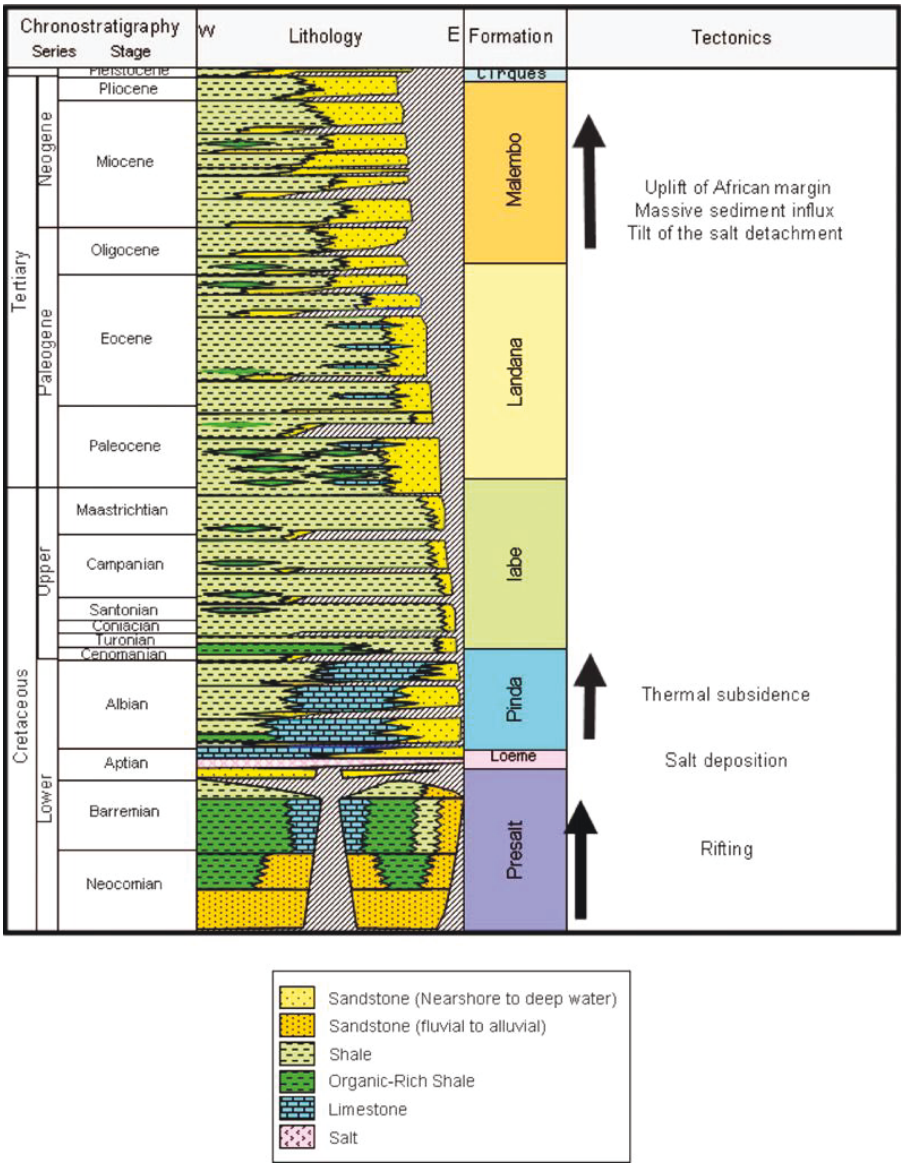


Figure 2.2 Stratigraphic column through the Lower Congo Basin showing the main tectonic events and sediments deposited within the basin from the Cretaceous to present day. Taken from Anderson et al. (2012).

During the Oligocene and Lower Miocene the sedimentation within the Lower Congo Basin was dominated by channel complex systems which can be mapped extending for hundreds of kilometres along the regional depositional dip in a broadly east-west orientation from the upper slope to the basin floor (Figure 2.3). Those which flowed through the study area were largely erosional and are referred to as third-order channel complex systems ranging from between 2 km and 3 km in width and 50 m to 200 m in thickness and depositing sediment as fan systems outboard of the study area (Figure 2.3, black box; Sprague et al., 2005, Mayall et al., 2006, Anderson et al., 2012). Although the updip extensional domain was dominated by active normal faults during this period, very little sediment was trapped in this region with most channel systems travelling through the area and out into the deeper basin (Figure 2.3; Anderson et al., 2012). Salt-influenced fold and thrust systems active within the vicinity of the study area led to some degree of confinement of the channels systems causing the position of the channels to shift in response to movement on the active structures (Anderson et al., 2012).

In the Lower Miocene from 23.05 Ma to 15.97 Ma the sediments deposited within the Lower Congo Basin changed due, at least in part, to the progradation of the shelf edge by 50 km to the west and the development of a shelf-edge delta (Figure 2.3; Anderson et al., 2012). Whist this delta delivered sediment to proximal areas it is thought that separate incised valleys were responsible for generating the main slope channel systems which are observed within the study area during this period. These third order channel complexes form the basis of the discussion on the interaction between channel complex systems and salt tectonics in Chapter 8. According to Anderson et al. (2012) the development of increasingly coalesced salt structures during this period, meant that channel complexes followed increasingly tortuous routes and ponding of sediments occurred elsewhere on the slope (Figure 2.3; Anderson et al., 2012).

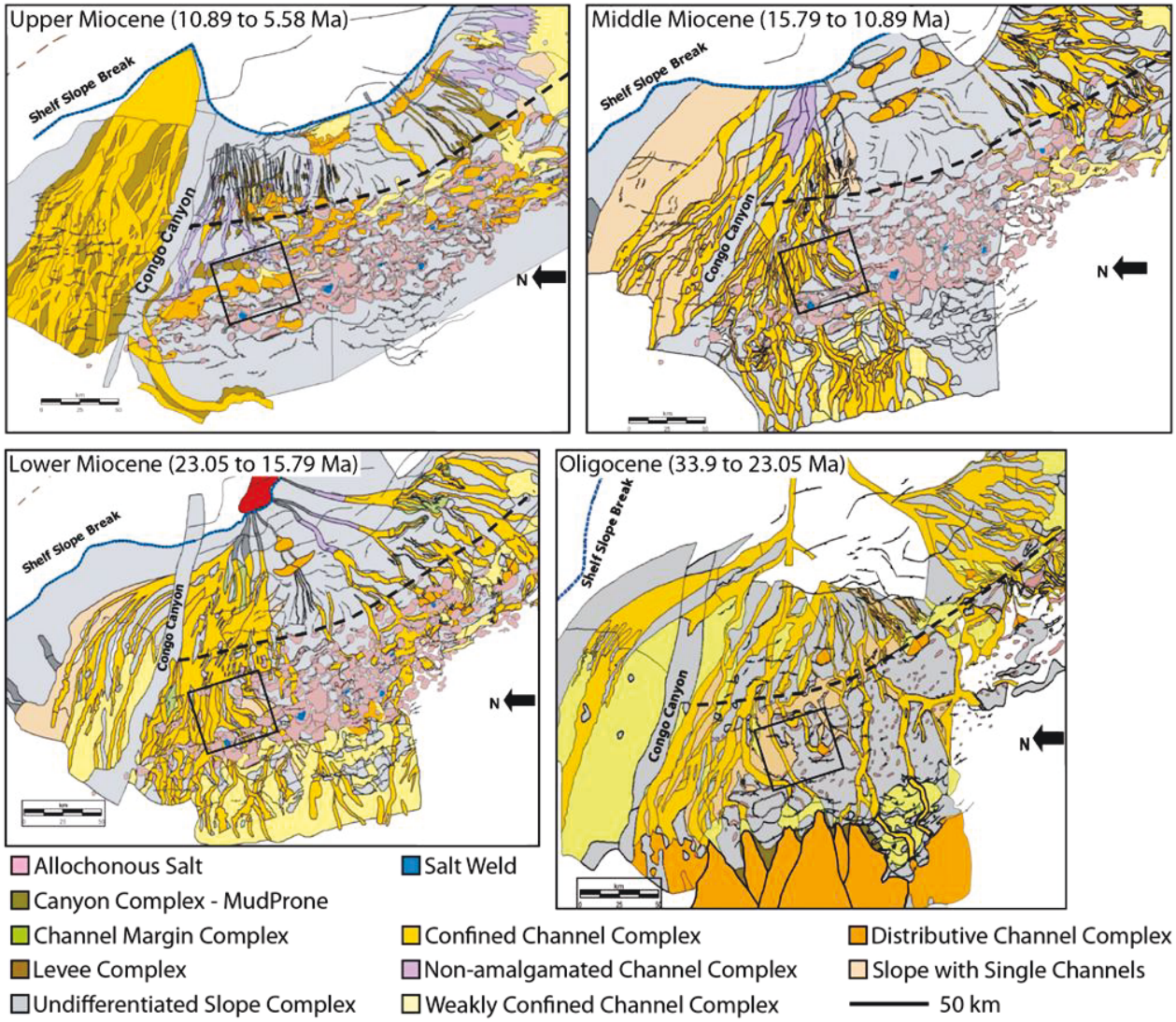


Figure 2.3 A series of palaeogeographic maps showing the distribution of the coarse clastic sediments and active structures across the Lower Congo at four periods during the evolution of the margin. The dashed line separates the extensional and contractional domains and the black box represents the approximate location of the study area within the Lower Congo Basin. Modified from Anderson et al. (2012).

In the Middle Miocene from 15.97 Ma to 10.89 Ma the sediment feeder systems started to become more entrenched in position with channel systems following the same route downslope from the extensional domain (Anderson et al., 2012). Also during this period the shelf-edge had prograded further into the basin, corresponding to the emergence of proto-Congo Canyon style sediment feeder systems. Within the study area the main sedimentation was still dominated by third-order channel systems up to 500 m deep and between 5 km and 10 km wide being both erosionally and levee confined (Anderson et al., 2012) and regional mass transport complex deposits (discussed in detail in Chapter 6). The channel complexes flowed through the north of the study area and eventually fed fans outboard of the area in the deepwater basin to the west (Figure 2.3).

Further changes in the regional sediment supply occurred within the Upper Miocene from 10.89 Ma to 5.58 Ma with the shelf edge prograding a further 20 km to 30 km to the west and the development of the large composite channel systems which make up the present day Congo Canyon to the north of the study

area (Figure 2.3; Ferry et al., 2005, Anderson et al., 2012). South of the present-day Congo Canyon, in the vicinity of the study area, the channel systems shown in Figure 2.3 are fairly straight and mud filled with occasional lag deposits (Anderson et al., 2012). This indicates that they mostly acted as by-pass conduits due to the steep up-slope gradient and terminated in salt-induced mini-basins, such as the basin studied here, in the contractional domain of the slope system. Ponded sediments formed within these mini-basins during this interval and are studied in detail in Chapter 7.

A reorganisation of sediment routing through the palaeo-Congo Canyon occurred at approximately 5.3 Ma with the main sediment supply being fed to the margin further to north and the onset of the modern Congo fan system (Anka et al., 2009). Within the vicinity of the study area the lack of clastic channel systems, or fan deposits after 5.58 Ma indicates that the sediment supply into the region shut off completely at this time with only background hemi-pelagic sedimentation recorded to the present day (Anderson et al., 2012).

Overall, the shelf edge prograded west into the basin by approximately 100 km to 200 km during the Oligocene and the Miocene (Figures 2.3 and 2.4; Anderson et al., 2000, Anderson et al., 2012). This progradation also affected the slope gradients with an estimated increase from less than 0.1° in the Rupelian (Upper Oligocene) to 2 – 3° near the shelf edge in the Messinian (Upper Miocene).

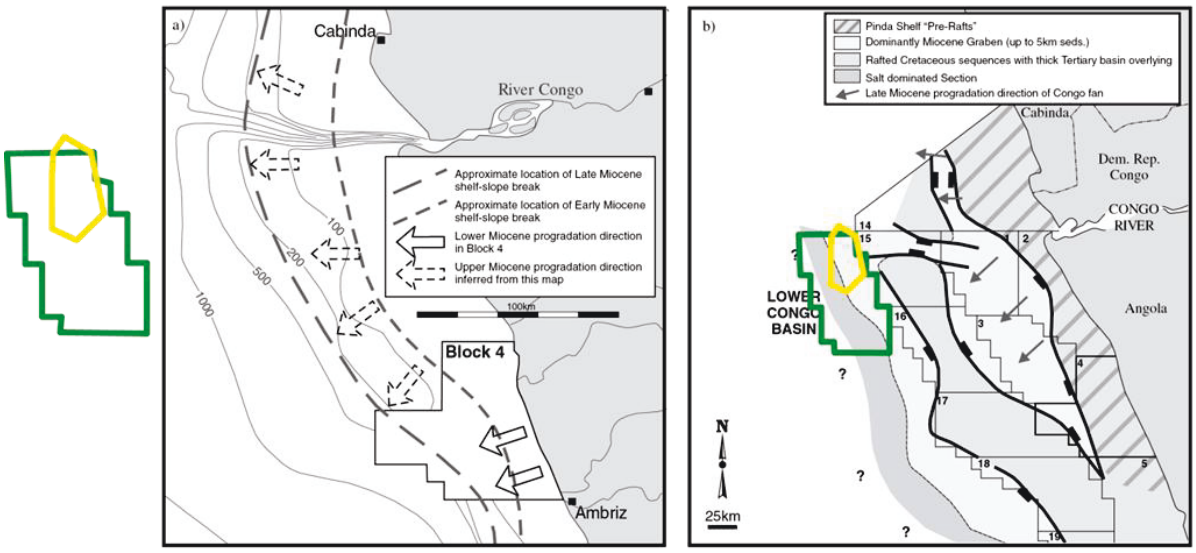


Figure 2.4 (a) Regional map showing the approximate location of the shelf slope break in the Lower Congo Basin during the Miocene, and how the shelf break has prograded relative to the Congo Fan, (b) major post-rift elements with approximate location of Block 31 outlined in green and the study area in yellow (Modified from Anderson et al., 2000).

2.3 Regional Structural Setting

The Angolan margin has a complex structural history starting with Cretaceous rifting and followed by gravity-driven salt-related deformation that spans the period from Cretaceous to Recent. Prior to salt deposition in the Aptian, large normal faults and associated grabens and basement tilted fault blocks formed during the Valanginian to Barremian rifting (Spathopoulos, 1996, Karner et al., 1997, Macdonald et al., 2003, Dupré et al., 2007). The Aptian Loeme salt acts as a mechanical detachment and decouples most of the post-salt deformation from the underlying rift-related structure. As a result, an understanding of the early

rift history of the margin is of less importance when investigating the gravity-driven post-salt passive margin deformation.

Two main phases of post-salt deformation are recognised in the Lower Congo Basin, the first of which is Albian to Cenomanian in age, and the second Oligocene to Holocene in age (Burke, 1996, Spathopoulos, 1996, Marton et al., 2000, Anderson et al., 2012 amongst others). Both are characterised by a gravitationally driven system of up-dip extension in the east with linked down-dip shortening and salt extrusion in the west (Figures 2.5 and 2.6; Spathopoulos, 1996, Dominey and Wiffe, 1998, Hartman et al., 1998, Anderson et al., 2000, Marton et al., 2000, Anderson et al., 2012). Such gravitational systems can be generated by a basinward tilt of the margin and increasing sediment load. As discussed previously, both of these processes has occurred along the Angolan margin: westward tilting has occurred in response the opening of the Atlantic and increased thermal subsidence basinward; and significant sediment loading has been provided by the thick Oligocene to Holocene Congo-fan related sedimentary systems that form the Malembo Formation.

The earliest Aptian to Cenomanian phase of passive margin deformation is thought to have been driven mainly by post-rift, thermal subsidence-related basinward tilt of the margin. In response to this tilt Quirk et al. (2012) propose that salt on both margins of the central South Atlantic started to move down-dip within only a few millions years of its deposition in the Albian. They cite the regional-scale inflation of the salt from about 2 km to 4 km in the Brazilian Santos and Campos Basins and the African Kwanza Basin (Hudec and Jackson, 2004, Davison et al., 2012) in support of this theory. A requirement of this model is outer volcanic highs and ridges situated close to the continent-ocean boundary which can act as 'sills' for the salt. Associated with the continued basinward flow of salt, Cretaceous strata were translated basinward and Cretaceous extensional listric normal faults are recognised on the Angolan shelf which formed in response to this tilting (Sahagian, 1988, Duval et al., 1992, Lundin, 1992, Lunde et al., 1992, Gaullier et al., 1993, Spathopoulos, 1996, Eichenseer et al., 1999, Seranne and Anka, 2005). Related Cretaceous contractional structures have proved more difficult to find because of overprinting by the Oligocene and younger deformation. However, Cramez and Jackson (2000) document an imbricate thrust belt of Cretaceous age in the northern Lower Congo Basin and Anderson et al. (2012) show Cretaceous-aged allochthonous salt sheets that flowed laterally along the ocean-continent boundary, imaged on recent seismic data.

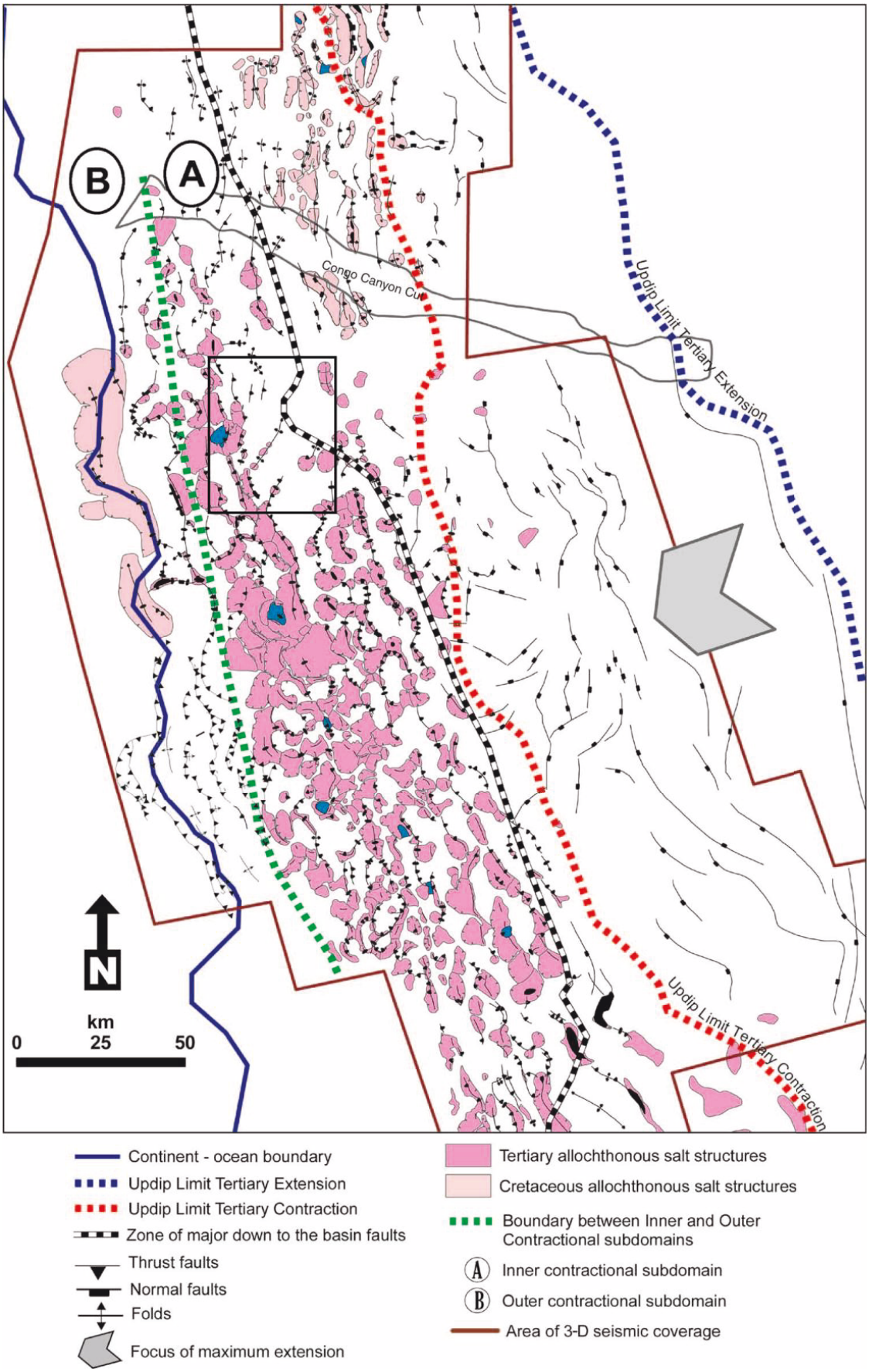


Figure 2.5 Structural elements map over the entire area covered by the Lower Congo Basin highlighting allochthonous salt structures, major faults and folds as well as limits of the contractional and extensional domains on the passive margin during the Tertiary. An approximate location of the study area investigated in this thesis is shown with a black box. The map is taken from Anderson et al. (2012).

The second major phase of post-salt passive margin deformation started in the Oligocene. In this case, both tilt of the margin due to the uplift of the African plate by a mantle plume, and the increased sediment load of the thick Congo-fan related clastic sediments are thought to have a played a role in driving the gravitational deformation (Bond, 1978, Hempton et al., 1990, Lunde et al., 1992, Burke, 1996, Jackson and Cramez, 2000, Marton et al., 2000, Hudec and Jackson, 2004, Al-Hajri et al., 2009, Roberts and White, 2010, Green et al., 2014, White and Hoggard, 2014). Based on the main salt tectonic features observed within the Lower Congo Basin, Anderson et al. (2012) divide the area into an extensional domain and a contractional domain (Figure 2.5). They state that the proximal extensional domain ranges in width from 150 km to 200 km whereas the contractional domain is smaller and ranges in width from 90 km to 100 km, corresponding to the area of the basin containing more allochthonous salt structures. Within these two broad domains other authors have identified four different salt-dominated provinces, again defined mainly on structures of Oligocene-Miocene age (Spathopoulos, 1996, Jackson et al., 1998, Marton et al., 2000), from east to west these are (Figures 2.5 and 2.6):

1. a raft domain,
2. a diapir domain in the central part of the basin,
3. a canopy domain outboard of this, and
4. a salt nappe furthest to the west

The following discussion of the main salt structures in the Lower Congo Basin will use the definition of the domains outlined by Anderson et al. (2012) identifying the main salt features within these two broader domains.

The extensional domain is characterised by a series of counter-regional down-to-the-basin listric normal faults, rafted blocks and thick Miocene-aged extensional basins; the original salt has been almost completely evacuated and the remaining salt structures include salt rollers in the footwalls of the normal faults, the occasional salt diapir, and small triangular salt rollers (Figures 2.5 and 2.6; Marton et al., 2000, Anderson et al., 2012). The greatest amount of extension on the listric faults has been observed to the south of the present day Congo Canyon and to the east of the study area (Figure 2.5; Anderson et al., 2012).

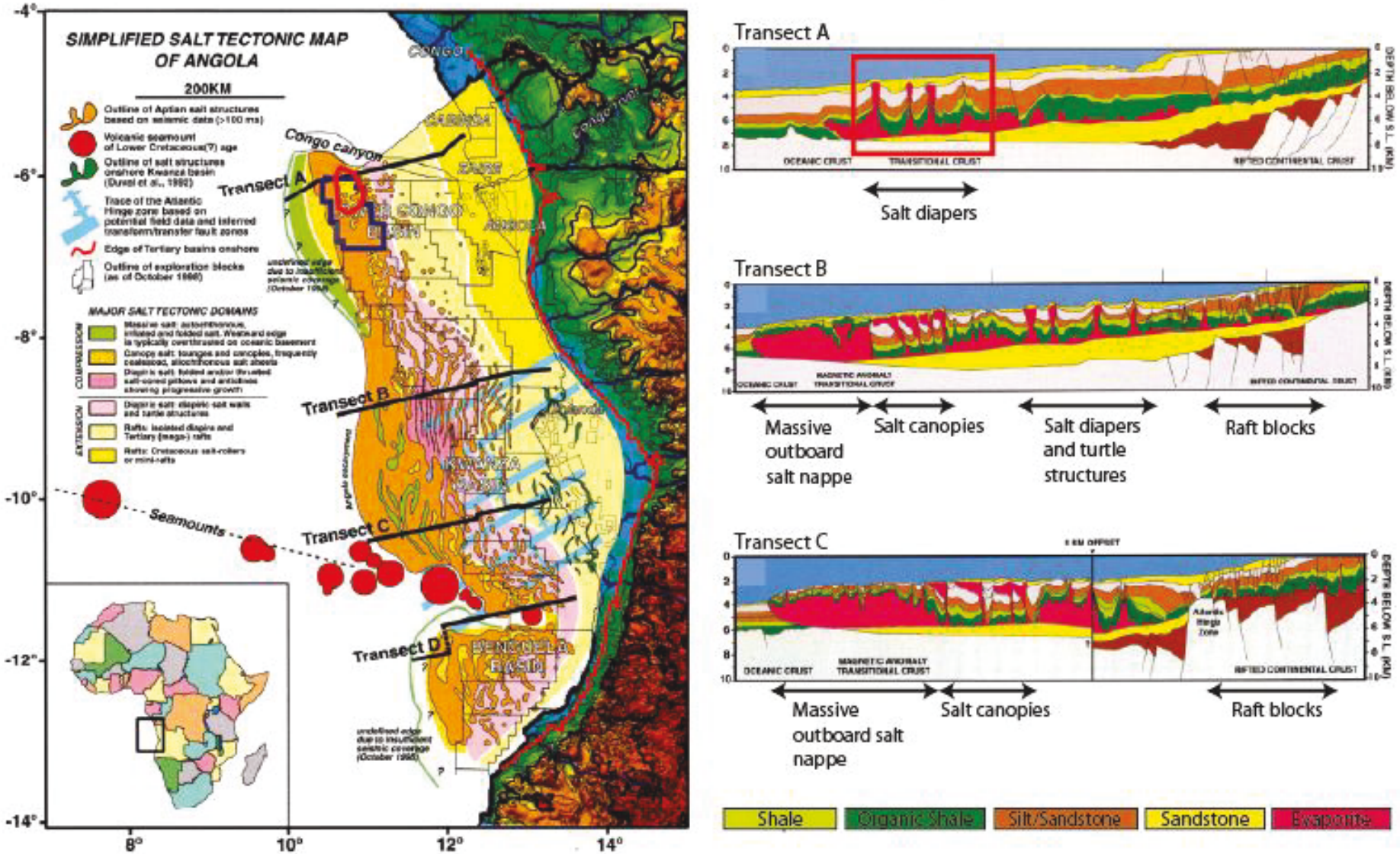


Figure 2.6 Overview of the regional salt tectonic providences offshore Angola, using a map and cross-sections to show variations along the margin. Blue outline on the map indicates the location of Block 31, orange shows the outline of the PSVM and the red box on Transect A shows the area of interest in this study (Modified from Marton et al., 2000, Tari et al., 1998).

The contractional domain is smaller than the extensional domain but contains within it significantly more variable salt structural styles, including: salt diapirs, extensive canopy salt structures, salt cored folds and salt nappes. It has been sub-divided into inner and outer contractional domains; the inner sub-domain is dominated by allochthonous salt structures whilst the outer sub-domain contains significantly less salt (Figure 2.5; Anderson et al., 2012). Shortening is accommodated on the slope within both these sub-domains through a complex interaction of folds, thrust faults and the extrusion or inflation of salt (Figure 2.5). This variability of structural styles has been attributed to the volume and distribution of the original salt, the magnitude of extension up-dip and contraction during the Neogene, the structural relief on the basal autochonous salt and the volume and location of sediment entering the Lower Congo Basin (Marton et al., 2000, Rowan et al., 2004, Anderson et al., 2012).

Working inboard to outboard across the Lower Congo Basin, the inner contractional domain contains predominantly salt diapirs in the east and salt canopies to the west (Figures 2.5 and 2.6; Marton et al., 2000, Anderson et al., 2012). In the eastern half of the inner contractional domain allochthonous salt structures such as large diapiric walls, turtle structures, salt pillows, salt sheets and cylindrical diapirs are commonly observed alongside thrust faults and detachment folds (Figure 2.5; Baumgartner and van Andel, 1971, Leyden, 1976, Marton et al., 2000). Anderson et al. (2012) document significant amounts of lateral flow within the allochthonous salt structures, thought to have occurred in response to shortening against the salt feeder stocks resulting in isolated to semi-isolated allochthonous salt bodies detached from the source salt layer. The western half of the inner contractional domain is dominated by salt canopies, some of which are anchored into the autochthonous salt layer (Anderson et al., 2012). These salt canopies are regularly covered by a thin veneer of Plio-Pleistocene sediment, suggesting recent activity, and may have formed as several of the allochthonous salt sheets were increasingly shortened, coalescing to form one allochthonous salt mass (Figure 2.5; Marton et al., 2000, Anderson et al., 2012).

The outer contractional domain is variable in character down the length of the Lower Congo Basin due to variations in the volume of outboard salt. In the southern half, there is little outboard salt and hence the structural style is dominated by tight detachment folds and thrust faults, whereas in the northern half there is more salt leading to the formation of an extensive salt nappe (Figures 2.5 and 2.6; Marton et al., 2000, Anderson et al., 2012). Where less salt is present in the south of the Lower Congo Basin, asymmetric basinward verging stacks of low angle thrust faults have been observed. This suggests a detachment layer with more friction, or the change from a salt detachment layer to one with more friction (Costa and Vendeville, 2002, Bahroudi and Koyi, 2003, Anderson et al., 2012). In contrast, in the north of the Lower Congo Basin, where more outboard salt is present, it is thought that the salt structures formed as autochthonous salt sheets during the Cretaceous and were subsequently inflated during the Oligocene shortening event then folded into the cores of Miocene detachment folds (Figures 2.5 and 2.6; Anderson et al., 2012).

Overall, the structures within the contractional domain formed early in the history of the basin and continued to grow, accommodating additional shortening throughout the Oligocene and Miocene (Costa and

Vendeville, 2002, Rowan et al., 2004, Anderson et al., 2012). This means they played a key role in the deposition of sedimentary systems within the basin at this time, controlling the distribution of these sediments and forcing them to shift in position in response to the changing local gradients driven by this salt movement (see also Anderson et al., 2000, Ferry et al., 2005, Gee and Gawthorpe, 2006, Kane et al., 2010, Mayall et al., 2010, Anderson et al., 2012). The impact that these evolving structures had on three very different types of sedimentary system (deepwater channel complex systems, mass transport complexes and ponded fan lobe complexes) is fully explored in this thesis.

3 Principles Behind the Study: A Sedimentological Literature Review

3.1 Introduction

It is well known that sedimentary systems within the deepwater environment react to changes in topography on the seafloor. This thesis aims to explore how a variety of deepwater systems respond to structurally induced changes in the local gradient within an area of contractional salt tectonics on the Angolan passive margin where the mini-basin development is controlled by the growth of salt walls, salt-cored anticlines and salt canopies. This thesis takes an integrated approach by combining a thorough structural analysis of the mini-basin (Chapter 5) with an in-depth investigation of parts of the Miocene sedimentary infill of the basin which include mass transport complexes (Chapter 6) and ponded fan systems (Chapter 7). Additionally, previously mapped older (Late Oligocene) channel complexes are included in the analysis to compare how three different depositional systems respond to the growth of structures and formation of accommodation space within the mini-basin (Chapter 8).

Mass transport complexes (MTCs) and ponded fan systems were chosen as a focus for the study because interactions between these sediment types and structural growth is a less-commonly explored topic in the literature and these two types of system are exceedingly well imaged within the seismic data. A review of the current literature on these sedimentary systems is presented in this chapter whist a review of the literature linked to the structural methods used in the analysis is provided in Chapter 4. As well as helping to fully understand the processes that impact on both the evolution of the basin and the sedimentary systems deposited, this literature review also highlights areas where less work has been carried out to date. These areas form the basis of the work presented in this thesis.

3.2 Sedimentation Types

3.2.1 Mass Transport Complexes (MTCs)

Gee et al. (2006) describe how MTC deposits were first recognised from folded, distorted sediments in the Black Sea (Arkhanguelsky, 1933), from distinctive, sharp breaks in submarine telegraph cables (Heezen and Ewing, 1952) and from topographic anomalies on the seafloor (Shepard, 1955). More recently, echo sounders, sonar and shallow 2D seismic data have been used (e.g. Masson et al., 1993, Gee et al., 1999, Talling et al., 2007) which reveal details on the frequency and estimates of the area affected by MTCs but have less information on the internal characteristics of MTCs and the structures on their basal surface. Advances in the resolution of 3D seismic data over the last few decades has allowed the internal characteristics of MTCs to be studied extensively with significantly better imaging of these systems (for example Brami et al., 2000, Posamentier et al., 2000, Posamentier and Kolla, 2003, Gee et al., 2006, Moscardelli et al., 2006, Posamentier and Walker, 2006, Sawyer et al., 2007, Alves and Cartwright, 2010). These studies have been used alongside detailed outcrop studies to significantly increase understanding of

the internal morphology of MTCs located in a variety of environments (Damuth and Embley, 1981, Martinsen, 1989, Martinsen et al., 2003, Posamentier and Kolla, 2003, Posamentier and Martinsen, 2011).

Mass movement of sediment on the seafloor has long been the subject of discussion in the literature, generating a plethora of associated terminology. Moscardelli and Wood (2008) highlight that it has been more than four decades since Dott (1963) and subsequently Lowe (1979) criticised confusion over the terminology used to describe the phenomena of sediment mass movement on the seafloor, which had resulted in many different classification schemes being developed (for example Carter, 1975, Varnes, 1978, Martinsen, 1994, Mulder and Cochonat, 1996, Weimer and Shipp, 2004, Frey-Martínez et al., 2006, Moscardelli and Wood, 2008, Nemec, 2009). This confusion is exacerbated by fact that scientists working in different geological environments (subaerial versus submarine) which have different flow parameters (Nardin, 1979, Shanmugam, 2000, Shanmugam, 2002, Moscardelli et al., 2006) use a mixture of different terms. Variations on the same terminology are also generated by scientists working in modern environments (Norem et al., 1990, Masson et al., 1997, Hovius et al., 1997, Masson et al., 1998, Gee et al., 1999, Gee et al., 2001) versus those studying older, often buried, rocks (Sohn, 2000, Wach et al., 2003, Frey-Martinez et al., 2005, Alves and Cartwright, 2010). Moscardelli and Wood (2008) broadly define submarine mass movement as the movement of sediment driven by gravity (gravity-induced deposits; based on earlier seminal work by Dott Jr, 1963, Nardin, 1979). This broad term therefore encompasses a spectrum of deposits that includes slides, slumps, debris flows and turbidites (Table 3.1). Other classifications would also include creep and rock falls in the overall spectrum of gravity induced submarine mass transport (e.g. Nemec, 1990 amongst others).

The classification scheme developed by Nardin (1979) was built on that first proposed by Dott (1963) and included a more comprehensive classification based on sedimentary characteristics identified within the deposits including sorting, grain size, stratification, grading and sedimentary fabric. This thesis follows the classification scheme Moscardelli and Wood (2008) adapted from the work of Nardin (1979) which focuses on the sedimentary fabric and seismically-recognisable criteria (see Table 3.1). Slides, slumps and debris flows are considered to be the three end-member constituents of MTCs and can occur within the same event or depositional unit (Table 3.1; Dott Jr, 1963, Nardin, 1979, Moscardelli and Wood, 2008).

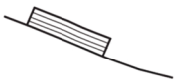
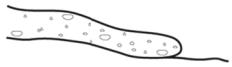
GRAVITY INDUCED DEPOSITS			Genetic Classification Transport Mechanism	Descriptive Classification Sedimentary Structures	Seismically Recognizable Features (Moscardelli et al., 2006; this work)
Mass Transport Complex	Slide		Shear failure along discrete shear planes with little or no internal deformation or rotation	Essentially undeformed, continuous bedding	Continuous blocks without apparent internal deformation. High-amplitude, continuous reflections.
	Slump		Shear failure accompanied by rotation along discrete shear surfaces with various degrees of internal deformation	Plastic deformation particularly at the toe or base. Flow structures, folds, tension faults, joints, slickensides, grooves, rotational blocks	Compressional ridges, imbricate slides, irregular upper bedding contacts, duplex structures, contorted layers. Low- and high-amplitude reflections geometrically arranged as though deformed through compressive stresses.
	Debris Flow		Shear distributed throughout the sediment mass. Strength is principally from cohesion due to clay content. Additional matrix support may come from buoyancy. Plastic rheology and laminar state.	Matrix supported, random fabric, clast size variable, matrix variable. Rip ups, rafts, inverse grading and flow structures possible.	Mega rafted and/or detached blocks, irregular upper bedding contacts, lateral pinch-out geometries, oriented ridges and scours. Low-amplitude, semitransparent chaotic reflections.
Turbidity Current	Turbidite		Supported by fluid turbulence (newtonian rheology)	Normal size grading, sharp basal contacts, gradational upper contacts.	Lobate features Laterally continuous

Table 3.1 The classification scheme proposed by Moscardelli and Wood (after 2008) but based on work from Dott (1963), Nardin et al. (1979) and Moscardelli et al. (2006). This definition of the main features within MTC deposits has been used throughout this chapter. Table taken from Moscardelli and Wood (2008).

Submarine mass flows can move as coherent slide sheets, internally deforming slumps and plastically deforming debris flows. The difference between slumps and slides is defined by the glide plane and the amount of deformation; a slide moves on a planar basal detachment and shows little internal deformation, whilst a slump moves along a concave-up glide plane generating a rotational movement which causes both brittle and plastic internal deformation. These are not clearly defined boundaries and many MTC deposits contain a mixture of slumps, slides and debris flow deposits, for example: slides and slumps can evolve into debris flows in situations where there is a down-slope increase in mass disaggregation (Moscardelli and Wood, 2008). Turbidity currents may also be generated from MTCs where the fluid content increases in the plastic debris flow and develops into a fluidal turbidity current (Shanmugam, 1996).

Submarine slope failure occurs when downslope-directed shear stresses acting along an inclined planar surface, such as a bedding plane, exceed the shear strength of the slope (Varnes, 1978, Hampton et al., 1996). However, it has been shown that sediments deposited in a state where shear strength exceeds shear stress will be stable but, if this balance changes either through an increase in shear stress or a decrease in shear strength, then failure can occur (see Biscontin et al. (2004) and Owen et al. (2007) for further discussion). Many factors, operating at different timescales can contribute to inducing slope instability and its subsequent failure. These include seismic events, tidal or storm loading/unloading, long-term sea-level changes, the development of over-pressure due to low porosity layers in otherwise high porosity rocks, gas hydrate dissociation, glacial loading/unloading, volcanic events, local changes in the seabed slope due to tectonics, and human activities such as construction in coastal settings (see Dugan and Flemings, 2000, Volpi et al., 2003, Biscontin et al., 2004).

After failure has been triggered, the material contained within the MTC is translated downslope along a decollement surface or basal shear surface (Figure 3.1). This motion continues until the balance between shear stress and shear strength is restored through erosion and shearing of the substrate by the over-riding material (Gee et al., 2006, Richardson et al., 2011). This basal layer has not been observed on all MTC deposits in the literature, but it is thought to significantly increase the volume of the MTC deposit and the run-out length. It has been documented on the Saharan debris flow (located offshore of the Canary Islands) where more than 450 km of the debris flow was underlain by an extensive shear layer (Masson et al., 1993, Gee et al., 1999, Gee et al., 2001). The basal surface can vary considerably in morphology with planar surfaces (i.e. little basal erosion) recorded in some areas (see Brami et al., 2000, Beaubouef et al., 2003, McGilvery and Cook, 2003) and considerable erosional relief in other areas with the removal of as much as 200 m of underlying sediment (for example Weimer, 1990, McGilvery and Cook, 2003). Basal surfaces are commonly characterised by groove scars which can vary in width and distance depending upon the size and type of material being transported by the flow of the MTCs (Posamentier et al., 2000, McGilvery and Cook, 2003, Newton et al., 2004).

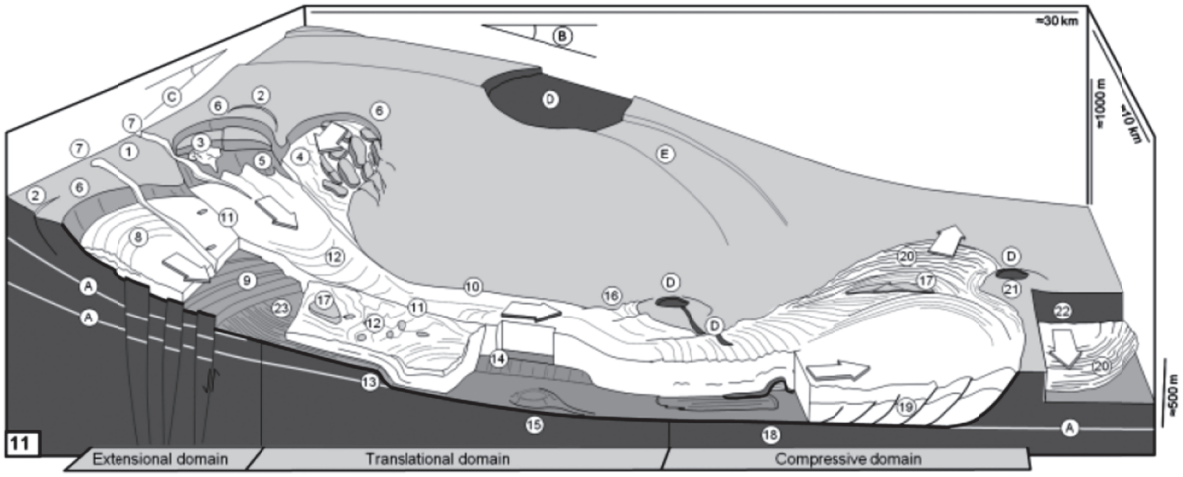


Figure 3.1 Diagram illustrating the main structures and domains associated with mass transport complexes and the syndepositional features associate with their development. The broad white arrows indicate the direction of transport with the sections through showing the features in that area. This is taken from Richardson et al. (2011) which is in turn modified from Bull et al. (2009) and Prior et al. (1984). *Key:* A, layers of weakness; B, slope created by basin margin; C, slope created by fold uplift; D, mud volcano (NB these are not present in Angola); E, curved grabens which emanate from mud volcano centre. *Extensional domain*: 1, headwall scarp; 2, crown cracks; 3, rotated blocks and residual debris; 4, rafted locks and sidewall fragmentation; 5, detached portion of the flow exposing evacuated basal shear surface; 6, arcuate scarps, showing divergent convex upslope orientations towards the fold flank and basin slope; 7, headless canyons incising the headwall; 8, convex upslope lineations; 9, normal ramps and flats in the basal shear surface located around fault traces. *Translational domain*: 10, lateral margin; 11, longitudinal shear zone; 12, flow fabrics, convex downslope and chaotic; 13 normal ramp, with coherent drape of mass transport deposit facies; 14, lateral ramp; 15 elongate strain shadow behind obstacle; 16, restraining bend in the lateral margin; 17,translated blocks. *Compressive domain*: 18, blocks and basal shear surface scours; 19, thrust sheet; 20, pressure ridges; 21 obstacle at mass transport deposit toe modifying frontal morphology; 22, older mass transport deposit travelling along the old layer of weakness; 23, basal shear surface grooves.

The size and shape of MTC deposits can vary greatly with some of the largest examples discovered elsewhere along the Atlantic Margin, extending for 700 km and involving thousands of cubic kilometres of material. Well-documented examples include the Saharan Slide, offshore the Canary Islands (see Embley, 1976, Masson et al., 1993, Gee et al., 1999), the Storegga Slide, offshore Norway (Bugge et al., 1988, Dawson et al., 1988, Haflidason et al., 2004, Solheim et al., 2005) and the Grand Banks Slide (Kuenen, 1952, Piper and Aksu, 1987, Mulder and Cochonat, 1996, Driscoll et al., 2000). The Pleistocene Storegga

Slide is thought to consist of sixty three quasi-simultaneous mass transport events over an area of approximately 95,000 km^2 and which led to the evacuation of 2,400 - 3,200 km^3 of sediment and generated a tsunami (Haflidason et al., 2004). This is a particularly large example, with the majority of MTCs deposited in unconfined settings ranging in size from between 50 - 75 km across and more than 200 km in dip direction, thus covering areas of at least 10,000 km^2 and 15,000 km^2 (Lee et al., 2004, Newton et al., 2004, Owen et al., 2007, Moscardelli and Wood, 2008). In confined settings, such as in intra-slope basins in the Gulf of Mexico, they can be considerably smaller and are commonly only 20 - 30 km^2 in area (Beaubouef et al., 2003). The thickness of MTC deposits also varies depending on the type of system, the lithology and the amount of failure along the slope margin, with thicknesses known to vary from 5 m to hundreds of metres (Kowsmann et al., 2002, McGilvery and Cook, 2003, Joanne et al., 2013). The plan-view shape of MTCs is variable depending on the local topography, but in general they tend to be elongate downslope (Figure 3.1). The shape is thought to reflect the initial failure area, the amount of confinement in the basin and the distance which the deposit has travelled downslope. In cross-section, the deposits are generally mounded or wedge-shaped with the thickest sediment deposited towards the toe of the system.

These differences in size, shape and coverage have led to the development of two main end-member models as proposed in a recent paper by Moscardelli and Wood (2008) based on MTCs offshore Trinidad (Figure 3.2): shelf- and slope-attached MTCs (Moscardelli et al., 2006) and detached MTCs. The slope- and shelf-attached MTCs are characterised by an evacuated headwall scarp and down-dip debris flows which are more likely to form regional units which can reach up to thousands of square kilometres in area and hundreds of metres in thickness (e.g. the Storegga Slide). In comparison, the detached MTCs are significantly smaller in extent and consist of clear extensional features in the headwall region and a compressional toe. Both attached and detached MTCs are observed in the study area with only the down-dip debris flow portion of the attached MTC sediments visible within the mini-basin studied. In the 3D seismic reflection datasets these deposits are characterised by low-amplitude, semi-transparent chaotic reflections which occasionally carry more coherent blocks of sediment. In some cases, particularly in areas with poor seismic resolution, the chaotic facies are often interpreted as debris flow deposits and may represent plastically deformed slump material. With improved quality seismic imaging it may be possible to resolve faults within the facies described previously as chaotic packages.

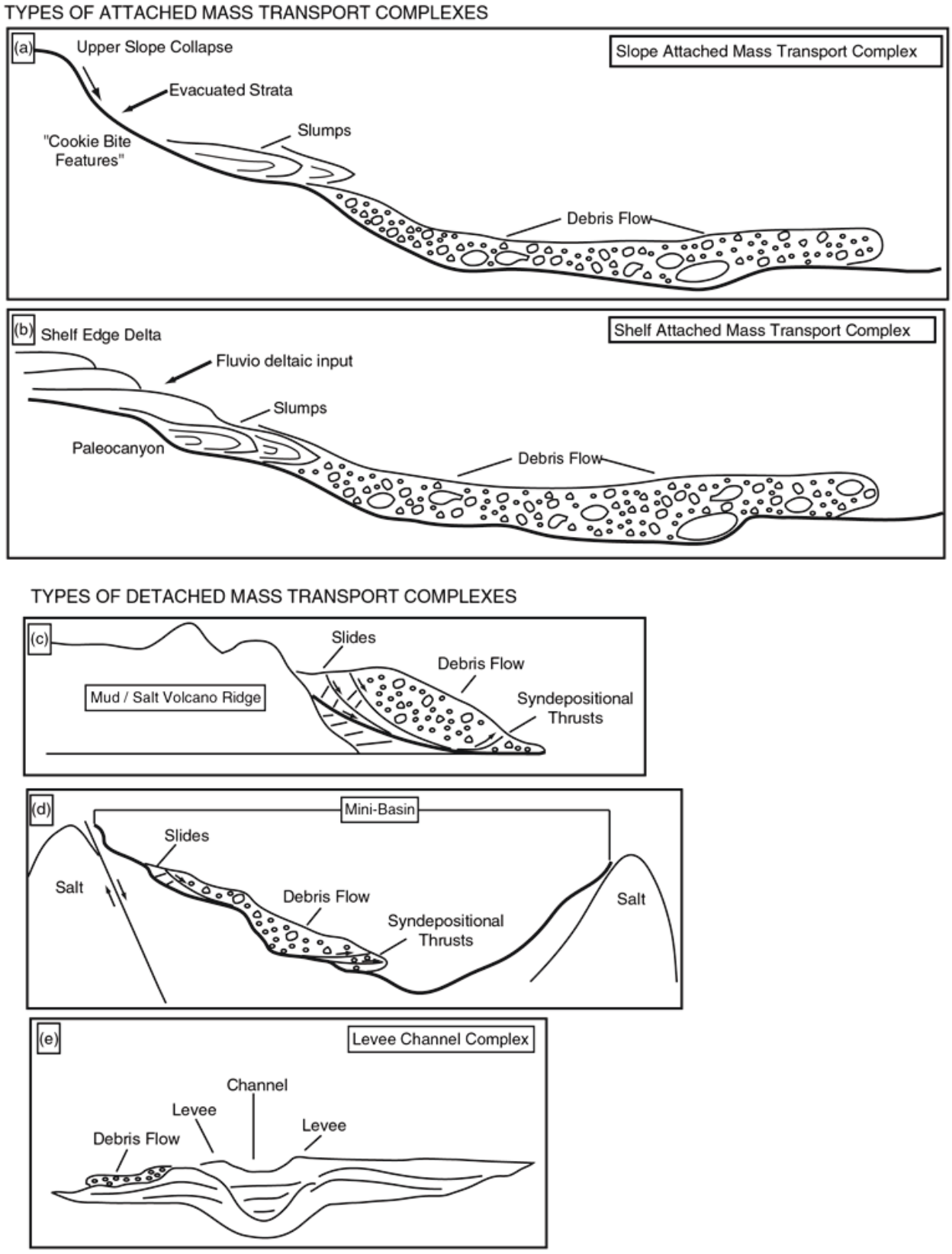


Figure 3.2 A series of diagrams illustrating the different kinds of mass transport complexes (MTCs) and the processes associated with their initiation, as outlined by Moscardelli and Wood (2008). (a) Slope-attached MTCs whereby the sediments are derived from catastrophic failure of the upper slope area. (b) Shelf-attached MTCs where shelf-edge delta collapse sources the material for the deposits. (c) Detached MTCs associated with the collapse along the flank of a mud volcano (in the case of the study area salt diapir growth could source this type of detached MTC). (d) Detached MTC associated with over-steepening of a margin along a deepwater mini-basin, and (e) detached MTC deposit whose genesis is associated with a levee-channel complex. Image taken directly from Moscardelli and Wood (2008).

MTCs located on the flanks of growing structures are also visible within the mini-basin and have been termed local MTCs. These contain clear extensional and compressional domains and, as such, would be classified as detached slides by Moscardelli and Wood (2008). In general, detached MTCs can be defined by three clear domains (Figure 3.1): an extensional domain in the headwall and scarp area, a translational domain in the middle of the MTC and a compressional domain towards the toe (Bull et al., 2009, Alves and Cartwright, 2010, Richardson et al., 2011). The extensional domain is characterised by a relatively thin deposit and extensional faulting, the translational zone may often contain relatively undeformed strata and semi-continuous horizons whilst the compressional domain is characterised by compressional features such as thrust faults (Figure 3.1).

The translational zone of MTC deposits commonly contains internally undeformed blocks which have been carried from the headwall (Figure 3.1). These blocks can vary in size and shape from several hundred to several thousand square metres, and are commonly surrounded by chaotic material (Lee et al., 2004, Moscardelli and Wood, 2008). Erosional remnants picked up, incorporated and transported by the flow can also be observed within the translational zone (Moscardelli et al., 2006).

The toe domain of MTCs contains compressional features such as thrust blocks (Weimer and Shipp, 2004) and syn-depositional thrusts (Frey-Martinez et al., 2005, 2006, Moscardelli et al., 2006). These tend to be associated with deceleration of the flow of the MTC and, as such, are found at the terminal end of the MTC deposits and in areas where flow of the MTCs is confined or altered by topographic changes on the seafloor (Marr et al., 2001). Frey-Martinez et al. (2006) discuss how MTC systems can be either frontally emergent or frontally confining depending on whether or not the systems runout over the top of a ramp within the compressional domain (Figure 3.3). This is important as the amount of run-out can be used to imply something about the amount of energy carried within the MTC; those that are able to emerge over the frontal ramp and onto the seabed have sufficient inertial energy to abandon their basal shear surfaces (for example Farrell, 1984, Martinsen, 1989, Martinsen and Bakken, 1990).

Both attached and detached MTC deposits are almost always bound by high amplitude seismic reflection events, with the lower boundary dominated by erosive features such as mega-scours. These can scour into the substratum and cover areas which are tens of metres deep, several kilometres wide and hundreds of kilometres long, effectively gouging out ‘channels’, or deep grooves, beneath the main erosive base (McGilvery and Cook, 2003, Posamentier and Kolla, 2003, Weimer and Shipp, 2004, Moscardelli et al., 2006, Moscardelli and Wood, 2008). The basal surface has also been found to contain smaller features such as those termed cat-claw scours (Moscardelli et al., 2006) or monkey fingers (McGilvery and Cook, 2003) which tend to occur down-dip of the mega-scours and are comprised of a series of smaller radiating shallow scours (Figure 3.1). Out-running blocks also cause scours on the basal surface of the MTC, gouging into the substrata and causing secondary scours and scratches (Moscardelli et al., 2006) or glide tracks (Nissen et al., 1999; Figure 3.1, features 18 and 23). The surface along which the initial slide occurred can also be visible within 3D seismic data as a high amplitude, continuous reflection which defines the basal boundary of the MTC (Lee et al., 2004).

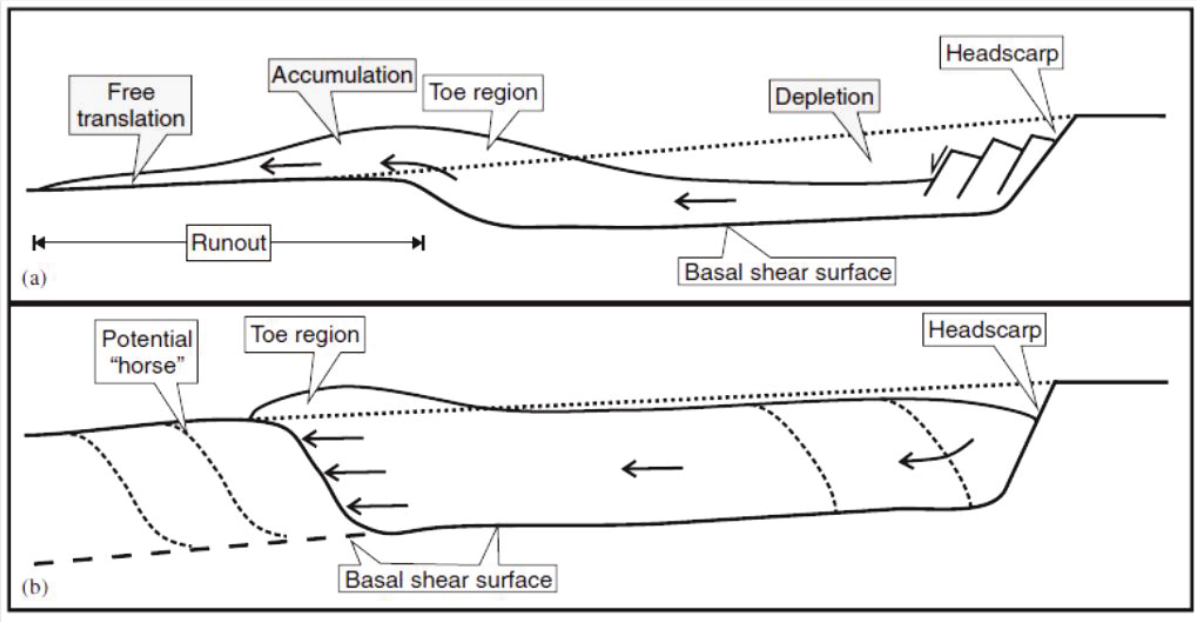


Figure 3.3 A comparison between MTCs defined according to the type of frontal emplacement exhibited. They have been defined as being either (a) frontally emergent whereby the material ramps up over the basal shear surface and out onto the seabed where it is able to travel a considerable distance over the unconfined seafloor or (b) frontally confined systems where the internal volume of the MTC is buttressed against the frontal ramp of the MTC and does not leave the original basal shear surface. Taken from Frey-Martinez et al. (2006).

The lithology of MTC deposits is dependent upon the lithology of the material which failed, and any material incorporated into it as it has moved. Both of these constituents effect the rheological characteristics of the MTCs (Shipp et al., 2004, Pickering and Corregidor, 2005). However, MTCs are mostly comprised of muddy sediments within which, whole, undeformed blocks may float, or may contain blocks that are extensively deformed, with dipping and folded beds (Macdonald et al., 1993, Piper et al., 1997, Shipp et al., 2004).

3.2.2 Ponded Fan Systems

Submarine fan systems form at the termination of deepwater submarine channel systems, down-dip of submarine feeder conduits (anything from short-lived gullies to long-lived leveed fan valleys), submarine channel mouths or 'transition points' (Posamentier and Kolla, 2003, Posamentier and Walker, 2006, Deptuck et al., 2008). Such systems were originally thought to consist of flat-layered deposits (sheet sands) resulting from flow freezing due to depletion at the termination of channel-levee systems (Normark, 1970, Mutti and Normark, 1991). However, more recent studies have revealed that submarine fans are comprised of a series of extensively channelised sandy depositional bodies most commonly termed lobes (Nelson, 1992, Twichell et al., 1992, Piper et al., 1999, Adeogba, 2005, Gervais et al., 2006, Saller, 2008, Prelat et al., 2009, Prelat et al., 2010). Prelat et al. (2010) proposed a hierarchical naming system whereby the components within these fan systems can be recognised from the individual bed scale, through lobe elements, lobes and finally lobe complexes following the basic principle that one or more components are stacked to form the next component in the fan hierarchy (Figure 3.4). Recent authors have suggested the presence of more sheet-like elements towards the edge of the individual lobes and the development of hybrid flows at the fringe of the lobes (Haughton et al., 2009, Hodgson, 2009, Talling, 2013), whereas Twichell et al. (1992) show that the

distal deposits on the modern Mississippi fan are comprised of a series of channel bifurcations which appear to result from distinct channelised flows. They argue that this indicates that the flows travelling through these channels are not travelling as unconfined sheet flows. Talling (2013) observes hybrid beds, which take the form of cohesive debrites towards the distal ends of submarine fans, tend to occur more often when the depositional setting fluctuates leading to progradation and retrogression of the submarine fan systems. He argues that as the lobe systems prograde they deposit intervals containing extensive hybrid beds which are overlain by channel-levee facies from the proximal lobes and underlain by distal fan facies including thin-bedded turbidites. This succession is reversed during retrogression of the lobe complex.

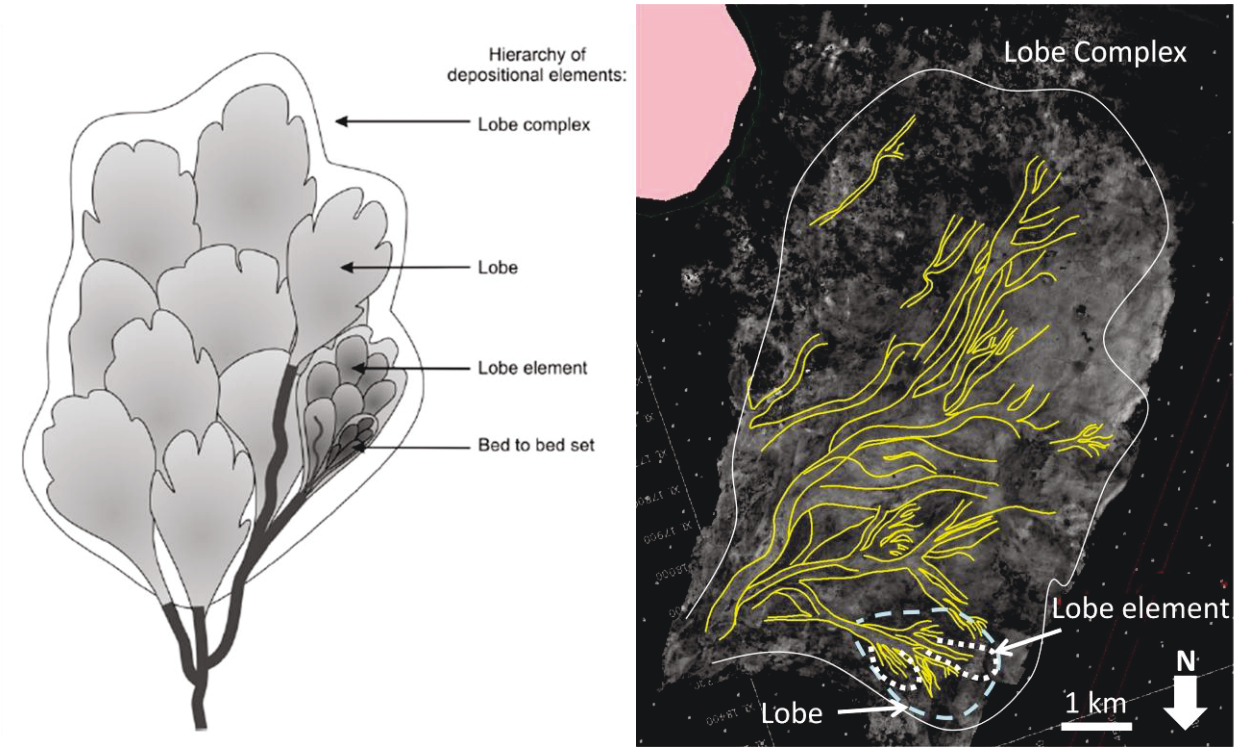


Figure 3.4 (a) Plan view of a typical deepwater submarine fan (from Prelat et al., 2009) showing the hierarchy of the depositional elements compared to (b) a typical fan found in the study area, note that the features can be recognised down to the lobe element scale.

In this thesis, the terminology used by Prelat et al. (2009) in the Karoo Basin, South Africa has been adopted throughout the study of deepwater fan systems; lobe elements, lobes and lobe complexes are all recognised in the seismic amplitude extractions (Figure 3.4). Lobe elements are formed of genetically related beds which are below the resolution of the seismic data. These lobe elements are defined as having lengths and widths in the order of a few kilometres and exhibit lateral changes in amalgamation and bed stratification. They are typically deposited within topographic lows which are generally established by older lobe element deposits either through compensational stacking or through the migration and instability of small-scale distributary channels (Prelat et al., 2009). Lobe elements combine to form lobes which are normally elongate in a downslope direction with their length up to twice their width (Figure 3.4). Prelat et al. (2009) record average mean length of 27 km, width of 13 km and thickness of 14 km with the volume estimated to range between 0.2 - 3.5 km^3. Again, these lobes can stack with spatial shifts in the centre of the lobes recorded through time and stacking at the scale of several kilometres observed in outcrop sections. These lobes stack to form discrete lobe complexes (Figure 3.4) which are commonly referred to as submarine fans

in older literature (for example Johnson et al., 2001). In outcrop data these discrete systems are generally separated by thick hemipelagic claystones indicating a sediment starvation to the area and that the systems are ultimately controlled by allogenic processes such as relative sea level changes.

Mutti and Normark (1987) were some of the first authors to recognise that deepwater fans which develop in relatively confined setting have distinctly different morphologies from those which develop in larger unconfined settings, with the former containing more sand-rich sediments and the latter being comparatively finer-grained. Subsequently, many authors have gone on to look specifically at fans that form in ponded settings, particularly those located in the Gulf of Mexico (Winker, 1996, Beaubouef and Friedmann, 2000, Steffens et al., 2003, Al Ja'Aidi et al., 2004, Adeogba, 2005, Covault and Romans, 2009b, Gamberi and Rovere, 2011, Prather et al., 2012). Building on this body of work Gamberi and Rovere (2011) identify four types of submarine fan system: basin plain fans, transient fans, terminal fans and ponded fans (Figure 3.5). This thesis is primarily concerned with ponded fans and transient fans. These two types of fan both form on the slope due to sediment interactions with the slope topography and topographical barriers (Figures 3.5 and 3.6). Ponded fans occur where turbidity currents encounter completely enclosed basins causing strong confinement of the sediment gravity flows whereas transient fans are controlled by a reduction of the slope along a stepped slope profile without major ponding. Transient fans are connected to a deeper base level and the majority of the sediment is ultimately deposited in terminal fans (Adeogba, 2005, Gamberi and Rovere, 2011).

Whilst it is generally accepted that the large-scale external controls on deepwater depositional systems which occur along continental margins are sediment supply, climate, regional basin tectonics and relative changes in sea level (Figure 3.8; Posamentier et al., 1988, Posamentier and Vail, 1988, Mutti and Normark, 1991, Reading and Richards, 1994, Johnson et al., 2001) these controls appear to have less influence on the fan morphology and lithology when the sediments reach a confining basin (Deptuck et al., 2003, Steffens et al., 2003, Covault and Romans, 2009b, Gamberi and Rovere, 2011). Individual lobe-scale characteristics are controlled by the interactions between intra-basinal controls such as topography and extra-basinal, controls such as climate and tectonics (Figure 3.8; Fildani and Normark, 2004, Stouthamer and Berendsen, 2007, Prelat et al., 2009, Groenenberg et al., 2010, Prélat et al., 2010). Steffens (2003) argues that the sediment delivery system and the receiving basin configuration become the primary factors influencing the fan morphology, thus incorporating the work carried out by Reading and Richards (1994) who proposed that the dominant grain size, sediment flux and the nature of the feeder system had the most influence on the submarine fan morphology. Gamberi and Rovere (2011) place more emphasis on the influence of the slope angle, seafloor topography and deformation of the slope in the development of internal architecture (see also Parsons et al., 2002, Deptuck et al., 2008, Eggenhuisen et al., 2010). Deptuck et al. (2008) cite even more factors as having a large influence on the internal fan architecture, including:

1. flow properties (volume, duration, grain size, concentration and velocity);
2. number, frequency and duration of flows;
3. gradient change and sea floor morphology at the feeder conduit;

4. lobe lifespan prior to avulsion and abandonment and;
5. feeder channel stability and geometry.

Covault and Romans (2009a) and Deptuck et al. (2008) both state that changes in these conditions normally result in changes in areal characteristics of the fan system (such as length-to-width and length-to-area ratios). Covault and Romans (2009a) observe that in settings where large volumes of sediment have entered the basin, the volume was confined by the basin margins and the fans were unable to expand spatially resulting in thick sediment sequences. In contrast, if less sediment reached the basin, the sediment did extend out to the basin margins resulting in a thinner than average sediment package. However, Deptuck et al. (2008) argues that these changes are mainly linked the location of the fans; those that are connected to shelf-incised canyons are longer, thicker and wider, tend to occur in more basinward settings and appear to be more architecturally complex, whereas those fed by slope gullies or erosive channels tend to result in smaller depositional bodies with poorly developed lobes which are clustered towards the toe of the slope. Covault and Romans (2009b) also recorded "healing" in the sediment packages whereby once near-shore basins were filled to capacity (i.e. the bounding ridges) the subsequent turbidity currents spilled into a seaward basin.

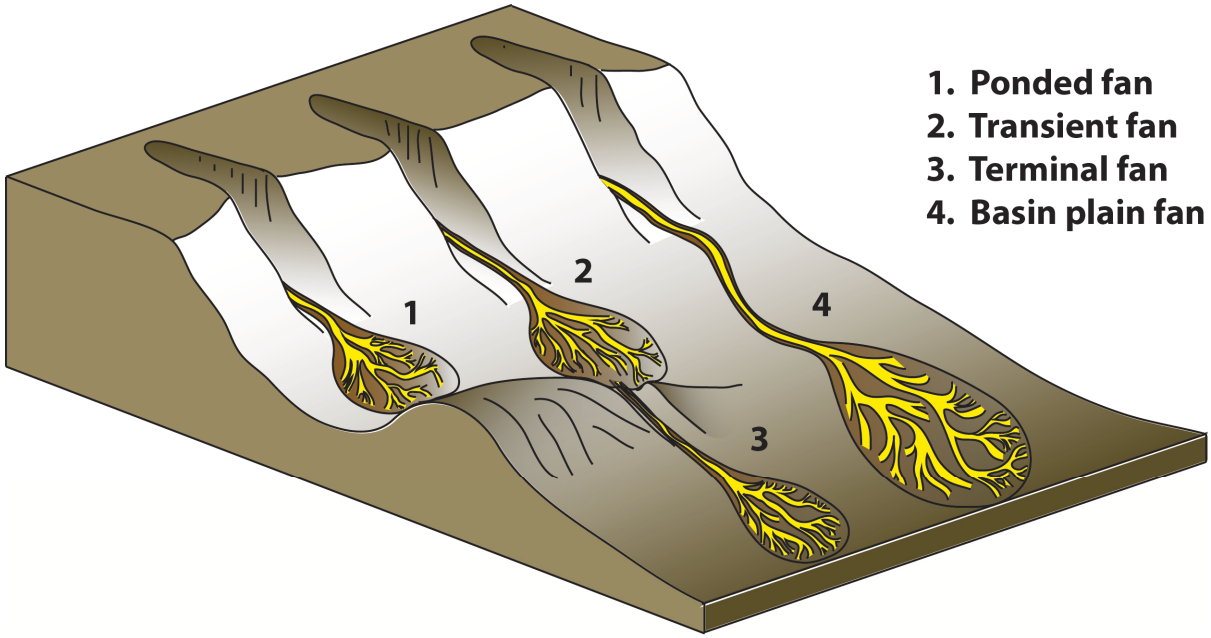


Figure 3.5 Cartoon showing the different types of submarine fans that develop along the continental margin depending on the slope topography (Modified from Gamberi and Rovere, 2011). Vertical scale highly exaggerated; approximate horizontal scale of 200 km.

Confined basin settings commonly occur in areas where complex seafloor has been generated, for example by active faulting or the diapiric movement of salt and mud (Ori and Friend, 1984, Brunt et al., 2004, Gamberi and Rovere, 2011, Jones et al., 2012). This topography generates depressions on the seafloor, commonly referred to as mini-basins, which have the potential to act as confining basins trapping all, or a proportion of the sediment that enters the basin until the negative topography is eliminated (Figure 3.6). This effect was first described in detail by Winker (1996) who noted that mini-basins in the Gulf of Mexico were regularly filled to their topographic spill point with the subsequent sediment by-passing the basin and entering those further seaward (see also Prather et al., 1998, Badalini et al., 2000, Beaubouef and Friedmann, 2000, Sinclair and Tomasso, 2002, Brunt et al., 2004). It is possible for the process to occur several times

within the same series of mini-basins with new accommodation space generated by changes in topography (Prather et al., 1998, Badalini et al., 2000).

When turbidity currents meet confining topography, such as that shown in Figure 3.6, depending on the kinetic energy which the current contains the sediment carried may be ponded behind the confining topography or the energy may enable all, or part of the current to surmount the topography (Sinclair and Tomasso, 2002, Clark and Cartwright, 2009, Mayall et al., 2010, Jones et al., 2012). Experimental results have shown that the height of the obstacle that a flow encounters has an impact on whether the flow is able to overtop the obstacle, or become ponded. Rottman et al. (1985) found that turbidity currents were able to overtop obstacles where the height of these was up to 2.5 times the body thickness of the flow and similarly Muck and Underwood (1990) found that that turbidity currents were able to overtop obstacles where the height of these was up to 1.5 times the head thickness (see also Kneller and McCaffrey, 1999).

The grain size and stratification of the sediments found within the ponded setting also varies according to the height of the confining topography. It is well documented that turbidity currents develop vertical gradients in suspended sediment concentration which in turn generates stratified flow both in terms of density and grain size (e.g. Middleton, 1993, Kneller and McCaffrey, 1999). Concentration and grain size are both greatest in the lowest proportion of the flow and decrease exponentially with height in the suspended sediment column, with finer material fairly well distributed throughout the flow (Kneller and Buckee, 2000). This means that in basin plain fans and terminal fans, deposits will decrease in thickness and grain size away from the sediment entry point as energy is lost through expansion and deposition (Figure 3.5; Middleton, 1967, Scheidegger and Potter, 1971, Garcia, 1994). However, when turbidity currents encounter a barrier to the flow, as in ponded and transient fans (Figure 3.5), only the highest sediment in the flow and hence the most dilute and finest sediment carried by these turbidity currents will be able to overcome the barrier and fill the basin. Brunt et al. (2004) state that as this process continues, and the upstream basins fill, progressively coarser sediment will enter the down-stream basin leading to the generation of a coarsening upwards sequence and a partitioning of grain sizes between subsequent basins. So the amount of partitioning that occurs between the basins and the grain size of the sediment escaping over the confining topography and into the subsequent basin in a ponded mini-basin setting is therefore dependent upon the effective confinement of the basin (i.e. the ratio of sill height to flow height), the intensity of the stratification within the flow and the kinetic energy of the flow. Through a series of experiments Brunt et al. (2004) concluded that if the basin was completely confined, this would cause the turbidity current to become trapped in an upstream basin generating a sedimentary sequence dominated by sand with a thick mud cap. However, if the basin was only partially confined, then at first the dilute upper fraction of the turbidly current would overtop the topography leading to a coarsening up sequence in the lower basin, but also in the upstream basin as progressively less mud is retained. Therefore, if this partial separation is retained by either upstream subsidence or the growth of the confining barrier between the basins then the coarsest sand-rich material will be preferentially retained in the upstream basin. If this does not occur and the basin fills to spill point, then essentially a full turbidity current will enter the subsequent basin (Brunt et al., 2004).

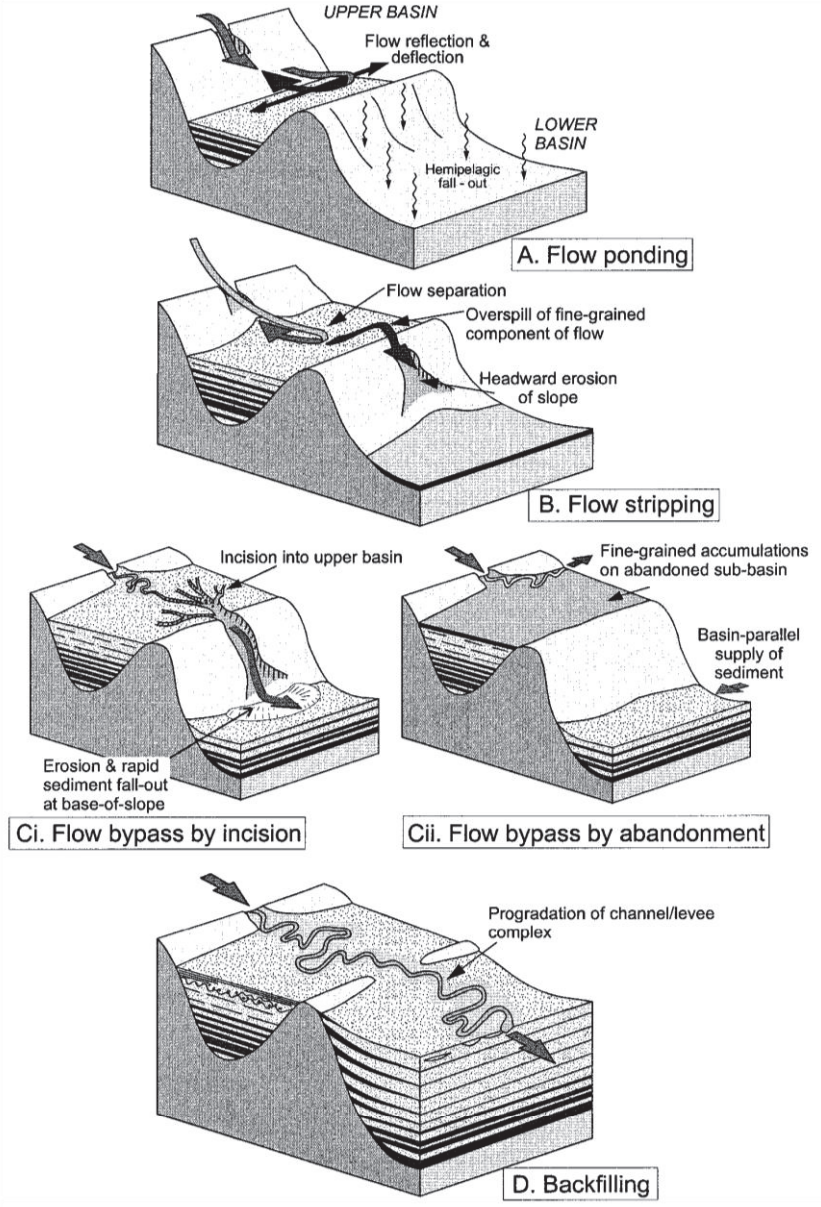


Figure 3.6 Cartoon showing the different methods by which ponded sediments can be deposited within a confined basin (Sinclair and Tomasso, 2002).

Sinclair and Tomasso (2002) use these ideas along with outcrop observations from Tertiary Alpine basins and subsurface data from the Gulf of Mexico to identify four clear and predictable phases of filling within confined deepwater basins assuming a steady sediment supply with no changes in the type of sediment entering the basin or sea level (Figure 3.6). These phases are as follows:

1. flow ponding whereby the initial flows are completely trapped and deposit a laterally continuous thick deposit of ponded mudstone and sandstones,
2. flow stripping, occurs where the finer, dilute proportion of sediment escapes over the edge of the basin leading to an increased sand/mud ratio in the basin. Then,
3. flow bypass occurs where the basin is filled to its spill point causing channel abandonment and the feeder channels to switch away from the basin or channel incision as the flows traverse across the now filled basin, this is followed by the final stage,

4. the area is blanketed due to rise in base level. There is also an important distinction to be made between ponded accommodation and healed slope accommodation when looking at these systems.

Hay et al. (2012) define the difference as ponded accommodation being associated with sheet sand deposition whereas healed slope accommodation being associated with alternations of channels, sheets and mass transport complexes (see also Booth et al., 2003, Prather et al., 2012).

3.2.3 Channel Complex Systems

Turbidite channels are commonly recognised features of the deepwater environment and represent important hydrocarbon reservoirs within many continental slope systems throughout the world (for example Beydoun et al., 2002, Mayall and O'Byrne, 2002, Weimer et al., 2004, Porter et al., 2006, Wynn et al., 2007, Cross et al., 2009, Armitage et al., 2010, Mayall et al., 2010). The terminology used to describe these deepwater channel systems varies extensively throughout the literature with many different schemes proposed covering a variety of different scales observed within seismic data and at outcrop scale, for example geobody, channel complex, channel storey, and channel complex set (Gardner and Borer, 2000, Navarre, 2002, Sprague et al., 2005). Added to this the clear definition of a 'channel' in the deepwater is not straightforward, Wynn et al. (2007) highlight the two main issues with the present commonly-used terminology: channels often gradually become termed canyons upslope, and they have highly variable morphologies, dependent upon the topography they encounter and the nature of the material being carried they can be termed V- or U-shaped in cross-section and occur with or without depositional levees (Shepard, 1965, Clark and Pickering, 1996a, Clark and Pickering, 1996b, Mayall et al., 2006). However, canyons can normally be recognised as separate features from deepwater channels as they typically connect directly to the shelf edge and, as such, occur primarily on the upper slope. They can be recognised as narrow, V-shaped cuttings which typically have a greater cross-sectional area and higher axial gradients than their down-slope channel counterparts (Wynn et al., 2010).

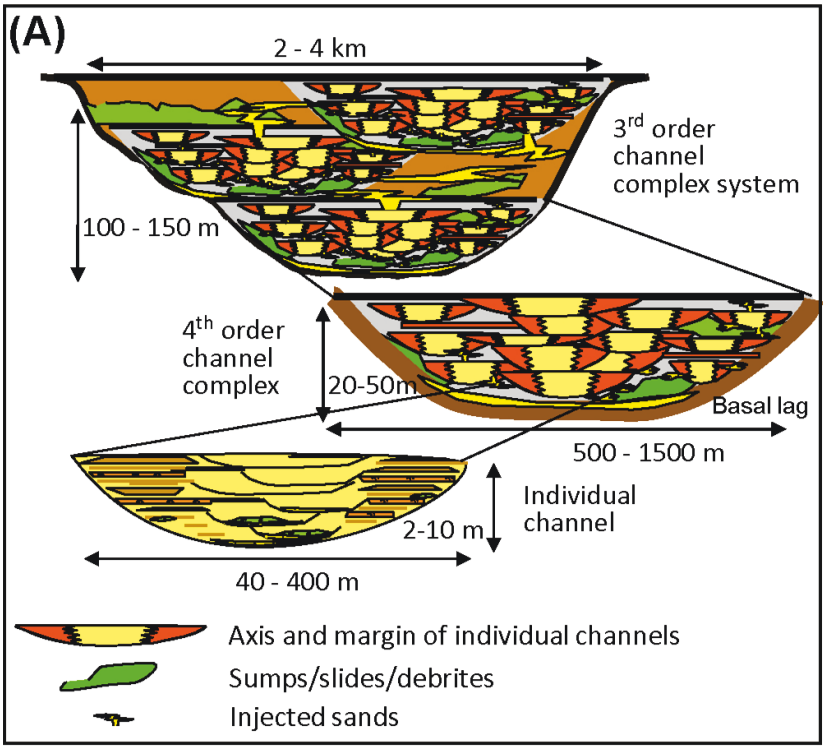


Figure 3.7 General model for the channel complex systems used throughout this thesis showing a third order channel complex system with a dominantly erosional base, several fourth order channel complexes in which axis and margin areas can be recognised and individual channels (modified from Mayall et al., (2006) and taken directly from Jones et al. (2012)).

In this thesis, the terminology outlined in Mayall et al. (2006) is used to describe the channel complexes seen in the mini-basin. This terminology is based on the sequence stratigraphic setting of the channels; they are largely confined within an erosional third-order basal bounding surface containing within it a series of fourth-order channels within which individual channels can be further recognised (Figure 3.7). Whilst not all channel systems of this size seen within the literature are erosional, the systems described within this thesis do conform to this broad definition. The third-order sequence boundaries used to define the main basal channel surfaces refer to the stratigraphic relationship these systems have with the major third-order maximum flooding surfaces; the majority of the third-order channel fill are associated with periods of third-order eustatic lowstand (Mayall et al., 2006). The sequence-stratigraphic fourth-order channel systems and individual channels within these erosional cuts are harder to identify on seismic data with confidence. However, the final fourth-order channel cuts deposited by a system can generally be recognised from high amplitudes in seismic amplitude extractions within the dataset used for this study.

3.3 Regional Boundary Condition Controls on Deepwater Depositional Systems

Changes in the regional boundary conditions surrounding a mini-basin act over an extended area and tend to occur over a longer period of time than the individual deepwater systems, resulting in gradual changes. The key regional parameters which act on deepwater systems include: variations in the source and rate of sediment supply, relative eustatic sea level change, climate change and regional basin tectonics (Figure 3.8; Posamentier et al., 1988, Posamentier and Vail, 1988, Mutti and Normark, 1991, Reading and Richards, 1994, Johnson et al., 2001, Kolla, 2007). Variations in these boundary conditions within the region will affect the facies and the distribution of sediments in deepwater basins.

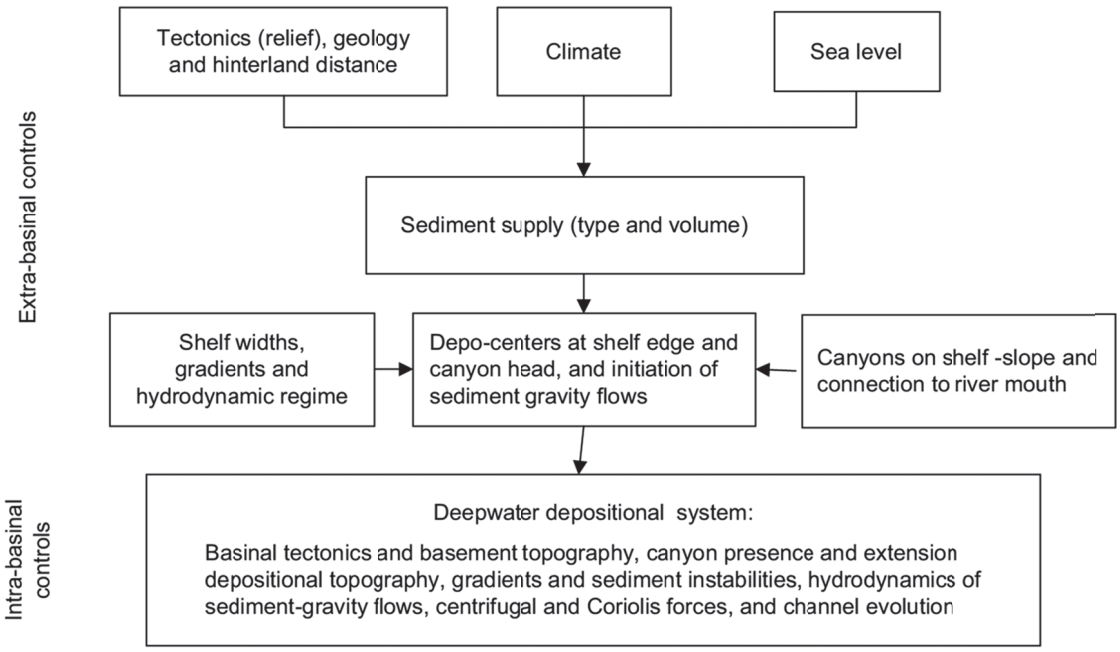


Figure 3.8 Flow chart showing how intra- and extra-basinal controls can impact deepwater systems. Image taken directly from Kolla (2007).

3.3.1 Sediment Supply

Sediment supply can have a significant effect on the type of deposits forming in a deepwater environment. It is controlled mainly by sediment source area and the processes which initiate the flow of sediment to the deepwater. Turbidity current generation depends on the initiating process which supplies suspended sediment into the water column (Normark and Piper, 1991). This initiation process generally takes three forms: slumping at the shelf edge, the discharge of rivers or subglacial melt water via hyperpycnal flows, or the suspension of coastal, shelfal or upper slope sediments by oceanographic processes including storms, tides and internal waves. All of these processes can form classical graded turbidites (Piper and Normark, 2009). The different processes generate turbidity currents composed of different types of sediment, but there is no simple relationship between the process that supplies the sediment to a region and the type of deposit that is produced. Work on Quaternary and Holocene systems indicates that events triggered by sediment failure tend to generate either mass transport deposits or proximal deposits in canyons, whereas direct freshwater flow tends to result in enhanced mud deposition in channels whilst only initiation by storm re-suspension of marine sediment generates the more traditional turbidites and massive sand filled channels (Piper and Normark, 2009). However, this work is based on recent sediments deposited during glaciations and/or modern high sea level conditions and, as such, may not be applicable to other times in the geological record. The clastic sediments that make up channel complexes and deepwater fans observed within the study area are sourced from material discharged into the area from the flow of the paleo-Congo (Zaire) River system (see Chapters 2 and 8), but more details of the sediment delivery mechanisms are unknown.

3.3.2 Sedimentation Rate

Sedimentation rate can have a significant impact on the type of system deposited within a basin and the resulting the morphology of that system (Broucke et al., 2004). This is particularly obvious in deepwater channel complexes where high sedimentation rates tend to generate stacked channel-levee complexes, whereas low sedimentation rates produce mixed turbiditic and hemipelagic deposits with erosive channel complexes and lobe formation down-dip. Sedimentation rate can also impact the topography of an area with the topography generated by active growth structures becoming buried during periods with high sedimentation rates (Burbank and Vergés, 1994, Burbank et al., 1996, Broucke et al., 2004, Shaw et al., 2004, Shaw et al., 2005). When the ratio of sedimentation to deformation is equal to or greater than one, sediment will bury the seafloor topography causing sedimentary depositional systems to be controlled by previous deposits; whereas when the ratio of sedimentation to deformation is less than one, topography will have a greater control on the sediment distribution within the basin (Broucke et al., 2004).

3.3.3 Climate Change

Climate change can have a marked effect on the type of sediment formed in the deepwater environment. One of the most obvious effects of a large scale change in climate is a change in eustatic sea level which controls the volume of sediment trapped on the shelf and hence changes the amount available to be transported to a deepwater setting (Broucke et al., 2004). During sea level lowstands, and as sea level falls, more sediment can reach the deepwater environment tending to accumulate at the base of the slope, whereas in highstands the deepwater is relatively sediment starved. However, this relationship is not always as clear-cut. For example in a study of the Lower Congo Basin, Broucke et al. (2004) show that the Burdigalian to Langhian (mid-Miocene) turbidite system which developed during a eustatic sea level rise displays a more erosive character than the Chattian (late Oligocene) system which developed during a major lowstand. Contrary to this, at present day in the Amazon system, the high sea level prevents the Amazon canyon in the deepwater from connecting to the Amazon river mouth and hence very little sediment reaches the Amazon fan (Broucke et al., 2004). Were the sea level to fall, then sedimentary depocentres from the Amazon River would move closer to the shelf edge resulting in turbidity currents and sediment reaching the deepwater channels. Kolla (2007) suggests that a minimum drop in sea level of 45 m is necessary for a river mouth to supply sediment to a canyon head and generate gravity flows. He argues that this increase in sediment can result in deepwater channel avulsions with extensive sand-prone high amplitude reflection packets (termed HARPs) indicative of sand-rich peak flows, underlying avulsed channel systems (Pirmez and Flood, 1995, Pirmez et al., 1997).

Climate change does not simply manifest itself in varying sea levels. It can also affect the water flux and sediment supply into a deepwater system with changes in rainfall, physical erosion rates and water chemistry modifying the sediment supplied to the deepwater (Broucke et al., 2004). Kolla (2007) suggests that increased rainfall in the Amazon River catchment area during the last glacial interval correspond to a higher sediment supply into the deepwater which in turn generates more turbidity currents and hence a greater

number of channel avulsions. A greater volume of sediment transported into a system can also affect the morphology of a deepwater system, for example leading to increased levee development.

3.4 Local Boundary Condition Variations – Topographical Changes

Local changes in topography can be caused by several processes, including salt movement, mud diapir movement and structural activity such as faulting or folding. Each of these can result in the formation of growth structures on the seafloor, inducing localised gradient and topographical change. Whilst the processes which drive this change in topography may vary, the response of deepwater sedimentary systems to the change in gradient within a basin can be similar. Topographical changes will affect the morphology of deepwater sedimentary deposits in different ways including triggering channel avulsions, inducing deflections in channel paths, altering the levee characteristics, altering width and depths of channel systems and forcing the system to pond (Gee et al., 2001, Gee and Gawthorpe, 2006, Gee et al., 2007, Clark and Cartwright, 2009, Mayall et al., 2010, Clark and Cartwright, 2011). As will be explored further in this thesis, structurally induced bathymetric changes can also influence the distribution of fans and mass transport complexes within the slope setting.

Channel avulsions can occur due to topographic change. However, Gee and Gawthorpe (2006) suggest that avulsion events related to salt activity specifically are rare because deepwater channels rapidly incise and establish a position on the slope. They imply that the ability of a channel to avulse is linked to the rate of movement of a structure and the maximum dip direction of the slope. This theory is supported by the work of Clark and Cartwright (2009) who found that avulsion was associated with a decrease in channel depth where a channel system exited a fold belt. This is commonly observed in actively deforming settings and is attributed to structural growth locally increasing the slope gradient leading to locally increased current velocities which trigger avulsions (Ferry et al., 2005a, Gee and Gawthorpe, 2006). Similar responses have also been observed in the vicinity of folds and mud volcanoes (Gee and Gawthorpe, 2006, Callec et al., 2010).

Morphological characteristics of deepwater channel systems vary as a result of local topographic change, the most commonly discussed characteristics include: channel sinuosity, channel width, channel depth and meander-arc width. Channel sinuosity has been shown to decrease over actively growing structures whilst the width to depth ratio increases and the seismic amplitude decreases. Where slope gradient is highest, low sinuosities are observed; whereas downslope of the structures, where slope gradient decreases, channels commonly broaden out and have higher sinuosities and moderate seismic amplitudes (Ferry et al., 2005a, Gee and Gawthorpe, 2006, Clark and Cartwright, 2009, Wood and Mize-Spansky, 2009). There are examples where this relationship does not hold, for example Cronin et al. (1994) record localised increases in channel sinuosity on steeper slopes in the Almeria Canyon, but this has been attributed to inherited sinuosity from a lower gradient, with sudden localised uplift accentuating the sinuosity. Ferry et al. (2005a) found that a local increase in gradient caused by fault activity generated straighter, narrower channel systems with more pronounced basal incisions and a twofold increase in the fill thickness. Whereas Gee et al. (2007) observed a

different reaction in channels offshore Angola with flows accelerating and becoming more erosive as they crossed a locally steeper section of the slope, causing them to increase in sinuosity or incise more in order to reach equilibrium. Pirmez and Flood (1995) suggest there is a limit to the amount this can be achieved by increasing sinuosity as the likelihood of loop cut-off increases, leading to a peak sinuosity beyond which only incision can be effective.

Channel widths and thicknesses also respond to local topographical changes; width decreases and depth increases as the channel systems incise in response to topographical uplift, often generating scalloped walls where the increase in gradient is the highest, then broaden and shallow in the subsequent sections (Deptuck et al., 2003, Huyghe et al., 2004, Ferry et al., 2005a, Ferry et al., 2005b, Gee and Gawthorpe, 2006, Gee et al., 2007, Clark and Cartwright, 2009). Channel systems have been observed to broaden and shallow rapidly as they enter slope depressions flanking salt intrusions where there is a localised decrease in the slope gradient. These channels also have less irregular basal indicators in seismic data and no incised notches (Gee and Gawthorpe, 2006). However, this response is not consistent, for example Wood and Mize-Spansky (2009) note a decrease in channel depth upstream of a mud volcano then an increase in channel depth and a decrease in width downstream of the mud volcano as the channel incises.

In regions where active topographic change is occurring, changes in the typical passive margin sequence from the continental margin to the basin of canyon, channel levee systems, then lobe deposition have also been observed. Callec et al. (2010) have recorded examples where active topographical change results in a reorganisation of the system such that channel levee systems develop upstream of canyon systems, with the sediment eventually deposited in channelised lobes. Channelised lobes and submarine fan systems are generally found basinwards where the deepwater system deposits the entrained sediment. However, ponded sediment and lobes can develop higher on the slope as a result of structural deformation and the creation of accommodation space (Broucke et al., 2004, Callec et al., 2010). This is also found in fill-to-spill salt mini-basins where basins fill with sediment (forming ponded deposits) until they reach the spill point of that basin, where channels erode the sill and fill successive basins downslope (see also discussion in Section 3.2.2; Satterfield and Behrens, 1990, Prather et al., 1998).

In addition to the changes in morphology, deepwater deposits can deflect and migrate in response to topographic activity (Cronin, 1995, Clark and Cartwright, 2009, Mayall et al., 2010). Channel systems migrate off actively growing structures shifting away from the axis of uplift and towards topographically lower regions. This produces lateral accretion surfaces adjacent to the structure and erosion on the far side of the channel system (Clark and Cartwright, 2009, Mayall et al., 2010). Channel systems also deflect from active structures resulting in a change in the channel pathway often resulting from obstruction by a feature at a high angle to the original channel course (Cronin, 1995, Clark and Cartwright, 2009, Mayall et al., 2010).

Hay (2012) observe changes in the spatial distribution and location of successive depositional fan lobe complexes in response to local changes in topography. They observe that changes in the local gradient within a basin can impact on the location, size and degree of cannibalisation of the depositional lobes within that basin. These systems behave in a similar manner to channel complex systems in response to active

structural growth; responding to topographical highs in the area by progressively shifting away from them and by deflecting from the structures which are thought to have had the highest topographical relief. They also observe an increase in the number of lobes and a corresponding decrease in lobe area through the system, although they attribute this to possible changes in the sediment supply to the fan system.

3.5 Summary

This literature review has summarised the variety of sediment distribution systems found within a deepwater setting and how these systems respond to changes both external to the basin (i.e. climate variations and changes in sediment supply) and internally within the basin (such as changes in the bathymetric relief). The response of channel complex systems to changes in the seabed relief of basins internally has been well-documented in the literature, but the effect which these changes have on fan complex systems and MTC deposits is less well-documented. Likewise, few studies have attempted to investigate in a more quantitative way the link between structural growth and the changes in deepwater systems, which is the focus of this thesis. The key themes revealed from this literature review have been summarised in Table 3.2 and will be explored in further detail in the subsequent chapters.

Issue	Key Literature and Themes	How is it examined?
Evolution of salt-controlled **structural growth** within mini-basin	**Chapter 2** and **Chapter 4** • Detailed understanding of the mini-basin evolution is required to fully understand the impact this can have on sedimentary systems • Strain analysis can highlight periods which have been subjected to greater structural growth	**Chapter 5** • A regional restoration, isopach analysis, sediment accumulation analysis and strain analysis within mini-basin • Guided by restoration algorithms and previous work on strain in literature
Differentiation between types of **MTC deposits**; internal characteristics and spatial distribution	**Section 2.3.1** • Large variety in the characteristics of MTC deposits • Slides, slumps and debris flows form main end-member classifications • Can be attached or detached	**Chapters 6 and Chapter 8** • Regional debris flows and local slumps investigated • Temporal distribution within the basin linked to strain analysis and inferred structural growth
Bridging the gap in knowledge between conventional seismic studies of **deepwater fan systems** and outcrop data	**Section 2.3.2** • Studies concentrate either on outcrop data or conventional-resolution seismic data • Ponded fan lobe complexes occur throughout world, but internal details of these systems is still poorly understood	**Chapter 7** • High resolution seismic data allows imaging of deepwater fans in unprecedented detail • Characteristics of lobes and changes in the lobe complexes observed as they response to structural growth
Impact of structural movement on sediment distribution and characteristics	**Section 2.5** • Well-documented responses of channel complex systems to bathymetric changes • Few studies linking rates of structural growth to sediment distribution patterns • Few studies investigate response of MTCs and fan systems to structural growth	**Chapter 8** • Strain analysis used to quantify changes in line length on intra-basinal and basin-bounding structures then linked to the response of sedimentary systems • Response of MTCs, ponded fan complexes and channel systems to structural growth investigated

Table 3.2 A summary table showing four of the most important issues highlighted by this literature review and the preceding discussion of the structural history of the study area in Chapter 2. The table shows how these topics will be examined further in the thesis.

4 Data Sources and Methodology

4.1 Data Sources

The majority of the work in this thesis has been carried out using two seismic datasets acquired for the purpose of oil and gas exploration, offshore Angola. They have different properties, having been collected for different purposes, and are comprised of: (1) a high-resolution three-dimensional (3D) seismic dataset covering the Plutão, Saturno, Venus and Marte fields (PSVM) and, (2) a merged, regional dataset containing both two-dimensional (2D) and 3D data. The sedimentological analyses (Chapters 6, 7 and 8) utilise the high resolution PSVM dataset, and the regional dataset was used primarily for the structural analysis (Chapter 5). Well data, including petrophysical data and biostratigraphic data were also available. However, because the majority of the study is concerned with shallow sediments, within the top 2 s twtt of the data, the petrophysical logs were of limited use as the majority of them were collected within the deeper sediments. The biostratigraphic data provides a good control on the main horizon ages.

4.1.1 PSVM Survey

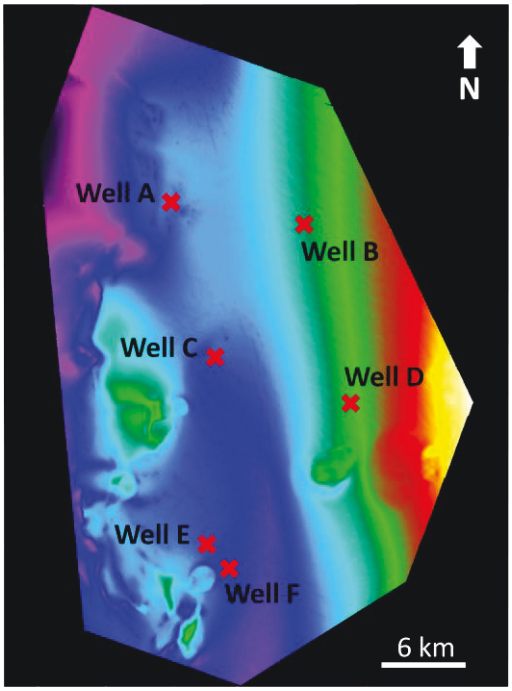


Figure 4.1 Extent of the PSVM data shown using the seafloor bathymetric profile, the six wells within the study area are labelled for reference.

The 3D seismic dataset covers an area of approximately 1,400 km^2 within Block 31, offshore Angola (Figure 4.1, see Chapter 2 for the regional location) and is higher resolution than 3D seismic volumes typically used for exploration and appraisal, with a sample rate of 2 ms as opposed to the more usual 4 ms of 'standard' 3D surveys. It also has a closer inline and crossline spacing of 6.25 m (bin size of 6.25 m) and hence has a particularly high resolution within the top two seconds of the dataset (Figure 4.2). The dataset has a variable frequency range with an overall average of 70 Hz generating a high vertical resolution (on average 9 m) which can increase to a vertical resolution of 5 m in the shallow sediments.

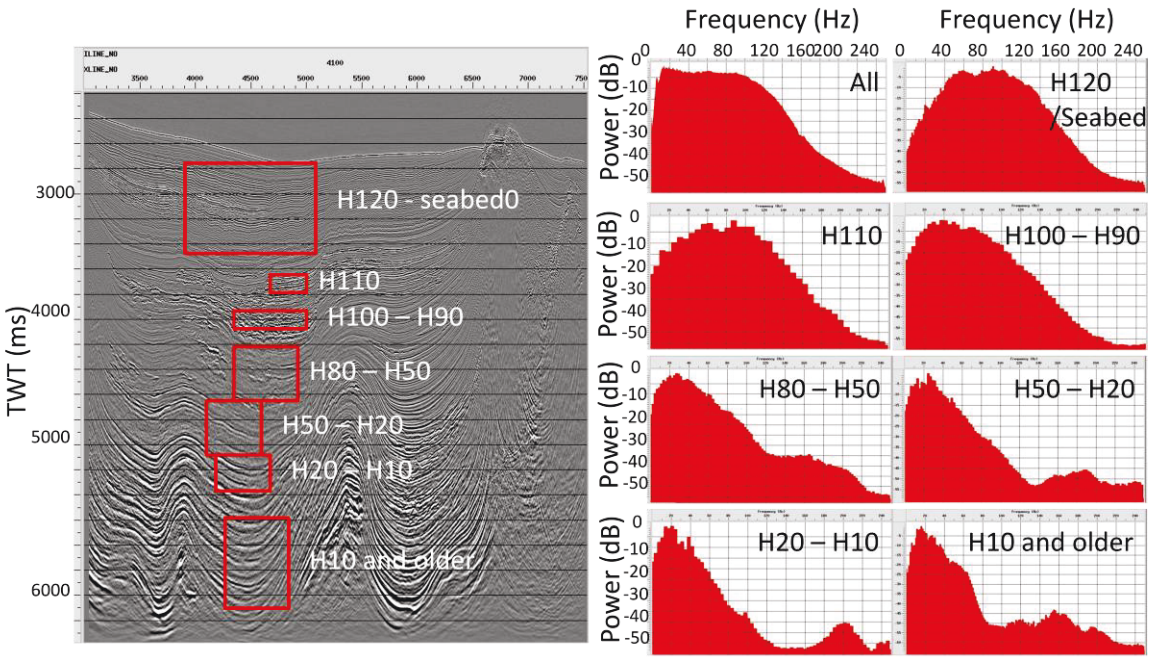


Figure 4.2 Analysis of the frequency change in the seismic data with depth; graphs show quality decreasing with depth.

The high frequency content of the data (and hence the high-resolution generated) is a function of the depth at which the source and receiver cables were towed (J. Verhaeghe, 2014, pers. comm.). In conventional seismic data these are normally towed at depths of between 8 m to 15 m in order to keep swell noise levels to a minimum. However, for this high-resolution survey they were towed at 4 m water depth resulting in a dataset rich in high frequency signals and relatively poor in low frequency signals (J. Verhaeghe, 2014, pers. comm.). The tow depth controls the useable frequency range by increasing the frequency at which the first ghost notch appears in the seismic frequency spectrum. Ghost events are those which occur due to reflections from the sea surface which contaminate the frequency spectrum generated and obscure the resulting images (Figure 4.3 (a)). The shallower the cable is towed then the higher the frequency at which the first ghost notch appears (for example in Figure 4.3 (b) the first ghost notch appears at 100 Hz). Conversely, this limits the amount of low frequency content in the seismic data (in Figure 4.3 (b) the lowest useable frequency appears at 20 Hz).

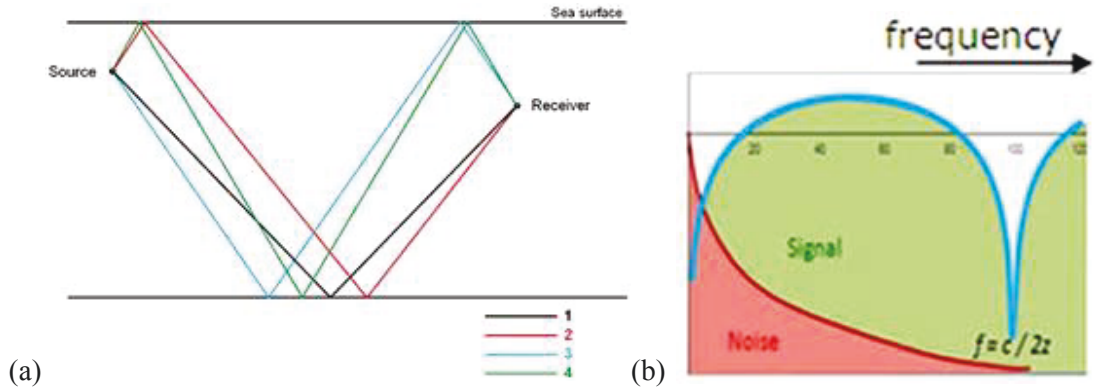


Figure 4.3 Diagrams showing how the high-resolution seismic dataset over the PSVM area was generated with (a) showing how the primary ray (event 1) pathway taken from the source array to the target receiver compares to those ghost reflector pathways (events 2, 3, and 4) generated from the sea surface which contaminate and obscure the seismic images of the subsurface, and (b) the impact of the ghost notches on the frequency of the signal received, in this example the first notch appears at 11 Hz frequency. Images provided by J. Verhaeghe, 2014, from BP internal documents.

Vertical resolution is much higher in the shallow data (Figure 4.2 and Table 4.1) which means that the imaging over these areas generates a much more accurate image of the subsurface. This enhances the ability to analyse the data using methods such as amplitude analysis. The majority of the sedimentological work carried out in Chapters 6 and 7 focuses on sediments deposited between the H20 and H70 horizons (deposited between approximately 17.29 Ma and 11.86 Ma) and the H100 to H110 interval (deposited between 8.29 Ma and 5.58 Ma).

Range	Frequency (Hz)	Average frequency (Hz)	Average velocity (m/s)	Average wavelength (m)	Average vertical resolution (m)
Seafloor – H120	40 - 140	90	1700	19	5
H110 – H100	20 - 130	75	1800	24	6
H100 – H90	10 - 100	55	2200	40	10
H80 – H50	0 - 70	45	2800	62	16
H50 – H20	0 - 70	45	3100	69	17
H20 – H10	0 - 50	25	3600	144	36
H10 and below	10 - 40	25	3700	148	37
Entire survey	10 - 130	70	2400	34	9

Table 4.1 Showing how the vertical resolution varies with depth through the section.

4.1.2 Regional Survey

The merged regional dataset comprises of nine 3D surveys covering Blocks 31, 15, 32, 16 and older 2D lines covering a larger area offshore Angola (Figure 4.4). It has an inline and crossline spacing of 25 m and as such a much lower horizontal resolution than the PSVM dataset. The vertical resolution of the 3D seismic data is also less than that of the PSVM 3D seismic data with an average vertical resolution of 15 m (Table 4.2).

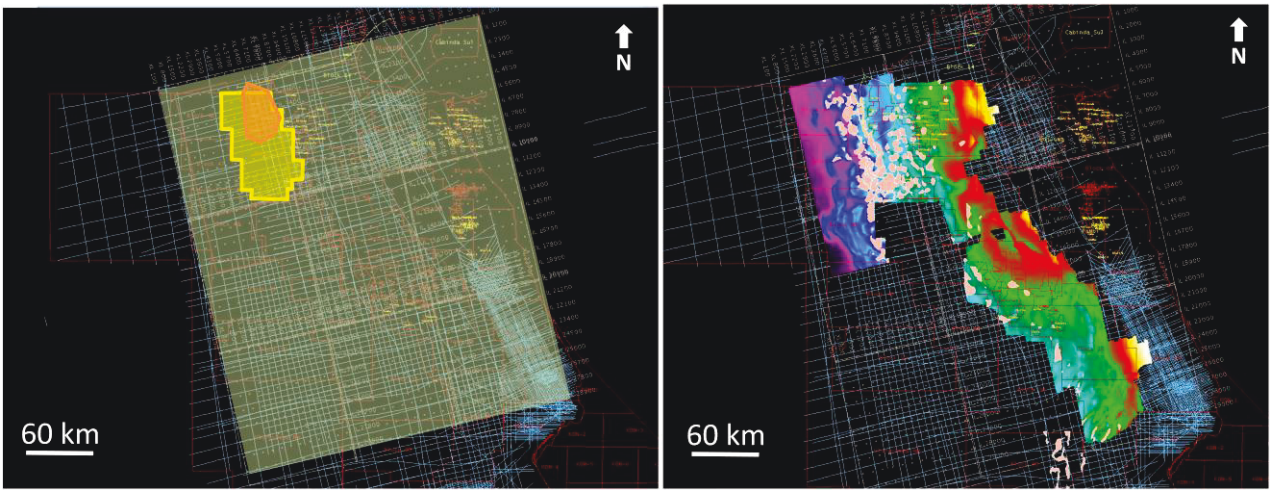


Figure 4.4 Extent of the regional dataset offshore Angola with the nine 3D surveys highlighted in green going from A to C north to south and 1 to 3 west to east, such that Block 31 (yellow) and the PSVM (orange) lie within 3D grid A1. Right-hand side shows regional bathymetry over the blocks that BP has access to and known salt in pink.

Regional magnetic and gravity data are also available, covering a very similar area to that shown by the 3D seismic data in Figure 4.4. The gravity data used in Chapter 5 has been subject to a high pass filter, filtering out wavelengths greater than 200 km to enhance the finer detail.

Range	Frequency Range (Hz)	Average frequency (Hz)	Average velocity (m/s)	Average wavelength (m)	Average vertical resolution (m)
Sea-level – H120	20 - 80	50	1700	34	9
H110 – H100	10 - 80	45	1800	40	10
H100 – H90	10 - 80	45	2200	49	12
H80 – H50	0 - 70	35	2800	80	20
H50 – H20	10 - 40	25	3100	124	31
H20 – H10	10 - 30	20	3600	180	45
H10 and below	10 - 20	15	3700	247	62
Entire survey	10 - 70	40	2400	60	15

Table 4.2 Vertical resolution of the regional data measured over a similar area to the PSVM with the same velocity values.

4.1.3 Horizon Ages

A range of horizons have been mapped across the two seismic datasets including horizons used directly from the BP database, horizons modified from the BP database and new horizons added to the existing database. The full set of horizons from H00 – H120 have been mapped within the PSVM dataset and tied to the wells that penetrate the area. Within the regional dataset, which was used for the bed length change analysis, there

are two additional horizons mapped between H00 and H10 (estimated to have been deposited at 25 Ma and 22.5 Ma) but the H20 to H50 horizons have not been mapped.

Horizon dating is based on calcareous nannoplankton events and bio-markers recorded within the well data and confidently dated within a world-wide framework (S. Payne, 2011, pers. comm.). The chronostratigraphy routinely used in the Angola area by BP, and hence used in this study, is based on two geological timescales produced by the International Commission on Stratigraphy (ICS) in 2004 and 2012. The version published in 2004 drew on calcarious nannofossil age events using results published in Lourens et al. 2004 for the Neogene and tables in Berggren et al. (1995a, b) for the Palaeogene. This work was superseded by the geological timescale produced by the ICS in 2012 where stratigraphic ages are given to two decimal places with error bars provided (Gradstein et al, 2012). Here, age dates are calibrated to magnetochrons and/or marine isotopes usually recorded from Ocean Drilling Program (ODP) and Deep Sea Drilling Project (DSDP) sites with calibrations given for up to eight global basins to show the diachroneity of some bioevents. This has been used to date the formations observed within the wells and then these have been tied to events in the seismic data. As well as errors arising from the accuracy of dating the nannoplankton events, errors are also introduced into the process where the dating is reliant upon well cuttings, as is the case in many of the wells in this study area, and through the process of tying the well data to the seismic data. Well ties are achieved through the matching of a synthetic seismic trace to the seismic data. The synthetic trace is generated through the integration of the velocity (sonic) and density logs to create an impedance contrast which in turn is used to generate reflection coefficients and synthetic wavelets which are combined into a synthetic seismic trace. The synthetic seismic trace is then matched with the peaks and troughs observed in the seismic data and hence the age of the main horizons can be back calculated. There are several stages where errors can be introduced into this workflow, with the main errors coming from inaccuracies in the location of the well or seismic line, poor quality logs or seismic data and incorrect modelling. The well tying process was undertaken internally within BP and has generated results that are consistent between the wells within the seismic volume. On this basis it is thought to be reliable, and the ages assigned to the horizons by BP have been used throughout this study.

The main horizons and their corresponding ages can be seen in Table 4.3. These were used during the study to investigate the sedimentation rates and rate of bed length change throughout the mini-basin (see Chapter 5). Note that the biostratigraphic data becomes more unreliable in the shallower sections (i.e. between H70 and the present day) as there are fewer true tops visible due to the sampling range; these horizons did not form the focus of the biostratigraphic studies as they are outside the reservoir sections (S. Payne, 2010, pers. comm.). However, only Well B and Well F have biostratigraphic data for the shallow sections above H70 and hence these were relied upon primarily to date the mapped units and constrain the growth rate and timing of deformation for the structures analysed within the mini-basin.

Horizon	Age (Ma)
H120	5.04
H110	5.58
P40	
P30	
P20	
P10	
H100	8.29
H90	9.68
H80	10.89
H70	11.86
H60	13.25
H50	*13.7*
H40	*14.4*
H30	*15.6*
H20	*16.5*
H10	18.26
Additional in regional data	22.5
Additional in regional data	25
H00	33.9

Table 4.3 Showing the horizon picks and ages available in the PSVM study area provided by BP. Those horizons which have been less reliably dated, with the ages interpolated between the reliably dated biostratigraphic picks are italicised.

4.1.4 Well Data

There are six wells within the PSVM area re-named Wells A – F for the purposes of this thesis (Figure 4.1). However, only Well B and Well F have biostratigraphic data for the shallow sections above H70 and hence these were relied upon primarily to date the mapped units and constrain the growth rate and timing of deformation for the structures analysed within the mini-basin.

The petrophysical logs recorded within the wells were also used during the sedimentological analysis with the shallow gamma ray logs in Well C studied in detail during the analysis of the ponded sediments in Chapter 7. The logs recorded within these shallow sections (i.e. deposited between H100 and H110) are much less reliable than those deeper in the wells as they are more likely to be washed out (E. Brown, 2013,

pers. comm.). Gamma Ray logs record the amount of natural gamma signal from radioactive formations, mostly contained within the clay minerals which form shale and mudstones. Thus, very simply, the amount of gamma ray radiation detected by the logging tool can give an indication of the amount of clay within a formation; high gamma ray signals indicate a high clay content (i.e. a mudstone) whilst low gamma ray signals indicate a clean, clay-free rock such as a quartzose sandstone.

4.2 Methods

The methods discussed in this section are those that are commonly used in all the chapters within this thesis, such as amplitude extractions, isopach maps and strain analysis. Those which are specific to each chapter will be discussed in more detail in the corresponding chapter. Background literature used to inform the choice of method used for the structural analysis is also discussed in detail here.

4.2.1 Seismic Interpretation

The horizons used in this study comprise a mixture of horizons used directly from the BP database, horizons modified from the BP database and new horizons added to the existing database in order to analyse specific areas in greater detail. Additional horizons have been mapped between the H100 and H110 horizons with the P10, P20, P30 and P40 horizons used to separate distinct packages within this ponded interval (Chapter 7). Additional horizons have also been mapped to investigate the regional and local mass transport complexes in more detail (Chapter 6).

The interpretation of the additional horizons and the faults within the PSVM dataset was carried out using PowerView® software. The mapping grid-size varied depending on the type of surface which was being mapped; the internal surfaces within the ponded section were generally mapped every 20th line (line spacing 6.25 m) whereas when mapping the complex base surface of the mass transport complexes mapping on every 10th line (spacing 6.25 m) was more appropriate. In areas where the relationships were more complex, such as the basal surface of some local mass transport complexes and in some areas within the ponded sections, the horizons were mapped on every line. The remaining horizon surfaces were then auto-tracked using the eZ-tracker within the PowerView® software. These surfaces were examined in the PowerView® software where the quality of the tracked picks was assessed visually. Depending on the quality of the auto-track horizons, smoothing and de-spiking algorithms were applied to the surface. Smoothing and de-spiking minimise the noise and minor surface irregularities on the horizons generated by the auto-tacking process. The quality of the smoothing was assessed to ensure that the surfaces had not been over-smoothed, which would have led to information being lost. The smoothing was applied incrementally with this routine carried out iteratively to check that the most accurate horizons were generated.

4.2.2 Seismic Attribute Analysis

Seismic attribute analysis allows the finer details of the geology from the sub-surface to be extracted from a 3D dataset by enhancing subtle phase variations and amplitudes in the seismic signal which may not be visible on the original seismic data (Chopra and Marfurt, 2008). There are many different types of seismic

attributes which can be extracted or derived from seismic data, such as dip, azimuth, amplitude extractions, coherency and spectral decomposition, each of which give a different insight into the properties of the subsurface (for some example see Taner et al., 1994, Marfurt et al., 1998, Liner et al., 2004, Chopra and Marfurt, 2005, Liu and Marfurt, 2007, Chopra and Marfurt, 2008). Attributes such as amplitude extraction record changes in acoustic impedance within the seismic signal, whereas attributes such as coherency, Sobel filter based edge detection, dip-azimuth and curvature are sensitive to seismic textures and morphology.

Those attributes which are sensitive to changes in the seismic texture such as coherency maps and dip maps have been used in Chapter 6 to investigate mass transport complexes. Whereas spectral decomposition, which focuses on amplitude variations, was carried out in Chapter 7 to investigate a section of the ponded sediments that were less coherent in conventional amplitude extraction maps. Details of the methodology followed to generate these seismic attributes is discussed in detail in the methodology section of the chapter corresponding to these features.

The seismic horizons have been used regularly throughout the thesis to generate a series of isoproportional amplitude extraction maps used to interpret the depositional features and geomorphological patterns contained within the mapped seismic units. Amplitude extractions are regularly used as a tool to analyse deepwater systems in 3D seismic data (for example Posamentier and Kolla, 2003, Gee et al., 2006, Deptuck et al., 2007, Mayall et al., 2010) and form the predominant method of analysis throughout this thesis because the high quality of the PSVM seismic data generates exceptionally high resolution amplitude extraction images.

Throughout the basin the geological features of interest and the stratigraphic timelines have been deformed during- and post-deposition, this means that the mapped horizons (H00 to H120) are not horizontal. Therefore, in order to investigate the intervals between the mapped horizons in more detail isoproportional sections are needed (Figure 4.5). These can be generated using the PowerCalculator® software where the shallow horizon is subtracted from the deeper horizon to give a thickness between two surfaces, and then divided by the number of widows to give an interval thickness:

$$Interval\ thickness, l = \frac{(H_1 - H_2)}{No.\ intervals} \qquad \text{(Eqn. 1)}$$

This interval thickness is then added to the base horizon to give a horizon surface, such as that shown in red on Figure 4.5. These new isoproportional horizons then form the top and base of intervals between which amplitude extractions were carried out.

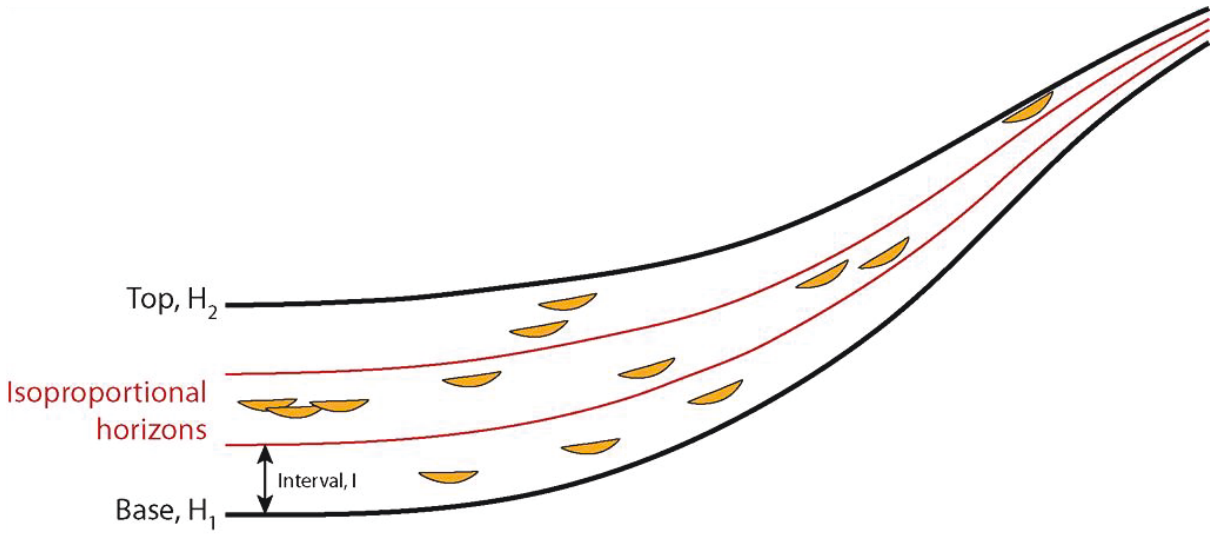


Figure 4.5 Diagram showing the definition of an isoproportional horizon. These were generated between mapped intervals of interest and used to produce amplitude extraction maps.

Amplitude extractions are one of the most commonly used processes to highlight sedimentary systems within 3D seismic reflection volumes. These highlight certain amplitudes within a portion of the seismic data to draw out information about the change in impedance within the subsurface. They can be carried out either on a single horizon or over a specified window between two horizons (Davies et al., 2007). In this study amplitudes were predominantly calculated over intervals, either using mapped seismic horizons, or isoproportional windows (see Figure 4.5 and the preceding paragraphs).

The root mean squared (RMS) amplitude extraction algorithm was used regularly throughout this work. It is applied to a section of the post-stack seismic volume and calculates the square root of the sum of the squared amplitudes divided by the number of samples taken within the window. This means that maximum positive and negative amplitude values are both highlighted. This method has the advantage of increasing the amount of information extracted from the dataset, but can result in an increase in the amount of noise generated when compared to some of the other amplitude extraction algorithms. However, squaring the maximum amplitudes does boost them, hence allowing a maximum opportunity to stand out above the background noise (Brown, 1999).

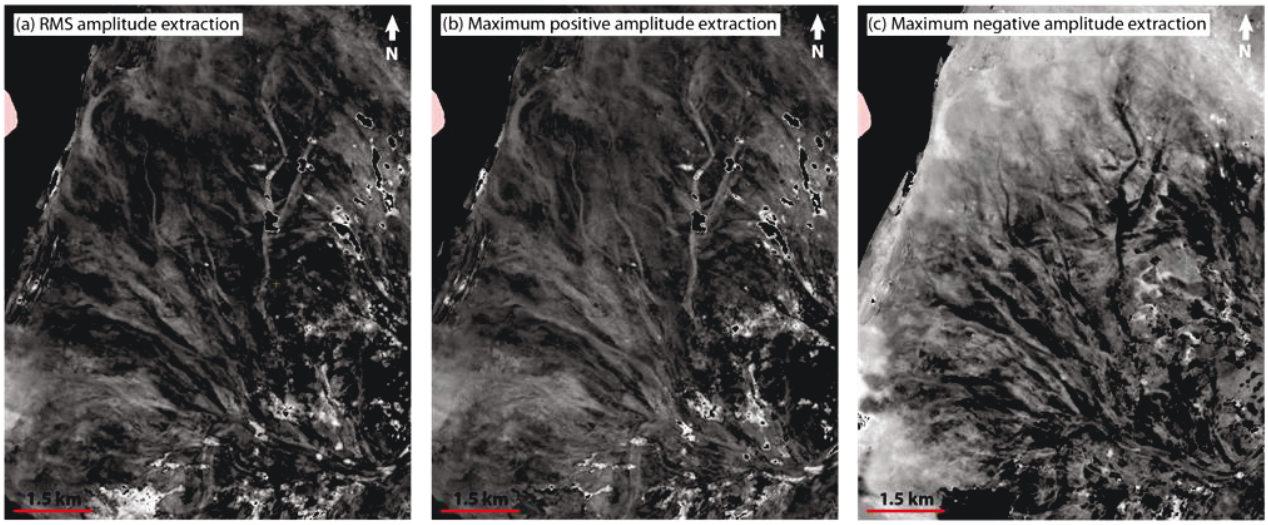


Figure 4.6 A series of amplitude extraction maps over the same 25 ms interval generated using three different types of algorithm: (a) a root mean squared amplitude algorithm is applied which calculates the square root of the summed amplitudes, (b) a maximum positive algorithm is applied to the same data highlighting the maximum positive amplitudes in white and negative amplitudes in black, and (c) a maximum negative amplitude extraction where the high negative amplitudes are white and positive amplitudes black.

Maximum positive and maximum negative amplitude algorithms, which calculate the maximum strength of the positive and negative amplitude respectively, within a given window were also tested but the RMS algorithm appeared to generate the most detailed images (Figure 4.6). When applied to seismic data, high-amplitude signals are generated by a high, positive impedance contrast between successive deposits thus normally indicating sand-rich sediments, whereas low seismic amplitudes indicate a low impedance contrast and hence mud-rich sediments (for normal polarity data).

4.2.3 Depth Conversion

The horizons have been picked in time-seismic data and then converted to depth surfaces using a depth variable velocity model (Figure 4.7). The three-dimensional velocity model was provided by BP and covers the PSVM dataset incorporating wells from within the area (see Section 4.1.4). Velocities within the subsurface start at approximately 1600 ms^{-1} in the shallow levels and increase to 3600 ms^{-1} at deeper levels (Figure 4.7). Velocities between 3600 ms^{-1} and 5000 ms^{-1} have been used in areas where salt is present, with the lower velocities indicating a transition between sediment and salt and the higher velocities true salt (Figure 4.7).

Whilst the majority of the analysis has been carried out using 3D time-seismic data, the depth converted surfaces have been used to generate isopach maps, which indicate true stratigraphic thickness, and sediment accumulation rate maps.

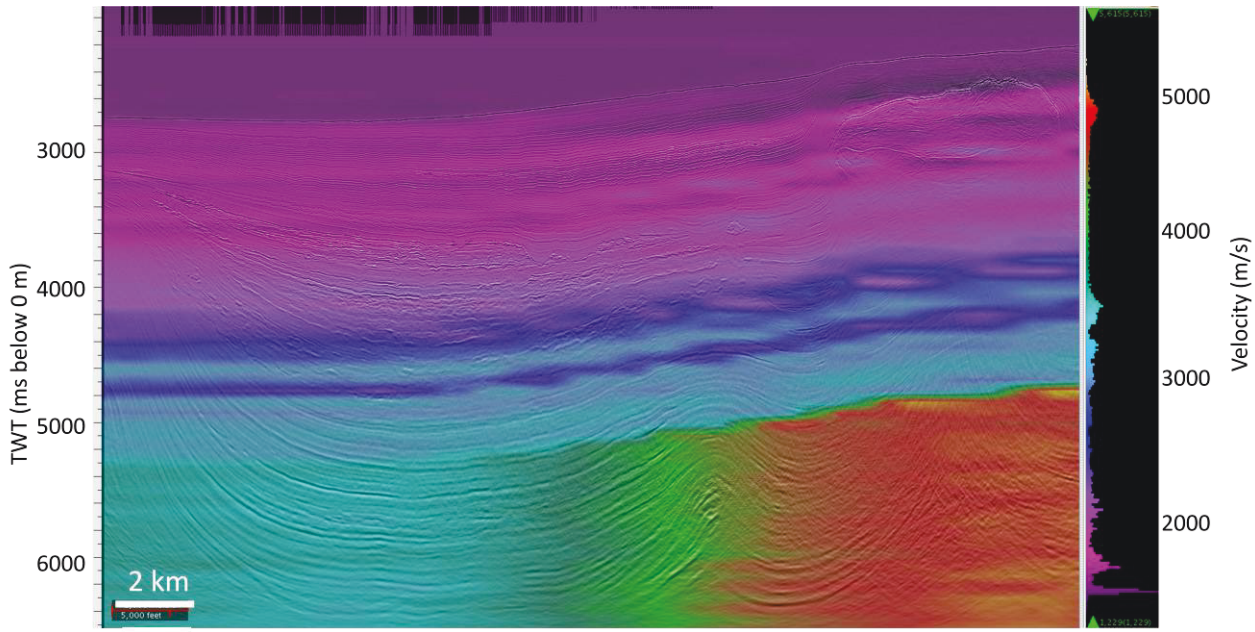


Figure 4.7 Velocity model overlaid on an inline of the PSVM data showing how the velocity varies with depth and sediment type. Velocity model used to calculate the vertical resolution and to convert horizons from time to depth.

4.2.4 Isopach Maps

A series of true stratigraphic thickness maps were produced using the calculation module within the PowerView® software to generate vertical thickness maps between the key horizons. Horizons were picked on time-seismic data and were converted to depth surfaces using a depth variable velocity model thus allowing the angle of dip of the beds to be calculated accurately (see Section 4.2.1 and Figure 4.7). Once the horizons were converted to depth an algorithm was used to calculate stratigraphic thickness maps between the horizons.

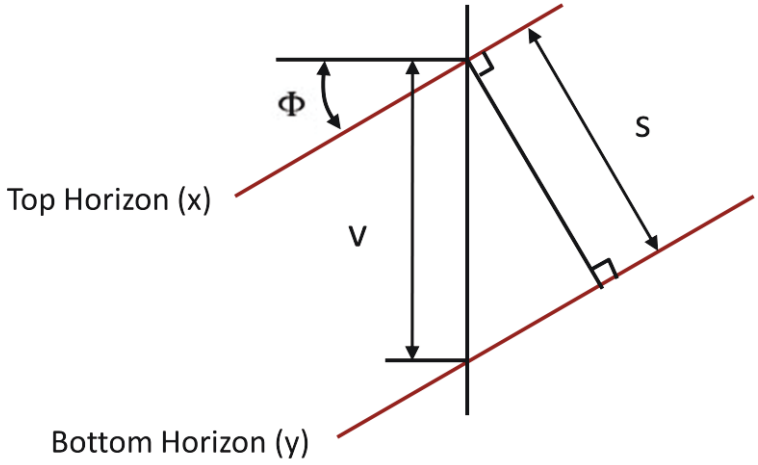


Figure 4.8 Diagram showing the difference between the vertical thickness (v) and the stratigraphic thickness (s) and hence how this can improve the accuracy of the measurement of bed thickness for steeply dipping beds.

Figure 4.8 shows the fundamental assumptions used by the algorithm to calculate the thickness between successive horizons, with vertical thickness (V) and stratigraphic thickness (S) related by:

$$S = Vcos(\Phi) \qquad \text{(Eqn. 2)}$$

where Φ is the slope (or the dip of the strata) and assuming a right angle triangle can always be formed by the vertical thickness line (V), the stratigraphic thickness line (S) and the base of the unit (a reasonable assumption over a short distance).

Figure 4.8 shows the dip as being one-dimensional, however this is not the case as it is measured in the direction of the gradient vector; the direction of the most rapid change in gradient. Therefore this algorithm measures maximum slope using the angle of the dip vector (B):

$$\frac{dz}{dn} = \frac{dz}{dx\cos(B)} + \frac{dz}{dy\sin(\mathrm{B})} \quad \text{(Eqn. 3)}$$

From this the declination angle (F) can be calculated:

$$F = \arctan\left(\frac{dz}{dn}\right) \quad \text{(Eqn. 4)}$$

Hence the stratigraphic thickness can be computed using equation 2. In areas where structural dip is greater than 25°, vertical thickness maps introduce errors of over 10% and hence are not appropriate (Figure 4.9).

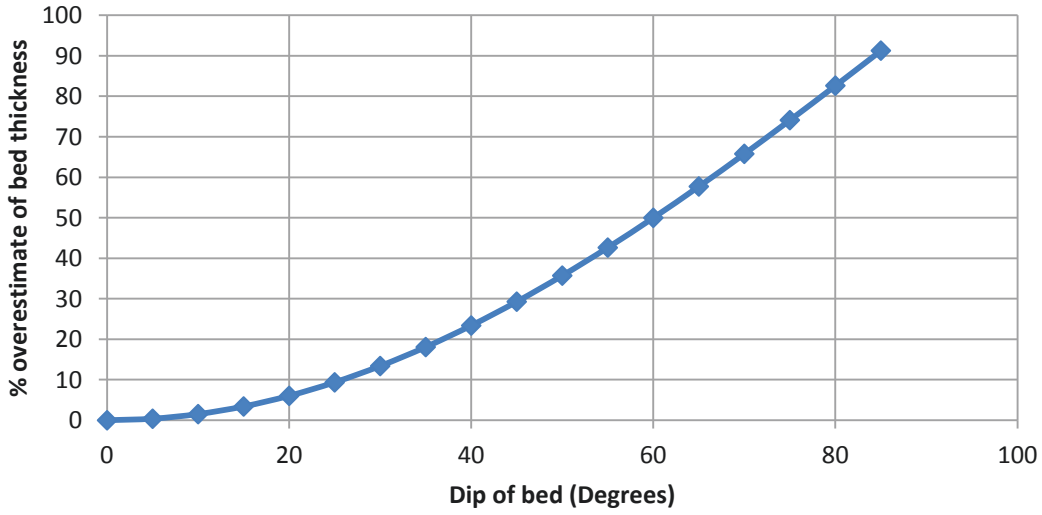


Figure 4.9 Percentage overestimate of bed thickness if calculated as a vertical thickness using the equation % overestimate = ((vertical thickness – stratigraphic thickness)/vertical thickness)*100

4.2.5 Structural Restoration

Structural restorations across the mini-basin create a step-by-step model of its evolution allowing visualisation of the structural setting through time. Structural restorations have been a commonly-employed technique since ground-breaking work carried out in the Canadian Rockies during the 1960s (Bally et al., 1966, Dahlstrom, 1969, Dahlstrom, 1970). This work was rooted in depth-to-detachment calculations (Chamberlin, 1910) and schematic evolutionary models such as those Buxtorf (1916) developed for the Jura Mountains (Rowan and Ratliff, 2012). Restoration, as reviewed by Rowan and Ratliff (2012), is a process by which the affects of deformation on an area are reversed, with sequential restoration calculating and removing the effects of processes that impact an evolving basin geometry during specified time intervals (in this case between interpreted, dated horizons). Restoration proceeds in the reverse sense by working backward through time, but can still be easily understood in the forward sense (Rowan, 1993b). Rowan

(1993b) summarises that the geometry of a basin, within an area where salt tectonics occurred, at a given point in time is modified during the subsequent period of time by some or all of the following factors:

- ***sedimentation*** – sediments are deposited with thickness variations across the basin dependent on the sediment provenance, facies, and seafloor topography encountered;
- ***compaction*** – this causes a decrease in thickness and increase in density of both the underlying and deposited sediments due to burial beneath the accumulating overburden;
- ***eustasy*** - global changes in sea level, not related to local tectonic events;
- ***fault-related deformation*** **-** primarily normal faulting and associated folding caused by regional extension and/or salt movement, but may also include localised reverse faulting;
- ***salt movement*** **-** salt withdrawal, diapirism and lateral flow in response to sedimentary loading and regional extension;
- ***isostasy*** **-** primarily subsidence due to sedimentary loading, but may also include either uplift or subsidence due to faulting and/or salt movement; and
- ***thermal subsidence*** - regional subsidence related to post-rift cooling of the lithosphere.

The restoration process is carried out by attempting to account for, and reverse, the effect of the above factors on the deformation sequentially and is most commonly attempted using 2D sections. The section restored for this study is of limited regional extent which means that it is likely that the isostatic compensation and thermal subsidence are uniform across the area, so there is no differential movement, and hence the affects of isostasy or thermal subsidence have not been included in the modelling. This in turn means that palaeowater depths cannot be estimated, and retrodeformation schemes are left with no vertical co-ordinate. However, as the sediments were deposited in a deep water setting, global sea level variations are considered to have minimal impact and so water depth changes are not included in the analysis.

Accurate restoration relies on several assumptions (Woodward et al., 1985 , Woodward, 1989, Rowan and Ratliff, 2012), one of the most fundamental of which is that deformation is in the plane of the strain, ensuring that there is no movement into or out of the plane of the cross-section, with the section orientated parallel to the overall transport direction. The second major assumption is that the cross-sectional area of the individual stratigraphic intervals must not be allowed to change during deformation. This can be accomplished using several different graphical restoration algorithms (see Figures 4.9 and 4.10 for illustrations of restoration techniques; Rowan and Klingfield, 1989, Nunns, 1991, Schultz Ela, 1992):

- bed-length restoration which preserves the line lengths of horizons;
- vertical-simple shear and inclined simple shear which maintain the lengths of vertical or inclined lines respectively;
- fault-parallel slip which keeps imaginary lines parallel to a given fault at a constant length;
- rigid-body rotation which maintains the exact shape and size of fault blocks; and
- area restoration relaxes the other constraints while still preserving unit area.

More recently finite element modelling and similar techniques have been employed (e.g. Maerten and Maerten, 2006, Smart et al., 2010, King and Backé, 2010).

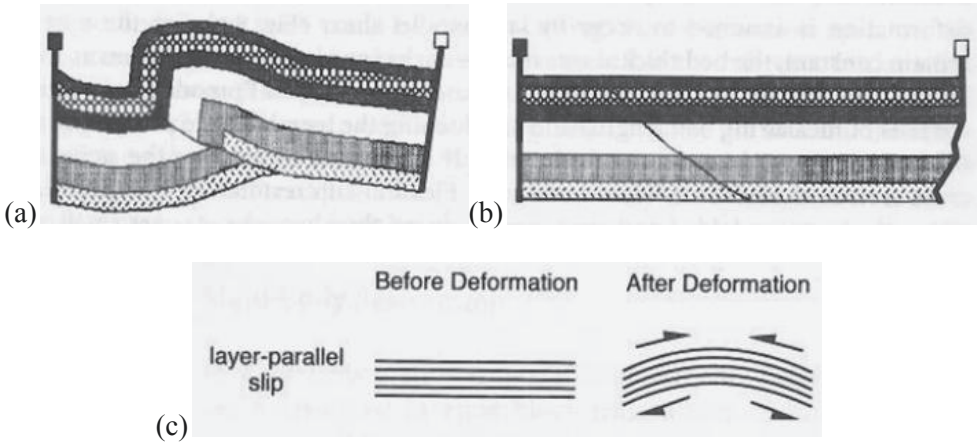


Figure 4.10 Diagrams illustrating the processes of restoration of a simple cross-section through flexural slip. This is based on the model that bed lengths do not change during deformation and that internal deformation occurs through layer parallel simple shear. (a) illustrating a deformed section prior to the process of (b) flexural-slip restoration, (c) shows the effect of constant bed-length thickness flexural slip model (after Klingfield et al., 1986)

As discussed in Rowan and Ratliff (2012), cross-sectional restorations through areas influenced by the movement of salt can often be challenging and have added uncertainty. This is primarily due to the fact that cross-sectional restorations typically assume that plane-strain deformation has occurred during which area has been conserved, assumptions that are generally invalid for salt due to the characteristic three-dimensional flow patterns (Rowan, 1993a, Diegel et al., 1995, Hossack, 1995) and possible dissolution (Lohmann, 1972, Jenyon, 1984, Hossack, 1995). Rowan (2012) also argues that the plane-strain assumption cannot be universally applied to the overburden. This assumption is invalid where the direction of salt movement is locally variable above salt canopies with significant salt-base relief (Rowan, 1996) and in mini-basins which have rotated about a vertical axes during lateral translation above salt bodies (Rowan and Vendeville, 2006).

The choice of a restoration algorithm is a fundamental decision in cross-section restoration, as it has a significant impact on the outcome of the restoration, particularly in salt-influenced areas. There are three main options in salt-influenced settings;

1. flexural slip (Figure 4.10),
2. vertical shear and,
3. inclined vertical shear (Figure 4.11).

Hudec and Jackson (2004) suggest algorithms based on the following logic: where deformation is primarily related to salt withdrawal they advocate vertical shear (Figure 4.11), where deformation is primarily in the hanging wall of a normal fault they suggest inclined shear antithetic to the normal fault and, finally, in contractional domains they suggest a flexural slip algorithm would be most appropriate (Figure 4.10). However, in nature many structures pass from one type of deformation to another as they evolve. Thus in the case of an inverted diapir, it might be appropriate to restore the most recent contractional deformation by flexural slip, but earlier diapir growth stages by vertical or inclined shear. A flexural slip algorithm is advocated in contractional salt domains as it accommodates slip between units thereby accounting for lateral

movement and not just vertical shear when restoring folds (Hudec and Jackson, 2004, Rowan and Ratliff, 2012).

Structural restoration is carried out in Chapter 5 where a section through the mini-basin is sequentially restored using 2D Move® software. Whilst this method is not used elsewhere in the thesis, the choice of restoration algorithms was pivotal to the quality of the resulting restoration and hence warranted discussion in this chapter of the thesis.

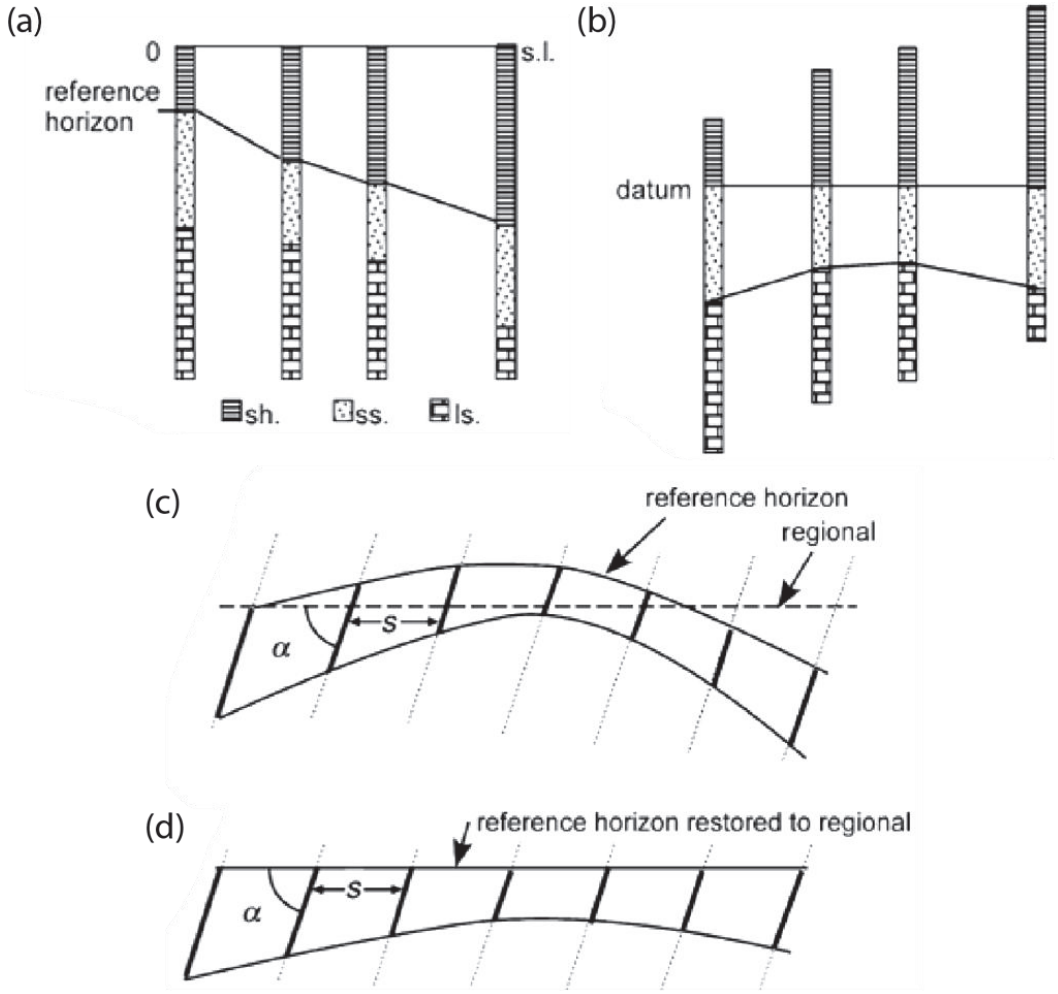


Figure 4.11 Diagram illustrating vertical and oblique simple shear, whereby a reference horizon is restored to a specified datum and underlying beds move accordingly, thus preserving vertical thickness but changing bed length and true thickness. This is illustrated using a vertical simple shear algorithm where (a) a cross-section based on a series of lithological logs where zero elevation is sea level (s.l.), sh: shale, ss.: sandstone, ls: limestone is also shown in (b) flattened to a datum at the top of the sandstone, thus revealing an anticline within the limestone beds. As well as by oblique simple shear. Here medium weight solid lines are marker beds, dotted lines represent the shear direction and are equally spaced at an arbitrary distance, S, and the shear angle is α, (a) shows a deformed cross-section while (b) shows this same section restored using the oblique, or inclined, simple shear. Diagrams taken from 2D Move user manual.

The structural restoration was carried out on a depth-converted section across the basin which originated from the regional seismic dataset (see Sections 4.1.2 and 0). A representative cross-section across the basin was taken as a screen-shot from the regional seismic data and then, using accurate coordinates taken from the interpretation software PowerView®, geo-referenced into the 2D Move® software. The 2D Move® software was used to depth convert the cross section using an algorithm derived from the local well data (see Section 4.2.6). The appropriate seismic horizons were traced from the 2D seismic section within 2D Move®

with the corresponding intervals assigned appropriate characteristics in terms of porosity and permeability. A sequential restoration was carried out using the 2D Move® software and the following steps:

1. the top sedimentary sequence was removed,
2. decompaction of the underlying unit was carried out using the standard Sclater and Christie (1980) depth-porosity relationships (see Section 0) and,
3. restoration using the flexural slip algorithm is performed (see Section 0).

This process was then repeated until all of the horizons had been stripped off. The salt volume was calculated in 2D Move® and was kept constant from 18.26 Ma (H10) until present day. This assumed that no salt was lost or gained during this period and hence that the amount of salt entering and leaving the plane of the section averaged out and there was no dissolution at the seafloor (following Marton et al. 2000). Prior to 18.26 Ma (H10), the base salt surface remained in the same position, allowing the salt volume to expand (following Rowan, 1993b) thereby assuming that most of the salt moved down-dip in this period.

4.2.6 Depth Conversion for 2D Move®

The section used for the 2D restoration was from the regional seismic dataset because this allowed a wider section through the basin to be observed (see Section 4.1.2). This dataset does not have a corresponding velocity model which could be used in 2D Move®, therefore the local well data were used to determine a time-depth function that could be applied to depth convert the seismic section. Figure 4.12 shows a graphical plot of the depth versus time taken from the well data, the algorithm shown on the graph was then used in 2D Move® to depth convert the section.

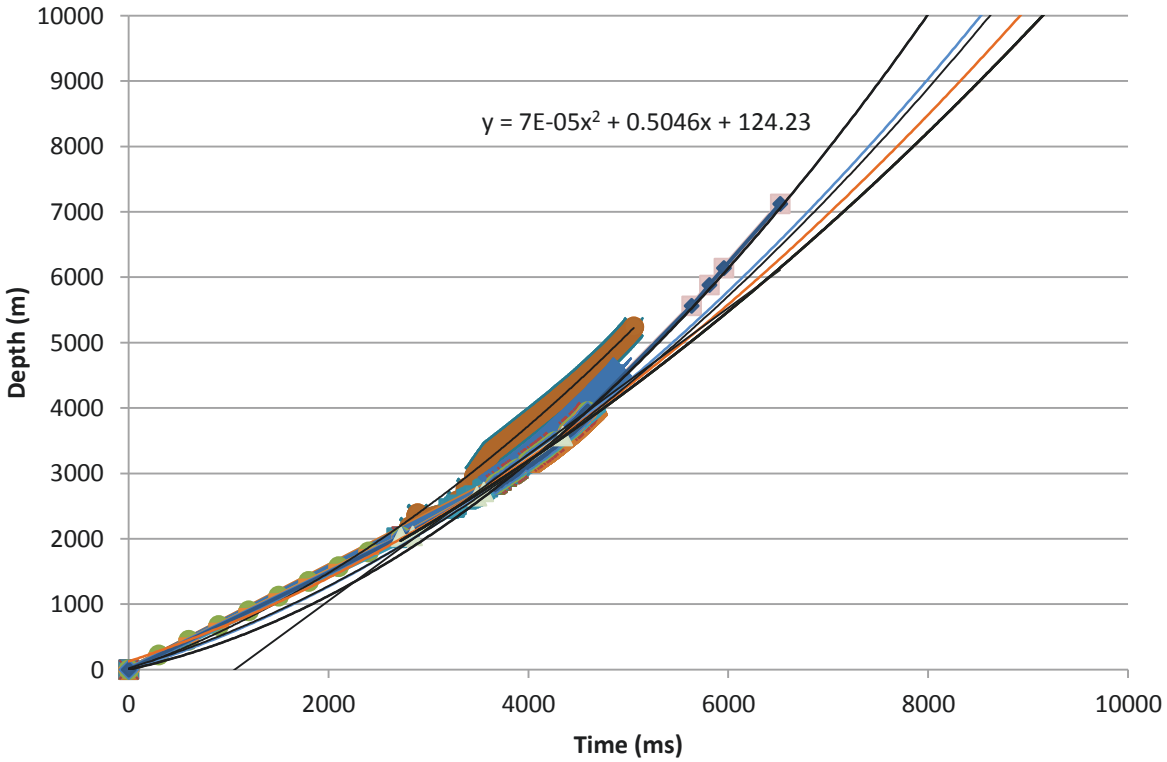


Figure 4.12 A graph showing all the well data from the area surrounding the basin. This is plotted to generate the algorithm used to depth convert the seismic section which was used for the structural restoration in 2D Move®.

4.2.7 Decompaction for 2D Restoration

As sedimentary rocks are buried they are subject to a reduction in thickness due to compaction which increases with increasing burial depth and overburden weight (Magara, 1980, Sclater and Christie, 1980). This compaction does not simply cause a reduction in the pore volume of a particular interval, but also incorporates all processes which result in volumetric strain being applied to the rock. Giles (1997) and Allen and Allen (2009) stress that this can be due to mechanical compaction, generally resulting from denser packing of the grains and pore fluid escape, physicochemical reactions, for example the removal of grain material by pressure solution, and cementation, a reduction in the pore space due to mineral precipitation (note this can also prevent mechanical compaction by stabilising the framework). In this study, as in the majority of studies, it will be assumed that there is no change in the solid volume of the rock during burial process, and consequently that the reduction in porosity is driven solely by the mechanical compaction process (Allen and Allen, 2009). This is not generally true as changes in the secondary porosity of sediments often occurs as a result of solution of grains or cement, fracture porosity, or retained higher porosities in over-pressured units where an over-hydrostatic pore fluid pressure can counteract mechanical compaction (Giles, 1997). However, reliable algorithms which incorporate these effects have yet to be created, so in the 2D Move® restoration only the effects of mechanical decompaction will be accounted for and removed.

Relationships between porosity loss and burial depth, or effective vertical stress, generally show a decreasing porosity with depth for most clastic lithologies (i.e. sandstones and shales; Magara, 1980, Bond and Kominz, 1984). Magara (1980) and Bond and Kominz (1984) both suggest that sandstones lose porosity linearly as a function of depth in the shallow surface (1 km to 5 km) but Allen and Allen (2009) stress that this linear relationship cannot hold at depth since it would result in the porosities becoming negative. Borehole data collected in many different studies suggest instead that sediments exhibit an exponential relationship between depth and porosity in the subsurface:

$$\emptyset_z = \emptyset_0 e^{-cz} \qquad \text{(Eqn. 5)}$$

Where $\emptyset_z$ is the porosity at a given depth, z, $\emptyset_0$ is the initial porosity at the time of deposition and c is a coefficient which is dependent on lithology and describes the rate at which the exponential decrease in porosity occurs with depth (Allen and Allen, 2009). This equation represents an over-simplification of the relationship between porosity and depth; it is well documented that porosity variations within sandstone units are affected by the amount of sorting, the clay content, and the lithology of the individual grains whilst shale porosities are affected by the arrangement of the clay minerals which form shale, and the effects of the expulsion of pore fluids (Giles, 1997). However, as discussed previously, most of these processes are not easily quantified therefore a simple porosity-depth function has been used to quantify decompaction within the 2D Move® restorations.

After testing a series of different restoration methods in 2D Move® it was decided that the section should be decompacted following the removal of each interval and that the expanded section should be attached to a deep baseline which acts as a fixed reference frame unaffected by compaction. This deep baseline, and the

sea level surface, forms a reference frame for the subsequent restoration acting to separate the effects of regional subsidence from compaction and deformation. The baseline needs to be placed below the mobile salt layer so that it is unaffected by salt movement and extensional faulting and is deep enough such that it is not effected by differential decompaction (R. Humphries, 2012, pers. comm.). A baseline at least 5000 m below the base salt is recommended because the effects of compaction decrease with burial (Rowan, 1993b), although Baldwin and Butler (1985) point out that even at this depth a small amount of compaction (approx. 2%) still occurs.

There is a lack of appropriate porosity-depth trend data and sand-shale ratio analysis in the region over which the structural restoration is being performed and hence a standard porosity-depth curve was applied using the 2D Move® software. The regional contraction which has led to shortening and uplift of the beds means that the porosity-depth curves generated by Sclater and Christie (1980) for the North Sea are not strictly appropriate. However, they have been used in the regional restoration as they were thought to produce the most reliable result given that they represent a similar lithology to that seen in Angola (a mixture of sandstone and shale). Any errors introduced by not taking these factors into account and the use of the Sclater and Christie (1980) porosity-depth data should not impact the overall shape of the structural restoration but does introduce inaccuracy into the absolute depth measurements. However, as the restorations are used purely qualitatively, this has very little impact on the study.

4.2.8 Algorithm Choice for Restorations

When sequentially restoring structural sections the choice of restoration algorithm has a significant effect on the outcome of the structural relationships generated at each stage of the process (Rowan and Klingfield, 1989, Nunns, 1991, Schultz Ela, 1992). As discussed in Section 4.2.5 this is particularly true in salt-influenced settings, where Rowan and Ratliff (2012) suggest the three best options are flexural slip, vertical shear and inclined vertical shear. In order to investigate this advice and to illustrate the impact of different restoration algorithms, three identical, hypothetical salt-cored folds were sequentially restored in 2D Move® using a series of different algorithms to assess the resulting impact on the structure: a flexural shear algorithm pinned on the centre of the fault, a flexural shear algorithm pined on the left hand side of the fault and a simple shear algorithm (Figure 4.13).

In general, the simple shear algorithm generates a much flatter, longer wavelength anticline, whereas the models generated by flexural slip appear to retain a more self-similar shape through time (Restoration 3, Figure 4.13). The point at which the section is pinned also effects the structural restoration of the section with the pin on the left side of the anticline causing the section to lose the symmetrical shape associated with the restorations that were pinned on the centre of the fold (compare Restoration 4, Figure 4.13; orange line is pinned to the left hand side of the fault whereas the blue line is pinned on the centre of the anticline). Pinning the section through the centre of the anticline appears to cause the section to distort the least thus generating the most self-similar shape through time, which has been deemed to be the most accurate anticline shape. However, it is important to note here that the real restoration section contains more than one

structure, so careful consideration will have to be given to where to situate the pin line. The restorations carried out in Figure 4.13 indicate that the flexural slip algorithm, pinned on the centre of the anticline is the most appropriate in this situation. This agrees with studies carried out elsewhere (see Rowan and Klingfield, 1989, Hudec and Jackson, 2004, Rowan and Ratliff, 2012) which emphasis that vertical simple shear produces very little layer-parallel strain thereby accounting more for the lateral movement and not just vertical shear when restoring folds.

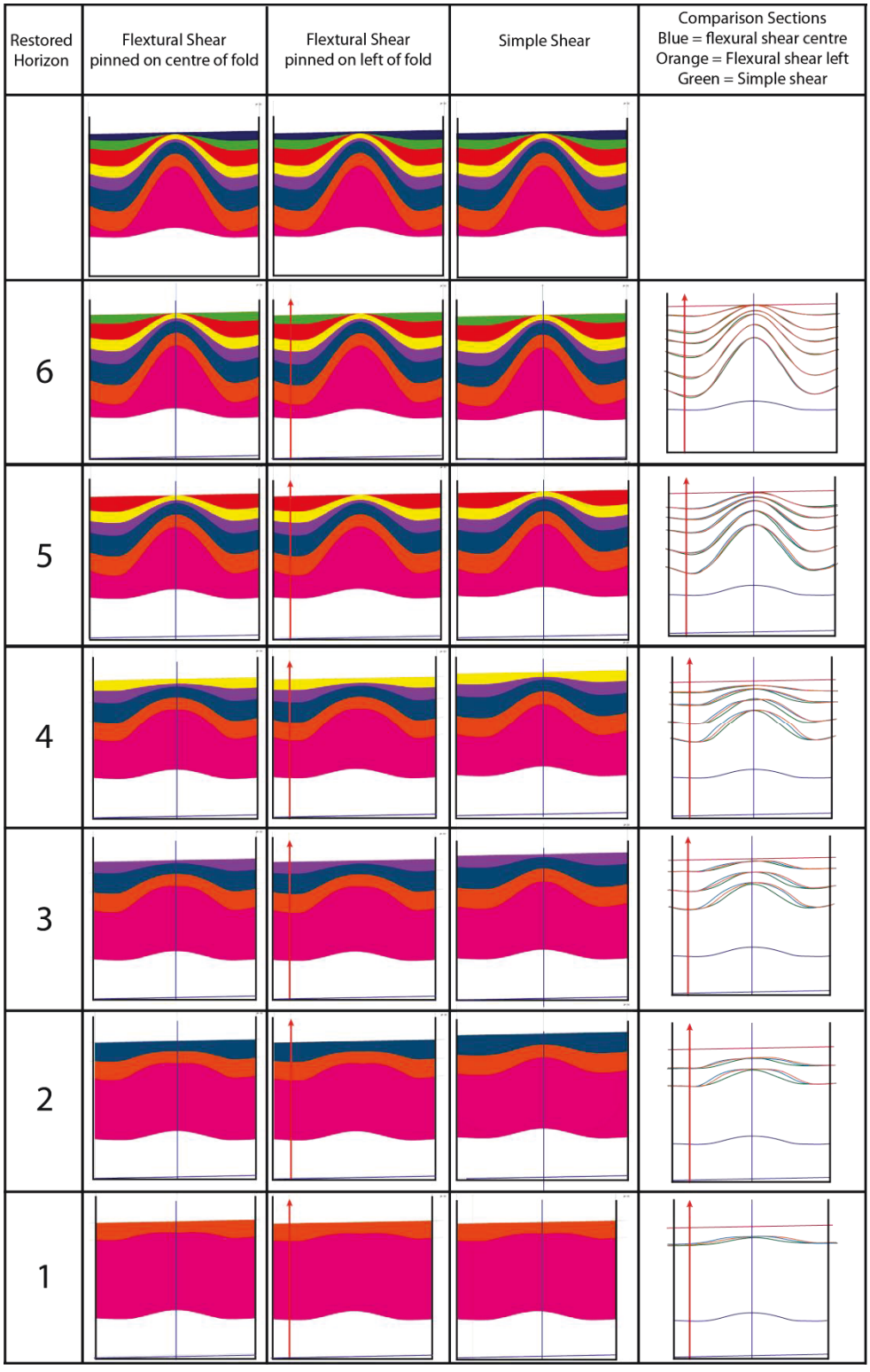


Figure 4.13 Comparisons between the patterns in stratigraphy generated by using three different restoration algorithms.

4.2.9 Strain Analysis

Structures that grow while sedimentation is occurring may affect the type and distribution of sediment within a basin. Therefore it is important to gain an understanding of the temporal and spatial evolution of faults and folds within the basin to fully understand the syn-kinematic sedimentary fill.

This is not only common in basins controlled by an underlying detachment surface such as salt and mud diapir controlled settings (e.g. Mayall and O'Byrne, 2002, Gee and Gawthorpe, 2006, Wood and Mize-Spansky, 2009, Mayall et al., 2010, Jones et al., 2012) but also in the external parts of foreland fold and thrust belts and foreland basins (e.g. Deramond et al., 1993, Zoetemeijer et al., 1993, Clark and Cartwright, 2009), as well as in rift basins (e.g. Gawthorpe and Leeder, 2000 amongst others). Structures within a contractional setting have been analysed using a variety of techniques including: geometric (e.g. Suppe, 1983, Moretti et al., 2006), mechanical (e.g. Braun and Sambridge, 1994, Hardy and Finch, 2007, Albertz and Lingrey, 2012) and analogue models (Costa and Vendeville, 2002 and references therein).

Geometric models using constraints such as the conservation of area, bed-length and bed thickness have been commonly used to investigate the relationship between slip, fault-shape and fold-shape, and syn-kinematic stratal geometries for fault-bend, fault propagation and detachment folds (e.g. Suppe et al., 1992, Hardy and Poblet, 1995, Poblet and Hardy, 1995, Hardy et al., 1996, Poblet et al., 1997, Storti and Poblet, 1997 amongst many others). While conceptually useful for understanding idealised syn-kinematic stratal geometries that might develop for a particular kinematic model, it is very difficult to apply these kinematic models in an area of salt-influenced folding where the folds do not necessarily comply with simple end-member fault-propagation or detachment fold models. Additionally, the subtle syn-kinematic stratal geometry variations predicted by these models were not observed in the study area seismic data. Hence, a simpler, model-independent approach of measuring bed-length change was preferred for this thesis, so that variations in structural growth between structures could be assessed for the entire mini-basin. Furthermore these studies do not, and were never intended to, link the geometries of the growth strata with the type of sediments deposited in the basin whilst the structures were deforming. The use of changes in the observed growth strata to determine the impact of the growth of a structure on depositional systems deposited within an area have been examined using outcrop data (e.g. Burbank and Vergés, 1994, Burbank et al., 1996, Ford et al., 1997). These ideas are discussed more extensively within Section 4.2.12.

Following the work of Dahlstrom (1969) and Hossack (1979) line-length balancing has been used as a standard method for measuring strain for decades but in this thesis the analysis has been modified to include growing structures and to calculate bed-length changes where stratigraphy onlaps structure following the approach of Schneider et al., (1996), Masaferro et al., (1999) and Poblet et al., (2004). To estimate strain from bed-length changes requires that the beds retain their cross-sectional length during deformation. However, in a salt environment a change in the bed length could result from a variety of, often indistinguishable, mechanisms; differential subsidence and subsequent salt growth, where the strata are pulled upward by the growth of salt wall, within the basin would result in a very similar geometric profile to that produced by the tectonic shortening of the area through the generation of faults and folds. Therefore,

within this environment a study of the change of the bed length is useful as a proxy for the structural growth, rather than calculating an absolute value for the tectonic shortening or strain on a structure in the strict sense. This means that the results cannot be directly compared to those calculated elsewhere in the literature, and therefore will be used primarily to broadly classify the structures into those that were growing at fast, moderate and slow rates at the different time intervals.

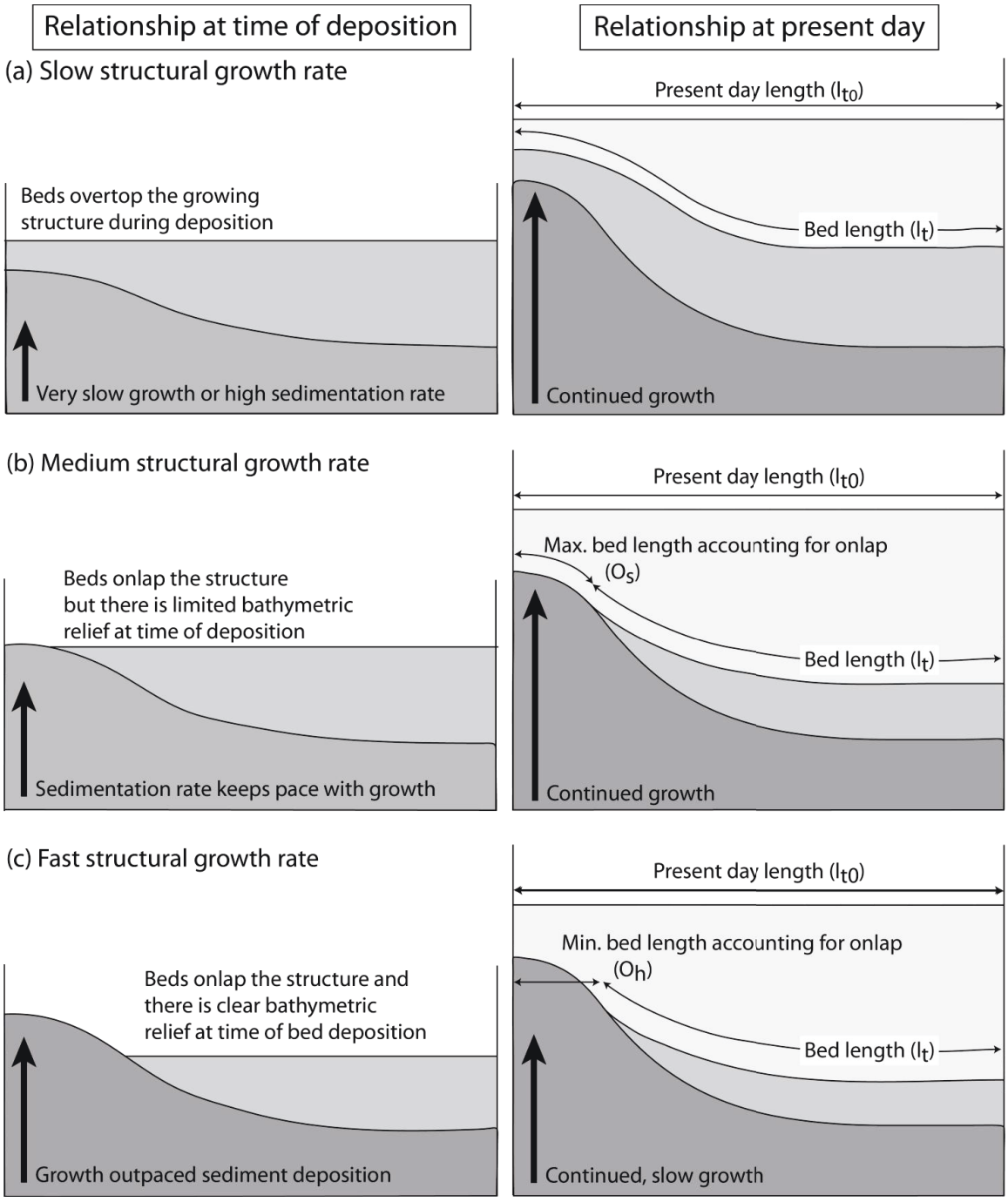


Figure 4.14 Diagrams illustrating the methodology used to calculate the bed length change of (a) structures with low growth rates, (b) structures with medium growth rates and (c) structures with high structural growth rates.

The bed length change, ΔB, of a horizon is calculated by subtracting the length of the present day cross-section from the folded length of the cross-section deposited at time t (Figure 4.14 (a)):

$$\Delta B = l_t - l_{t0} \quad \text{(Eqn. 6)}$$

In cases where the growth strata onlap growing bathymetry then a decision needs to be made about how to continue to measure the bed length taking account of this onlap (i.e. Figure 4.14 (b) and (c)). If it is assumed that no significant bathymetry occurred at the seabed and that the crest of the anticline generated minimal positive bathymetric relief whilst the subsequent beds were deposited (i.e. Figure 4.14 (b)), then the length deposited at time t_0 includes the length over the top of the present day structure, O_s. Therefore, it would be calculated as follows:

$$\Delta B = (l_t + O_s) - l_{t0} \quad \text{(Eqn. 7)}$$

This results in a maximum estimate for the bed length change over the structure, as this method assumes that most of the folding of the onlap surface has occurred after this event. However, if the top of the fold was visible above the seafloor whilst the beds were deposited (i.e. Figure 4.14 (c)), then the bed length is more accurately estimated as a horizontal line measured from the onlap point on the flank of the fold, O_h, thereby assuming that growth after the time of deposition had less of an impact on the change in bed length. This method would result in a minimum value for the change in bed length and is calculated using the following equation:

$$\Delta B = (l_t + O_h) - l_{t0} \quad \text{(Eqn. 8)}$$

The rate of change of bed length has also been used throughout this study to normalise the results. In order to calculate this, change in bed length must be divided by the time period over which it has occurred, i.e. $\Delta B / \Delta t$.

The results in this study use Equation 7 to calculate the change in bed length where beds onlap growing structures as it is believed that a significant amount of the change in bed length occurred after the deposition of the beds. Therefore, it should be noted that the results presented in this study give a maximum change in bed length through time.

In order to accurately measure the bed length and cross-sectional length of the main structures constraining the basin, 5 km cross-sections were taken through them from the PSVM dataset and loaded into 2D Move® software using a geo-referencing tool which insured they were correctly positioned spatially. The sections were depth converted and the bed lengths measured digitally. Bed length change measurements across the folded layers were recorded on sections where the horizontal and vertical scales were the same. Measuring the lines in this way gives the cumulative bed length change through time (i.e. the cumulative summed difference in recorded between adjacent stratigraphic layers). This means that the maximum cumulative bed length change is recorded at present day (0 Ma) and represents all the bed length change recorded on the strata. These measurements have also been used to determine an average interval rate of change of bed length between the dated, sequential stratigraphic surfaces.

Graphical representations of the bed length change results have been carried out in several different ways. Most commonly the cumulative change of bed length has been plotted for sections on the flanks of the structures located within and along the margins of the mini-basin, with cumulative bed length change plotted against the horizon age of several of the structures. This enables differences in the growth history of several

of the structures to be compared together, and is shown in Chapter 5. In order to highlight the variation in bed length change along one specific structure the bed length change on each surface has been plotted against distance along the structure. This analysis is often used on extensional fault systems and on thrust faults (e.g. Davies and Stewart, 2005, Higgins et al., 2009) where displacement is plotted against distance.

The results of the bed length change analysis are also used in Chapter 8 to define six intervals within the history of the basin where the amount of structural movement occurring during that time can clearly be linked to the depositional systems active in the basin. These were used to highlight changes in the interactions between sedimentary systems and structural growth through time. Also within this chapter, the bed length change results are mapped along the main structures for the relevant time intervals coding it as 'high' (red), 'medium' (green) or 'low' (yellow). High rate of change of bed length was defined as rates greater than 30 mMa^{-1}, medium rates of bed length change between 10 and 30 mMa^{-1}, and low rates of bed length change as rates below 10 mMa^{-1}.

4.2.10 Errors Associated with Bed Length Change Measurements

Errors associated with quantifying the cumulative bed length change and rate of bed length change can be either induced by the key bed length change assumptions not holding true in all cases (e.g. length preservation during shortening) or can be introduced through the methodology used in this study. The derived values, and associated interpretations, are only reliable if they exceed the magnitude of the errors associated with the measurements.

There are some uncertainties involved with this method of using the changes in bed length as a proxy for the amount of structural growth in an area. Moretti and Callot (2012) recently stated that the length preservation during shortening assumption is unlikely to hold true in the majority of cases. They state that variations in length can be introduced by:

- compaction by burial and ductile strain (Mitra, 1994, Koyi et al., 2004, Roure et al., 2005) and;
- the behaviour of non-competent rocks such as salt and shale which are known to flow and hence follow either viscous or plastic-viscous laws (Weijermars et al., 1993).

Moretti and Callot (2012) observed that in addition to these known problems the horizon length will be changed as it is faulted and folded, resulting in continuous measuring generating artificial lengths and either increasing or decreasing the real length of a line. They show that a 38% reduction in shortening imposed on a system artificially resulted in a computed of shortening as little as 26%. This is attributed to incorrect measurements across fold and fold offsets as well as the impact of horizontal compaction and layer parallel shortening (also discussed by Koyi and Sans (2003)). The majority of the structures studied in this thesis are compressional with some faulting over the crests of the anticlines, and therefore the measurements of the bed length may be unintentionally increased during the mapping process. In a series of experimental plots Poblet et al. (2004) measured the bed length variations at stages through the deformation of a fold train (Figure 4.15) and found that the bed length increased/decreased by < 3.4% during the applied deformation, from

which they concluded that the assumption of constant bed length was approximately valid. They attribute this bed length change primarily to thickening within the crest of the folds and transtensional fault development over the fold crest causing an overestimate of the degree of bed length change (Figure 4.15; Poblet et al., 2004).

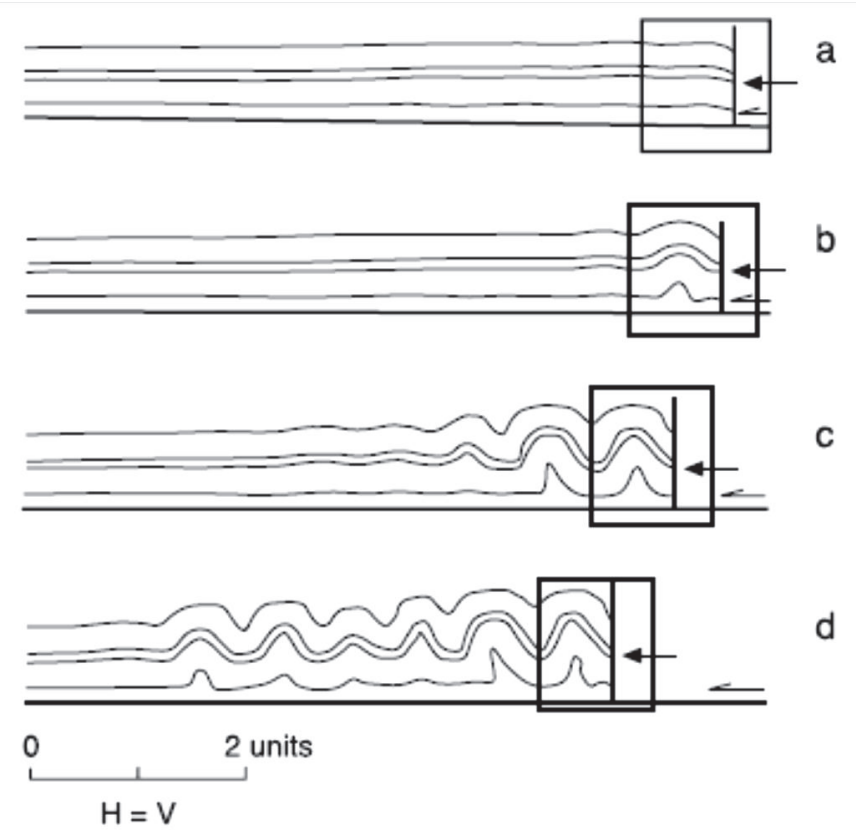


Figure 4.15 Illustration showing the deformation in an experimental detachment fold train. Taken from Poblet et al. (2004) but ultimately modelled after Price and Cosgrove (1990).

Therefore, it is likely that the bed length change measurements in this study are over-estimates of the true bed length change with both of the factors observed in the preceding paragraph increasing as bed length change on the horizons continues. From these studies it is possible to conclude that an over-estimate of the bed length change by between 3 - 10 % is likely in the results, with this increasing in the older beds which have been subjected to larger amounts of bed length change. As well as this, the percentage error associated with the bed length change measurement will be greater at smaller values of strain.

As previously discussed, the individual horizons were first mapped using PowerView® software and then imported into 2D Move® software where they were depth converted. Selection of the lines on which to carry out the strain analysis can introduce errors into the process with perpendicular lines required for an accurate bed length change analysis. In order to address this issue, the lines were carefully selected from the seismic data using timeslices through the structures to identify the main structural trends. Secondly, errors may have been introduced to the analysis during the depth conversion process. A depth conversion was carried out within 2D Move® using the methodology outlined in Section 4.2.6. The algorithm was calculated using well-data and is thought to be accurate. Once the sections were correctly referenced and depth converted with 2D Move® the horizons were re-traced and the lengths of these measured. These new

traces were more coarsely picked than the seismic horizons within the PowerView® software as they did not automatically trace the horizons and hence errors in the length could be introduced, for example, where the curve of the beds is not picked as accurately.

Errors are also associated with the biostratigraphy used to calculate the rates of bed length change on the structures. As discussed in Section 4.1.3 it is difficult to quantify the errors associated with these picks, but it is known that these values become less reliable shallower in the seismic data due, in part to the fact that these areas lie outside the main reservoirs and hence fewer tops were biostratigraphically analysed (i.e. from H70, 11.86 Ma, onwards; S. Payne, 2010, pers. comm.).

It should be noted that error bars have not been shown on any of the graphical plots presented in this study. This decision was made because many of the error bars lie within the area of the data points shown by these graphs and so adding them to the plots would, in many cases, mask the data points on the plots. As comparison of the bed length changes between and along structures is the main objective of this analysis, and not the absolute value of bed length change, the approach adopted is considered appropriate.

4.2.11 Interpreting Bed Length Change Graphs

Two graphs showing change in bed length generated from theoretical cross-sections are shown in Figure 4.16, these were generated in excel and then input into 2D Move® for the analysis. Measuring the change in bed length on these sections and understanding the resulting graphs helps aid understanding of the bed length change graphs measured from anticlines which show different growth scenarios. The theoretical sections contain a series of pre-growth horizons (the dark blue to green beds deposited between 50 Ma and 30 Ma), deposited flat and parallel. If bed length is preserved on these beds no incremental bed length change should be recorded, as would be expected for pre-kinematic strata. However, the artificial construction of the folds used in this example has resulted in changes in bed thicknesses with the pre-kinematic strata and hence small increases in bed length between layers resulting in negative bed length change values.

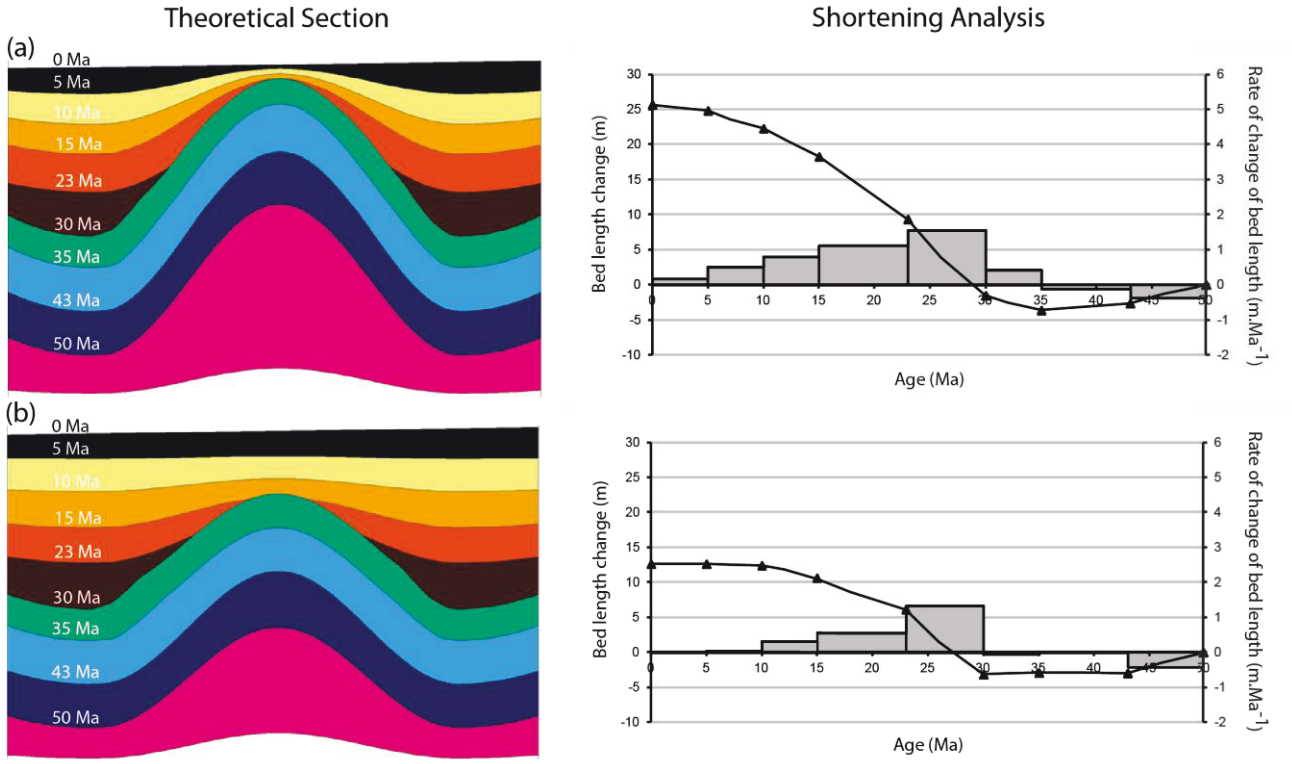


Figure 4.16 A visual comparison between two theoretical cross-sections through anticlines and the corresponding bed length change graphs.

The sections both contain periods where the growth of the anticline resulted in onlap and thinning of the overlying sediment packages. As the intervals were deposited over approximately the same periods, it can be assumed that periods where the beds onlap have the highest growth rates as this would have generated the most seafloor topography. This is the case when comparing the rate of bed length change between Figure 4.16 (a) and (b) between 5 Ma and 10 Ma while the yellow bed was deposited; Figure 4.16 (a) has a higher rate of bed length change than Figure 4.16 (b) with correspondingly thinner yellow beds deposited over the top of the anticline during the earlier period. Onlapping beds can be seen in the brown interval deposited between 23 Ma and 30 Ma on Figure 4.16 (a) and (b) corresponding to the highest rates of bed length change observed in both of these anticlines.

The section shown in Figure 4.16 (b) has much lower overall cumulative bed length change because of the lower amplitude and longer wavelength configuration of the anticline, which indicates lower growth of the structure. These models illustrate how different patterns of growth inferred from seismic sections can be compared.

4.2.12 Stratal Growth Pattern Analysis

Onlap patterns have long been used to infer qualitatively the rate of movement of structures, providing a fundamental dataset for documenting and interpreting salt movement (Schlische, 1992, Giles and Lawton, 2002) and structural growth in outcrop examples (Burbank and Vergés, 1994, Burbank et al., 1996, Ford et al., 1997, Shaw et al., 2004, Shaw et al., 2005). Four end-member scenarios relating to actively growing topographic features are shown in Table 4.4 (Burbank and Vergés, 1994, Ford et al., 1997):

1. uplift following a period with no structural growth whereby beds are deformed, but retain an even thickness over the structure;
2. medium rates structural growth generating some topographic relief and causing beds to thin over the structure but still overtop it;
3. high rates of structural growth resulting in high positive topographic relief causing sediment to onlap the structure, and
4. in areas where structural growth continues to outpace sedimentation offlapping strata can be observed whereby the strata are deposited progressively away from the flanks of the structure due, in part, to rotation of the fold limbs during their evolution.

These different stratal relationships can be used to infer information about the relative rate of sediment accumulation versus the rate of uplift of the structure (Burbank and Vergés, 1994) and ultimately information about the amount of the structure which was emergent during a specific period (Broucke et al., 2004, Shaw et al., 2004, Shaw et al., 2005); onlapping and offlapping stratal geometries both suggest emergent topography.

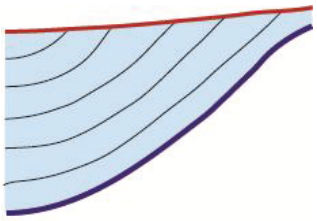
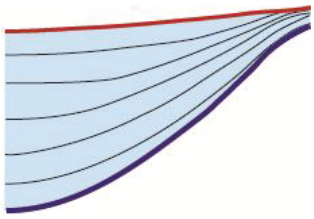
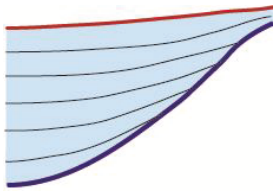
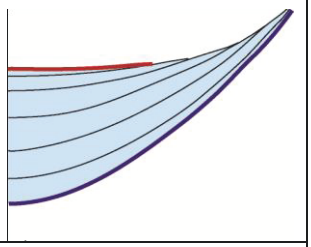
Increasing structural growth and/or decreasing sediment deposition →			
Truncated horizons parallel to anticline	Overtopping of strata over the anticline	Onlapping strata onto anticline	Offlap of strata off the growing structure
			
• Strata upturned and truncated by overlying beds, • strata removed by erosion after deposition, • parallel bedding indicates no topographic growth during deposition, then subsequent uplift.	• Active, but relatively slow, growth on the anticline during sediment deposition, • anticline had had limited seafloor expression • sediments continue over the top of the anticline.	• Sediments onlap anticline, • anticline was a topographic high on the seafloor causing sediment to onlap and become truncated, • typical of under-filled basins and high structural growth.	• Strata thin towards structure and sequentially offlap further away from the main growth, • anticline formed a topographic high and continued to grow rapidly, • sediment cannot keep pace with growth.

Table 4.4 A series of cartoons illustrating the types of stratal relationships with structural growth.

In areas where strata flank passively growing salt diapirs, thinning and upturning of beds near the diapirs along with the development of localised unconformities has long been recognised both in outcrop data and in the subsurface (Bornhauser, 1969, Johnson and Bredeson, 1971, Steiner, 1976, Lemon, 1985, Schultz-Ela et al., 1993, Davison et al., 1996, Schultz-Ela, 2003, Giles and Rowan, 2012). Giles and Rowan (2012) observe patterns acting at two scales (Table 4.5):

1. over a large area where strata flanking passive diapirs often thin towards the structures due to differential subsidence of mini-basins into the underlying salt or regional shortening of the diapirs and mini-basins; or
2. over a smaller area where restricted drape folding and stratal thinning is common due to local topographic relief

They refer to the second, local changes as halokinetic sequences which they define as packages of halokinetic growth strata bound by angular unconformities. Accordingly Giles and Rowan (2012) define two types of halokinetic sequence, which stack laterally to form composite halokinetic sequences (Table 4.5). They state that the type of halokinetic sequence which forms, relates to the relationship between the rate at which the salt structures grow compared to the sediment accumulation rate. When sediment accumulation rate is rapid relative to structural growth rate, thick roofs develop over the top of the salt diapir leading to the generation of tapered halokinetic sequences. On the other hand, if sediment accumulation rate is relatively slow compared to diapir growth rate then a thin roof will form leading to a tabular composite halokinetic sequence (Table 4.5).

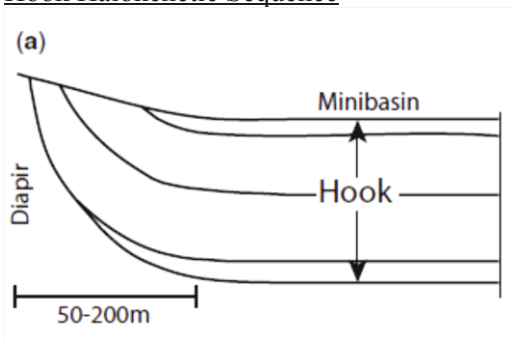
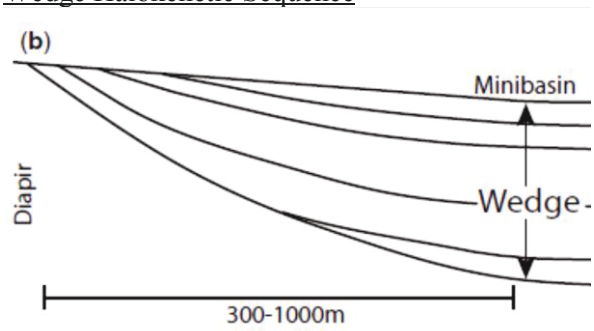
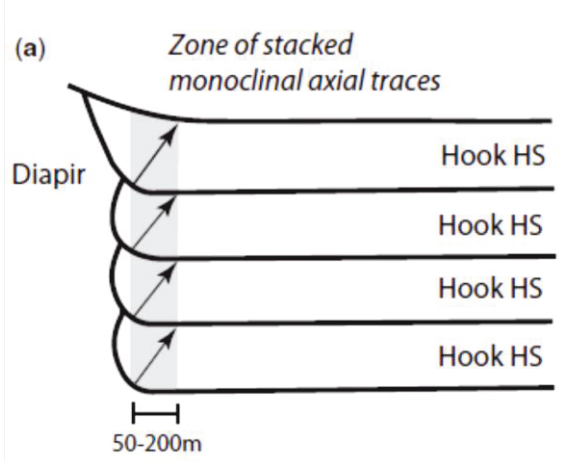
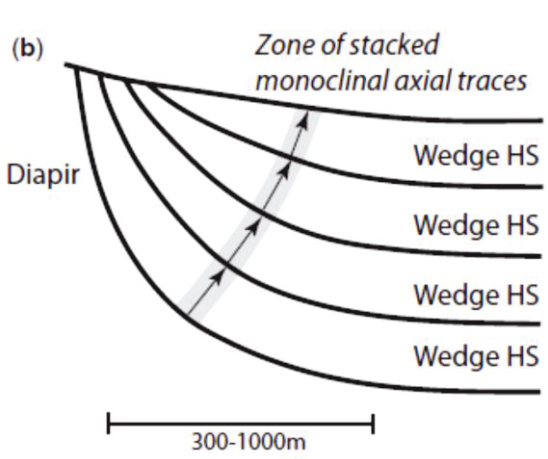
Hook Halokenetic Sequence	Wedge Halokenetic Sequence
	
Tabular Composite Halokenetic Sequence	**Tapered Composite Halokenetic Sequence**
	
• Drape folds 50 – 200 m from diapir • ≤ 90° unconformities • Near-diapir abrupt facies change • Mass transport complex generation common	• Drape folding 300 – 1000 m from diapir • < 30° angular unconformities • Broad zone of gradational facies changes • Mass transport complex generation less common

Table 4.5 Two types of halokinetic sequence described by Giles and Rowan (2012) with the main characterises outlined below the images.

As well as discussing the onlap patterns at this large scale it is possible to analyse the beds contained within one hook or wedge halokinetic sequence (Table 4.5). As previously discussed, analysing individual growth strata within these sequences can give some indication of the amount of topography present at the time of deposition (Broucke et al., 2004, Shaw et al., 2004, Shaw et al., 2005), as well as giving some indication of the rate at which the structure was moving (Burbank and Vergés, 1994, Schlische, 1995, Burbank et al., 1996, Ford et al., 1997). To this end, and to compliment the results of the strain analysis, the growth strata are examined in Chapter 8. This includes spatially mapping the onlap and offlap locations of the key surfaces within the ponded interval (i.e. P20 – P50) and a full discussion of the growth stratal geometries within the intervals containing channel complexes and MTC deposits.

4.2.13 ArcGIS Analysis

Several of the chapters within the thesis contain work carried out using ArcGIS software to gather accurate measurements. This program was used because standard seismic interpretation and visualisation software has not been designed to allow measurements of spatially referenced data to be extracted from seismic reflection volumes. Therefore, in this study geographic information software (GIS) has been integrated with

the seismic interpretation software in order to allow documentation and analysis of the deepwater fan systems (Chapter 7), to facilitate accurate mapping of the structures in the area (Chapter 5) and to fully integrate the seismic amplitude extractions with the accurately mapped structural elements map (Chapter 8).

The ArcGIS software coordinate system was set using the Camacupa/TM 12SE projected CRS which uses the Camacupa geographic 2D CRS as its base CRS and the TM 12 SE (Transverse Mercator) as its projection, making it suitable for referencing measurements offshore Angola (J. O'Brien 2012, pers. comm.). The amplitude extraction maps were imported into ArcGIS using the georeferencing tool and a series of geographical co-ordinates collected from the seismic interpretation software, PowerView®. The individual features (for example channel edges, the main fault trace, the location of the anticline hinges etc) were then digitalised using the curve or line drawing tools and converted from a graphic to a feature. Any changes were subsequently made using the editing tool and then the maps either exported as images, or the channel morphology data (i.e. channel orientations within the fan lobe complexes) exported into excel for further analysis.

5 Structural Analysis of the Mini-Basin

5.1 Abstract

Analysis of the interaction between actively growing salt structures and coeval deepwater sedimentary systems form the basis of the work within this thesis. This chapter uses a variety of different approaches to thoroughly analyse the growth of the structures which bound the basin, generating a clear description of its evolution and how the spatial distribution of the actively evolving structures varies through time. As well as being of interest here, this information will be incorporated elsewhere in the thesis to analyse the response of various sedimentary systems to this growth.

Structural restoration, isopach maps and sediment accumulation rate maps have been used alongside to identify periods of high structural growth within the basin. These indicate two main periods of basin-wide higher structural growth; the first in the Oligocene from 33.9 Ma to 25 Ma, where rate of change of bed length analysis and isopach maps indicate clear thinning over structural highs, and a second in the Mid Miocene from 18.26 Ma to 13.25 Ma, also indicated by high rates bed length change and the thinning of sediment growth packages. The lack of correlation between high sediment accumulation rates in the main depocentres and periods of high structural growth suggested that these two periods of basin-wide growth were driven by regional-scale processes as opposed to local sediment loading.

The correlation between high rates of bed length change and the thinning of sediment packages recorded throughout this history of the basin indicates that it is valid to use bed length change as a proxy for the amount of growth and hence the presence of positive bathymetric relief on the seafloor. This novel approach uses the values calculated during the bed length change analysis to generate maps which indicate the spatial location of the high, medium and low rate of change of bed length structures (and hence inferred high, medium and low growth-rate structures) through the history of the basin. These maps will also be used in subsequent chapters of the thesis to thoroughly investigate the response of sedimentary systems to structural growth.

5.2 Introduction

This chapter aims to give a broad overview of the structural evolution of the salt influenced mini-basin; constraining the rate at which the structures within and bounding the basin developed and the spatial distribution of the structures with the highest change of bed length. Within salt provinces the term mini-basin is often used for structural lows formed by removal of an underlying mobile substrate (normally salt), which become sites of significant sediment accumulation. The most common explanation for the formation of the simplest type of mini-basin is that salt is forced from beneath the basin by the weight of sedimentary fill and flows into the adjacent structures. Thus the basin forms by density-driven subsidence (Hudec et al. 2009). However, other processes such as extension and shortening are considered to play an important role in the subsidence mechanism for more complex mini-basin types (Hudec et al., 2009). For

example, in areas of shortening, such as the study area of this thesis, while the salt walls or diapirs are shortened and uplifted, the intervening mini-basins will form a bathymetric depression. In this case diapir 'inflation' (essentially uplift) is a more important mechanism for generating a bathymetric low than salt withdrawal (Rowan 2002).

The way in which sedimentary systems interact with the bathymetry in a mini-basin is strongly controlled by the geometry of the basin, the rate at which the salt structures deform through time and the volume of sediment deposited in the basin. In this chapter several different approaches are taken to understand how the geometry of the basin within the study area evolved, the timing of the growth of the structures situated on the basin margins and within the basin, and sediment thickness distributions within the basin.

The structural restoration of a representative line through the mini-basin is used at the start of the study to show the mini-basin evolution through time in a broad context. This analysis is complemented by a detailed bed length change analysis of the individual structures that affect the depositional systems. The results from this are discussed in detail in this chapter and then used in subsequent chapters to investigate the response of three types of deepwater sedimentary systems to this growth: mass transport complexes (MTCs) which are, in general, linked to periods of high structural growth (Chapter 6); a ponded fan system which formed in a period of low structural growth (Chapter 7); and third-order slope channel complexes which respond to the growth in different ways depending on the rate of growth of the structure they encounter (Chapter 8, where MTC and ponded fans are also discussed).

Isopach maps and sediment accumulation rate maps are also used in this chapter to give a slightly different insight into the structural development of the basin. These provide both a broad overview of the depocentre evolution though time, and at a more local scale provide insight into structural growth, where reduction in sediment thickness close to a structure is an obvious indication that the structure was active. In addition, because the isopach and sediment accumulation rate maps cover the entire basin they allow growth to be identified on the structures not included in the bed length change analysis.

5.3 Methodology

The structural evolution of the mini-basin has been analysed using a series of different methods which approach the problem at differing levels of detail; from structural restoration of a section across the basin, through isopach analysis across the whole basin and down to finer-scale analysis of the bed length change recorded on individual structures. The analysis starts at the broad scale by restoring a representative section across the centre of the mini-basin. A complete discussion of the reasoning behind the choice of algorithm and restoration technique can be found in Chapter 4, Sections 4.2.5 to 4.2.8.

A full discussion of the methodology used to generate the isopach maps shown in this chapter is presented in Chapter 4, Section 4.2.4. Given the available biostratigraphy, the isopach maps were normalised using the horizon ages to generate sediment accumulation rate maps which allowed direct comparisons to be made between the sediment accumulated during the time periods defined by mapped surfaces.

The methodology used for the bed length change analysis is also outlined in full in Chapter 4, Sections 4.2.9 and 4.2.11 with a full discussion of the errors associated with this analysis presented in Section 4.2.10. The values were calculated for the main structures within the vicinity of the mini-basin. These were chosen as they either bound the basin, or were in the centre of the basin and thus affected the sedimentary depositional systems which entered the basin. Changes in thickness recorded in the isopach maps and sediment accumulation maps were also used to guide the selection of structures to be analysed. Bed length change was calculated for 21 lines, each of which was oriented perpendicular to the main strike of the structures and is 5 km in length at the present day. The results are presented both graphically and in map view. Further analysis focussed on one structure within Area C, allowing the linkages between the three anticlines in this region to be observed and discussed. For this part of the study 18 transects across the structure were investigated at 1 km spacing. Again, each was 5 km in length at present day, thus allowing direct comparisons between all the bed length change results.

5.4 Regional Overview

5.4.1 Gravity and Magnetic Analysis

Gravity and magnetic data over the region can be used to provide some insight on the deep, sub-salt structure and regional depocentres on the Angolan passive margin. The deposition of salt in the Aptian had a major influence on the overlying structures and is likely to have prevented the overlying basin infill from being directly influenced by the underlying rift structures that formed during the initial development of the passive margin (see Chapter 2 for further discussion of the evolution of the passive margin). However, some of the salt structures generated along the Angolan margin may have been influenced by the underlying basement topography which can be interpreted on free air gravity data and magnetic data (Figure 5.1).

Regional-scale gravity data indicate that Block 31 is bisected by an elongated high gravity anomaly trending NW-SE with significantly lower gravity anomalies to either side. This relatively high gravity anomaly could be indicative of a basement ridge in this area, which would lie under the salt wall that defines the western margin of the study area within Block 31. However, the corresponding magnetic data in the region does not correlate to this signal with three parallel high magnetic intensity areas which may suggest more isolated basement highs (Figure 5.1 (b)).

The gravity high is postulated to be one of a series of basement highs imaged elsewhere along the Angolan margin with more thought to occur outboard of this area (BP internal document). These basement structures may impact the initial distribution of the salt within the area and hence the location of the salt structures which form as the basin develops.

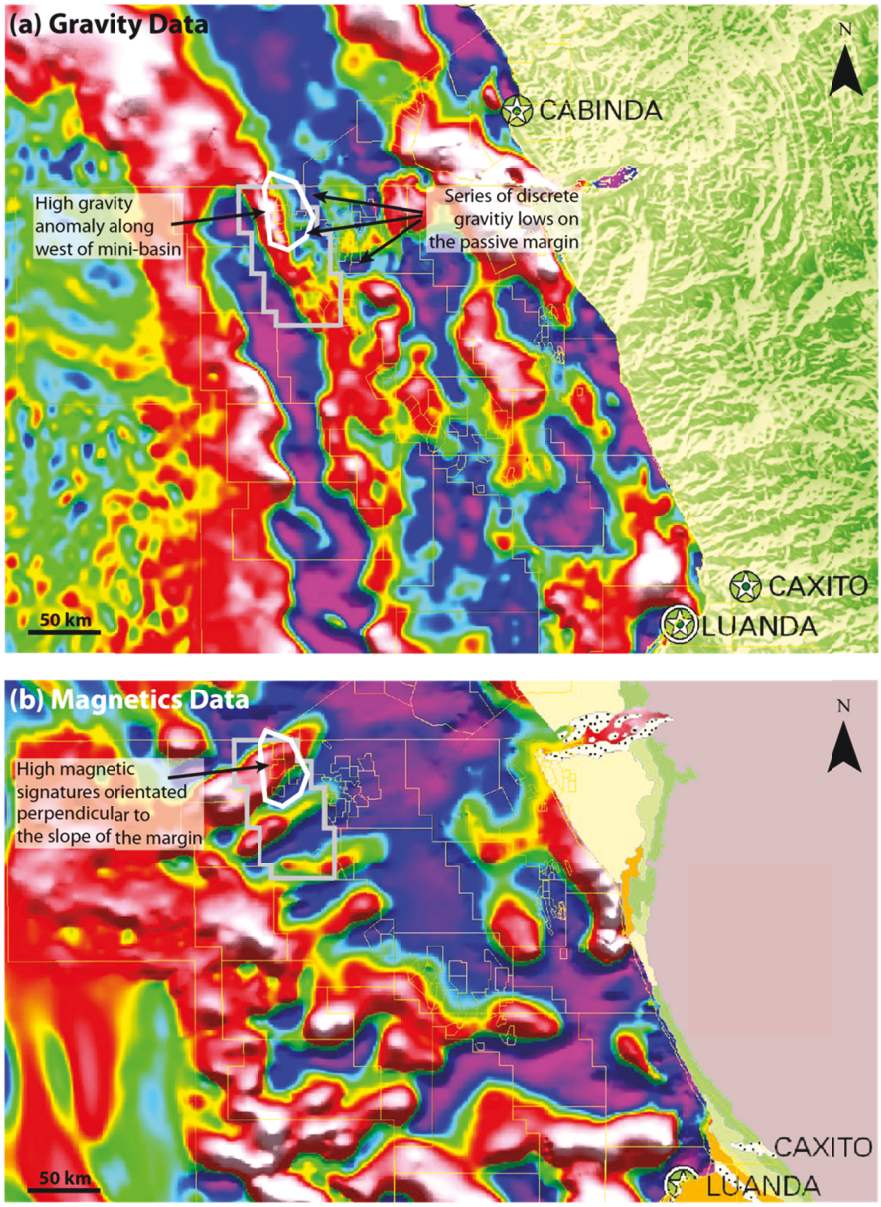


Figure 5.1 Maps over the region offshore Angola showing (a) regional gravity with a 200 km wavelength filter applied, red is high gravity and purple low and (b) regional magnetic intensity map where red is high intensity and purple is low intensity. In both maps Block 31 is outlined in grey and the study area in white.

5.4.2 Regional Salt Setting

Regionally, the study area is located in the downdip compressional domain of the Lower Congo Basin on the Angolan passive margin. It is located within an area dominated by salt canopies, salt diapirs and salt-cored anticlines (Figure 5.2). There are four main salt provinces along the Angolan passive margin; the extensional province, the salt diapir province, the salt canopy province and the salt nappe province (see Chapter 2 for further discussion of these). The study area is bordered to the west by the salt nappe province which, in this area, is characterised by a relatively small volume of allochthonous salt. There is a long-lived salt wall on the western margin which extends the length of the area terminating at the strike-slip fault indicated in Figure 5.2 (a). The shape of the salt canopy indicates salt movement from the east, consistent with the salt having been driven basinward by up-dip extension, in response to differential subsidence across the passive margin and an increase in sediment loading (Figure 5.2 (b)).

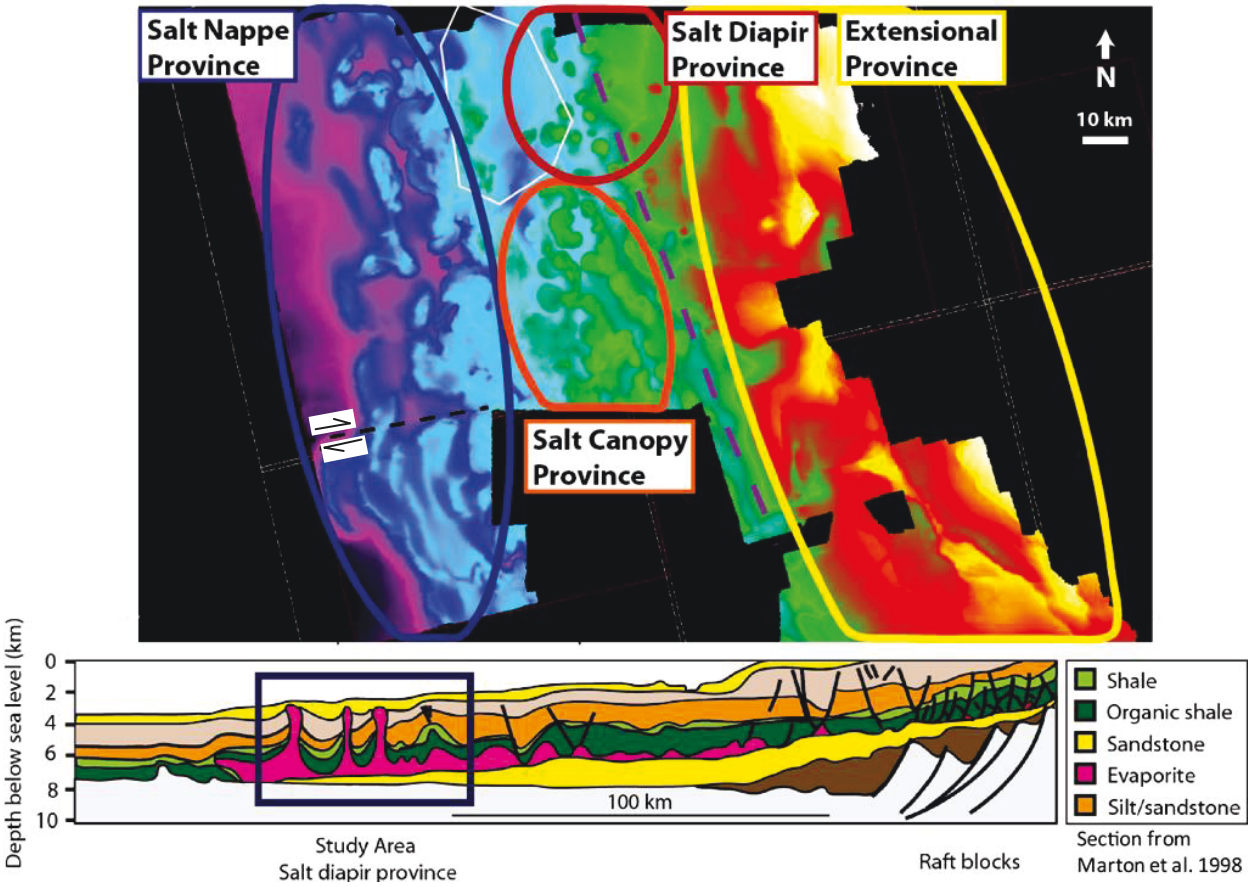


Figure 5.2 Bathymetry map of the top H120 surface which highlights the main salt domains off the Angolan Passive margin. The study area is outlined in white. The section is a stylised section located slightly to the north of the basin (i.e. located almost directly north of the bathymetric map) which has similar features to those seen near to the study area. The approximate location of the study area on the passive margin is also shown, modified from Marton et al.(2000).

The early history of salt movement, soon after deposition, is likely to have involved salt flow down-dip, due to oceanward tilting of the margin in response to thermal subsidence. This may have contributed to early salt inflation in the study area, as is considered to have occurred in similar structural settings in the Santos and Campos Basins of Brazil, and Kwanza Basin to the south in Angola (Quirk et al., 2012). However, the increase in sediment load since Oligocene times, following the initiation of the large Congo (Zaire) fan system in the Lower Congo Basin, is likely to have been the main trigger for the Oligocene and younger salt tectonics in this part of the Angolan margin (Brice et al., 1982, Marton et al., 2000, Babonneau et al., 2002, Anderson et al., 2012). As discussed in detail in Chapter 2, this initiation is thought to be driven by a variety of factors including (Reyre, 1984, Droz et al., 1996, Anderson et al., 2012):

- structural deformation and uplift onshore west Africa which increased the amount of bedload in river systems;
- a world-wide lowering of sea level; and
- the development of a more humid climate in the drainage area.

To the south of the study area the salt front appears to be offset dextrally (Figure 5.2), which may also indicate some deeper basement control on either the original salt depocentres or the later salt tectonics. The trend of the strike-slip offset is parallel to one of the high magnetic anomalies shown on Figure 5.1, which would corroborate the idea that this feature exploits an existing basement structure.

5.5 Mini-Basin Structural Setting

The mini-basin is characterised by contractional features such as salt-cored anticlines, diapiric salt bodies and thick, allochthonous salt canopies which have formed predominantly by down-dip shortening, concomitant with salt movement (Figures 5.2 and 5.3). The western edge of the basin is defined by a series of broadly north-south trending salt-cored anticlines, with continued salt movement along this trend generating a series of salt walls. The major salt walls are labelled Areas B and D on the west side of the basin (Figure 5.3; pink anticline symbols indicate the inferred existence of anticlines). North-south trending salt-cored anticlines form the eastern boundary of the basin, some of which have formed young allochthonous salt canopies (post H110, 5.58 Ma), whose salt stocks remain attached to the source salt (Area F; Figure 5.4 (c)). A series of northeast-southwest trending anticlines, along which less salt movement occurred, formed in the centre and south of the basin area (Figure 5.3; Areas C and E). A few of the diapirs which subsequently punctuated the cores of these anticlines are connected to the original Aptian autochthonous salt layer but the majority form isolated to semi-isolated allochthonous salt bodies which are detached from the source salt layer. Sub-parallel, north-south trending salt-cored anticlines form the western border in the northern part of the basin (Area A; Figure 5.4 (b)).

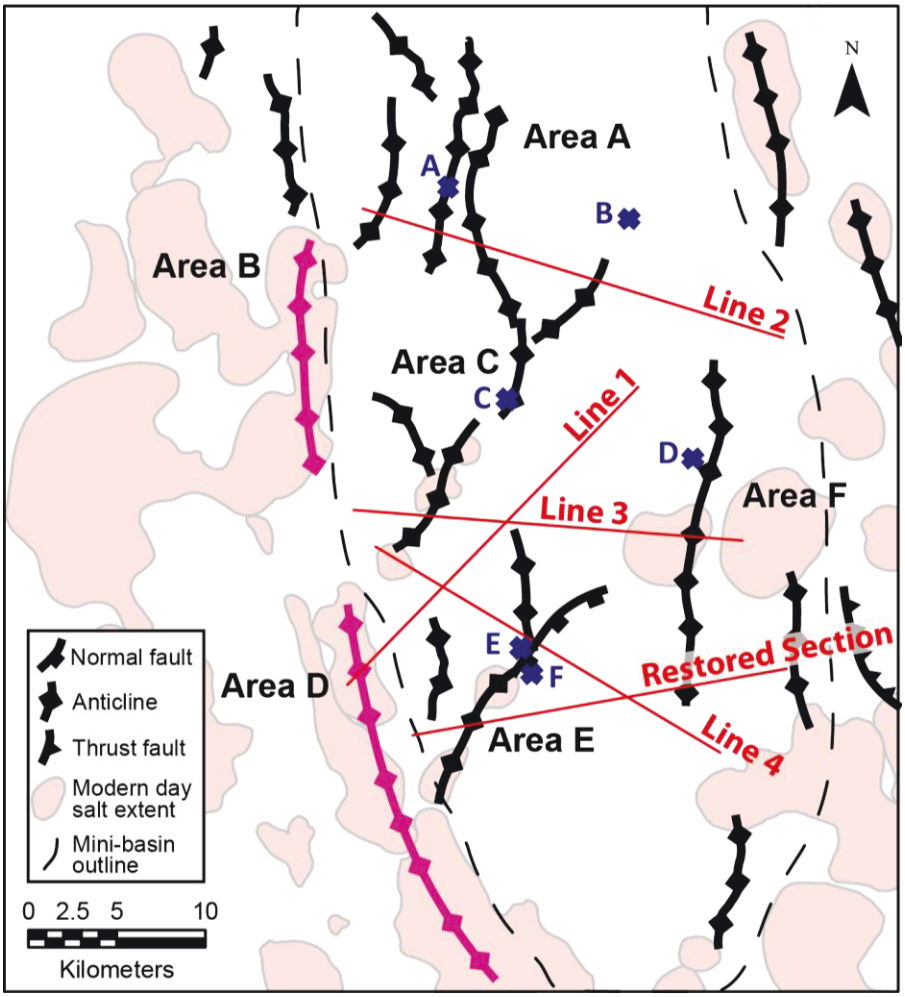


Figure 5.3 Structural elements map showing the location of the main structures in the area. Salt distribution (pink) is that seen at or near the surface at present day; black lines indicate anticlines visible in the seismic data, pink lines indicate anticlines inferred from the seismic data, red lines 1 – 4 relate to seismic sections in Figures 5.4 and 5.5. The blue crosses represent locations of the six main wells in the area.

Growth on the western salt structure, along the length of the basin, has been extensive throughout the history of the basin and continues to present day. Thinning of the sediment packages suggest that the main structural activity started in the Oligocene (i.e. before the H10 was deposited at 18.26 Ma) with the main canopy salt features forming from H80 (10.89 Ma) onwards (Figure 5.4 (a), (b) and (d)); A. Hutchinson 2014, pers. comm.). The two southerly seismic sections indicate that some of these salt structures are still growing at present day, generating positive topography on the seafloor (Figure 5.4 (c) and (d)). The structures along the western margin of the mini-basin appear to have been subject to the most growth, and in places units deposited between the H10 and H60 horizon (18.26 – 13.25 Ma) crop out on the seafloor due to this salt activity (Line 1, Figure 5.4 (a)). The high gravity anomaly seen in Figure 5.1 (a) has a similar orientation to this active salt wall, indicating that the continued growth in this area may be in some way linked to this feature.

The eastern edge of the basin is less uniform in its structural pattern with a greater change in structural style and timing of the main periods of structural growth. The main structure on this side of the basin is a salt-cored anticline which has been locally pierced by salt movement towards the centre of Area F (Figures 5.3 and 5.4 (c)). The southern tip of this anticlinal fold has also been imaged east of the normal fault in Figure 5.4 (d) where an increase height of the top of the salt can be observed. It is difficult to constrain timing of growth of this structure; whilst the beds deposited between the H00 and H70 (33 Ma and 11.86 Ma) do not appear to change in thickness towards the structure it might be that there is some degree of thinning in the beds close to the salt sock that has been obscured by the later salt growth (Figure 5.4, (c)). It is however, clear from the seismic data that lateral salt flow and canopy development took place in the last 5 Ma (post H120). This detail is also supported by the isopach and bed length change analyses discussed in detail later in this chapter.

The smaller structures located within the centre of the mini-basin tend to have a distinctly different orientation to the structures along the basin margins; trending more northeast-southwest compared to the basin-bounding structures which tend to be orientated more north-south (Figure 5.3). In general the structures located towards the centre of the mini-basin were more active in the early history of the basin from H00 until the H10 or H20 interval (i.e. between 33 Ma and 18.26 Ma) with units thinning over the top of them during this period (Figure 5.4 (b), (c) and (d)). After this time these folds are mostly buried and appear in-active.

A northeast-southwest trending arcuate normal fault is also identified on the structural elements map and the seismic sections (Figures 5.3 and 5.4 (d)). This has a similar orientation to the structures within Areas A, C, and the southern half of Area E, and downthrows to the south. Seismic data indicates that it has been active since at least 9.68 Ma (H90) with a thickening of the sediment south of the fault after this time and evidence of tilting in the hanging wall (Figure 5.4 (d)). The offset of the fault decreases from the southwest to the northeast indicating that it is likely to be linked to collapse over the top of an anticline structure related either to salt withdrawal at its south-western tip or to lateral flow of salt into the diapir situated in Area E (Figure 5.3).

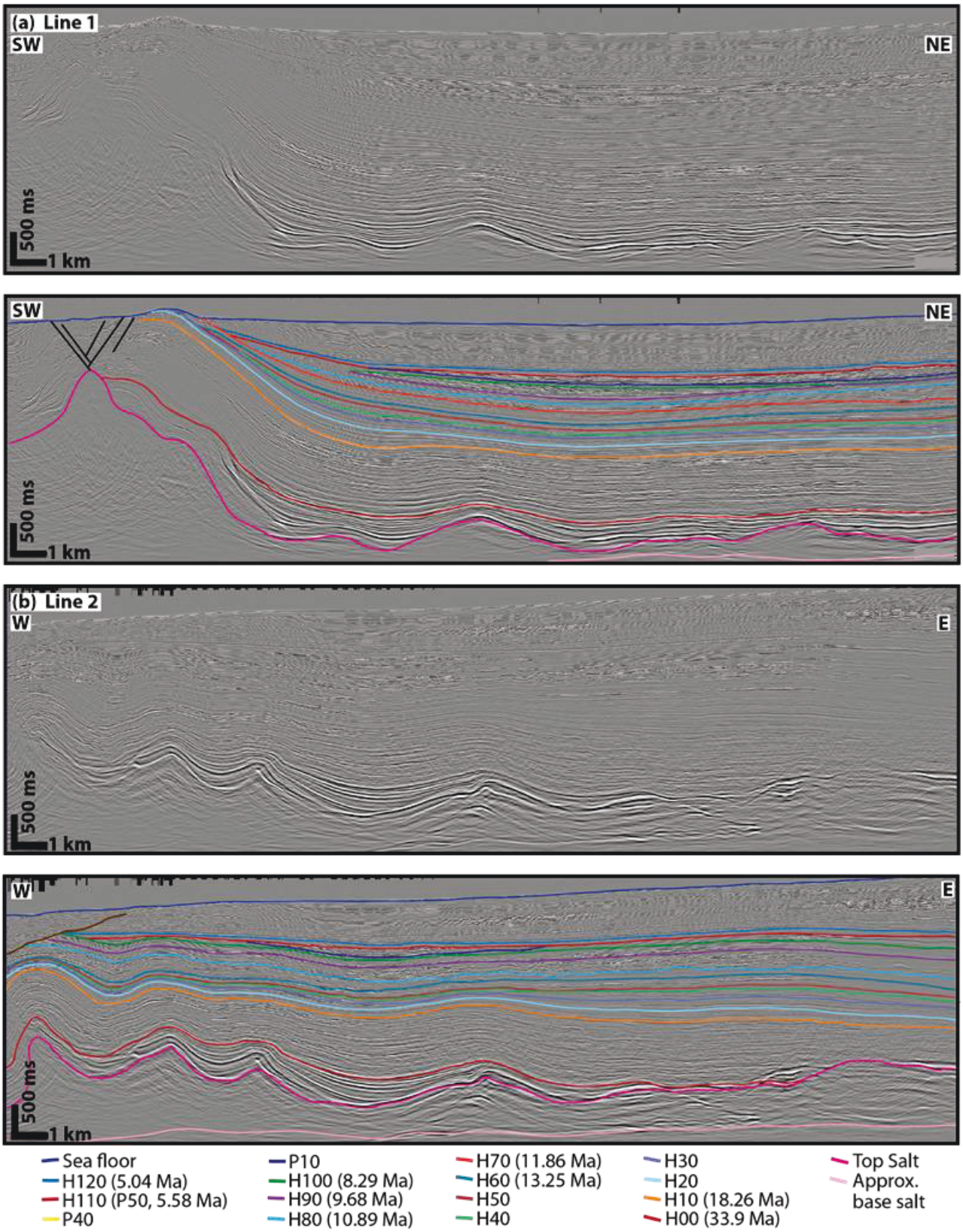


Figure 5.4 Seismic sections through the basin showing (a) Line 1, selected through the length of the basin and (b) Line 2 in the north of the area. Locations of these lines are shown in Figure 5.3. Black lines show fault locations and brown line indicates the base of a slump.

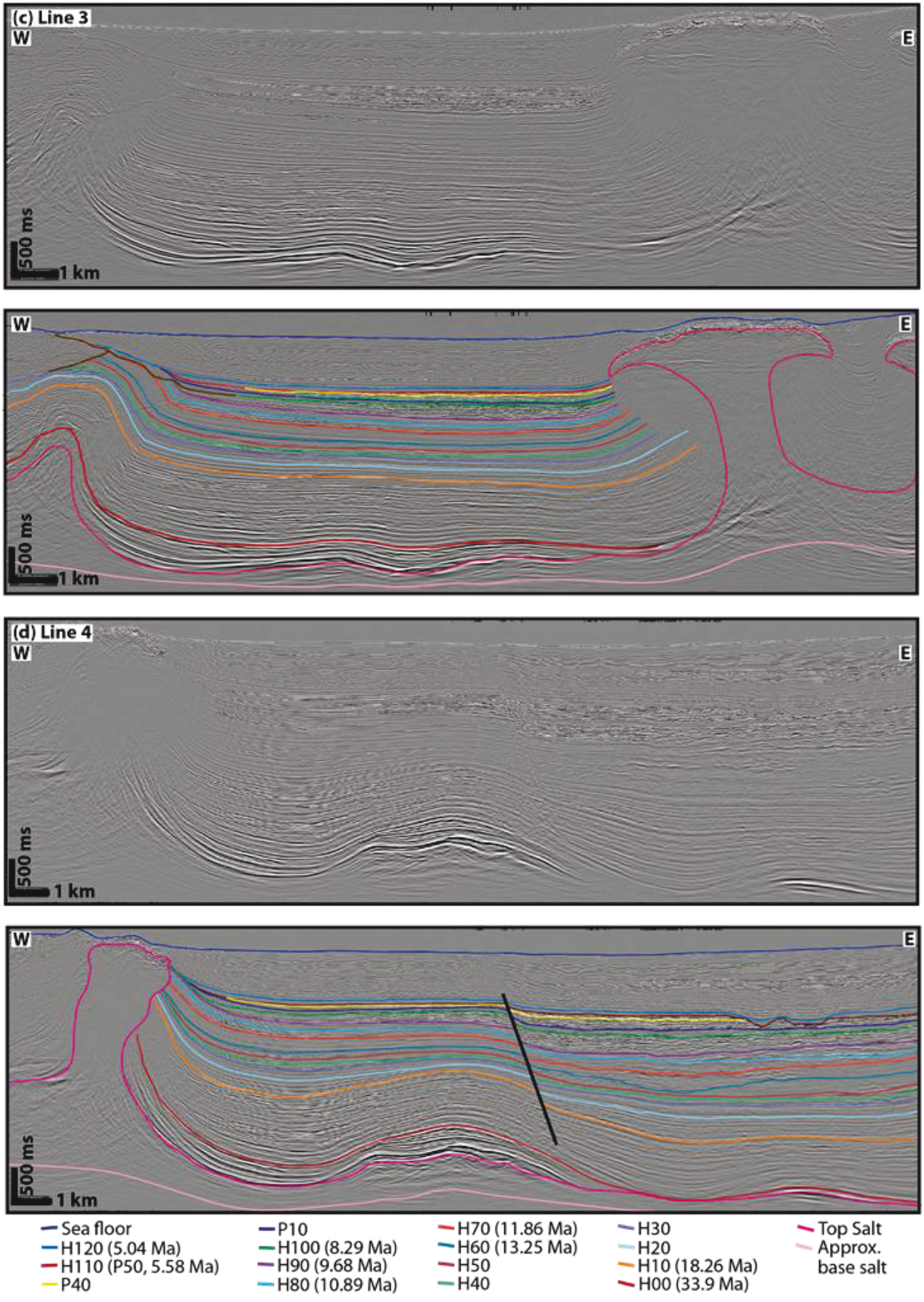


Figure 5.4 cont. Seismic lines perpendicular to the main basin orientation, (c) Line 3 across the centre of the basin and (d) Line 4 across the south of the area and showing the normal fault. The locations of both of these lines are shown in Figure 5.3. Black lines show the location of the normal fault and brown lines indicate the possible location of slip surfaces at the base of slide deposits.

5.6 2D Reconstruction across the Mini-Basin

A sequential restoration of a section across the mini-basin reveals one potential scenario for the evolution of the mini-basin through time (Figure 5.5). The salt volume has been kept constant from 18.26 Ma (H10) until present day, thus assuming that the majority of the salt had moved down-dip before the deposition of H10; prior to this period the salt volume was allowed to expand. Retaining a constant salt volume from 18.26 Ma to present day assumes that no salt is lost or gained through time which should be valid if the amount of salt entering and leaving the plane of the section is averaged out and there is no dissolution at the seafloor (Marton et al., 2000). This implies that all deformation is confined to the post-salt sections and that salt movement was largely a function of local withdrawal in response to sediment loading and shortening within the mini-basin, causing the squeezing of salt in to the core of the folds or the salt walls. Obviously, this does not represent a true image of the salt volumes and movement through time but, given the lack of constraint on the original salt thickness and its complex 3D history, this was thought to give the most accurate depiction of salt movement within the basin (R. Humphries 2011, pers. comm.). Given that the restoration is based on the sequential removal of known sediment thicknesses, and hence that the timing of the main growth phases is pre-determined, the results given by this structural restoration are thought to be an accurate representation of one potential model of basin evolution.

The base salt is poorly imaged, and hence difficult to identify within this area, leading to two different models: (a) salt deposited across the region was approximately uniform in thickness then tilted due to the effect of sediment loading and/or thermal cooling at the basin-margin scale, or (b) the original salt deposited thinned onto a basement high at the western edge of the basin (Figure 5.5). As discussed above regional gravity data indicates the presence of a basement high along the western edge of the basin (Figure 5.1). Such a high could also have provided some structural control for development of the prominent salt wall in this location. The high could have allowed thinning of salt over it and then provided a buttress against which the salt inflated during early tilting and/or subsequent salt movement, fixing the salt wall in this position (Figure 5.5, H00). This second model, whereby salt movement is constrained by an earlier buttress, has been used during the restoration.

The restoration shows that the majority of the bed length change occurs within the H60 – H120 interval from the Mid to Late Miocene (13.25 Ma to 5.04 Ma; Figure 5.5). It is also clear that underlying topography, or early salt movement, affected sediment distribution at the mini-basin scale from 33.9 Ma (H00) onwards, with thicker sediment deposited in the west and less to the east. However, the main western structure begins to grow between H00 to H10 (33.9 Ma to 18.26 Ma), as indicated by a decrease in sediment thickness towards the developing western structure. Both the western and eastern structures were active during the H60 to H70 (13.25 Ma to 11.86 Ma) interval. Strata thinned over the eastern fold, but onlapped onto the western salt wall where the H00 to H10 (33.9 Ma to 18.26 Ma) horizons appear to be already emergent at the sea floor.

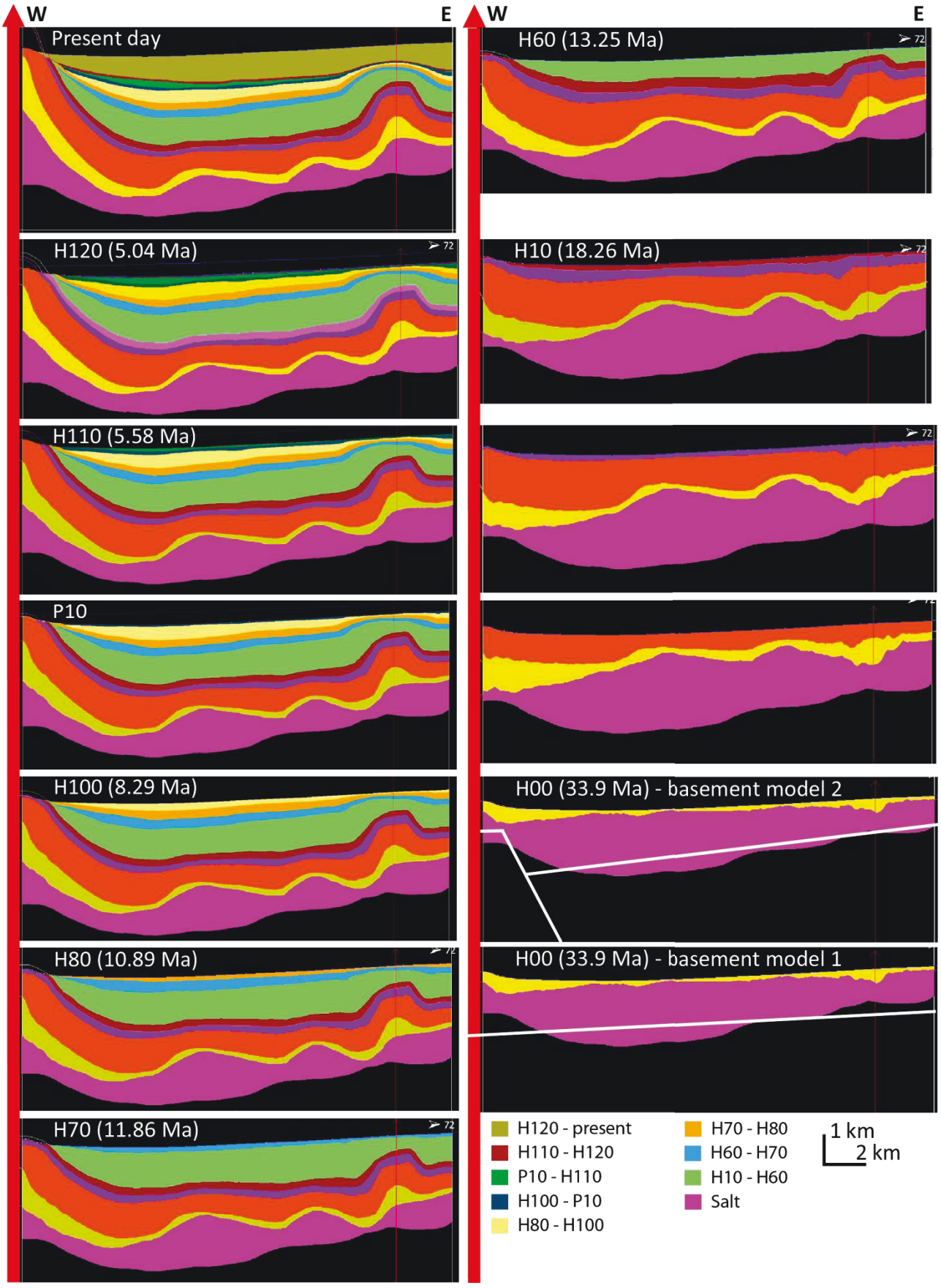


Figure 5.5 A structural restoration using a seismic section across the southern part of the basement (the location is seen in Figure 5.3). Two alternative basement structure models are also shown to give an indication of how basement structure could impact the original salt distribution. The white lines on the two oldest sections indicate two alternative basement models, these cut across the known salt, but are drawn as schematic sections.

Between 8.29 Ma and 5.58 Ma both the P10 and the H120 horizons onlap both sides of the eastern anticline, indicating that the structure was growing at a faster rate at this time, with growth outpacing the sediment supplied to the area (Figure 5.5). The thickest sediment packages were deposited at the western side of the basin adjacent to the western salt structure. This indicates that at this time there was increased growth of the salt wall either due to increased salt flow into the wall or increased shortening and the generation of more accommodation space adjacent to the structure. The salt wall structure continued to be active until the present day (5.58 Ma onwards) with an inflation of the salt beneath the structure and increased tilting of the horizons deposited between H00 to H10 (33.9 Ma to 18.26 Ma). Some thinning of the sediment continued over the eastern structure on the restoration, but stopped sometime within the last 5 Ma as there is no evidence of growth at the seafloor at present day. However, north of the restoration line on the same anticlinal structure within Area F, later salt canopy formation occurred between 5.58 Ma (H110) and the present day generating clear seabed bathymetry (Figure 5.4 (d)).

The two salt swells in centre of the restored section are related to the Oligocene or older history of the basin. They are orientated broadly northeast-southwest in a similar orientation to the older anticlines observed towards the centre of the mini-basin. They affect the thickness of sediment deposited between the H00 to H10 interval (33.9 Ma to 18.26 Ma) and hence relate to the early history of salt distribution and movement in the basin. There is no significant sediment thickness variation over these folds after 18.26 Ma (H10 horizon) and hence they do not appear to have grown after this time (Figure 5.5).

Overall, growth on the salt structure to the west has been active since at least the Oligocene at approximately 33.9 Ma (i.e. the H00 to H10 period) whereas it would appear that the salt cored anticline in the east became most active from the Mid Miocene (13.25 Ma, H60, onwards). It should be noted that the bed length change analysis discussed subsequently indicates that the main fold on the east of the basin did start growing earlier, albeit at very slow rates. Both structures continued to be active until the present day. The reconstructions indicate that sediment was consistently thicker near the western salt between the Upper Miocene (8.29 Ma, H100) and the Pliocene (5.04 Ma, H120) and thins in an eastwardly direction. This reversed between the Pliocene and present day where sediment thickened in the east (H120 – present day, 5.04 Ma onwards).

As previously discussed the location and longevity of the western salt structure could be due to a basement high running north to south in this region. This high could have prevented the salt from easily flowing further down-dip, hence pinning the salt wall in place, and focussing evacuated salt into the wall from the adjacent basin. This would have also led to enhanced stratal rotation through time which has been observed on the flanks of the salt wall, as seen in results of the restoration and on seismic sections through the structure (Figures 5.4 and 5.5).

5.7 Isopach and Sediment Accumulation Analysis

Whilst the structural restoration through the mini-basin allows observations to be drawn about the timing of growth and the general evolution of the mini-basin it only relates to a single section across the southern part of the basin. Therefore, it is useful to use isopach maps generated at different periods in the growth history of the mini-basin to give an indication of the spatial development of more of the structures shown in Figure 5.3. Depocentres identified on isopach maps indicate areas of greatest accommodation space during a specific time window due to tectonic movements (fold and salt wall or diapir growth) or salt withdrawal. Thinned sedimentary packages represent areas where accommodation space is reduced due to growth of folds and associated salt structures. Thus sediment thickness changes on an isopach map can indicate when individual structures in the basin were active, without the need to restore all the structures through time. Examining sequential isopachs allows changes through time to be investigated. However, there is an inherent bias in comparing isopach maps between different time intervals, because a thicker isopach may be purely a function of a longer time interval. Instead sediment accumulation maps, which show a normalised thickness recorded in metres per millions of years, give a much better indication of sediment thickness changes through time. Therefore, a series of sediment accumulation maps, generated using the detailed biostratigraphy discussed in Chapter 4, are presented alongside the isopach maps which also preserve thinning relationships onto growing structures (Figures 5.6 and 5.7).

Isopach maps were produced by depth-converting basin-wide horizons. As most of these basin-wide surfaces were mapped by BP, they did not focus on details across or adjacent to structures, therefore the horizons are less reliable in these areas. A few clearly anomalous features can also be attributed to miss-picks within the horizons, such as the strong line in the north-eastern corner of the maps generated between H80 and H90 (Figures 5.6 and 5.7 (d)). The area covered by the isopach maps also varies between the intervals, again depending on the area covered by the mapped horizons, this is particularly apparent close to Area C which has not been mapped in as much detail between H80 and H100, most likely due to the fact that the sediments thin and become almost non-existent in this area (Figures 5.6 and 5.7 (c) and (d)). The results of the isopach and sediment accumulation analyses are used to illustrate broad depocentre locations and their spatial variation through time as well as to identify the major active structures, which become the focus of the detailed bed length change analysis. The aim of this study is to quantify growth for structures that interacted with the studied depositional systems. Therefore a full understanding of how the mini-basin depocentres and related salt structures formed and evolved is beyond the scope of this thesis.

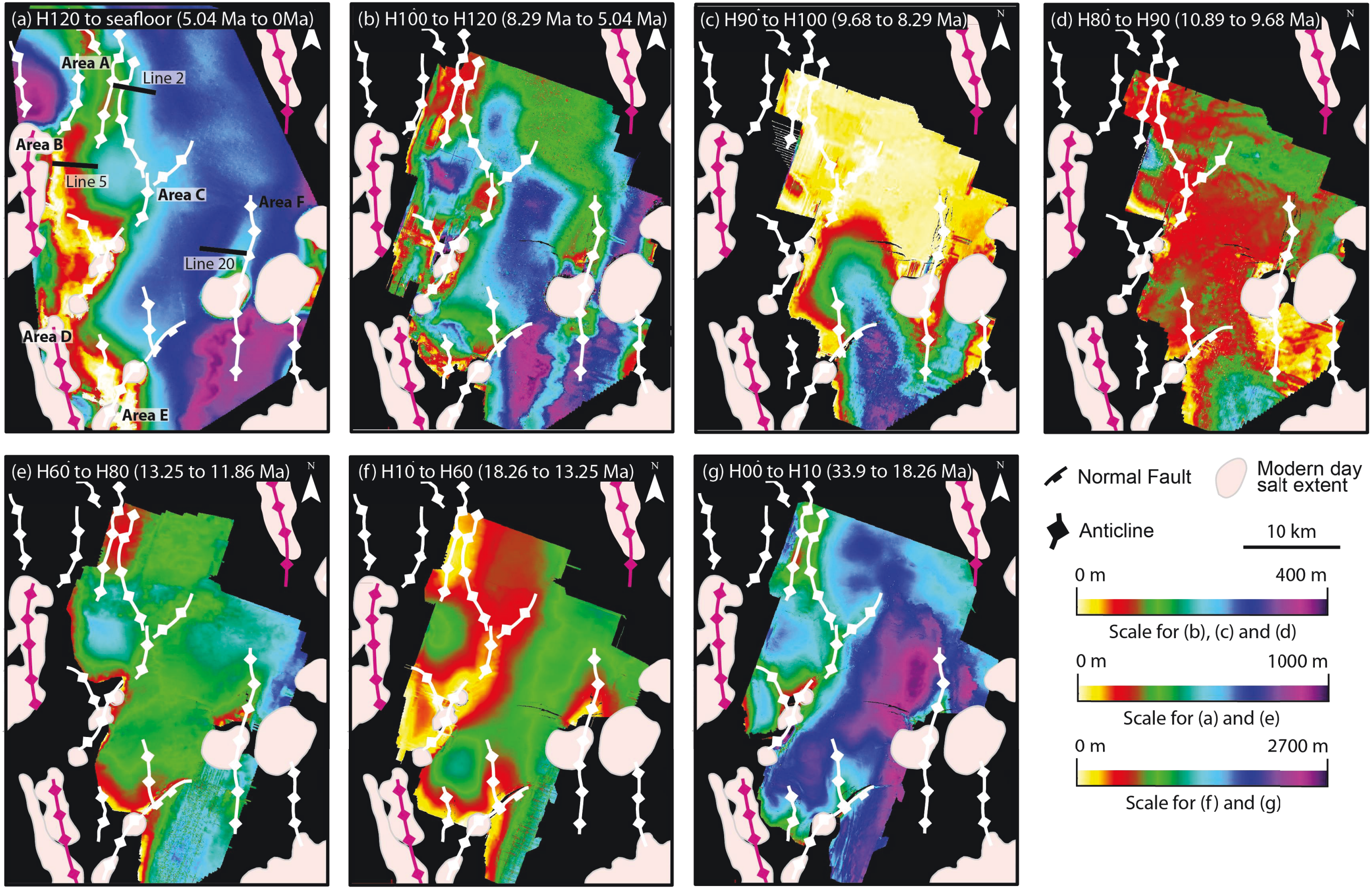


Figure 5.6 Isopach analysis showing how sediment thickness varies through time from (g) the H00 to H10 (33.9 Ma to 18.26 Ma) period through to (a) the H120 - seafloor period (5.04 Ma – 0 Ma). Pink anticlines indicate inferred anticlines where horizons are obscured by recent salt growth. Note that the interval 11.86 Ma to 10.89 Ma was thought to be unreliable and as such has been omitted. Seismic sections though Lines 2, 5 and 20 are shown in Figure 5.8.

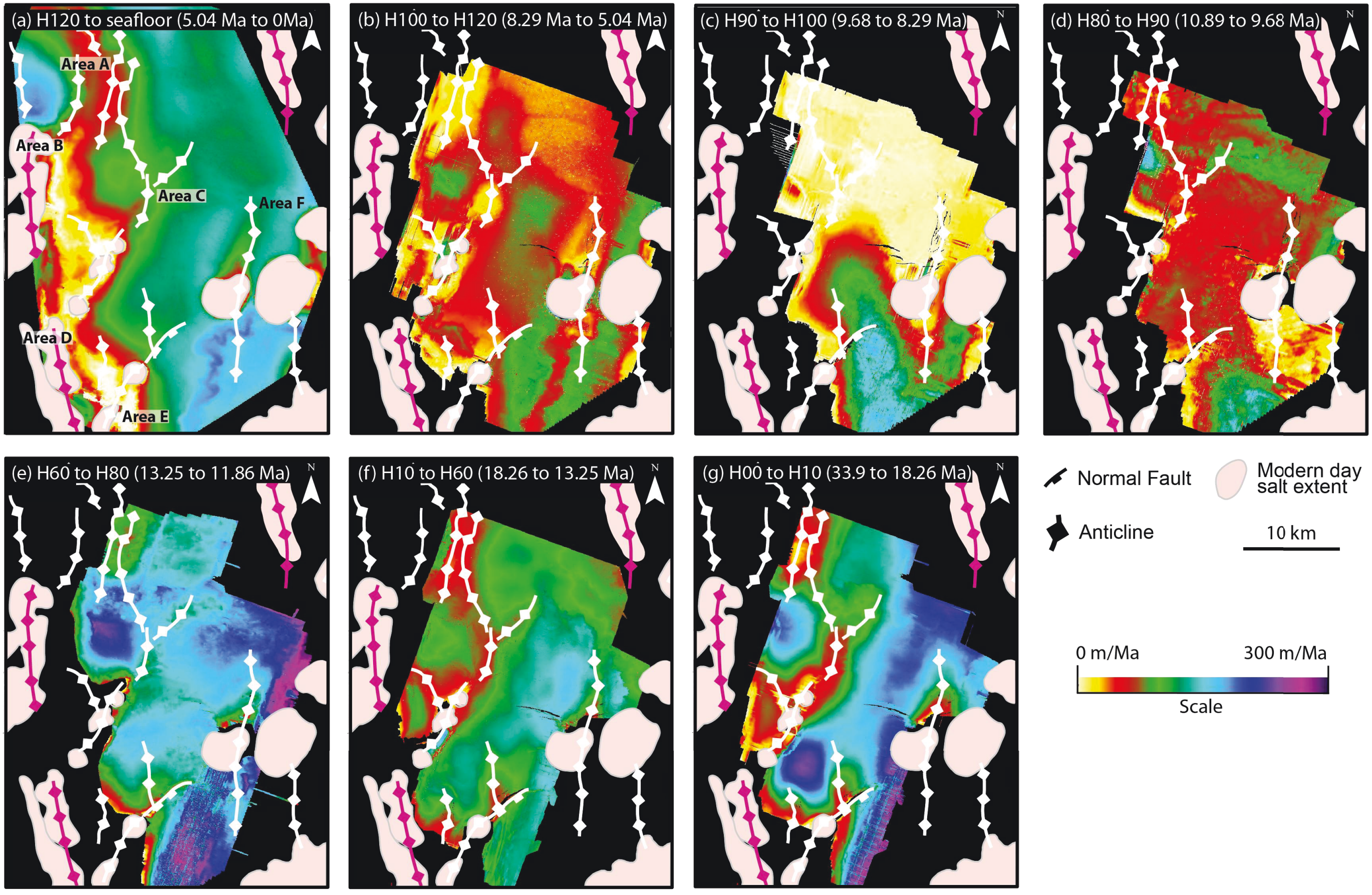


Figure 5.7 Sediment accumulation rate maps through the different periods of the basin evolution, corresponding to the periods seen in the isopach map in Figure 5.6. Note that again the interval 11.86 Ma to 10.89 Ma was thought to be unreliable and as such has been omitted.

The greatest thickness of sediment occurs in the centre of the mini-basin through the entire period of its development from 33.9 Ma until the present day (Figures 5.6 and 5.7). However, changes in both the thickness and the sediment accumulation rate indicate that the shape and orientation of the basin axis has varied considerably through time, as has the development of sub-basins within the area. The salt structures along the western margin of the basin, particularly those in Areas B and D, have been active throughout the history of the mini-basin discussed previously in this chapter (i.e. from 33 Ma onwards). This growth history is not clearly shown by the isopach and sediment accumulation maps as these do not have sufficient coverage. However, thinning of the sediment packages is observed in the seismic sections shown in Figure 5.8 (a) and (b) and is also observed in the structural reconstruction (Figure 5.5). The eastern margin of the basin is also poorly covered by the isopach and sediment accumulation maps in the older phases of mini-basin development, with the seismic sections through Area F suggesting a small amount of thinning of the sediment over the structure during this time (Figure 5.8 (c)). This implies that this structure was growing very slowly during this early period, which is contrary to what the results of the structural restoration showed in Section 5.6 and it may be that during the periods between H10 to H80 (33.9 Ma to 11.86 Ma; Figures 5.6 and 5.7 (e), (f) and (g)) the mini-basin is actually constrained on its eastern margin by structures located to the east of Area F outside the study area.

The period from 33.9 Ma to 18.25 Ma (H00 to H10 interval) contains some of the thickest sediment packages deposited in the basin. This results in a high sediment accumulation rate of up to 230 mMa^{-1} along the eastern edge of the basin. A further two locally confined sub-circular mini-basins occur at this time between Areas C, D and E and a shallower basin has developed further north between Areas B and Area C (Figures 5.6 and 5.7 (g)). Sediments appear to thin onto all of the structures within the basin during this time. The exception to this is in the southern half of the anticline within Area F where coverage of the isopach maps is poor but the sediment appears to thicken towards it, this is supported by the observations from the structural reconstruction (Figure 5.5) and the seismic line through this area (Figure 5.4 (d)). Structures within Areas A and C appear to be particularly active at this time; sediments thin along the length of the structure within Area C with the thickness of the sediment deposited over the crest of the anticline decreasing towards the south (Figure 5.6 (g)). The northern tip of the anticline within Area E also appears to be more active during this interval than in any other part of the history of the basin with thinner sediment deposited over the southern half of the crest. North of the salt diapir within Area F there is some evidence of thinning of sediment over the anticline (Figure 5.6 and 5.7 (g)), this can also be observed within the seismic line though this location (Figure 5.8 (c)). This slight thinning is indicative of some structural growth during this period.

The isopach maps and sediment accumulation maps show a similar distribution pattern with the main basin in the subsequent interval, deposited between 18.26 Ma and 13.25 Ma, with a depocentre forming to the east of Area C and a local sub-circular mini-basin between Area B and Area C (Figures 5.6 and 5.7 (f)). The basin trends broadly north-northeast to south-southwest thinning onto the structures within Areas A, C, D and E of the western margin of the basin, indicating that these structures were most active during this period. Due to poor horizon coverage along the eastern boundary fold in Area F, it is only possible to say

conclusively that the section of the anticline in the north of the Area F diapir was active during the period between 18.26 Ma and 13.25 Ma (Figure 5.6 and 5.7 (f)).

The interval deposited between the H60 to H80 horizons (13.25 Ma to 10.89 Ma) has a broadly similar sediment distribution pattern to that seen during the previous interval with packages thinning onto all of the main structures (Figures 5.6 and 5.7 (e)). A main north-northeast to south-southwest trending basin develops that deepens to the south, and local sub-circular mini-basin situated to the west of Area C persists and contains some of the thickest sedimentary deposits in the basin at this time (Figure 5.6 (e)). In contrast the sub-circular basin between Areas C and E in no longer a separate feature and this is likely due to a reduction in growth of the north-south trending anticline at the northern end of Area E.

The active structures within the basin impact on the formation of the main depocentres within this interval. For example, the northeast to southwest trending anticline towards the centre of Area C appears to partially subdivide the basin with a thicker depocentre forming to the west of this structure (Figures 5.6 and 5.7 (e)). The sediments deposited south of the normal fault are significantly thicker than the deposits north of the normal fault with an average thickness of approximately 550 m, indicating that the normal fault formed at this time (Figure 5.6 (e)). The fold structure within Area F also continues to be subtly active; separating an easterly depocentre from the main basin and having more control on sediment thickness on its northern segment than south of diapir where there is no horizon coverage.

The most obvious feature in the 10.89 Ma to 9.68 Ma maps (generated between H80 and the H90; Figures 5.6 (d) and 5.7 (d)) is a change in focus of deposition to the south in the study area. This occurs along a more north-south trend with much lower rates of sediment accumulation in the northern part of the basin, leading to lower overall sediment thicknesses. The normal fault still appears to be active within this interval. However, rather counter-intuitively there is a slight thinning of the sediment observed on the southern, downthrown side of the fault (Figure 5.6 (d)). This is the first interval (10.89 Ma to 9.68 Ma) that the southern half of the anticline within Area F is fully imaged in the isopach and sediment accumulation rate maps with clear thinning associated with the southern half of this structure (Figure 5.7 (d)). The seismic sections though Area A and the northern half of Area F show very little change in sediment thickness across these structures during this interval supporting the observations from the isopach analysis (Figure 5.8).

The development of this southerly depocentre also dominates in the next youngest interval deposited between 9.68 Ma and 8.29 Ma (the H90 to H100 horizons). The main depocentre of the mini-basin, which now trends broadly north-south, extends further north into the central parts of the basin and thins significantly onto the salt walls in Area D and onto the southern end of the anticlinal folds in Area C. It also thins onto the anticline which forms the southern half of Area F and appears to be bisected by this structure in the southern half of the basin (this is particularly apparent in the sediment accumulation maps, Figure 5.7 (c)). The northern half of the basin has the lowest sediment accumulation rates of all the intervals during this period with the majority of the area ranging from 0 m to 30 m in thickness. This suggest that the sediment supply to the northern half of the basin has switched off during this interval, possibly driven by

changes in the sediment supply pathways updip of the mini-basin. However, this cannot be independently corroborated due to a lack of resolution and detailed mapping within the regional seismic dataset.

Overall the period between 8.29 Ma and 5.04 Ma (the H100 to H120 interval) contains some of the lowest sediment accumulation rates in the basin (Figure 5.7 (b)). The main axis of the basin remains orientated broadly north-south with thicker sediment deposited in the south of the basin. A younger channel complex cuts through the sediment south of the normal fault. Horizon H120 has been picked along the base of this channel and hence shows a thinner sediment package in the H100 to H120 interval and a thicker sediment package in the H120 to seafloor interval (Figure 5.7 (a) and (b)). The normal fault was active during this interval with both the isopach and sediment accumulation maps showing thicker sediment deposited south of the normal fault (Figures 5.6 and 5.7 (b)). The sub-circular basin bound by structures in Area A, B and C also appears to have formed again during this period, possibly due to renewed structural activity on surrounding structures (Figure 5.7). Clear thinning towards the structures during this interval within Area B can be observed on the seismic sections that partly cut through this depocentre (Figure 5.8 (b)). Interestingly thinner sediment appears to be deposited in the north-eastern corner of the basin which does not appear to be linked to underlying structural activity.

The most recent map covering the last 5 Ma of sediment accumulation within the area represents a period when the main sand rich systems were no longer feeding into the basin, with the sediment deposited in the basin being composed almost entirely of hemipelagic fill. The main sediment distribution within the mini-basin more or less replicates the pattern of the underlying intervals, and shows continued major control of active structures on the west of the basin (i.e. Areas A, B, D and E) and depocentre limits (Figures 5.6 and 5.7 (a)). The sediments thin along the length of the western margin, in particular around Area B, the southern half of Area C and Area E, and locally on the eastern edge of the basin near Area F where the salt canopy extruded laterally during this time interval (Figures 5.6 and 5.7 (a)). The isopach thickness map also indicates a thicker sediment package in the southern half of the basin with no thickness change across the southern part of the Area F fold, thus implying that the southern half of this structure was not active during this period (Figure 5.6 (a)).

This series of isopach maps and sediment accumulation rate maps thus reveal substantial local variations in shape, orientation and location of the main depocentres through time. The details of these changes in sediment distribution allow constraints to be placed on the activity, or growth, of the various structures on the margin and within the basin through time. The isopach maps show that the basin has developed significantly since the start of the Oligocene (33.9 Ma). Until the end of the Middle Miocene (Figure 5.7 (e)), the thickest sediment is deposited within a main depocentre which trends northeast-southwest, thinning onto the structural highs on the western margin of the basin and developing a second semi-circular mini-basin west of Area C. This changed between 10.89 Ma and 9.68 Ma (H80 – H90) when the thickest sediment was deposited in the south of the basin, extending northwards though time along a north-northwest to south-southeast trend (Figure 5.7 (c) and (d)). Following this, there is a reestablishment of the earlier pattern of sediment distribution with depocentres observed in similar locations within the

earliest and latest periods of the basin history (i.e. Figure 5.7 (a) and (b) have a similar sediment distribution pattern to (e), (f) and (g)). This implies that the sediment distribution patterns observed within the intervals between the H80 and H100 horizons (i.e. 10.89 Ma to 8.29 Ma) are anomalous and resulted from a change in the sediment supply to the area, correlating with observations on the regional sediment variations in Anderson et al. (2012) which shows a series of very small upper slope channels and the formation of small fans on the mid to lower slope (Figure 2.3, Chapter 2).

5.8 Bed Length Change Analysis of Basin Structures

Isopach analysis gives a general outline of basin depocentre evolution through time and allows active structures to be identified. However, understanding how depositional systems link with structural growth requires the individual structures to be examined in greater detail. Bed length change analysis allows the amount of bed length change accumulated on a structure though time to be investigated, this in turn can be used as a proxy for the amount of growth of that structure through time. Here the results are presented graphically to document variation in growth histories of an individual structure, or groups of related structures. The results are also presented in map form to allow the spatial variation in bed length for different time periods in the basins history to be documented (Section 5.10).

Bed length change analysis has been carried out on the majority of the structures which bound and are internal to the mini-basin. These were identified as having been active from the isopach and sedimentation accumulation rate maps (Figures 5.6 and 5.7). Bed length change was measured at a total of 21 positions in the basin, using sections positioned perpendicular to the trend of the structures and on their flanks (Figure 5.9). The Area C structure was studied in more detail using more closely spaced intervals (discussed in Section 5.9). Three positions were chosen on the most easterly anticline within Area A in order to prevent the analysis unintentionally recording the bed length change accumulated on two linked anticlines to the west (Figure 5.8 (a) shows a section through the main anticline in Area A and the linked western anticline). Four lines were positioned in Area B to avoid the parts of the structure where salt had broken through. A further four lines were positioned on the linked anticlines which constitute Area C, again chosen to avoid the southern half of Area C where canopy salt prevents the accurate measuring of the bed lengths. Whilst isopach analysis suggests that Area D has been active throughout the history of the basin, the structures in that area have been extremely affected by later salt movement which obscures the horizons and hence only two lines were positioned here (Figure 5.9). The interaction of the structures between Area D and Area E also prevent accurate bed length measurements from being recorded in the south of Area D. The lines in Areas E and F are positioned such that they show representative sections through the structures and avoid areas containing canopy salt. Structures south of Line 18 were outside the area covered by the high resolution PSVM seismic dataset, so these were not studied (see Figure 5.9 for all line locations).

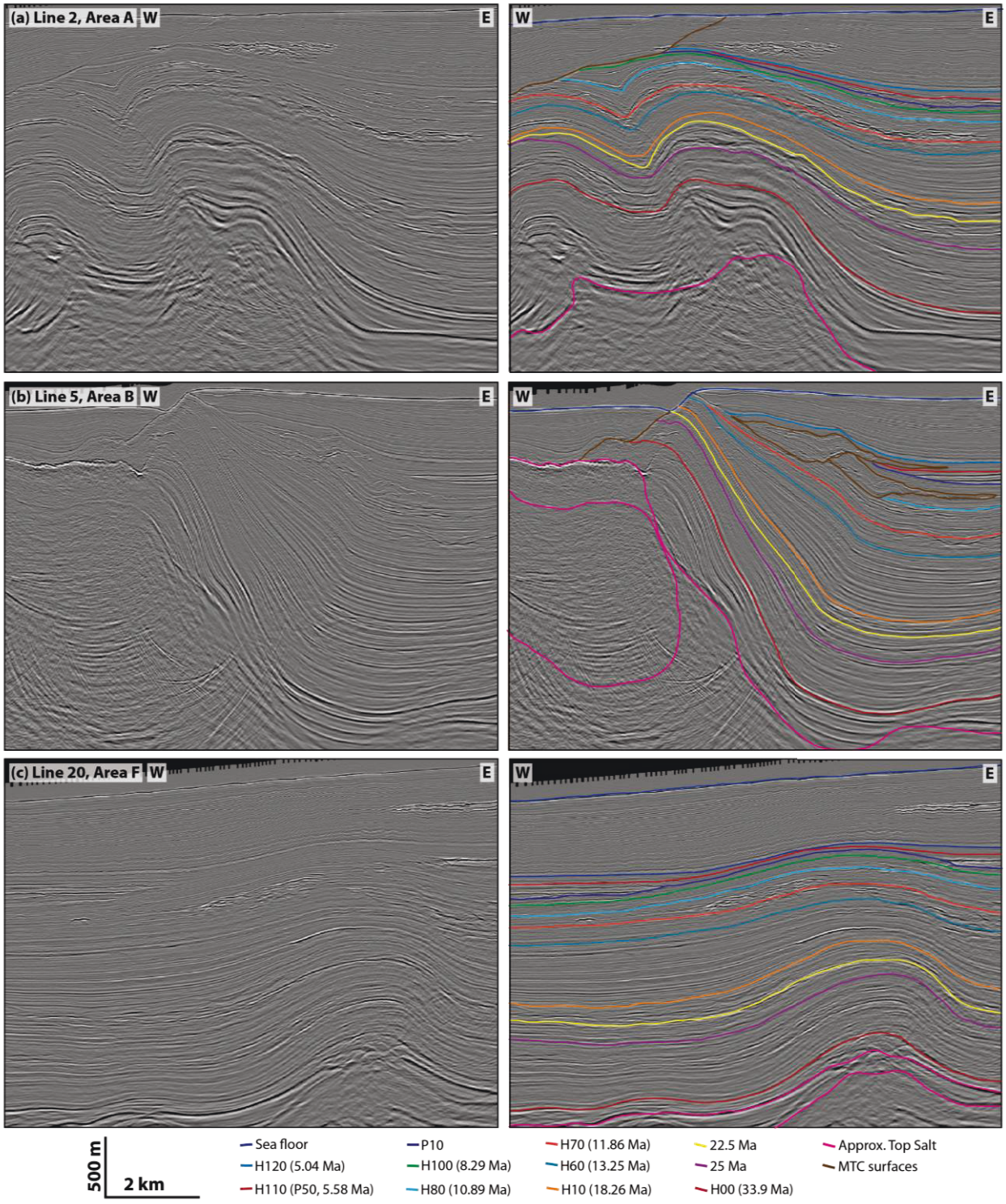


Figure 5.8 A series of close-up seismic sections through three of the most influential structures with (a) showing Line 2 within Area A in the north of the mini-basin, (b) showing Line 5 a section through the flanks of the long-lived salt wall within Area B and (c) Line 20 north of the salt diapir within Area F on the eastern margin of the mini-basin. The location of these lines can be seen on Figure 5.7 (a) and 5.9.

Overall the amount of bed length change in the area ranges from a total cumulative bed length change of 100 m (Line 19; Figures 5.9 and 5.10) to 1700 m (Line 18; Figures 5.9 and 5.10). The highest rate of bed length change, is also recorded from Line 18 between 18.26 Ma and 13.25 Ma (H10 – H60) when the rate of bed length change is 115 mMa^{-1}. The structures within the mini-basin have a broadly similar pattern of growth: during the Oligocene from 33.9 Ma to 25 Ma they all undergo a period of mostly rapid bed length

change, this slows between 25 Ma and 18.26 Ma, before they undergoing a second period of rapid bed length change in the Lower to Mid Miocene between 18.26 Ma and 13.25 Ma (H10 – H60). After this the majority of structures have a very low rate of bed length change and hence very little growth (Figure 5.9), subtle changes in the growth during this period still occurred on some structures effecting the sediment distribution observed in the isopach maps (Figure 5.6). The structures represented by Lines 17 and 18, in the southwest of the basin have a slightly different pattern in that they continue to grow from 18.26 Ma to 9.68 Ma (H10 – H90; Figures 5.9 and 5.10). Line 17 is also unusual as shows very little bed length change during the initial period from 35 to 25 Ma.

Area A is comprised of three salt cored anticlines (Figure 5.4 (b)) which bed length change analysis indicates have grown very little during the history of the basin. The maximum rate of change of bed length of 18 mMa^{-1} is recorded on Line 3 between 33 Ma and 25 Ma and a second period of consistently high bed length change is seen on all lines within the area between 18.26 and 13.25 Ma (H10 – H60; Figure 5.10), with Line 2 having a maximum rate of change of bed length of 12 mMa^{-1}. This follows the general pattern of structural growth seen throughout the mini-basin and corresponds to low rates of sediment deposition across these structures (Figure 5.7 (g) and (f) respectively). Lines 2 and 3, in the middle and southern part of this structure have slightly higher bed length change rates than Line 1, with Line 2 (shown in seismic section in Figure 5.8 (a)) recording a short-lived pulse of high growth, and hence high bed length change, between 11.86 Ma and 10.89 Ma when the rate of change of bed length increases to 13 mMa^{-1}.

Area B, one of the major structural features along the salt wall which defines the western edge of the basin, has some of the highest rates of change of bed length in the mini-basin (Figure 5.9 (b)). This structure has a significantly higher overall rate of bed length change with a cumulative bed length change of 1230 m on Line 6 towards the centre of the anticline, and lower cumulative bed length change towards the anticline tips (e.g. Line 4, Figure 5.9 (b)). Again, the highest rate of bed length change is recorded within the interval between 18.26 Ma and 13.25 Ma (H10 – H60) towards the centre of the structure on Line 6 where a rate of change of bed length of 69 mMa^{-1} is calculated.

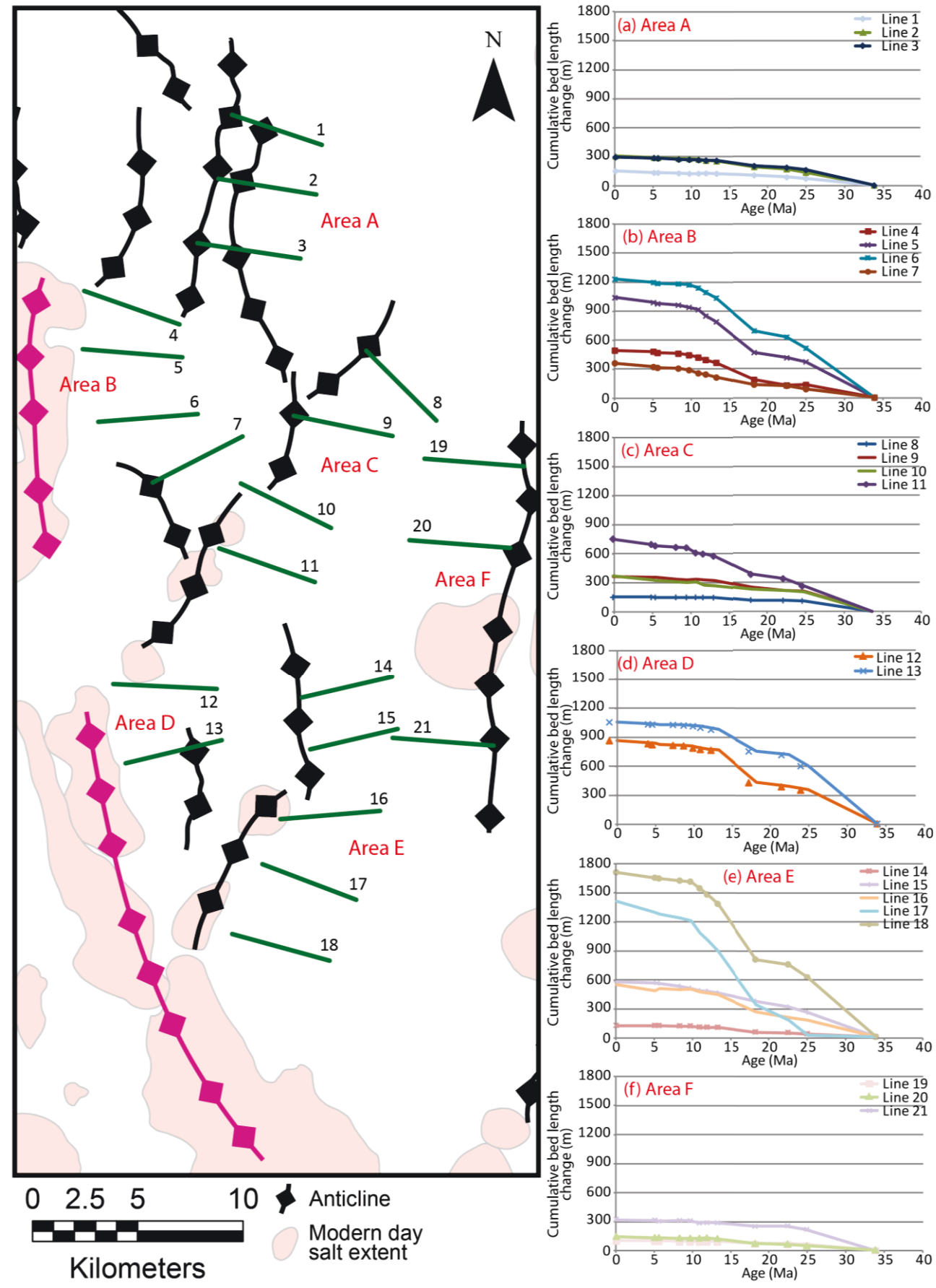


Figure 5.9 The location of the lines used in the bed length analysis of the basin bounding structures is shown alongside the graphical analysis of the cumulative bed length change of the structures which bound the basin. The graphs are grouped according to the structural areas, the location of which are shown in the map on the left.

The structures in Area C extend through the centre of the basin, and comprise a series of linked anticlines which trend northeast-southwest and are explored in significantly more detail in Section 5.11. Overall this structure has less bed length change and consequently a lower rate of change of bed length than the structures in Areas B, D and E (Figure 5.9). The pattern of the variation in bed length change also varies slightly, with less of an increase in the rate of bed length change in Lines 8 – 10 during the 18.26 Ma to 13.25 Ma interval (H10 – H60; Figure 5.9). Overall the highest cumulative bed length change along this structure is 690 m, recorded on Line 11, with the majority of the bed length change accumulating between the intervals between 33.9 Ma and 25 Ma, 18.26 Ma and 13.25 Ma (H1 - H60) and 10.89 Ma to 9.68 Ma (H80 to H70) when the highest rate of change of bed length were 28 mMa^{-1}, 35 mMa^{-1} and 41 mMa^{-1} respectively. Lines 10 and 11 also have fairly high rate of change of bed length of up to 10 mMa^{-1} in the period between 5.04 Ma and the present day (H120 to present), whereas bed length change on Lines 8 and 9 is negligible within this period. Line 8 has the least cumulative bed length change on this structure with only 140 m of bed length change recorded. Lines 9 and 10 have very similar cumulative bed length change values at 335 m and 340 m respectively, but the graphical analysis indicates that they grew at different rates and during different periods; Line 9 had a rate of change of bed length of 13 mMa^{-1} between 18.26 Ma and 13.25 Ma (H10 – H60), whereas Line 10 grew more steadily during that period, with a rate of change of bed length of 7 mMa^{-1} but then had a short-lived increase in growth rate to 30 mMa^{-1} between 11.86 Ma and 10.89 Ma (H70 – H80) when growth on Line 9 was negligible (Figure 5.9).

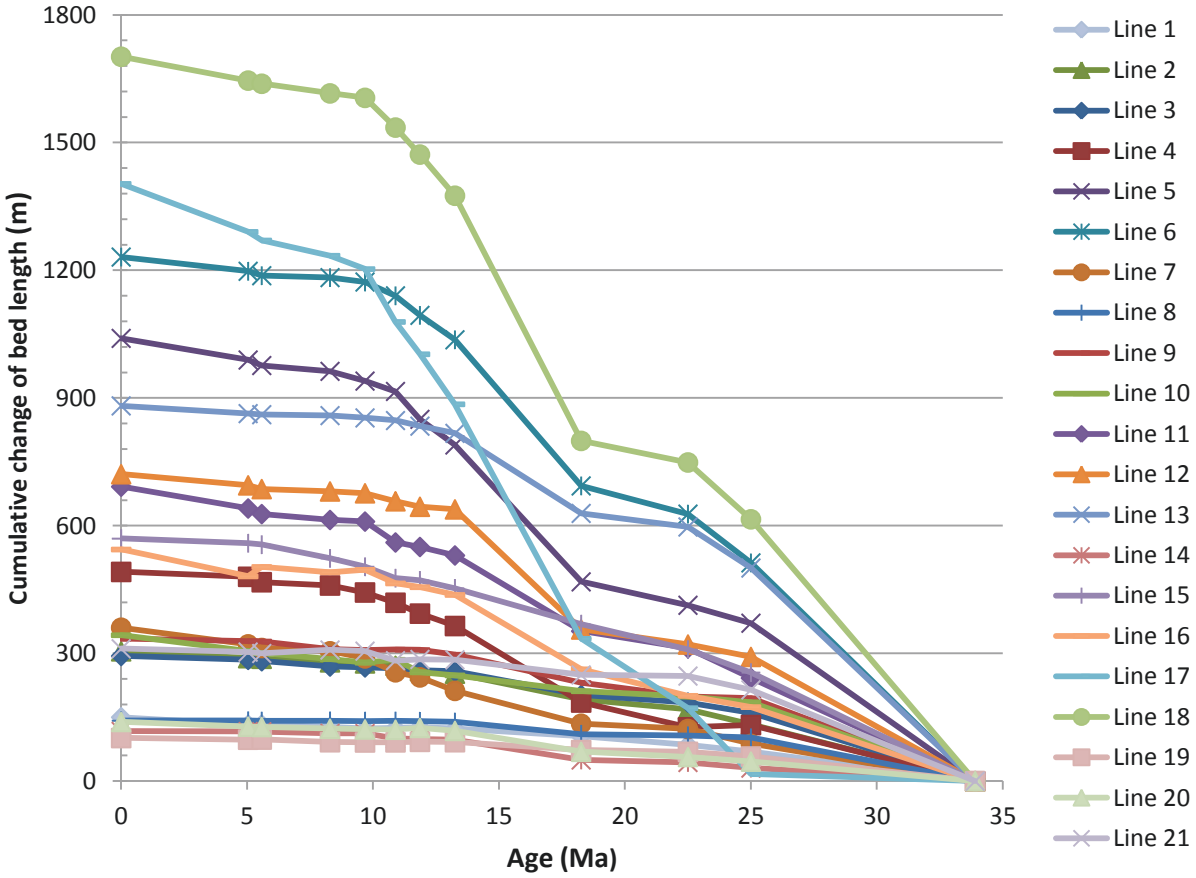


Figure 5.10 A graph showing the cumulative bed length change for all of the structures analysed within the study area. Note how all of the structures within the area, with the exception of Line 17, have a broadly similar pattern of development through the history of the basin.

The structures within Area D have a very similar pattern of cumulative bed length change to those in Area B; two periods of increased rate of change of bed length and two where the rate of bed length change of the structures plateaus (Figure 5.9 (b) and (d)). Line 13, again towards the centre of the structure, has the highest cumulative bed length change within this area with an overall bed length change of 880 m. Both lines indicate a period of increased rate of bed length change between 18.26 Ma and 13.25 Ma (H10 – H60) which ranges from rates of change of bed length of 38 mMa^{-1} (Line 13) to 56 mMa^{-1} (Line 12).

Area E has the highest cumulative bed length change of any of the structures with 1700 m bed length change recorded on Line 18 (Figure 5.9 (e)). Lines 17 and 18, through the most southerly structures studied here, both have the most rapid rate of bed length change and hence the inferred highest growth between 18.26 Ma and 9.68 Ma (H10 - H90). In this period the maximum rates of change of bed length of up to 109 mMa^{-1} (Line 17) and 114 mMa^{-1} (Line 18) are calculated. Line 17 is unusual in that very little bed length change occurred between 33 Ma and 25 Ma (Figure 5.9), which was followed by a period of high rates of change of bed length of up to 62 mMa^{-1} between 25 Ma and 22.5 Ma. This means that this structure was growing at a greater rate than any of the other structures in the basin during this period, suggesting a period of localised salt movement. The consistently higher cumulative rates of change of bed length recorded on Line 18 could be attributed to the proximity of this structure to the main salt wall on the western margin of the mini-basin (Figure 5.9). Lines 14 and 15 have experienced lower cumulative bed length change, and a much more

gradual increase in bed length change through time suggesting that they have been growing at a steady rate since 33 Ma (Figure 5.9 and 5.10). Whilst this structure has been grouped with the other anticlines in Area E, it is an intra-basin structure and therefore it might be expected to have a similar bed length change pattern to those seen on the anticlines within Area A and at the northern end of Area C which are also intra-basinal.

Area F bounds the basin on the eastern margin. The salt diapir through the centre of the anticline makes recording the bed length change in the centre of the structure very uncertain and for this reason has been omitted from this study. Overall, the cumulative bed length change on this structure is significantly less than that seen on the structures within Areas B to E. The maximum cumulative bed length change is recorded on Line 20, close to the region where the salt has broken through, and is 310 m (Figures 5.8 (a), 5.9 and 5.10).

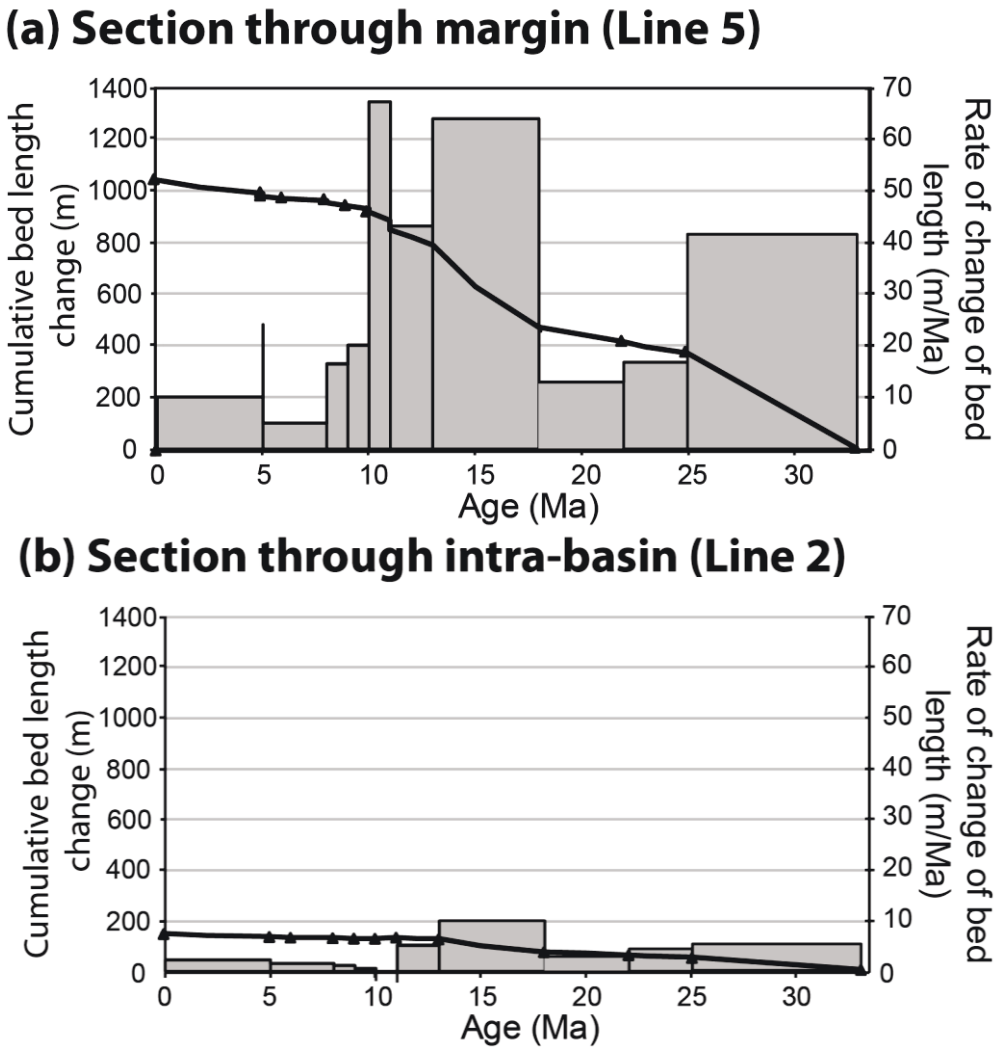


Figure 5.11 Sections at the same scale showing the variation in the cumulative bed length change and rate of change of bed length on (a) the margin of the basin compared to those seen at (b) towards the centre of the basin.

Overall, the structures that bound the basin to the west have significantly higher cumulative bed length change than those which are situated within the basin: the average cumulative bed length change in Areas B and D is 780 m and 870 m respectively compared to 380 m in Area C (Figures 5.9 and 5.11). The pattern of evolution of the structures through time is broadly similar between the structures it these two areas, but the magnitude is greater on the margins (Figure 5.11). Both structures situated within the basin and on the margins of the basin have a high growth rate phase between 33.9 Ma and 25 Ma with growth rates remaining high, but decreasing from 25 Ma to 18.26 Ma (Figure 5.11). All structures within the mini-basin have a high growth phase between 18.26 Ma to 13.25 Ma, but this is significantly smaller on the intra-basin structures, for instance the rate of change of bed length on Line 2 (Area A) at this time was 10 mMa^{-1} compared to 63 mMa^{-1} on Line 5 (Area B). Both the structures show a decrease in growth following this period, with markedly less bed length change shown on the structures which are within the basin.

A full discussion of the errors associated with this bed length analysis has been carried out in Chapter 4, Section 4.2.10. However, it is useful to consider here that some of the patterns observed in the rate of bed length change could be a function of the spacing of the dated horizons. For example, spike of high rate of change of bed length around 10.89 Ma seen on many of the structures within the mini-basin would disappear if they were averaged between lower rate of change of bed length columns on either side. That said, two main periods of consistently high in growth rates (i.e. between 33.9 Ma and 25 Ma and 18.26 Ma and 13.25 Ma) do appear to be robust and occur throughout the mini-basin. However it is noted that the first of these growth periods comprises almost the entire Oligocene, a large period of almost 10 Ma, and it is entirely possible that growth started sometime later than 33.9 Ma in this interval. Were the age controls within the mini-basin more detailed, there may be more variation in the growth rates of the structures recorded, implying that structures may have more irregular growth rates at finer temporal resolutions. This idea will be discussed in more detail throughout the subsequent chapters.

5.9 Bed Length Change Analysis of a Single Structure

The growth of a single structure within Area C is investigated in more detail in this section; analysing the rate of bed length change along the length of the linked anticlines. This analysis has the dual purpose of testing the robustness of the bed length change approach, as only three or four lines per structure were analysed in the rest of basin, and testing whether the folds are composed of linked segments. Area C was chosen as it is situated in an intra-basin location at the northern end and becomes increasingly basin-bounding towards the south. The isopach maps illustrate how the growth along this structure, at least in the south, affected sediment thicknesses throughout the history of the basin (Figures 5.6 and 5.7). Eighteen transects were taken along the length of structure at 1 km intervals (Figure 5.12) with bed length change measured over a 5 km distance (Figure 5.13); it is noted, however, that the transects taken from 12 km to 16 km have been subject to recent salt movement making the results less reliable.

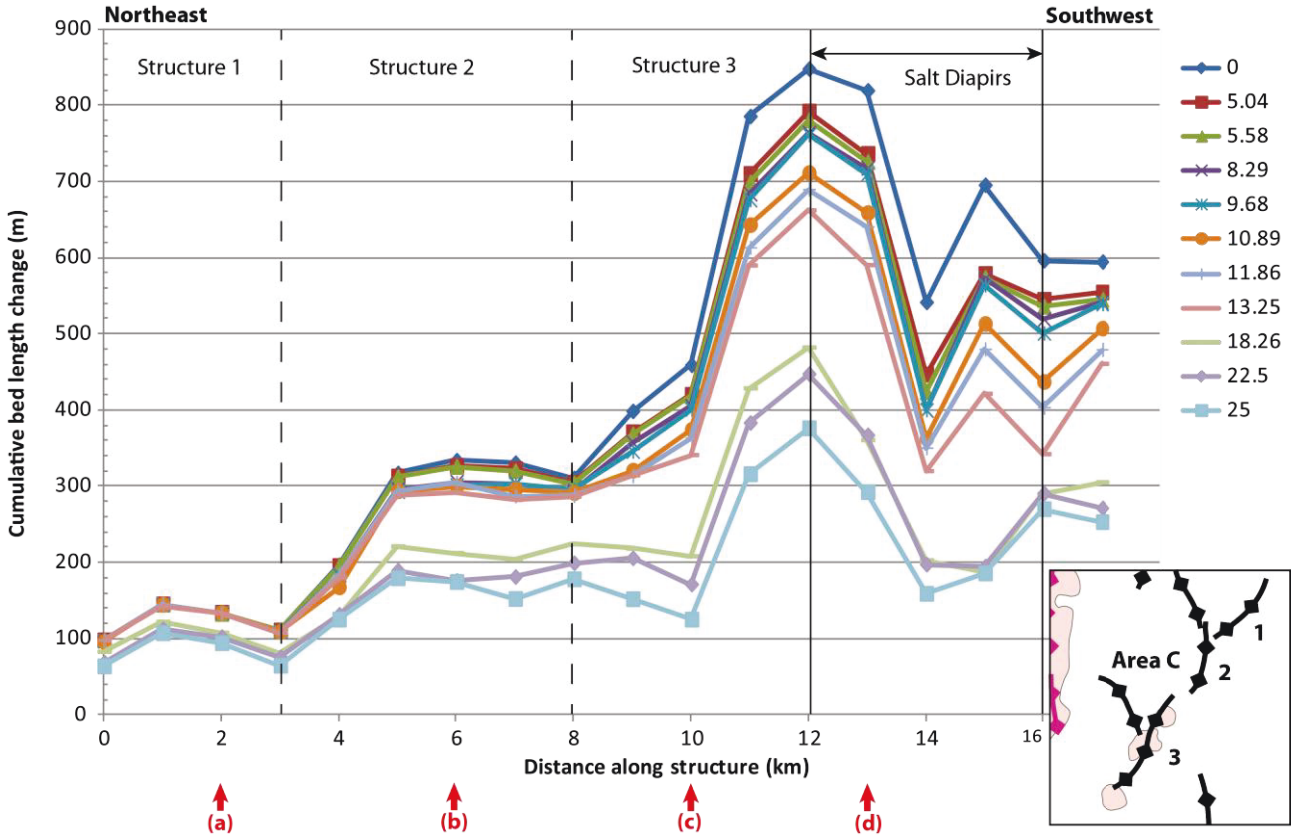


Figure 5.12 A plot showing the variation in bed length change along the length of the main structure within Area C. The area between 12 km and 16 km has been affected by salt breakthrough and hence the data is less robust than in other areas along the length of the anticline. The arrows labelled (a) – (d) link to the rate of change of bed length graphs shown in Figure 5.14.

Bed length change along the length of the structure was analysed in detail with bed length change on each surface plotted against distance along that structure, a technique routinely used in extensional fault systems where displacement is plotted against distance. Three salt-cored anticlines link to form this structure, and a typical section through one of these anticlines is interpreted in Figure 5.13. The three separate structures can be distinguished by a series of bed length change minima located towards the tip of the structures and a clear increase in bed length change in the centre, in a pattern similar to that seen in fault analysis (Figure 5.12). The three structures behave in a similar way through time, but the total cumulative bed length change increases from the northeast to the southwest along the structure as towards the basin margin. The maximum cumulative bed length change increases from 145 m on Structure 1, to 335 m on Structure 2, and up to 850 m on Structure 3 (Figure 5.12).

The bed length change values shown in Figure 5.12 are cumulative, and measured from the time of deposition of the pre-growth strata at 33.9 Ma, until present day. This means that the lowest bed length change values are seen at 25 Ma and all increase towards a maximum cumulative bed length change recorded at present day. However, the difference in bed length change (i.e. the gap between one dated horizon and the next) gives an indication of the amount of bed length change that occurred in that time period; a larger gap indicates more bed length change occurred in this period and hence there was greater growth on the structure (Figure 5.12). The graph reveals that there were two main periods of growth along the length of the structure; the first between 33.9 Ma and 25 Ma, and the second between 18.26 Ma to 13.25 Ma (H10 – H60; see Figure 5.12). Graphical analysis of the bed length change on representative lines through these structures

also shows that these two periods consistently had the highest rate of change of bed length (Figure 5.14). During the initial phase of bed length change from 33.9 Ma to 25 Ma the pattern of bed length change seen in Figure 5.12 indicates that there could have initially been four structures; the first from Lines 0 to 3 (similar to today), the second from Lines 3 to 7, the third from Lines 7 to 10 and then a fourth from Line 10 onwards. This persisted until 13.25 Ma (H60) when the boundary between Structure 2 and Structure 3 is established (Figure 5.12). These are very small variations in bed length change and therefore could be attributed to errors within the measuring process. However, the fact that the pattern is consistent over the interval and does not occur after 13.25 Ma indicates this is a reliable observation. There is also an anomalous, consistent low bed length change recorded at Line 14 along the structure. However, this is within the area of the structure affected by subsequent salt movement so these results are less reliable and the possibility of a fifth anticline segment here has been dismissed.

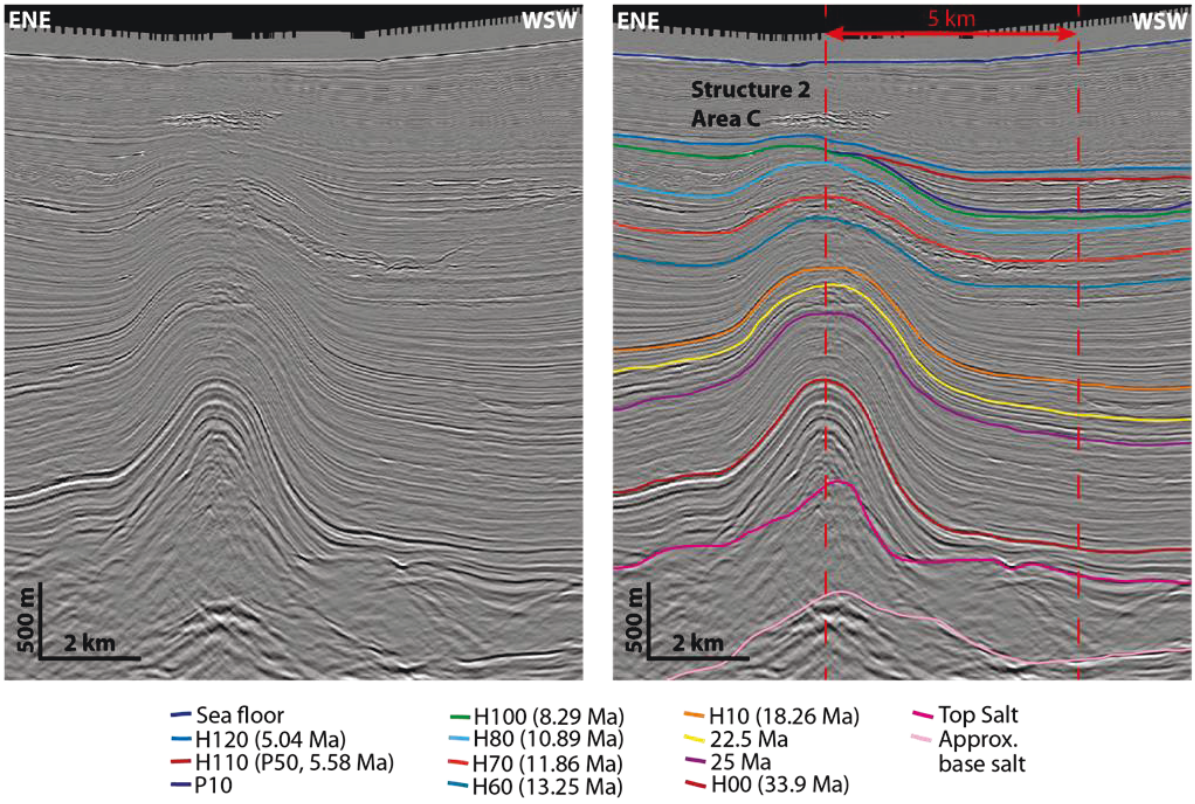


Figure 5.13 Seismic line through Line 7, Structure 2, Area C. This shows the typical structure through this part of the anticline with a salt-core and sediment packages thinning towards the actively growing structure.

Overall, the growth between 18.26 Ma and 13.25 Ma (H10 – H60) was the most variable along the length of the structure (Figure 5.12) with a substantially smaller, and more constant, change in the amount of bed length change towards the northern end of the structure. For example, Structure 1 (Line 2; Figure 5.14 (a)) has a rate of change of bed length of 4 mMa^{-1} as opposed to 13 mMa^{-1} on Structure 2 (Line 6; Figure 5.14 (b)) and 36 mMa^{-1} on Structure 3 (Line 13; Figure 5.14 (d)). Structure 1 subsequently stopped growing, with the detailed analysis of Line 2 indicating negligible rates of change of bed length until present day (Figure 5.14 (a)). In contrast, Structures 2 and 3 continued to grow from 13.25 Ma (H60) onwards, however the values recorded between 12 km and 16 km are less reliable due to salt movement which obscures some of the horizons (Figure 5.12). Structure 2 has a third period of higher growth between 8.29 Ma and 5.58 Ma (H100

– H110) where a higher rate of change of bed length of 6 mMa^{-1} is recorded on Line 6. This interval corresponds to a time when rate of change of bed length was consistently low within the mini-basin and on the margins (Figure 5.8) during which time ponded fan sediments were deposited. This growth is less obvious on the lines through Structure 3 (Figure 5.14 (c) and (d)) both of which have a higher rate of change of bed length phase between 10.89 Ma and 9.68 Ma (H80 – H90) when the rate of change of bed length on Line 13 is 41 mMa^{-1}. A period of growth is also recorded between 5.04 Ma and the present day on Structure 3 (Figures 5.12 and 5.14), during which time the major clastic sediment supply to the basin switched off.

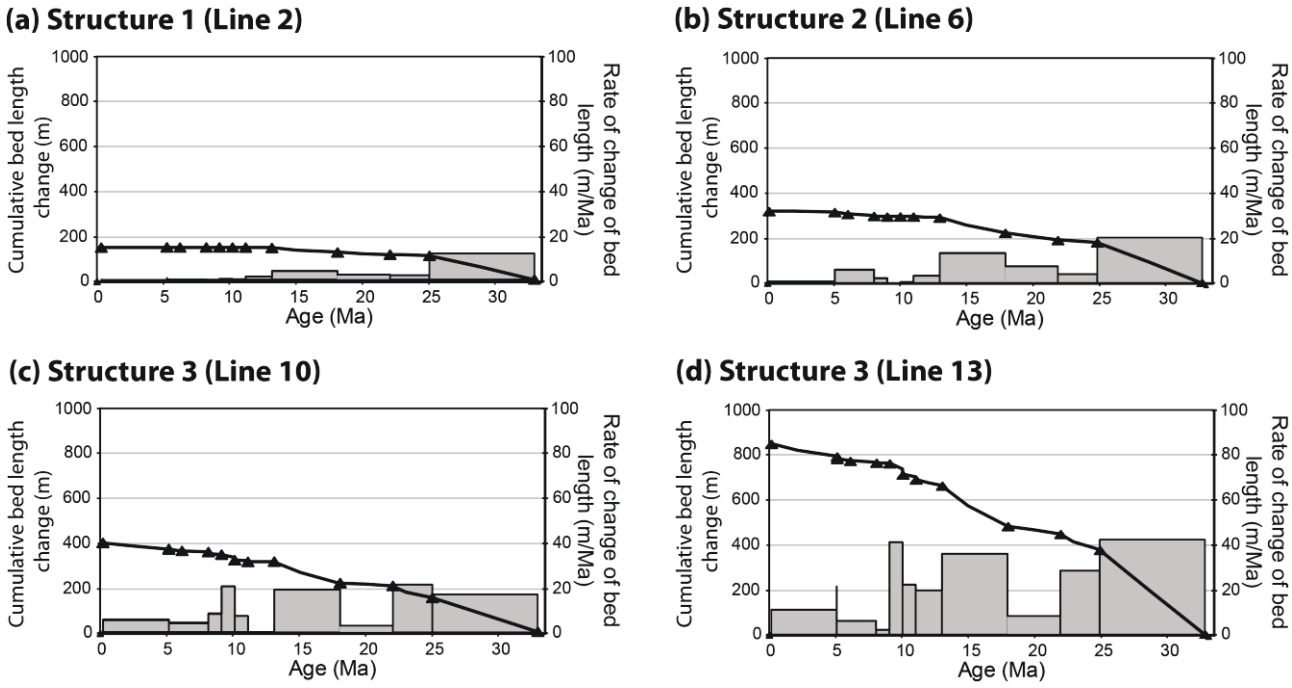


Figure 5.14 Bed length change analysis through four of the structures within measurements taken from lines which are orientated perpendicular to the anticline within Area C.

5.10 Maps Showing Rate of Change of Bed Length

The bed length change analyses carried out in the previous sections give an indication of the behaviour of the individual structures within the vicinity of the mini-basin. They are very useful in that they provide an absolute value for the bed length change of individual structures and allow comparisons to be made between the rate of bed length change through time. However, they do not provide the type of spatial overview seen in the isopach and sediment accumulation maps. In order to link these analyses the rate of change of bed length measurements have been grouped according to the amount of bed length change on the structure and colour-coded accordingly; low rates of change of bed length (< 10 mMa^{-1}) coloured yellow, medium rates of change of bed length (10 – 30 mMa^{-1}) coloured green and high rates of change of bed length (> 30 mMa^{-1}) coloured red (Figure 5.15). The rate of change of bed length has been mapped using these colours along the anticlines on the structural elements map (Figure 5.15), for time intervals which correspond to those shown in the isopach and sediment accumulation maps (Figures 5.6 and 5.7). These maps will also be used in Chapter 8 to discuss how the sediments deposited in the basin react to changes in structural growth.

The structures had consistently higher growth during the early history of the basin evolution from 33.9 Ma to 9.68 Ma (i.e. Figure 5.15, maps (d) to (g)). The highest growth rates in Area A occur during the early part of the basin history from 33.9 Ma to 13.25 Ma (Figure 5.15, maps (f) to (g)) and after this it slowed down substantially. In contrast to this the salt cored anticlines within Area E at the southern end of the basin have the longest life in terms of growth, with high to moderate growth rates recorded from 33.9 Ma until present day. Higher rates of growth along this structure occur during the 33.9 Ma to 10.89 Ma intervals (Figure 5.15 (e) to (g)), which coincides with higher growth rates seen on the structures within Areas C and D. The anticline within Area F has the lowest rate of change of bed length through the history of the basin with some medium rates of bed length change during the intervals between 33.9 Ma to 18.25 Ma and 10.89 Ma to 9.68 Ma suggesting these were the periods when it grew the most.

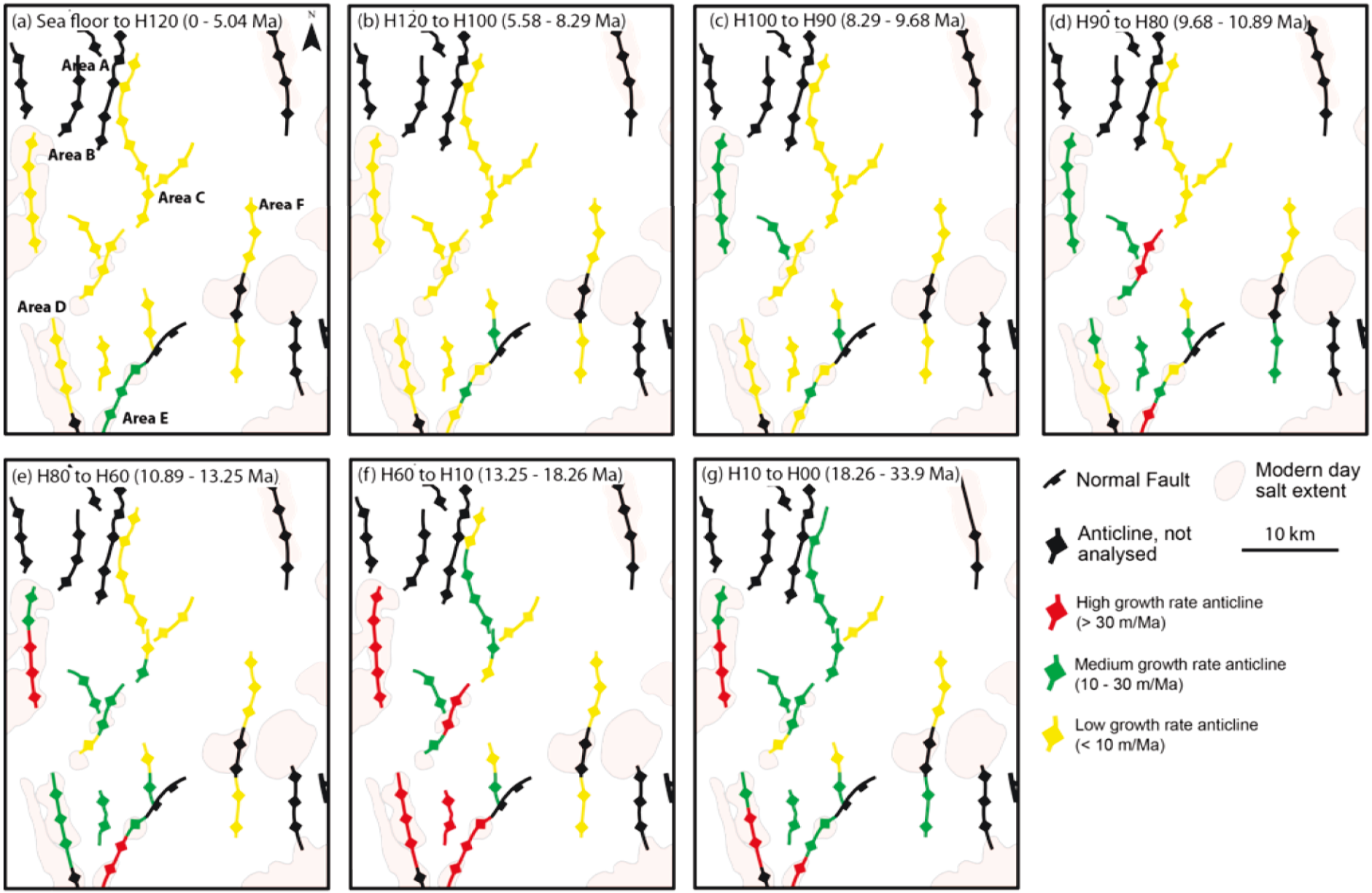


Figure 5.15 A series of maps showing the growth of the structures which surround the basin at time periods corresponding to those seen in the isopach maps and sediment accumulation rate maps.

5.11 Discussion

5.11.1 Structural Driving Forces

Analysing the structural development of the basin using a series of different methods allows an insight into the structural evolution of the basin at different scales. Since the deposition of the Aptian salt, the Angolan passive margin has experienced a complex history of structural deformation. The predominantly compressional structures described and analysed in this chapter are linked to movement which has occurred on a late Aptian salt detachment (also observed by Burollet, 1975, Duval et al., 1992, Lunde et al., 1992, Lundin, 1992, Gaullier et al., 1993, Spathopoulos, 1996, Anderson et al., 2000, Cramez and Jackson, 2000, Hudec and Jackson, 2004, Anderson et al., 2012).

Bed length change analysis of the evolution of the main structures which surround and intersect the basin indicate that the basin evolution was punctuated by two periods of more rapid growth; the first occurred from 33.9 Ma to 25 Ma and a second pulse in growth was observed between 18.26 Ma and 13.25 Ma (Figure 5.10). During the early part of basin development from 33.9 Ma to 18.26 Ma, bed length change analysis indicates that structures within Areas B, D and E along the western edge basin were particularly active (Figures 5.9 and 5.10). The sediment accumulation maps and isopach maps corroborate this with sediment thinning onto all of the structures within the area and particularly thinning over the crest of the anticline within Area C (Figure 5.7 and 5.13). Maximum rates of change of bed length of 69 mMa^{-1} were recorded, and seismic sections across the basin during this period show that beds taper and thin towards the structures on the western margin of the basin in particular (Figure 5.4).

The interval between 18.26 Ma and 13.25 Ma (H10 and H60) also has consistently high rates of change of bed length across the basin, with thinning observed on the sediment accumulation maps, indicating that the majority of the structures within the basin were active (Figure 5.7). Sediment thinning is observed in Area A, which contains structures with the lowest cumulative bed length change in the mini-basin, with approximately 150 m of sediment deposited adjacent to the structure thinning to less than 50 m over the crest of the anticlines (Figure 5.6 (f)). The seismic sections and bed length change analysis also indicate that the amount of structural movement is consistently higher during this period than during any other period in the history of the basin (Figures 5.4, 5.10 and 5.13); the highest bed length change is recorded in Area E which had a rate of change of bed length of 115 mMa^{-1}.

The onset of the period of high structural growth corresponds to a well documented episode of uplift along the African margin which is thought to have occurred between 30 Ma and 22 Ma (Green et al., 2014, Paul et al., 2014, White and Hoggard, 2014). This uplift and tilting has been attributed to epeirogenic uplift triggered by a possibly associated with the initiation of the superplume beneath subequatorial Africa (Burke, 1996, Al-Hajri et al., 2009, Roberts and White, 2010). Denudation of between 150 m and 500 m has been recorded elsewhere in the Lower Congo Basin (Cramez and Jackson, 2000) thought to be associated with this phase of growth (Walgenwitz et al., 1990, Lunde et al., 1992, Cramez and Jackson, 2000, Hudec and Jackson, 2007). This uplift would first have caused sliding and gravitational movement of the salt from the

uplifting high down-dip, and secondly generated an increase in solid sediment flux from the interior African hinterland (Al-Hajri et al., 2009, Roberts and White, 2010, Paul et al., 2014). This is manifested as major coarse, clastic, channel systems which entered the basin south of the present day Congo Canyon during the Oligocene feeding large third-order channel systems that dominate the stratigraphy of the Lower Congo Basin until the Middle Miocene (10.89 Ma), after which there was a major shift in the main locus of the Congo Fan (Anderson et al., 2012). Thus the timing of the two periods of high bed length change observed and measured in this study is consistent with a the regional-scale sediment loading on the shelf through the Oligocene and Miocene, tilting of the margin, and concomitant extension driving the down-dip shortening.

Whilst the deformation measured can be explained by the regional tectonic setting of down-shortening, driven by up-dip extension, it is also possible that sediment loading in the local mini-basin may have driven some salt withdrawal from beneath the main basin depocentre with flow of salt into, and hence growth, of the basin-bounding salt-structures. If this is the case, one might expect periods of high sediment accumulation rates in the centre of the mini-basin to coincide with periods of enhanced growth rate on the salt wall in Areas B and D and possibly the Area F salt diapir.

However, direct comparison of the sediment accumulation maps with the maps which show the structures colour coded according to growth (i.e. Figures 5.7 and 5.15), indicates that in the majority of cases the spatial location of the thickest sediment accumulations does not directly correlate to the location of structures which have the highest rates of change of bed length. The two earliest sediment accumulation rate maps cover the period from 33.9 Ma to 13.25 Ma (i.e. the intervals from 33.9 Ma to 18.26 Ma and 18.26 Ma to 13.25 Ma) due to a lack of basin-wide accurate horizons whereas this period is sub-divided into three intervals by the rate of change of bed length calculations (i.e. 33.9 Ma to 25 Ma, 25 Ma to 22.5 Ma, and 18.26 Ma to 13.25 Ma). In order to resolve these inconsistencies the rate of bed length change for the 33.9 Ma to 18.26 Ma interval has been shown on the maps in Figure 5.15. Despite the non-optimal time intervals, when the rate of bed length change is averaged and plotted along structures in the same temporal windows as the isopach maps some key observations can be made. The first two maps (Figure 5.15 (f) and (g)) show no substantial difference in averaged bed length change rates along structures, but the average sediment accumulation rates in main depocentre is between a half and a third less between 18.26 Ma and 13.25 Ma (Figure 5.7 (f)), when compared to the previous time period. The disparity between the location of the thickest sediment accumulations and the location of structures which have the highest rates of change of bed length can be observed most clearly between 10.89 Ma and 9.68 Ma (H80 to H90) and 9.68 Ma and 8.29 Ma (H90 and H100) where the highest sediment accumulation rates are in the south of the basin near Areas E and F (Figure 5.7 (c) and (d)), and yet the highest rates of change of bed length are seen in Area B on the northwest margin of the basin (Figure 5.15 (c) and (d)). This lack of linkage is also observed in the relatively small time interval between 13.25 Ma and 10.89 Ma (Figures 5.7 (e) and 5.15 (e)) where a significant increase in sediment accumulation rate occurs in a local basin between Areas C and B; and again east of Area E, but none of these structures demonstrate a substantial increase in growth rate when compared to earlier interval. This means that the growth on these structures during this interval cannot be simply a factor of localised sediment loading adjacent to the structures.

Therefore it can be concluded that, at the resolution of the temporal intervals investigated, there appears to be little correlation between sediment accumulation rates in the main depocentres and variations in the rate at which the structures on the margins of the mini-basin have grown. This appears to suggest that salt flow driven only by local sediment loading has not played an important role in the inflation of the salt structures in the study area. It is of course possible, that had the isopach maps been made over shorter time intervals, another result might have been obtained. If the results presented here are valid, it seems that the structural growth observed in this region of the Angolan margin is driven mainly by the regional shortening, and that salt movement driven by sediment loading in the local mini-basin depocentre cannot explain variations in the rate of bed length change seen at the mini-basin scale.

5.11.2 Linking Bed Length Change Rates, Growth and Topography

The main objective of this thesis is to investigate links between the growth of basin-bounding and intra-basin structures and the distribution and facies development of the sedimentary systems which infill the mini-basin. Therefore, it is particularly important to try and identify areas which formed structural highs during the evolution of the basin. These can then be used to look in detail at the impact of positive bathymetric relief on the distribution and morphology of the different types of sediment deposited throughout the mini-basin.

In this study, the cumulative bed length change and rate of bed length change recorded on a structure has been used as a proxy for the amount of structural growth of that structure. Structures which have high rates of change of bed length are likely to have grown at a proportionally high rate as the horizontal bed length change is translated into vertical growth. One issue which has not been addressed is how the horizontal bed length change and hence the horizontal component of strain translates into a vertical component of growth. In order for a sedimentary system to 'see' and react to a structure it has to have some degree of bathymetric relief. Therefore, it would be more useful ultimately to be able to quantify the amount of vertical uplift of a structure and the associated bathymetric relief. However, this is not a simple calculation as there are two linked problems:

1. whether it is possible to find an accurate structural method to convert horizontal bed length change to vertical uplift; and
2. if it is possible to convert vertical uplift to bathymetric relief, given that this would also have to take into account the sedimentation rate at the time of structural growth.

There are several models in the literature investigating fold growth where horizontal bed length change has been converted into a value for vertical uplift. It is well documented that vertical uplift on simple detachment folds continues with increased shortening, and hence increased bed length change, but this is not the case for fault-bend folds. In fault-bend folds when the lowest unit in the hanging wall reaches the upper footwall flat it causes the fold to broaden and increase in width without growing vertically (Suppe, 1983). In contrast detachment folds have a very simple relationship with shortening directly resulting in vertical uplift (Hardy and Poblet, 1994) but applying different kinematic models to these folds can result in different

predicted amounts of vertical uplift for the same amount of slip and shortening inputted into the model. For example two models where individual detachment folds form by limb rotation of a competent unit detached over a ductile horizon generate very different growth geometries (Figure 5.16); the De Sitter (1958) model suggests that the relationship between uplift and slip is non-linear with more uplift at lower slip values and decreasing uplift as slip increases (e.g. Hardy and Poblet, 1995, Poblet and Hardy, 1995, Storti and Poblet, 1997) whereas in the Dahlstrom (1990) model the relationship between uplift and slip is linear. This difference occurs because in the De Sitter (1958) model the fold grows by an increase in limb dip, or progressive limb rotation, whilst the limb length remains constant whereas in the Dahlstrom (1990) model the fold limbs become longer as the dip increases and the fold grows (Figure 5.16; Poblet and Hardy, 1995).

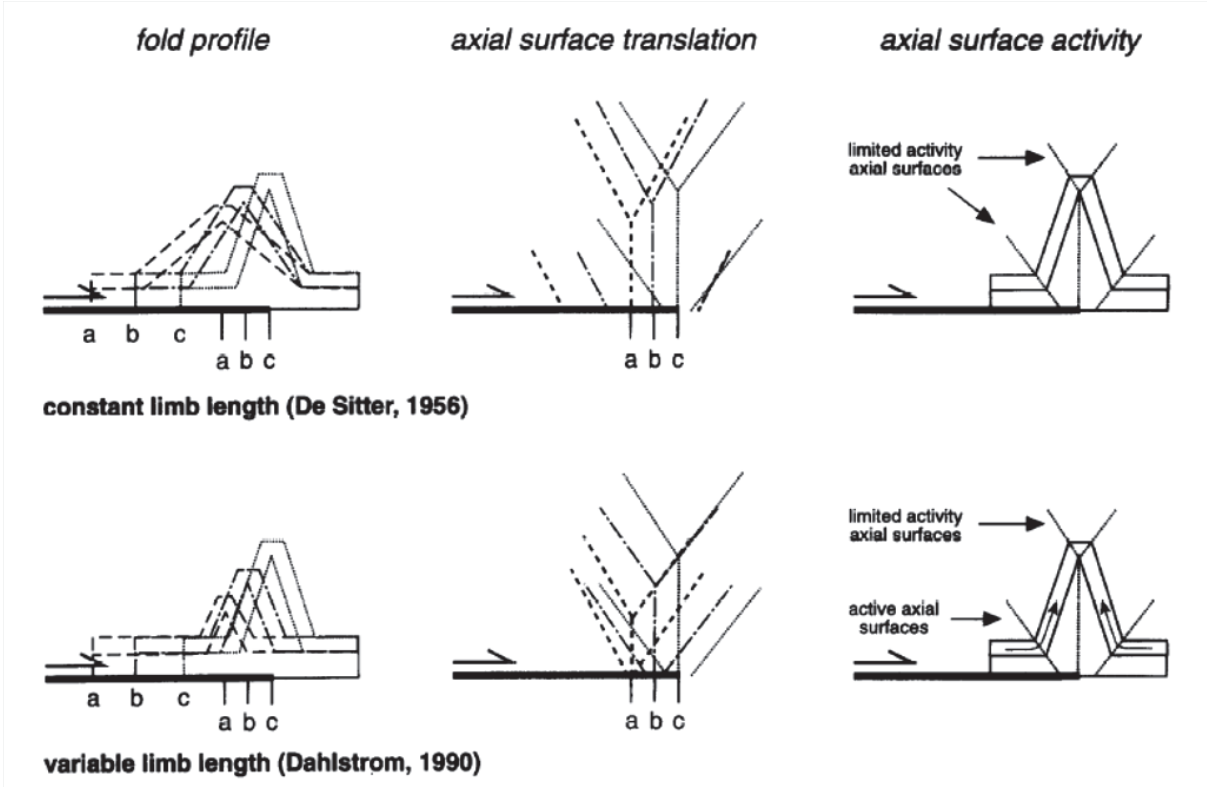


Figure 5.16 Contrasting models of fold growth impacting on the shape and topography observed at the seafloor surface. From Poblet and Hardy (1995).

These different outcomes suggest that the amount of uplift calculated on a structure is highly dependent upon the kinematic model chosen and hence in order to accurately convert horizontal shortening or bed length change into a vertical component of uplift requires knowledge of an appropriate geometric and kinematic model for the fold type observed in the study area. Given that the structures observed within the study area are unlikely to be simple detachment folds, it is not obvious which, if any, of the kinematic models for fold growth presented in the literature would be appropriate for the structures observed within the study area. Therefore, in order to reduce the number of errors introduced into the study, it was decided that a numerical analysis of vertical uplift was beyond the scope of this thesis.

Even if vertical uplift rate had been calculated for the structures within the study area it cannot be used as a direct indicator of the topographic relief of a structure as sedimentation can compensate for this growth. The ratio of the amount of sediment accumulation to the rate of structural uplift determines whether a structure

develops a topographic expression on the seafloor as discussed in Chapter 4, Section 4.2.12 (Burbank and Vergés, 1994, Burbank et al., 1996, Ford et al., 1997, Broucke et al., 2004, Shaw et al., 2004, Shaw et al., 2005). In areas where sedimentation rate is greater than the rate of uplift of a structure the sediment can blanket the growing topography, thinning towards the structure, but ultimately infilling the topographic relief created along the flanks of the structure (Figure 5.17). In contrast to this in areas where the rate of uplift of a structure is greater than the rate of sedimentation the structure will form topography on the seafloor causing the sediments to onlap against the flanks of the structure (Figure 5.17). In extreme cases where the rate of structural growth and vertical uplift is significantly higher than the sedimentation rate in the basin the onlapping stratal geometries will actually start to offlap the structure (Figure 5.17; Ford et al., 1997). However, Shaw et al. (2004) argue that this is a function of the fold model used and hence is not applicable in the case of limb rotation folds, such as those observed within the study area. Analysis of the onlap patterns within the sediment packages alongside analysis of the rates of change of bed length can give more indication of the topographic relief generated by certain structures in the history of the basin. If structures are growing more rapidly, sediment is less likely to be able to over-top the structure leading to onlap (see Figure 5.18 (b)). In reality the strata geometries observed on the flanks of structures are not this well defined with a mixture of more than one stratal geometry often observed as the structures grow (Shaw et al., 2004; Figure 4) due to variation in the rate of the sediment entering the area or the rate of the structural growth.

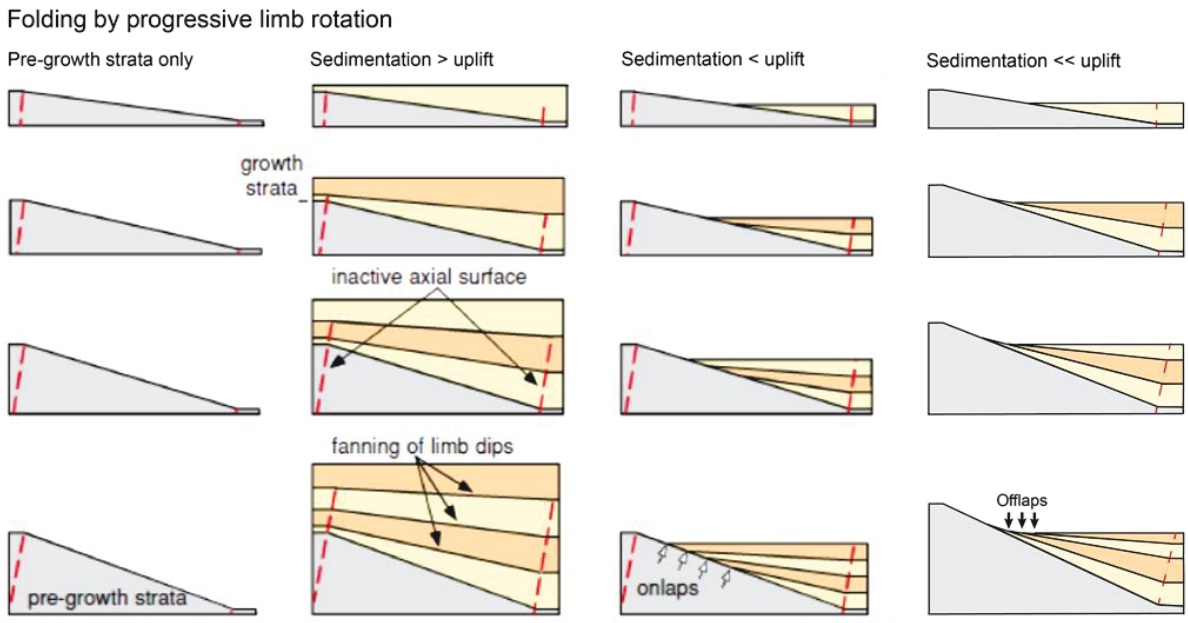


Figure 5.17 Diagram illustrating the development of growth strata as a record of fold kinematics developed by growth of a detachment fold by limb rotation. Modified from Shaw et al. (2005).

It is possible to gain some idea of the topographic relief expressed on the seafloor by comparing the rate of change of bed length maps (Figure 5.15) and the sediment accumulation rate maps (Figure 5.7): in areas where high rates of change of bed length are coupled with sediment thinning it would be expected that there was a relative topographic high on the seafloor (i.e. Figure 5.7 (a)). High rates of change of bed length can be seen to correspond to a thinning of sediment packages throughout the history of the basin. It is particularly apparent in the 18.26 Ma to 13.25 Ma (H10 to H60) interval where sediment thins, but ultimately overtops the structures within Area C and the linking anticline between Areas A and C, which has medium rates of bed length change at the time (Figures 5.7 and 5.15 (f)). Areas of the basin which have high rates of bed length change but show little evidence of sediment thinning could indicate that the high sediment accumulation rates have kept pace with, or overwhelmed the structural growth, leading to very little topography developing (Figure 5.18). This can be seen in the 10.89 Ma to 9.68 Ma (H60 to H80) interval within the vicinity of the Structures 1 and 2 within Area C which have low rates of bed length change towards the centre and yet there is very little, if any, change in surrounding and overtopping sediment thickness (Figures 5.7 and 5.15 (d)). In contrast, thinning of the sediment is observed on the eastern flank of Structure 3 where the rate of change of bed length is high.

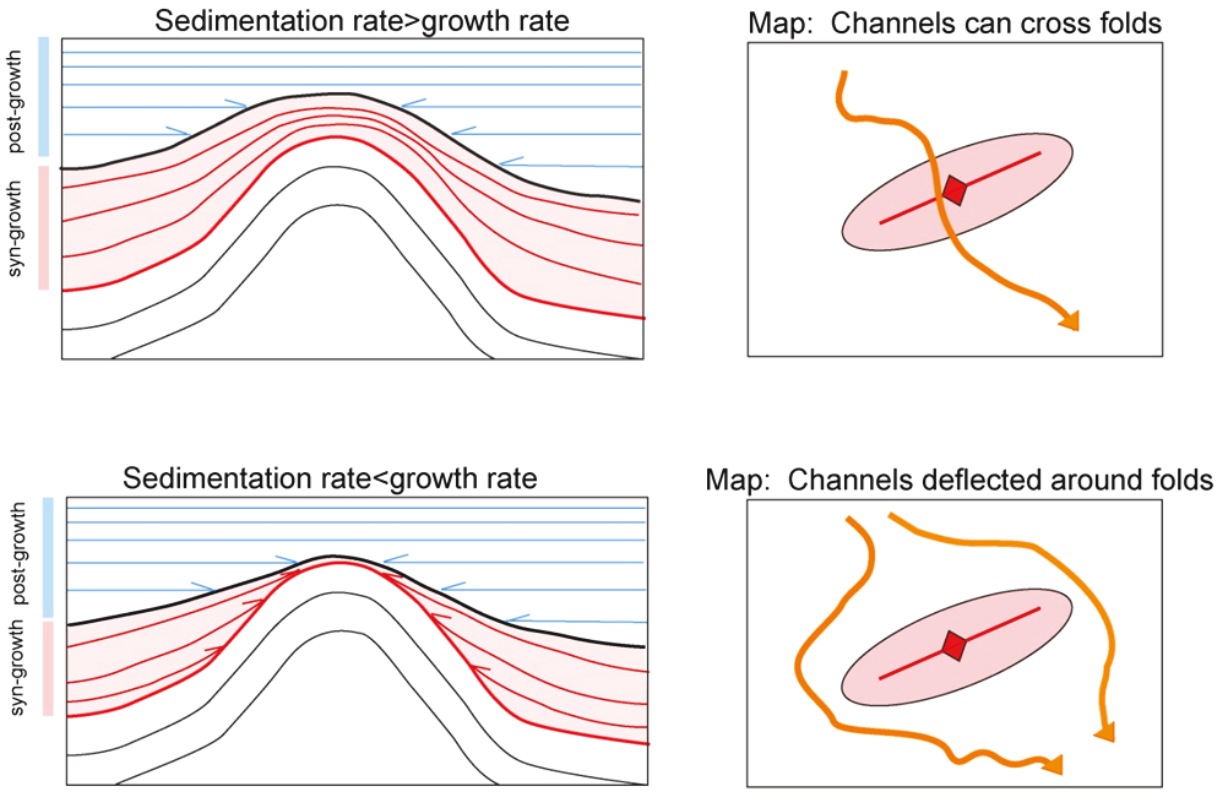


Figure 5.18 Illustration linking the impacts and effects of relative changes in growth rate of a structure and sedimentation rate. Note the passive onlap geometries in the post-growth sediments and the rotated onlap in the syn-growth sediment. Image from L. Lonergan.

5.12 Conclusions

This study has investigated the structural history of a salt influenced mini-basin in the compressional domain of the Angolan passive margin through a variety of methods. By investigating the structural activity on a variety of different scales and time intervals an accurate representation of the evolution of the basin has been presented which indicates two main periods of growth on the basin bounding structures; the first during the Late Oligocene and the second during the Mid-Miocene.

Given the lack of correlation between thickness changes within the centre of the mini-basin and the rate of structural growth of the basin bounding structures, at the temporal resolution of the isopach maps it is possible to conclude that structural growth is primarily driven by regional-scale changes which drive salt movement as opposed to local sediment loading. The main phase of structural activity within the mini-basin occurred in the Oligocene from 33.9 Ma until 25 Ma and coincides with regional uplift of the African margin driven by a plume event beneath subequatorial Africa. This resulted in periods of high supply of sediment to Lower Congo Basin from the Congo (Zaire) River system (Al-Hajri et al., 2009, Roberts and White, 2010, Paul et al., 2014) which continued until approximately 10 Ma when the location of the Congo (Ziare) Fan moved further north (Anderson et al., 2012). The results presented in this chapter suggest that, at least in this part of compressional domain, rates of change of bed length have not remained constant through time but vary with increased activity in two periods followed by a slowing of bed length change on all structures within the basin at approximately the same time as the shift in location of the Congo (Zaire) Fan. Whilst the first period of increased structural growth is observed elsewhere along the margin and extensively documented (for example Al-Hajri et al., 2009, Roberts and White, 2010, Anderson et al., 2012) the second main period of growth observed within the mini-basin has not been documented elsewhere in published literature. Further work is required to understand the processes driving this period of basin-wide growth, with further discussion of this result presented in Chapter 9.

In the majority of cases, structures which have high interval bed length change rates have correspondingly low sediment accumulation rates over the top of the structure. Therefore, it is acceptable to use these rates of change of bed length measurements to give an indication of local changes in topography within the mini-basin. As discussed in the preceding section the rate of change of bed length alone does not translate easily into a vertical uplift rate or into a value for bathymetric relief. However, given the strong correlation between the thinning of sediments and high rates of change of bed length on structures within the basin it is considered to give a good proxy for bathymetric relief. Therefore, rate of change of bed length will be used alongside stratigraphic onlap analysis in subsequent chapters to investigate the response of different sedimentary systems to relative structural growth along the margins and within the mini-basin.

In summary, the main conclusions from this chapter which will be developed further in subsequent chapters are as follows:

1. There were two major basin-wide periods of structural growth within the mini-basin, the first between 33.9 Ma and 25 Ma and a second higher pulse in growth between 18.26 Ma and 13.25 Ma.
2. The growth observed on the structures in these two major intervals of growth appears to be driven by folding and salt movement in response to regional shortening as opposed to local sediment loading.
3. The two youngest intervals in the history of the mini-basin, from 8.29 Ma until present day, have the lowest growth rates on the structures, which corresponds to the northward movement of the main sediment entering the Lower Congo Basin from the Lower Congo River thought to begin at approximately 10 Ma (Anderson et al., 2012).
4. Rate of change of bed length provides a reliable indication of the amount of growth on a structure. Analysis of isopach maps or onlap patterns needs to be used to complement this analysis in order to confirm whether this growth translates directly into bathymetric relief.

6 Mass Transport Complex Deposits Generated by, and Subsequently Influenced by, Active Salt Growth Structures

6.1 Abstract

Mass transport complexes (MTCs) are generally readily identifiable on seismic datasets, here two types of MTC deposit are studied: local slide deposits and regional debris flows. Both of these deposits are observed within the mini-basin, dominating the sedimentary succession at different periods of its history. The two types of MTC have distinctly different topography, internal characteristics and distribution within the mini-basin; features which are all analysed in this chapter.

Local MTCs usually show classic extensional features towards the head of the system and compressional features at the toe. The strike of the normal faults and toe thrusts on amplitude extraction maps allows the transport direction to be reliably interpreted, with the direction of flow indicating that these MTCs are all sourced from the flanks of active salt structures. The anticlinal structures which source the best developed local MTCs show the highest rates of uplift in the preceding periods and the flanks of the anticlines appear to be exposed and emergent during the time that the MTCs were generated.

It is not possible to trace the source of the widespread, well-developed regional MTCs to an initial failure surface within the dataset. However, biostratigraphic analysis of recovered cuttings shows that at least one of the MTCs contains remobilised outer shelf to upper bathyal biofacies indicating that the sediments were transported from significantly further landward. They can be recognised in seismic sections by a relatively planar basal surface with little to no visible erosion, topped with internally chaotic, semi-transparent beds which tend to thin onto salt structures. The thinning observed towards the anticlines with high structural growth rates suggests that these structures constrained the extent of the deposition of the debris flows. Studying these regional MTCs allows observations of how active structural growth has influenced the locus of debris flow deposition within the mini basin; high growth rates on certain structures have generated seabed topography that was too high for the debris flows to surmount, with down-dip terminations of MTCs on the flanks of the structures suggesting that flows were halted by relatively low seafloor dips.

6.2 Introduction

Mass transport complexes (MTCs) transport large amounts of material into deepwater settings and, as such, are responsible for a significant proportion of the stratigraphic fill of basins along the continental margins (Hampton et al., 1996, Moscardelli et al., 2006, Alves and Cartwright, 2010). Posamentier and Walker (2006) observed that in some deepwater areas, MTCs and their associated deposits can make up more than 50% of the slope and stratigraphic column, with other authors suggesting this might be up to 75% in more ancient outcrops and basins (Martinsen, 1989, Martinsen, 1994, Maslin et al., 2004, Newton et al., 2004). MTC deposits constitute a large volume of material within the mini-basin studied in this thesis, therefore it is important to understand the nature of these deposits and what triggers their formation.

Moscardelli and Wood (2008) broadly define mass transport complexes (MTCs) as the movement of sediment driven by gravity (gravity-induced deposits; based on work by Dott Jr, 1963, Nardin, 1979). This broad term therefore encompasses a spectrum of deposits including slides, slumps, debris flows and turbidites, all of which can co-occur within the same event or depositional unit (see Chapter 3, Table 3.1). Other authors have included creep and rock falls in their classifications (for example Nemec, 1990). However, this work follows the scheme outlined by Moscardelli and Wood (2008) and adapted from the work of Nardin (1979), which focuses on the sedimentary fabric and seismically-recognisable criteria and is therefore most appropriate for this study.

MTCs are thought to be generated in areas where deformation of the seafloor generates instability which in turn leads to the formation of slumps, slides and debris flows from intra-slope highs. Having previously investigated the degree of movement on the structures which bound and are internal to the mini-basin, this study area is an ideal place to investigate the effect that structural growth has on the development of the MTCs. The size of the MTCs recorded in the subsurface and on the seafloor can range from small, local slumps and slides with limited lateral movement, to debris flows covering tens of square kilometres (Hampton et al., 1996, Huvenne et al., 2002, Haflidason et al., 2004, Frey Martinez et al., 2005, Moscardelli et al., 2006, Owen et al., 2007, Moscardelli and Wood, 2008, Posamentier and Martinsen, 2011). In this chapter, both of these scales are investigated: local MTCs are analysed in Sections 6.7 and 6.8 and the toe region of a series of regional MTCs are analysed in Section 6.9.

Two main types of MTC are observed within the study area: local and regional MTCs which are broadly classified as slides and debris flows respectively. The slides form as coherent blocks of material which move along a planar basal detachment with little internal deformation whereas debris flows are comprised of disaggregated material containing matrix supported clasts and are seismically recognisable through their low-amplitude, semi-transparent, chaotic seismic character (Moscardelli and Wood, 2008). Recent work on MTC deposits offshore Trinidad by Moscardelli and Wood (2008) can be drawn upon to classify the local slides and regional debris flows as detached and attached MTCs respectively. They define detached MTCs as those deposits which are formed when local instabilities affecting local bathymetric highs trigger partial collapse along the flanks of structures generating cascading debris flows, slides and slumps. Whereas attached MTCs are larger in scale and characterised by debris flows which form regional units. These are triggered by regional events which have the capacity to destabilise the outer-shelf/upper slope regional of the passive margin generating massive collapses responsible for the initiation of mass wasting processes (see Chapter 3 for further discussion of this classification scheme; Moscardelli and Wood, 2008).

The generation of MTC events can have an often catastrophic impact on the surrounding area, generating tsunamis, avalanches, major rock falls, and mudslides (for example Holmes, Bolt et al., 1977, Voight, 1978, Brunsden and Prior, 1984, Fisher and Smith, 1991, Martinsen, 1994, Bondevik et al., 2003, Posamentier and Martinsen, 2011). Richardson et al. (2011) emphasise their potential large impact on several parts of a petroleum system as they:

- are potential geohazards affecting the stability of offshore installations (Prior and Coleman, 1982, Hampton et al., 1996, Locat and Lee, 2002, Solheim et al., 2005)
- transport significant volumes of sediment offshore (Hjelstuen et al., 2007, Talling et al., 2007)
- induce possible global climate change mechanisms due to gas hydrate disassociation (Maslin et al., 2004)
- can create issues when drilling (Barley, 1999, Weimer and Shipp, 2004) and
- occasionally form unconventional hydrocarbon trapping mechanisms (Weimer and Shipp, 2004, Butler and Turner, 2010, Mosher et al., 2010)

Here, two distinctive types of MTC are investigated which both impact on the ability to drill in the region and have the potential to impact the petroleum system by forming local seals.

In this Chapter the internal characteristics of both the locally derived smaller MTC deposits and a portion of one of the larger regionally derived MTC deposits will be described. The relationship between these two types of MTC and the structures which grow along the margin will also be discussed in detail, in particular focussing on how the rate of change of bed lengths discussed in Chapter 5 relate to these; do high rate of change of bed lengths correlate directly with periods of MTC formation, or it is the relationship more complex?

6.3 Methods

This chapter uses the high resolution PSVM seismic dataset to investigate the characteristics of both the local and regional MTC deposits. Whilst the regional deposits extend outside the area covered by the PSVM dataset, the resolution of the regional seismic dataset does not allow them to be traced back to the source. Therefore, in both cases the PSVM dataset has been the focus of the work and used alongside biostratigraphic data and paleontological analysis of the wells which intersect these deposits.

The local MTCs have been mapped in detail with the upper and lower bounding surfaces mapped on MTC 1 and the basal surfaces mapped on MTCs 2a to 2c (Figure 6.1). These surfaces were mapped at a spacing of 20 lines, the equivalent of 125 m, and then interpolated using the methodology outlined in Chapter 4. The top and base surface of regional MTC β was also mapped throughout the basin using the same inline and cross-line spacing. Again, these surfaces were interpolated and smoothed following the procedure outlined

in Chapter 4. Amplitude extraction maps through MTCs α and γ were generated using horizons already picked near the lower and surfaces of these MTC deposits (surfaces H20 and H60 respectively).

Extensive attribute analysis was performed on both the local and regional MTC deposits. Root mean squared (RMS) amplitude analysis was carried on 10 ms windows above and below the basal and top surfaces of MTC 1 and on 20 ms windows above the mapped basal surface within MTCs 2a, 2b, 2c and 3. Similar size windows were also used to analyse the regional MTC deposits. The amplitude extractions are beneficial to highlight morphological similarities and variations within the MTC deposits as changes in amplitude can result from variations in the fluid content, bed thickness, porosity and geometry of the beds (Hart, 1999). Therefore, by analysing intervals within the MTC deposits using the 3D seismic data it is possible to discern structural features, variations in sedimentology and lithological changes which will facilitate observations of the internal characteristics (Enachescu, 1993).

Alongside this, volumes were generated and loaded into Geoterric® software, these were flattened to the corresponding mapped surface and a range of attributes extracted. The volumes generated included coherency volumes, dip volumes, azimuth volumes and spectral decomposition volumes. Generating a volume which can be flattened to the basal surface of the MTC deposit means that it can be horizontally sliced allowing more information on the aerial extent and lateral continuity of the internal material within the MTC to be analysed (Dalley et al., 1989, Peyton et al., 1998).

6.4 Structural Constraints

The local MTC deposits can be clearly linked back to their source on a specific structure along the margin of the basin (Figure 6.1). The deposits generally flow towards the basin centre, but have locally varying transport directions in response to local fold-related topography. Six local MTC deposits have been mapped in Figure 6.1 and represent the largest, most dominant slides within the study area. MTC 1 is sourced from the structure within Area D on the west of the basin and is constrained in extent partly by growth on Area E, and partly by erosion from the deposit which is not studied here, but is sourced from the Area C structure. MTC 2 consists of three separate, mapable MTC deposits which occurred in a very similar location but at different times during the history of the basin; MTC 2a (oldest) to MTC 2c (youngest). A portion of the sediments which make up MTC 2a were derived from the southeast where two anticline trends converge and flowed towards the northeast whilst the two later deposits MTCs 2b and 2c were sourced from growth on the anticline within Area B and flowed to the east (Figure 6.1). MTC 3 has been sourced from the structures within Area F and flows from the east to the west.

In contrast to these aerially-confined systems the regional MTC deposits can be mapped throughout most of the basin area with the easterly and westerly limits defined by the structures within Areas C, D, E and F. Late canopy salt growth on the structure within Area F which occurred after the deposition of the regional MTC has partially obscured any changes in thickness in response to this structure.

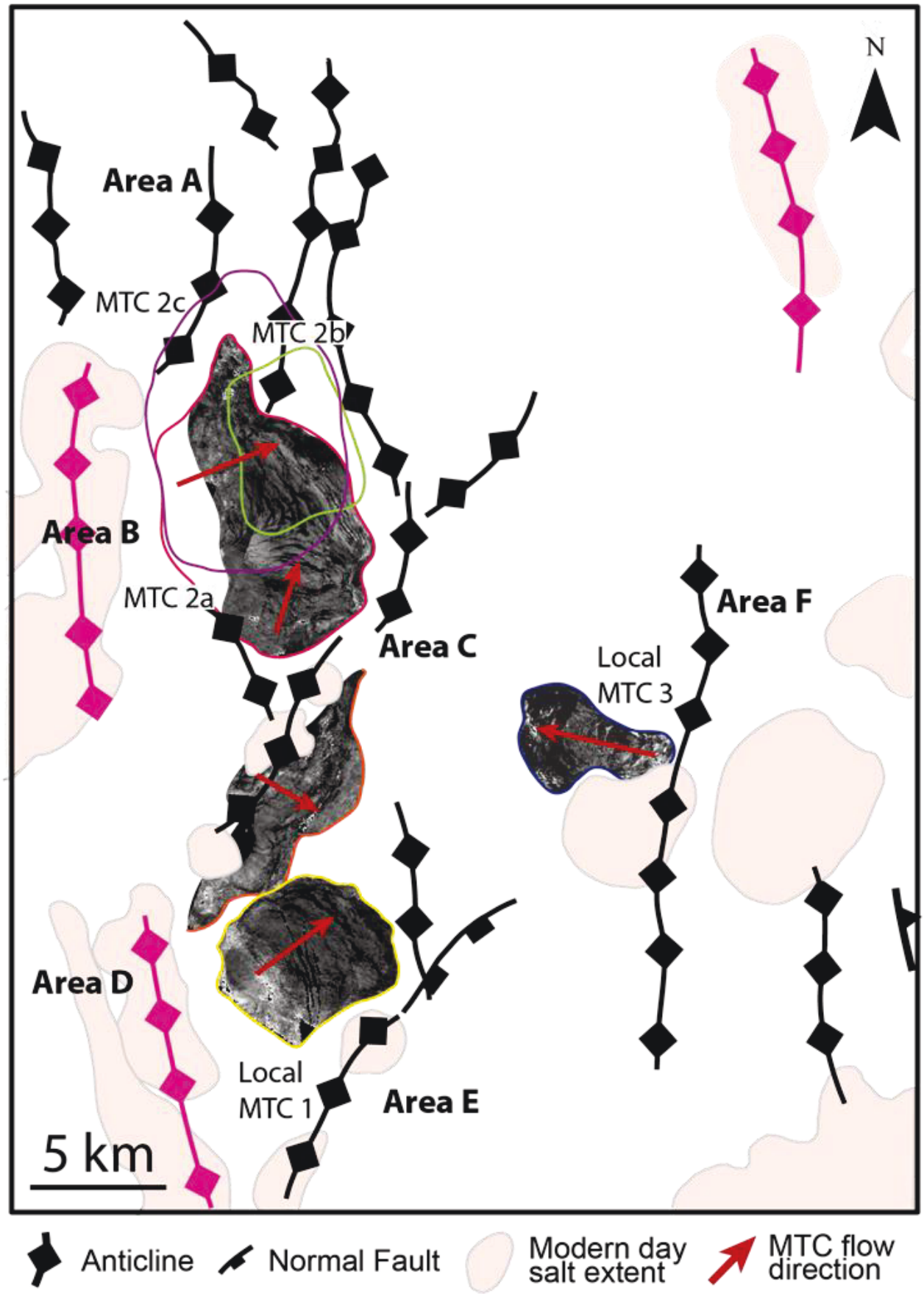


Figure 6.1 Map showing the location of the main local MTC deposits studied in this chapter and the flow directions of these. Note that the majority of the locally sourced MTCs are derived from the structures along the western margin of the basin. The main local MTCs are highlighted using the relevant root mean squared (RMS) amplitude extractions where white indicates high amplitudes and black low amplitudes.

6.5 Age of MTCs

Local MTC deposits are observed throughout much of the history of the mini-basin, but this study concentrates on the largest of these deposits which are located between the H90 and H120 horizons and, as such, were deposited between 9.68 Ma and 5.04 Ma within a 4.64 Ma period. This period also corresponds to the main deposition of ponded sediment within the basin, with the local MTCs deposited before, during and after the deposition of these fan systems (see Chapter 7 for more discussion of these). The basal shear surface of the compressional domain of MTC 1 runs conformably along the top of the H100 interval and is onlapped by sediments deposited between H100 and H110 (8.29 Ma and 5.58 Ma; ponded sediments), onlap patterns also suggest that MTC 2a and 2b were deposited at the same time as this (see Figures 6.4 and 6.7). The two other local MTCs discussed in detail here, MTC 2c and MTC 3, are both younger. These were both deposited within the interval between the H110 and H120 horizons, a period between 5.58 Ma and 5.04 Ma when sediment input into the area switched off (see Figures 6.7 and 6.10). MTC 3 appears to be older than MTC 2c as the compressional domain of MTC 3 is conformable with the H110 horizon, whereas the MTC 2c basal shear surface was deposited above the H110 surface. This means that MTC 2, taken as a whole, is the most long-lived structure with a series of MTC deposits generated from the one structure.

The regional MTC deposits, are mainly confined to the period between the H10 and H60 horizons (18.26 Ma to 13.25 Ma) with the majority deposited between the H50 and H60 horizons towards the latter half of this interval.

6.6 Local Mass Transport Systems – MTC 1

The main boundaries and internal features of one of the largest and best-imaged locally derived MTCs has been analysed in detail in this chapter (MTC 1, Figure 6.1). Once the main features have been described and discussed in detail, this system will be compared to MTC 2 and MTC 3 which contain subtly different features due to the variation in movement and timing on the structures they are derived from. The extensional and compressional domains of the MTC deposits are well-imaged within all the MTCs, whilst the translational domain is hard to identify, possibly because these are all relatively coherent slides and material has not moved laterally very far from the source. The internal features seen within each domain of MTC 1 will be discussed in detail in the following sections, broadly focusing on the bounding surfaces and the domain boundaries discussed in Section 3.3.1; the extensional domain, translational domain and compressional domain. Faults which are clearly located within the extensional and compressional domains are colour-coded in Figure 6.2 giving an indication of the extent of the extensional and compressional domains.

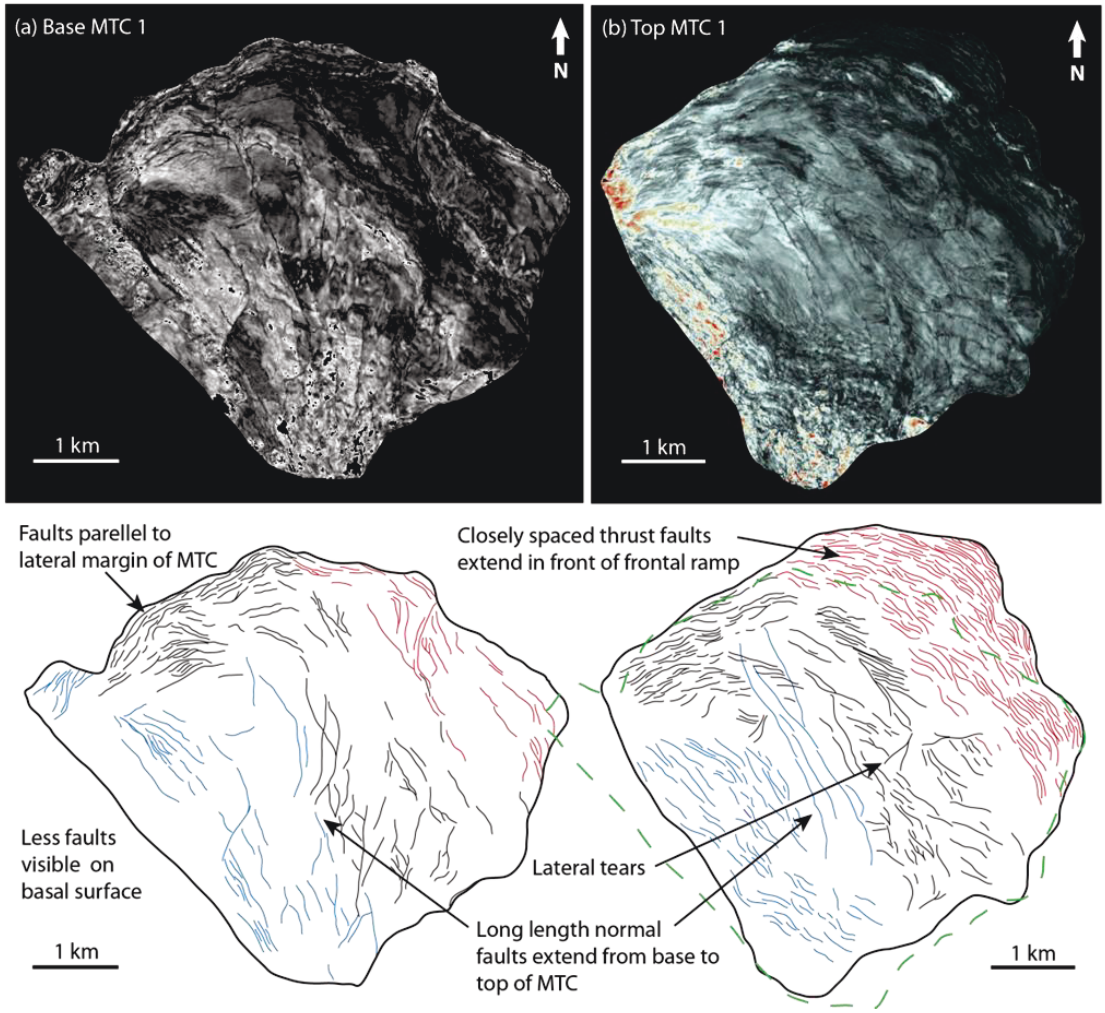


Figure 6.2 RMS amplitude extraction maps and sketch maps highlighting the main features of MTC 1 with (a) showing an RMS amplitude map extracted over a 10 ms twtt window above the base of the MTC where white indicates high amplitude and black low amplitude and (b) showing an RMS amplitude extraction through an isopachous interval between the top and the middle of the MTC where white indicates high amplitudes, red middle amplitudes and black low amplitude. The main faults are highlighted in the sketch maps where blue and red lines have been used to colour code extensional and compressional faults respectively, the outline of the base of the MTC is shown in dashed green lines on the top MTC sketch map to highlight the inferred edge of the frontal ramp. The middle of the upper half of the MTC contains a band of unclassified faults containing both normal and thrust fault.

6.6.1 Bounding Surfaces

Basal Shear Surface

The basal shear surface is a detachment surface along which the sediment slides, it is normally concordant to bedding but can be affected by faults or variations in the lithology of the bedding plane (Varnes, 1978). In MTCs consisting of coherent stratigraphy the basal shear surface is sometimes observed to ramp-up in stratigraphy in the compressive domain and along the lateral margins of the slide (Frey-Martínez et al., 2006). This is the case in MTC 1 where once the basal shear surface has cut down at the headwall scarp it is generally concordant with the underlying sediment packages in the extensional domain and towards the centre of the MTC (Figure 6.4). However, there are some small ramps within the area which are on average 30 m high and cut both down into the underlying strata and up from the underlying strata (Figures 6.4 and 6.5). These ramps truncate the underlying sediment packages and appear to trend perpendicular to the main direction of flow.

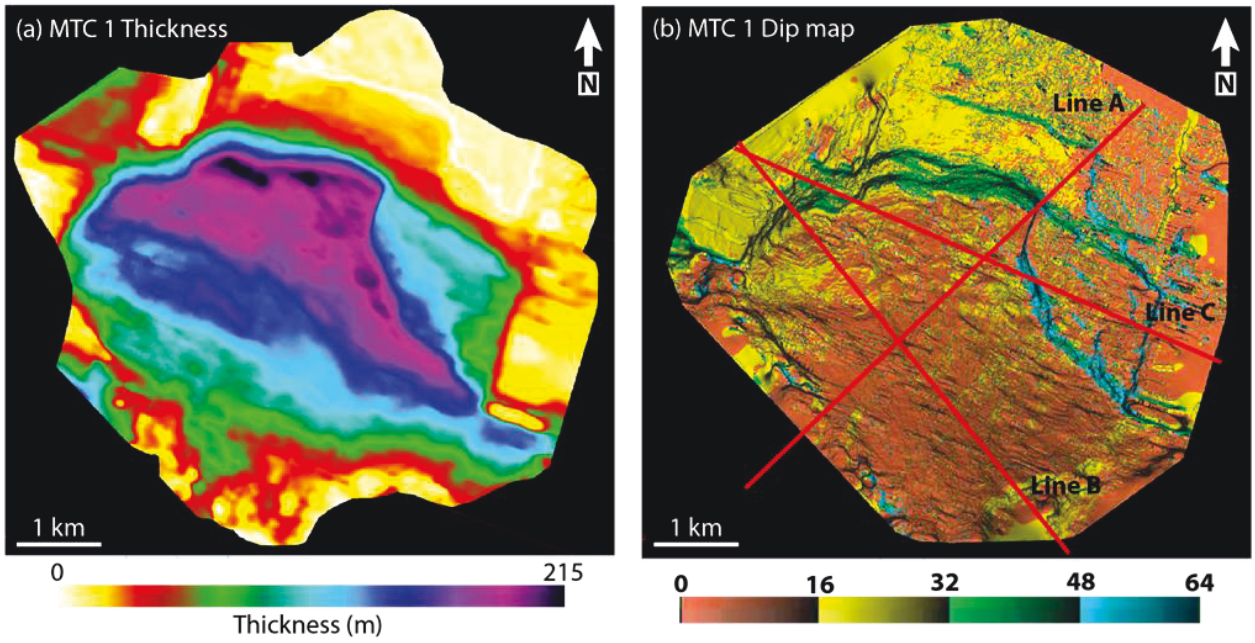


Figure 6.3 Maps showing (a) the thickness of MTC 1 calculated using the stratigraphic thickness algorithm discussed in Chapter 4 applied to the top and base mapped surfaces, note the interval of thick sediment extends further into the basin on the western side of the MTC deposit, this shape is reflected in (b) a dip/azimuth map over the basal surface of MTC 1. The location of the seismic lines seen in Figure 6.4 are also shown on this dip map.

The basal shear surface is more complicated towards the margins of the MTC, both within the compressional domain and along the lateral margins. Here, it cuts up through the stratigraphy generating a distinctive frontal ramp towards the front and variable height ramps along the margins (Figures 6.3, 6.4 and 6.5). The frontal ramp is on average 200 m high cutting up through stratigraphy deposited between 10.98 Ma to 8.29 Ma (the H80 to H100 horizons) and decreasing in height towards the edges of the MTC (Figures 6.4 and 6.5). The basal dip map and thickness map indicate that the frontal ramp steps back towards the source area towards the east of the MTC (Figure 6.3). The ramps within the basal surface which form along the lateral margins of the MTC are discussed in more detail in a subsequent section.

Top MTC Surface

The upper surface of MTC 1 has been mapped revealing an undulose top surface reflecting underlying internal deformation within MTC 1. A more irregular topography occurs towards the back of the extensional domain reflecting the movement on the underlying normal faults and in the compressional domain where a series of arcuate folds are generated in response to movement on thrust faults in this area (Figures 6.4 and 6.5). The majority of faults towards the back of the extensional domain and the front of the compressional domain extend up to the top surface of the MTC, with those between these two extremes less likely to extend through it (Figure 6.4). There is some evidence of ponding and onlap of younger sediments against the MTC surface (Figure 6.4).

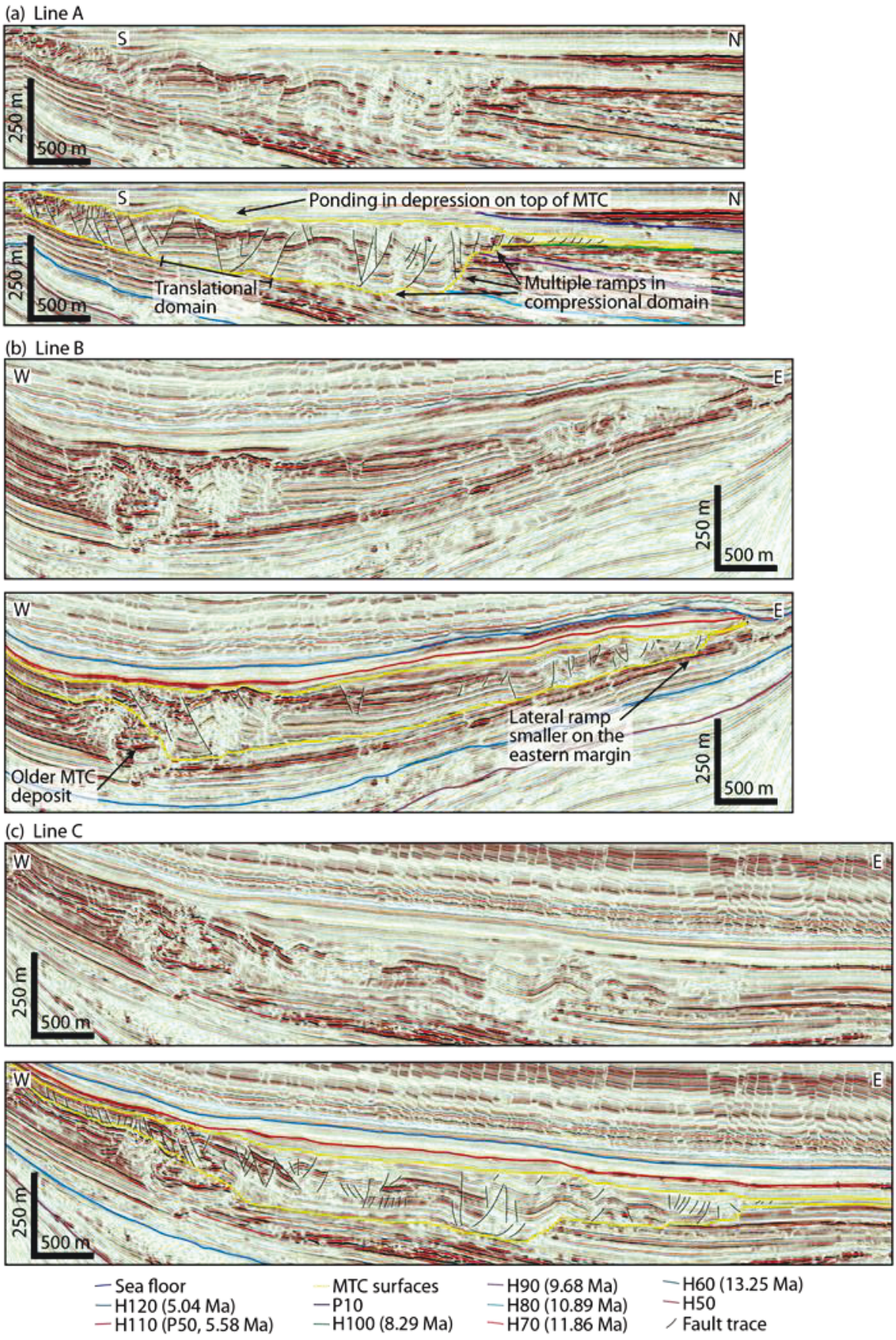


Figure 6.4 Seismic sections through MTC 1 showing (a) Line A, a strike section parallel to the direction of flow of the MTC and flattened on the H120 surface. This flattening simulates the topography present at the time of deposition of MTC 1, (b) Line B, an un-flattened seismic line perpendicular to the main flow direction which shows a section through the lateral margins of the MTC and how it relates to the older MTC to the west of the area. The third seismic section, (c) Line C is also an unflattened seismic section perpendicular to the flow direction but further basinwards than Line B. The location of all three of these lines is shown on Figure 6.5.

Lateral Margins

These are the down-dip parallel side-boundaries of a MTC which cut through the surrounding material and commonly form parallel to the main direction of flow of the system (Bull et al., 2009). Strike-slip movements have been recorded along these lateral margins (see Martinsen and Bakken, 1990, Martinsen, 1994, Frey Martinez et al., 2005) with the formation of transpressional or translational structures if the MTC narrows or widens. Here, the basal shear surface or decollement cuts down into stratigraphy at headwall and material above the basal shear slides in relatively coherent way above this surface. At the lateral margins this material cuts up to higher levels in stratigraphy but does not disaggregate enough to form a debris flow unit (Figure 6.4). These lateral margins extend along the edge of the structure and merge with the frontal ramp in the compressional domain.

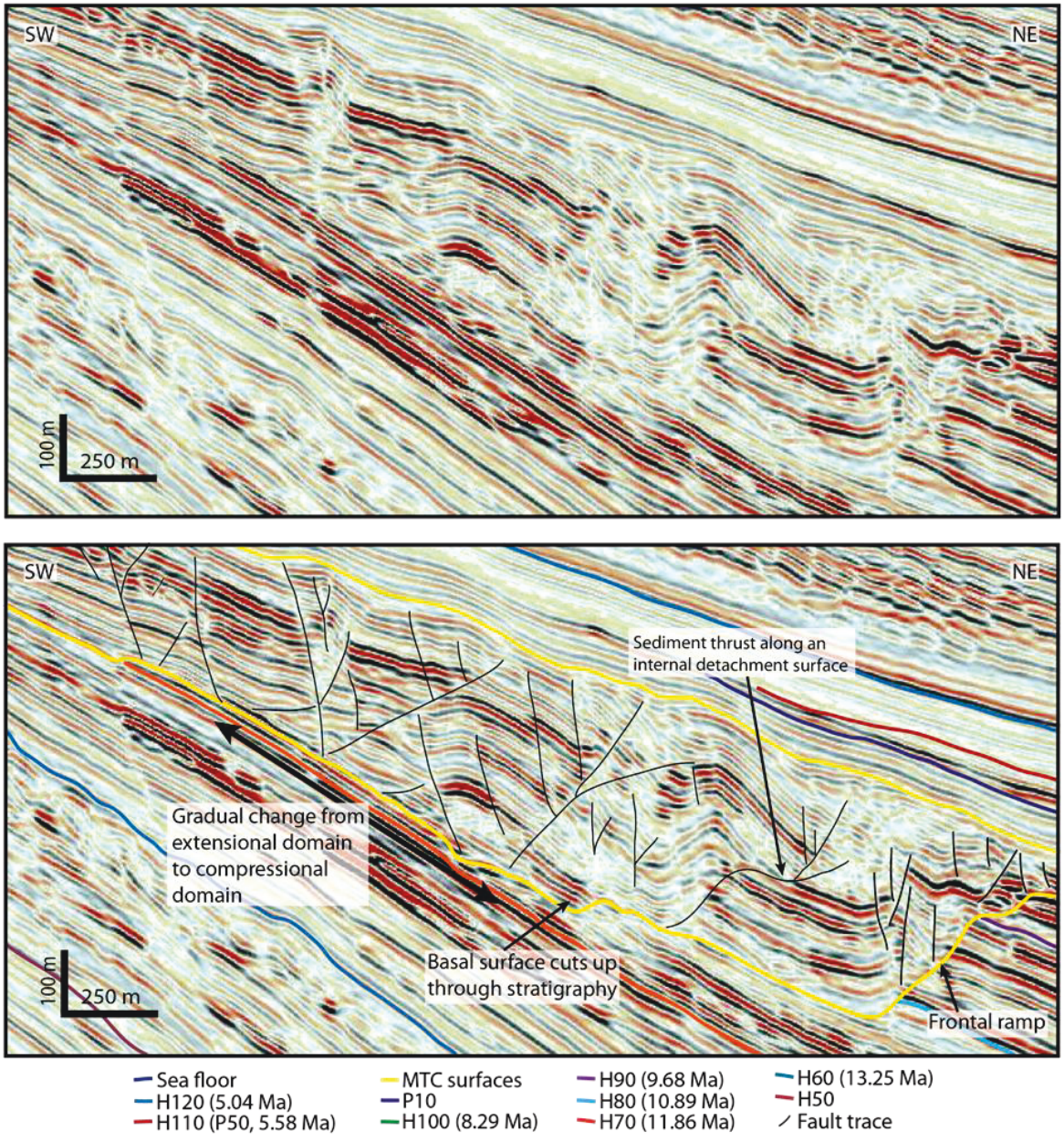


Figure 6.5 A close-up seismic image showing the detail within the compressional domain of MTC 1, highlighting the thrust faulting and folding within this domain. Note how the frontal ramp cuts up through the stratigraphy and the development of a series of folds and thrusts behind this ramp.

MTC 1 is confined on at least one margin by positive topographic relief (Figure 6.1) which may have had an impact on the type of margin formed. The lateral margins of MTC 1 show the slide cutting up into younger stratigraphy by up to 200 m from a low basal detachment surface on both the eastern and the western margins on the MTC (Figure 6.4 (c)). The basal surface on the western margin of the MTC cuts through an older MTC deposit truncating the underlying sediment packages (Figure 6.4 (b) and (c)), this older MTC has not been studied in detail but is shown in Figure 6.1. The lateral ramp is significantly higher on both margins towards the back of the MTC with a height of approximately 180 m and a very steep ramp gradient in this area (Figure 6.5 (b)). This corresponds to an increase in the number of compressional faults observed parallel to the lateral margin (Figure 6.2). Towards the front of the MTC, the ramp has slightly smaller overall relief (approximately 130 m) and the ramp surface has a shallower gradient surface being comprised of a series of steps (Figure 6.5 (c)).

The morphology of the eastern margin of the basin varies significantly down the length of the margin (compare Figure 6.4 (b) and (c)). The eastern margin remains fairly concordant with the underlying stratigraphy near the headwall region of the MTC with a small ramp forming near the margin which has a maximum height of 50 m (Figure 6.4 (b)). Whereas closer to the front of the MTC a second, larger ramp cuts up through the stratigraphy further to the west of this first one (Figure 6.4 (c)). This ramp surface has also been imaged on the thickness map and dip map of the basal surface, both of which indicate the presence of a curved ramp which starts near the middle at the front of the MTC and curves towards the middle of the eastern lateral margin (Figure 6.3). The ramp curves in the opposite direction to what would be expected within the compressional domain of a slide and the faults imaged on the amplitude extraction maps to do not appear to follow the trend of this ramp. In contrast those faults imaged on the western margin do mimic the trend of the western margin (Figure 6.2).

6.6.2 Internal Characteristics

Extensional Domain

Overall, the extensional domain is narrower towards the northwest edge of MTC 1 and widens along the axis of the structure to the south; going from approximately 500 m wide in the northwest to over 1,750 m in the south, as shown by the colour-coded faults in Figure 6.2.

The extensional headwall of the locally derived MTCs are not easily imaged on the seismic data as the material has been evacuated from the area. However, it can be seen on the seismic sections through MTC 1. The erosive down-cutting surface on the southwest end of the dip-section through MTC 1 is interpreted to be its preserved headwall scarp (Figure 6.4 (a)). This is a clean, clear break orientated perpendicular to the maximum transport direction of the MTC, with all the associated material removed from the area. The space which was evacuated by the MTC deposit has subsequently been infilled by younger sedimentary units (Figure 6.4 (a)). The headwall scarp has not been fully mapped, but analysis of the area using the 3D seismic data indicates that it ranges in height from 100 m to approximately 300 m.

The extensional domain is dominated by extensional normal faults separating discrete blocks of un-deformed material (Figures 6.2 and 6.4 (a)). These tend to be parallel to sub-parallel to the headwall scarp with the blocks typically elongate in the along-strike direction. Amplitude windows taken through MTC 1 highlight the orientation of the blocks and normal faults (Figure 6.2). The normal faults are broadly linear and appear to be smaller and more discrete nearest the headwall scarp of the MTC (Figure 6.2). The normal faults extend throughout most of the MTC unit but show a slight increase in frequency towards the upper surface of MTC 1 where they tend to branch (Figure 6.4 (a)). Strike sections perpendicular to the flow direction indicate that the blocks separated by the normal faults range in width from less than 100 m to over 300 m (Figure 6.4 (a)).

Translational Domain

The translational domain lies between the extensional and compressional domains within the centre of the MTC (see Chapter 3, Section 3.2.1). Bull et al. (2009) define it as the main translated body of the MTC, containing extensive sediment deformation due to the movement of the failed material along the basal shear surface. MTC 1 does not contain a well defined translational domain with extensional structures visible right down to start of compression. Elsewhere in the literature several of the MTCs termed slumps and slides also do not contain a well-defined translational zone (for example see Frey Martinez et al., 2005, Frey-Martínez et al., 2006). There is a small zone between the boundaries of the extensional and compressional domain where both extensional and thrust faults co-exist but this is not well developed enough to warrant a full discussion of a translational domain (Figures 6.4 (a) and 6.5).

Compressional Domain

The compressional domain within MTC 1 covers the largest area within the system. It is also referred to as the toe domain and, as such, represents the downslope region of the MTC including the termination point or toe (Bull et al., 2009). The main features within this area of the MTC includes pressure ridges and thrust and fold systems which Frey Martinez et al. (2006) argue occur to varying degrees depending whether the system is frontally confined or frontally emergent (see Section 3.2.1). All of the locally derived MTCs described in this chapter are frontally emergent with the seismic cross sections indicating that the mass of material generated by the slide is able to move up from the original basal surface in the translational domain and then flow freely across the unconfined sea floor (Figure 6.4 (a)). There are two distinct zones within the compressional domain: a fold and thrust domain where the material has buttressed against the ramp in the basal shear surface and a much thinner region containing small imbricate thrusts.

Fold and thrust systems develop behind the frontal ramp of the MTC with the internal deposits buttressing against it generating a series of folds and thrust faults (Figures 6.4 (a) and 6.5). As the previous discussion on lateral margins highlighted, the western edge of the frontal ramp extends further into the basin than the eastern edge, possibly defining two separate lobes of movement within the MTC, and impacting on the distribution of fold and thrust features (Figure 6.3). The thrust faults imaged within this section typically affect the entire thickness of the MTC body, detaching into the basal shear surface and generating positive

topography of up to 40 m on the top MTC surface (Figures 6.4 (a) and 6.5). The body of the MTC affected has a maximum thickness of 215 m with offsets of up to 50 m recorded between the beds (Figure 6.4 (a)). Several pop-up style features are also visible within this domain, these are generated by pairs of opposite-dipping thrust faults which are also imaged in the RMS amplitude extraction maps (Figure 6.2). The compressional domain of MTC 1 contains at least one internal detachment zone which has enabled a second thrust fault to piggy back over the sediment package nearest to the ramp edge, generating a fault propagation fold (Figure 6.5).

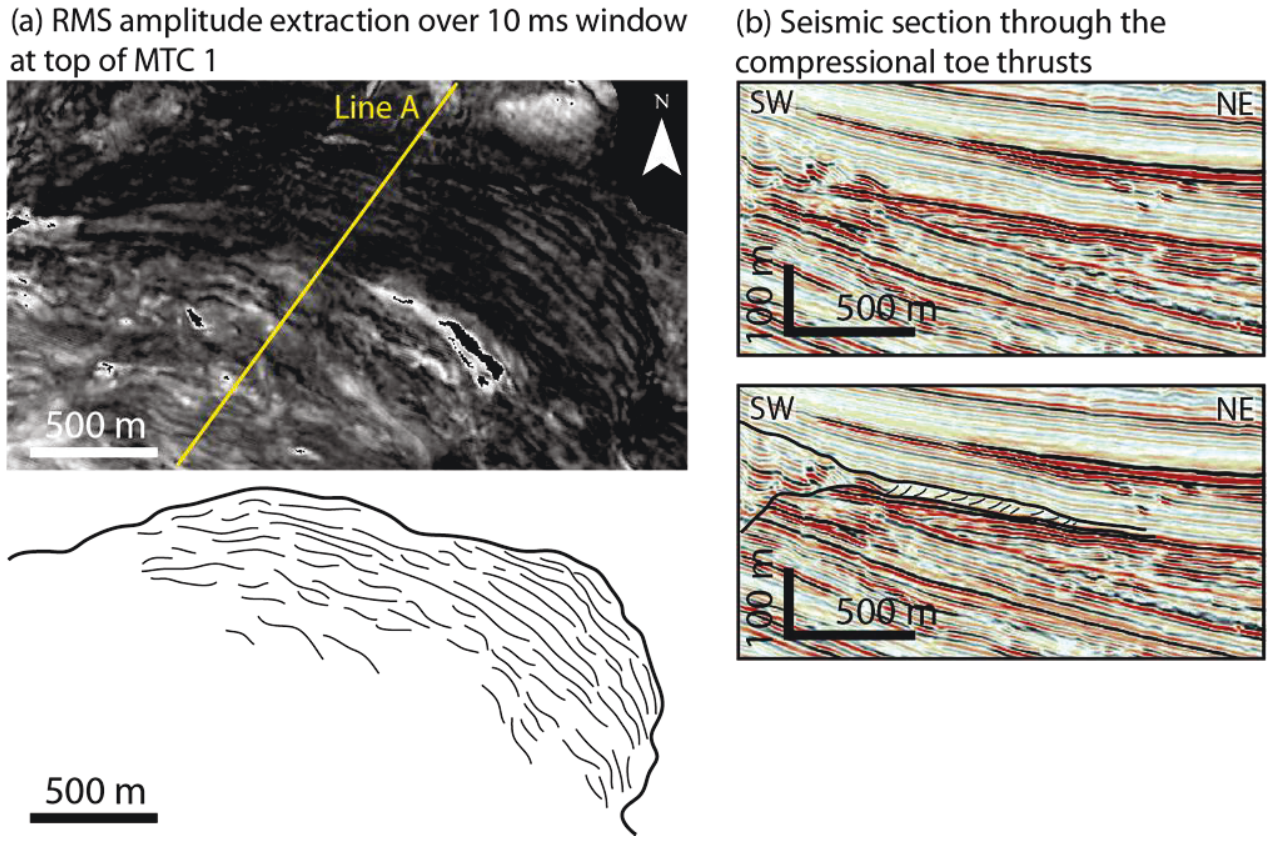


Figure 6.6 A close-up on the thrust faults within the compressional toe of MTC 1 with (a) showing an RMS amplitude extraction map over this toe region and a sketch map highlighting the trend of these faults on the map, note how these are slightly more obvious in the amplitude extraction map than in (b) the seismic section, where the fault traces are still visible, but slightly harder to identify. Note that both the amplitude extraction maps and the seismic sections are at the same horizontal scale.

MTC 1 also has a frontal wedge-shaped zone containing small imbricate thrusts that detach into the basal decollement basinwards of the frontal ramp (Figures 6.2, 6.4 and 6.6). These small thrust faults are regularly spaced, arcuate fault traces which mimic the shape of the terminal edge of the MTC and are orientated parallel to the headwall (coloured red in Figure 6.2 and shown in more detail in Figure 6.6). They are closely spaced, with the amplitude extraction indicating a maximum spacing of 50 m between the faults, although the seismic cross-section indicates that the spacing could be closer than this in some areas (Figure 6.6). The imbricate thrust faults form exclusively in an area containing significantly thinned sediment in the frontal part of the MTC which has a maximum thickness of 50 m; bed offsets cannot be measured in this area because the individual packages are hard to resolve. These features have been imaged elsewhere in the literature where they have been referred to as pressure ridges by other authors (for example Prior et al., 1984, Masson et al., 1993, Posamentier and Kolla, 2003, Frey-Martínez et al., 2006, Moscardelli et al., 2006).

However, given the quality of the images seen in this study it is possible to resolve the individual thrust faults which make up this section of the MTC and hence infer that shortening is transmitted within a thinner layer of stratigraphy at the distal end of the slide and localised into a weak zone. When movement on the basal detachment at the seabed stops, then the translating sediments behind are internally deformed and shorten into coherent thrust faults driven by the force of the MTC sliding down-dip.

6.7 Comparison between MTCs 1, 2 and 3

Whilst all the local MTC events were deposited within a similar timeframe between 8.29 Ma and 5.04 Ma they are derived from different structures which bound the basin and, as such, have slightly different characteristics reflecting their source area and subsequent evolution (see Figure 6.1 for the locations of MTCs 1, 2 and 3). They all have a similar lithology being comprised primarily of hemipelagic mud deposited along the flanks of the main structures within the mini-basin. This discussion will focus on comparing the features seen, and previously discussed, in MTC 1 with those observed in MTC 2, which has been sub-divided into MTC 2a, 2b and 2c, sourced from Area B on the western margin of the mini-basin and MTC 3 on the eastern edge of the basin.

6.7.1 Bounding Surfaces

Basal Shear Surface

The basal shear surface is similar in all of the local MTCs studied; mostly concordant with the underlying stratigraphy cutting down at the headwall and up at the frontal ramp and lateral margins of the MTC (Figures 6.4, 6.7 and 6.10). Several small ramps are imaged on the basal surface towards the centre of the MTCs which range in size from 10 m in MTC 3 to 30 m in MTC 2c (Figures 6.7 and 6.10). Basal striations and imbrications running parallel to the flow direction are not observed on any of the amplitude extractions or dip maps through the MTCs. This could be because the slides did not travel far from their source or it could be a function of the type of material carried in the slide.

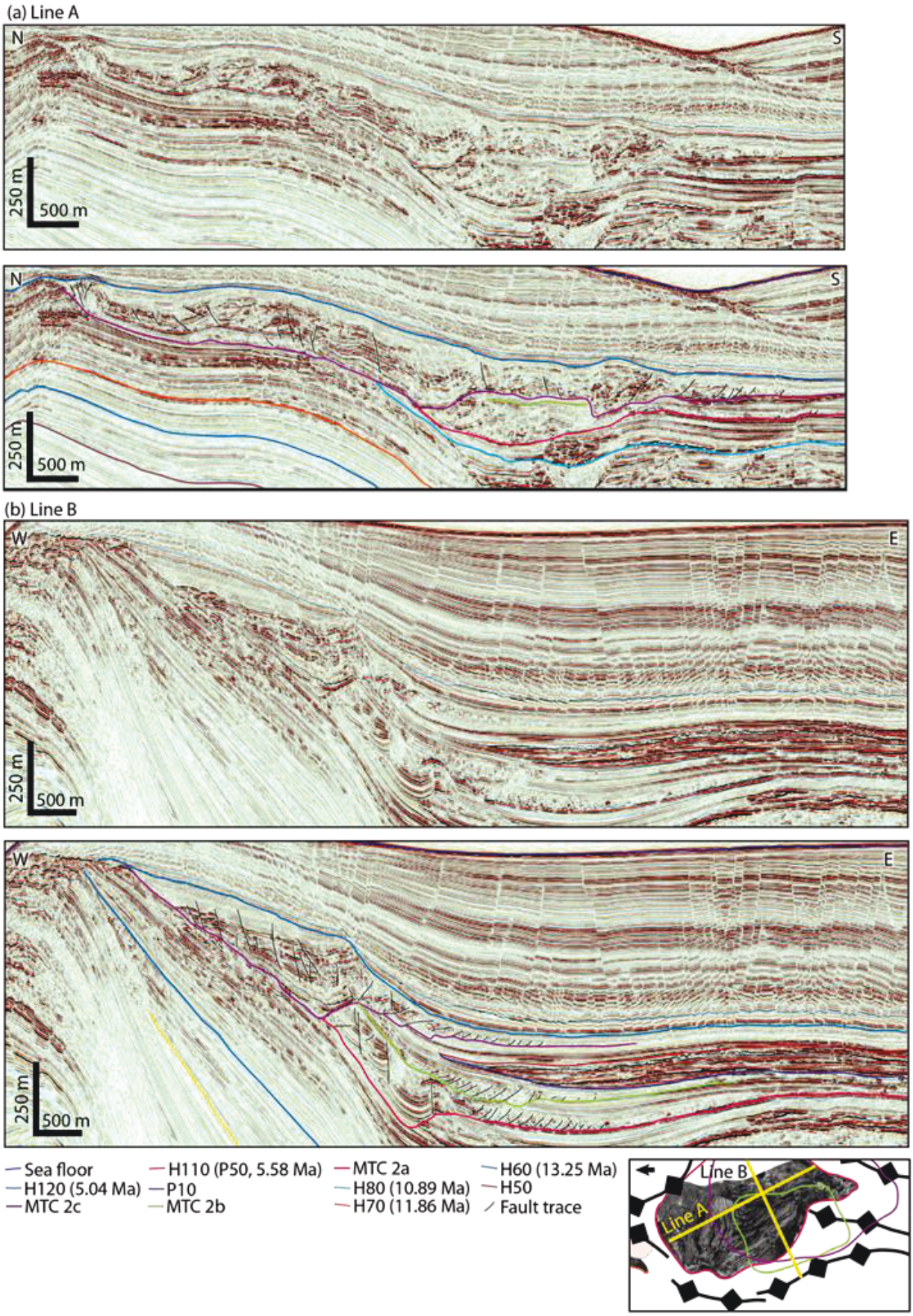


Figure 6.7 Two seismic section through the second cluster of MTCs, highlight MTC 2a, 2b and 2c. (a) Line A is orientated perpendicular to the flow direction to highlight the complex nature of the lateral margins of the deposits and their interactions with topography whilst (b) Line B is orientated along strike of the MTCs parallel to the flow of the slumps The section is taken through the older portion of MTC 2a, in order to also bisect MTC 2b.

Frontal ramps occur within all of the MTCs where one dominant ramp cuts up through the stratigraphy within the compressional domain. These range in height from up to 300 m in MTC 1, to 130 m in MTC 3, possibly reflecting the fact that there is less volume of sediment contained within MTC 3 (Figures 6.4 and 6.10). Interestingly MTC 2c had a medium size frontal ramp height with an average of 150 m relief, but has a series of smaller frontal ramps basinwards of this surface (Figure 6.7).

Top MTC Surface

The top surfaces of all the local MTCs have an undulating appearance which is reflective of the underlying internal deformation within the MTC. Later sediments clearly pond against the top surface of MTC 2a with well defined onlap patterns in the compressional toe area (Figure 6.7), this seen to a lesser extent within MTCs 1 and 3 (Figures 6.4 and 6.10). However, the depressions formed on the top surface of the MTC may have led to the formation of ponded sequences within these below the resolution of the seismic data, meaning that onlap patterns are not visible, even though ponding is occurring. The topography formed on the top of the MTCs is generated by the seafloor expression of the underlying extensional and thrust faults and therefore tends to form three-dimensional topography composed of slightly curved, thin, elongate depressions bound by ridges. The depressions within MTC 1 range in width from 50 m to 210 m and in length from 150 m to 400 m with the broader basins forming above the translational domain of the local MTCs. The basins are significantly shallower in the extensional and translational domains of MTC 2c as the faults do not extend as close to the top surface of the MTC, but the basins are broader and longer; in MTC 1 the ridges form depressions of up to 40 m in height whereas in MTC 2c these are only a maximum of 20 m but can extend to lengths of between 200 m to 400 m and have widths up to 300 m (Figures 6.7 and 6.8). In contrast to this the largest basins to form in the depressions on top of MTC 3 have developed within the contractional toe domain (Figure 6.10 (b)). The depressions have a similar shape to those observed on the upper surfaces of the other MTCs but are broader because they have formed between ridges across the top of a series of imbricate thrust faults. They are, on average, 700 m wide and up to 10 m high, estimating the connectivity and lengths of the individual depressions is not possible as the upper surface has not been mapped and that level of detail is not visible on the RMS amplitude extraction (Figures 6.9 and 6.10).

Lateral Margins

The majority of the locally derived MTCs within the study area are confined on at least on one margin by positive topographic relief (Figure 6.1). The relationship between the three MTCs which form the MTC 2 complex makes identifying, and accurately describing, the margins of these very difficult using seismic sections. The lateral margins of MTC 2c appear to be constrained by the confining topography to the north and south, infilling the topographic low and cutting up through the underlying stratigraphy in the south (Figure 6.7 (a)). This pattern of the lateral margin cutting up through stratigraphy is also seen in MTC 2a (Figure 6.7 (a)) and MTC 1 (Figure 6.4). The lateral margins of MTC 3 are significantly less pronounced than the other MTCs and do not cut up from the basal surface (Figure 6.10 (a)).

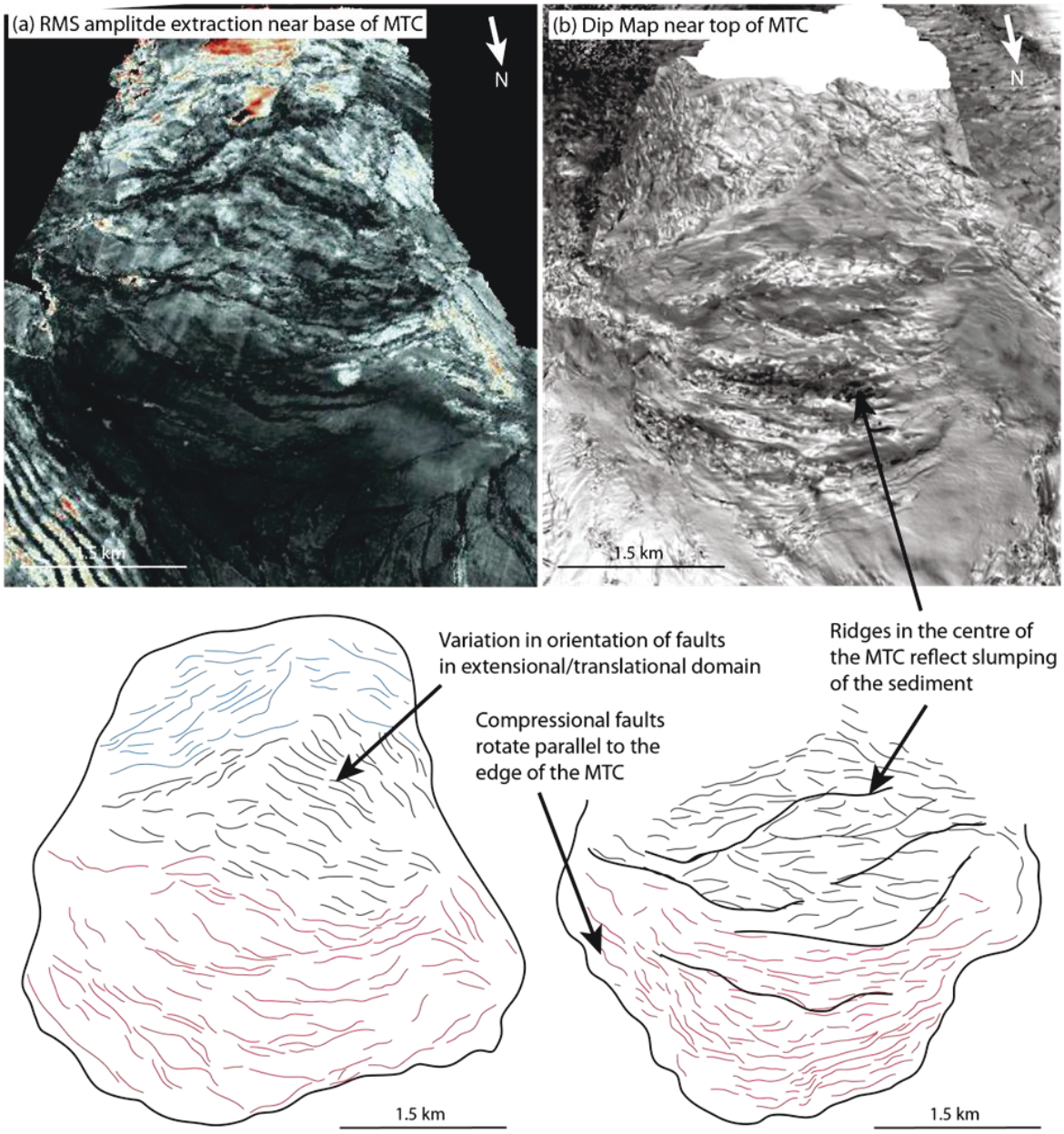


Figure 6.8 Top and base maps through the northern section of MTC 2a with (a) showing an amplitude extraction through a 20 ms window from the base of the MTC 2a with the main faults and structures observed within this window sketched below, and (b) a section though the top of a dip map which has been flattened on the base of MTC 2a highlighting the compressional thrust faults in the toe and clear ridges towards the centre of the MTC.

6.7.2 Internal Characteristics

Extensional Domain

The headwall has been imaged in MTC 1 and MTC 2c, where strike sections through the MTC indicate an erosive down-cutting surface which has been interpreted as the headwall scarp (see Figure 6.7 for a clear image of this). The maximum height of the headwall scarp seen in MTC 2c is 175 m and, as such, is smaller in part than the headwall scarp observed in MTC 1 (100 m to 300 m). The headwall scarp in MTC 3 does not appear to have been preserved or may be filled with material which has not evacuated the area. If the latter is the case then it contains predominantly small extensional blocks making estimating the height and dip of the slide scars difficult to estimate (Figure 6.10).

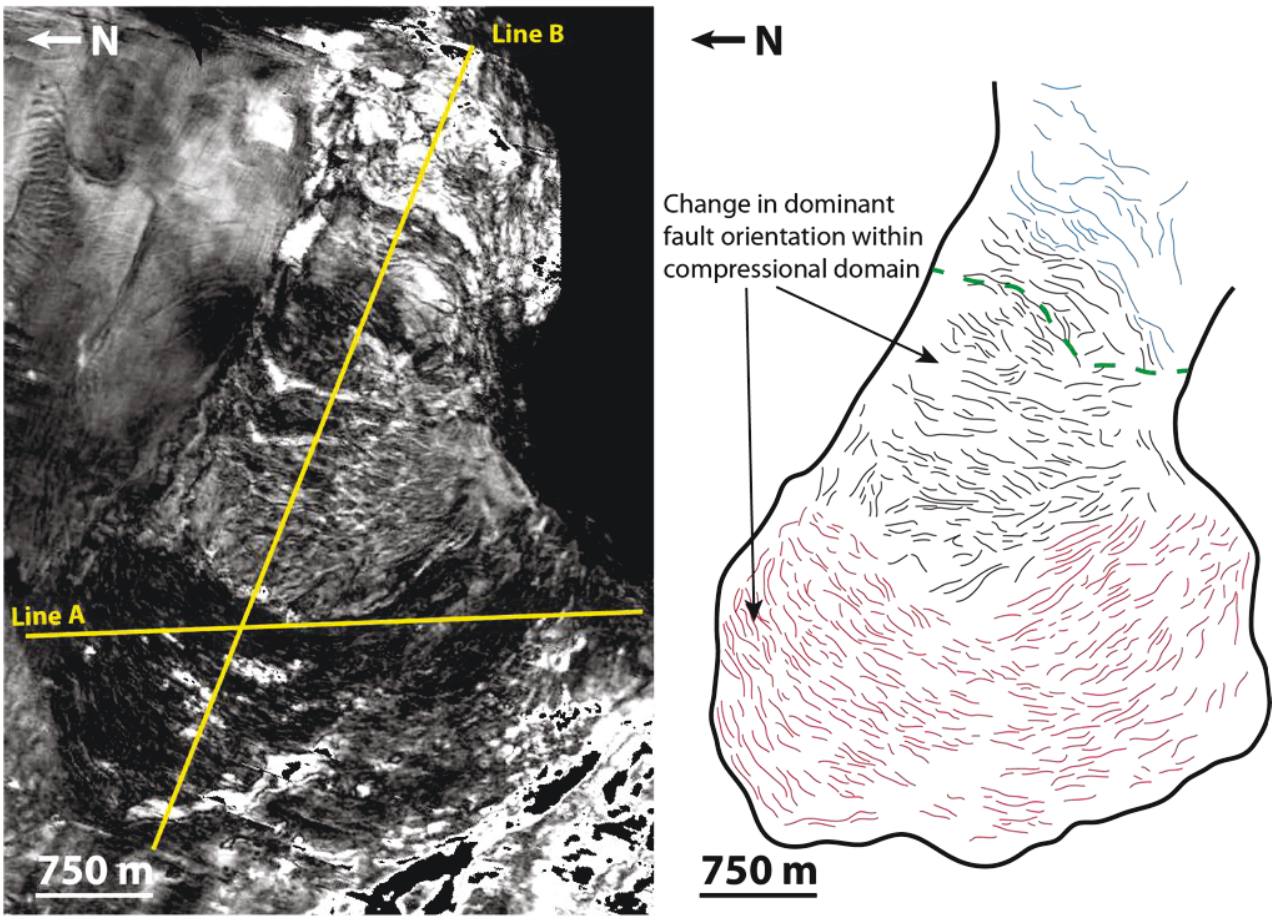


Figure 6.9 An RMS amplitude extraction map and corresponding sketch highlighting the main features within MTC 3 which is sourced from the eastern margin of the basin (see Figure 6.1 for the location of this deposit). Note how the faults become more closely spaced towards the toe end of the deposit and rotate to become orientated parallel to this margin. The yellow line indicates the position of the seismic sections shown in Figure 6.10. Red faults are clearly compressional, blue fault traces are clearly extensional and the green line indicates the position of the start on the frontal ramp on the basal shear surface.

The extensional domain in all of the MTC deposits is dominated by extensional structures such as normal faults which separate discrete blocks of un-deformed material. These discrete blocks have very similar volumes in all three of the main, un-eroded local MTCs, ranging from 7 x10^6 m^3 in the extensional domain of MTC 3 to 8 x10^6 m^3 in the extensional domains of both MTC 2c and 1 compared to a range of between 1 x10^5 m^3 (MTC 3) and 1 x10^6 m^3 (MTC 2c) in the compressional domain. The undeformed blocks in the compressional domain are longer in length perpendicular to the flow direction (for example 600 m in length as opposed to 180 m in MTC 1) but significantly smaller in height, being on average 27 m as opposed to 155 m. The extensional domain is best imaged in seismic sections taken perpendicular to the main direction of movement through MTCs 1, 2c and 3 (Figures 6.4 (a), 6.7 (b) and 6.10 (b)). MTC 2c has a small extensional domain which contains few faults that extend thought to the basal surface whereas MTCs 1 and 3 contain slightly closer spaced normal faults (compare Figure 6.4 (a) to Figure 6.10 (b)).

MTC 2a is comprised of two discrete episodes of MTC development, an earlier one in the south and a later system in the north. A significant proportion of the extensional domain of MTC 2a in the north has been eroded away by the subsequent development of MTC 2c (Figure 6.7 (b)). However, the southern half of MTC 2a contains a clearly defined extensional domain with an amplitude extraction map and dip map over the area highlighting a series of small discrete faults and fractures (Figure 6.8). Within the extensional

domain, there are two patterns of extensional fault orientation with those in the southeast corner trending from east to west and those in the southwest corner trending southeast to northwest and a convergence of these trends towards the middle of the MTC (Figure 6.8). This pattern could have resulted from the fact that the extensional domain of the MTC is sourced from an area where two salt-cored anticlines converge with the two distinct fault trends reflecting the orientation of these two distinct extensional fault packages (Figure 6.1, MTC 2a). The extensional faults observed within MTC 2a have a very similar length and spacing to those observed in MTC 1, both having an average length of approximately 500 m and a spacing of less than 250 m on average (Figure 6.11).

Translational Domain

None of the local MTC deposits examined contain a clearly defined translational domain. Strike sections taken through these show that the extensional faults occur down the length of the MTC until the start of compression (Figures 6.4, 6.7 and 6.10). The seismic section through MTC 3 shows that there are less faults present towards the middle of the MTC where the translational domain would be located (Figure 6.10 (b)). However, amplitude extraction maps and sketch maps of the faults indicate that these are clearly present down the length of the deposit, but may be below the resolution of the seismic section (Figure 6.10). There is a slight change in the main orientation of the faults towards the centre of MTC 3 with the faults going from having a broadly linear trace to being more curved in orientation, reflecting the shape of the front of the MTC, as they become dominated by compressional features (Figure 6.9). Faults which are located between the clearly defined extensional and compressional domains within MTCs 2a, 2c and 3 do not extend down to the basal surface (Figures 6.7 and 6.10), whereas they do in MTC 1 (Figure 6.4). This could reflect the more complex nature of the faults and their orientation overall within MTC 1 and the development of lateral tears (Figure 6.2).

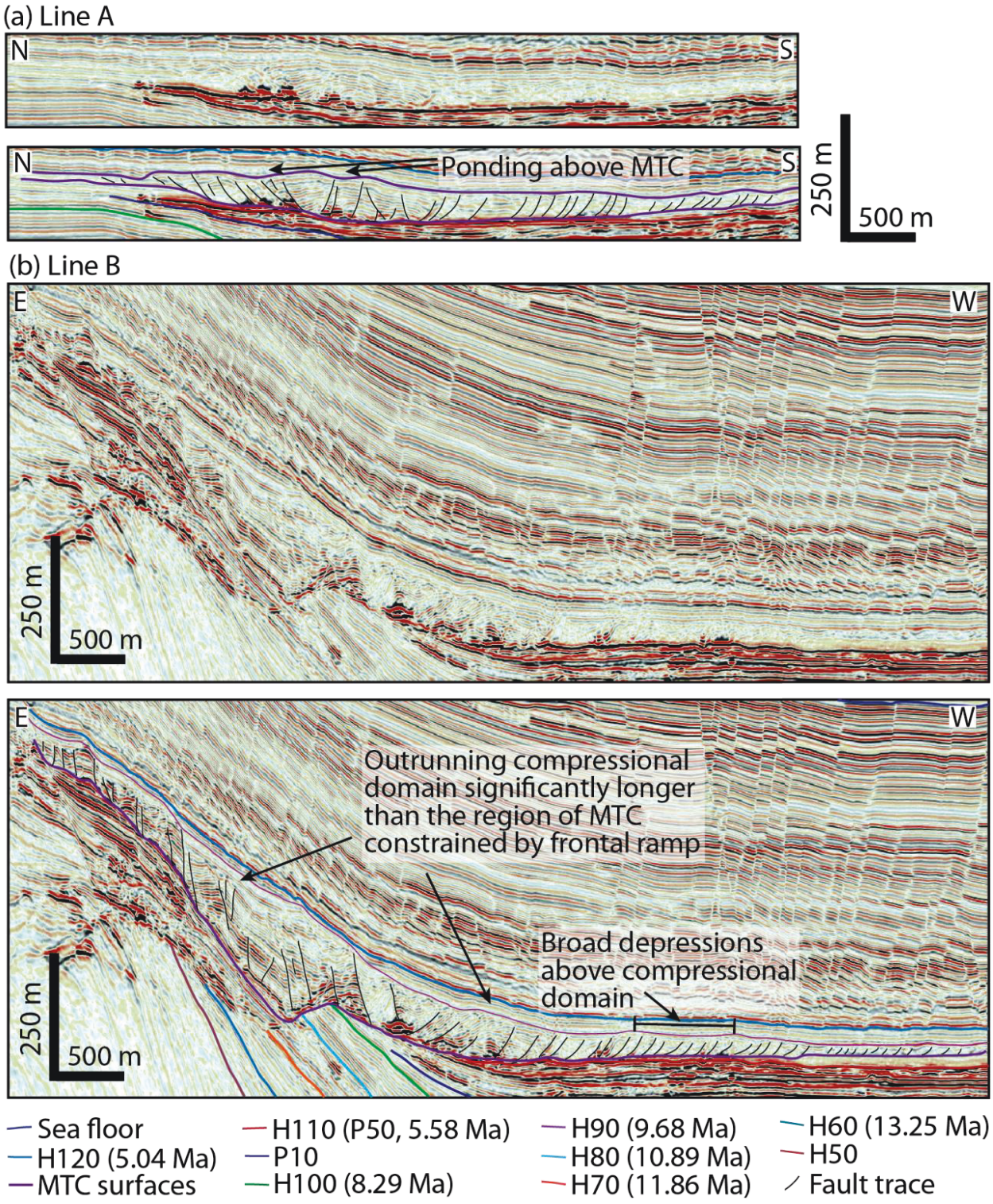


Figure 6.10 Cross-sections through MTC 3 (a) Line A is orientated perpendicular to the flow direction of the MTC within the compressional domain and (b) Line B, a strike section parallel to the flow direction within MTC 3, with a relatively small extensional domain and a long compressional domain overlying the H110 ponded section in the west. Location of the sections are shown in Figure 6.9.

Compressional Domain

The local MTCs are all frontally emergent with material moving up from the original basal surface in the main part of the MTC and onto the sea floor (Figures 6.4, 6.7 and 6.10). All the MTCs recorded here, including the smallest one MTC 2b, have two distinct zones within the compressional domain; a fold and

thrust domain where the material has buttressed against the ramp in the basal shear surface and a much thinner region of run-out containing small imbricate thrusts.

The fold and thrust domain has been fully described in MTC 1 and contains a series of thrust faults and at least one internal detachment surface (Figure 6.5). Cross-sections parallel to the direction of movement of the MTC 2 complex also indicates the presence of thrusts and fold within MTCs 2a, 2b and 2c all buttressed against the frontal ramp. These all contain extensively folded sediment over the ridge of the main ramp which has in turn generated small-scale pop-up structures within the area. The pop-up structures are offset to a maximum of approximately 35 m and do not appear to generate as much positive relief on the top of the MTCs 2a and 2c as that seen in MTC 1 (compare Figures 6.4 and 6.7). MTC 3 also contains a clear thrust and fold dominated zone within the compressional domain, but there is less of a focus of thrust faults around the frontal ramp and this series of fold and thrust systems extends basinwards, away from the frontal ramp surface (Figure 6.10). This may be because the fontal ramp is smaller in size in this MTC and hence did not form as much of a buttress to the down slope movement of the MTC.

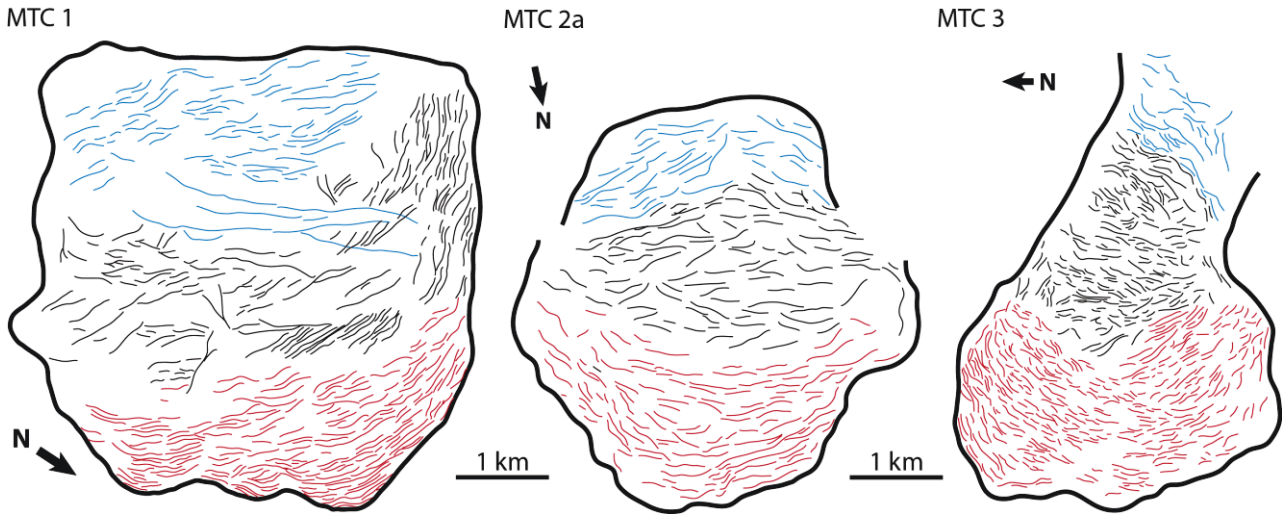


Figure 6.11 Comparison between three different local MTCs within the area, all shown at the same scale. MTC 2a is an amalgamation of the features seen in the extensional domain and recorded in the amplitude extraction map and the features in the compressional domain recorded in the dip map in Figure 6.7. The fault traces coloured blue are clearly extensional and those coloured red are clearly compressional thrust faults.

All the local MTCs contain a frontal wedge-shaped zone with small imbricate thrusts that detach into the basal decollement (Figures 6.4, 6.5, 6.7 and 6.10). These appear to be formed from coherent basin sediments which have been subsequently deformed by the down-dip movement of the MTC deposit. These frontal wedges all have very similar characteristics: they are composed of a series of closely spaced, high frequency, slightly concave, duplex-style thrust faults, with very little offset observed and the faults detaching onto the basal shear surface. The area containing these thrusts has a maximum thickness of approximately 85 m, recorded in MTC 2a, and with thickness decreasing towards the terminal end of the system. MTC 2a also has the longest zone of closely space imbricate thrusts extending up to at least 4.5 km into the basin beyond the frontal ramp (Figure 6.7). MTC 3 is slightly different in that larger thrust faults grade into the thinner outbound wedge; whereas in MTCs 1 and 2a, the change in scale of thrusting coincides with the position of the prominent frontal ramp (Figures 6.4, 6.6 and 6.7). The thrust faults generate positive relief on the top

surface of the MTC, forming ridges of up to 15 m in height in MTC 1. They have been well imaged in all the amplitude extraction maps, where sketches indicate they are well organised, on average 500 m in length and orientated parallel to the front of the MTC (see those faults coloured red in Figure 6.11). MTCs 1 and 3 have a slightly closer spacing of these faults which corresponds to a slightly smaller fault trace length, whereas MTC 2a contains slightly less closely spaced faults but the fault traces are overall more organised (Figure 6.11). MTC 3 contains the largest areas of imbricate thrust faults but is one of the smallest MTCs studied here. The thrust faults in all three of the MTCs appear to rotate and reorganise to become orientated almost parallel to the front edge of the MTC, curving towards the lateral margins (Figure 6.11). This would support the idea that these thrust faults propagate back from the front of the MTC at the end of the basal shear surface with imbricate thrusts forming as the down-slope movement of the slide material continues to apply compressional force to the area.

6.7.3 Volume and Area

The local MTCs studied here all cover a similar area along the edge of the basin ranging from 15.9 km^2 (MTC 1) to 28.9 km^2 (MTC 2a) with run-out distances of up to 6.3 km (Figure 6.1 and Table 6.1). Maps of the upper and lower surfaces of MTC 1 allow calculation of a thickness map and estimation of an approximate volume of 1.9 km^3 for the deposit (Figure 6.3). The internal structures within the MTC indicate that this volume largely consists of translated material that has moved down-slope and internally deformed, but that has not moved very far from its original depositional location. Broadly speaking, there is a net accumulation zone where the translated sediments have been buttressed behind the frontal ramp forming thicknesses of up to 215 m (Figures 6.2 and 6.4) and an updip zone where they have been thinned.

Name	Area (km^2)	Maximum run-out length (km)
MTC 1	15.9	5.5
MTC 2a	28.9*	4.7
MTC 2b	7.2*	2.3
MTC 2c	20.7	6.3
MTC 3	11.5	5.4

Table 6.1 Table outlining the area covered by the local MTCs discussed in this section. * indicates that MTC deposit has been partially eroded by later MTC and hence area represents an underestimate.

These local MTCs are predominantly small submarine slides, where the material on the edge of the anticlines has slid and internally deformed in a relatively coherent manner down the flanks of the anticlinal folds. This relatively small amount of translation of the sediment means that they have small volumes and no associated debris flow or disaggregated slide facies. They form as the seabed along the flanks of emergent folds becomes unstable with continued growth triggering failure on the slope. It is well documented in the

literature that slides of a similar scale and containing similar internal features can form on very low slopes, for example those observed in the Gulf of Mexico are commonly only 20 km^2 to 30 km^2 in area (Beaubouef et al., 2003, Owen et al., 2007).

6.8 Regional Mass Transport Systems

These regional mass transport systems are common within the mini-basin between the H20 and H70 horizons, a 5.38 Ma interval deposited between approximately 17.29 Ma and 11.86 Ma (Figure 6.12). Within this interval, at least eight separate regional MTC events can be mapped across the basin ranging in thickness from 20 m to over 300 m in the centre and southern half of the basin (Figures 6.13 and 6.14). These systems appear to respond to some of the structural topography present at the time thinning onto areas which would have formed topographic highs and thickening towards the centre of the mini-basin (Figure 6.12). These regional MTCs can be recognised on seismic sections from their distinctive chaotic seismic facies which tends to extend throughout the seismic sections, concordant with the underlying stratigraphy (Figures 6.12 and 6.18).

This section of the chapter will look in detail at the regional MTC deposits exploring:

- how common these are within the basin fill;
- the thickness and extent of these deposits and whether it varies through time;
- the main, identifiable internal characteristics of regional MTC deposits and what this implies about the nature of the deposit;
- their source area and derivation.

Three of the regional scale MTCs identified within Figure 6.12 will be analysed in detail within the mini-basin, with the discussion in Section 6.9 focussing on how these deposits relate to the structural evolution of basin and contrast with the local submarine slides. The interaction between regional MTC deposits and the main structures within the basin will be explored in further detail in Chapter 8 using maps showing the spatial distribution of the structures with the highest bed length change during the interval when the regional MTCs were deposited.

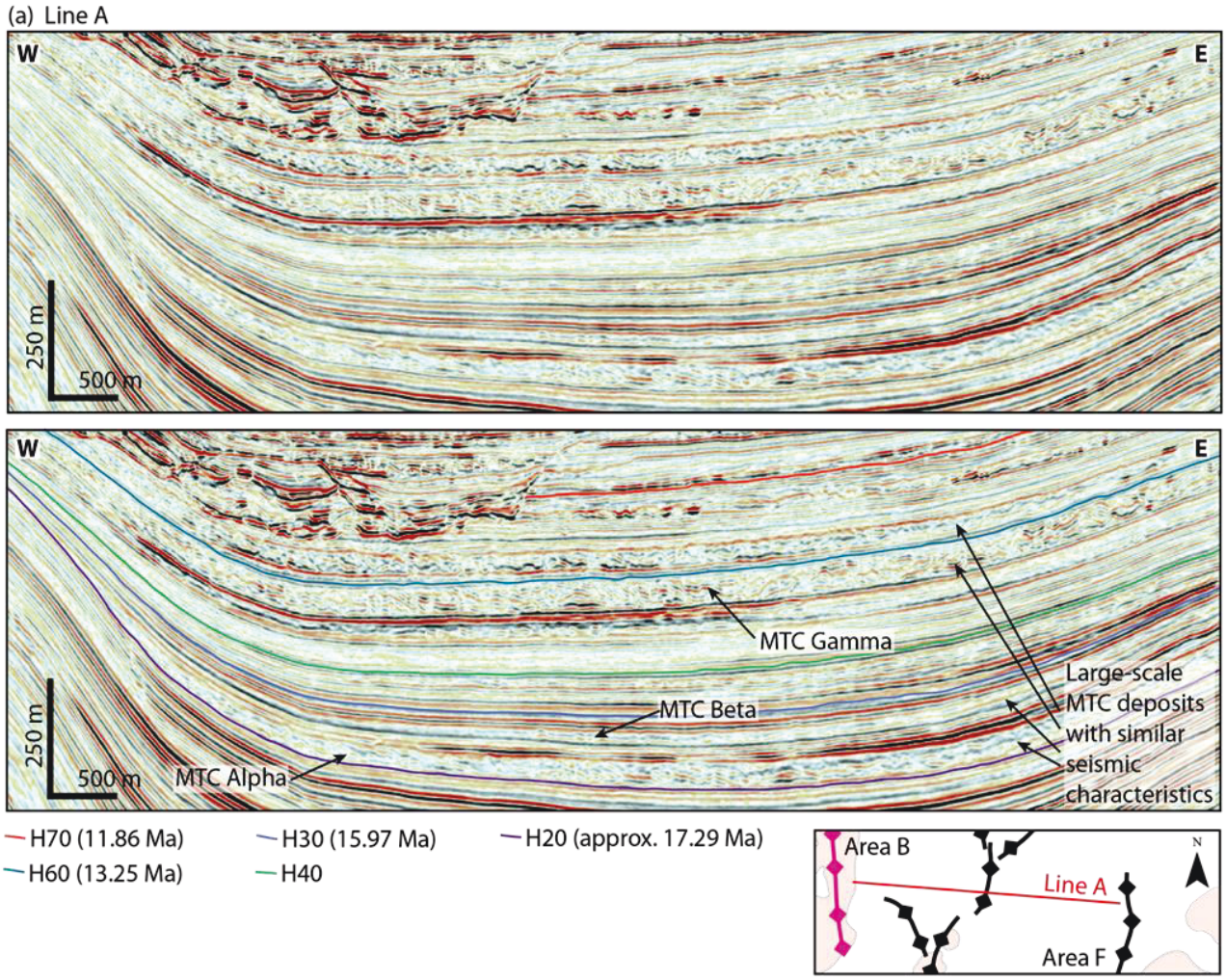


Figure 6.12 A seismic cross-section through the centre of the basin highlighting the regional MTCs and showing the change in thickness and the distribution of the regionally derived MTCs. The three main MTCs (α, β and γ) which are discussed in detail in the text are also highlighted; amplitude extractions from within these deposits are shown in Figure 6.13.

6.8.1 Age and Frequency

These regional MTC deposits are a common component of the mini-basin fill between approximately 17.29 Ma and 11.86 Ma (a 5.38 Ma interval between the H20 and H70 horizons). At least eight can be identified within the seismic sections during this period (Figure 6.12), covering slightly different areas within the basin (Figure 6.13). Thinner regional MTCs appear to be more frequent within the basin with the proportion of thicker MTCs increasing as the sediments become younger (Figure 6.12). The larger MTCs often occur in pairs separated by intervals containing almost parallel thin sediment drapes (for example MTCs α and β, Figure 6.12). This implies that the events triggering the formation of these MTC deposits could have occurred over a sustained period generating more than one event at a time.

6.8.2 Thickness and Extent

The regional MTC deposits range in thickness from 100 m to over 300 m with the thickest deposits consistently found in the south of the mini-basin and towards the centre. They constitute up to 40 % of the

basin fill within the interval between the H20 and H70 horizons (approximately 17.29 Ma to 11.86 Ma) and, as such, are the dominant sedimentary facies within the basin at this time.

The three regional MTC deposits analysed in detail do not cover the same area within the basin (Figure 6.13). However, they are all broadly constrained by the main structures in the area, in particular those in Areas C and D. The youngest and oldest MTC deposits (MTC α and γ) extend further to the west of the mini-basin with sediment deposited within the area between Areas A, B and C whereas MTC β does not extend west of the tip of the structures within Area C (Figure 6.13). The two older MTC deposits (MTC β and γ) extend south of the normal fault whereas the youngest deposit (MTC α) terminates to the north of this structure. All three of the MTCs appear to respond the structure within Area F, even though this has low growth rates during this period, with MTC γ deposited the furthest from this structure (Figure 6.13). Area C also appears to control the deposition of MTC deposits throughout this period with MTC α terminating furthest from the hinge of the anticline on the eastern margin of the structure.

An isopach map of MTC β illustrates that the thickness of the deposit is controlled by the basin bounding structures (Figure 6.14). The anticlines that form Areas C, D and E along the western edge of the mini-basin in particular appear to have influenced the thickness of the deposit (Figure 6.14). This implies that these structures had positive seafloor topography at the time at which this MTC was deposited. MTC β is thickest in the south and south-eastern edge of the basin where thicknesses of up to 300 m are recorded, and thins to the north with an average thickness of approximately 100 m north of the normal fault. The full extent of the thinning is masked in some areas by the subsequent development of the salt structures and canopy salt, particularly in Area F where cross-sections through the salt indicate that the canopy had not formed by this period. The limits of the high resolution PSVM seismic dataset prevent the southern and eastern extents from being mapped.

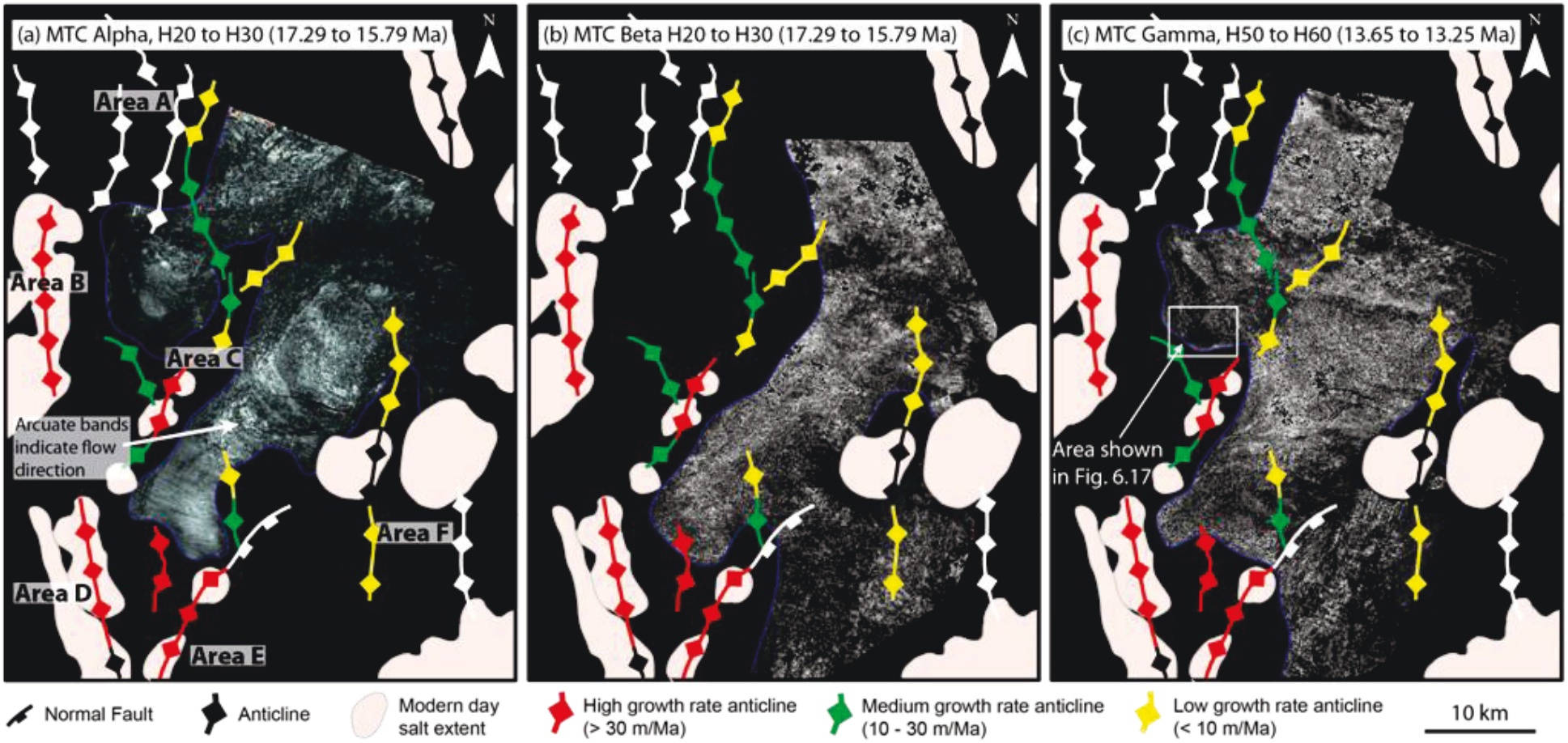


Figure 6.13 RMS amplitude extraction maps taken through approximately 10 ms windows towards the centre of three of the large scale MTC deposits identified in Figure 6.14. (a) shows MTC α, the oldest regional MTC investigated, located above the H20 horizon, note how clear ridges can be seen in the amplitudes here, indicating the flow direction of the deposit, (b) shows a 10 ms widow thought the centre of MTC β which does not extend as far throughout the basin, note how this MTC has a more chaotic, speckled appearance and (c) the youngest MTC, MTC γ which covers the most

6.8.3 Internal Characteristics

Analysis of the internal characteristics of the regional MTC deposits reveals several persistent trends; they predominantly contain largely chaotic material with very little internal organisation, but where they encounter topography a series of small scale imbricate thrust faults tend to form. It is possible to observe large-scale arcuate flow patterns and translated blocks within some of the MTC deposits, but the striations and megascours described in similar-scale MTCs elsewhere are not observed.

Cross-sections through the regional MTCs indicate that the basal surface is mostly conformable with the underlying sediment (Figures 6.12 and 6.18). A seismic section through MTCs β and γ indicate the presence of small ramps within the basal surface which cut up through the underlying stratigraphy. These occur throughout the MTC with ramps of up to 15 m observed in the base of MTC β (Figure 6.18). In areas where down-cutting ramps are present the sediment packages beneath the MTC also appear to become thinner, suggesting that either some of the sediments within these were eroded and amalgamated into the MTC or that the rapid deposition of the regional MTC material onto the underlying sediments caused compaction. The ramps within the basal surface of MTC γ appear to be mainly confined to areas where the imbricate thrust faults are observed with a ramp of up to 25 m observed along the edge of the margin (Figure 6.17). This is very similar to the frontal ramp observed in the local MTC deposits with the ramp forming a buttress and leading to the development of these thrust faults.

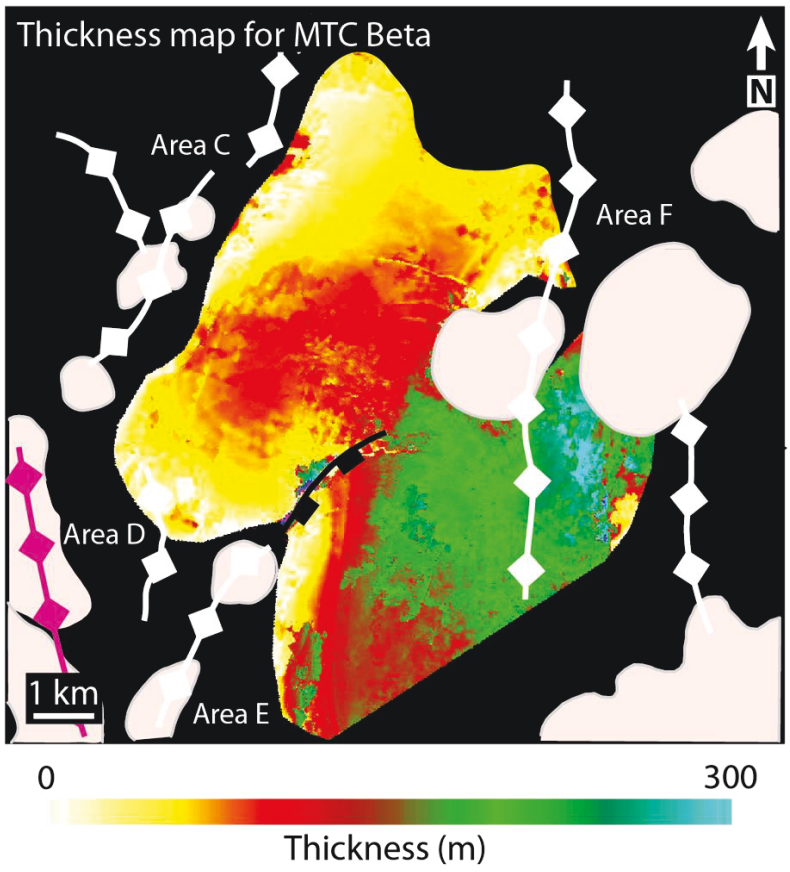


Figure 6.14 Isopach map showing the thickness of MTC β and highlighting the interactions with the basin bounding and internal structures. Note that this does not extend as far north as the amplitude extraction shown in Figure 6.15 due to thinning of the MTC package in this area.

The upper surface of the regional MTC deposits are often concordant with the overlying horizons, but can become uneven where the MTC deposit thickens with some sediment ponding on top of this (Figure 6.18). This upper surface appears to respond more to the slight changes in topography within the basin, with a more uneven, rugose top to the MTC deposit observed within the centre of the basin and a flatter, more concordant top seen at the edges of the basin where the MTC thins towards the structures (Figures 6.12 and 6.18). This could correspond to a decreasing amount of energy within the MTC deposit in areas where it encounters relative topographic highs.

Amplitude extraction maps generated through small intervals (windows of 10 ms) within the regional MTC deposits show a dominant speckled, blotchy seismic facies (Figure 6.13). This implies that the sediment being transported is chaotic in nature and contains a mixture of small, discrete blocks and sediment (Figures 6.15 and 6.16). There is, however, some suggestion of the presence two ridges running from the northeast to the southwest within the semblance maps which may have been generated by the movement of the sediments in this area (Figure 6.15). However, this semblance map confirms the observations from the RMS amplitude extraction maps with the chaotic, disjointed nature of the semblance data implying that the sediment was carried as a mass flow and deposited as a jumbled mix of blocky coherent sediments and a finer grained matrix.

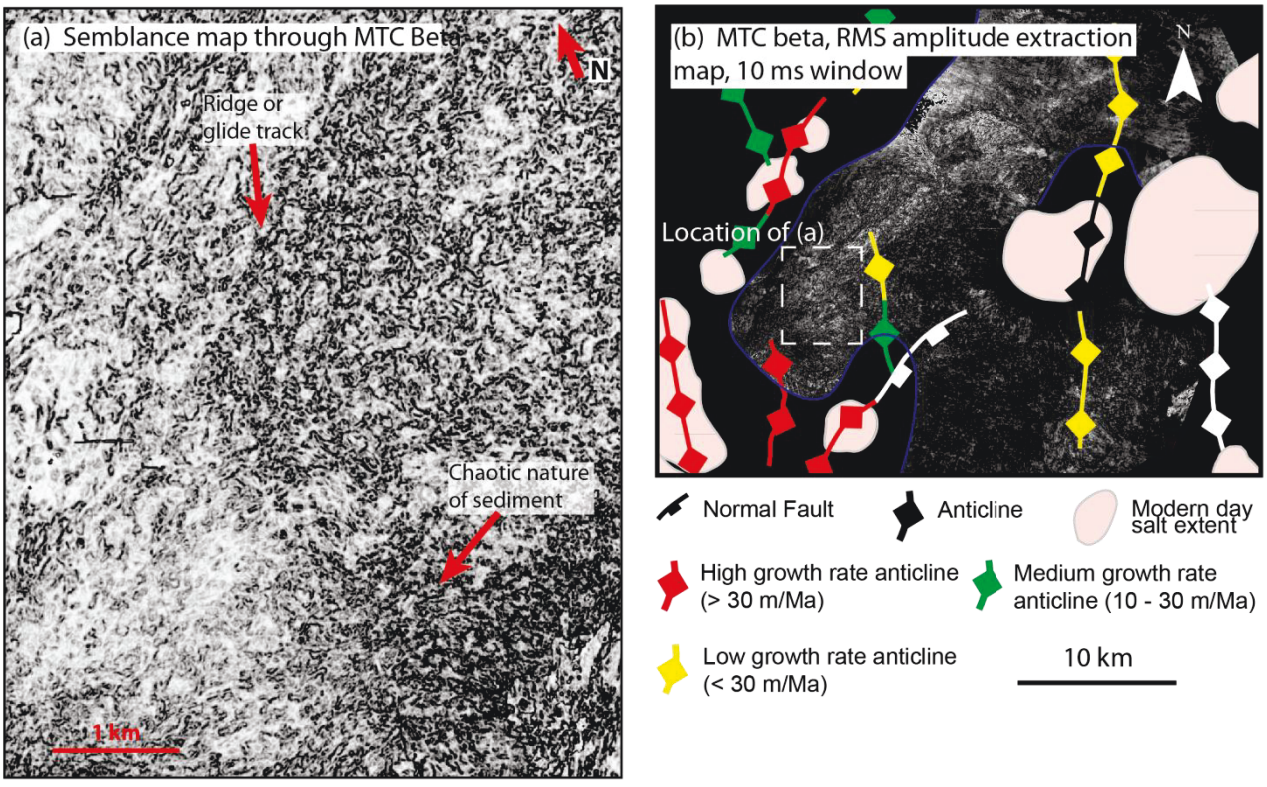


Figure 6.15 (a) A semblance map and (b) an RMS amplitude extraction map through MTC β highlighting the chaotic nature of the sediments carried within the MTC deposit.

There is some indication of small, discrete blocks being carried within the chaotic sediment, with high amplitude blocks imaged within a muddy surrounding matrix within MTC β. These are particularly clear in the north-eastern corner of the RMS amplitude extraction map seen in Figure 6.16. They tend to be rectangular in appearance and range in size from a maximum length of 50 m to 250 m generating areas of up

to 17,000 m^2, and are randomly distributed throughout the basin. There is a wide band which contains a higher concentration of these high amplitude patches which appears to be aligned the northeast to the southwest within this area of MTC β (Figure 6.16). This band is orientated parallel to the orientation of the strictures within Area C (Figure 6.13) and could represent a zone of more concentrated flow containing less disaggregated material.

Texture is observed within some areas of the debris flows, particularly where the flow encounters topography towards the edge of the basin. In these areas arcuate ridge geometries can be observed in the amplitude extraction maps which corresponds to the development of imbricate thrust structures within the MTC deposits (Figures 6.16, 6.17 and 6.18). These have been observed towards the edge of the basin in MTCs β and γ which could suggest that the sediments are responding to topographic relief on the seabed or are forming where the flow thins (Figures 6.17 and 6.18). The duplex-style thrust faults observed in the seismic sections though MTC γ have a spacing of approximately 60 m and extend throughout the thickness of the MTC (Figure 6.17). Those observed in MTC β are less defined and less extensive within the deposit, but they also extend throughout the thickness of the MTC and have a slightly closer spacing with an average of 45 m (Figure 6.18). These features imply that the debris flows were travelling along a basal surface and which stopped abruptly causing a series of thrust faults to propagate back through the system.

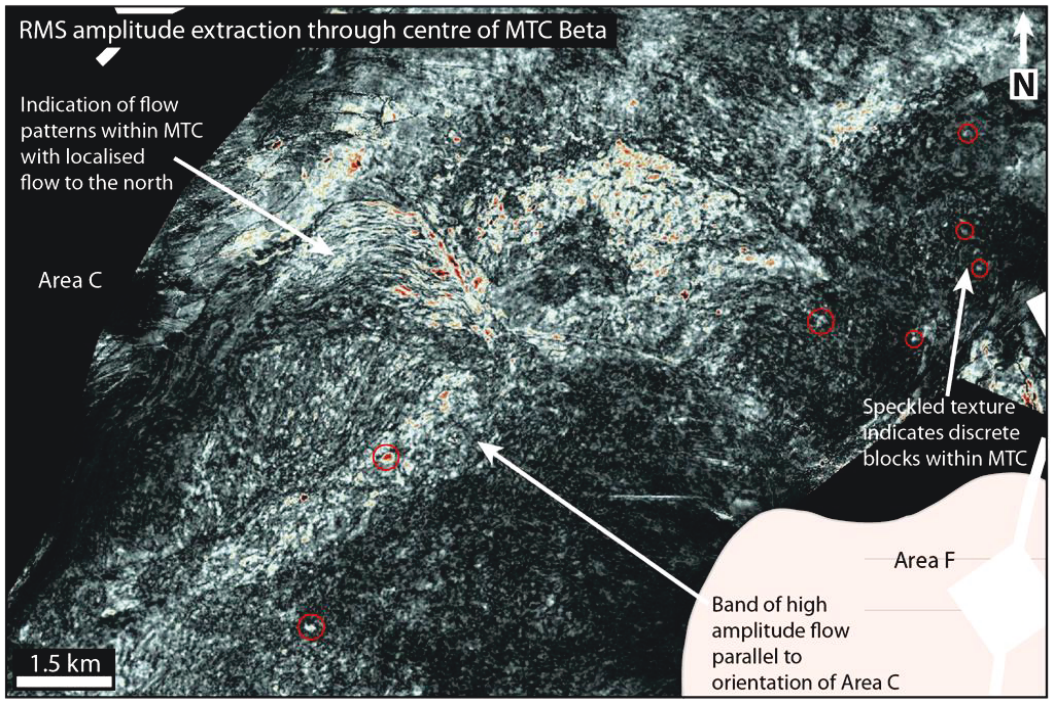


Figure 6.16 An RMS amplitude extraction map through a 20 ms window within the centre of MTC β with high amplitudes shown in white, medium amplitudes shown in red and low amplitudes black. These shown smaller blocks of high amplitude within the internal matrix, a few of which are highlighted by red circles.

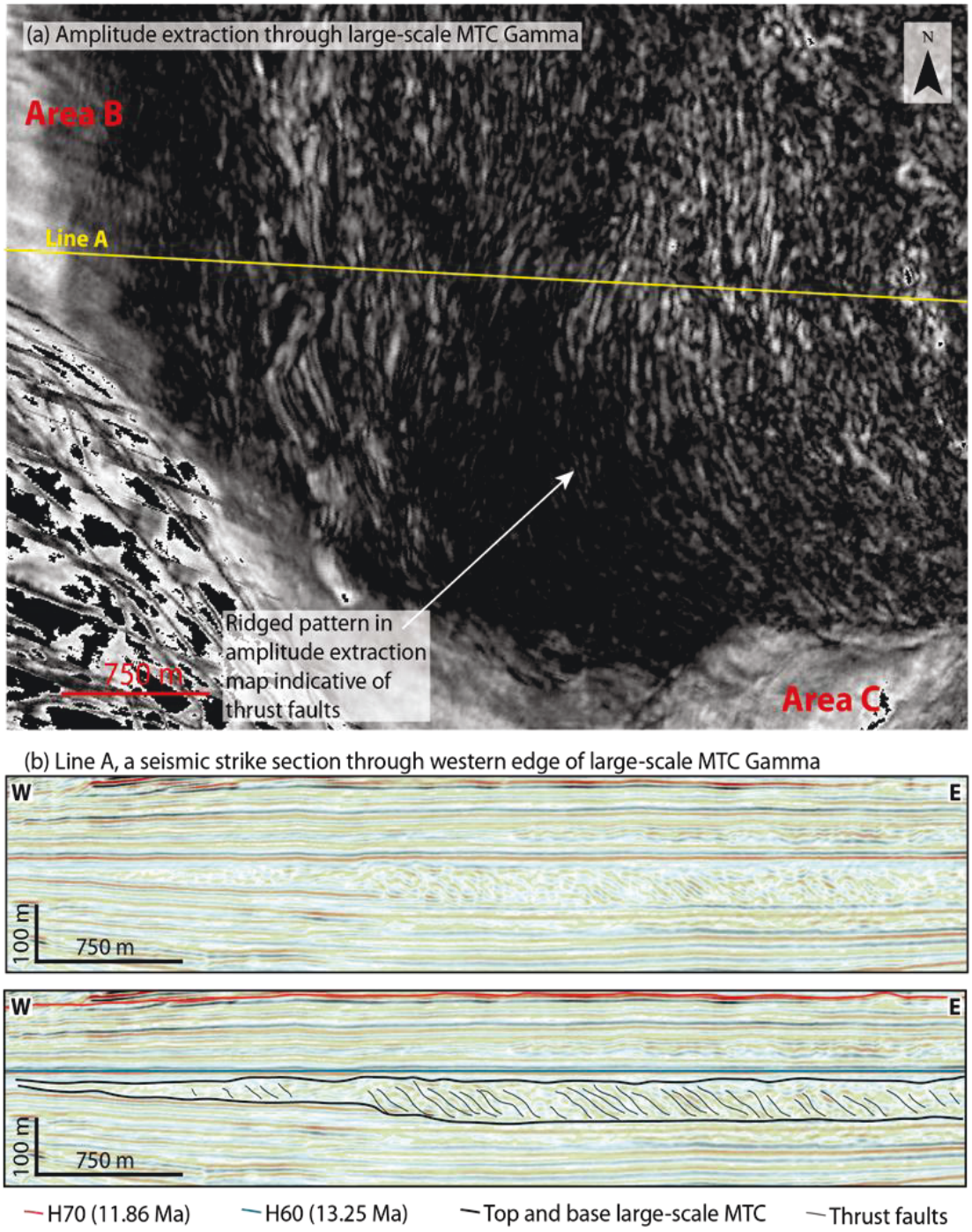


Figure 6.17 (a) An RMS amplitude extraction map highlighting the thrust fault traces within MTC γ and the location of (b) a seismic section through MTC γ flattened on the H70 surface in order to highlight the thrust faults within the regional MTC deposit in this section of the basin. The location of the amplitude extraction map is shown in Figure 6.13.

A change in seismic character can also be observed in the areas where the MTC deposits flow over structures within the basin, with a change in the overall amplitude and nature of the deposit observed (Figure 6.13). This is particularly apparent with a dimming of amplitude observed over the anticline which links the structures within Areas A and C in amplitude extraction maps for MTC α and γ (Figure 6.13 (a) and (c)). This could occur in response to a thinning in the sediment deposited within this area which could have generated a more organised flow pattern, such as that previously observed to occur along the flanks of the basin-bounding structures.

It is possible to identify some large-scale flow patterns within the amplitude extraction maps which indicate the flow direction within the basin. These are particularly clear on the amplitude extraction through MTC α where slightly arcuate bands can be seen in the area between the structures within Area C and those in Area E (Figure 6.13). This would imply that the debris flow was travelling from the northeast comer of the basin to the southwest and would fit with the assumption that it terminates down-dip against the structures within Area B and D. These broad high amplitude bands can also be seen in MTC γ and indicate that, although the overall debris flow was chaotic there was some degree of organisation in how the sediments flowed.

Overall, these regional MTCs are predominantly composed of chaotic material with some areas of organisation (for example the thrust faults observed towards the edge of MTC γ and the bands of larger high amplitude blocks observed in MTC β). It has been argued that the arcuate structures observed in MTC γ relate to changes in the topography at the edge of the basin, but it is difficult to understand the significance of the higher-amplitude bands at this seismic resolution suggesting that there is little systematic variation in the deposit. Given the scale of these deposits it is unusual that striation and megascours have not been observed in the amplitude extraction maps. However, this could be a function of the mapping method used in this study or could relate to the large distance these sediments have been transported from the source area.

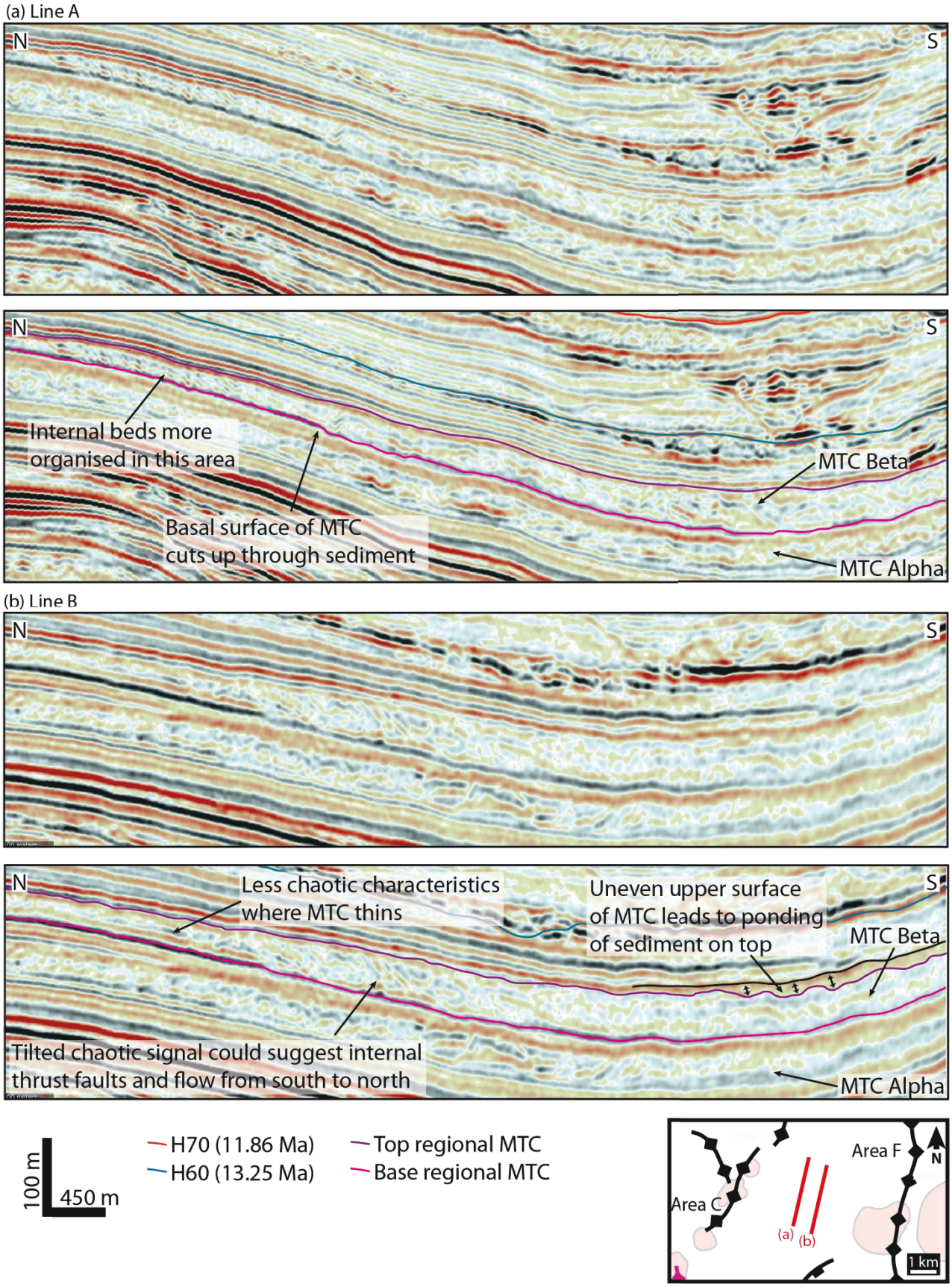


Figure 6.18 Two seismic sections through MTCs α and β which highlight the topography on the upper and basal surfaces of the regional MTCs and some of the key internal characteristics associated with them.

6.8.4 Source Area and Derivation

Due to the limited resolution of the regional seismic data it is not possible to trace the regional mass transport packages back to their source. However, micropalaeontological analysis from cuttings through MTC β in Well E suggests that it contains allochthonous shallow-water forams alongside the mid-lower bathyal agglutinating forams which would have been deposited in situ (S. Payne 2011, pers. comm.). These calcareous forams include species which would have lived in an outer-shelf to upper-bathyl setting and hence imply that the sediment contained within these MTC deposits originated in an outer shelf environment. The other regional MTC deposits are also known to contain forams which have been sourced from the outer shelf (S. Payne 2011, pers. comm.). The outer-shelf is located at least 100 km to the east of this area which would suggest that the deposits seen in the mini-basin have travelled at least this far from their source.

The biostratigraphic evidence when taken alongside the amplitude extraction maps implies that the regional MTC deposits observed within the mini-basin are simply one portion of a significantly larger MTC. It is well known that sediments remobilised by submarine landslide events are able to travel exceedingly long distances from their source area (for example >800 km; Bugge et al., 1988, Masson et al., 1993, Gee et al., 1999). Therefore it is likely that the sediment described in the previous sections forms part of the runout deposits of a system which initiated on the outer shelf, at least 100 km to the east of this area. Mohrig et al. (1998) suggest that hydroplaning of the sediment, whereby the leading edge of the debris flow rises to ingest a thin water layer beneath the moving mass and the substrate, might allow this type of enhanced runout length. This is in contrast to other authors who suggest that significant basal erosion occurs generating an increase in the volume of material being transported. They argue that this contributes towards the development of a low friction basal shear layer which would also allow a long runout distance to develop (Gee et al., 1999, Gee et al., 2001, Posamentier and Kolla, 2003, Gee et al., 2006).

Regional MTC deposits have been documented elsewhere along the Angolan Margin within Block 17, to the south east of the study area (Gee et al., 2006). They are located in approximately 1.5 km water depth, within the top few hundred meters of the seafloor and are, as such, significantly younger than the deposits described in this section. However, the giant landslide discussed in detail by Gee et al. (2006) is thought to have a volume of ~ 20 km^3 and extends at least 26 km from the headwall scarp flowing towards the deeper shelf. Given that the study area where these regionally derived MTC deposits have been recorded is approximately 100 km basinwards of the break of shelf it is very likely that the regionally derived MTC deposits described here were generated by a giant submarine landslide with similar characteristics to that described by Gee et al. (2006), but encompassing a much larger volume of sediment.

Analysis of the regional seismic dataset indicates that the shelf break is dominated by large extensional, rotated fault blocks. Thickening patterns across these rotated blocks indicates that they were active between 18.26 Ma and 13.25 Ma when the regional MTC deposits were generated. It is likely that the movement of these faults generated instability on the slope which in turn triggered the formation of these regional MTC deposits.

6.9 Discussion

The two types of mass transport complexes described in this chapter exist on very different scales and probably relate to end-member scenarios within a spectrum of MTCs. They conform to the ideas of attached and detached MTCs outlined by Moscardelli and Wood (2008) with the attached MTCs being regional in extent and comprised primarily of debris flows towards the toe end of the flows (i.e. a similar distance from the shelf area as is observed here). The local MTCs observed and described in this basin would be classified as detached MTCs with an extensional headwall situated on the flank of a structure and a compressional toe located within a confined basin. Here, the similarities and differences between these types of MTC are discussed in detail along with how the timing of their formation links to structural evolution of the mini-basin.

6.9.1 Comparison between Debris Flows and Slides

The MTCs within the mini-basin can be classified as two distinctly different types according the scheme outlined in Section 3.2.1: local detached MTCs which are dominated by slides and regional attached MTCs dominated by debris flows (Moscardelli and Wood, 2008). The slide deposits contain material which has been translated from an in-situ position along a discrete basal shear surface to a maximum of run-out length of 6.3 km whereas the debris flow deposits have been transported at least 100 km from the shelf of the passive margin, possibly entraining additional material as they flow. This very different transport mechanism in turn generates different internal characteristics and relationships with the surrounding stratigraphy (Table 6.2).

The top surfaces of both the local and regional MTCs are undulating reflecting the underlying deformation within the MTC and are overlain by sediment which tends to pond and onlap against them. This is more prominent in the local MTCs where undulations in the top surface are more pronounced (compare Figure 6.4 to Figure 6.18).

The basal surfaces are very different between the two types of MTC deposit, partly due to the limited area of the regional MTC studied. The local MTCs have clear erosion at the headwall and subsequent ramp formation on the lateral margins and frontal ramp where the deposit steps up through the stratigraphy, whereas the regional MTCs have a much more concordant basal surface (again compare Figure 6.4 to Figure 6.18). Small ramps are recorded in the middle, translational domain of the local MTCs which are similar in scale to those observed towards the end of the regional MTCs; ramps of up to 30 m are recorded in the local MTCs and up to 25 m in the regional MTCs. The polarity of the basal surface indicates that the lithology at the base of these two deposits has very different characteristics; the local MTC deposits have a predominantly normal polarity at their base indicating a transition from soft to hard sediment whereas the base of the regional MTC deposits has a reverse polarity of the seismic data which would indicate a transition from hard to soft sediment. This polarity reversal could indicate the presence of a weak lithology at the base of the MTC or a more coherent debris flow. Alternatively, this polarity reversal could be indicative of trapped over-pressured fluids beneath the MTC, these could have induced the formation of a

low shear-strength surface and contributed to the decoupling of the debris flow unit from the underlying basin sediments thus allowing propagation of the regional MTC for at least 100 km (Moore et al., 1995, Sultan et al., 2009, Harders et al., 2010, Joanne et al., 2013).

Feature	Local MTC	Regional MTC
Source and derivation	Locally derived (up to 6 km from source) and can be traced back to the flanks of specific basin-bounding anticlines	Regionally derived (at least 100 km), thought to be generated by movement of extensional faults on shelf edge
Classification (according to Moscardelli and Wood (2008))	Slides	Debris flows
Top surface	Undulated top surface reflects internal deformation within MTC, clear onlap of later sediments	Mostly concordant with overlying stratigraphy, some evidence of ponding on upper surface
Base surface	Largely erosional with clearly defined frontal and lateral ramps up to 300 m high	Mostly concordant with underlying stratigraphy, some ramps where interact with topography but up to 25 m
Maximum thickness	Thicknesses of up to 350 m recorded in thickest section immediately behind frontal ramp	Maximum thickness in centre of basin where thicknesses of up to 300 m are observed
Main internal characteristics	Composed of translated blocks of material with clearly defined extensional and compressional domains containing normal faults and thrust faults respectively	Mainly composed of chaotic sediment with some blocks carried in flow and some evidence of thrust faults developing at topographic barriers

Table 6.2 A table detailing the main characteristics of the two scales of MTC deposit examined in this chapter, note how they are for the most part very different in composition and morphology.

The main difference between the local and regional MTC deposits is the internal characteristics of these deposits; the local slides are composed of well organised translated material whereas the regional debris flows contain predominantly chaotic, disaggregated material (Table 6.1 and Figures 6.4 and 6.12). This difference in the internal morphology is thought to have resulted from the distance these deposits have travelled from their source and the coherent nature of the sediment carried within these. The local MTC deposits are comprised of coherent, mostly rigid translated material which has internally deformed with the

development of normal faults in the extensional domain and thrust faults in the compressional domain (for example Figure 6.10). In contrast to this, the regional MTC deposits (classified as debris flows according to the scheme outlined in Section 3.2.1) deform plastically, or at least semi-plastically, during displacement with the material transported as an incoherent mass which is deposited as such on the seafloor surface (for example Figure 6.18). The only exception to this appears to occur when the debris flow thins or encounters local increases in the topography surrounding the basin. In these instances, ridges tend to form within the debris flows with imbricate duplex-style thrust faults forming back from the area where the debris flow encounters this change in topography (Figure 6.12). These are similar in size and appearance to those recorded in the toe of the compressional domains of the local MTC deposits; the thrust faults within the local deposits have an average spacing of between 50 to 100 m whereas those observed in the regional MTC deposits have an average spacing of between 45 to 60 m and they both thin towards their terminal end. This similarity implies that the sediment slurry carried within the debris flow can behave in a more coherent manor when it thins and encounters topography. Joanne et al. (2013) also observe this phenomena towards the distal end of a debris flow which they attributed to high friction on the basal surface and the build-up of compression at the frontal end of the debris flow which they termed 'bulldozing' (also described by Frey-Martinez et al., 2005).

The area covered within the basin and the volume of material transported within these two types of MTC deposit varies significantly. The local MTC deposits cover areas of between 11.5 km^2 and over 28.9 km^2 along the edge of the basin whereas the regional MTC deposits cover up to approximately 1300 km^2 within the mini-basin and would cover a significantly larger area than this if the region between the mini-basin and the source area at least 100 km to the east, were to be taken into account.

6.9.2 Structural Evolution and Corresponding MTC Deposits

The local slides and regional debris flows described in the preceding sections not only have very different characteristics but also occurred at different times during the history of the basin, with very few instances where they were both present at the same time. Submarine slope failure, which generates MTC deposits, is known to occur when down-slope directed shear stresses acting along an inclined planar surface, such as a bedding plane, exceed the shear strength of the slope (Varnes, 1978, Biscontin et al., 2004, Owen et al., 2007). Thus, the generation of MTC deposits is intrinsically linked to the structural evolution of the mini-basin and the passive margin as a whole. Increased structural movement could have generated over-steepened slopes on the flanks of the anticlines which bound the mini-basin and structures elsewhere on the passive margin where the shear stress acting along the inclined surface could have exceeded the shear strength of the slope. Investigating the structural evolution of the basin alongside the development of these MTC deposits may help explain why either local slides or regional debris flows dominate the mini-basin fill during different phases of structural growth of the mini-basin.

The regional MTC deposits were deposited within the basin during the interval which contains the highest rate of change of bed lengths and hence the inferred highest growth rates overall (Figure 6.19). High rate of

change of bed lengths have been recorded on all structures which bound the basin and lie within the basin during this interval. As discussed in Chapter 5, this interval links to a period during which large extensional faults were active at the shelf edge; movement and rotation on these fault blocks could have lead to the formation of these regional MTC deposits. As well as generating regional MTC deposits this activity at the shelf edge would have been partially responsible for driving the movement seen on the structures within this basin at this time, with the growth of the anticlines within the area driven by the down-slope movement of the failed sediment and the underlying salt. Rotation of the fault blocks, alongside a concomitant increase in up-dip sediment loading from the regional MTC deposits, could have driven the salt down-dip into the salt structures within the mini basin.

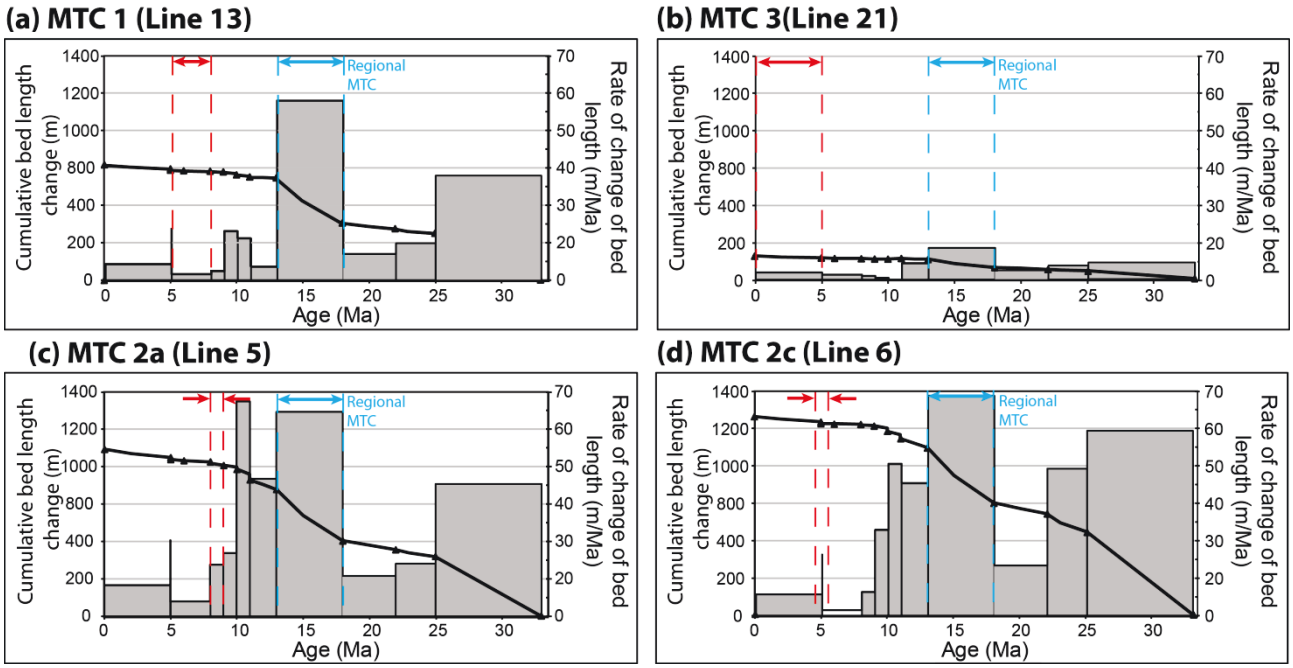


Figure 6.19 Bed length change graphs showing the amount of cumulative bed length change and the rate of bed length change recorded through the structures associated with the local MTCs. The red arrows indicate the period during which the respective regional MTCs were deposited whilst the light blue arrow indicate the period when the regionally MTCs were deposited throughout the basin. The line numbers are the same as those used in the study of all the structures within the basin in Chapter 5.

The timing of the initiation of the local MTCs does not clearly correspond to periods of high growth on structures in the basin (Figure 6.19). Instead, these slide sediments appear to be triggered during periods with relatively low bed length change and hence low structural growth on the associated structures. MTC 1 was triggered in the period with the lowest rate of change of bed length out of the structures; at the time at which the MTC was deposited the rate of change of bed length over the structure was calculated to be 2 mMa^{-1} and an overall bed length change of 690 m on the structure. A similar rate of change of bed length also occurred during the time in which MTC 3 was triggered with a rate of change of bed length of 2 mMa^{-1} also recorded on the structure within Area F. The overall accumulated bed length change on this structure is significantly less, with only 140 m of bed length change accumulated at this time (Figure 6.19). Whilst low rates of bed length change during this time period does not indicate a high rate of movement on these structures, there may have been short periods of rapid-salt related movement during these intervals which, when averaged over the entire period, do not look significant. This pulsing of salt activity could have generated rapid, but short-lived, uplift which triggered the deposition of these MTC deposits. This period

also contains ponded fan systems deposited within the centre of the basin. The stratal onlap patterns observed within these ponded sediments indicate that the basin was under-filled but confined on the margins and had an emergent, exposed bathymetric relief during this period. The emergent slopes on the flanks of the anticlines which bound the basin may have been more prone to gravitational instability and hence could have failed, forming the relatively small submarine slides documented here. Smaller MTCs and ponded sediments are not commonly identified deeper in the basin, suggesting it was not under-filled to this extent in the past, and that in this area local MTC deposits only form during periods of under-filled basin development. The co-existence of ponded fan systems and slide deposits has also been imaged in the Niger Delta (Adeogba, 2005).

In contrast, the MTCs within the MTC 2 complex do correspond to periods which have relatively high rate of change of bed lengths on the structures they are sourced from (Figure 6.19). MTC 2a occurred in the period between 9.68 Ma and 8.29 Ma when rate of change of bed lengths of 16 mMa^{-1} were recorded, and follows a period of relatively high rate of change of bed lengths on this structure from 18.26 Ma (Figure 6.21). The formation of the youngest MTC within this cluster, MTC 2c, also corresponds to a peak in the growth rate of the structure between 5.58 Ma and 5.04 Ma with a rate of change of bed length of 19 mMa^{-1} recorded during this interval (Figure 6.19 (d)). MTC 2a and MTC 2c transported the largest area of sediment out of all the local MTCs investigated which could imply that higher rates of structural growth generates larger MTC deposits (see Table 6.1).

The MTC 2 complex contains a series of individual failures which occurred successively within the area and link to growth on one individual structure within Area B. Whilst it is not possible to define the headwall scarp in all three of these MTCs, the location of the remnant extensional domain implies that the headwall scarp retrogressively moved up the main structure. This indicates that there was growth on this structure throughout the interval when these MTCs were deposited from 9.68 Ma to 5.04 Ma. The bed length change analysis in Figure 6.19 implies that growth was episodic during this interval and hence most likely related to pulsing of the salt. Owen et al. (2007) suggest that episodic structural growth is more likely to trigger failure than steady growth, arguing that whilst steady uplift will increase a slopes susceptibility to failure it still needs a secondary trigger to initiate the generation of the MTC. This trigger can be a rapid change in slope angle by as little as < 1°, with the increase in slope causing an increase in the downslope shear stress (Owen et al., 2007).

6.10 Conclusions

The high resolution seismic dataset allows the identification of two types of MTC deposit within the mini-basin fill; local, detached slides and regional, attached debris flows. These two mechanisms transport very different volumes of sediment and, as such, have very different internal morphologies and distributions.

Local MTCs have a very self-contained distribution consisting of translated material which can clearly be sub-divided into an extensional domain, containing the headwall scarp which cuts down into the stratigraphy and extensive normal faults, and a compressional domain dominated by thrust faults, folds and ramps cutting

up through the stratigraphy. These slide deposits can be clearly traced back to their source area on the flanks of anticlines that bound the basin and occur during periods when the mini-basin is under-filled and these structures are exposed on the seafloor surface.

Regional debris flows are sourced from at least 100 km east of the mini-basin, near the shelf of the continental margin. These MTCs are mostly comprised of chaotic material carried within the flow with some discrete high amplitude blocks of sediment also transported. More organised internal features can develop within the regional MTCs when these debris flows encounter topographic highs, generating closely spaced imbricate thrust faults. In general the regional MTCs tend to react to topography within the basin, depositing further down the flanks of actively growing structures and with significantly thicker deposits found in the centre of the mini basin.

From the observations outlined in the preceding paragraphs and in this chapter as a whole, it is possible to draw some over-riding conclusions related to the development of MTCs within the mini basin:

- The location and frequency of local, detached MTCs does not necessarily correspond to high periods of structural growth within the resolution measured by the bed length change analysis. However, a period of uplift of the seafloor would seem to be the most likely trigger for generating the local MTCs. Therefore it is possible to assume that either they form due to salt movement beneath the biostratigraphic resolution of this study or that longer periods of emergence at the seabed (i.e. during the under-filled period of the basin development) led to greater sediment instability on the flanks of the structures. If the former is the case, then it is possible to conclude that the frequency of the salt movement is higher than can be observed within the bed length change analysis. Hence the spatial distribution of the local MTCs can be used to aid understanding of structural growth below the temporal resolution provided by the biostratigraphically dated horizons.
- Similar style imbricate thrust faults can be observed in local and regional MTC deposits. They are thought to form as the flow at the front of the MTC freezes as it moves over the basal shear surface and encounters more resistance on the surface of the seafloor. This causes the flow to stop abruptly and generates a series of thrust faults which propagate back through the system as the material carried within the MTC continues to apply pressure. When observed within the regional MTC systems these allow an independent verification that the high rates of bed length change within an area generated bathymetric highs.
- In these examples local MTCs have more impact on the bathymetry within a basin; the frontal and lateral ramps erode into the underlying stratigraphy by up to 300 m and the positive topography generated within the compressional domains impacts the sediments subsequently deposited. They have more potential to alter a petroleum system within an area, both positively and negatively, than the regional MTCs; they can potentially form traps within the largely undeformed blocks in the extensional and compressional domains but can

also scour into the underlying stratigraphy potentially eroding into underlying petroleum systems and breaching seals.

- The ponded sediment accumulated within the depressions on the surface of local and regional MTCs has the potential to form effective reservoirs. However, the volume and connectivity of these packages varies between the two systems; the sediments deposited within the depressions which form on top of local MTCs are thicker than those imaged above the regional MTCs, but the packages above the regional MTCs cover a larger area and have better connectivity.

7 Development of Deepwater Ponded Fan Systems within a Mini-Basin; their Characteristics and Evolution

7.1 Abstract

This is the first time that images of this resolution and detail have been recorded from subsurface submarine fan systems. The quality and resolution at which these can be observed and analysed is without parallel in a subsurface setting and, as such, allow the full extent of these submarine fan systems and the interactions within these to be explored in detail.

A succession of four deepwater fan lobe complexes deposited within the salt-controlled mini-basin have been imaged in unprecedented detail. The relatively shallow depth of the sediments (approximately 850 m beneath the seabed), coupled with the high resolution of the three dimensional (3D) seismic data allows the plan-view morphology of the fan lobe complexes to be imaged in exceptional detail using amplitude extractions and frequency decomposition. Examining each of the four fan lobe complexes on slices made at approximately 25 m vertical separation through the stratigraphy shows how the growth is controlled by both autogenic events within the sedimentary system and allogenic events external to the sedimentary system.

The ponded interval was deposited over a period of approximately 0.8 Ma and consists of four discrete packages, each of which contains at least one fan lobe complex. There is a systematic change in the shape and orientation of the lobe complexes through time: the two older lobe complexes are oriented broadly north-south and are up to 10 km long by 5 km wide, whereas the youngest lobe complexes are orientated southeast-northwest and have a rounder shape (9 km long by 8 km wide). The gradual north to south movement of the main feeder channel entry point and the distinct change in the lobe complex orientation is attributed to growth of the basin-bounding salt structures.

Each fan lobe complex is composed of multiple individual lobes which are formed of a trunk channel and a diverging network of smaller distributary channels commonly fringed by a high amplitude band. The lobes are on average 1.6 km long by 1.3 km wide and are fed by trunk channels which range from 60 m to 200 m wide, with thicknesses up to 15 m. These trunk channels branch into distributary channels with widths of less than 30 m. Variation in lobe shape and spatial location is driven by both allogenic and autogenic events, with lobes responding to topographic growth along the edge of the basin and as well as inherited seabed relief generated by previous lobe growth. Compensational stacking of the lobes is observed where lobes develop in topographic lows between older lobes. In areas where lobe development is constrained by structural growth along the edge of the basin the lobes become elongated and divert away from the growing topography. Where changes in topographic relief are highest, along the edge of the basin and on the downthrown side of a normal fault, the distributary channels within the lobes amalgamate.

Fan lobe complexes of similar scales have been described in detail in outcrops and in unconfined settings on the seafloor but this is the first study to describe these systems in such detail in the subsurface; resolving the individual lobes and lobe elements within a ponded intra-slope basin. These high resolution plan-view

images link the fine-scale sedimentological studies that have been carried out on fan lobe complexes and sheet sands for the past twenty years with less well resolved seismically imaged fan systems. The sheet sands described in outcrop studies can be correlated with features seen in the plan-view amplitude extraction maps: we record densely channelised lobes (channelised sheet facies) passing laterally into more branched, thinner channels and lobe elements (channelised and amalgamated sheets) then terminating in a high amplitude fringe (amalgamated and layered sheets). These features are often hard to link spatially in outcrop settings where only dispersed sections are available but this unique dataset allows the linkages between these facies to be explored. Bridging this gap between outcrop resolution and seismic resolution is important when thinking about reservoir properties; if it is possible to identify features at a seismic scale and link these to properties recorded from outcrop studies then this allows a much more thorough understanding of the potential reservoir characteristics. This new Angolan example can be used as a unique analogue to enhance the understanding of reservoir heterogeneities within deepwater fan systems in ponded basins throughout the world.

7.2 Introduction

Submarine fan systems in deepwater settings have long been documented, with researchers as early as 1959 recognising three principal areas of deposition in the deepwater: the basin floor, submarine fans and slope aprons (Gorsline and Emery, 1959). Subsequent work on submarine fan systems, both in modern and ancient settings, led to the formation of a more general deepwater submarine fan model (Menard, 1960, Walker, 1966, Jacka et al., 1968, Normark, 1970, Haner, 1971, Walker, 1978) and the recognition of inner fan, middle fan and outer fan facies (Mutti and Ricci Lucchi, 1972). The advent of high resolution seismic datasets and side-scan sonar imaging led to an expansion of work in this field (e.g. Nelson, 1992, Twichell et al., 1992, Gervais et al., 2006, Deptuck et al., 2008, Jegou, 2008, Saller, 2008). More recently, increased hydrocarbon exploration and production success in deepwater settings, where submarine fan systems act as important hydrocarbon reservoirs, has driven this field of study further. This work frequently relies upon high resolution seismic data, often imaged three-dimensionally to analyse near surface deepwater systems for use as analogues in deeper less well-imaged but hydrocarbon-bearing zones (for example Beaubouef and Friedmann, 2000, Deptuck et al., 2003, Fonnesu, 2003, Saller et al., 2004, Adeogba, 2005, Mayall et al., 2006, Prather et al., 2012).

Normark (1970) carried out some of the earliest work on modern submarine fan systems looking at outcrops on the Californian Borderland and offshore Baja, California. Subsequent work at the outcrop scale has provided much detail in terms of lithofacies distribution and bed-scale hierarchy (Normark, 1970, Walker, 1978, Mutti and Normark, 1987, Mutti and Normark, 1991, Remacha, 2003, Hodgson, 2006, Prelat et al., 2009). Whilst outcrop studies are invaluable in advancing understanding of these details, in many cases the palaeogeographic location of the outcrop with relation to the original fan system and lateral facies changes is poorly constrained due to insufficient lateral continuity (Deptuck et al., 2008, Saller, 2008). Significant amounts of work have also been carried out using flume tanks to simulate the flows that generate these submarine fan complexes, but these are hard to scale up and, as such, are difficult to validate using modern

systems (Parsons et al., 2002, Al Ja'Aidi et al., 2004, Baas et al., 2004, Kubo, 2004, Cantelli et al., 2011, Talling, 2012). Side-scan sonar imaging and industry standard multichannel reflection seismic profiles, often ground-truthed using piston core data, have been used to link the observations seen in outcrops and have provided useful insights into the interactions within, and between, the lobes within submarine fan systems (Nelson, 1992, Twichell et al., 1992, Piper et al., 1999, Gervais et al., 2006, Deptuck et al., 2008, Jegou, 2008, Saller, 2008). However, in the case of conventional seismic data, poor resolution has meant that it is not possible to image some of the fine detail and architecture within the individual lobes which can often appear as single cycle seismic reflections (Fonnesu, 2003, Adeogba, 2005), or in the case of North Sea studies and the Jeanne d 'Arc Basin, as sub-circular to elongated 'mounds' of sand-prone deposits up to 60 m thick (Sarg and Skjold, 1982, Deptuck et al., 2008). High-resolution and ultra-high resolution seismic data, capable of resolving individual sand beds, ground-truthed by piston cores has attempted to bridge the gap between outcrop studies and conventional seismic data. This has lead to a collection of detailed analogues which provide information on the dimensions and distribution of lobes within submarine fans along with a more precise understanding of paleogeography (e.g. water depths, gradients, distance from the shelf-break) and hence more understanding of some of the controls on the initiation and character of the turbidity currents that deposited the lobes (Piper et al., 1999, Booth et al., 2003, Deptuck et al., 2008, Hay, 2012).

In imaging a series of submarine fan complexes fully, the work presented in this chapter builds on these previous studies and attempts to bridge the gap between outcrop data and conventional resolution seismic data by using a high-resolution 3D seismic dataset. The submarine fan lobe complexes investigated here are all contained within one structurally controlled mini-basin, and hence this work focuses on the characteristics and evolution of submarine fan lobe complexes within a ponded setting. These discrete fan lobe complexes were deposited in the mini-basin over a period of approximately 0.8 Ma during a lull in structural activity (see Chapter 5).

7.3 Methodology

As discussed in Chapter 4, a high-resolution, 3D seismic dataset covering approximately 1,400 km^2 has been used throughout this study. It has an inline and crossline spacing of 6.25 m and a vertical sample rate of 2 ms twtt. The frequency content of the dataset yields a vertical resolution of approximately 5 m within the interval between the H100 and H110 surfaces where the ponded fan systems are located.

Four surfaces have been mapped between the H100 and H110 surfaces resulting in four intervals based on the seismic signature within the package (see Chapter 4). The area between these surfaces has been isoproportionally sliced to generate intervals which mimic the topography of the basin and are up to a maximum of 25 ms twtt thick towards the centre of the basin. A root mean squared (RMS) amplitude extraction algorithm has been applied to each interval which calculates the square root of the sum of the squared amplitudes divided by the number of samples taken within the window. This means that the both maximum positive and negative amplitude values are highlighted, increasing the amount of information extracted from the dataset but also creating slightly more noise than some of the other extraction algorithms (see Chapter 4 for further discussion of this). The channels identified and interpreted from the amplitude extractions have been checked on sections perpendicular to the fan and can be linked clearly to high positive or negative amplitude anomalies in cross-section, clear examples are highlighted with arrows in Figure 7.1.

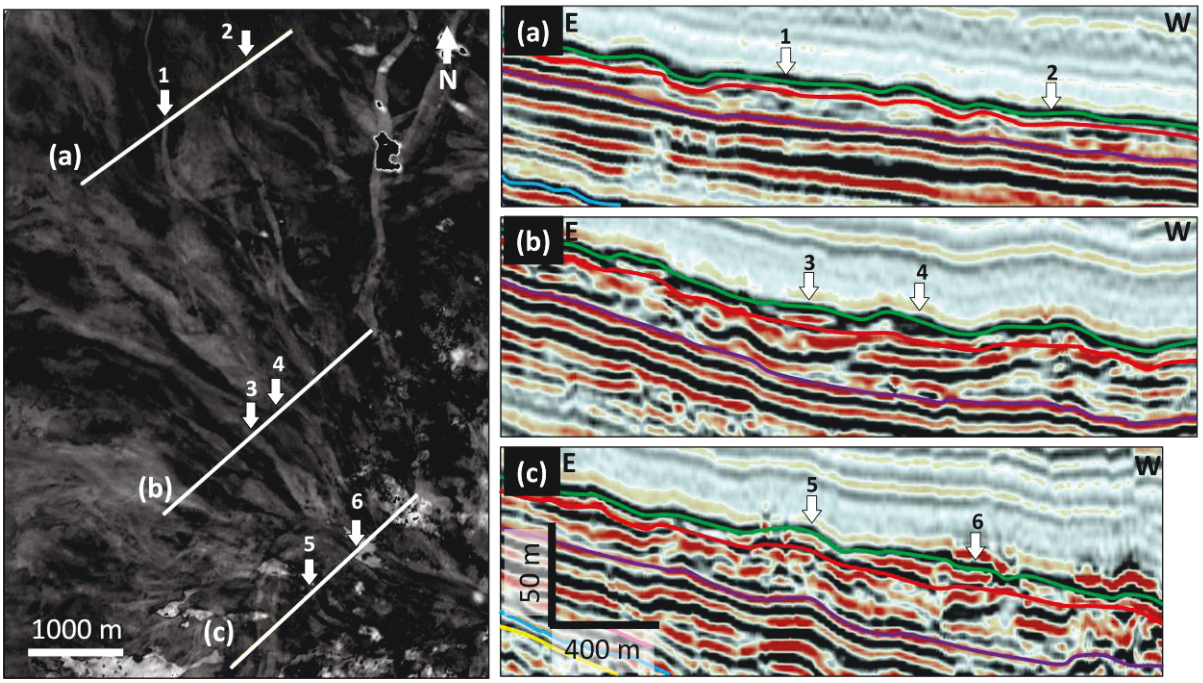


Figure 7.1 A root mean squared (RMS) amplitude extraction map through the interval between the green (P50) and the red horizons. The section is the top isopachous interval of four taken between the P40 and P50 horizons, with the P40 horizon shown in purple. Sections illustrate how the amplitude extractions identify real channels. The correlation in section (a) is not as easy to identify as the red line partially covers the amplitude event.

In the south of the area details within the stratigraphic packages were poorly resolved using standard amplitude extraction techniques and so a spectral decomposition analysis was carried out. This was applied over a portion of the seismic data south of the normal fault which was flattened on the upper-most ponded horizon. In this process volumes are band limited according to their frequency magnitude and then blended

using a red-green-blue (RGB) colour scheme (McArdle and Ackers, 2012). In order to do this the frequency spectrum for the section was calculated and then a constant Q bandpass filtering method was applied where the bandwidth of each frequency response increases with the frequency such that the integral of energy over frequency remains constant in each band (McArdle and Ackers, 2012). Three frequency magnitude volumes are created with different central frequencies and overlapping bandwidths, each of which is ascribed a different colour and then all three are superimposed or 'blended' in RGB colour space (Figure 7.2).

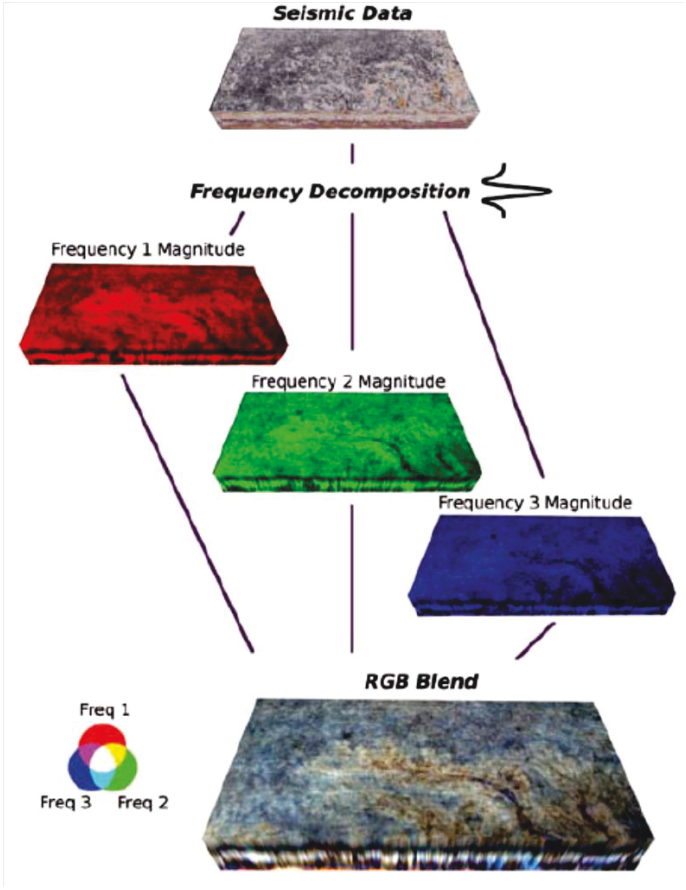


Figure 7.2 Flow diagram showing the method used to create a frequency decomposition colour blended volume. Here the three main frequencies are ascribed to a red, green or blue colour and then blended such that areas where one frequency dominated will be associated by the dominant assigned colour and areas where the frequencies overlap will be coloured according to the diagram on the bottom left side of the figure (From McArdle and Ackers, 2012).

A comparison between an RMS amplitude extraction and a frequency decomposition volume calculated within a 25 ms twtt window south of the normal fault indicates that it can be effectively used to identify features in the seismic data (Figure 7.3). This shows how the use of frequency decomposition instead of amplitude extractions can highlight different features in the seismic data; for example the boundaries between the channel edges appear to be sharper in the higher frequency blend (Figure 7.3 (c)). Overall, the channels appear to be much sharper in the frequency decompositions than in the amplitude extraction windows. This may be due to the fact that the frequencies are sampled over a smaller window than the RMS amplitude extraction meaning that more channels are imaged together in the RMS extractions which could cause the image to blur. However, using the frequency decompositions makes it more difficult to identify the exact depth of the channels as they are identified between surfaces within a flattened volume. This has meant that amplitude extractions have been used for the majority of the analysis.

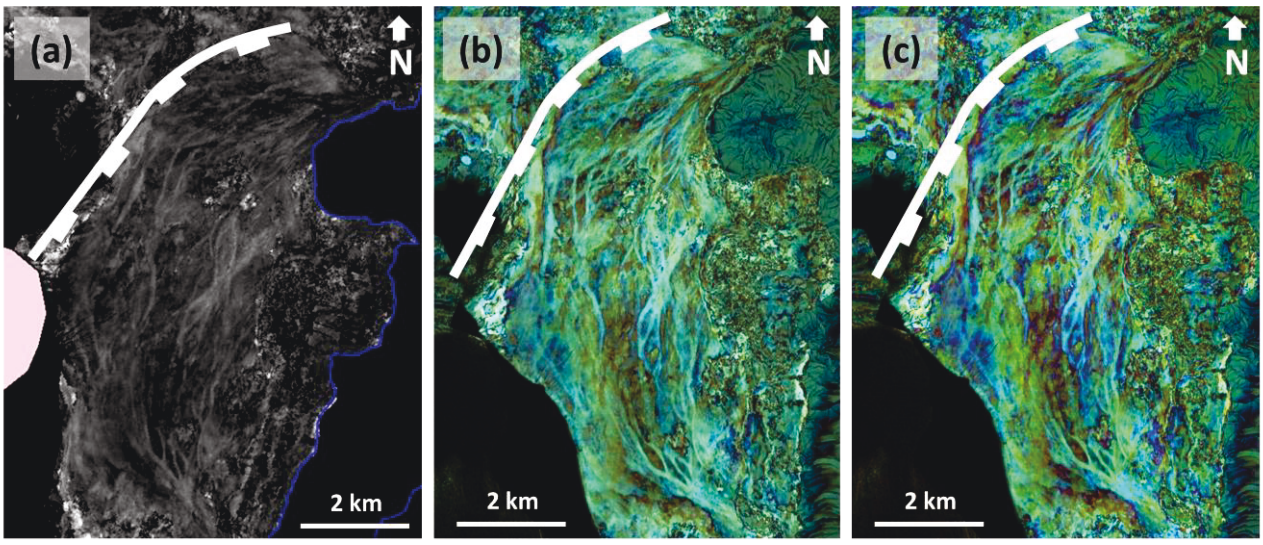


Figure 7.3 Comparison between (a) root mean square (RMS) amplitude extraction (b) lower frequency decomposition blend and (c) a higher frequency decomposition blend. Note how the different methods highlight different features from within the data.

7.4 Structural Constraints

The ponded deposits studied here are primarily located in the south of the study area and bounded on all sides by salt-influenced structures. The major boundary which prevents sediments exiting the mini-basin is in the west of the area where a long-lived salt wall prevents sediment flow down the slope and out into the basin (Figure 7.4, Areas B, D and E). A series of linked salt-cored anticlines in Area C further constrain the northwest boundary. These linked structures are discussed in further detail in Chapter 5, and show increased movement within the interval prior to the deposition of the ponded fan sediments. The eastern boundary, Figure 7.4 Area F, is formed by a salt-cored anticline which has been pierced by a salt diapir subsequent to the formation of the ponded interval. The two younger ponded intervals extend south of the normal fault which was active at the time the ponded sediment was deposited.

The area is cut by two younger channel systems; one to the north of the ponded area and one to the south of the normal fault. Analysis of the most southern half of the ponded area is also constrained by the extent of the high-resolution seismic data, which stops at the southern end of the Area E structure (Figure 7.4).

Shortening analysis, discussed in detail in Chapter 5, indicates that the spatial extent of the ponding is primarily constrained by the topography which formed due to structural growth n the previous time interval. It indicates that the period during which the ponded sediments were deposited was a period of relative structural quiescence with slower structural growth. However, previous intervals had significantly higher growth rates throughout the area which would have resulted in the generation of significant bathymetirc relief. Analysis in Chapter 5 shows that Areas C, E and F had particularly high growth rates during the preceding interval, but that structural movement slowed significantly between H100 to H110 (8.29 Ma to 5.58 Ma), when ponding occurred, thus allowing the sediments entering the basin to largely passively infill the topographic lows (Figure 7.4).

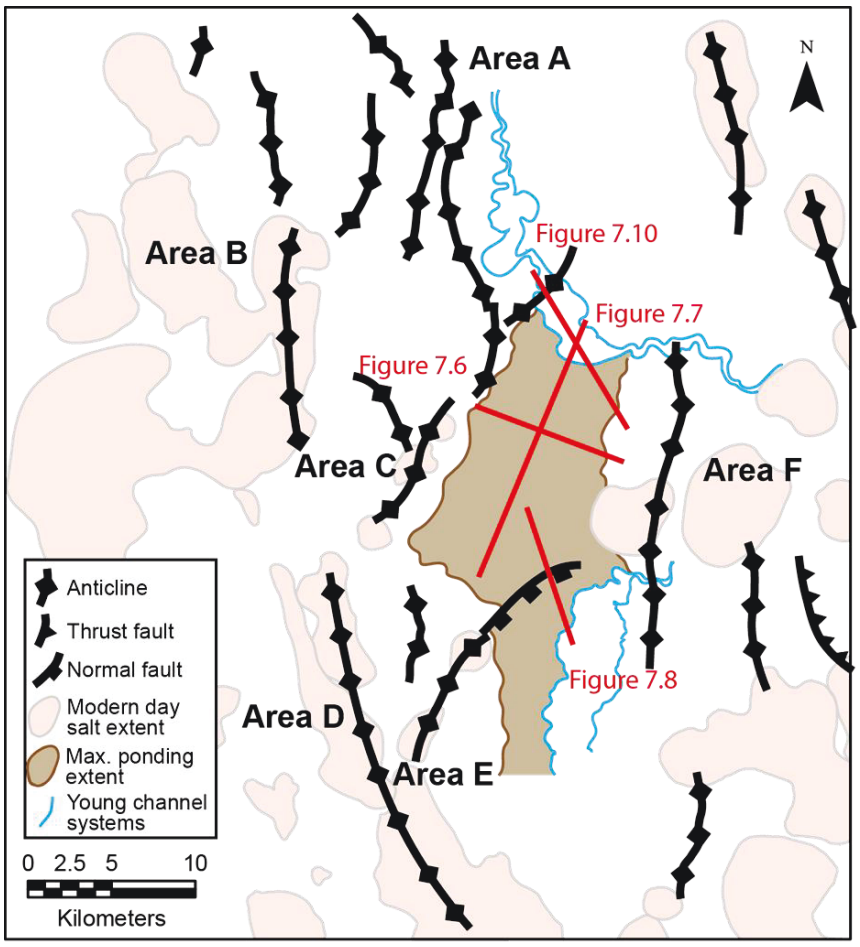


Figure 7.4 Location of the ponded area with respect to the main structures within the basin. This shows the maximum extent of the ponded sediments. The high-resolution seismic data does not extend further south than the Area E label and the blue channel outlines are younger systems that cut the ponded material. Red lines indicate the locations of seismic sections referred to later in the chapter.

A northeast-southwest trending arcuate normal fault has exerted control on thickness of the ponded sediment during its deposition (Figure 7.5). The section of the fault visible in the seismic data is approximately 6 km in length, and downthrows to the south resulting in a tilting of the hanging wall. Displacement along the normal fault is greatest towards the western end, closest to the salt diapir in Area C (Figures 7.4 and 7.5). Growth of the fault is likely to be linked to the salt structure beneath it, forming due to collapse related to salt withdrawal and/or lateral flow into the larger salt structure at its south-western end (Figures 7.4 and 7.5).

A few local mass transport complex (MTC) deposits occur before, during and after the deposition of the ponded fan systems. These take the form of slides and are largely sourced from the eastern salt-cored anticline and salt structure within Area F. The largest of these systems seen interacting with the ponded sediments (MTC 3) is discussed in detail in Chapter 6, but several smaller MTCs have been imaged within the ponded interval earlier in the history of the basin.

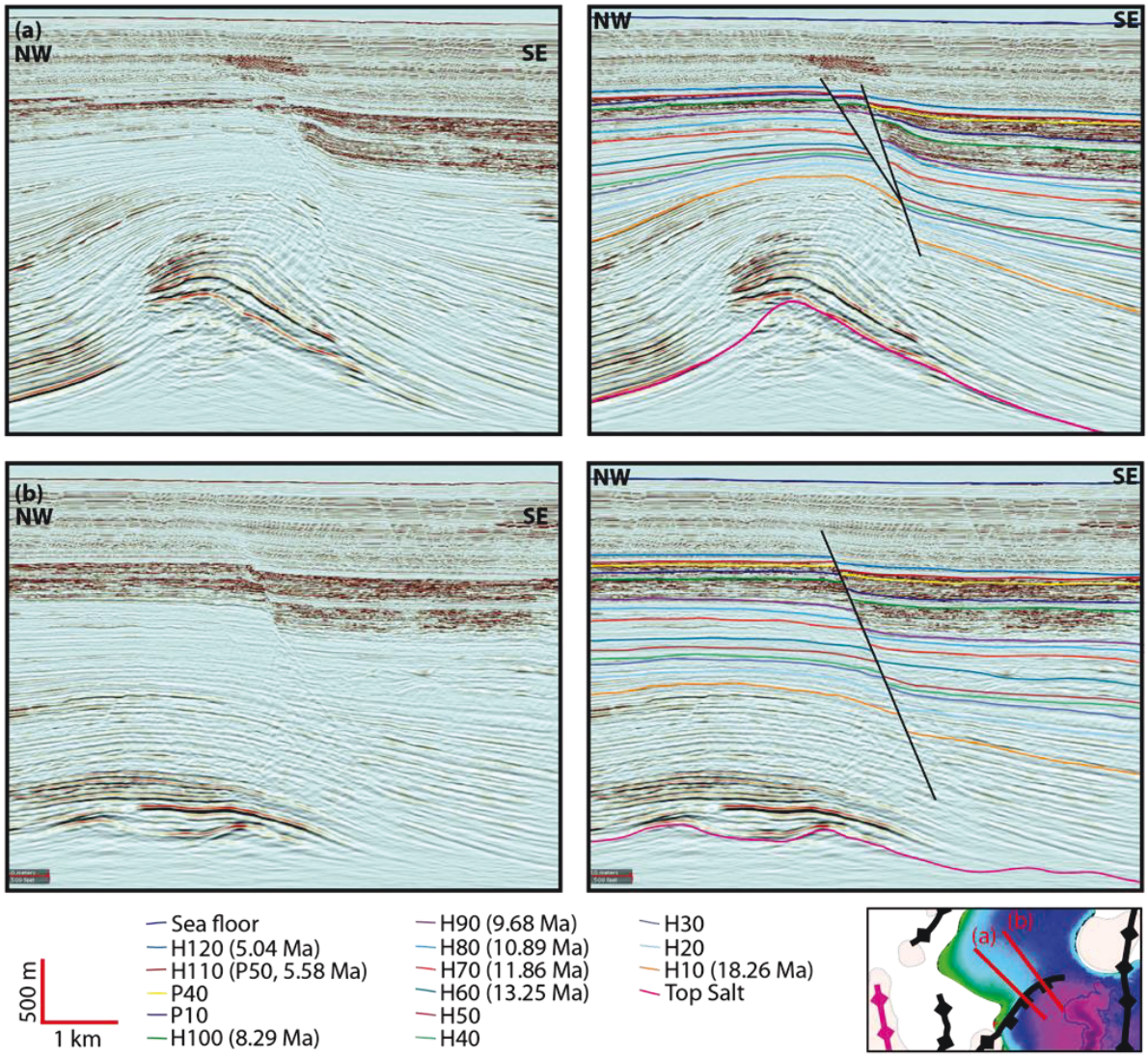


Figure 7.5 Seismic sections along the length of the normal fault from (a) a section across the central area of the fault and (b) towards the eastern fault tip. These show how the throw on the fault decreases to the east, away from the salt structure within Area C, corresponding to a decrease in the difference in thickness either side of the normal fault. Line locations are shown in the location diagram in the bottom right corner.

7.5 Stratigraphy

Ponded sediments occur primarily between 9.68 Ma and 5.58 Ma (H90 and H110). Within this period two packages of ponded sediments were deposited (Figures 7.6 and 7.7); the oldest between 9.68 Ma and 8.29 Ma (H90 to H100) and the younger between 8.29 Ma and 5.58 Ma (H100 to H110). The deposition of a unit of laterally extensive, parallel, low-amplitude layered reflections between the two ponded intervals suggests a hiatus in sediment input into the area with only background mudstones being deposited (Figures 7.6 and 7.7). In this work the younger of the two ponded packages will be analysed in detail north and south of the normal fault. Within the younger ponded interval five sequence boundaries have been recognised and mapped; P10 (oldest) to P50 (youngest) (Figures 7.6 and 7.7). The intervals contained within these sequence boundaries have been analysed in detail and their seismic stratigraphic characteristics are discussed in the following paragraphs.

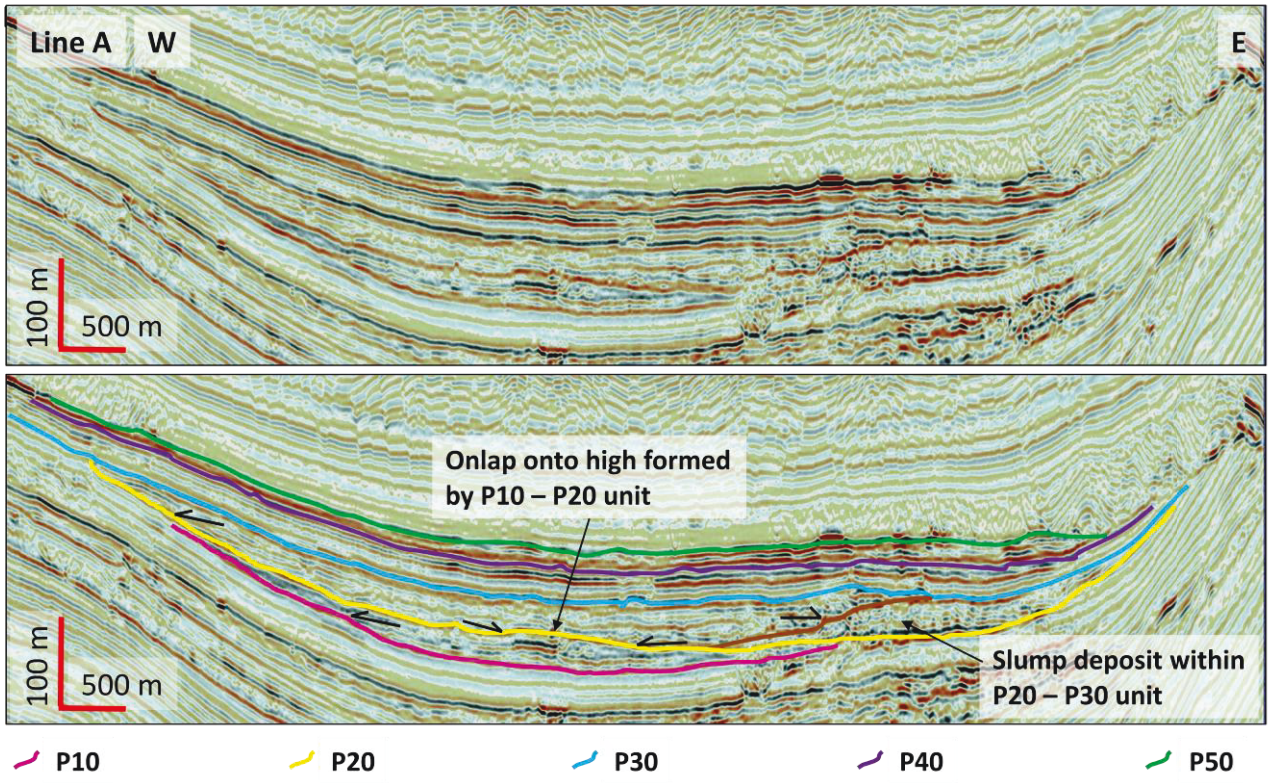


Figure 7.6 Cross-section though the ponded basin highlighting the four packages within the ponded interval, brown line indicates the western boundary of a slump within the P20 – P30 interval. Note how the basin is bound to the east and west by folded anticlinal structures which the packages onlap onto. Line location shown in Figure 7.4.

Cross-sections through the basin illustrate how the package thicknesses vary through time (Figures 7.6 and 7.7); in the earliest phases (P10 – P30) thicker sediment is deposited towards the north of the basin, whereas in the P30 – P50 intervals the thickest sediment packages are deposited towards the south of the area. All of the packages appear to thin towards the western edge of the basin with all but the interval between P40 to P50 also thinning towards the east. This indicates that the structures on both sides of basin were either active throughout the deposition of the ponded sediments or had topographic relief at this time (Figure 7.6).

The ponded unit is bound at the base by the P10 event, which is a strong reflection that is concordant with the beds beneath it (Figure 7.6). This horizon terminates on the flanks of both the eastern and western structures in Areas C and F respectively (Figure 7.6). The southern boundary to the ponded unit appears to have formed due to gentle change in topography and the P10 horizon decreases in amplitude such that it can no longer be traced. The lowermost package within the ponded section is defined at its base by the P10 and at its top by the P20 horizon, which is concordant with the beds within the P10 – P20 unit but forms a clear boundary with the beds in the P20 – P30 unit as they downlap onto it (Figure 7.7). This first unit within the ponded interval is comprised of fairly continuous horizons that appear to thin towards the confining edges of the basin, onlapping in the west and onto the topographic high seen towards the north of the area in Figure 7.7.

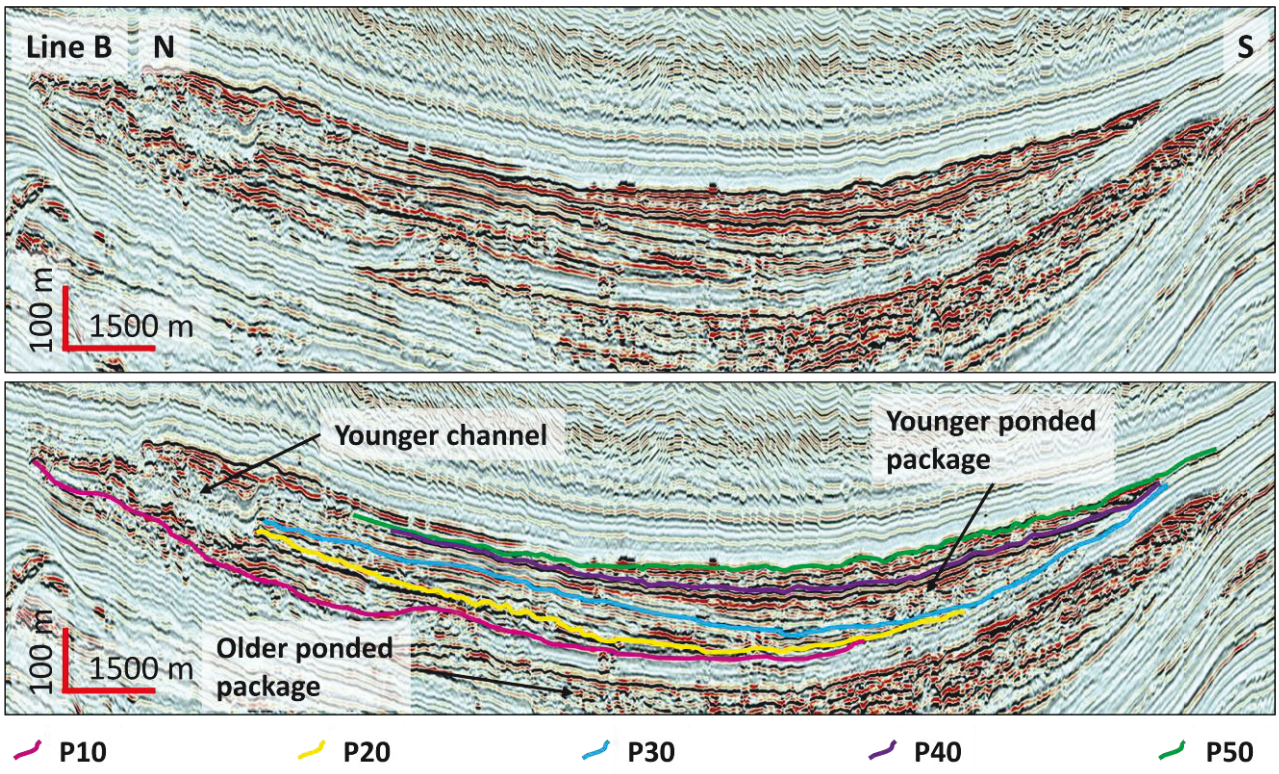


Figure 7.7 Cross-section along the strike of the basin. Note the younger channel cutting through the north of the basin and the change in thickness between the four packages from north to south. The top of the older ponded package is also identified. Line location is shown on Figure 7.4.

The next unit is bound by the P20 and P30 surfaces. The P20 surface lies conformably above the horizons within the P10 – P20 unit, but there are clear onlap and downlap of reflections onto the horizon from within the P30 – P20 unit; this occurs mainly within the centre of the unit and away from the edge of the basin (Figure 7.6). In the west of the mini-basin the beds extend a substantial distance up the edge of the anticline within Area C, onlapping onto, and terminating against it (Figure 7.6). The terminations in the east are complicated by the presence of a coeval slide unit, and here the individual horizons within the interval appear to downlap against the P20 surface as well as terminating against the slide. Some of the youngest beds within the package continue over the slide, and lie conformably above it indicating that the slide stopped moving within this interval. The other bounding surface, the P30 horizon, clearly onlaps the structures on both sides of the basin and also blankets the older slide in the east (Figure 7.6). It is a continuous horizon that can be traced across the basin and is conformable with series of younger horizons within the P30 – P40 unit. Within the P20 to P30 unit the reflections are highly discontinuous; they become more opaque in appearance towards the base of the section and more continuous and stronger as they become younger.

The P30 and P40 horizons are strong, high-amplitude, continuous reflectors that extend across the basin bracketing a package consisting of highly continuous bright reflections. In a similar way, the P40 surface is the last easily traceable continuous reflection within this package (Figure 7.6). The reflections within this package onlap against the structure to the east but thin and continue over the western structure. The package appears to thin towards the north and thicken to the south (Figure 7.7). The P30 and P40 horizons can both be traced south of the normal fault with the P30 horizon becoming the base of the ponded package south of

the normal fault. The P30 horizon is offset by an average of approximately 50 m which means that the P30 - P40 interval is almost twice as thick south of the normal fault (Figure 7.8). The package has very similar seismic characteristics, but has slightly higher amplitude signals and less reflection continuity to the south of the normal fault (Figure 7.8).

The P40 – P50 unit is the thinnest of the mapped packages and has a very similar distribution to the P30 - P40 unit with the beds onlapping the structure to the east, this is not visible in Figure 7.6 due to the activity of a later slide deposit, but can be imaged elsewhere in the basin. The interval also thins towards the structure in the west, continuing almost to the crest of the anticline (Figure 7.6). The P50 horizon is cut by the younger channel system in the north, with the younger infill of this channel being deposited on top of the older ponded sediments (Figure 7.7). Overall the P40 – P50 interval is comprised of high amplitude, discontinuous reflections that thin towards the north and are cut by the normal fault to the south. Although the P40 and P50 horizons are offset by the fault there appears to be very little growth across it at this stage (Figure 7.8).

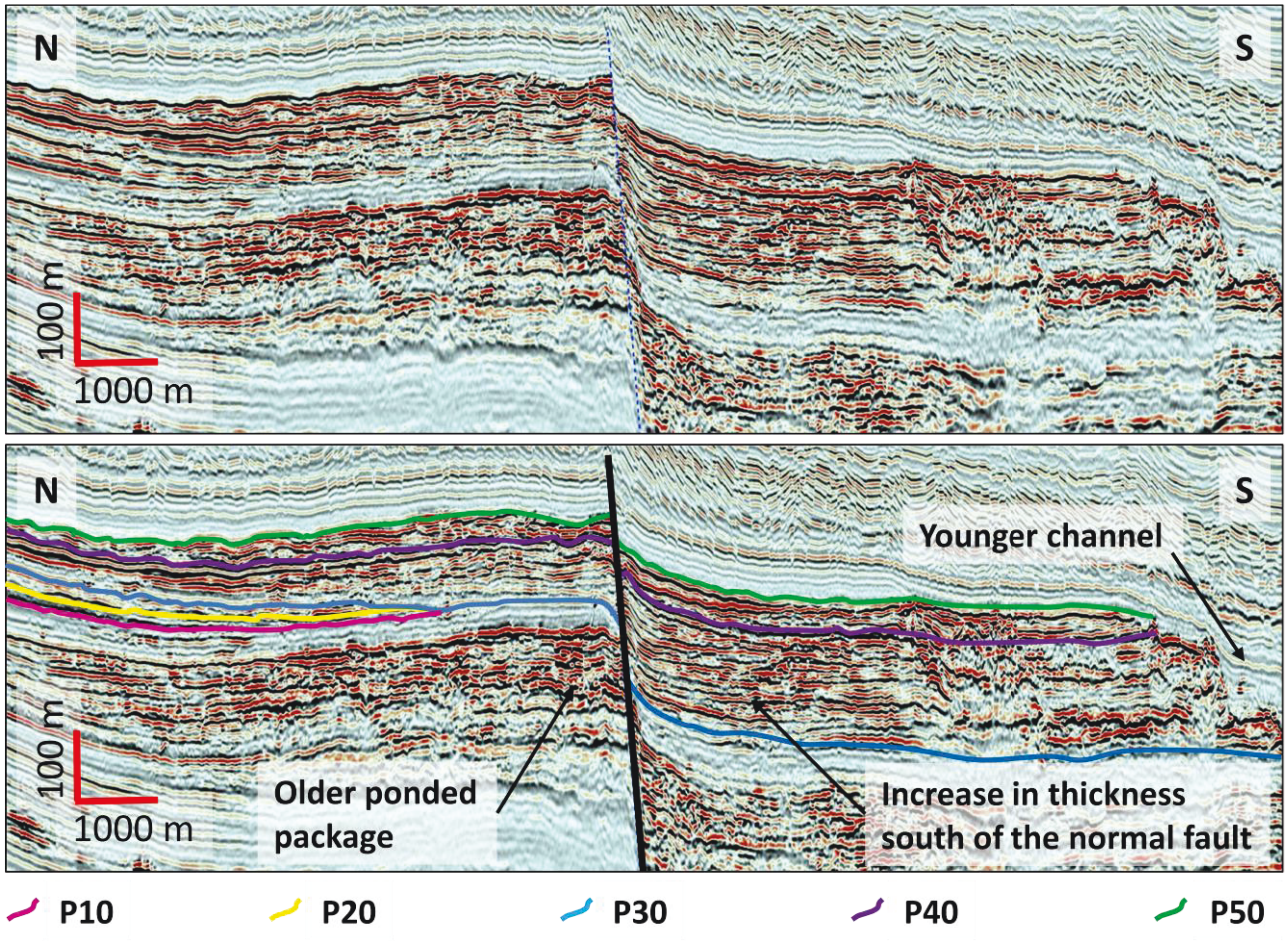


Figure 7.8 Section across the normal fault that cuts through the P30 – P40 unit and the P40 – P50 unit. The P30 – P40 unit almost doubles in thickness across this section of the normal fault. The second older ponded interval is clearly imaged beneath the ponded interval which is imaged here. A second younger channel is also imaged south of the normal fault which cuts through the ponded interval. Line location is shown in Figure 7.4.

The thickness of the units within the ponded interval varies through time. Assuming that the thickest part of the sedimentary packages correlates with the main sediment input point to the basin, Figure 7.9 illustrates a gradual change from the sediment entering primarily from the north of the area during the P10 – P20 unit to

sediment entering the basin primarily from the south of the area in the P40 – P50 unit. Between these two end points there is a continuous change which appears to occur in a step-wise clockwise rotation from the sediment entering from the northeast to an entry point in the southeast. The units identified here have been defined by their seismic characteristics and not by their duration and hence each occurs over a different time period, however we can see that the thickest sediment has been deposited within the P30 – P40 unit (Figure 7.9 (c)). The P30 – P40 unit is particularly interesting as the sediment appears to enter the basin through an area that contains an active salt body at present day, thus indicating that this salt was not active at the time of sediment deposition. Also during this period the thickest sediment is deposited in the southeast of the basin, directly to the south of the normal fault (Figure 7.9 (c)). Thick sediment is also deposited south of the normal fault during the P40 – P50 unit indicating that a similar sediment feeder system may have sourced both these ponded sediments (Figure 7.9 (c) and (d)). The normal fault that separates the north and south of the basin affects the sediment distribution from P30 times onwards. Prior to this the sediment packages thin towards the normal fault and terminate to the north of it (Figure 7.9 (a) and (b)). This thinning could be indicative of fault movement prior or during P10 – P30 times where movement on the fault caused rotation and tilting of the footwall to the northeast generating a relative topographic high along the length of the footwall.

Two younger channel complex systems occur to the north and southeast of the ponded unit (Figures 7.4, 7.7 and 7.8). The channel complex to the south of the normal fault cuts through the entire ponded unit and, as such, is younger than the ponded interval. Although the four youngest horizons, P20 – P50, terminate against the northerly channel system (Figure 7.7) the isopach maps show that the oldest packages, P10 – P20 and P20 – P30, thin away from this channel system thus indicating that they could be related to it (Figure 7.9). This channel system will be studied in detail in the subsequent section in order to determine whether it evolved at the same time as the ponded material or after it was deposited in the mini-basin. If it formed at the same time it may have sourced the fan lobe complex imaged in the P10 – P20 unit; with the ponded unit actually a crevasse splay formed as the channel turned north abruptly.

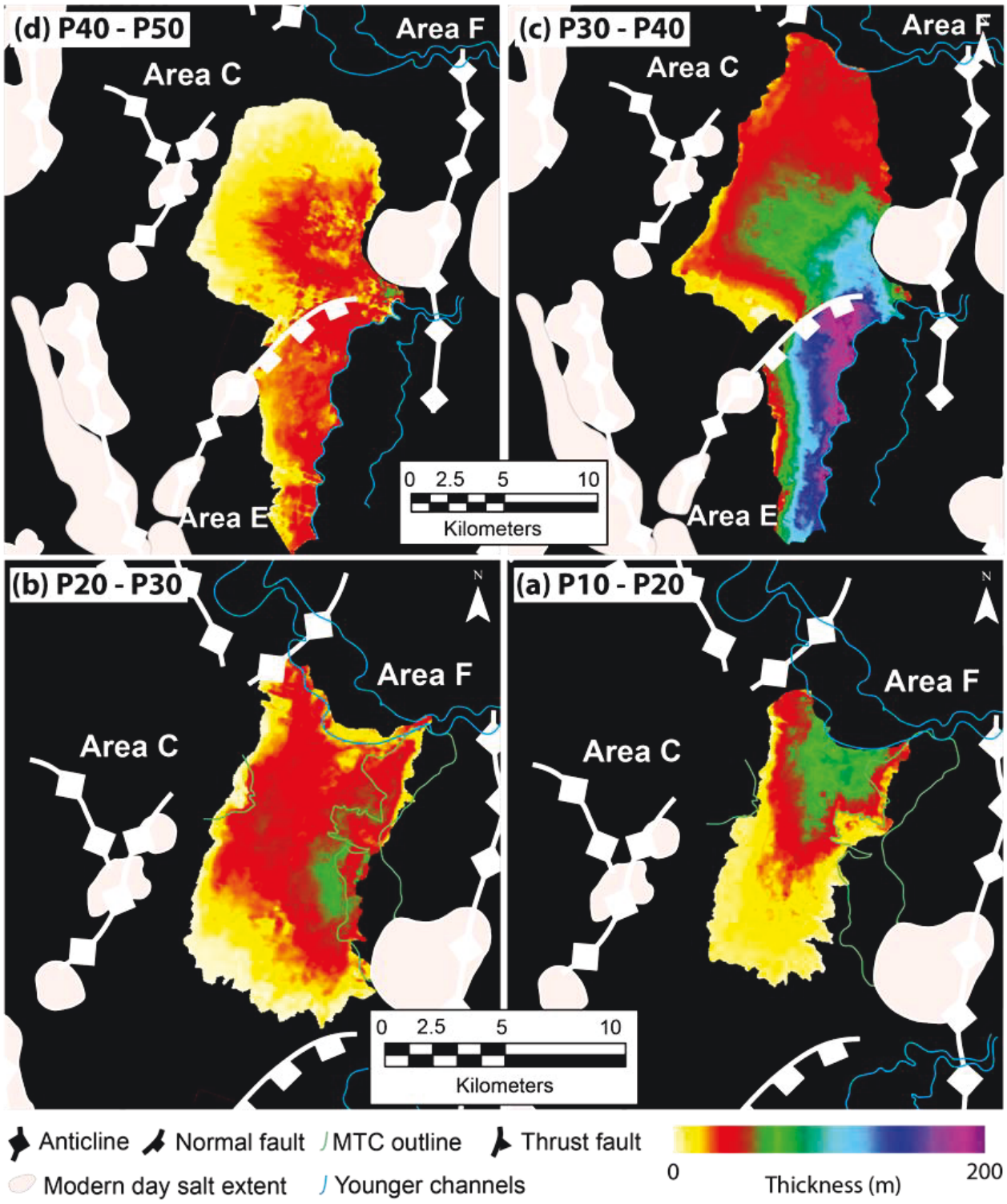


Figure 7.9 Isopach maps showing the sediment thickness through the ponded interval. In all images the thickness ranges from 0 m (yellow) to 200 m (purple) according to the scale shown in the bottom right corner; (a) the P10 – P20 unit (oldest interval) where the sediment is thickest in a triangle spreading out from the north-east and thinning towards the south, (b) P20-P30 unit which has thicker sediment either side of the previous high in the P10 – P20 unit whereas in (c) within the P30 – P40 unit the sediment is thickest in the southeast, something which continues in (d) P50 – P40 unit where the thickest sediment is again in the east of the mini-basin. Note how the distribution of sediment within the two oldest unitss is effected by slump deposits (mass transport complexes; MTCs).

7.6 Northern Channel Complex

A channel system cuts through the ponded sequence in the north of the region. As explained previously it is important to establish the origin of this feature and whether it is directly related to the ponded sediment package. The channel complex enters the mini-basin from the east in a topographic low between two anticlines, and then turns to the north as it encounters the topographic barrier along the western margin of the basin (Figure 7.4).

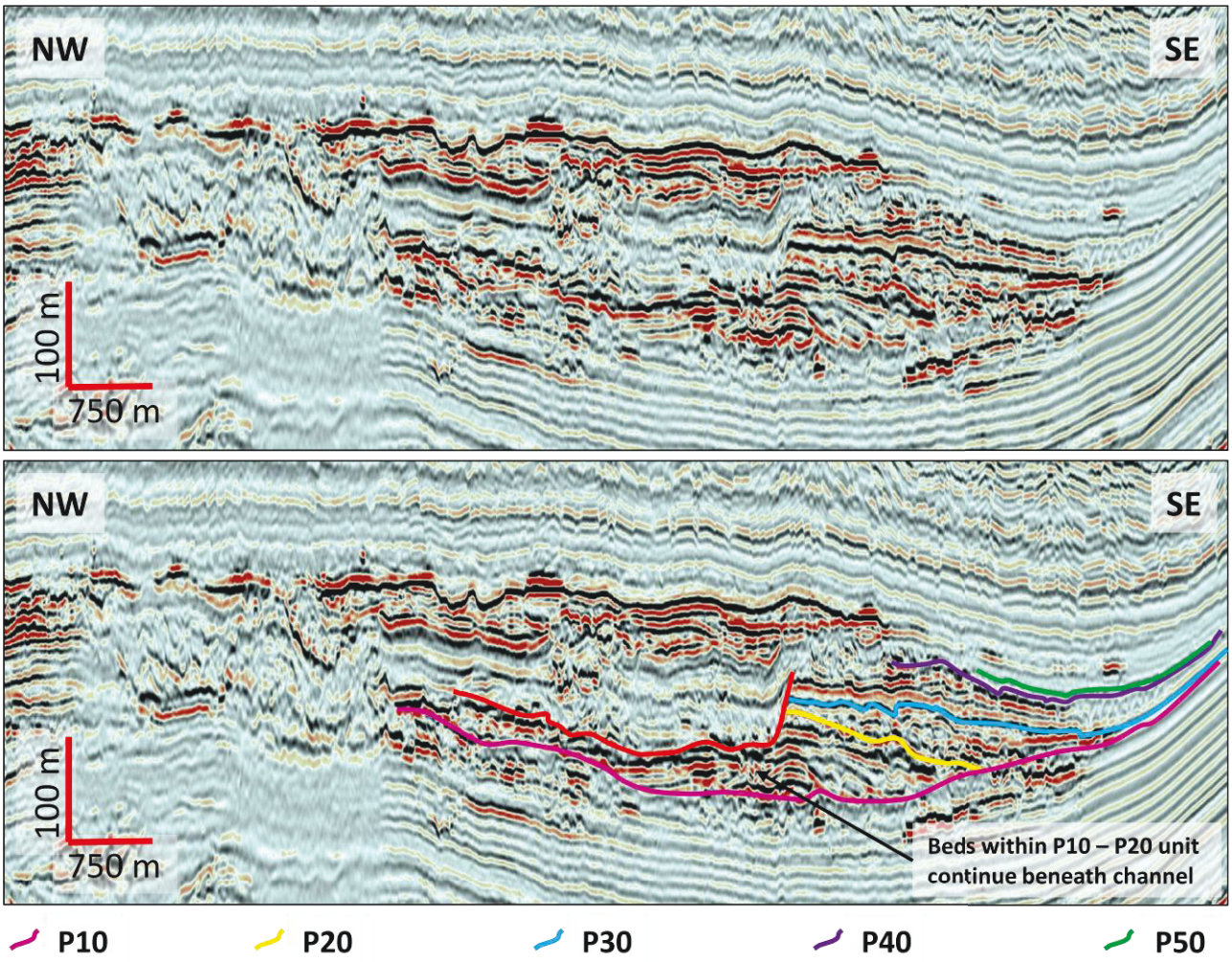


Figure 7.10 Cross-section through the channel complex in the north of the area. The P10 – P20 unit extends beneath the channel and, as such, was clearly active prior to the formation of this later channel complex. The edge of the channel complex is outlined in red and clearly erodes through units P10 – P20, P20 – P30 and P30 – P40. The P40 – P50 unit does not extend this far north. The line location is shown in Figure 7.4.

In order to investigate the origins of the four ponded intervals discussed in Section 7.5, it is first necessary to establish how this northern channel relates to them; whether it is a later feature which truncates the packages, or whether sediment gravity flows moving down the channel system sourced the distributary channels within the fan-lobes that make up the P10 – P20 and the P20 - P30 units. The channel system has a clearly defined erosive margin on its south-eastern side which truncates the P20 and P30 horizons (Figure 7.10) whereas the P10 – P20 unit contains beds which are continuous beneath the main channel cut. This implies that the channel complex is at least younger that the oldest parts of the P10 – P20 package.

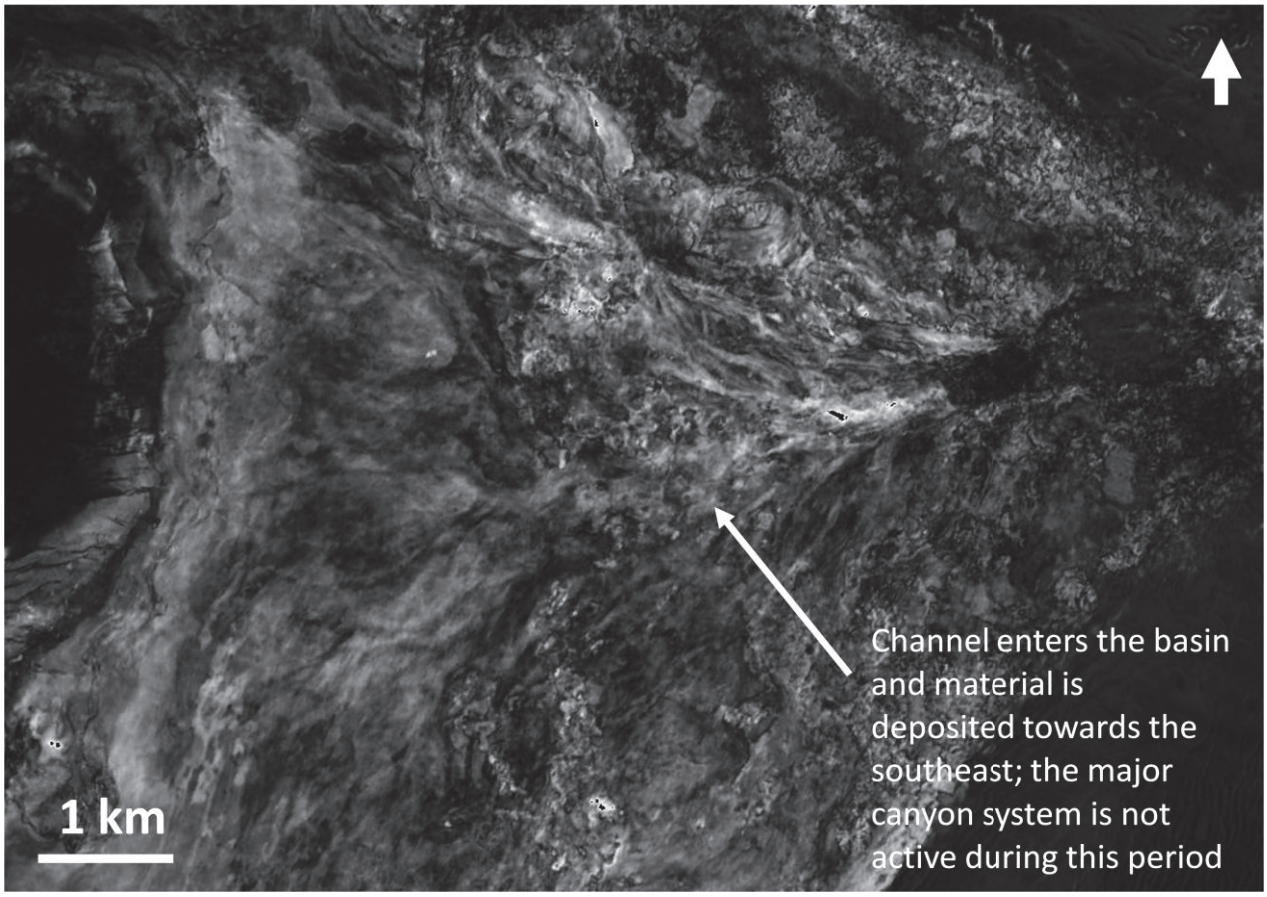


Figure 7.11 Root mean squared (RMS) amplitude extraction beneath the channel complex that cuts through the north of the area. This indicates that the channels that form the lobe complex within the P10 – P20 unit are sourced from a channel feeder system which enters the basin from the northeast and are not simply a crevasse splay feature that relate to the younger channel system in this area, a cross-section through which is shown in Figure 7.10.

The amplitude extraction made in a 20 ms twtt interval through the continuous beds between the P10 horizon and the base of the channel indicates that the channels within the P10 – P20 unit were fed by a feeder channel that entered the basin in a similar location to the younger channel complex, but at a different orientation (Figure 7.11). The younger channel complex turned abruptly northwards after entering the basin (Figure 7.12) whereas the channels in the P10 – P20 unit enter the basin and flow in a northeast – southwest direction. This clear entry point and swing to the south indicated in the amplitude extraction maps coupled with the fact that P10 – P20 unit extends beneath the base of the channel surface indicates that the P10 – P20 unit was sourced by an older system which entered the area through a similar entry point to the much younger channel cut. No evidence was found to suggest that the P20 – P30 interval was formed in a different manner and hence the P10 – P30 intervals are interpreted to be earlier fan lobe complexes sourced from feeder channels which enter the basin from the east, as opposed to channel overspill features from a long-lived channel complex.

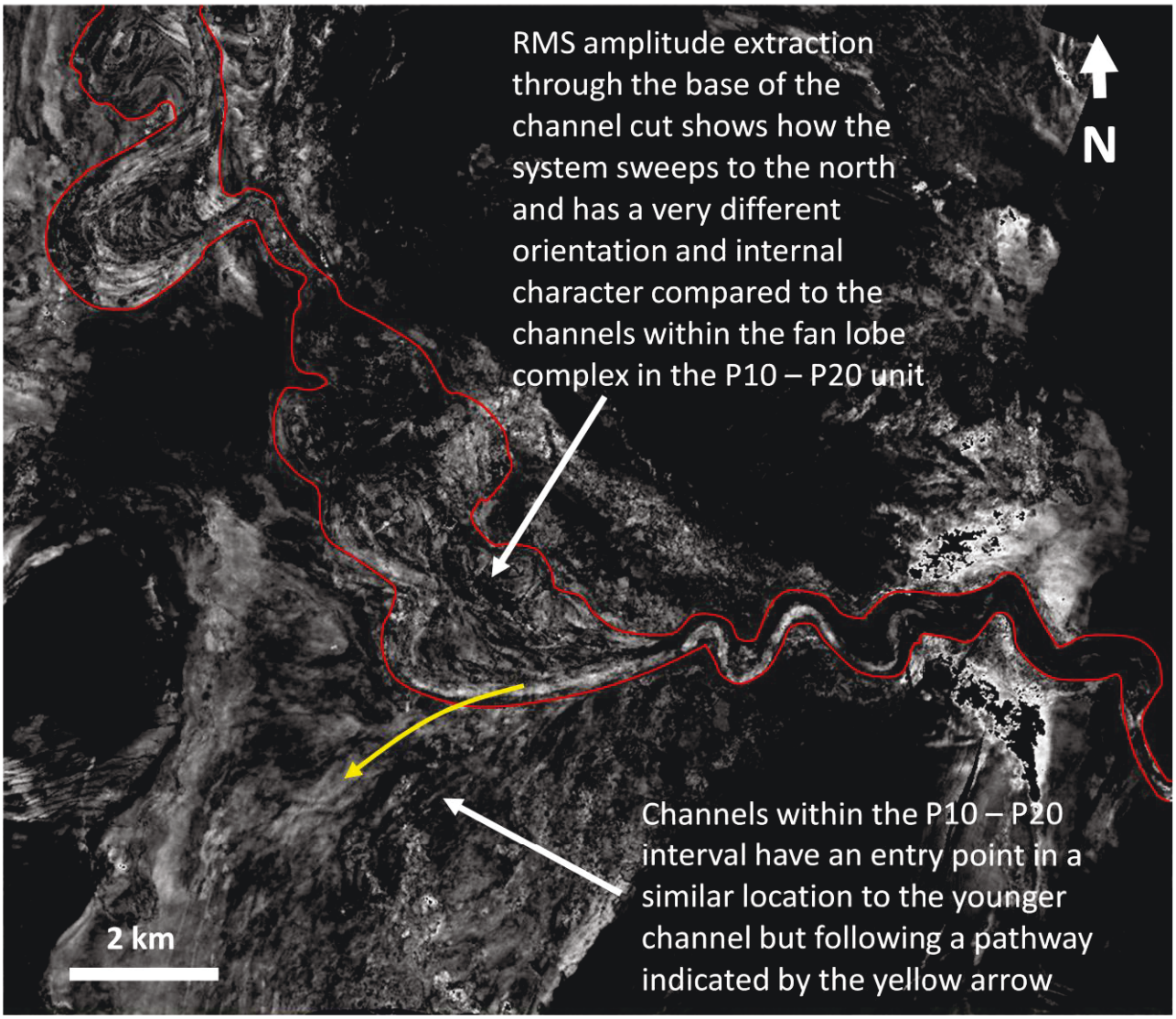


Figure 7.12 An RMS amplitude extraction map taken from within the channel system is outlined in red and superimposed on top of an RMS amplitude extraction taken from a 20 ms Twtt window within the P10 – P20 interval beneath the younger channel system. Note how the younger channel turns to the north in this area whilst the older underlying system swings to the south (as shown by the yellow arrow).

7.7 Ponded Interval Analysis

As discussed in Chapter 3, the submarine fan systems have been described following the scheme developed by Prelat et al. (2009) whereby the elements which make up the submarine fan are stacked to form progressively larger elements. This classification was developed in the Karoo Basin using outcrop data which enabled resolution down to the bed scale. Here, features down to the lobe element scale are identified within some of the RMS amplitude extraction maps. These lobe elements stack to form lobes which further can be grouped together as fan lobe complexes (Figure 7.13).

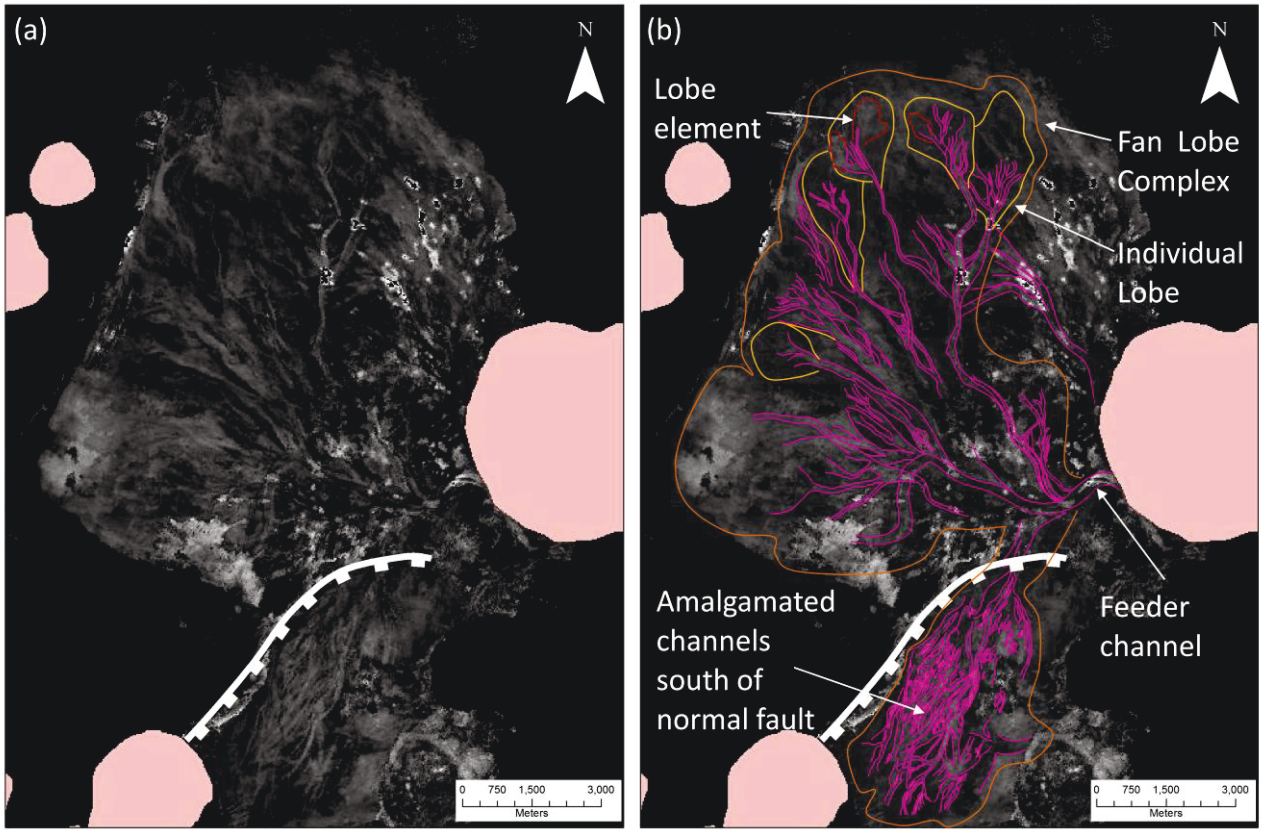


Figure 7.13 Fan lobe complex imaged using a root mean squared (RMS) amplitude extraction across a variable window (maximum thickness 25 m towards centre of mini-basin) with (a) uninterpreted and (b) interpreted with the lobe complex (orange), lobes (yellow), lobe elements (red) and channels (pink) highlighted. The present day salt diapir locations are also shown in light pink along with the normal fault, active at the time of lobe complex deposition (white).

Each fan lobe complex imaged in the mini-basin is fed by a single feeder channel which can mostly be imaged within the mini-basin. This channel branches to form smaller trunk channels down the axis of the flow resulting in the formation of a lobe which is formed of a trunk channel and a diverging network of smaller distributary channels commonly fringed by high amplitude sediment (Figure 7.13). The lobe is inferred to occur when the trunk channel starts to break down into its finest scale of splaying within the basin (see Chapter 3 for further discussion of this classification scheme).

Local slide deposits are also visible within some of the ponded intervals, particularly along the margins of the basin. These have been identified with a slightly dim chaotic seismic signature in cross-section and a generally low-amplitude disorganised, blotchy seismic signature in the amplitude extraction maps.

7.7.1 P10 – P20

The P10 – P20 unit is the oldest package within the ponded section. The deposit is triangular in shape thinning from 90 m in the north towards the southeast, east and west of the basin; confined in extent by the relative highs generated by the salt structures to the east and west (Figure 7.14). A later slide has cut out some of the sediment deposited towards the eastern edge of the basin (Figure 7.15) and, as discussed in Section 7.6, it is cut by the younger northeast-southwest trending channel system to the north.

A series of four isoproportional amplitude extractions through the interval indicate that the sediment entering the basin during this period was comprised of narrow, high amplitude channels. During the oldest interval

(Figure 7.15 (a)) these channels appear to have entered the basin from an entry point to the north-northeast of the younger channel complex that cuts down through this ponded interval (Section 7.6). This means that the part of the fan lobe complex imaged in this area is a more distal location. It is comprised of dispersed, small channels up to 25 m in width which branch frequently, but can ultimately be traced for a distance of up to 6 km into the mini-basin. The majority of the channels are orientated in a northeast-southwest orientation with a cluster of channels in the northwest corner oriented in a more east-west direction.

The next youngest interval, Interval 2, consists of channels which cover a very similar area to those observed within Interval 1, with slightly fewer channels on the eastern edge of the basin (Figure 7.15 (b)). At this stage the fan lobe complex is still comprised of multiple small, branching, high amplitude channels which are oriented in a primarily northeast-southwest direction along the axis of the mini-basin and are on average 90 m wide. Some features which appear more like typical lobes can be observed towards the southern end of the basin. Channels on the western edge of the basin appear to be responding to a topographic high in that area with a series of channels amalgamating to form one thick channel up to 50 m in width which bends away from the basin edge (Figure 7.15 (b)).

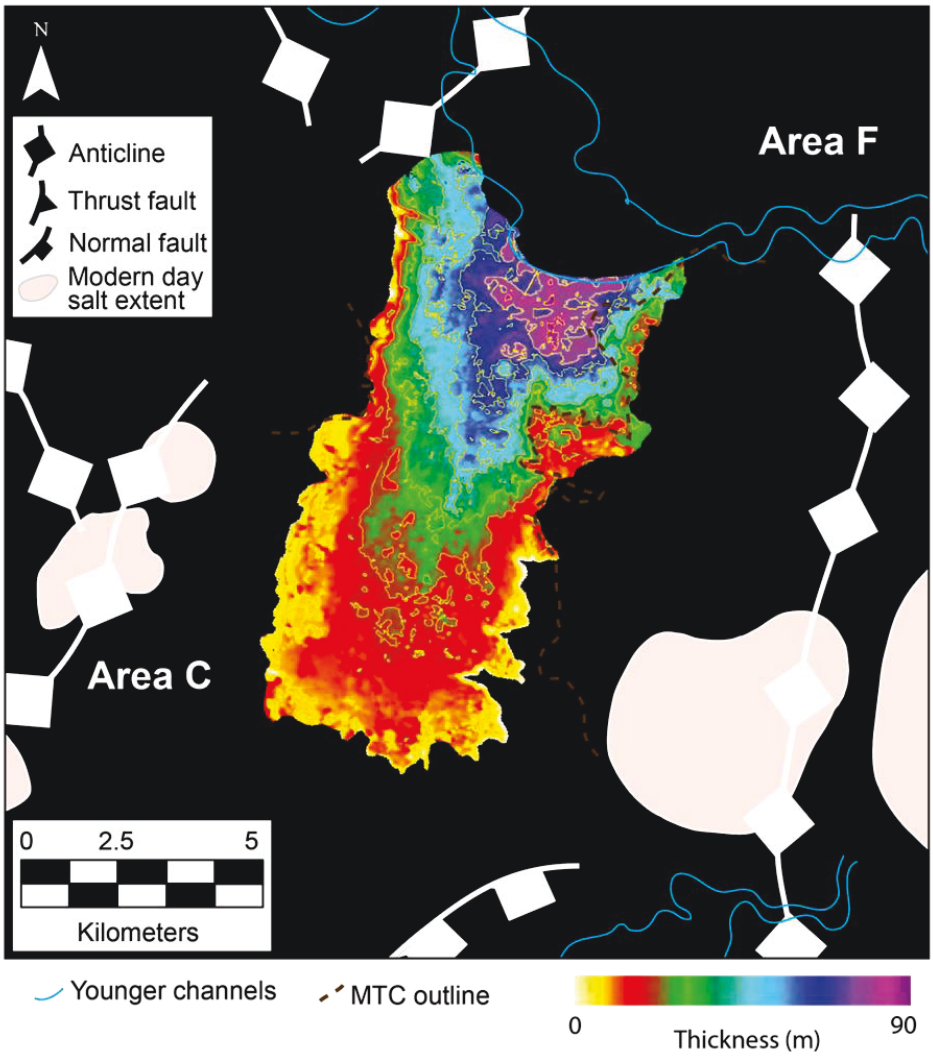


Figure 7.14 Isopach showing the thickness variations across the P10 – P20 unit. The edge of the slump deposits are highlighted with dashed brown lines, note how the eastern slump is related to a reduction of sediment thickness of the P10 – P20 unit in that part of the mini-basin.

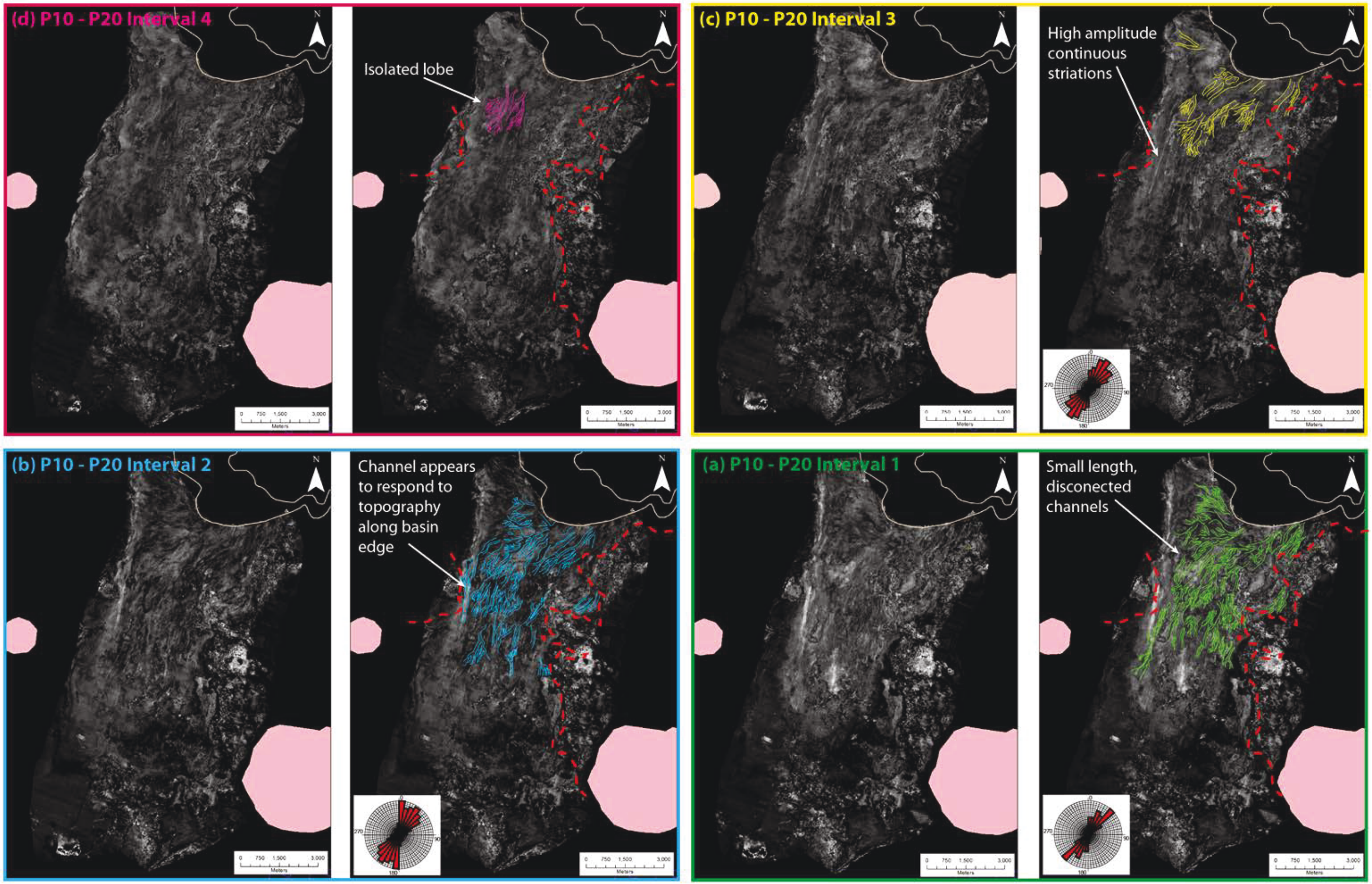


Figure 7.15 Isoproportional RMS amplitude extraction maps from four intervals within the P10 – P20 unit. Red dashed lines show the extent of the slump deposits and rose diagrams indicate orientation of channels within each interval.

As the system becomes younger it recedes from the basin with the maximum deposition point retreating closer to the sediment entry point in the north (Figure 7.15 (c) and (d)). At the same time these intervals both contain long, slightly curved, high amplitude lines that run from the north-northeast to the south-southwest of the mini-basin almost parallel to the western margin. These unusual features are only seen in these two amplitude extractions and do not appear to be linked to any obvious features in seismic cross-sections. It is possible that they have been formed by the activity of a mass transport complex (MTC) flowing along the basin axis with boulders and debris at the base carving scars into the basin floor. This activity could also be responsible for the fact that fewer channel systems are present during these two intervals. Interval 3 contains significantly fewer channels than seen in the previous interval with a cluster of more northeast-southwest trending channels in the north of the area extending approximately 3 km into the basin (Figure 7.15 (c)). Whereas within the youngest interval in the P10 – P20 unit it is only possible to identify one small cluster of channels in the northwest corner of the basin and MTC deposits dominate the eastern edge of the basin (Figure 7.15 (d)).

7.7.2 P20 – P30

Within the P20 – P30 unit the thickest sediment is deposited in the east of the basin within an 80 m thick sediment depocentre (Figure 7.16). The overall depositional thickness of the sediment is controlled by the thickness of the underlying package, the P10 – P20 unit, with the P20 – P30 unit thickest on either side of the main P10 – P20 triangular depocentre (compare Figures 7.14 and 7.16). Onlap of individual events within the P20 – P30 interval can be observed on the margins of the thickest part of the P10 – P20 unit, indicating that the underlying P10 – P20 package formed depositional relief within the basin during P20 – P30 times and influenced the position of flows entering the basin at this time (Figure 7.6). Part of the interval has been eroded and cut out by a subsequent MTC which appears to be contained primarily within the P20 – P30 interval and, as such, is inferred to have occurred immediately following the deposition of these sediments, but prior to the overlying package (Figure 7.6).

A series of four isoproportional RMS amplitude extraction maps through the P20 – P30 unit reveals the details of the channels and lobes that make up this package. The main feeder channel in the P20 – P30 unit enters the area from the northeast and follows a northeast-southwest trend (Figure 7.17). The oldest channels within the lobe complex shown in Interval 1, are partially cut by the local slide deposits in the northeast. However, it is still possible to observe some individual channels entering from a feeder channel in the northeast corner of the mini-basin as well as a cluster of smaller channels in the northwest corner of the basin (Figure 7.17 (a)). These range in size from 10 m, clustered in the northwest corner of the basin, to over 210 m where the main feeder channel enters the area (Figure 7.19). The small cluster of channels in the northwest corner of the basin which have a more lobe-like appearance appear to have a different origin to the other channels and may be linked to the lobe observed in this location in P10 – P20, Interval 4 (Figure 7.15 (d)). Overall, this is a different channel distribution pattern to that observed in the previous P10 – P20 unit

where the channels did not have a clear entry point, were more diffuse in their distribution and extended further into the basin.

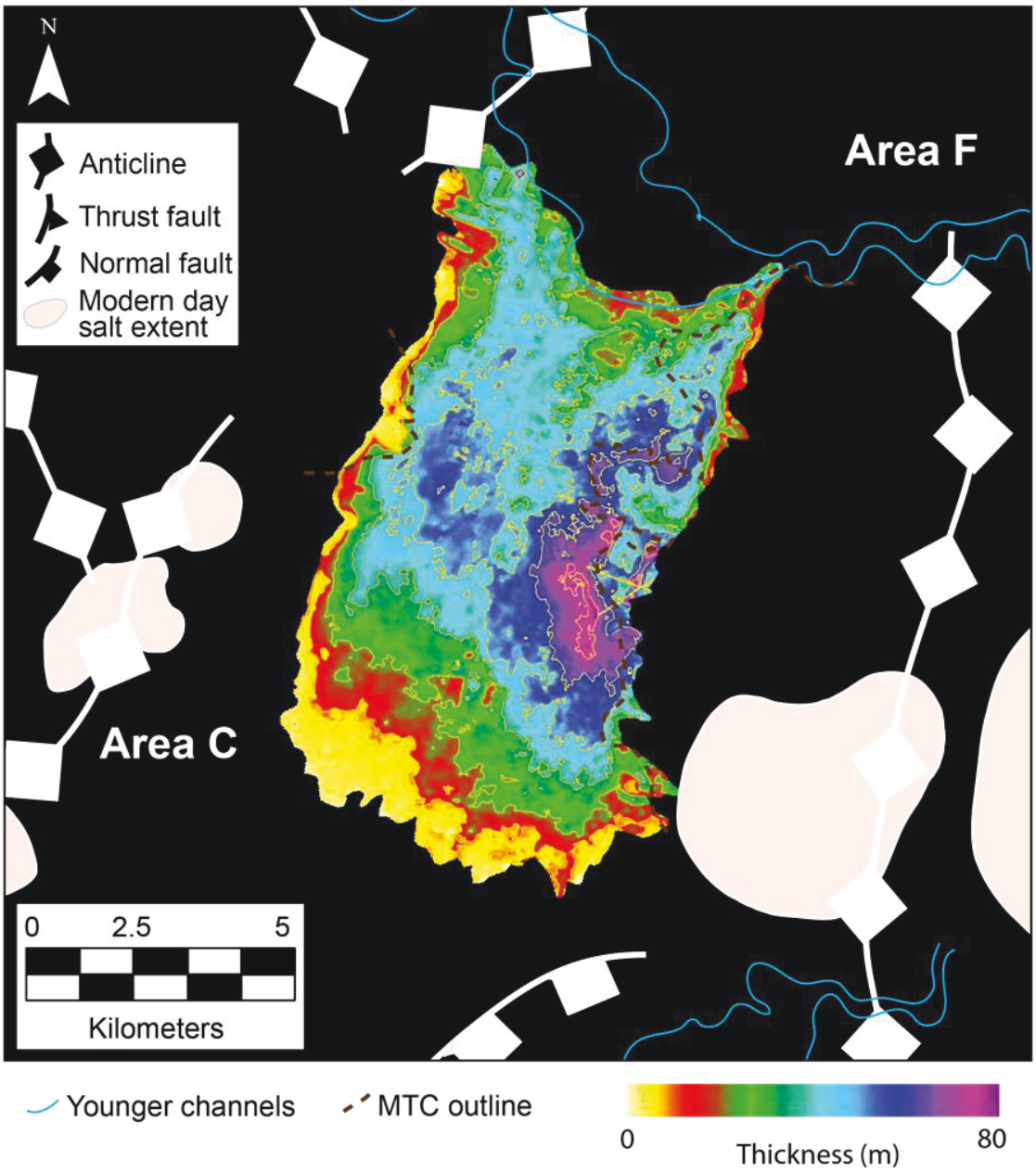


Figure 7.16 Isopach map showing the thickness variations across the P20 – P30 unit. It is interesting to compare the thickness patterns in this unit to that observed in the P10 – P20 unit (Figure 7.16) with thicker sediments in this unit distributed to the east and west of those in the preceding unit.

The next youngest interval within the P20 – P30 unit, Interval 2, contains a much better imaged and more established submarine lobe complex with one main feeder channel entering the mini-basin and splitting into at least four channels, each of which feed a lobe (Figure 7.17 (b)). Again, it is sourced from a main feeder channel in the northeast corner of the basin. The individual distributary channels range in size from 100 m up to 400 m in width, with the largest approximately 6000 m in length (Figure 7.19). The main channels have a slightly lighter amplitude signature and, as such, are thought to contain a higher sand percentage than the surrounding sediments. The channel systems all branch towards their ends and terminate in an area of between approximately 0.7 km^2 and 2.5 km^2. These areas are slightly lighter in amplitude and contain more

diffuse, narrower channels, which are interpreted as indicating the presence of lobes (Figure 7.17 (b)). The individual channel systems which branch within the lobes are harder to identify, which could indicate that they are below the resolution of the seismic data (i.e. thinner than 5 m). In this interval lobe elements and the lobe fringe are also not easily identifiable within the amplitude extraction map (Figure 7.17 (b)). The trunk channel systems which feed the lobes are deflected by a slide deposit the southeast of the basin; deflecting away from this towards the centre of the basin (Figure 7.17 (b)).

The fan lobe complex within P20 – P30, Interval 3 has a broadly similar feeder channel pattern to that of Interval 2 (Figure 7.17 (b) and (c)). The feeder channel enters from the northeast corner of the basin and has the same orientation as in the previous two intervals. However, in Interval 3 the channels are less constrained within the northeast corner and are slightly narrower (Figures 7.17 (b) and (c) and Figure 7.18). The feeder channels have a very similar orientation to the anticline which constrains the eastern margin of the mini-basin in Area F, with a few of them orientated almost straight and parallel to this. The channels extend further into the basin than in the previous interval with the fan lobes deposited closer to the edge of the basin (Figure 7.17 (b) and (c) and Figure 7.18), particularly in the southwest corner. The majority of the lobes are orientated northeast-southwest and occur within the western half of the basin. Again, it is not possible to easily discern the most distal lobe characteristics. However, the majority of the lobes are elongate in shape and range in area from about 1.7 km^2 to over 5 km^2, with multiple branching of the trunk channels observed. In this interval the channels are cut by a slide in the east; it is possible to trace them up to this deposit and exiting the other side, implying that the event occurred after the channels were active.

Channels become wider in the youngest interval within the P20 – P30 unit and there are less individual systems feeding into the area (Figure 7.17 (d)). Overall the amplitudes observed in the area appear to be higher than in the previous intervals, implying that there is more sand present in the system. The main feeder channel into the fan complex has a width of approximately 380 m which is significantly larger than the other feeder channels in the P20 - P30 unit (Figures 7.17 and 7.19). There are a series of well-defined lobes present towards the western edge of the basin within which very narrow channels are visible. Outside of the channels the lobes appear to be composed of low amplitude sediment and the high-amplitude lobe fringes imaged elsewhere in the system are not visible. The southwest corner of the basin contains a large area dominated by high amplitude signals. This may represent an area of sand deposited as one large fan lobe consisting of small channels within a sheet-sand beneath the resolution of the seismic data. It is tempting to suggest that the three lobes on the western edge of the basin represent a southward movement and lateral switching of the lobes within the fan lobe complex through time.

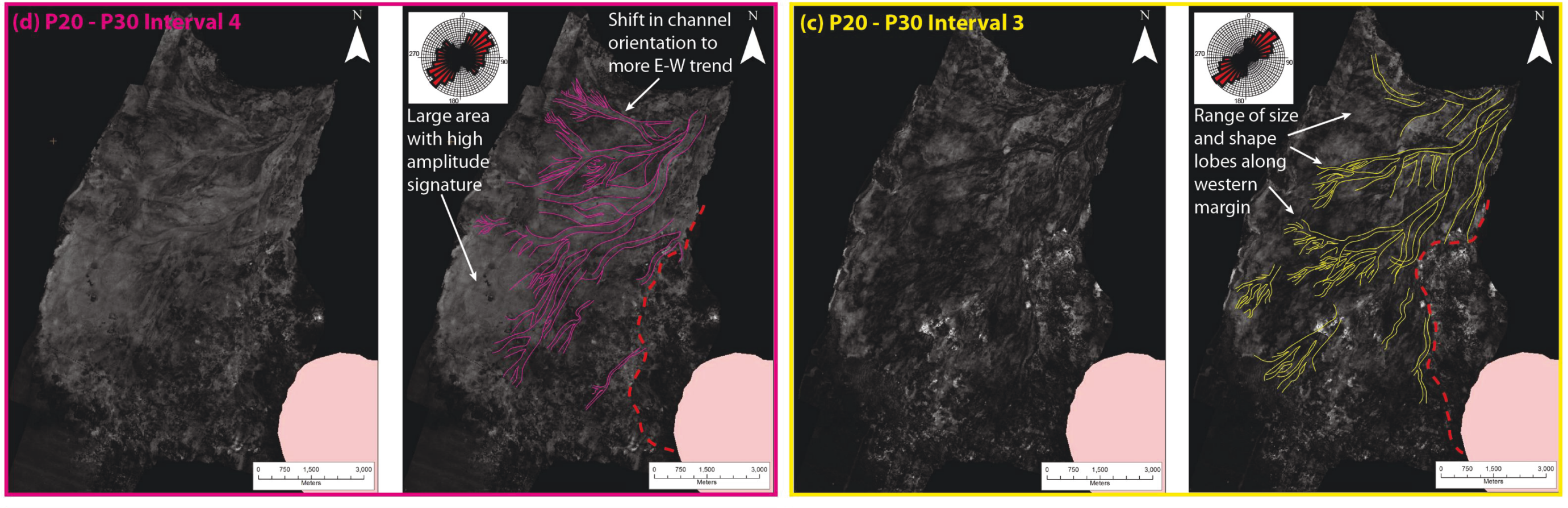


Figure 7.17 RMS amplitude extraction maps generated using isoproportional intervals within the P20 – P30 unit. Note how the extent of the slump deposit (dashed in red) has less impact on the channel distribution through time. Interval 1 is the oldest and Interval 4 is the youngest interval within the P20 – P30 unit.

By overlaying the channel outlines from the amplitude extractions it is possible to track some of the changes in the distribution of the lobes throughout the P20 – P30 unit (Figure 7.18). One of the clearest trends is the compensational stacking of the channels and the lobes (Figure 7.18). Within the two oldest intervals there are clear changes in the systems in terms of depositional patterns: in Interval 2 there are several instances where the location of the lobe has moved in order to switch away from a relative high generated during the deposition of channels in the previous interval (Figure 7.18 (a)). This has occurred in two main ways: either by the lateral movement of the fan body, or by progradation of the channel system further into the basin. Channel progradation appears to occur frequently with at least three of the systems prograding further into the basin as the available accommodation space within the basin becomes full (Figure 7.18 (b)). As the fan lobe complex develops further, the channels and corresponding lobes appear to take a step back towards the main feeder channel and away from the edge of the basin in the south of the fan lobe complex (Figure 7.18 (c)). However, there is also a change in style between the older and younger systems with the orientation of systems in the northwest of the basin changing; in the older fan lobe complexes the channels and the lobes both tend to trend north-south (i.e. Figure 7.18 (a), (b) and (d)) whereas the younger systems appear to primarily trend east-west (Figure 7.18 (c) and (d)). This could be in order to exploit a local topographic low, or alternatively may be driven by a structural change in the topography.

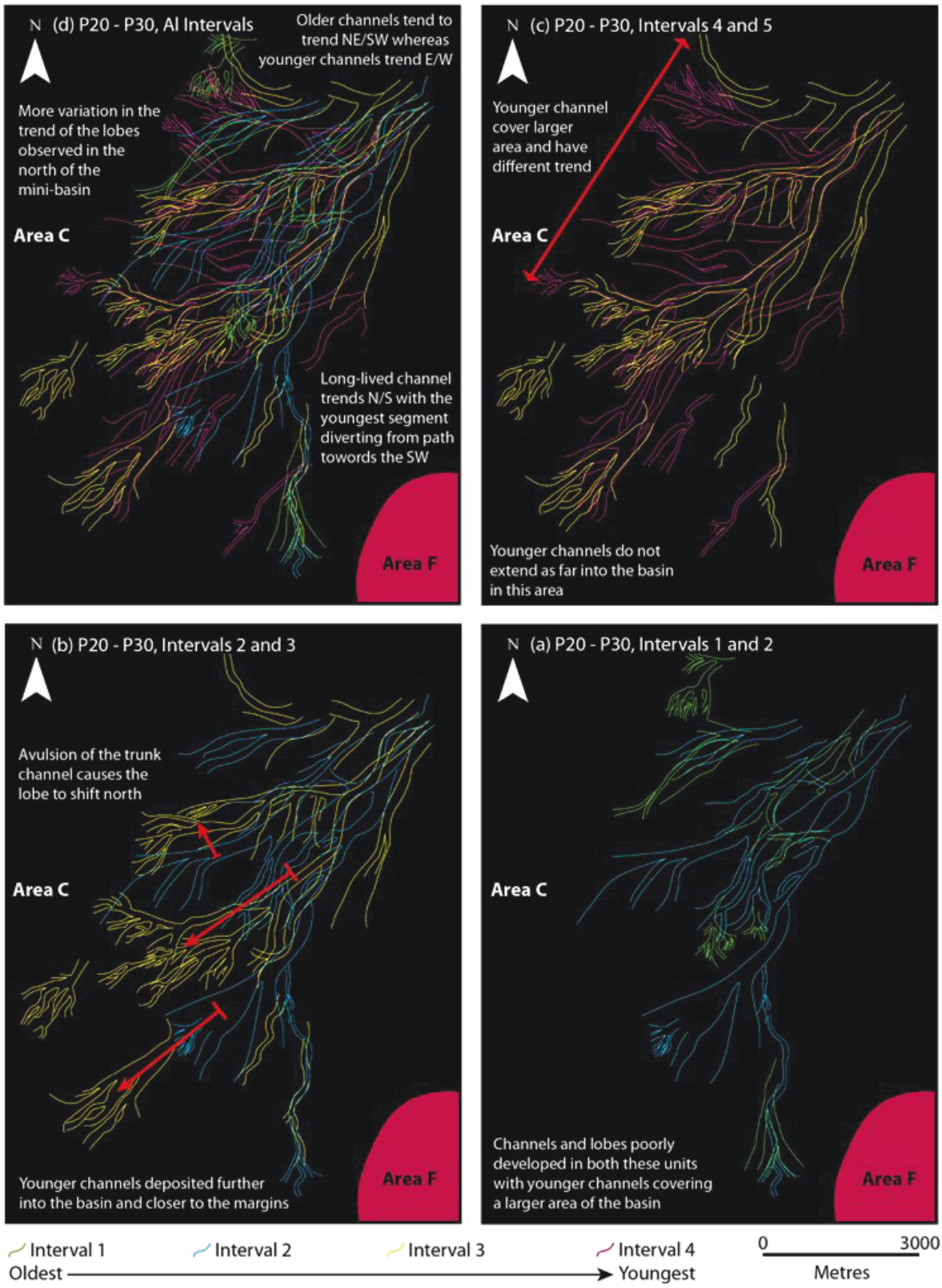


Figure 7.18 Annotated diagrams showing how the individual channels behave within the four intervals that comprise the P20 – P30 unit. Using these it is possible to identify periods when the lobes are stepping onto the basin and compensational stacking of the lobes which is particularly apparent in Intervals 3 and 4.

One channel system terminating in a lobe can be identified which has been active over the entire period. The lobe is located in the southeast corner of the basin and can be traced off the main trunk channel extending almost the length of the basin (Figure 7.18 (d)). During this entire period the main sediment entry point has

remained in the northeast corner of the basin and appears to be confined to a corridor approximately 1 km wide. The northeast corner of the mini-basin is one of the most interesting areas throughout the P20 – P30 interval. Here, the oldest channels enter from a single entry point, as well as from a minor entry point and small lobe in the northwest. This mimics what is seen in the P10 – P20 interval where the main entry point was from the north. However, as the system becomes younger the northeast-southwest trend dominates in the channels and controls the pathways with most sediment bypassing the proximal area of the fan complex and being carried deeper into the basin. In the final stages of fan development there is a third switch in channel orientation with the final system being deposited in a southeast-northwest orientation and the individual channels becoming more visible within the lobes (Figure 7.18).

Overall, a wide range of channel widths have been recorded within the fan lobe complexes in the P20 – P30 intervals. These range from 10 m to over 300 m in width depending on the location of the channels within the lobe complex. The modal width of all channels within these systems is between 30 m and 120 m (Figure 7.19), with the number of wider channels decreasing steadily until a maximum of 300 m width. There are very few channels recorded with widths of less than 30 m, however this could be in part due to the resolution of the seismic data. Overall, the frequency of the wider channels increases in the youngest sections through the fan lobe complex (Figure 7.19).

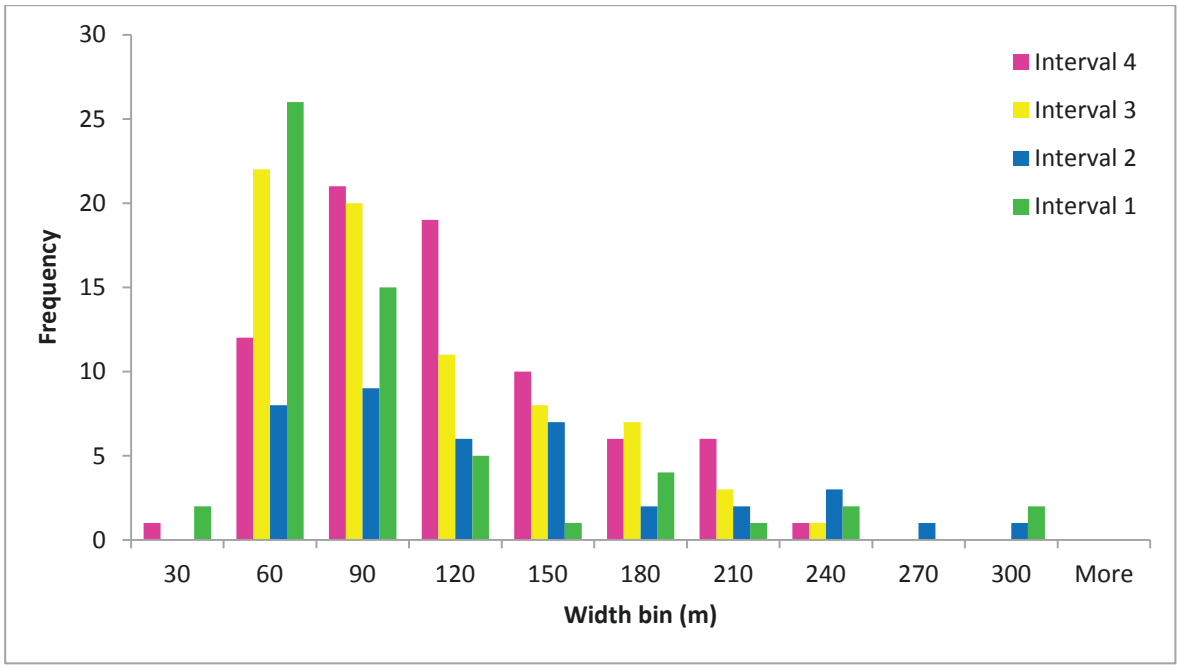


Figure 7.19 Histogram illustrating the range of channel widths within the channels in each of the intervals within the P20 – P30 unit. These channels were systematically measured towards the branching point to ensure consistency.

7.7.3 P30 – P40

This is the oldest ponded interval found both north and south of the salt-withdrawal normal fault. The sediment package is significantly thicker in the downthrown hanging-wall block south of the fault, with a maximum thickness of 120 m here as opposed to a maximum of approximately 80 m north of the normal fault (Figure 7.20). As well as being affected by the fault activity, the distribution of the main depocentre

north of the fault has also changed; the thickest sediment is found deposited in the southeast corner of the basin, as opposed to in the north and northeast in the previous time intervals (compare Figures 7.14 and 7.20). There is a clear thinning in the north of the area which could be due to the relict depositional topography in the previous interval. Although the P30 – P40 interval extends both north and south of the fault, the amplitude extractions show that the depositional fill within the two parts of the basin has responded differently on either side of the fault and therefore the northern and southerly sub-basins have been treated separately.

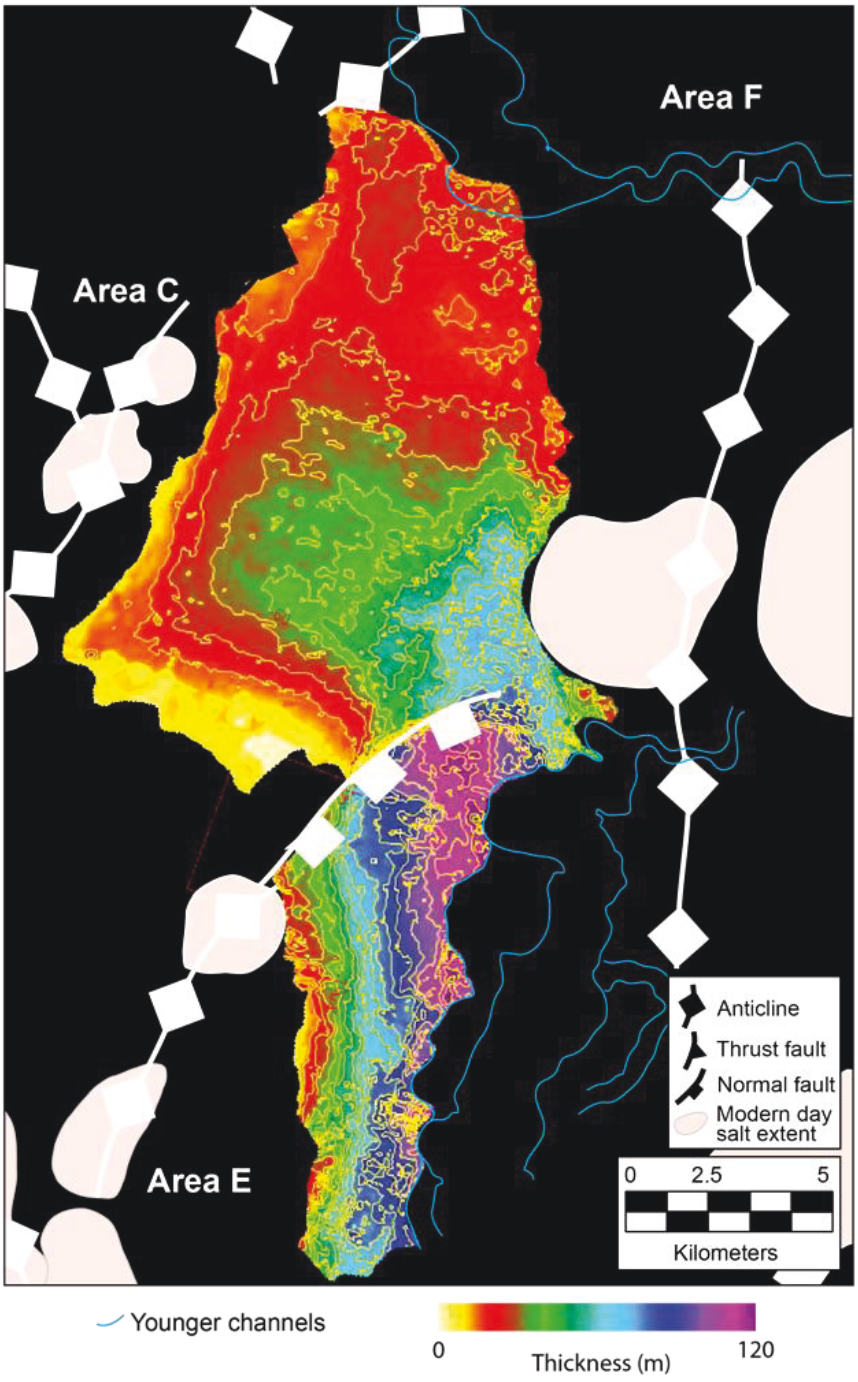


Figure 7.20 Isopach thickness map of the P30 – P40 unit. The sediment distribution is very different to that observed in the previous unit with significantly thicker sediment identified south of the normal fault. The slump deposit is not outlined in this interval as it no longer appears to impact the thickness of the sediment.

The oldest intervals in the P30 – P40 unit are dominated by MTC deposits (Figures 7.7 and 7.8). These extend throughout the basin and their origin is uncertain, but this increase in MTC activity does correspond to the switch in the sediment entry point during this period. This could suggest that either the MTC deposits in here are sourced from structures which have growth between the deposition of the P20 – P30 unit and the P30 – P40 unit or that they formed from structures that were exposed in the basin during a period of relative sedimentary quiescence. The P30 – P40 unit has been sub-divided into six intervals, however it is only possible to discern clearly defined fan lobe complexes within Intervals 3 to 6, and so these are discussed here.

Northerly Sub-Basin

The first interval contains evidence of widespread MTC activity throughout the area, whereas it is possible to identify some dispersed channels within Interval 2. Neither of these maps have been shown in Figure 7.21 as the image quality is so poor. However, a change in the sediment entry point can be observed between the P30 – P40 unit and the previous unit with the majority of the channels now trending east to west across the basin and an inferred entry point to the southeast, possibly beneath the present day salt location in Area F.

Interval 3 is poorly developed, consisting of multiple, high amplitude, narrow channels and lobe systems which extend almost to the western margin of the mini-basin (Figure 7.21 (a)). As per the other intervals within this unit, the main entry point for the channels has been cut out by later salt movement and concomitant MTC deposit development in the east, near Area F. Given the dispersed nature of the channels and lobes in the mini-basin it is likely that the feeder channel system was located further to the east. The trunk channels branch extensively towards their ends indicating the development of lobes, which are comprised of high-amplitude channels surrounded by low-amplitude lobe elements. Both the channels and lobes within this interval of the P30 – P40 unit trend southeast-northwest with the edges of the lobe complex defined by particularly high amplitudes (Figure 7.21 (a)). Within the mini-basin the channels in the south-eastern corner feed the clearest, most well-developed lobes whilst further to the north many of the lobes are deposited towards the centre of the basin.

The main channels, and the lobes that develop at the distal ends of these, step backwards away from the basin margin during the subsequent Interval 4 (Figure 7.21 (b)). This is particularly apparent along the southern half of the anticlinal structure within Area C, where the lobes are otherwise very well developed. The channels become harder to trace through the MTC dominated area in the southeast, but they do appear to be similar in width to previous intervals within this unit and branch to form lobes towards their ends. The channels enter the area from the southeast branching from a feeder channel now obscured by salt in Area F. The width of the area through which the channels enter the basin decreases between Interval 3 and Interval 4, suggesting that the feeder channel has moved closer to the basin in the east (Figure 7.21 (a) and (b)). There is a subtle change in the trend of channel orientation between this interval and the previous interval with these channels trending more to the northwest than in the previous interval (Figures 7.21 and 7.22). Overall, the lobe complex appears to be fairly unconstrained by topography during this interval and has a rounded shape on the basin floor.

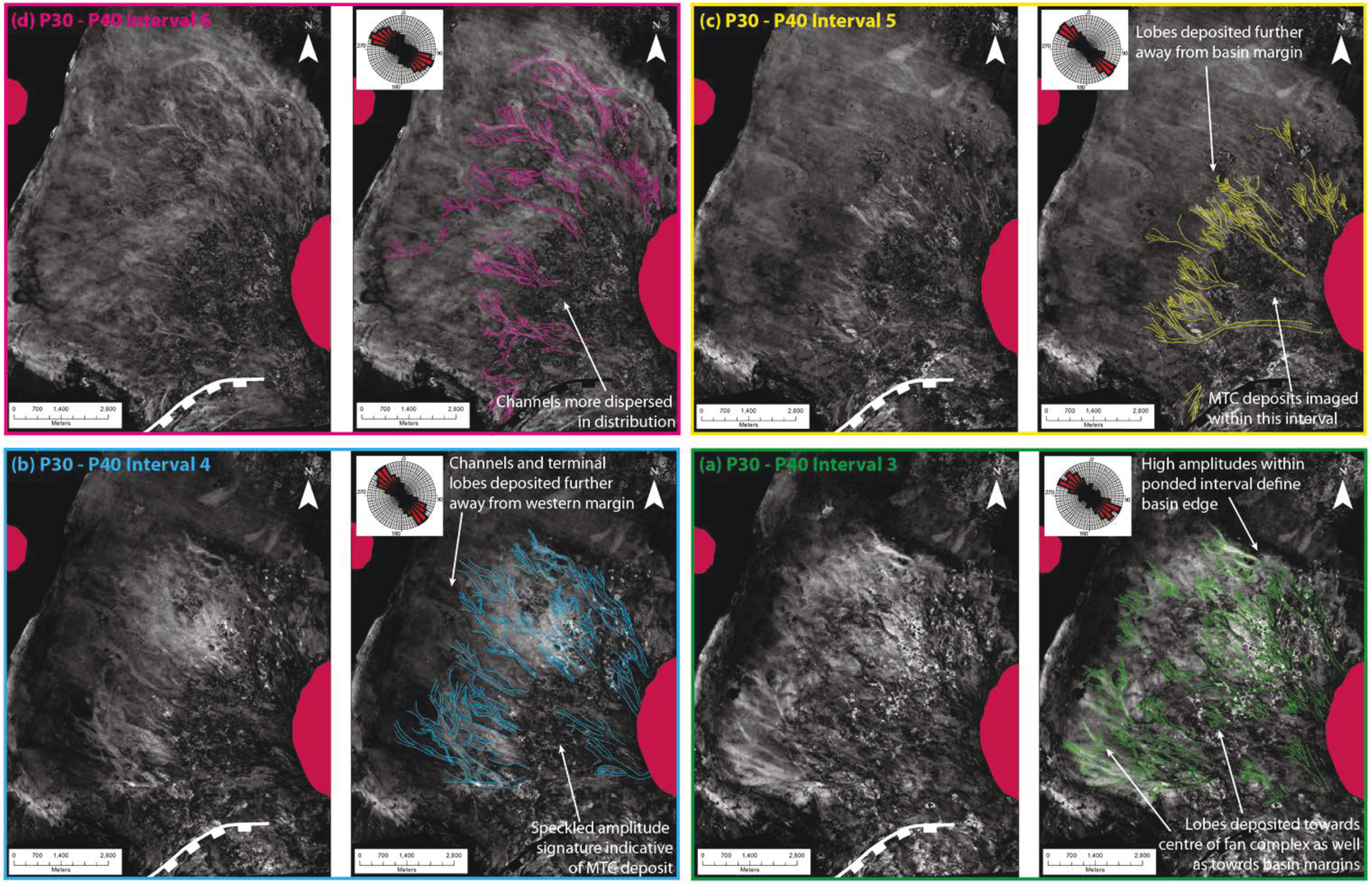


Figure 7.21 RMS amplitude extraction maps from the P30 – P40 unit north of the normal fault highlighting variations in the extent of the fan lobe complex through the history of the mini-basin. Note that maps start at Interval 3 as Intervals 1 and 2 contain predominantly MTC material.

The fan lobe complex imaged in Interval 5 has a distinctly different depositional pattern to that observed in the previous intervals within the P30 – P40 unit. The terminal edge of the sediment depositional area, as defined by the channel and lobe limits, has stepped back away from the edge of the basin with the channels now terminating on average 2 km away from the western salt wall as oppose to 1 km away in the previous few intervals (Figure 7.21 (c) compared to (a) and (b)). This implies that either there was more activity of the western salt wall during this period, or there may have been a change in the nature of the sediment supply or energy of the flows entering the basin at this time. The channels and lobes deposited within this interval are also more focussed in their extent, from which it is also possible to infer that one main feeder channel is located closer to mini-basin during this time. In Interval 5 it is clearly possible to trace the individual channel systems back through the area which has now been obscured by salt in Area F (Figure 7.21 (c)). There are five main channel feeder systems that enter in this area which we can infer will merge into one main feeder system some way east, updip of the ponded basin. The MTC deposit is still influencing the deposition of some of the channel systems, but extends a shorter distance into the basin possibly due to the fact that it generates less associated seabed relief as the basin becomes filled. The lobes are composed primarily of narrow, discrete, high amplitude channels surrounded by lower amplitude lobe elements, making it hard to discern the edges of the lobes (Figure 7.21 (c)). The trunk channels for these lobes are up to 150 m in width with the channels within the lobes as narrow as 40 m, overall the modal average channel width within this interval lies between 60 m and 90 m. The best-imaged lobe in the south of the mini-basin covers an average area of 1.8 km^3.

Within Interval 6 it is possible to observe a more distinct fan lobe complex containing clear channels and lobes (Figure 7.21 (d)). Trunk channel widths range from 80 m to 230 m and have a high amplitude signature, particularly towards the western edge of the basin, indicating the presence of extensive sandier sediments generally located in the lobes. The MTC observed in the other intervals again appears to impact the basin during this time with the channels being eroded by this later feature. The channels follow a predominantly straight pathway across the basin, with very little deviation from a west to west-northwest trend (Figure 7.21 (d)). The channels cannot easily be traced back to one central feeder channel in the area, implying that they originate outside the present day basin boundaries and that the basin may have extended further to the east during this time (i.e. the salt structure in Area F did not form any topographical barrier or obstruction). Four of the fan lobes terminate approximately half way across the basin whereas the other trunk channels branch to form lobes closer to the western margin of the mini-basin (Figure 7.21 (d)).

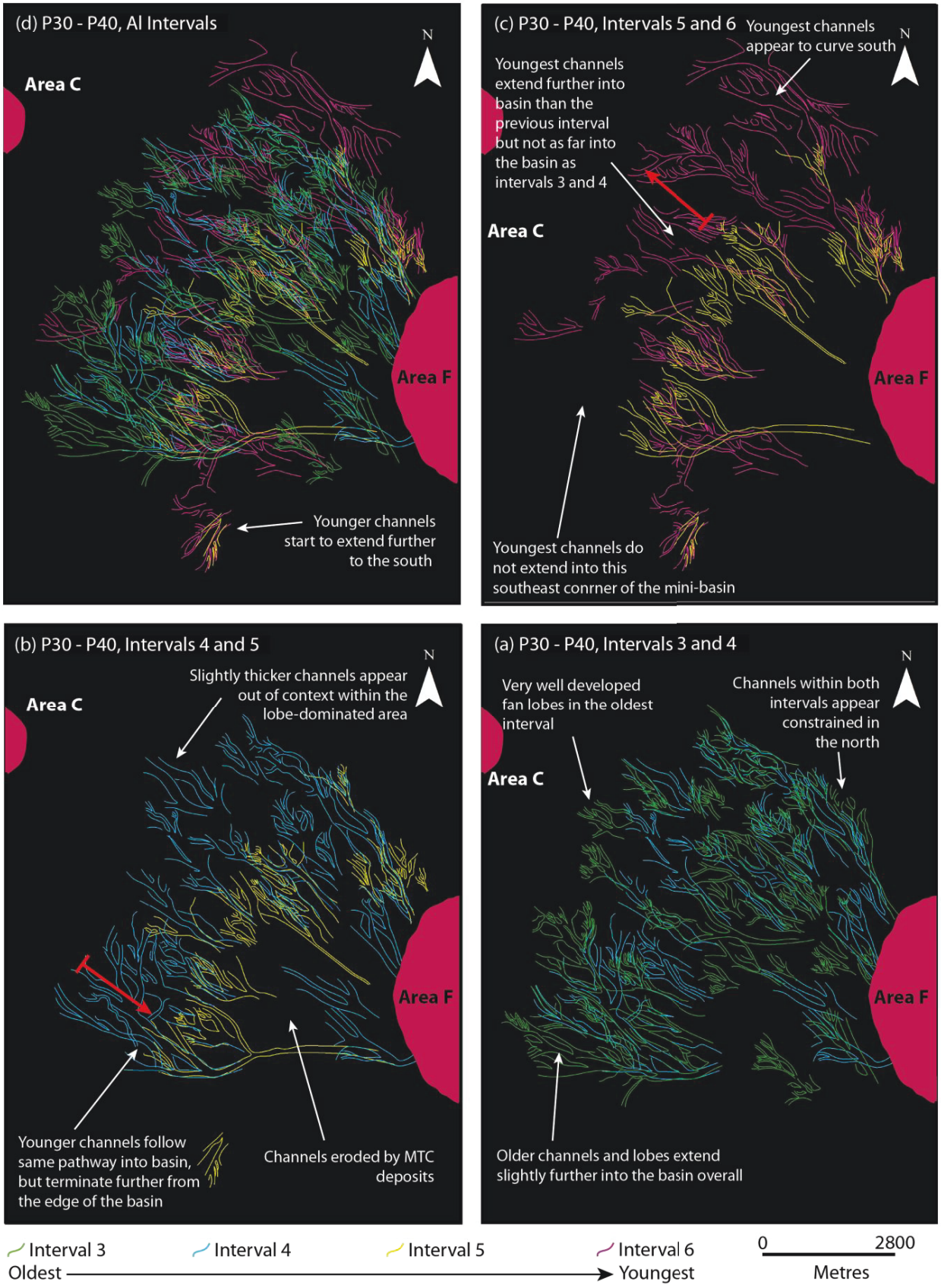


Figure 7.22 A series of sketches showing how the fan complex develops during the P30 – P40 unit. Note how the system steps away from the western edge of the basin during Interval 5. Compensational stacking at the lobe scale is also clearly visible between Intervals 3 and 4

The main development in the evolution of the fan lobe complex in the northern half of the mini-basin during the P30 – P40 unit is the variation in the western extent of the fan lobe; it steps away from the western edge of the basin during Interval 5 before prograding back into the basin in Interval 6 (Figures 7.21 and 7.22). The lobes deposited within Interval 6 appear less well developed than the lobes in Interval 5, indicating a change in the system entering the area. The movement of the distal extent of the lobe complex could indicate that the salt on the western edge of the basin may have been more active during this brief interval and generated a more prominent topographical high. The lobe complex covers a fairly large area throughout the history of the basin, with a slight change in channel orientation observed in the youngest intervals (Figure 7.22). One of the most striking observations from the composite map of the channels during this interval is that compensational stacking of the lobes occurred; lobes deposited in subsequent intervals infilled gaps between the channels and lobes in the previous intervals (Figure 7.22).

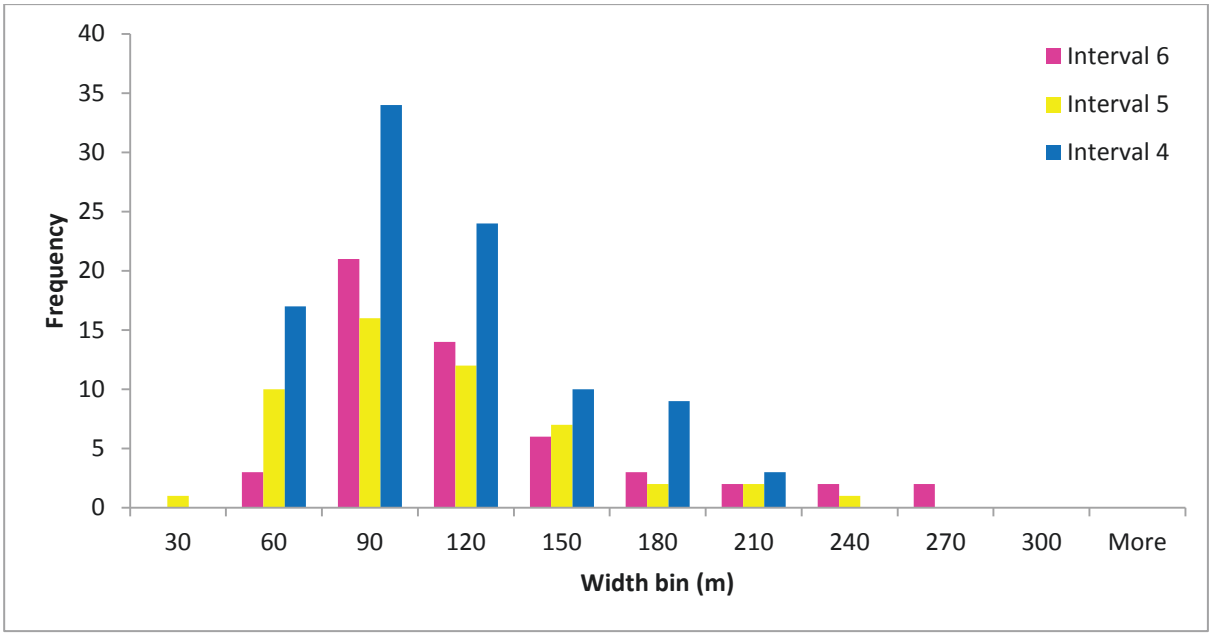


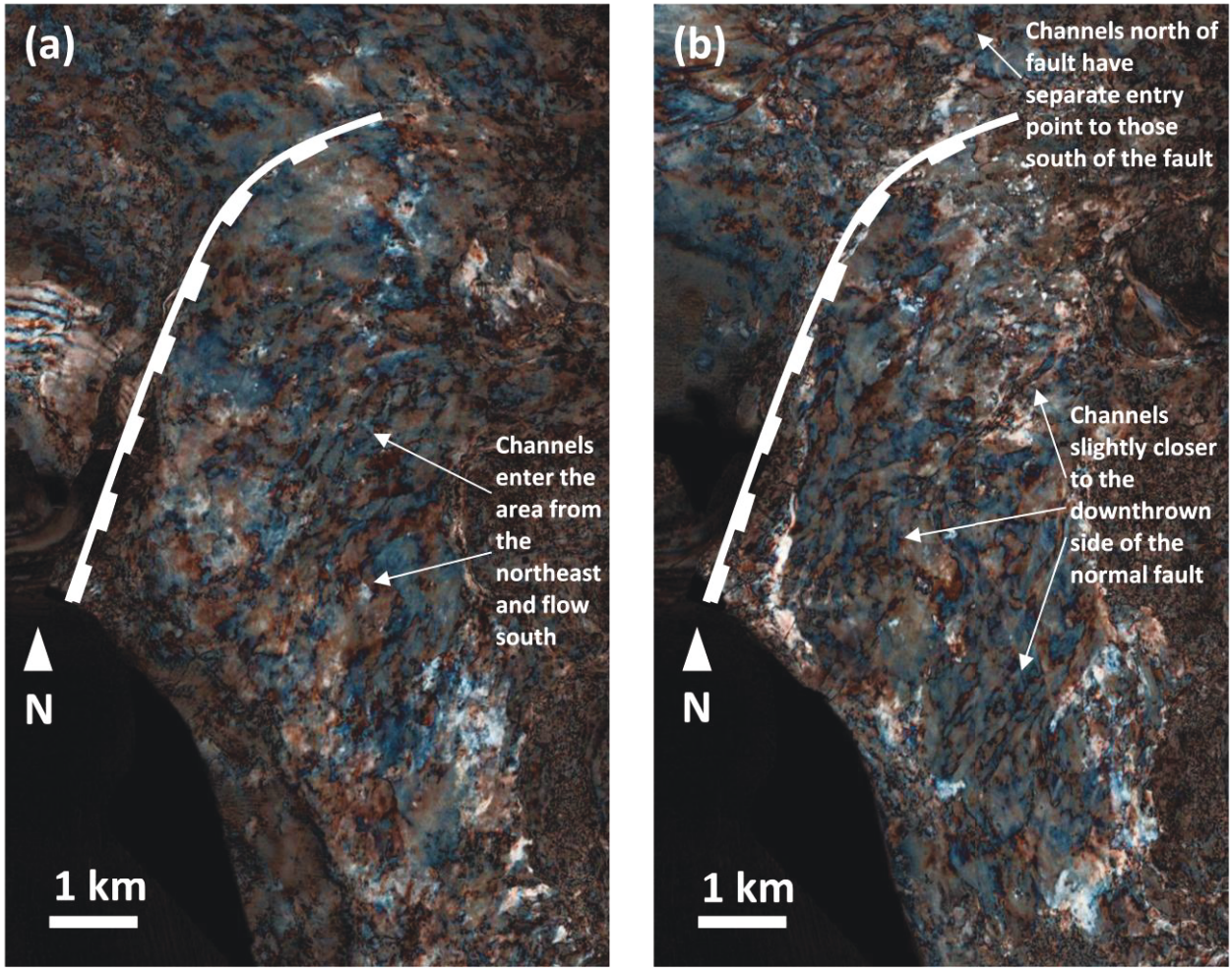
Figure 7.23 Bar chart illustrating the variety seen within the channel widths during the P30 – P40 unit with the majority of widths within the 60 m to 90 m width bin in all the intervals. Note that Interval 4 also appears to contain the highest frequency of channels overall within the P30 – P40 unit and bars are colour coded according to colours used in map in Figure 7.22.

Overall the pattern of channels and lobes seen in this fan lobe complex is different to that observed in the previous two units, P10 – P20 and P20 – P30. As well as having a different sediment entry point these systems contain much narrower channels with the majority ranging in size from 30 m to 180 m and a modal width of 80 m (Figure 7.23). The lobes at the distal end of these lobe complexes are more broadly distributed throughout the basin floor than in the previous units which could indicate a change in the energy of the system or a change in the grain size of sediment carried into the fan lobe complexes.

Southerly Sub-Basin

As previously mentioned, the section of the P30 – P40 unit which extends south of the normal fault has been treated separately for the purpose of this analysis. The amplitude extractions south of the normal fault were not included within Figure 7.21 as they did not show any interpretable details of the depositional facies through this interval. However, frequency decomposition blends generated through a flattened volume of

this interval do indicate that larger channel systems may have been present within the P30 – P40 unit south of the normal fault (Figure 7.24). These channels appear to have a separate entry point into the mini-basin from the channels north of the normal fault, they are slightly wider with widths of up to 300 m and trend in a broadly northeast-southwest orientation. The spectral decomposition does not indicate the presence of any terminal lobes in this area, but some of the younger channels do show branching towards their ends (Figure 7.24 (b)).



7.7.4

Figure 7.24 Frequency decomposition images showing channels south of the normal fault within the P30 – P40 interval with (a) an older slice compared to (b) a younger slice through the blended decomposition volume.

7.7.5 P40– P50

The P40 – P50 unit is the youngest within the ponded sediment package and also extends south of the normal fault. It has a maximum thickness of up to 75 m, concentrated just to the north of the fault and a locally thick depocentre immediately south of the fault (Figure 7.25). The isopach thickness map indicates that the thickest sediment volume has been deposited along a broadly east-west orientation north of the normal fault and within the northeast corner south of the normal fault (Figure 7.25).

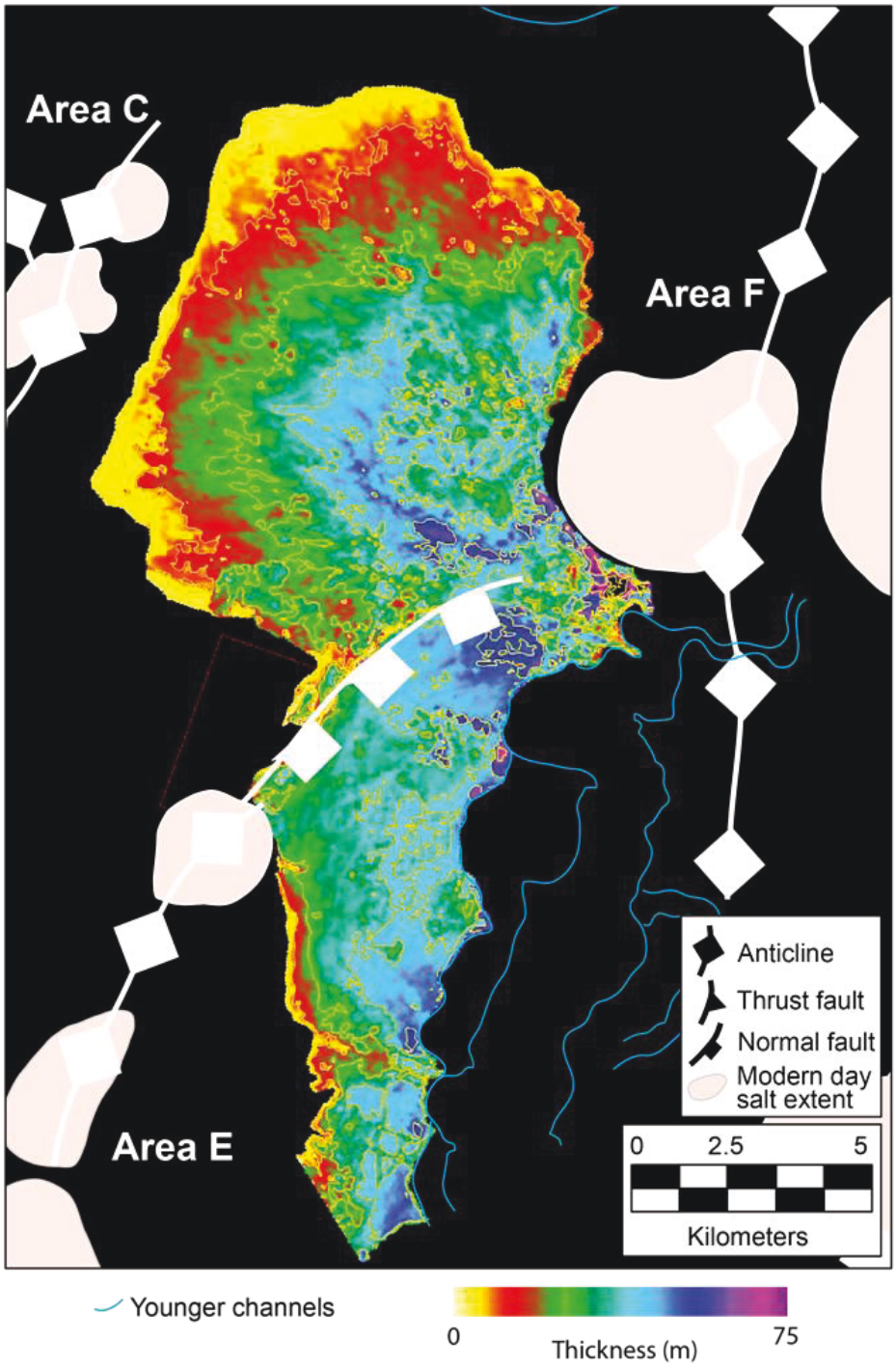


Figure 7.25 Isopach thickness for the P40 – P50 unit. Note how this unit extends south of the normal fault and the thickest sediment in the north follows a pattern mimicking the main channel systems within this interval (Figure 7.25). A younger channel complex in the south (blue line) has eroded part of the ponded sediment.

The P40 – P50 unit has similar lobe complex characteristics to the previous interval. However, the difference between the channels north and south of the fault and the impact this fault activity has on the ponded fan system varies through time as the amount of growth on the fault changes. As the system gets younger the normal fault appears to have had less of an impact of the lobe complex characteristics and the sediments entering the basin have a common entry point (Figure 7.26 (a) to (d)). As was done in the other units, four isoproportional intervals were generated through this unit to explore these relationships further and RMS amplitude extraction maps generated (Figure 7.26).

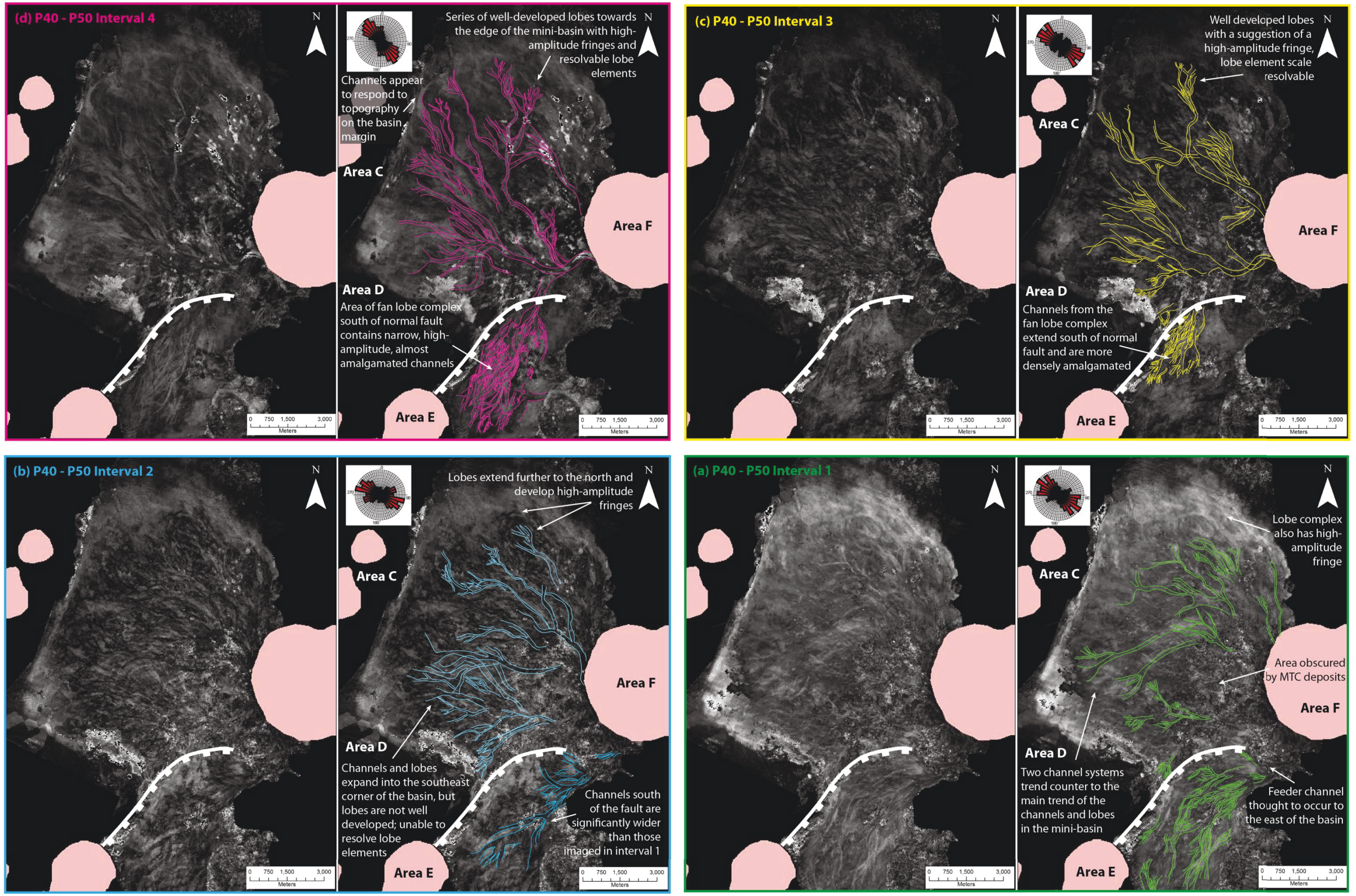


Figure 7.26 A series of isoproportional amplitude extractions from the P40 – P50 interval north and south of the normal fault. Note how the entire lobe complex in this unit has a high-amplitude fringe.

Within the northerly sub-basin the channels and corresponding lobes deposited in the oldest interval (Interval 1), have a broadly similar overall trend and distribution pattern to the channels seen in the previous interval (compare Figure 7.26 (a) to Figure 7.21 (d)). Again, a MTC appears to have partially eroded the channels in the east of the basin. There are three distinctly different channel orientations within this interval (Figure 7.26 (a)): in the north of the area the channels enter the basin from the southeast, directly below the present day Area F and then trend in a southeast to northwest direction; in the south there is a cluster of channels that trend from east to west and in between these two areas there are two very straight channels that trend in a different orientation from the northeast to the southwest across the basin. Overall, there are fewer lobes imaged here than in the later intervals (Figure 7.26 (a)) and the average channel width is also less, with an average of between 60 m and 90 m (Figure 7.28). The three different channel trends in the mini-basin are likely to all stem from a feeder channel in the east of the mini-basin. However, the links between these systems have been obscured by a subsequent MTC deposit and movement of the salt within Area F.

South of the normal fault within Interval 1 the channels enter from the east of the area and sweep towards the south in an arc shape that broadly follows the same orientation as the normal fault (Figure 7.26 (a)). The channels are clustered together and have a more amalgamated, braided style, most likely due to the topographic constraint imposed by the movement of the normal fault, which meant that the flows were entering a narrow, elongate depocentre. The channels appear to originate from a source outside the present day basin boundary, potentially linked to the source for the fan lobe complex in the northern sub-basin (Figure 7.26 (a)).

As the system becomes younger, the lobe complex expands into the available accommodation space. Within Interval 2 it is clear from the un-interpreted RMS amplitude map that the area is extensively channelised with the systems stacking on top of each other and forming a dense network of channels terminating in lobes (Figure 7.26 (b)). In this interval there still appears to be three distinct feeder systems for the three main lobes, but the entry point for all of three of these has shifted further south. The trunk channels contain more branches than in the previous interval and extend almost to the western edge of the basin. They appear to swing out from the main entry point area in an arc shape with the channels in the north trending southeast-northwest and those in the south trending east-west (Figure 7.26 (b)). The trunk channels range in width from 60 m to 225 m terminating in lobes which contain smaller high amplitude channels immediately surrounded by low amplitude sediment and in turn by a high amplitude fringe.

The channels imaged within this interval south of the normal fault are located further away from the normal fault and have a broadly northeast-southwest orientation; no longer trending parallel to the fault orientation (Figure 7.26 (b)). This could indicate that there was less movement on the normal fault during this interval and hence the channels were less constrained. The channels south of the normal fault are wider than those observed in the previous interval with widths of on average 300 m (Figure 7.28) and do not terminate in obvious lobes.

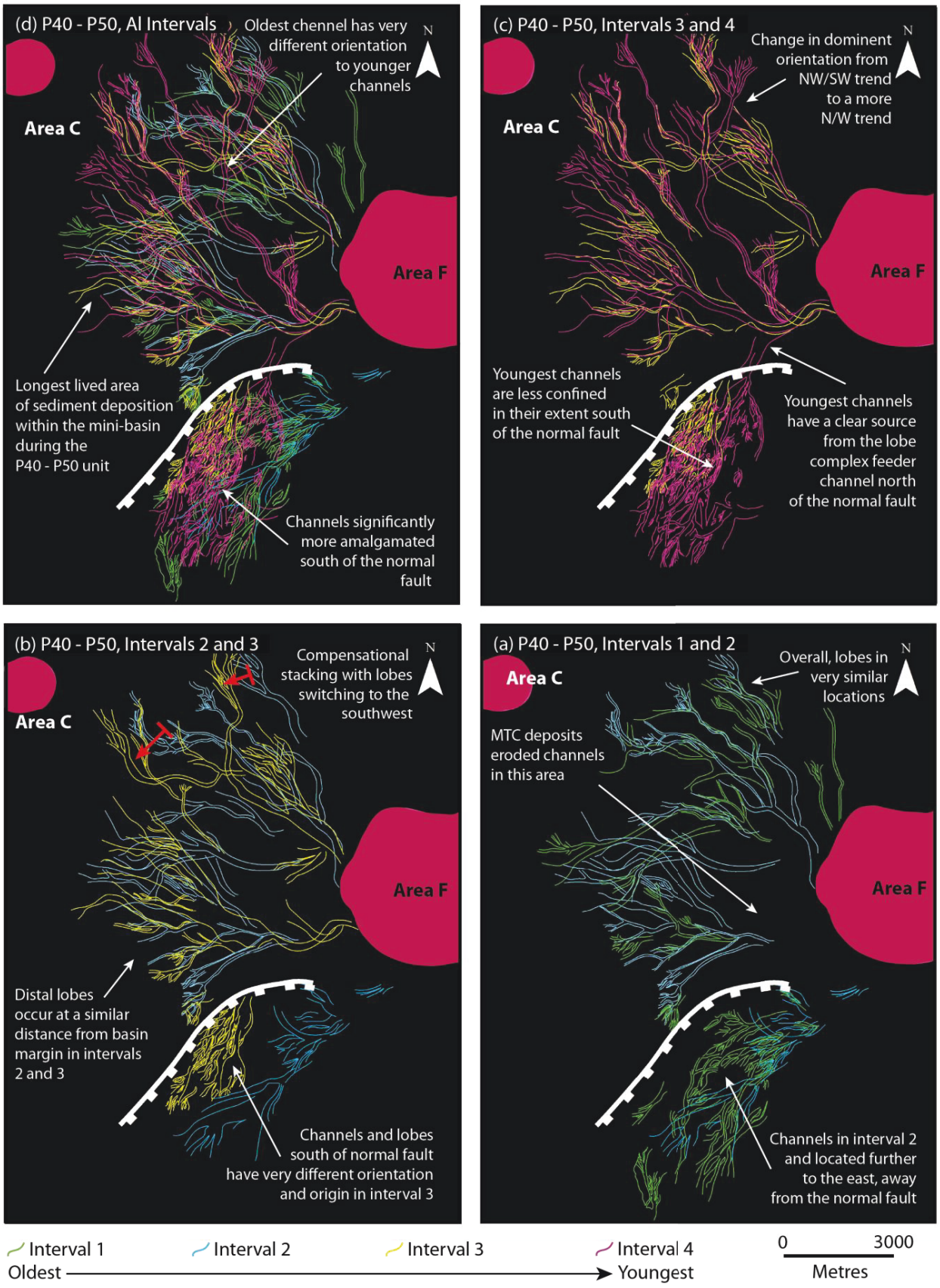


Figure 7.27 A series of diagrams showing how the channels within the ponded fan systems vary through the history of the basin within the P40 – P50 unit. This clearly highlights the change in channel orientation and entry point south of the normal fault.

Within the third interval two distinct channel feeder systems are observed north of the fault, both of which feed into fairly well established lobe complexes (Figure 7.26 (c)). The lobe complex in the north appears to be longer and thinner than the system in the south with a few well developed lobes at the distal end of the channels. The second fan lobe complex enters the basin further to the south and trends in a more westerly direction. The main feeder channel is approximately 350 m wide and has a slight bend before the whole system branches out and expands into the southwest corner of the basin. Channels south of the normal fault can be directly traced back to the fault and, as such, are interpreted as being linked to a splay from the southerly larger channel within the fan lobe complex to the north of the fault. The channels which form this splay feature are much narrower than the channels north of the fault (an average of approximately 40 m compared to 90 m north of the normal fault) and again trend parallel to the normal fault (Figure 7.26 (c)). This implies that there may have been some activity towards the southern end of the fault system during this time, but possibly not sufficient throw to prevent the channels from overtopping the relative high caused by rotation in the footwall.

The final stage of ponded fill in the mini-basin is represented by P40 – P50 Interval 4. A single entry point is now evident from the southerly part of the salt diapir (Figure 7.26 (d)). This feeder channel branches into three main systems which spread, extending further into the basin than any of the older lobe complexes within the P40 - P50 interval. The trunk channels diverge and branch into lobes at their termination near the basin edge, particularly towards the western and northern basin margins. These lobes are comprised of high amplitude channels surrounded by low amplitude lobe elements and fringed by a high amplitude band. This high amplitude band is up to 150 m wide surrounding the lobes in the north of the area, with the high amplitude suggesting that the fringes are composed of sandier sediment than the lobe elements (Figure 7.26 (d)). The channels can be continually traced up to 7 km away from the main sediment entry point (Figure 7.26 (d)). There is some indication in the northwest corner of the basin that the orientation of the channel systems is driven by the orientation and growth of the structures along the edge of the basin with one of the channels deflected to the north parallel to the salt-cored anticline.

The channels south of the normal fault can be traced back across the fault and form one of the three main branches of the feeder channel (Figure 7.26 (d)). Whilst the origins of this section of the fan lobe complex is the same as that observed north of the normal fault the characteristics of these two systems are very different. South of the normal fault, within the hanging wall, the lobe complex consists of significantly thinner channels which are almost braided in appearance, and somewhat similar in style to the channel system developed in this area within the first interval in the P40 – P50 unit. These channels follow an orientation similar to that of the normal fault but extend further south than those seen in Interval 3. Again, this suggests that the fault may have been active towards its southern tip during this period generating a more elongate restricted basin.

Compilations of the fan lobe complexes super-imposed on top of each other during this interval reveal how the system develops through time and how the channels and lobes shift within the P40 – P50 unit (Figure 7.27). North of the normal fault, Intervals 1 and 2 follow a broadly similar pattern with two main

areas of deposition: one in the north and one in the south. Both these main depositional areas are composed of highly branching, stacked channels with the northern channels trending southeast to northwest and the channels in the south following a broadly east-west trend. There is some evidence of compensational stacking between Interval 2 and Interval 3 with the later channels tending to follow pathways that have not been previously exploited by the older channels (Figure 7.27 (b)). By the time of the youngest interval, Interval 4, very little sediment is entering the basin from the more northerly sediment entry point; the remaining system appears to be fairly short and does not extend as far into the basin as the other older channels did in this area. In contrast the feeder channel in the south of the northern sub-basin has formed the main sediment supply to the area. Here there are three main branches to the feeder channel with the main one following a very similar pathway to that seen in Intervals 2 and 3, supplying sediment to the western corner of the basin, and new systems developing to either side of this depositing sediment north and south. The new system north of the normal fault trends broadly north-south with the main sediment flowing from the south to the north in direct contrast to the trends seen in the P10 – P20 and P20 – P30 intervals. This channel system also appears to run almost perpendicular to the previous channels in the basin observed in the P40 – P50 unit. This may be a response to either a change in the bathymetry of the basin, or the infilling of the north-eastern portion of the basin by the previous sediments.

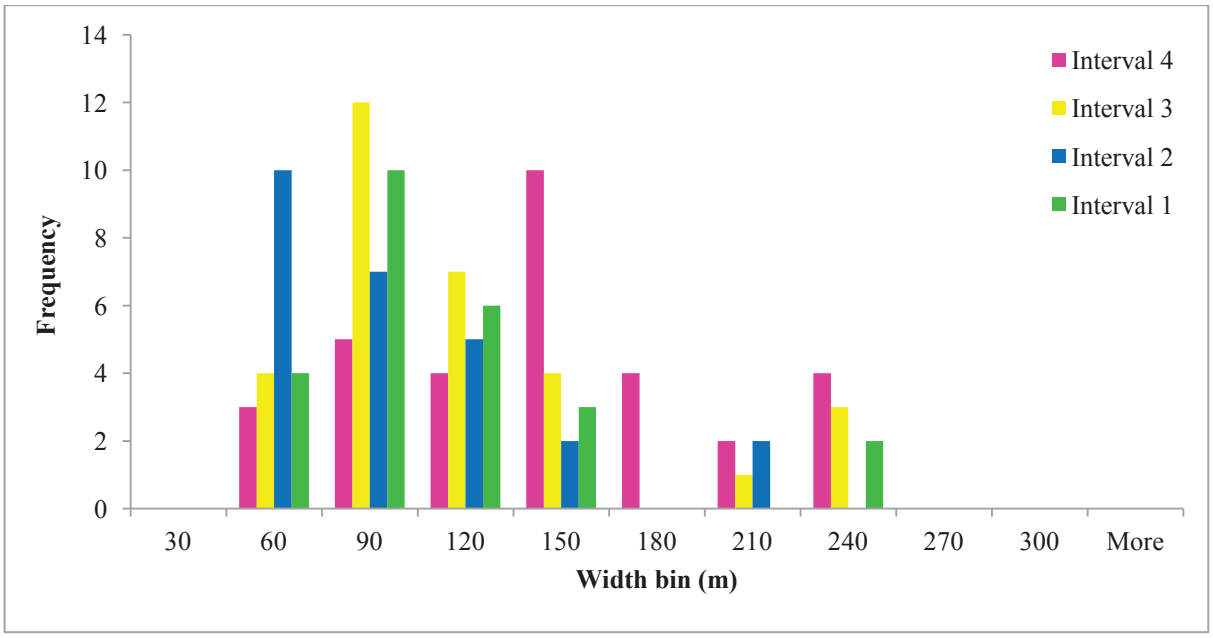


Figure 7.28 Width measurements recorded within the four intervals within the P40 – P50 interval, note how there is more variety within the frequency bins than in the width measurements from the other units.

In the southern half of the basin the normal fault has had a significant impact on the sediment distribution patterns. In the two oldest intervals the channels enter the basin from a separate entry point both north and south of the normal fault (Figure 7.27 (a)). To the south of the fault, the channels in the oldest interval are aligned sub-parallel to the fault, but by Interval 2 times the fault-related topography appears to have exerted less control on the channel geometries. The channels within Interval 3 appear to form as a localised fan lobe that has spilled over from the footwall side of the fault and thus are part of the main lobe complex which was developing to the north of the normal fault. In the youngest interval the channels and lobes south of the fault

can be clearly seen to be sourced from the main feeder channel north of the normal fault. Despite having the same entry point (and hence the same sedimentary characteristics, such as grain size) the channels are narrower, more closely spaced and more amalgamated in plan view than the other channels of the same age (Figure 7.26 (d)). Taking into account the variation in geometry of the channel systems through this package south of the fault, each interval shows evidence for having been affected by the presence of the fault, whether this was topographic expression related to the fault itself, or a response to the narrower and more elongated basin shape developed in the hangingwall.

7.8 Well Data

There are two wells within the study area drilled through the ponded interval, and although these mostly just intersect the edge of the ponded sediment, they still give some indication of the sand content of the ponded sediments. Due to the shallow position of the P10 to P50 units only gamma ray and resistivity data were collected, the gamma ray data is thought to be the most reliable and gives some indication of the sand content of the units. The two wells in the north of the study area have been drilled through the northeast edge of the ponded sediments and intercept a section approximately 40 m thick (Figure 7.29).

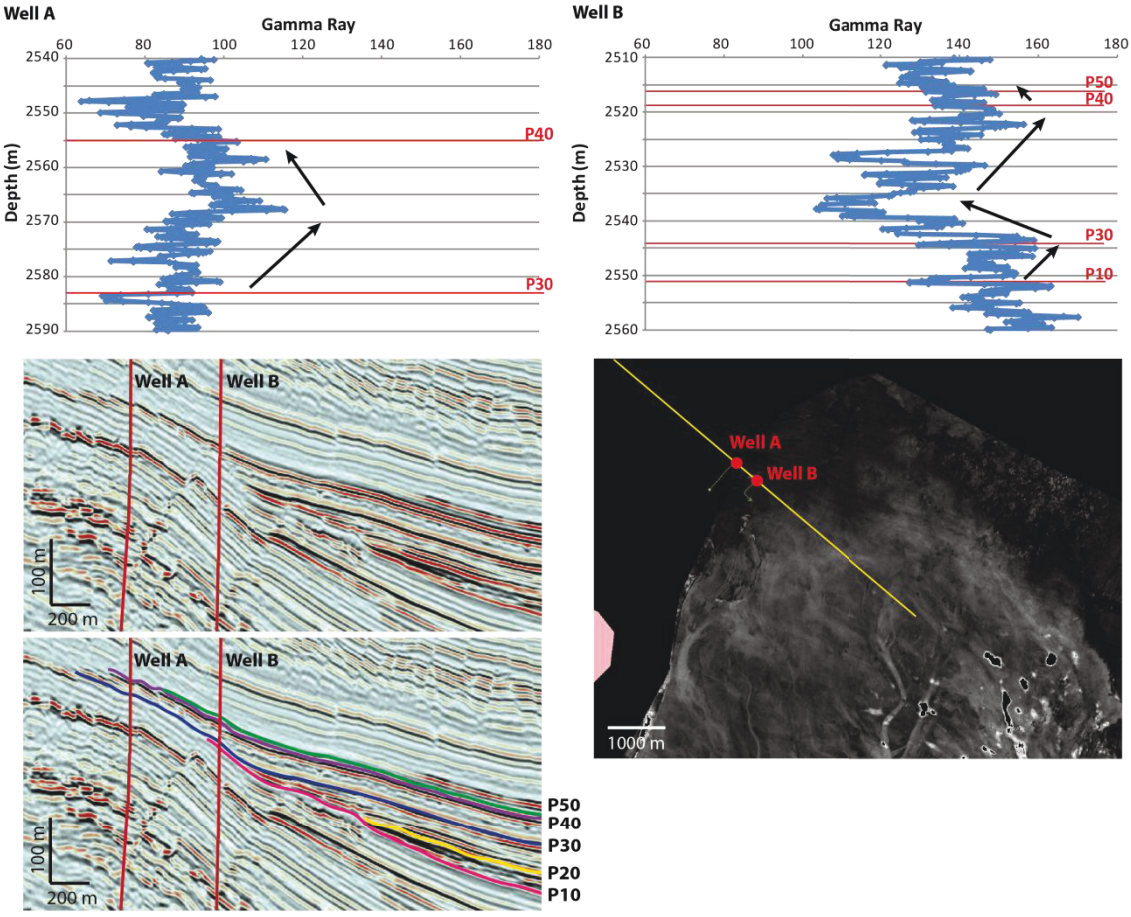


Figure 7.29 Gamma Ray analysis of two wells which intercept the ponded interval in the northwest corner of the basin. Arrows on the well logs indicate the broad changes in grain size within between the mapped horizons.

The gamma ray signature shows the trend within the P30 – P40 unit in the most detail, however the signature appears to differ between the two wells. The seismic section indicates that Well B intercepts more material

within the ponded interval and so analysis will focus on this well. In this location there are two main packages within the P30 – P40 interval (Figure 7.29); the lower package which contains a coarsening up sequence and the upper package which is thicker and the grainsize fines upwards. This corresponds to the amplitude signatures seen in the amplitude extraction maps with the lower packages containing more MTC derived material and the upper packages containing increasingly more channels and better developed fan complex systems (Figure 7.22).

The gamma ray signature through the P40 – P50 interval indicates the presence of much finer sediments (Figure 7.29, Well B). This well is located at the fringe of one of the lobes within the fan system during this interval and hence indicates that these fringes contain dominantly fine grained material. This supports the high-amplitude signature often observed towards the fringe of the lobes in the RMS amplitude extraction maps.

7.9 Comparison to Other Systems

In order to use fan lobe complexes as analogues for other buried ponded successions that may not be as well imaged it is necessary to compare what has been observed here to ponded fan systems elsewhere. However, it is important to exercise caution when using examples like those shown here as direct analogues; for example in deepwater Brunei Darussalam seismic facies types similar to those seen in the Gulf of Mexico contained significantly less net sand when drilled, due to less accommodation space and a mud-rich provenance (Demyttenaere et al., 2000, Adeogba, 2005).

7.9.1 Seismic Studies

Studies of fan lobe complexes have mostly been carried out in the shallow sections of the seafloor where the distribution of fan lobe complexes has been extensively mapped and some vertical architecture resolved (for example Beaubouef et al., 2003, Booth et al., 2003, Adeogba, 2005, Saller, 2008, Hay, 2012, Prather et al., 2012). However, the limits of the resolution mean that these systems have only been imaged down to the lobe scale and the individual channels within these lobes are very hard to image within the amplitude extraction maps.

The lobes observed in this mini-basin are similar in size and scale to those described from salt and shale-influenced basins elsewhere. However, documented examples elsewhere typically consist of a series of MTCs overlain by distributary channel-lobe complexes (Prather et al., 1998, Beaubouef and Friedmann, 2000, Adeogba, 2005). MTCs and fan lobe complexes are observed within the study area, but not necessarily together in the sequence described by other authors. Leveed-channel systems are also commonly observed in the vicinity of ponded-fan systems, but were not observed in a similar temporal interval in the study area. Adeogba et al. (2005) also record a lack of leveed channel systems and attribute this to having a sand-rich system without sufficient fine sediment to build levees (a theory supported by Reading and Richards, 1994, Richards and Bowman, 1998, Richards et al., 1998).

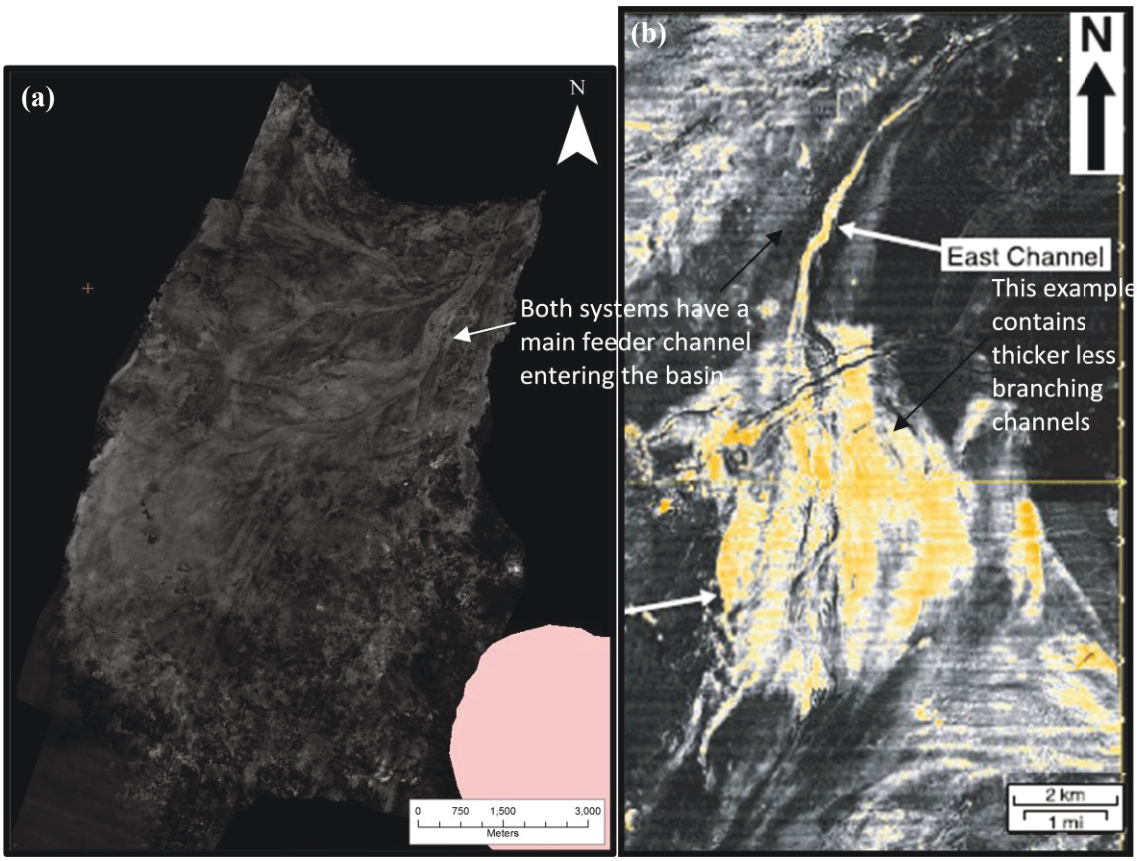


Figure 7.30 A direct comparison between (a) one of the lobe complexes seen in this area and (b) a channel and fan systems studies by Adeogba (2005) at a similar scale.

There are degrees of ponding observed within the deepwater setting; ponding within almost completely enclosed basins such as those observed in the Gulf of Mexico (i.e. Booth et al. 2003) or less strongly ponded, stepped shelf systems where ponding occurs briefly before the gradient of the system flattens out and bypass occurs (e.g. Adeogba et al., 2005, Hay et al., 2012). The ponding observed in this system is somewhere between these extremes with an almost completely enclosed mini-basin, but less repeated cycles than are observed in the Gulf of Mexico. However, a discussion of the key features observed within these different types of systems is worthwhile as it allows characteristics which are common to all settings to be identified.

Booth et al. (2003) investigate the development of confined fan systems in the Auger and Macaroni Fields, Gulf of Mexico. They observe differences in the stratigraphic architecture that they believe can be mainly attributed to paleo-bathymetric controls on the basin. The Auger field is substantially smaller than the mini-basin studied here, with a width of approximately 2.5 km as opposed to approximately 10 km and a length of 4.8 km as opposed to 20 km, but the shape is broadly the same and the system is confined by salt structures on each flank. The stratigraphy within the Auger Field is similar to that which is seen in this study with alternating cycles of sand-rich sheet/lobe deposition followed by intervals containing more channels. A series of sand-rich submarine fan deposits (fan lobe complexes in the terminology used here) onlap the salt structures and are often topped by erosional channel complexes or MTCs. The fan lobe complexes are very similar in style to those observed in the study area in Angola. The Auger Field also contains a normal fault which appears to have been active during the deposition of the submarine fan systems, Booth et al. (2003) state that there was considerable expansion in sediment thickness in the downthrown side of the fault and

that the expanded section has a higher percentage of sand. They note that the channelised sections are generally less erosive on the downthrown side of the fault, with better sand preservation seen in borehole analysis. These observations are somewhat analogous to the changes seen in this dataset within the P40 – P50 unit, where amplitude extractions indicate that the channels are much better preserved on the downthrown side and appear to cluster near the fault, mirroring the fault orientation. Due to the lack of well data through this section it is not possible to comment on the sand content of the sediments observed on the downthrown side of the normal fault within the study area. However, the clustering of high amplitude channels south of the normal fault in the P40 – P50 interval would suggest a higher sand content in this area (Figure 7.26).

The scale over which Adeogba et al. (2005) record the occurrence of major cycles of MTC deposits, distributary channel-lobe complexes and hemipelagic drape in a study on the Niger delta slope is not seen within the relatively thin interval investigated in this study. The cycles recorded in their work encompass basins between 300 m to 2000 m thick with MTC deposits comprising about a third of the material deposited in these cycles. In contrast to this, the cycles seen in this study are up to 200 m thick, but consist almost entirely of distributary fan-like sediments with approximately 20% MTC material contained within it, as opposed to forming a discrete package beneath it.

Adeogba et al. (2005) also infer that the majority of the non-MTC depositional facies is comprised of sand-rich unleveed distributary channel-lobe complexes (equivalent to fan lobe complexes). This inference is based on moderate to high reflection amplitude and continuity; onlapping reflection geometries, compensating and locally erosional internal reflection geometries and fan-shaped pattern in the amplitude extraction data (Figure 7.30). They state that a transient fan developed after a 50% reduction in slope gradient with a terminal fan developing after a 57% reduction in slope gradient. The fan lobe complexes imaged within the P20 – P30 unit are a very similar scale to those observed by Adeogda et al. (2005). The feeder channels are a similar size, both approximately 300 m wide entering the fan system and both fan lobe complexes have a similar distribution pattern, although the fan lobe complex imaged in the P20 – P30 Interval 4 is larger; it covers an area of approximately 28 km^2 compared to approximately 19 km^2 in the Niger Delta example (Figure 7.30). The high resolution of the seismic data in this chapter allows significantly more detail to be imaged in the fan complexes within the study area.

Hay (2012) observes similar patterns in the spatial location and development of the fan systems in the Kwansa Basin, Angola to those seen in this study of the Lower Congo Basin, Angola. She clearly observes a confined feeder-channel network that expands on entry to the basin to form depositional lobes, and that the deposition of the lobes changes as the basin topography varies. She documents the erosional front shifting updip during the overall downdip propagation of the system. A similar pattern to this is visible within the P30 – P40 unit in this study where the lobes appear to move progressively further into the basin whilst the entry point widens, indicating a back stepping of the system (Figure 7.31).

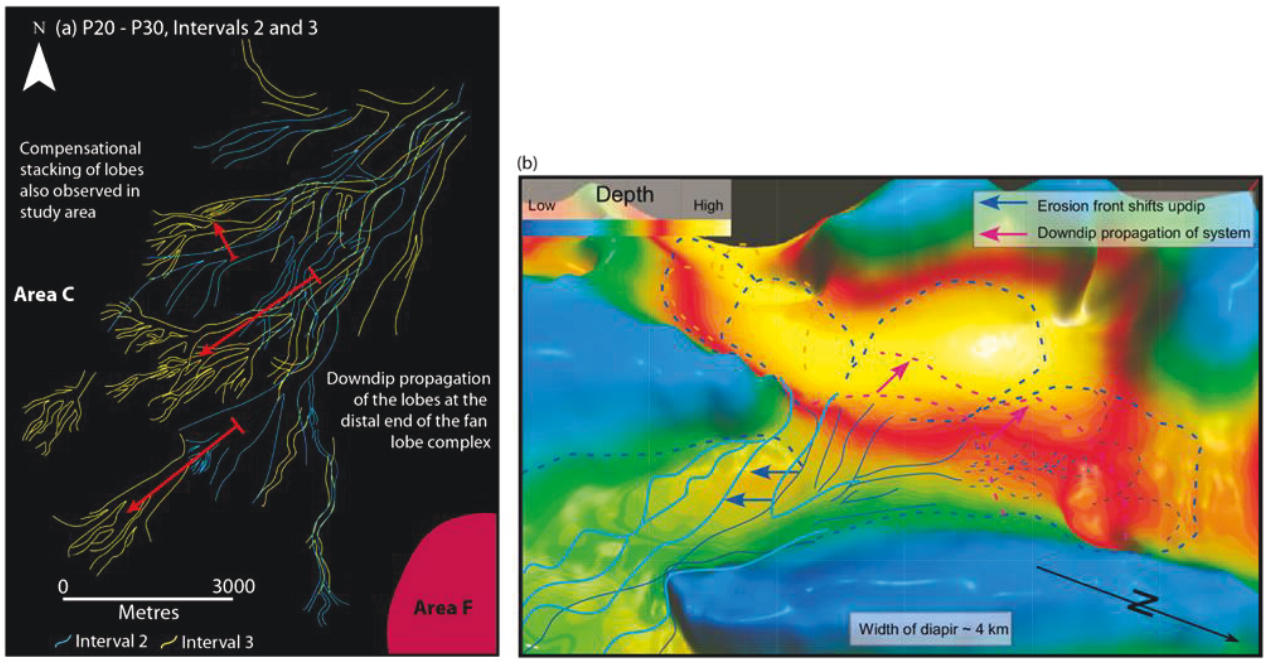


Figure 7.31 Comparison between the downdip propagating channels and lobe systems seen (a) within the P20 – P30 unit in this study compared to those lobes observed in (b) the Kwanza basin also offshore Angola where in an updip shift of the erosion front occurs alongside the downdip progradation of the system (Hay, 2012).

7.9.2 Modern Seafloor Studies

Studies of deepwater submarine fan lobe complexes on the modern seafloor are extensive with high resolution sidescan sonar, back scatter and bathymetric data used to explore these systems in many locations including the Gulf of Mexico, Corsica, Barbados and Indonesia (Belderson et al., 1984, Twichell et al., 1992, Ercilla et al., 1998, Kenyon et al., 2002, Decker et al., 2004, Deptuck et al., 2008). These systems are often imaged to a high resolution and the analysis is often coupled with information from piston cores to aid understanding of the lithology. However, imaging in this way only allows a snap-shot in the development of a fan system to be observed as very few details of the vertical architecture of these systems are resolvable making it difficult to understand the evolutionary history of the system.

The scale of the fan lobe complexes and the patterns observed as they develop within the mini-basin are very similar to that recorded by Twichell et al. (1992) on the modern-day outer Mississippi Fan in the deepwater Gulf of Mexico. They observed crosscutting channels within the fan system using sidescan sonar data and infer that the cross-cutting relationships indicate that only one channel was active at a time and hence many depositional events were responsible for the construction of each depositional lobe. Cross-cutting relationships are frequently observed in the amplitude extractions shown in this chapter and hence we can infer that was also the case in the lobes studied here (for example, see Figures 7.18 and 7.27). The channels observed towards the distal end of the fan by Twichell et al. (1992) are on the same scale as the smallest channels seen within the lobes in the study area; those recorded by the backscatter data over the Mississippi are typically less than 100 m wide and have a relief of less than 2 m, whereas those recorded in this area typically 100 m wide (Figure 7.32). The termination patterns within the lobes in this study are quite similar to the 'fronds' observed by Twichell et al. (1992).

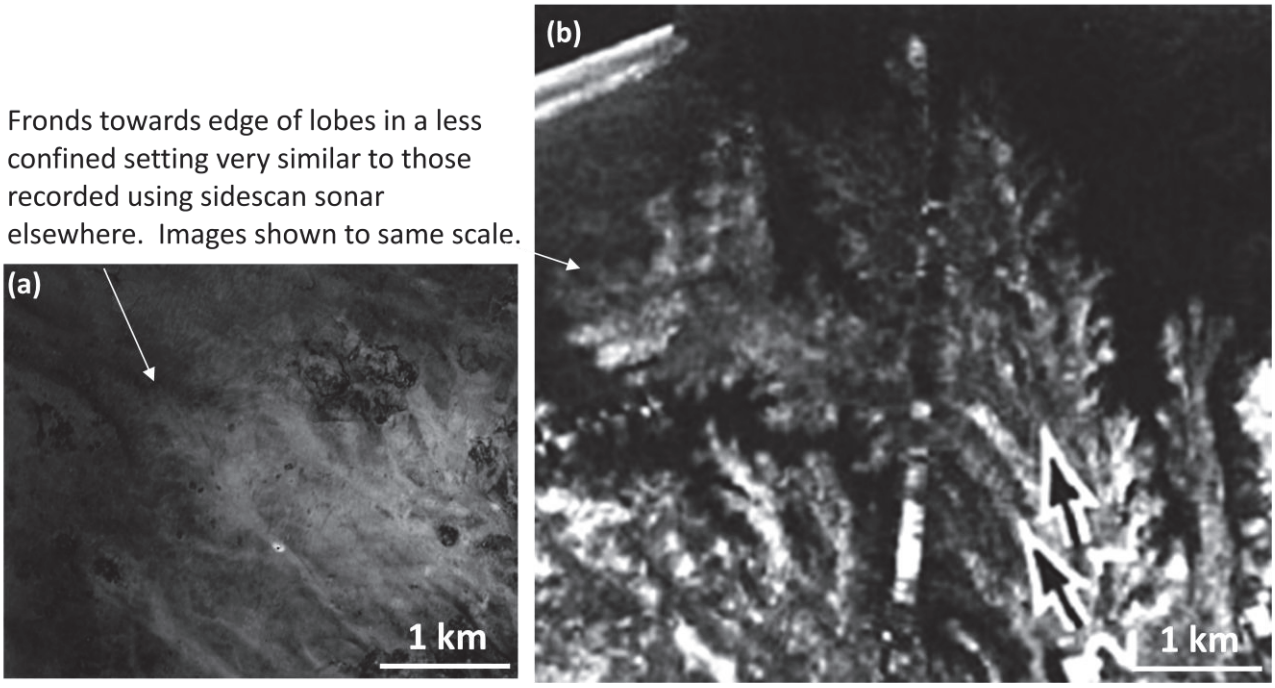


Figure 7.32 A comparison between (a) RMS amplitude extraction data from the P30 – P40 interval and (b) the fronds recorded by Twichell at al. (1992); shown at similar scales.

Whilst braided channels have been recorded in a number of modern deepwater settings, they are not a common features of deepwater fan systems and mostly occur at channel mouths or confluences and at channel lobe transitions (Belderson et al., 1984, Kolla and Coumes, 1987, Wuellner and James, 1989, Kenyon and Millington, 1995, Klaucke and Hesse, 1996, Ercilla et al., 1998, Hesse et al., 2001, Wynn et al., 2007). In a fluvial setting the formation of braided channels traditionally requires a high gradient setting, with high discharge and a predominance of bedload material (Schumm et al., 1987). However, Wynn et al. (2007) state that in the deepwater environment they appear to be associated with the rapid deposition of sand-rich sediments, resulting from abrupt changes in turbidity current parameters, for example reduced flow thickness and velocity resulting from changes in gradient and degree of confinement. A pattern of channel deposition that closely resembles a braided channel system occurs in the P40 – P50 interval south of the normal fault (Figures 7.26 and 7.33). This arrangement of channels is very similar to that observed on the Orinoco submarine fan system, offshore Barbados (Belderson et al., 1984, Ercilla et al., 1998). However, the braided channels recorded from the Orinoco deepwater fan system are significantly larger than those seen in the present study (Figure 7.33); the individual channels in the Orinoco system are approximately 500 m wide compared to a maximum width of approximately 100 m for the Angolan ponded fan system. The braided systems recorded by Klaucke and Hesse (1996) on the Northwest Atlantic Mid-Ocean Channel (NAMOC) system in the Labrador Sea, are very similar in scale to those of the Orinoco Fan with a braid plain up to 550 km long and 120 km wide. This magnitude difference in scale of the systems suggests that the underlying processes creating the systems in the Orinoco Fan and the NAMOC fan might be different to those responsible for the braiding imaged south of the normal fault in this study. The braided pattern seen in this study could have been influenced by the movement on the normal fault; either the channels may have formed as part of a fan lobe constrained in its extent by movement on the normal fault or the braiding could

occur in direct response to a change in the velocity of the flow as it travels over the incline produced by the normal fault. This would have caused rapid deceleration of the sediment into the relative low formed in the hangingwall of the normal fault.

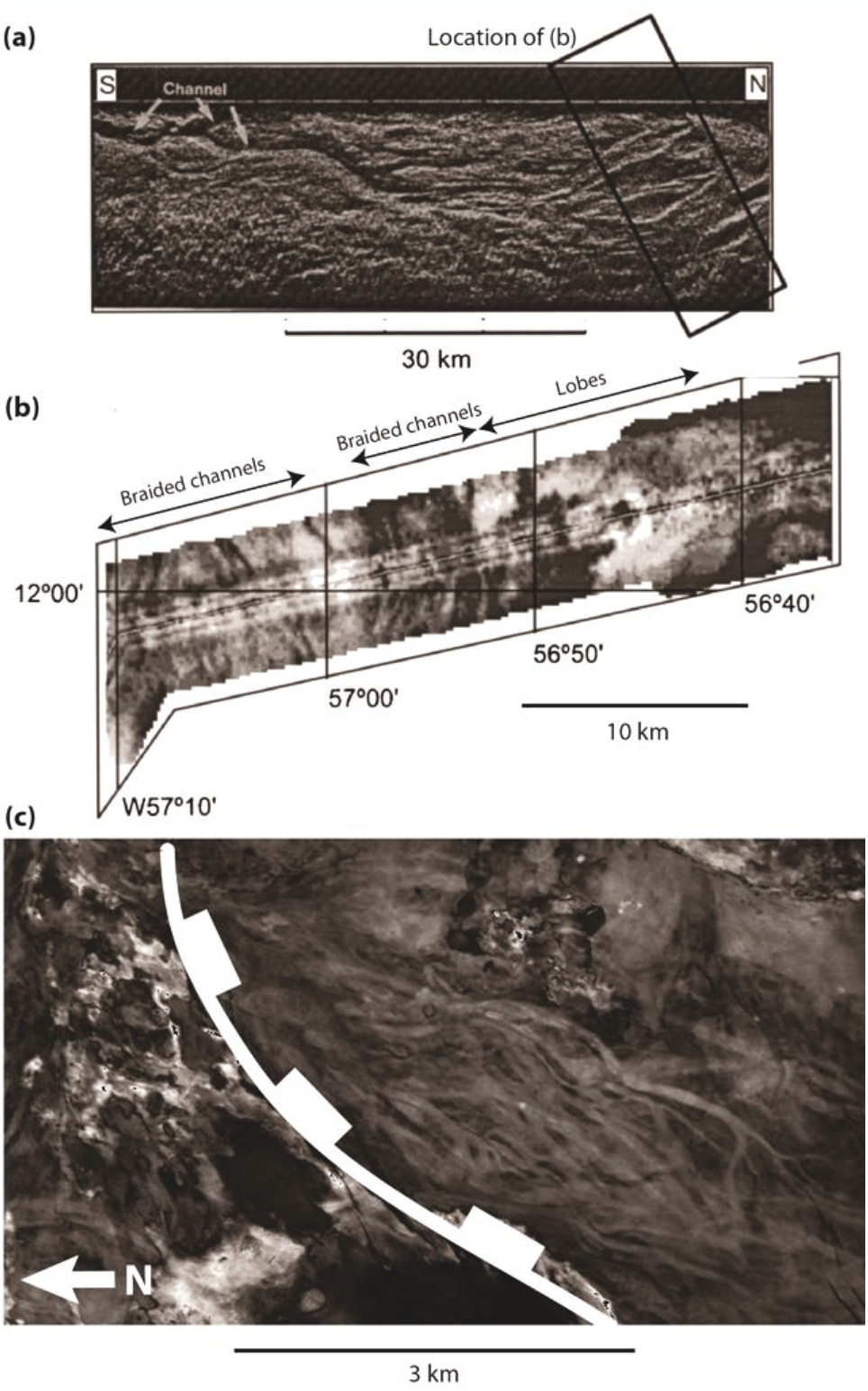


Figure 7.33 Comparison between the braided channel systems recorded in the Orinoco submarine fan, Barbados and those recorded in seismic data offshore Angola, (a) shows the GLORIA side-scan sonar image of the Orinoco system (Belderson et al., 1984) with a section of this further interpreted in (b) using backscatter data (modified from(Ercilla et al., 1998), note that the backscatter images show a cluster of braided channels in the west with a series of lobes in the east. (c) shows the braided system recorded within south of the normal fault within P40 – P50 interval 4, here the channels are approximately 10 times smaller than those seen on the Orinoco submarine fan system, but also occur alongside lobe features.

7.9.3 Outcrop Studies

Outcrop studies exploring deepwater lobe complexes are extensive with studies carried out throughout the world including the Karoo Basin in South Africa, the Ross Formation in County Clare, Ireland, the Brushy Canyon Formation, West Texas and the Precambrian Kongsfjord Formation, Norway (for example Carr and Gardner, 2000, Gardner and Borer, 2000, Sullivan et al., 2000, Drinkwater and Pickering, 2001, Gardner et al. 2003, Wach et al., 2003, Sullivan et al., 2004, Hodgson, 2006, Hodgson, 2009, Prelat et al., 2009). The comparisons in this study have mostly relied upon examples from the Karoo Basin in South Africa and the Ross Formation in County Clare as these are two of the best studied examples in modern literature. These studies have enabled extensive, detailed descriptions of the facies within lobe complexes to be fully explored from the proximal to distal locations and have provided insights into the vertical architecture of these systems. However, due to the nature of the outcrop locations this work only allows limited spatial mapping of the lobe complexes. Despite this, there are several comparisons which can be drawn between the work carried out on outcrops and this high resolution seismic study.

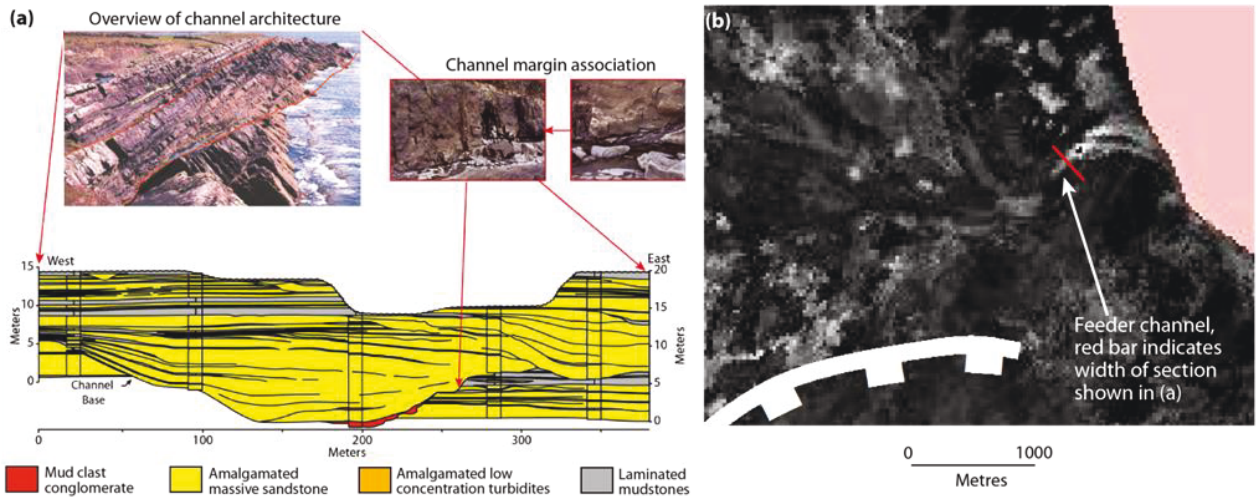


Figure 7.34 (a) Proximal channels observed in the Ross Formation by Sullivan et al. (2000, 2004) compared to (b) feeder channels on a similar scale seen within the lobe complex within P40 – P50, Interval 4.

Previous studies using outcrop data have sub-divided the lobe complexes into proximal, medial and distal fan settings according to key characteristics such as channel size, aspect ratio of the sand bodies (width to thickness ratio), and key reservoir characteristics such as net-to-gross and the continuity of sand bodies (Sullivan et al., 2000). Sullivan et al. (2000) observe that the proximal fan of the Skoorsteenberg Formation, South Africa can be characterised by a low aspect ratio, high net-to-gross, erosional contacts between the sand bodies and excellent vertical but poor lateral connectivity. In all the lobe complexes imaged within the study area from the P20 – P30 unit onwards the proximal fan is dominated by a series of feeder channels entering the basin. These are best imaged in the P20 – P30 and P40 – P50 units where they are between 250 m and 300 m in width and tend to have a high amplitude signature indicating a high sand content. As such, they are a very similar scale to those observed in the Ross Formation in the Clare Basin, Ireland (Figure 7.34) where sand-rich amalgamated channels have been observed in outcrop (Sullivan et al., 2000, Sullivan et al., 2004).

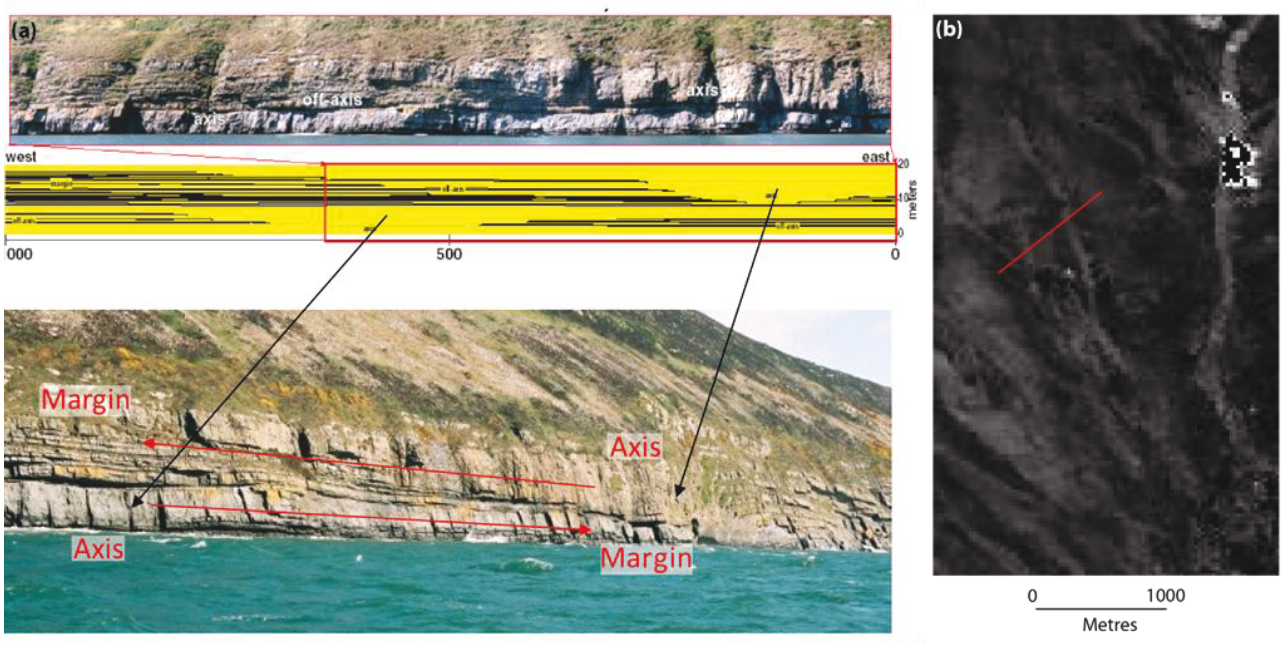


Figure 7.35 Compensational stacking observed within the transitional domain observed in (a) outcrop data from the Ross Formation, County Clare by Sullivan et al. (2004) and (b) commonly within the transitional domain of the fan lobe complexes in the study area, as imaged here in P40 – P50 interval 4. The red line shows 1 km on the amplitude extraction map, showing a similar distance as illustrated in the sketch cross section.

Towards the centre of the fan lobe complexes a transitional domain has been described by Sullivan et al. (2004) containing the type of channelised and amalgamated sheet facies observed in outcrop in the Ross Formation of the Clare Basin, Ireland (Figure 7.35). It is possible to trace the beds from the axis to the margins of the lobes within the Ross Formation with beds thinning and becoming less amalgamated towards the margins. This domain appears to exist towards the middle of the lobe complexes in the study area where trunk channel branch prior to the development of lobes; channels are more amalgamated towards the centre and thin towards their margins (Figure 7.35). Channels in the study area have very similar widths to those observed in outcrop with ranges in this area from approximately 50 m to 200 m in the fan complexes observed here compared to up to 350 m in the Ross Formation (Figure 7.35; Sullivan et al., 2004).

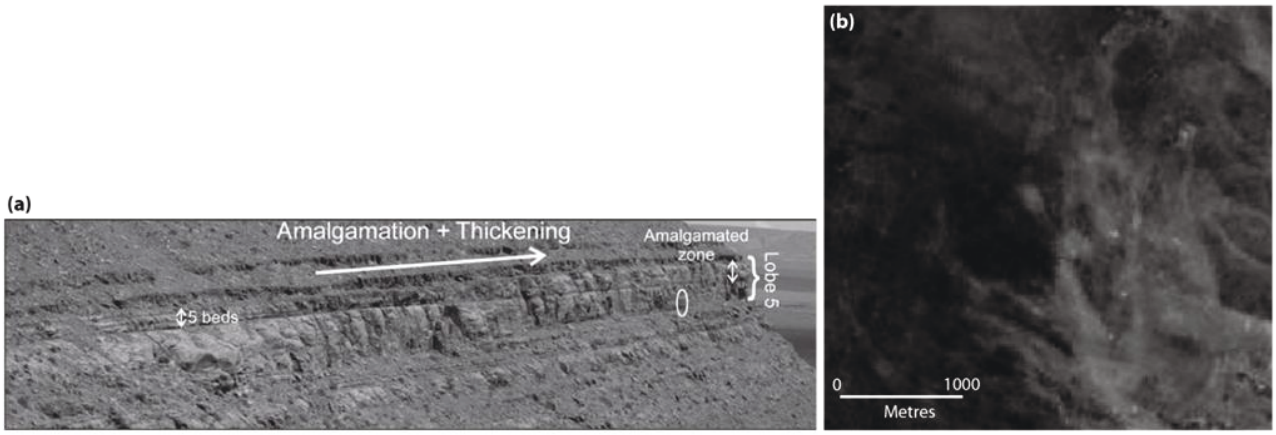


Figure 7.36 Two images showing (a) an cross section through amalgamated and densely channelised lobes in an outcrop in the Karoo Basin (Prelat et al. 2009) compared to (b) an amplitude extraction map showing a similar area within the lobe complex in the P30 – P40, Interval 2.

Similarities between the level of detail observed in outcrop and within this study are also apparent in the densely channelised lobes which form in a more distal location within the lobe complexes. These have often been described as channelised sheet facies with channel amalgamation occurring within the lobe axis. The occurrence of a series of discrete, but amalgamated, channels towards the centre of one of the lobes in the study area has been frequently observed which corresponds to observations made from outcrop studies in the Karoo Basin, South Africa (Figure 7.36). In outcrop a thickening of the beds which make up the individual lobes occurred towards the axis of the lobe along with increased sand content and amalgamation (Figure 7.36; Prelat et al., 2009). In this study clear evidence of lateral migration and compensational stacking of the lobes could imply that they thicken towards the lobe axis (Figures 7.18, 7.22, 7.27 and 7.40).

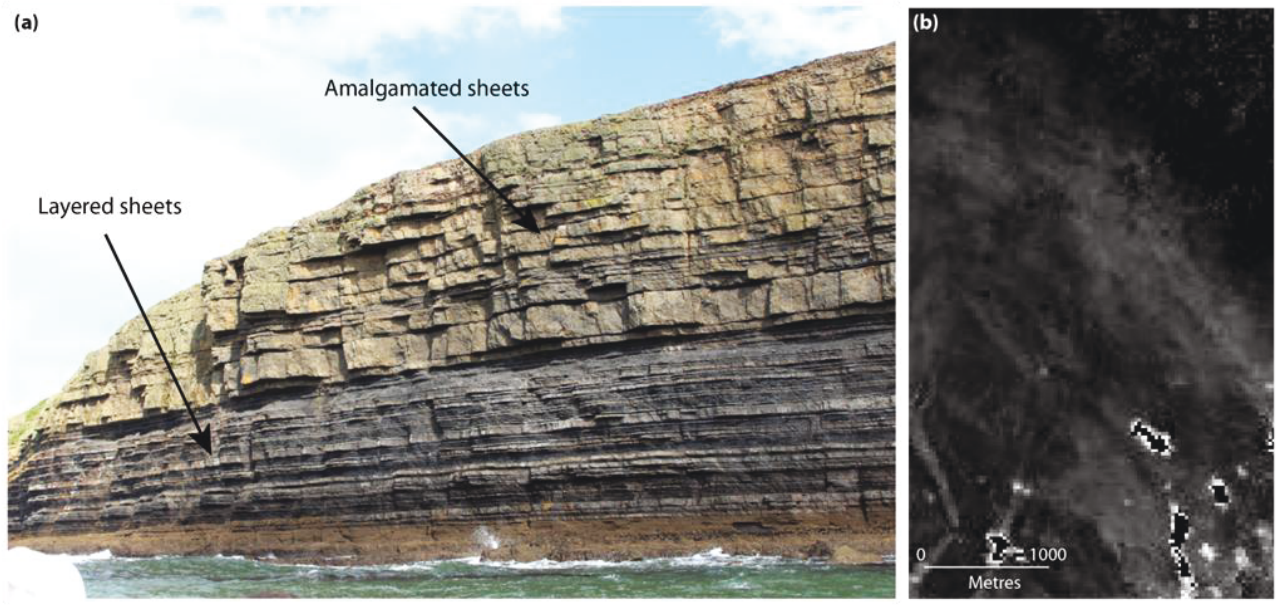


Figure 7.37 A comparison between (a) the layered and amalgamated sheets observed in outcrop section in the Ross formation, County Clare (image courtesy of M. Mayall) and (b) the high amplitude fringes observed in the study area towards the edges of individual lobes and lobe complexes.

High amplitude fringes are imaged towards the edge of both individual lobes and the lobe complexes observed within the study area (Figures 7.28, 7.38 and 7.40). These correspond to the location of amalgamated and layered sheets observed within the Ross Formation of the Clare Basin, Ireland (Figure 7.37). The amalgamated sheets contain a higher proportion of sand and, as such, are more likely to be similar in style to the high amplitude fringes observed in the study area (Figures 7.37 and 7.40). Recent studies of submarine fans have concentrated on the idea of hybrid event beds (e.g. Hodgson, 2009, Talling, 2013) located towards the fringes of submarine fan systems and thought to be generated during fan initiation and growth (Hodgson, 2009). These hybrid beds have been observed in more than 20 modern and ancient systems worldwide but not described in terms of seismic amplitude characteristics (Talling, 2013). Hodgson (2009) recognises three types of hybrid system, all comprising of a weakly graded, fine grained sandstone turbidite system overlain by a clast supported matrix. Whilst these deposits have been readily identified in outcrop section and in the subsurface from well data (for example Barker et al., 2008, Haughton et al., 2003, Kane and Pontén, 2012) the thin nature of the deposits and their random debris-flow like seismic characteristics make them very hard to detect in seismic data. The high resolution of the dataset used in this

study, gives a limit of vertical resolutions of up to 5 m at this water depth and the root mean squared (RMS) amplitude extractions do reveal areas around the individual fan lobes and the edge of the submarine fan that are paler (in this case indicating higher amplitudes) in comparison to the surrounding area, suggesting a slightly higher sand content (Figures 7.38 and 7.40). It is proposed that these pale fringes associated with the edges of the lobe deposits seen in Figure 7.40 are the amplitude signature of these event beds.

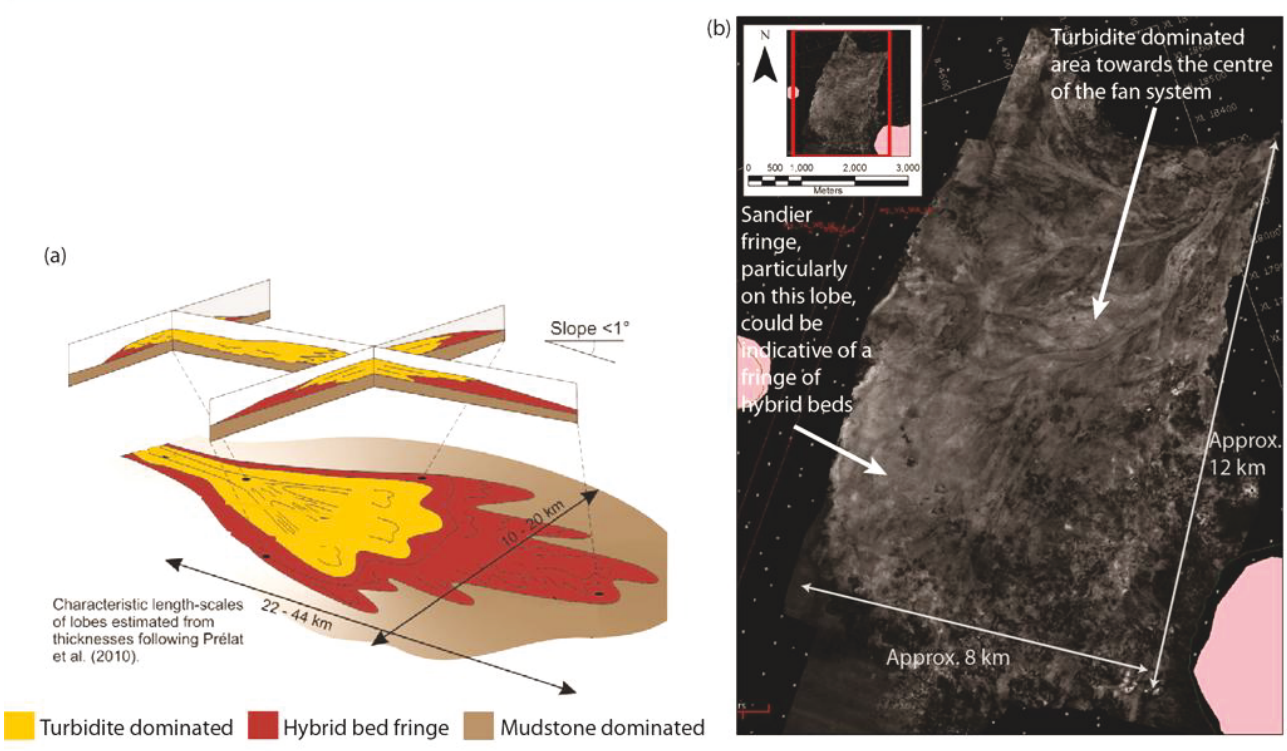


Figure 7.38 (a) conceptual model showing the distribution of hybrid beds around the fringes of a submarine fan system (modified from Kane and Pontén, 2012, Hodgson, 2009), compared to one of the intervals within this fan system (P20 – P30, interval 4) which has a series of high amplitude channel systems which bifurcate to form lobes towards the end of the system and these lobes are surrounded by high amplitude, undefined beds, postulated to be hybrid beds.

7.10 Discussion

7.10.1 Morphological Variations

Overall four distinct phases of submarine fan formation have been recognised within the ponded material, each containing a single long-lived fan lobe complex; one feeder channel branching into several channels within the fan and terminating with a series of lobes. However, the orientation of the fan systems and the geomorphological characteristics of the channels and lobes that make up the fans vary between the intervals. There are two drivers for changes in the fan characteristics within the basin; autocyclic controls and allocyclic controls; those changes driven by factors within the basin and those driven by factors external to the basin respectively. Both these controls are observed acting at different scales within the ponded fan intervals.

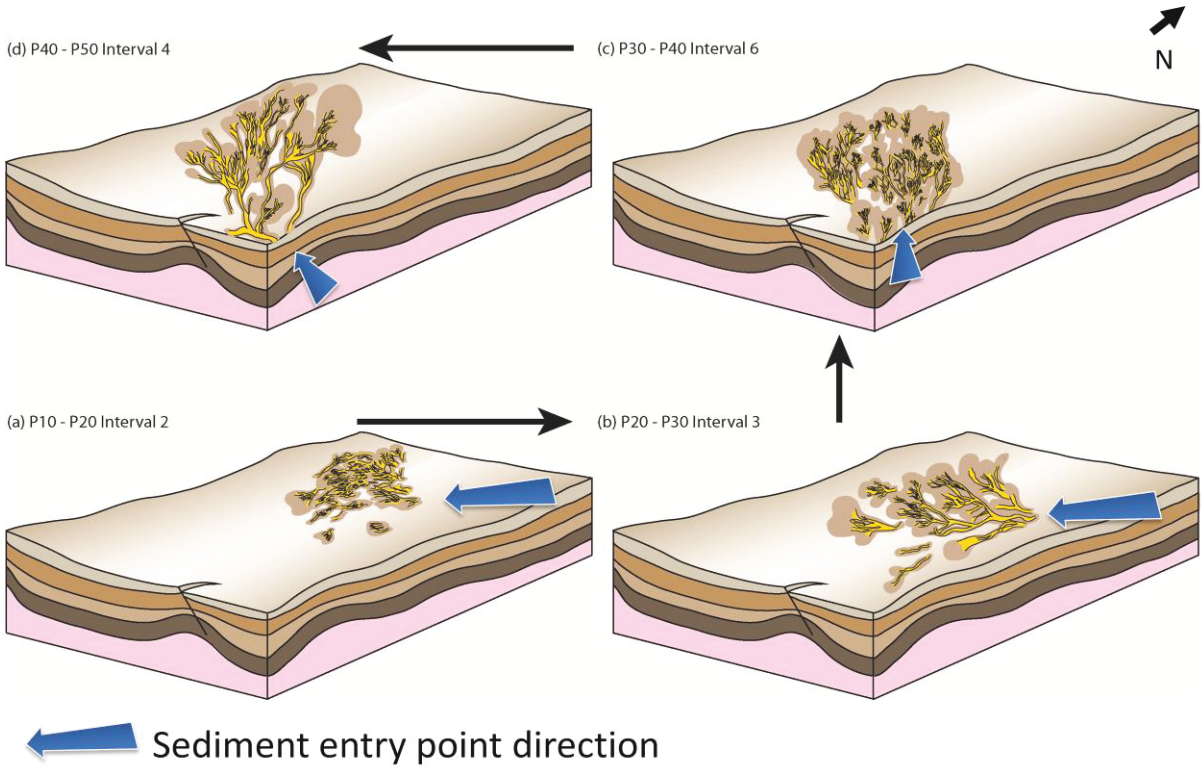


Figure 7.39 Sketch showing the development of the lobe complex units north of the normal fault through time illustrating the change in main sediment entry point through time with a switch from a sediment entry in the north to the entry point in the east.

There is a clear shift in the feeder channel entry point from the northeast to the southwest between the P20 - P30 unit and the P30 – P40 unit (Figure 7.39). This switch is likely to have been caused by changes in the feeder channel pathway prior to its entry into the basin. This could either have been caused by structural change (e.g. growth of a salt body up-dip of the basin) or a stratigraphic change (for example avulsion of the channel prior to entry into the basin). Given the nature of the salt growth in this area it appears most likely that the channel may have been forced to switch pathways by the growth the salt either on the eastern margin of the basin or outside the bounds of the basin further to the east. The orientation of the channels within Interval 4 of the P20 – P30 unit (Figure 7.17 (d)), the interval directly before the switch in sediment entry point, is much more varied that those recorded in the previous intervals with a slightly more east-west orientation overall. This could indicate that even by this stage the channels are responding to changes in the salt structures to the east of the mini-basin, thus implying a structural driver to the main switch in orientation.

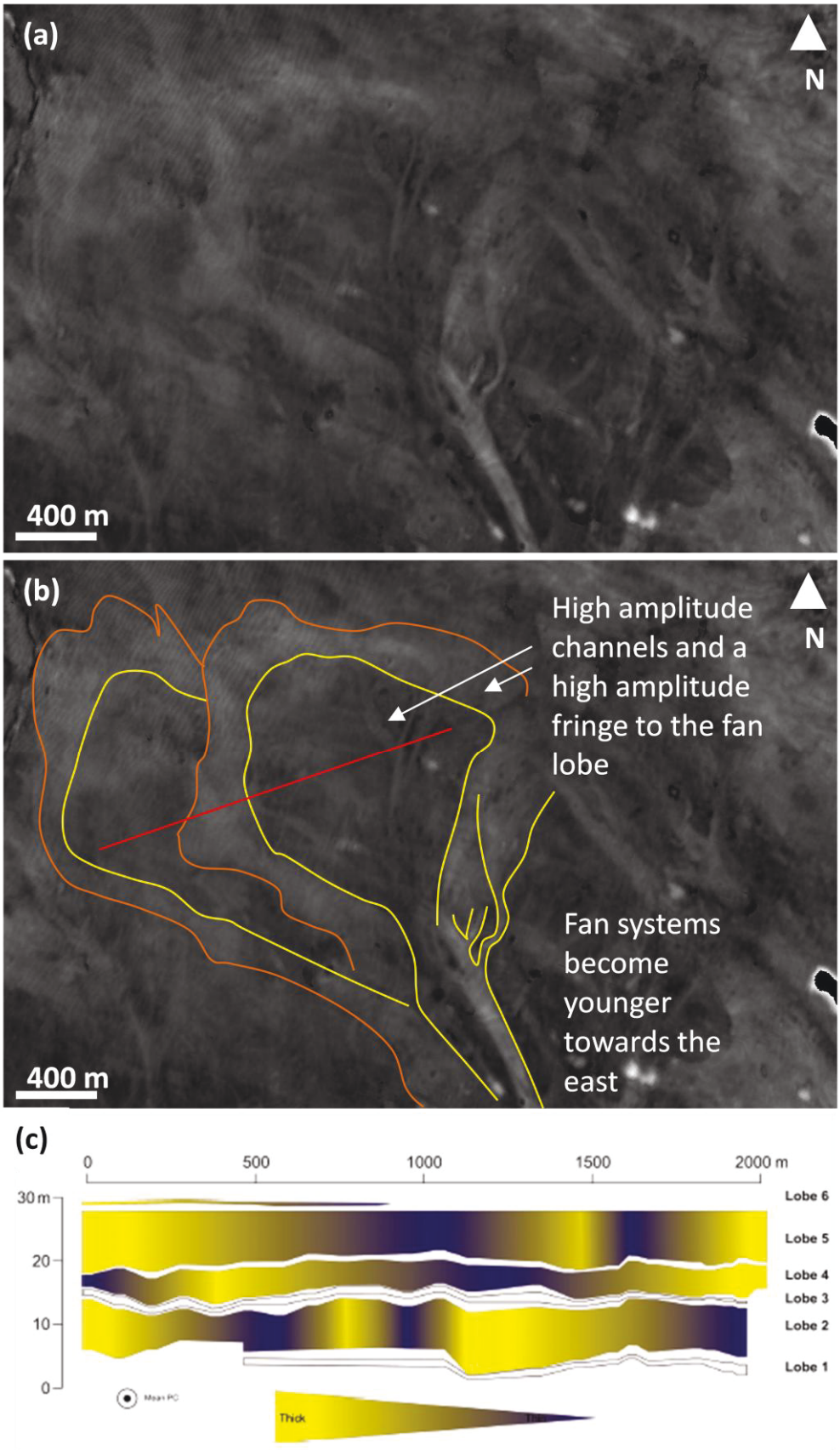


Figure 7.40 (a) Uninterpreted RMS amplitude extraction map highlighting the main channel and lobe systems within P40 – P50, interval 4 alongside (b) an annotated image showing the main fan outlines and also highlighting the high amplitude fan fringes. White shows high amplitudes and black low amplitudes indicating sand and shale respectively, red line shows location of inferred similarities at same scale as (c) shows this in comparison to the compensational stacking observed at the lobe scale in a schematic correlation panel from the Karoo Basin, South Africa, taken from Prelat et al. (2009).

There are changes in the distribution of the sediments deposited within the fan lobe complexes which appear to be responding to topography within the basin. Within the study area it is possible to observe responses of the channels within the lobe complexes to topography generated by the previous lobe complex system. This is particularly apparent between the P10 – P20 unit and the P20 – P30 unit. Isopach analysis of the P10 - P20 unit indicates that there is a thick triangular wedge of sediment towards the north of the basin (Figure 7.14), which corresponds to the area surrounding the feeder channel which contained the largest number of channels during this time period (Figure 7.15). However, in the following unit, P20 – P30, the thickest sediment was deposited on either side of this relative high (Figure 7.16). The oldest channels that develop within the fan system during the P20 – P30 unit (i.e. those in Intervals 1 and 2) appear to respond to the presence of this relative topographic high with the majority of them clustering down the eastern side of the basin (Figure 7.17 (a) and (b)). The younger feeder channels within this fan lobe complex (i.e. those imaged in P20 – P30 Intervals 3 and 4) are still located mostly to the east of the relative high, but trunk channels branch away from these terminating in lobes towards the western edge of the mini-basin. This implies that by the time Intervals 3 and 4 were deposited the relative topographical lows have been filled by sediment from Intervals 1 and 2.

Within the individual fan lobe complexes (i.e. P40 – P50) there are clear changes in the channel geometries within the component intervals (for example Figures 7.18, 7.22 and 7.27). These changes in sediment distribution patterns between successive intervals through each fan lobe complex appear to be driven both by the underlying structure and by lobe compensation, with autocyclic processes controlling the distribution of many of the lobes within the fan lobe complexes. There are several intervals where it is possible to see lateral movement of a lobe or the avulsion of a channel system driven by relative high topography generated by an earlier fan. One such example can be seen within Figure 7.40 where the amplitude extractions indicate that the fan has laterally migrated eastwards across the basin. The scale of these lateral migrations and corresponding compensational stacking of lobe systems is similar to that observed in outcrop data in the Karoo Basin, South Africa by Prelat et al. (2009). They observe clear thinning and stacking of individual lobe systems within a schematic correlation panel (Figure 7.40 (c)).

In some instances it is possible to see autocyclic and allocyclic processes working together to control the development of the fan lobes. Within the P40 – P50 unit a slightly braided channel system entering the area from the north appears to be constrained by the relict topography formed by the edge of an older fan lobe to the east and the high topography generated by the growth of a salt-cored anticline within Area C to the west (Figure 7.41). This has caused the channels to become increasingly amalgamated closer to the western topographic high until they are indistinguishable in the amplitude extraction data. The system follows the edge of the basin as it remains constrained by the two highs to the east and west before branching out away from the western high at its most northerly point where it becomes significantly less confined by the fan system (Figure 7.41).

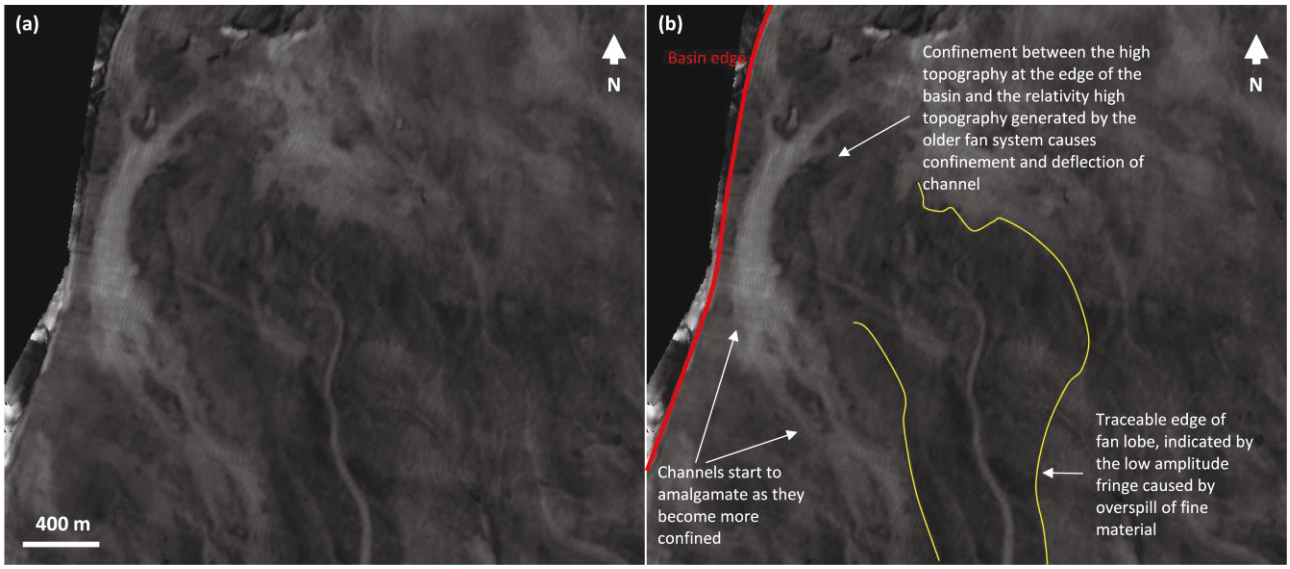


Figure 7.41 RMS amplitude extraction map highlighting some of the detail within the P40 – P50 unit, interval 4 shown both (a) un-annotated to show all detail and (b) annotated illustrating how the confinement of a channel system between the high topography of the basin edge and the relatively high topography caused by an older fan system can impact on the characteristics of the resulting channel.

Allocyclic controls can have a large impact on the sediment distribution with a basin, with a fairly long-lived normal fault controlling the distribution of sediment throughout the period over which the fan lobe complexes develop (Figure 7.42). During the deposition of the P10 - P20 and P20 – P30 units, the fault appears to have exerted less control over the sediment distribution. However, it is possible that movement on the fault during these periods caused uplift and rotational tilting of the footwall which in turn would have created a subtle topographic high on the southern margin of the basin next to the fault. This high may have been enough to prevent sediment from being deposited any further south and may be responsible for the slight western bend observed in the channels deposited in the southern half of the basin during the P20 – P30 interval (Figure 7.17). The fault has a direct impact on the sediment distributed within the basin during the P40 – P50 interval with clear variation in the characteristics and distribution of the channels deposited north and south of it (Figures 7.26 and 7.27). It appears that the throw of the fault decreases as the system becomes younger causing the tilt on the footwall to decrease and allowing the channels to flow across the eastern tip of the fault (Figure 7.42). At the same time the main sediment entry point into the basin moves closer to the fault and hence the sediment is more likely to flow across it.

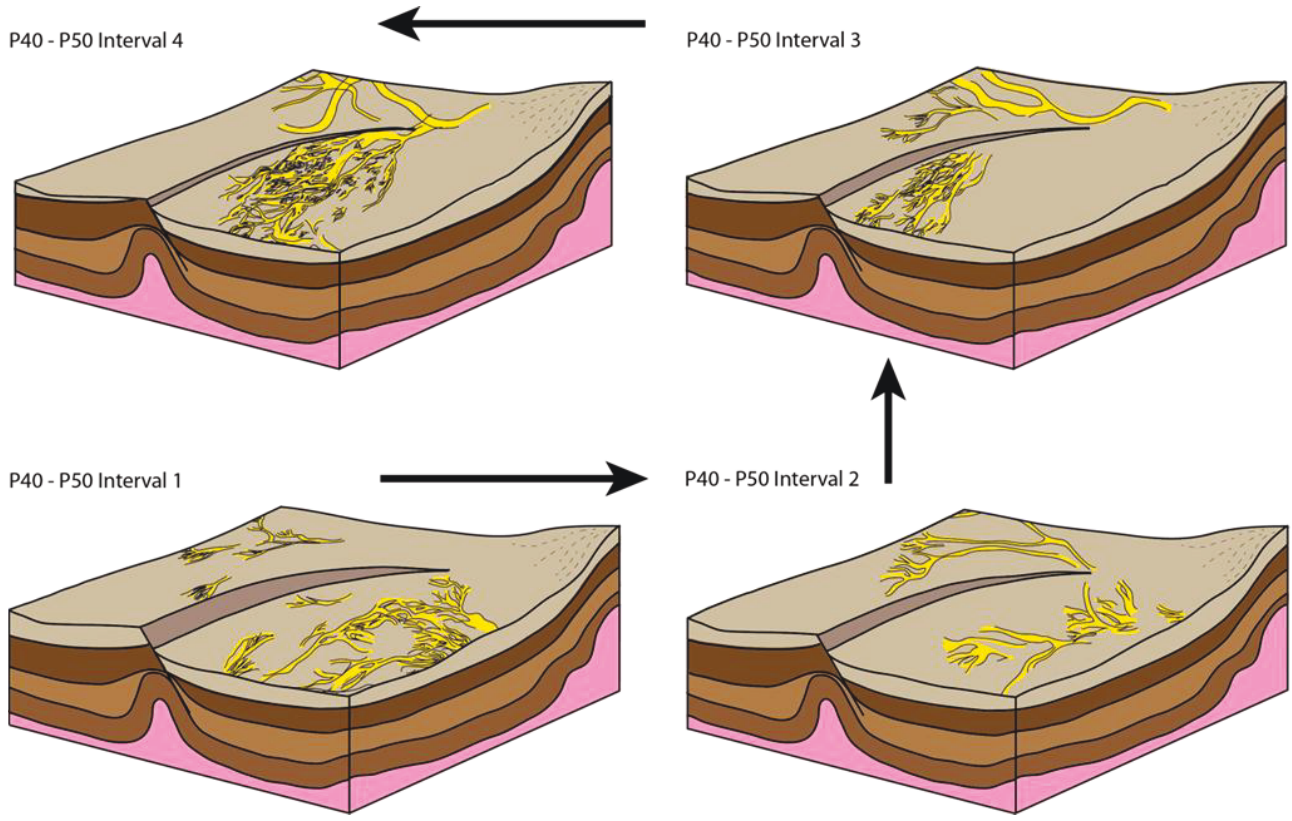


Figure 7.42 A series of diagrams indicating how large scale allocyclic controls (in this case a normal fault) can impact on the sediment distribution and fan lobe complex characteristics within a mini-basin.

7.10.2 Observational Scales

As discussed in Section 7.9 lobe complexes can be observed from a variety of different types of dataset most commonly: seismic data, modern seafloor datasets such as sidescan sonar and backscatter data, and outcrop data. Each of these datasets presents advantages and disadvantages and each highlight certain features within the lobe complexes better than the others. Conventional resolution seismic data is mostly able to resolve detail down to the lobe scale, but rarely images the channels and fringe sediment associated with these lobes. Whereas on modern day seafloor data it is possible to image to this resolution but the vertical architecture and details of the development and evolution of the complexes cannot be discerned. Outcrop data allows the fine-scale details of the fan architecture and lithological variations to be explored, showing detail significantly greater than that seen in either seismic studies or modern-day studies and expanding the understanding of the lithologies and facies which make up the fans. However, the conclusions drawn from outcrop data are difficult to link spatially.

This dataset is unique in that the high-resolution of the seismic data used allows the differences between these three scales to be bridged. In particular, it allows links to be made between observations at the outcrop scale and those seen in more conventional seismic data. Here, the smallest resolvable channels within the fan lobes can be linked to details seen in outcrops such as the Karoo Basin, South Africa and the Clare Basin, Ireland. This allows observations to be drawn on the facies expected within these elements when observed in seismic data. This is most exciting within the transitional area between the more proximal channelised parts of the fan complex to the more distal channelised parts. Here, beyond the resolvable channels, smooth

relatively featureless amplitudes have been imaged (for example Figure 7.40) which are know from outcrop examples to contain more amalgamated and layered stratigraphy (Figure 7.37) but have not been previously imaged in seismic data. This information clearly has implications for predicting the reservoir quality and internal architecture of lobe complexes and individual lobes. Models incorporating this facies towards the distal parts of lobe complexes have been described elsewhere in the literature using outcrop examples (for example Sullivan et al., 2000, Sullivan et al., 2004). The amplitude extractions generated from this data confirms that these models can be applied to the subsurface and the detail imaged within these amplitude extractions could be used in the future to help refine the reservoir models used for ponded fan lobe complexes.

7.11 Conclusions

This is the first study in which images of this resolution have been generated for submarine fan lobe complexes in the subsurface. This high resolution has generated exceptionally detailed images in amplitude extraction maps which allow unparalleled levels of detail to be observed about the facies which make up these systems and their evolution and development through time. These images illustrate how fan systems respond to variations in the basin geometry and changes in sediment entry points on a large scale by changing the distribution of the lobe complexes and their spatial extent. Small-scale intra-basinal variations in the location of the channels and lobes which combine to form these lobe complexes are also observed. These can mostly be attributed to lateral migration of the channels and compensational stacking of the lobes as they encounter topography from previous systems.

Lobe and channel distribution within the lobe complex responds to subtle changes of the basin-bounding structures and local topography. The spatial distribution of the distal lobes varies significantly between the short-lived intervals; assuming a steady sedimentation rate each interval within the four main units is deposited over approximately 0.04 Ma with compensational stacking of the lobes and channel avulsions observed between every interval. The key recognisable shape of an individual lobe (i.e. the branching lobate pattern and tear-drop shape) can also be significantly affected by topographical constraints. For example, south of the normal fault the channels become significantly amalgamated and do not appear to deposit tear-drop shape terminal lobes and toward the edge of the basin they can become significantly narrower and amalgamate.

On a broader scale this unique study makes it possible to start to bridge the gap between information known from current outcrop studies and conventional resolution seismic studies. Elsewhere systems of a similar scale have been described from outcrop data and on the seafloor but this is the first study to describe these systems in such detail in the subsurface; resolving the individual lobes, lobe elements and the fringes to these lobe elements. The fan lobe complexes described in detail in outcrop can be correlated with features observed here in the plan-view amplitude extraction maps. This is particularly interesting at the lobe and lobe element scale where such features have previously been simply described as ‘sheet sands’ when imaged in seismic data. This study enables the variation within these to be resolved and linked to known facies in

outcrop data; densely channelised lobes (channelised sheet facies) pass laterally into more branched, thinner channels and lobe elements (channelised and amalgamated sheets) then terminate in a high amplitude fringe (amalgamated and layered sheets). The high amplitude (i.e. sandy) fringes visible at a lobe and lobe element scale are particularly interesting as they surround the lobes, fringing lower amplitude lobe elements and are therefore likely to represent the amalgamated and layered sheet sands observed in outcrop data but never before recognised in seismic data. The new insights gained from this high-resolution Angolan example can be applied in the future to enhance the understanding of reservoir heterogeneities within deepwater fan systems throughout the world.

8 Interactions between Deepwater Sedimentary Systems and Active Salt Structures

8.1 Abstract

The infill history of a salt withdrawal mini-basin in the contractional domain of the gravity-driven salt system on the Angolan passive margin has been reconstructed using a high resolution three-dimensional seismic dataset. Well-constrained biostratigraphy has allowed calculation of the rate of change of bed length, used as a proxy for vertical growth rate, for the basin-bounding and intra-basin structures which have been fully discussed in Chapter 5. This information has been used alongside an analysis of the growth strata relationships to fully investigate how the depositional style of sediments preserved within the mini-basin has changed in response to changes in the rate of growth of the coeval, adjacent salt structures. Three different types of sedimentary system have been analysed which form the main constituents of the basin fill: channel complex systems; regional and local MTC deposits; and ponded fan lobe complexes. These different sedimentary systems have very different characteristics and associated flow characteristics, and hence react in different ways to bathymetric highs on the seafloor.

The channel complexes show the widest range of responses to the creation of seafloor topography by contemporaneous salt movement, with channels deflected, diverted, off-set or deeply incised as they interact with the developing slope topography. A cut-off rate of change of bed length of 15 mMa^{-1} has been calculated, below which channels are able to overtop the growing topography. Local MTCs do not appear to respond immediately to growing structures in the mini-basin but form after periods of high growth when the flanks of the structures are emergent on the seafloor. These two systems can be linked directly to structural growth of an area and hence have been grouped together as processes which exhibit an active response to structural growth. In direct contrast to this, regional MTCs and ponded fan lobe complexes infill the mini-basin avoiding areas where growth rates are high and/or the strata indicate topography formed a barrier to flow on the seafloor. These systems have been grouped together as having passive responses as they do not deviate from the original flow pathways and are simply funnelled or terminate against the resulting topographical barriers.

An early version of this chapter was presented at the 2012 Bob F. Perkins Research Conference organised by the Gulf Coast Section of the SEPM, and published as paper in the conference proceedings (Jones et al., 2012). Maps of the Miocene channel systems used in that paper, and subsequently for this thesis, were provided by BP, with the assistance of Mike Mayall.

8.2 Introduction

On many slope systems, deformation of the seafloor by salt diapirs, shale diapirs and/or faults has had a major impact on the facies deposited and their distribution. Limited or aerially restricted areas of seafloor deformation may cause channels to deflect or divert from their course (Cronin, 1995, Rowan and Weimer,

1998, Mayall and Stewart, 2000, Haughton, 2000, Hodgson and Haughton, 2004, Morgan, 2004, Smith, 2004, Gee and Gawthorpe, 2006, Mayall et al., 2006, Heinio and Davies, 2007, Clark and Cartwright, 2009, Cross et al., 2009, Mayall et al., 2010, Clark and Cartwright, 2011; Anderson et al., 2012). Depending on the relationship between the timing of the seafloor topography, channel formation and channel erosive power, the channels may also show off-set stacking on the flanks of structures and increased incision adjacent to, and across, the developing structures (Clark and Cartwright, 2009, Mayall et al., 2010, Clark and Cartwright, 2011). Where deformation of the seafloor is more extensive, completely enclosed basins may form. Lobes of sand may be deposited as the system is temporarily ponded within these intra-slope basins (see Chapter 7 and also Prather et al., 1998, Booth et al., 2000, Winker and Booth, 2000, Prather, 2003; Hay 2012).

Deformation of the seafloor commonly creates instability of the sediment leading to the formation of slumps, slides and debris flows sourced from intra-slope highs. The mass transport complexes (MTCs) that are generated can vary from being very local in extent with limited lateral movement of the original sediment (i.e. slumps and slides) to large deposits covering tens of square kilometres (Hampton et al., 1996, Huvenne et al., 2002, Haflidason et al., 2004, Frey Martinez et al., 2005, Moscardelli et al., 2006, Posamentier and Martinsen, 2011). Both local slides and regional debris flows have been imaged in the basin at different periods during its evolution and are fully discussed in Chapter 6.

Interactions between sediment deposition and contemporaneous structural development has been a significant factor in a number of slope channel systems which have become major hydrocarbon provinces (Kolla et al., 2001, Beydoun et al., 2002, Mayall and O'Byrne, 2002, Samuel et al., 2003, Broucke et al., 2004, Weimer et al., 2004, Porter et al., 2006; Anderson et al., 2012). One such area where this has occurred is offshore Angola. Here, Oligocene and Miocene sequences in the Lower Congo Basin containing turbidite channels and sheets have been deformed by the halokinetic activity of late Cretaceous salt, as the salt evolves in response to differential subsidence on the continental margin and increasing sediment load (Marton et al., 2000, Anderson et al., 2012). This deformation has generated the hydrocarbon plays that have led to the development of the deepwater Lower Congo Basin as a major oil producing area over the last ten to twelve years.

This chapter presents a study of the interaction between the growth rate, and resulting seafloor topography, of actively evolving structures and the sediment depositional systems within a salt-controlled mini-basin. Both active and passive responses are observed within the mini-basin with the channel systems showing the greatest range of active responses to the growing structures; large channel complexes deflect, are diverted, exhibit offset stacking and incise deeply into the salt-cored anticlines, salt walls and salt diapirs in the study area. In contrast to this the regional MTC deposits and the ponded fan lobe complexes react in a very passive way to the topography present in the area; infilling the areas with low bathymetry and terminating against structures which form a barrier to the sediment flow. The local MTCs do not behave in a predictable manner, but appear to be always sourced from structures which had high growth rates in preceding intervals and emergent bathymetry when the slides initiated.

8.3 Methodology

The growth of individual structures within the area was examined by calculating the bed length change at different times during the history of the basin. A full discussion of the methodology used for the bed length change analysis is presented in Chapter 4, Section 4.2.4. The results of this analysis are fully discussed in Chapter 5 where 21 sections have been examined throughout the basin and a further more detailed analysis was made of the linked folds in Area C. Throughout this thesis the rate of change of bed length of individual beds which cross the structures are used as a proxy for the growth rate of that structure; when the rate of bed length change is high this implies that the rate of structural growth during that interval was also high. This horizontal bed length change is assumed to result in a corresponding vertical uplift and hence the development of significant structural relief on structures within the mini-basin. This assumption is tested through the investigation of stratal growth geometries alongside the results of the bed length change analysis.

The results from the bed length change analyses are presented in map form for the relevant time intervals when the key depositional systems were active within the basin. The structures have been colour-coded according to the rate of bed length change for the relevant time interval shown as 'high' (red), 'medium' (green) or 'low' (yellow) and plotted along strike of the folds or salt walls they were measured from. High bed length change has been defined as rates greater than 30 mMa^{-1}, medium bed length change as rates between 10 mMa^{-1} and 30 mMa^{-1}, and low bed length change as rates below 10 mMa^{-1}. As discussed previously, the pink areas on the maps show the location of shallow salt, either in salt walls or diapirs that pierce through folds. Areas of extrusive, or canopy, salt are thought to have started to move laterally at approximately 10.89 Ma.

A key issue is the assessment of whether any seabed topography existed associated with the growing structures. Growth strata relationships are inherently very useful in this regard as they give some indication of the bathymetry associated with the structures through the assessment of the sediment packages along the flanks of the structures (see discussion in Chapters 4 and 5; Burbank and Vergés, 1994, Burbank et al., 1996, Ford et al., 1997, Broucke et al., 2004, Shaw et al., 2004, Shaw et al., 2005). Therefore relationships such as onlap, offlap and overtopping of strata on the flanks of the growing structures have also been examined for the key periods of sediment deposition in the basin. Furthermore for the interval containing the ponded fan lobe complexes the onlap locations of key stratigraphic surfaces have been mapped around the margins of the fan unit packages. These results are used to complement the mapping of the bed length change trends within the basin and assess the response of the deepwater sedimentary systems to changes in the growth rate and, ultimately, bathymetry within the mini-basin.

8.4 Structural Controls on the Mini-Basin

The limits of the main sediment depocentre are defined by a series of broadly north-south trending salt-cored anticlines which flank the western and eastern margins of the basin (Figure 8.1). Continued salt movement generated a series of salt walls, the most influential of which are labelled Areas B and D on the west side of the basin (Figure 8.1). The eastern border is also composed of a series of less continuous north-south

trending salt-cored anticlines. Northeast-southwest trending anticlines, along which less salt movement occurred, are located in the central and southern parts of the area (Figure 8.1; Areas C and E). Sub-parallel, north-south trending salt-cored anticlines form the western border in the northern part of the basin (Area A). A few of the diapirs in the core of the anticlines can be seen to be connected to the original Aptian autochthonous salt layer but the majority form isolated to semi-isolated allochthonous salt bodies which are detached from the source salt layer.

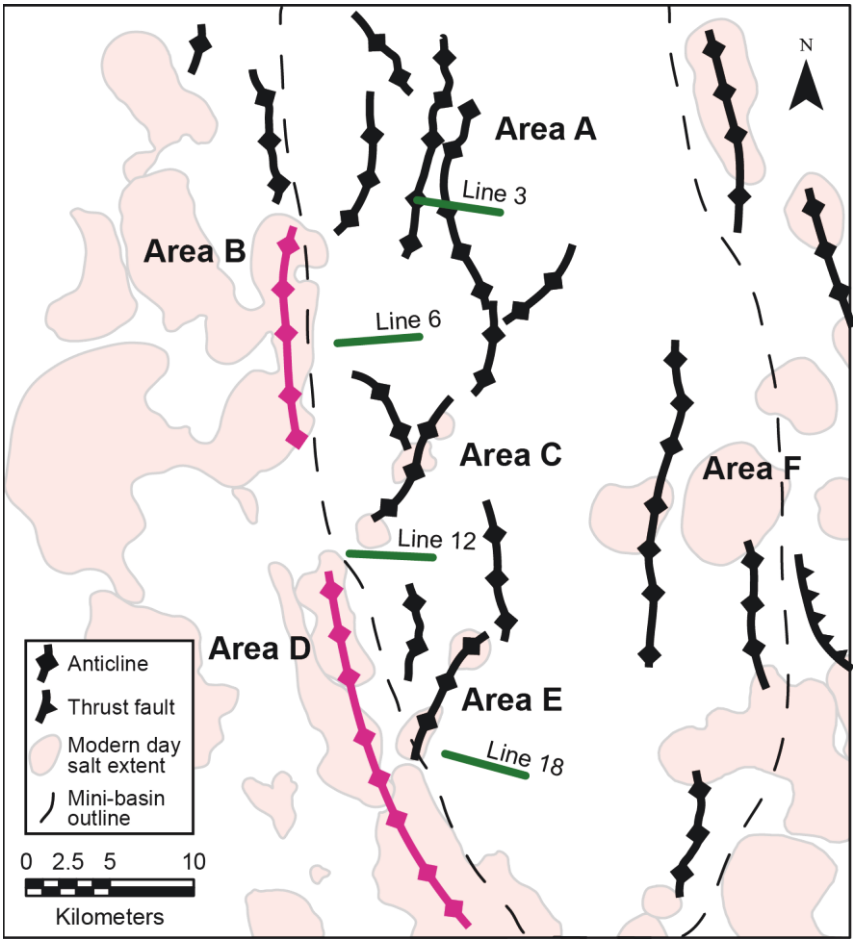


Figure 8.1 Structural elements map showing the location of the main structures in the area. Salt distribution (pink) is that seen at or near the surface at present day, black lines indicate anticlines visible in the seismic data, pink lines indicate anticlines inferred from the seismic data, green lines 3, 6, 12 and 18 relate to graphs shown in Figure 8.2. Line numbers are the same as those shown in Chapter 5.

A selection of graphs showing the amount of bed length change recorded on sections through the most significant structures in the basin emphasises that consistently high rate of change of bed length occurred until approximately 11.86 Ma (H70) implying a rapid rate of structural growth during these times (Figure 8.2). The rate of bed length change decreases across all structures from then onwards, however this decrease is less rapid on the structures seen in Areas B and E, where higher than average growth rates occur throughout (Figure 8.2, Lines 6 and 18). The lowest rate of change of bed lengths are seen from 8.29 Ma (H110) onwards where there is very little movement on any of the structures (Figure 8.2). The variation in the structural history of the mini-basin through time is discussed in more detail in Chapter 5.

Alongside the variations in structural growth rate, the type of sedimentary system being deposited in the basin also varies, allowing links between growth rate and different types of depositional systems to be

investigated. This chapter focuses on how three different types of depositional systems respond to the changes in bathymetry created as the structures grew: channel complexes; mass transport complexes (MTCs); and ponded fan lobe complexes. Although channel complexes occur throughout the history of the basin they show the greatest response to structural growth between 25 Ma and 18.26 Ma and hence it is this interval that is examined in more detail (Figure 8.2). The highest rates of structural growth occur between 18.26 Ma and 13.25 Ma (H10 to H60) which corresponds to a time when regional MTCs were deposited, whereas the lowest rates of structural growth occur in during between 8.29 Ma and 5.58 Ma (H100 to H110) when sediment ponding was extensive which may appear somewhat paradoxical.

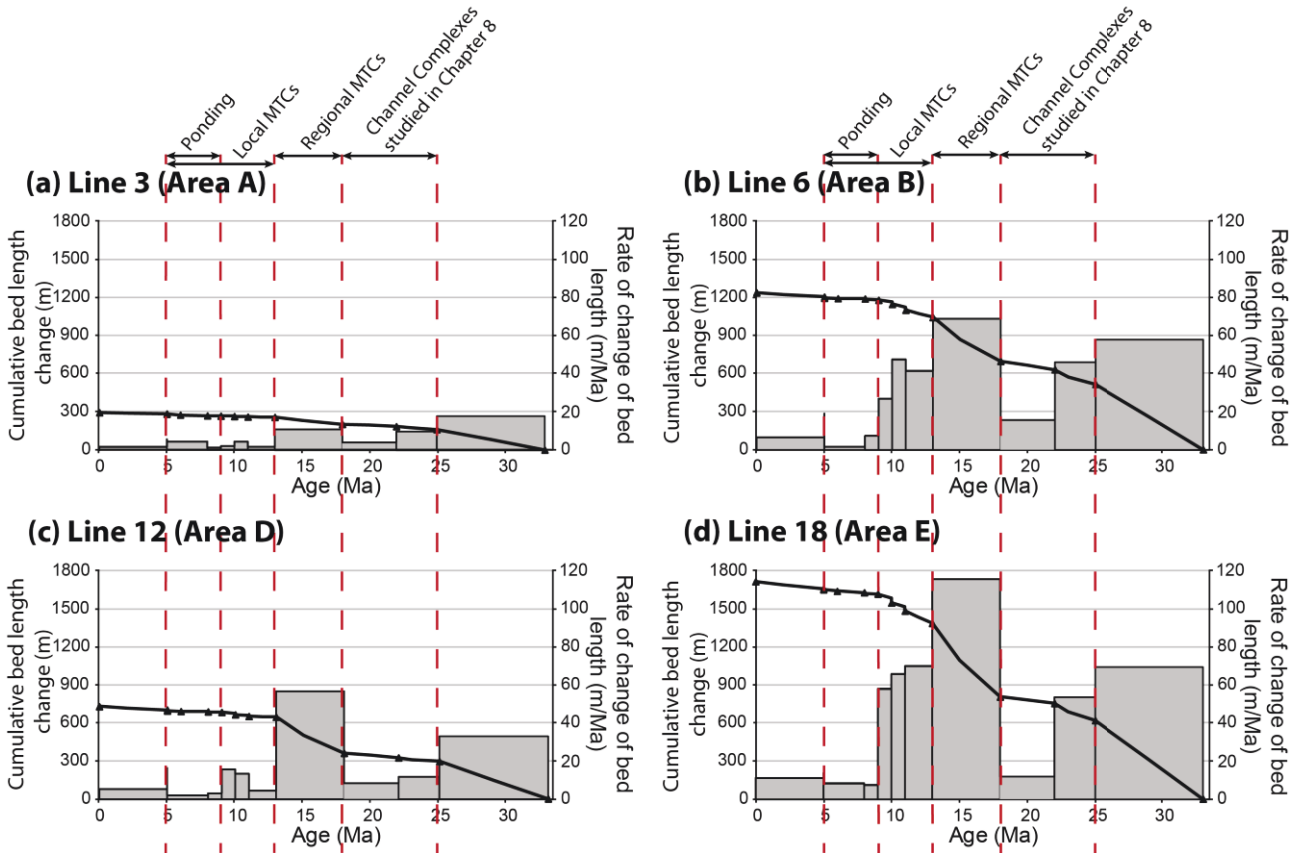


Figure 8.2 A series of graphs showing the absolute bed length change (black line) and the rate of change of bed length change (grey bar chart) across four of the structures bounding the western edge of the basin. Lines located in Figure 8.1. The graphs have been sub-divided to show the dominant sedimentary packages.

8.5 Interactions between Active Structural Growth and Channel Complexes

As the channel complexes have not been previously discussed in this thesis the relationship between structural growth rate and channel distribution is examined in detail and then followed by a discussion of some of the key points highlighted by this work. The theories presented on how the channels react to the variations in bed length change rate and hence inferred vertical growth of the structures are then tested using stratal relationships on the flanks of the active structures. This stratal analysis is somewhat hindered by poor imaging and bed rotation on the flanks of some of the key salt-cored structures. However, as discussed in Sections 4.2.12 and 5.11.2 (Chapters 4 and 5 respectively), generation of seabed topography is a function of the ratio between the rate of active structural growth and rate of sediment accumulation, and hence the growth rate of structures as measured through bed length change analysis cannot be considered in isolation.

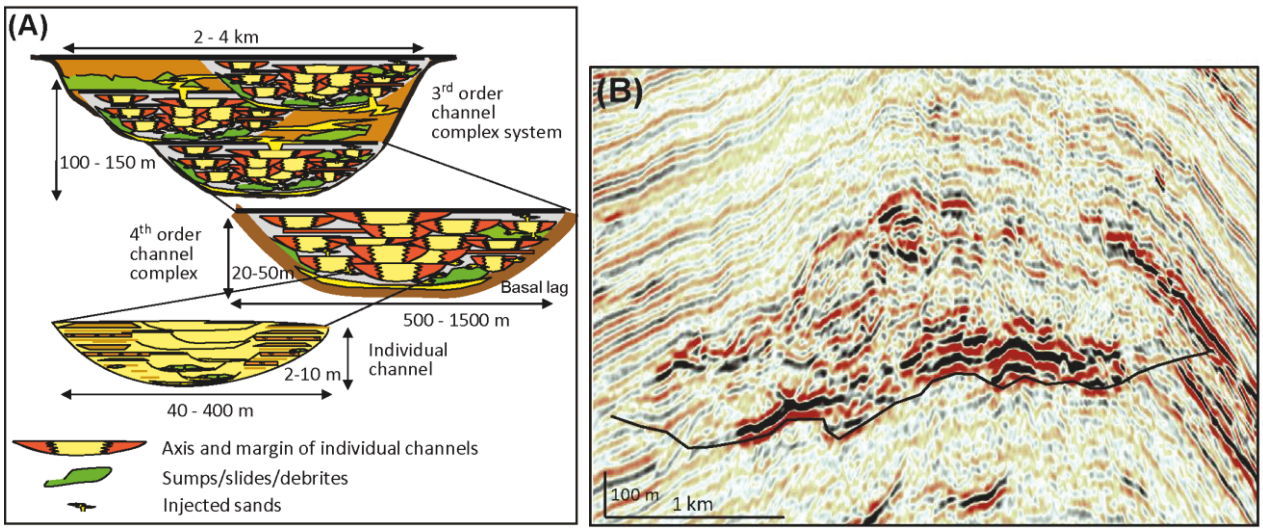


Figure 8.3 General model for the channel complex systems in the area studied. (A) General model includes a third order channel complex system with a dominantly erosional base, several fourth-order channel complexes in which axis and margin areas can be recognised and individual channels (modified from Mayall et al., 2006). (B) Representative seismic section through a channel complex system with the third order base interpreted. Figure from Jones et al. (2012).

The channels shown in this section of the thesis have been mapped by BP and third-order systems have been isolated from the amplitude extraction maps (Figure 8.3; as per terminology of Mayall et al., 2006); fourth order smaller-scale channels are also sometimes identifiable in the amplitude maps. During the interval from 25 Ma to 18.26 Ma studied here, the deposition of the channels and how they respond to salt movement are examined in two time periods referred to as Early and Late Channel intervals. Biostratigraphic data indicates that these two periods are approximately 2 to 4 Ma years in duration (S. Payne, 2012, pers. comm.). During both of these periods the relative ages of the channels (Figure 8.4; 1.1, 1.2 *etc*) were assigned by observing the erosional and onlapping stratigraphic relationships. It is possible that the more discrete channel clusters in the north and the south of the mini-basin may have both been active at the same time.

8.5.1 Response of Channels to Structural Growth during Early Channel Interval

During the earliest time period between approximately 25 Ma and 22.5 Ma (Figure 8.4 (b)) structures in Areas B, D and E have the highest bed length change values and a correspondingly high growth rate. The structures in the southern half of Area B had particularly high rates of change of bed length with up to 49 mMa^{-1} recorded. The channels respond to the presence of this structure with major diversions of the channel complex systems in this area; Channel 1.3 diverts to the south and Channels 1.4 to 1.7 are deflected to the north (Figure 8.4 (b)), indicating that the high rates of bed length change did correspond to the generation of seabed topography with a local increase in the slope gradient in the vicinity of the anticline (and resulting salt wall). A significant change in flow pathway orientation is particularly noticeable for the fourth order channels within Channel 1.3 which are deflected by almost 90^{o}. These become increasingly sinuous as the channel orientation switches from an east-west to a northeast-southwest orientation directly west of the Area B salt wall which has the highest rate of change of bed length (Figure 8.4 (b)). Where the channel system goes through the gap between the anticlines within Area C the third order channel complex system was able to incise directly across the structure.

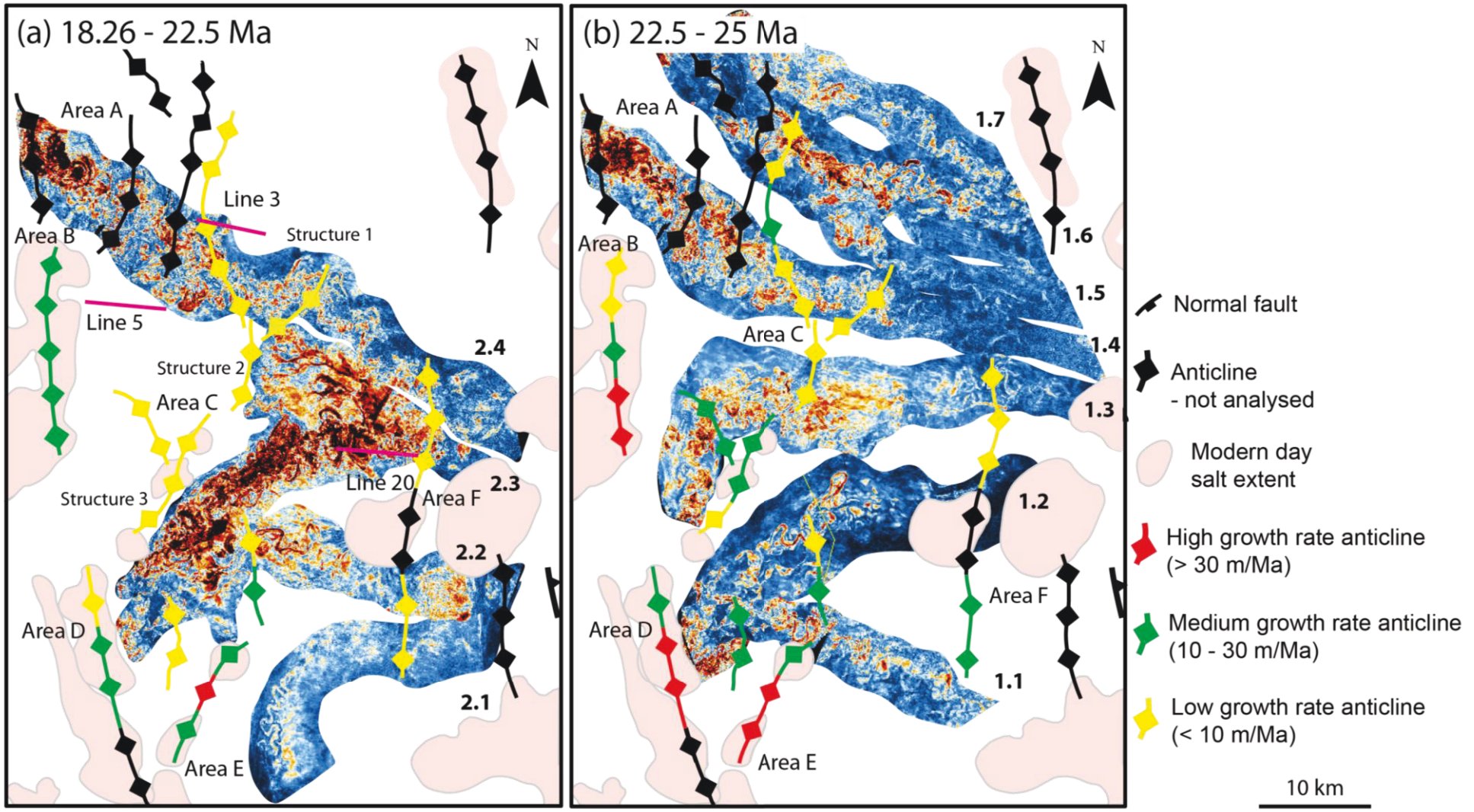


Figure 8.4 Distribution of channel complex systems from 25 Ma to 18.26 Ma, (a) shows the channel systems within the Late Channel interval from 22.5 Ma to 18.26 Ma during which time the channel complex systems continue to deflect around Areas B and D but also deflect around Area C, divert in front of Area E, cut across the structure within Area A and divert around Area F, and (b) the Early Channel interval from 25 Ma to 22.5 Ma which shows channel complex systems deflect to the north and south around Areas B and D (the areas of greatest salt movement), divert around Area C, cut across Areas A and E and show northwards offset stacking from Area F. Both these maps highlight the channels using root mean squared (RMS) amplitude maps calculated using 50 ms Twtt window. General regional slope direction is east to west. Red coloured anticlines indicate high rates of bed length change, green indicate medium rates of bed length change, yellow indicate low rates of bed length change and black indicates where no bed length change analysis was conducted. Cross-sections Lines 3, 5, and 20 shown in Figure 8.6.

The growth on the salt-cored anticline in Area C, which has a high maximum rate of change of bed length of 28 mMa^{-1}, caused Channel 1.3 to be slightly diverted around the northern end of the structure. It then deflected sharply to the south because its pathway to the west was blocked by the Area B salt wall. Although imaging is difficult in the vicinity of the Area D salt walls, it appears that Channel 1.3 may have exited the basin north of Area D (Figure 8.4 (b)). In contrast Channel 1.2 was diverted to the south of the Area C structure and continued to run almost parallel to this structure until it exited the basin between Areas D and E (Figure 8.4 (b)). Fourth order channels, clearly visible in the amplitude signal show an increase in sinuosity away from structure tips, presumably where the palaeo-seabed gradient was lower. Channel 1.2 is inferred to enter the area approximately mid-way along the Area F structure. A younger salt canopy has developed from the salt diapir through the anticline at this location, this, along with a second salt canopy directly to the east, obscure the underlying strata, and prevented bed length measurements from being calculated in this location. The implications of the presence of Channel 1.2 in this area is that either the structure did not have seabed expression at this time, or it may be a relay between two segments of the Area F anticline and thus have provided a topographic low for the channel to exploit.

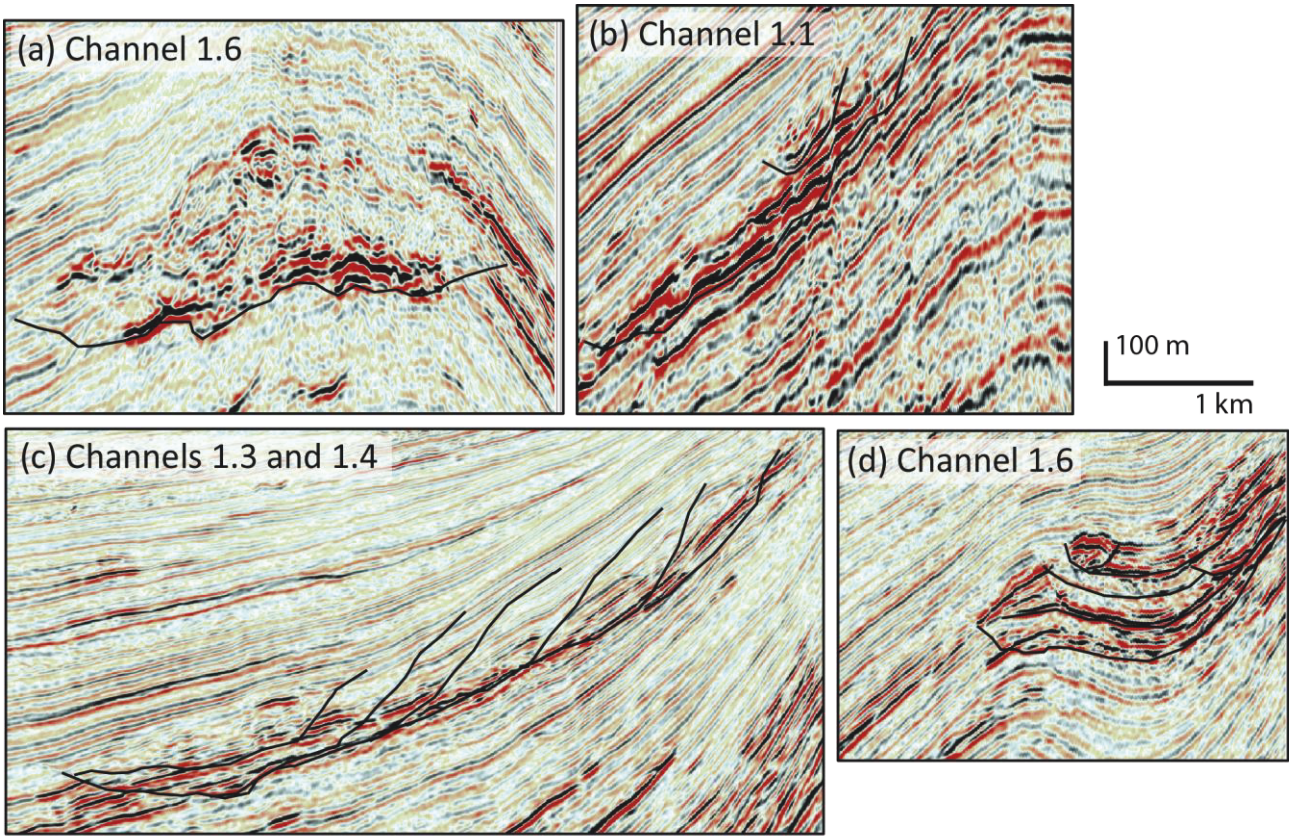


Figure 8.5 Typical seismic lines through four of the channel systems as they encounter actively growing structures: (a) Channel complex 1.6 cutting into the structure as it approaches Area A with the third-order channel base highlighted, (b), Channel complex 1.1 showing the system offsetting and cutting into the structure in Area E, (c) Channel complexes 1.3/1.4 showing offset stacking of the channel complexes away from the growing structure in Area F, and (d) Channel complex 1.6 showing multiple incisions into the growing structure towards the crest of the anticline in Area A. This figure is slightly modified from one published in Jones et al. (2012).

Channel 1.4 which exits the mini-basin to the north of the Area B salt wall exhibits a more gradual change from an east-west orientation to a broadly southeast-northwest orientation, which again corresponds to the growth on structures within Area B. The channel complex system also widens rapidly and is deflected

slightly around the anticline with the medium rate of change of bed length in the middle of Area A. This anticline has a maximum rate of change of bed length of 14 mMa^{-1} during this interval and appears to have generated enough of an increase in topography to cause this channel to deflect slightly (Figure 8.4 (b)). The channels to the north of this area also respond to the growing structure within the centre of Area A with Channels 1.6 and 1.7 passing to the north. However, channel incision appears to have kept pace with structural growth in the north of Area A where rate of change of bed lengths of up to 6 mMa^{-1} were recorded in this interval. Channels 1.5 and 1.6 were able to cut through the structure, although both did avoid the centre of the structure which had the highest growth rate (Figure 8.4 (b) and Figure 8.5 (a) and (d)).

Channel 1.1 has a very different entry point and orientation to the other channels within the study area; it is orientated southeast-northwest and enters the basin from the southeast of the area (Figure 8.4 (b)). It follows a straight, direct route within the basin and has cut through the medium growth-rate structures towards the centre of Area E (Figure 8.5 (b)). These have a fairly high maximum rate of change of bed length of 22 mMa^{-1} during this interval. In contrast to the changes in channel morphology observed in other channels, Channel 1.1 does not appear to respond to the growth on this structure, with only a slight increase in the width of the sinuosity after it has traversed the structure. However, seismic sections through the channel complex indicate that it deeply incised across the growing seafloor structures (Figure 8.5 (b)). This shows that the channel truncated sediment packages within the older part of fold but as the fold continued to grow the channel location switched and the remnant part of the channel was folded. This resulted in a high degree of focusing of the channel axes and extensive periods of erosion at the fourth order scale. The repeated deep erosion has resulted in the early fourth order channel being highly eroded and often only preserved as erosional remnants (Figure 8.5 (b)). Channel 1.1 is then diverted to the south due to the high growth rate structures within Area D and appears to have exited the basin following the same pathway as Channel 1.2.

It appears that the growth of the fold and salt diapir in Area F on the eastern edge of the basin caused offset and northward stacking of Channels 1.3 to 1.7 (Figure 8.5 (c)). Therefore, it is assumed that this growth occurred towards the latter half of this interval and after the deposition of Channel 1.2. This repeated offset stacking of the third order channel complex systems meant that only the oldest systems have been preserved updip (Figure 8.5 (c)). Growth on anticline to the south of the present day salt canopy within Area F could also have been responsible for the more southerly entry point of Channel 1.1 (Figure 8.4 (b)).

8.5.2 Response of Channels to Structural Growth during Late Channel Interval

During the Late Channel Interval between approximately 22.5 Ma and 18.26 Ma (Figure 8.4 (a)) the greatest amount of growth occurred on the structure in Area E although the salt walls on the western edge of the basin, Areas B and D, also continued to develop, albeit at a slower rate than in the Early Channel Interval (Figure 8.4). The structures in Area B in particular continued to form a major regional barrier and locus for diversion of the channel complex systems either to the north (Channel 2.4) or to the south (Channels 2.3). These structures had an average rate of change of bed length of 15 mMa^{-1} which increased from north to south along the structure. Channel 2.4 exited the basin to the north of Area B crossing the lowest growth tip

of the anticline in Area A, following a similar pathway to that observed by Channel 1.4 in the previous time interval. Whilst the growth on the structures within Area A and the northern tip of the structures within Area C were low in this period, they do appear to have had an influence on the morphology of the third order channel system and the fourth-order channels contained within these (Figure 8.4 (a)). Within Channel 2.4 the high amplitude fourth-order channels deflect north around the tip of the anticline in Area C and increase in width after they have crossed the structure to the south of Area A, which had a rate of change of bed length of 4 mMa^{-1}.

Structures 2 and 3 in Area C also formed a complete barrier to westward flow of the channels at this time, even though they had relatively low rate of change of bed lengths, with a maximum of 9 mMa^{-1} recorded towards the south of Area C (Figure 8.4 (a)). Channels 2.2 and 2.3 deflected southwards to the east of Area C and both channels exited the basin between the structures in Areas D and E. As Channel 2.3 was deflected to the southwest on the west side of the anticline in Area F a large splay was deposited at the point where the channel sharply turned south (see Mayall et al., 2010 for further discussion of this feature). Whilst the maximum bed length change recorded within Area C was only 9 mMa^{-1}, Channels 2.2 and 2.3 do appear to respond to these structures. This could indicate that these channels are responding to relict bathymetric highs within the area which resulted from the previous higher growth on these structures in the Early Channel Interval.

The Area E anticline continued to be prominent in this interval and caused Channel 2.1, which entered to the south of Area F, to be deflected sharply to the south as well as causing Channel 2.2 to deflect north around its northern tip (Figure 8.4 (a)). Channel 2.1 appears to contain lower amplitude fourth-order channels which are slightly narrower in width than those seen within the other third-order channels in this period. This could indicate that the system is less well-developed than those imaged elsewhere in the basin. The distinct 90^{o} change in orientation of Channel 2.1 as it approached the structures within Area E contrasts with a channel in a similar location in the previous time period (Channel 1.1) that crossed the northern tip of the structure (Figure 8.4 (a) and (b)).

Despite structural growth of the main Area F anticline, albeit at a low rate, all channels entering the mini-basin do so over this structure. Channels 2.2 and 2.3 appear to deflect slightly around the location of the present day salt canopy, suggesting that this part of the structure may have acted as a topographic barrier. Unfortunately it is not possible to measure bed length variations in this location as the beds are obscured beneath the younger salt canopy. There could be a number of reasons why the channels are able to make their way across the structures within Area F:

- channels are already cutting the structure so they can keep pace with slow growth (however, this does not appear to be the case when compare to previous time interval);
- the structure is buried (possibly just on the eastern flank) with no seabed relief and hence channels don't directly encounter it;
- the structure has been buried briefly and channels have enough erosional power to remain entrenched in one place as structure has grown.

8.5.3 Discussion of Channel Interactions

The channel systems examined in the preceding sections have not been studied in depth elsewhere in the thesis and show unique responses to the inferred change in bathymetry generated as bed length varied on the structures bounding, and internal to, the basin. Therefore a discussion of the key observations will be presented in this section of the chapter and then the more active response of the channel systems compared to the passive response of the regional MTCs and ponded sediments outlined in the main discussion sections (Sections 8.8.1 and 8.8.2).

Analysis of channels in both the Early Channel interval and the Late Channel interval has shown that the magnitude of horizontal bed length change, which is used here as a proxy for growth rate and hence vertical uplift, can explain some of the response of channel systems. In particular, the structures which have the highest growth rates (i.e. those with rate of change of bed lengths of >30 mMa^{-1}) have been clearly documented to form the most significant bathymetric barriers. Using only the results from the bed length change analysis it is possible to conclude the following:

- structures with high to medium growth rates cause deflection of channels which implies that they had associated seabed expression. Therefore it is possible to conclude from the observations outlined in the preceding sections that when rate of change of bed lengths are greater than 30 mMa^{-1} the associated structures have seabed expression;
- in a few isolated cases channels are able to make it across structures with moderate growth rates, c. 15 mMa^{-1} (for example Channels 1.1 and 1.3);
- low growth rate structures are more frequently crossed; low horizontal rate of change of bed lengths mean a concomitant lower vertical uplift with relatively minor seabed topographic expression. These structures are more likely to be overtopped by sediments; though some do deflect channels, in particular the linked anticlines in Area C during the Early Channel interval.

Therefore it is possible to define a cut-off of approximately 15 mMa^{-1} horizontal bed length change for this particular study area below which a structure is not likely to generate enough topographic relief to affect the response of the channels within the study area.

However, the interactions between the channels in the vicinity of Area C suggest that either low rate of change of bed lengths, or relict topography may have an impact on the distribution of channels within the mini-basin. When comparing the responses of the channels between the Early and Late intervals it is noticeable that Channels 1.3 and 1.4 are able to make it across the structures in the north of Area C whilst Channel 2.3 is deflected south by this structure. This occurred during a period when the maximum rate of change of bed length on the structure which was crossed by Channel 1.3 but not by Channel 2.3 increased from 2 mMa^{-1} to 8 mMa^{-1}. A detailed analysis of the three linked anticlines which form the structures within Area C was carried out in Chapter 5, Section 5.9 and can be used to give further insights into the how relatively small variations in bed length change and hence bathymetric relief can impact distribution of the

channel systems and decide whether they incise into an anticline or are deflected by it (Figure 8.6). In this part of the study Area C has been separated into three segments, the locations of which are shown on Figure 8.4.

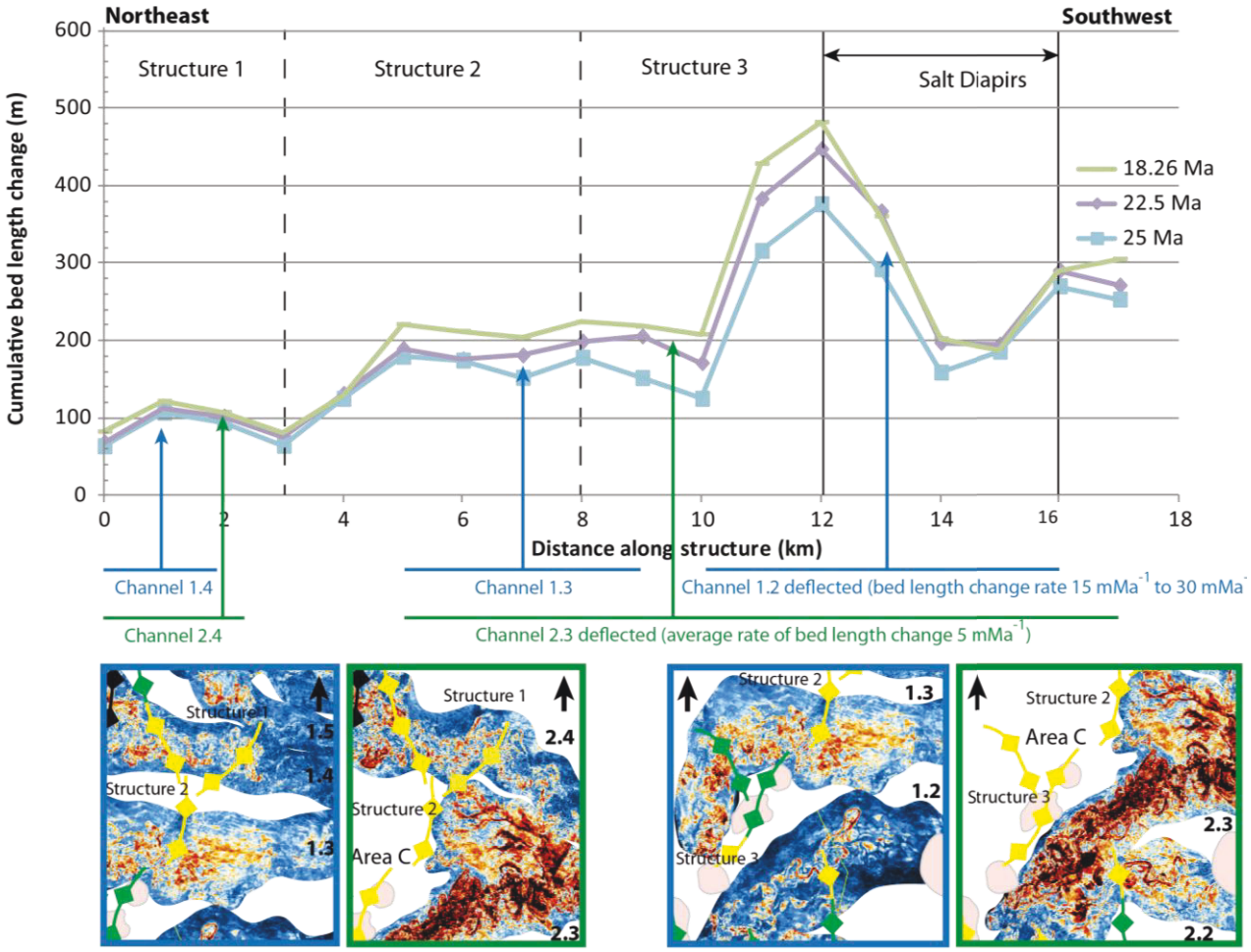


Figure 8.6 Three anticlines which link to form Area C presented alongside the location and maps showing the main channel complexes. Note that Channels 1.4 and 2.4 cross the structure in the northeast where the bed length change is the lowest and the lowest rate of change of bed lengths are observed whereas Channels 1.3 and 2.3 are deflected by the anticlines in regions where bed length change, and hence structural growth, is highest.

During the Early Channel interval between 25 Ma and 22.5 Ma there is no significant bed length change on Structure 1 and most of Structure 2; but Structure 3 shows significant bed length change (Figure 8.6). The results of the bed length change analysis indicate that the average rate of change of bed length across Structure 1 during this interval is 3 mMa^{-1} whilst the average on Structure 2 is 5 mMa^{-1} these low rates of change of bed length imply low vertical growth, allowing Channels 1.3 and 1.4 to cross the resulting structures (Figures 8.4, 8.5 and 8.6). In contrast to this Structure 3 has significantly higher rates of bed length change during this interval which range between 15 mMa^{-1} and 30 mMa^{-1} towards the northern end of the structure which decreases to an average of 6 mMa^{-1} in the southern two kilometres. These higher rates of change of bed length in the northern part of Structure 3 cause Channel 1.2 to be deflected and it is unable to cross the resulting bathymetry.

In comparison to this, during the Late Channel interval between 22.5 Ma and 18.26 Ma only Structure 1 of Area C has a very low bed length change rate recorded with an average of 2 mMa^{-1} whilst the rate of change

of bed length on Structure 2 appear to have increased slightly in some places along the structure with a maximum bed length change of 9 mMa^{-1} recorded from the centre of the anticline (Figure 8.6). In contrast the bed length change has decreased on Structure 3 with a similar range now recorded to Structure 2, both of which range from between 1 mMa^{-1} to 10 mMa^{-1} with an average of 5 mMa^{-1} on Structure 3 and 4 mMa^{-1} on Structure 3. Consequently the only part of Area C to be crossed by channels in Late Channel interval from 22.5 Ma to 25 Ma is Structure 1 which is crossed by Channel 2.4 (Figure 8.6). No channels cross Structures 2 and 3 and although they are all classified as being in the 'low' growth rate bracket, they have higher growth rates than Structure 1. Therefore it would seem that a small increase in bed length change along Structure 2, between the older and younger intervals was enough to force the younger Channel 2.3 that was previously following similar flow path to Channel 1.3 to divert and flow to the east of Structure 3 as opposed to crossing through Area C over Structure 2. Some of the deflection could also be explained due to the presence of relict bathymetric highs formed in the younger interval which remained as highs on the seafloor. Deciphering whether relict topography was present during the later interval is not possible through the use of stratal relationships in this area as the beds on the flanks of the structures have been subsequently folded too much to allow decent resolution. However, this study does show that there may be more detail in areas assigned to the low growth rate (i.e. <10 mMa^{-1}) category which might be resolved with more closely spaced measurements.

As shown in the response of Channel 2.3 in the Late Channel interval between 22.5 Ma and 18.26 Ma it is still possible for channels to be deflected by structures which have low rates of bed length change (Figure 8.6). This indicates that the structural growth rate is only part of the story and as discussed in Chapter 5, Section 5.11.2 bed length change analysis can only reveal which of the structures were growing during this stage in the development of the basin but not necessarily the amount of topographic relief generated by those structures. So an obvious explanation for areas where channels appear not to respond to a growing structure is that sedimentation kept pace with structural growth so that no seabed topography was generated. Additionally there are number of other factors that might be important when considering the response of channels to bathymetry such as:

- channels in an established position (i.e. antecedent channels) may keep pace with structural growth; or
- higher growth rate from the previous interval can affect channel pathways, even though growth at time of channel formation itself has slowed, through the generation of relict topography.

The stratal relationships along the flanks of actively growing structures can be assessed to test whether the rate of change of bed lengths calculated for a structure are an accurate predictor of bathymetric relief. This has proved difficult to do accurately at the depth at which the channels are located due in part to the steep dips on the flanks of the structures which have formed due to continued folding or salt movement, and limits of the seismic resolution. This means that subtle onlap and offlap reflection geometries cannot be

ascertained with confidence, and therefore it has not been possible to assess the strata rigorously in all areas of the basin. However, a few examples are presented and discussed here to illustrate some of the key points.

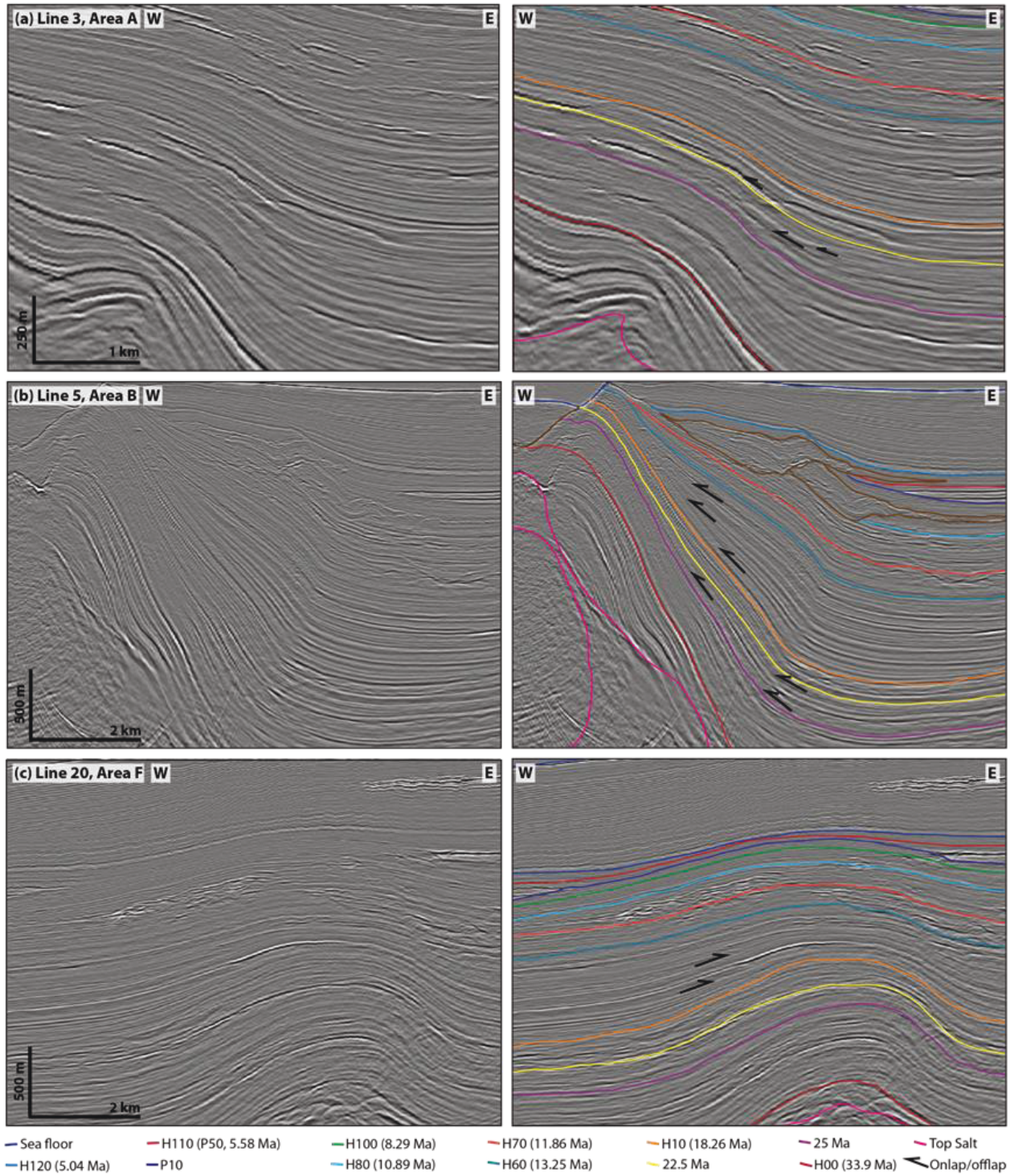


Figure 8.7 Sections through some of the key structures where channels respond to structural growth, with the Early channels deposited between the purple and yellow horizons (25 Ma to 22.5 Ma) and the Late channels between the yellow and orange horizons (22.5 Ma to 18.26 Ma). Black arrows indicate onlapping and offlapping strata and have also been shown within the interval containing regional MTCs (the orange to blue horizons deposited between 18.26 Ma and 13.25 Ma) which will be referred to in Section 8.6.1. Line locations shown in Figure 8.4. (a) shows a section through Area A on the north-western margin of the mini-basin where onlap can be observed in the packages containing the channel complexes, (b) shows a section through Area B which had consistently higher growth rates throughout the history of the mini-basin resulting in extreme folding of the sediments and the generation of local MTC deposits (outlined in brown), and (c) a seismic section taken through Area F directly to the north of the diapiric salt.

Channel complexes are clearly able to cut through the actively growing structure in the south of Area A in both the Early and Late Channel intervals (Figure 8.4). However, Channel 1.5 in the Early Channel interval deflects further away from the tip of the anticline than Channel 2.4. This corresponds to medium growth rates in the Late Channel interval but also to changes of the growth strata along the eastern flank of the anticline (Figure 8.7 (a)). During the Early Channel period (between 25 Ma and 22.5 Ma) there is clear thinning of the main sediment package towards the anticline and a series of onlapping strata observed in the youngest part of this package. At least one offlapping relationship is also observed (Figure 8.7 (a)) indicating that there was clear topographic relief in this area during the time the channel complexes were active. In the Late Channel interval (from 22.5 Ma to 18.26 Ma) less onlapping relationships are observed within the strata with the majority of the youngest strata overtopping the structure. This change in the stratal relationships corresponds to a movement of Channel 2.4 slightly to the north closer to the centre of the anticline within Area A.

In the anticline in the north of the Area F, almost directly to the north of the salt diapir, channels are able to continue to move across the slow growth rate structure. Whilst these structures are categorised as low growth rate, they were still active during both the Early and Late Channel periods with rate of change of bed lengths of 4 mMa^{-1} and 3 mMa^{-1} respectively. The seismic section through this structure shows clear overtopping of the sediments throughout this interval (i.e. from the purple 25 Ma horizon until the orange H10 horizon) with almost no change in bed thickness recorded (Figure 8.7 (c)). This section corresponds to the northern edge of Channel 1.3 and in the middle of Channel 2.3, and therefore supports the observation that when sedimentation rate is greater than the growth rate on a structure then the structure can become blanketed by sediment and channels no longer detect the structures on the seafloor.

Area B is one of the most active structures within the basin (see Chapter 5) and movement on this structure appears to have caused Channel 1.3 to deflect within the Early Channel interval. Continued movement on this structure is thought to be a contributing factor to the lack of channel complexes in this area during the subsequent Late Channel period (Figure 8.4). Variations in the thickness of the sediment packages between 25 Ma and 22.5 Ma support the results of the bed length change analysis in this area during the M2 Early period and explain the clear deflection of Channel 1.3; the sediment package thins dramatically towards the crest of the anticline and some strata can be observed onlapping the flanks of the anticline suggesting that the structure had topographic relief during this period (Figure 8.7 (b)). However, the sediment package deposited between 22.5 Ma and 18.26 Ma thins less dramatically across the anticline with the majority of the strata overtopping the structure (Figure 8.7 (b)). This implies that there was less bathymetric relief on the structure during the Late Channel period suggesting that the lack of channel deposits in this area might be attributed solely to topographic highs formed by the structures within Area C to the east (Figure 8.4 (a)). Therefore this example shows that in the case of structures which have a high growth rate, it is possible to observe clear stratal patterns which support the assumption gained from the channel response and the rate of change of bed length calculations that there must be a significant topographical barrier in the area.

The patterns and links between the stratal relationships, bed length variations and channel responses observed in Areas B and F represent end-member scenarios; in Area B the rates of bed length change are high and extensive onlap is recorded indicating that the structure formed a topographic barrier to down-dip flow and caused channels to deflect, whereas in Area F the structural growth is low and correspondingly the channels are able to overtop the structure. Therefore, this analysis has shown that the magnitude of horizontal bed length change, which is used as proxy for growth rate with related vertical uplift, can explain many of the responses of third-order channel complexes and that the structures with the highest rate of change of bed length do indeed form the most significant topographic barriers. However, other processes should also be considered, as it has been observed that some channels can cross structures that are actively growing, and hence knowledge of processes associated with channel formation become important. These include factors such as the change in erosive power of channel systems and the volume of sediment transported by the channel complexes.

It has also been observed that existing topography from the preceding period of growth affects the flow pathways of the channels. Therefore it would be useful to know whether channelised turbidity currents can surmount obstacles and if so what the topographic cut off is. These are questions which were beyond the scope of this study, but might be interesting to consider in further studies of this kind. It is also probable that some of controlling factors may be beneath the resolution of the observations made here. The rate of change of bed lengths recorded may not be constant even over a 2 Ma time span and thus there may be periods where a slowdown in growth has allowed sediments to overtop a fold; a channel then can cross a structure and may keep up with growth incising into structure as rate subsequently increases.

8.6 Interactions between Active Structural Growth and Mass Transport Complexes

Mass transport complexes (MTCs) are common offshore Angola within the Tertiary stratigraphy (Gee et al., 2006). MTCs can vary in size and shape, from local slumps and slides to regional unconfined debris flows capable of transporting sediment from the continent to the abyssal plain (Hampton et al., 1996). The MTCs studied here have been divided into two categories; regional MTCs and local MTCs. The former extend throughout the entire area, occur earlier in the sedimentary succession and contain shelfal biofacies, indicating they have been transported regionally, whilst the latter are smaller in their extent, form later and do not contain shelfal material. A full discussion of the main features associated with these MTCs can be found in Chapter 6. Here, the main distribution patterns of these systems will be discussed with respect to the relative structural movement recorded on the anticlines within the mini-basin as they were deposited.

8.6.1 Regional MTCs

Widespread, well-developed regional MTCs occur primarily between 18.26 Ma and 13.25 Ma (H10 and H60; Figure 8.2). Several are easily recognisable in the seismic data as they are internally chaotic and thin onto the salt structures which bound the basin, particularly those in the west of the area. Whilst horizons have been mapped within the interval between 18.26 Ma and 13.25 Ma (H10 to H60), the bed length change

analysis was carried out across this entire period and hence the analysis in map view shows the same rates of change of bed length for both of the MTCs studied here.

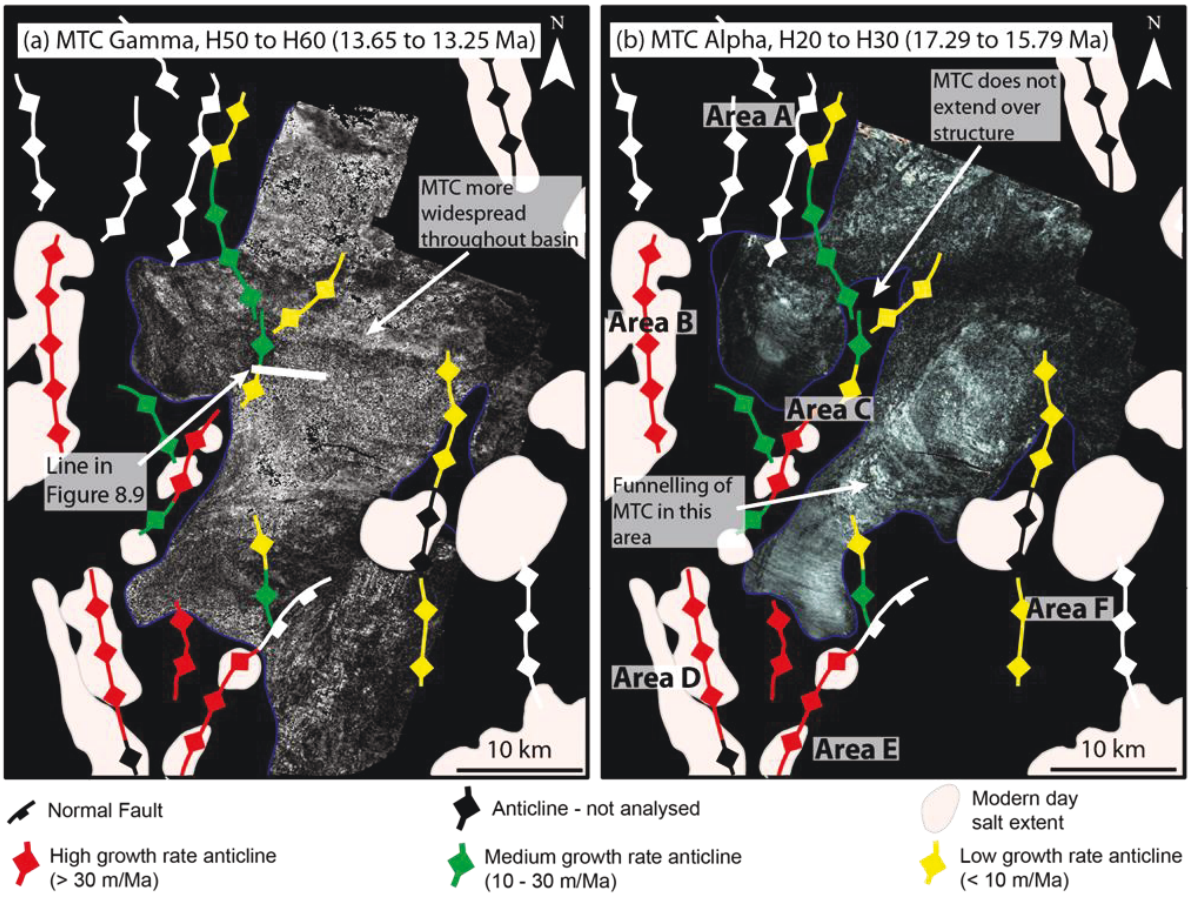


Figure 8.8 Maps illustrating the areal extent of two of the regional MTC deposits with anticlines coloured according to bed length change values from the whole interval from 13.25 to 18.26 Ma. (a) shows the extent of MTC γ, a younger system deposited in the mini-basin and (b) shows the extend of MTC α, the oldest system. The maps show RMS amplitude extractions taken through the centre of each of the MTC deposits using a 10 ms twtt window to highlight the main features. Red coloured anticlines indicate high rates of bed length change, green are medium rates of bed length change, yellow are low rates of bed length change, and black are areas where no bed length analysis was conducted.

This interval has high rates of bed length change and hence high growth on all the structures within the mini-basin, particularly on the western margin of the basin (Figure 8.8; Areas B, C, D and E). It is not possible to trace the source of MTCs to an initial failure surface within the mini-basin and the basal surfaces and internal characteristics cannot be traced further east due to limits in the resolution of the data. However, biostratigraphic analysis of recovered cuttings shows that at least one of the MTCs contains remobilised outer shelf to upper bathyal biofacies (S. Payne 2011, pers. comm.) indicating that the sediments may have been transported from significantly further landward. As discussed within Chapter 6, this indicates that the generation of the regional MTCs was not influenced by the high rates of structural growth within their immediate vicinity (Figure 8.8).

Here the focus is on two of the regional MTCs which vary in spatial extent throughout the basin; the older unit (MTC α; Figure 8.8 (b)) which is thinner and covers less area than the younger unit, especially in the vicinity of the growing structures. Additionally, the older MTC deposit splits into two tongues around the northeast-southwest trending anticlinal ridge that links the Area A and C structures (Figure 8.8 (b)). In comparison the younger MTC unit blankets these same structures (Figure 8.8 (a)). This could be explained through a series of different scenarios (Figure 8.8 (a) and (b)):

1. the structures did not form significant topographic highs during this time interval; or
2. that the younger debris flow was thicker and therefore able to surmount any subtle seabed topography; or alternatively
3. the anticlines linking the Area A and C structures were more active whilst MTC α was deposited.

There is evidence that growth on the structures within Area A affected the distribution of both of these regional MTCs, with both deposits terminating along the flanks of these structures almost parallel to the trend of the anticlines.

Areas B, D and E have the highest rates of bed length change during this time interval, with a maximum rate of change of bed length of 115 mMa^{-1} recorded on the most southerly anticline within Area E. The high growth rate structures within Area B have a significant impact on the distribution of both the regional MTCs, with MTC α and γ terminating at least 3 km away from the main anticlinal ridge in Area B along the trend of these salt walls/salt-cored anticlines. The structures within Area B have an average rate of change of bed length of 52 mMa^{-1} with the highest rates found towards the centre of the structure. This could explain the shape of the termination point of both the MTCs near this structure; the deposit has a slightly curved, convex shape with the maximum distance away from the anticline towards the centre of the structure (this is more pronounced in MTC γ; Figure 8.8 (a)). The younger system, MTC γ, terminates higher up the flanks of the anticline than MTC α; the former terminates on average 5 km from the crest of the anticline while the latter terminates on average of 6.25 km from the crest. This could imply that there was more topography in this area at the end of this period of time, or that MTC γ contained more energy than MTC α.

The older MTC unit does not extend quite so far to the south as the younger deposit (Figure 8.8 (a) and (b)). This applies both to the position of the deposit on the flanks of the anticline within Area D and the extent of the MTC south of the normal fault; the older MTC does not extend south of the normal fault and terminates approximately 700 m further down the flank of the anticline in Area D. Again, this could be due to a multitude of factors, but is most likely to be related to the thickness of the deposit and, linked to this, the amount of energy carried within the system. The older system, MTC α is on average 50 m thick whereas MTC γ is on average 70 m thick in the centre of the basin. The thinner system would have contained less material and correspondingly less energy and hence not travelled as far into the mini-basin.

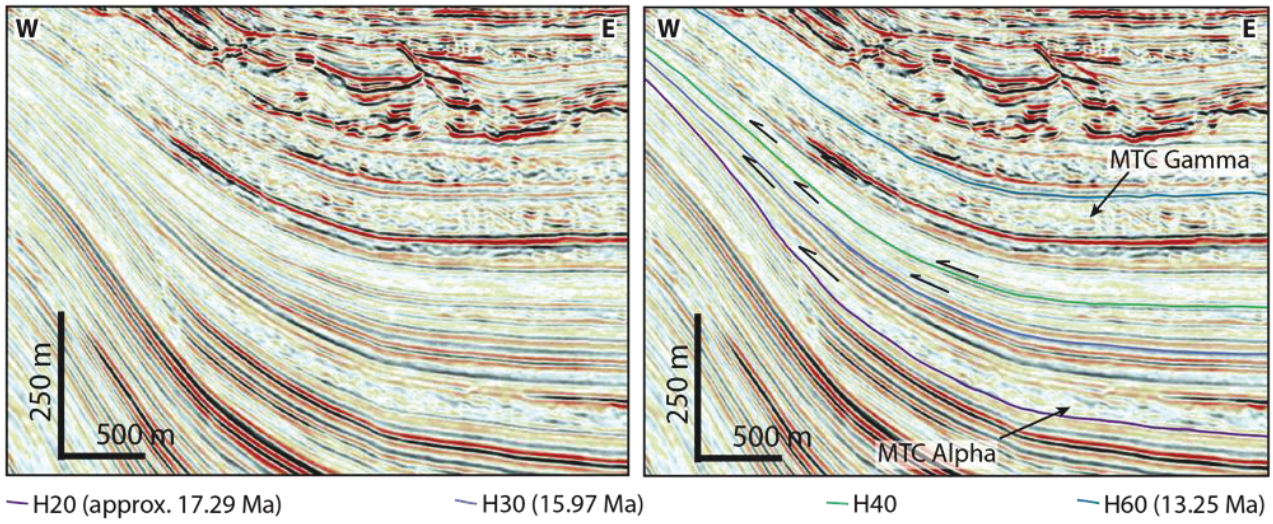


Figure 8.9 Section through Area C showing details on the stratal relationships within the 18.26 Ma to 13.25 Ma interval containing the regional MTCs. Note how the younger strata overlap the structure whereas the older strata onlap. Line location shown in Figure 8.8.

In conclusion, although the regional MTCs were most likely sourced outside the study area, we can still observe how structurally related bathymetry within the area has influenced the locus of debris flow deposition within the mini-basin; high growth rates on the Area B, C and D generated seabed topography that was too high for the thick debris flows to surmount, resulting in ponding. Seismic sections through the area indicate that MTC γ is 20 m thicker than MTC α which could partly explain the differences in distribution recorded in the basin. The thicker deposit being able to more easily over-top the growing structures and containing more energy which would allow it to travel further up the flanks of the deforming anticlines.

8.6.2 Stratal Relationships of Regional MTCs

The largest difference in the spatial distribution of the regional MTC deposits is towards the north of Area C (Figure 8.8) where the older MTC α is deflected by the structures whilst the younger MTC γ blankets the structures. The bed length change analysis within this interval is at too coarse a resolution to be able to resolve differences in the growth rates of these two structures, as it is measured over the entire interval from 18.26 to 13.25 Ma. However, the stratal relationships in the growth packages surrounding these two MTC deposits can give some indication of the topography present at the time they were deposited within the mini-basin (Figure 8.9). The stratal relationships are more reliable at this depth, with onlap and overtopping recognised with more confidence within the stratigraphy.

The strata deposited beneath MTC α thin towards the anticline within Area C but ultimately overtop the structure whereas MTC γ clearly onlaps the flank of the anticline (Figure 8.9). This indicates that the structure clearly had positive topography at the time that MTC α was deposited. Between the H30 and the H40 horizons (i.e. the period between the deposition of MTC α and MTC γ) the majority of the strata either onlap the flank of the anticline or thin towards it, indicating that the anticline formed a topographic barrier for most of this period. The structure does not appear to have a prominent topography during the subsequent

period as MTC γ clearly overtops the anticline with very little change in thickness observed as it nears the crest (Figure 8.9). The beds above the H60 horizons (i.e. those deposited after 13.25 Ma) also exhibit very little change in thickness thus indicating that the structure was less active after this time. This suggests that changes in the topography may be responsible for the spatially variations observed within the regional MTC distribution, at least in the vicinity of this part of Area C.

Both the regional MTC deposits terminate along the flanks of the anticline within Area B, with the older MTC α travelling higher up the flank of the structure than MTC γ (Figure 8.9). The seismic sections through this structure indicate significant onlap and thinning of the sediment packages during the interval when these MTCs were deposited between 18.26 Ma and 13.25 Ma (H10 to H60). This significant thinning and onlap indicates that there was topography present in this time during this interval. The higher termination points for MTC γ could imply that the sedimentation from the earlier intervals has, at least partly, infilled the basin.

8.6.3 Local MTCs

MTC deposits are more localised in their extent between 13.25 Ma and 8.29 Ma (H60 to H100) and can be traced back to specific headwall scarps on the flanks of the structures which bound the basin (Figure 8.10; see Chapter 6 for further discussion of these). Biostratigraphic analysis of cutting supports this observation, as the fauna found are indicative of a deeper water slope depositional environment with stratigraphic ages representative of the source stratigraphy. Analysis in Chapter 6 showed that overall the timing of the initiation of the MTC deposits does not correspond to particularly high growth rate periods on the basin margins (Figure 8.8). This was attributed to a series of factors:

1. The salt movement may have occurred as a series of pulses as opposed to a steady rate and hence the salt movement when averaged over the time intervals does not appear significant,
2. Ponded sediments and stratal onlap patterns indicate that the structures these MTCs were triggered from were emergent at the time of MTC generation. These emergent slopes may have been more prone to gravitational instability and slope failure.

In general the local MTCs are smaller in size and significantly thicker than the regional MTC deposits. They are up to 250 m thick and extend for up to 6 km into the basin (Figure 8.10). The three illustrated in Figure 8.11 all show clear extensional faults on the headwall escarpment with rotational blocks formed internally within the MTCs. All the local MTCs have erosional bases and cut up through the stratigraphy. The MTC 2 complex illustrated in Figure 8.11 (b) shows a younger MTC that has eroded through the updip portion of two older, underlying MTCs. All of the MTCs terminate in a series of toe thrusts, with MTC 1 being extensively folded towards the toe of the slide (Figure 8.11 (c)). The strike of the normal faults and toe thrusts on amplitude maps allows the transport direction to be reliably interpreted and indicates that the MTCs are all sourced from the flanks of active salt structures (Figures 8.10 and 8.11), suggesting that the movement of these structures may have contributed to instability in the sediments and eventual failure of the overlying sediment. The local MTCs have been mapped within two separate time intervals which occurred during and after the deposition of ponded fan systems within the mini-basin (Figure 8.2).

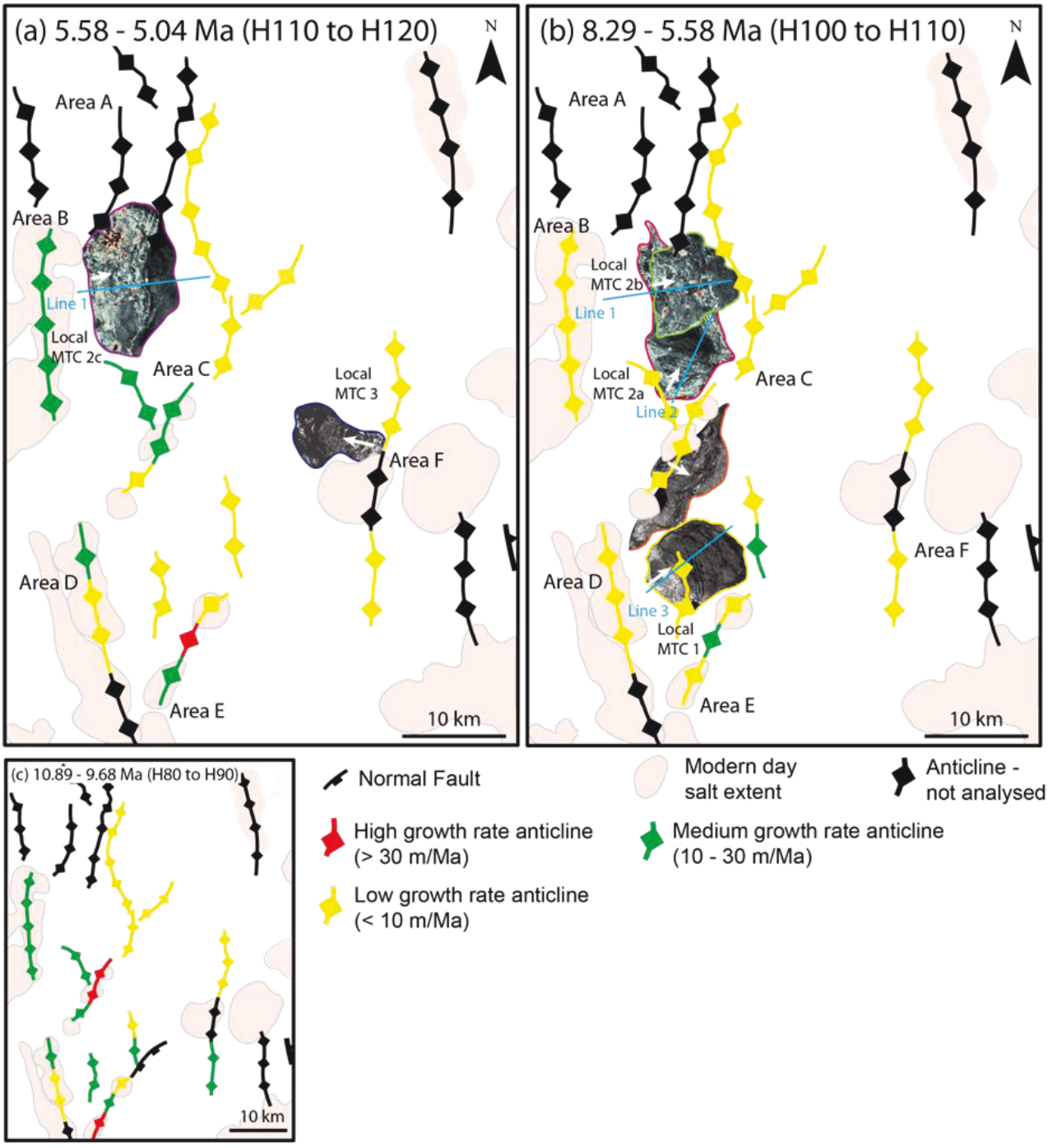


Figure 8.10 Location and extent of a selection of local MTCs. (a) shows a older anticlines deposited with the interval between 8.29 Ma and 5.58 Ma (H100 to H110) whist (b) shows the MTCs deposited in the period following this between 5.54 Ma and 5.04 Ma (H100 to H120). Note how all these local MTCs are sourced from anticlines along the margin of the basin and are cover a broadly similar area. (c) highlights the higher rates of bed length change recorded in the preceding intervals. Rates of bed length change are coloured as in previous maps. Map show RMS amplitudes extracted through windows of between 10 - 25 ms Twtt. White arrows show the direction of movement of the MTCs. Location of sections through the MTCs are labelled 1 – 3 (Figure 8.11).

Four MTCs have been mapped within the older time interval from 8.29 Ma to 5.58 Ma (between the H100 and H110 horizons): two within the MTC 2 complex and two to the south of the basin. These all link to structures along the western margin of the basin, which, paradoxically all show a low rate of change of bed length during this interval (Figure 8.10 (b)). However, with the exception of the structures in the south of Area D, all of these structures had medium to high rate of change of bed lengths in the preceding periods (for example 10.89 Ma to 9.68 Ma; Figure 8.10 (c)). The local MTC north of MTC 1 was sourced from growth on the anticline within Area C which had a maximum rate of change of bed length of 40 mMa^{-1} during the

preceding period and a maximum rate of change of bed length of only 3 mMa^{-1} when the MTC was triggered. This is indicative of the episodic nature of the anticline growth in the mini-basin generated by movement of the underlying salt, which could have caused instability on flanks of the structures. Extensive ponding of sediment against this western margin of the basin was also recorded during this interval with clear onlap of the sediment within the mini-basin (Figure 8.11 (c)). This implies that the flanks of the structures were exposed in the interval between 9.68 Ma and 8.29 Ma which could also have made them more prone to instability.

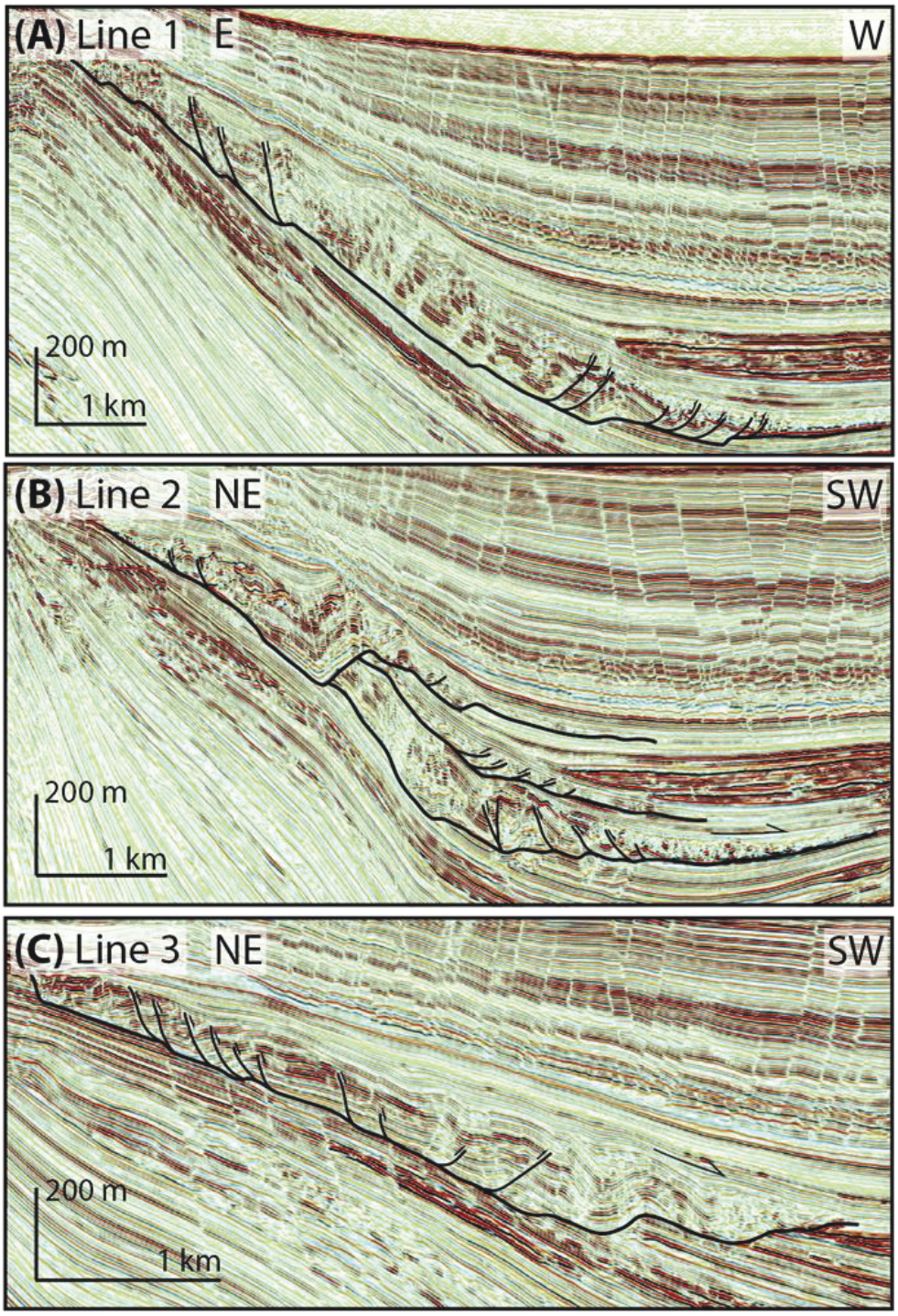


Figure 8.11 Sections through the local MTCs. (a) and (b) are taken through the MTC 2 complex whilst (c) shows a section through MTC 1. Note extensional structures in the headwall area, with contractional structures seen towards the toe of the slides. Location of sections is shown in Figure 8.10.

There are higher rates of structural movement on most of the structures within the mini-basin during the interval between 5.58 Ma and 5.04 Ma (H110 to H120) than in the preceding interval (Figure 8.10). However, less local MTCs are triggered within this interval with only MTC 2c and MTC 3 observed. MTC 2c is clearly sourced from the flanks of the anticlines which constitute Area B. In contrast to MTC 2a it is sourced solely from the north-south trending anticline along the western margin. This structure has an average rate of change of bed length of 21 mMa^{-1} during this interval which is significantly higher than its rate of change of bed length in the preceding interval. The movement during this interval, coupled with the fact that the flanks of anticline were exposed on the seafloor, could have generated this relatively large local MTC (Figure 8.10 (a)).

The other local MTC generated in this period is sourced from the eastern margin of the basin and is the largest and clearest of the few examples observed along the eastern edge of the mini-basin. During this period, and throughout much of the history of the basin, very little bed length change and hence very little growth is recorded within Area F. The section of the anticline this MTC was sourced from had a very low a rate of change of bed length of 2 mMa^{-1} during this interval, however growth strata observed in the seismic sections through here do indicate that the flanks of the structure were exposed at the seafloor. This could indicate that the MTC was triggered by structural growth which led to emergent bathymetry and hence instability of the flank of the anticline. The canopy salt to the south of MTC 3 is thought to have extruded fairly late in the development of the mini-basin, most likely at about the same time that this MTC formed, which may also have impacted on its development.

8.6.4 Discussion of MTCs and their Interactions with Structural Growth

The main differences in the affect that the growing structures have on the two different types of MTC deposit studied here results from the different mechanical properties and energy carried within the systems. The regional MTCs found within the mini-basin are at least 100 km from the initiation point and hence the resulting debris flow deposits simply passively infill the bathymetric lows encountered within the basin, whereas the local MTCs are sourced on the flanks of structures along the basin margins, that were actively growing or had recently grown and formed emergent seabed topography. This means that the actual rate of growth of the structure is less important in the distribution of the regional MTC deposits and they are more affected by the amount of bathymetry visible on the seafloor that they encounter when entering the basin. In contrast the local MTCs are triggered from the flanks of the basin-bounding structures and hence it might be expected that they relate in some way to structural growth.

Given the large intervals over which bed length change was measured, the rate of change of bed lengths of the individual structures which effect the distribution of the regional MTCs cannot be determined. However, it is possible to conclude from the distribution of the MTCs that the thickness of the debris flow may have had an impact on the distribution with the older, thicker MTC able to blanket growing structures. Both the regional MTCs terminate along the flanks of the structures where the highest rate of change of bed lengths

were recorded (i.e. in Areas B and D), indicating that rate of change of bed lengths of >30 mMa^{-1} and the resulting positive seafloor topography these create can prevent the down-dip flow of regional MTCs.

The fact that the distribution of the local MTCs does not mirror the spatial distribution of the structures with the highest growth rates, or indeed the intervals with the highest growth rates seems counterintuitive. However, the stratal relationship analysis indicates that they were deposited during an interval when the basin was underfilled and extensive onlap and offlap of sediment occurred. This implies that the flanks of the structures were emergent for a prolonged period of time which may have generated gravitational instability on the flanks of the anticlines as the emergent topography made slope degradation more likely. These ideas are discussed in more detail in Chapter 6.

8.7 Interactions between Active Structural Growth and Ponded Fans

During the youngest stratigraphic interval investigated in this study (8.29 Ma to 5.58 Ma), ponded sediments comprised of sandy deposits formed by multiple small distributary channels infilled part of the mini-basin. This was a time of low rates of bed length change; but significant topographical relief must still have existed from the previous higher growth rate intervals to allow the extensive ponding of thick units (up to 300 m) in the relative topographic lows formed during the previous phase of structural activity (Figure 8.12). Ponded sediments are deposited from 9.68 Ma to 5.58 Ma infilling the topographic lows within the centre of the mini-basin. This thesis is primarily concerned with the ponded fan systems observed within the basin between 8.29 Ma and 5.58 Ma (discussed in detail in Chapter 7) the distribution of which are shown in Figure 8.12. Ponding occurs primarily in the southern half of the study area and consists of fan-like systems bound by the structures in Areas C, D, E and F (Figure 8.12). These ponded fan complexes are described in Chapter 7 which fully explores the evolution of these systems and how they change in orientation through time.

8.7.1 Spatial Distribution of Ponded Fan Lobe Complexes

The extent of the ponding is broadly constrained by the topography formed by structural growth that occurred in the mini-basin from 18.26 Ma (H10) onwards. Areas C, E and F had particularly high growth rates between 18.26 Ma (H10) and 9.68 Ma (H90), which is reflected in the rate of change of bed length measurements (Figures 8.12 (e) and 8.2). When the ponded sediments examined here were deposited between 8.29 Ma and 5.58 Ma, structural movement had slowed significantly allowing the sediments entering the basin to passively infill the topographic lows (compare the rate of change of bed lengths recorded in Figure 8.12 (a) and (e)). For example, the rate of change of bed length in the anticline in the middle of Area C decreased from 40 mMa^{-1} during the period between 9.68 Ma to 10.89 Ma to 5 mMa^{-1} in the period when these ponded sediments were deposited.

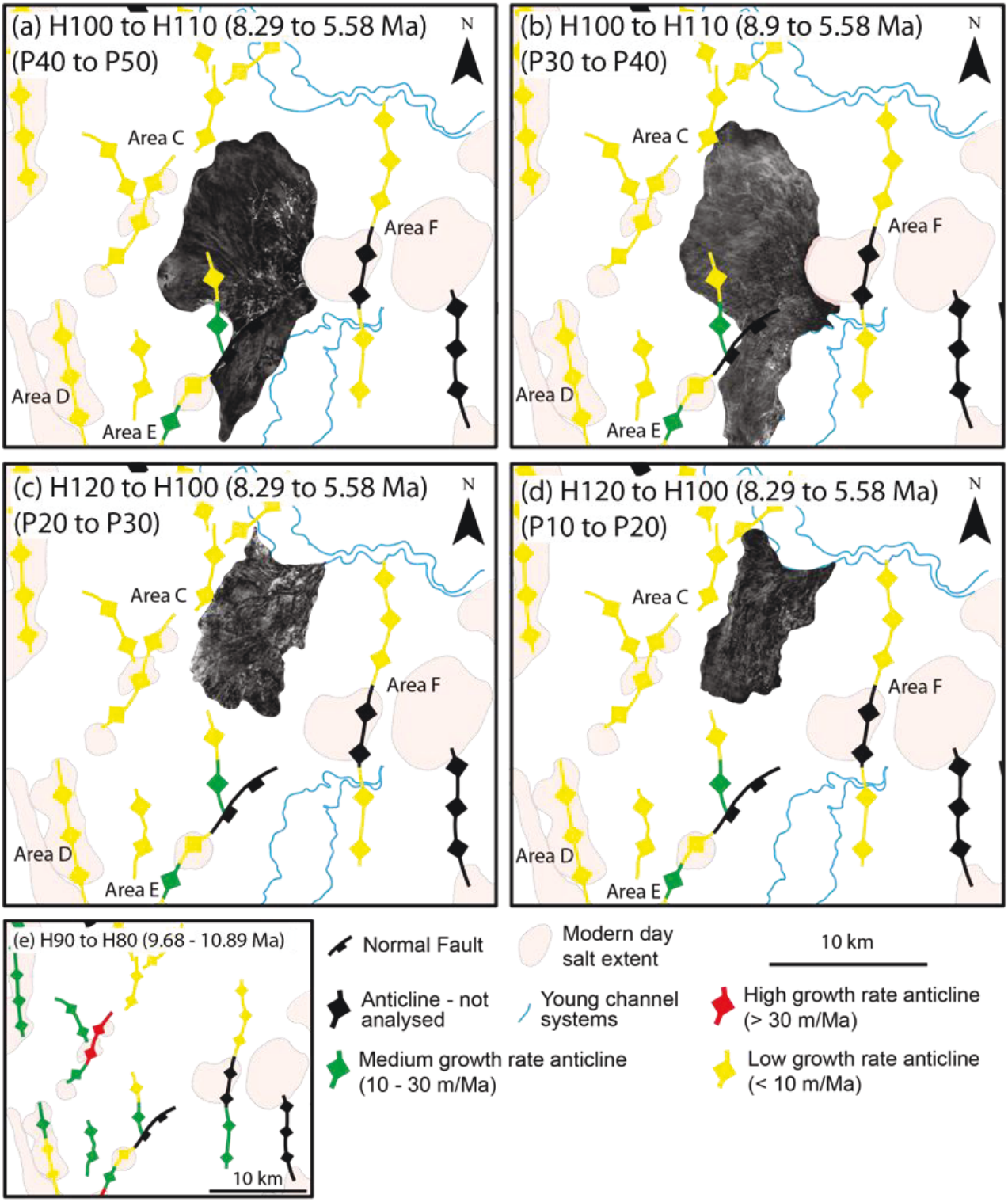


Figure 8.12 Ponded sediments deposited within the mini-basin between 8.29 Ma and 5.58 Ma are examined with (a) showing the youngest fan system feeding in from the south and extending north and south of the normal fault, (b) an older system with channels branching away from Area F, (c) a fan systems feeding into the basin from the north, (d) the youngest fan system feeding into the mini-basin from the north and trending broadly north to south along the basin axis, and (e) the rate of change of bed lengths from the preceding interval give an indication of the relict topography in the basin when the ponded sediments were deposited. Rate of change of bed lengths are indicated by red, green and yellow in the same manner as previous maps. RMS amplitude extraction maps are used over an isopachous interval with a maximum thickness of 25 ms Twtt. More detailed RMS amplitude maps are shown in Figure 8.13 and Chapter 7.

The ponded sediments are stacked sheet sands comprising multiple small channels, most of which have developed into distributary fan-like systems (Figure 8.13). The main sediment entry point into the mini-basin switched whilst the ponded fan lobe complexes were deposited with the main feeder channel first

entering from the north (Figure 8.12 (c) and (d)) and then switching further to the south (Figure 8.12 (a) and (b)). The oldest lobe complex (Figure 8.12 (d)) enters from the north of the area branching out to form an elongate fan-shaped deposit. This fan system is not as organised as the subsequent systems but appears to be controlled by the structures in Areas C and F with the channels forming parallel to the northeast-southwest trends of the main anticlines which make up these structures. Some of the channels within this fan lobe complex appear to slightly deflect away from the anticlines within Area C, again indicating that this had positive topographic relief at the time of deposition (Figure 8.12 (d)).

The next-youngest ponded fan system has a very similar overall trend within the mini-basin (Figure 8.12 (c)) but is much more organised. The main feeder channel has a northeast-southwest trending axis, parallel to the anticlines in Areas C and F, with the smaller channels branching to form a distributary geometry away from the apex and fanning out to the west and southwest. This implies that the relict topography from an earlier interval was, at least in part, controlling the deposition of these sediments as the channels developed away from the relative high near to Area C and towards the eastern margin of the mini-basin. This eastern margin (Area F) had a significantly lower rate of change of bed length in the preceding interval (between 10.89 Ma and 9.68 Ma) with a rate of change of bed length of only 1 mMa^{-1} recorded on the anticline in the north of Area F (Figure 8.12 (e)). Contrary to the other structures within the study area, growth on this structure actually increased slightly within the ponded interval to a rate of change of bed length of 2 mMa^{-1} which could have generated some topography on the seafloor thus preventing the sediment from being deposited any further to the east (Figure 8.12 (c)).

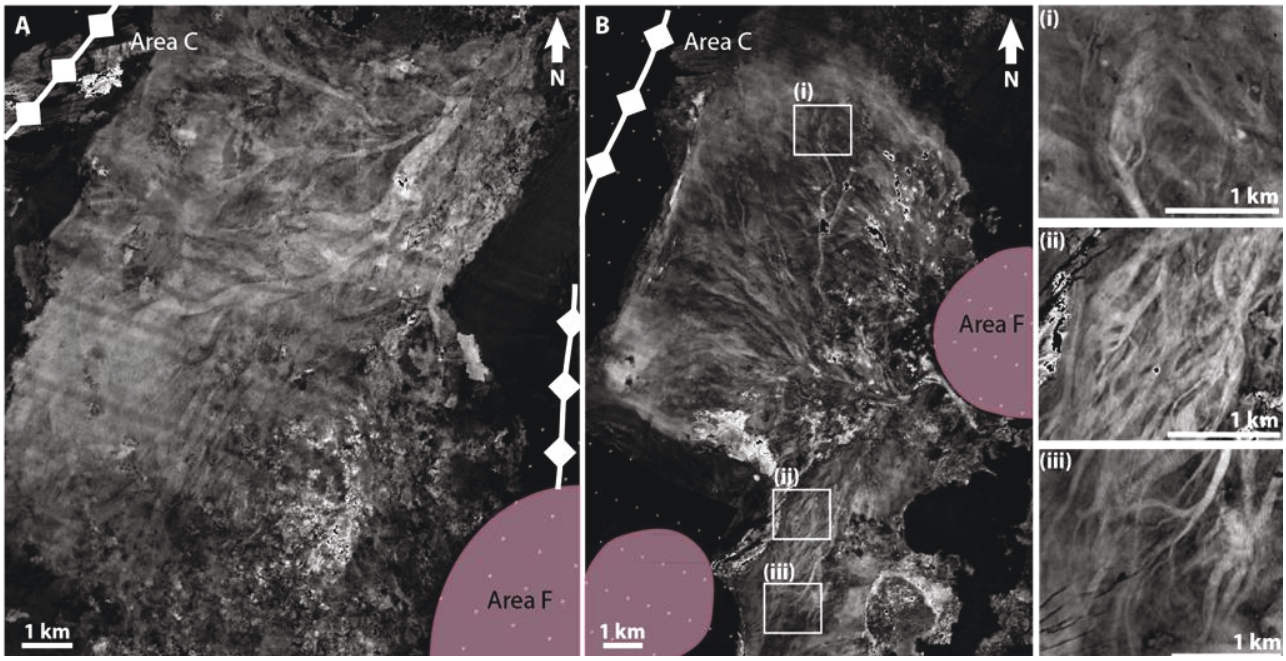


Figure 8.13 RMS amplitude maps calculated using 10 ms Twtt windows to illustrate the details within the deepwater ponded fan systems seen in Figure 8.12 with (a) showing a more detailed view of the second oldest fan system (seen in Figure 8.13 (c)) and (b) showing a detailed image of the youngest fan system (seen in Figure 8.12 (a)), i, ii and iii on Figure 8.13 (b) highlight some of the main details; individual channels branch towards the edge of the basin and more amalgamated channels are observed south of the normal fault.

The distribution of the sediments within the two youngest fan systems (Figure 8.12 (a) and (b)) is also partly controlled by a normal fault that trends northeast-southwest across the basin. North of this fault the fans are more diffuse with a lobate shape and distributary channels branching from a single entry point. Whereas in both systems south of the fault and southeast of Area E the individual channels are more confined in their extent; the majority trend in a northeast-southwest direction and have a more braided, less sinuous appearance (Figures 8.12 (a), (b) and 8.13). These different characteristics could be attributed to the response of the system to movement on the normal fault and continued movement on structures in Area E; the medium growth rate structure north of the normal fault had a growth rate of 11 mMa^{-1} whist the one south of the normal fault had a rate of change of bed length of 13 mMa^{-1}. In the youngest fan system the braided channels flow along the downthrown side of the normal fault which could have formed a localised depression and acted as a conduit to the channels (Figure 8.13). This could indicate that the fault was more active towards the end of this interval.

The distribution of the two youngest fan systems is controlled to the northeast by the structures within Area C which appear to have formed a topographic barrier at this stage. Neither system reach as high up the flanks of the anticline as two older systems, however this could be because they are at the terminal end of the fan systems where the channels have less energy (Figure 8.12 (a), (c) and (d)). The actively growing anticline north of the normal fault appears to have influenced the distribution of both of these fan systems and prevented sediment from depositing there (Figure 8.12).

8.7.2 Stratal Relationships of Ponded Fan Lobe Complexes

Analysis of the onlap locations of the fan lobe complexes can help aid understanding of the relict topographic relief on the basin bounding structures during this interval. This is particularly useful given the low rates of change of bed length measured throughout the basin at this time. Using seismic cross-sections along the margins of the basin (e.g. Figure 8.14) the location of the onlap has been mapped for the P20 to P50 horizons (Figure 8.15).

The onlap location for the oldest horizon mapped within the ponded interval (the P20) has a different pattern to the subsequent horizons; terminating substantially further away from the structures within Areas D, C and F during this period. The exception to this is in the north of the mini-basin where it onlaps and overtops the most northerly anticline within Area C, which had no significant growth during this period or that immediately preceding it (see Chapter 5, Section 5.9 for more discussion if the structural evolution of Area C). Along the western margin of the basin the P20 horizon onlaps the structure significantly further away from the anticline axis than any subsequent horizons (Figures 8.14 and 8.15). The onlap point is consistently about 2 km east from the main anticline axis of Structure 2, Area C with this distance decreasing to 1.5 km towards the southern tip of the structure and the area between Structures 2 and 3 (Figure 8.15). This suggests that there was less of a topographic high towards the tip of the structures and between the structures, a fact that is supported by the rate of change of bed length analysis in Chapter 5 with less bed length change recorded where the structures link. The distance between the axis of the anticline of Structure 3, Area C and

the onlap of P20 increases along the length of Structure 3 from approximately 3 km in the north to almost 4 km in the south. This change from north to south could be accounted for by the increased rate of bed length change along this structure during the interval within which the P10 – P50 beds were deposited; the analysis carried out in Chapter 5 suggests that the average rate of change of bed length increases from 4 mMa^{-1} in the north of Structure 3 to 6 mMa^{-1} in the south during this period. Another explanation for this change could be the decrease in depositional power of the sediment towards the termination of its depositional area; this section of the anticline is furthest away from the sediment entry point during this period and, as such, the sediment would contain less energy and be more influenced by small changes in topography.

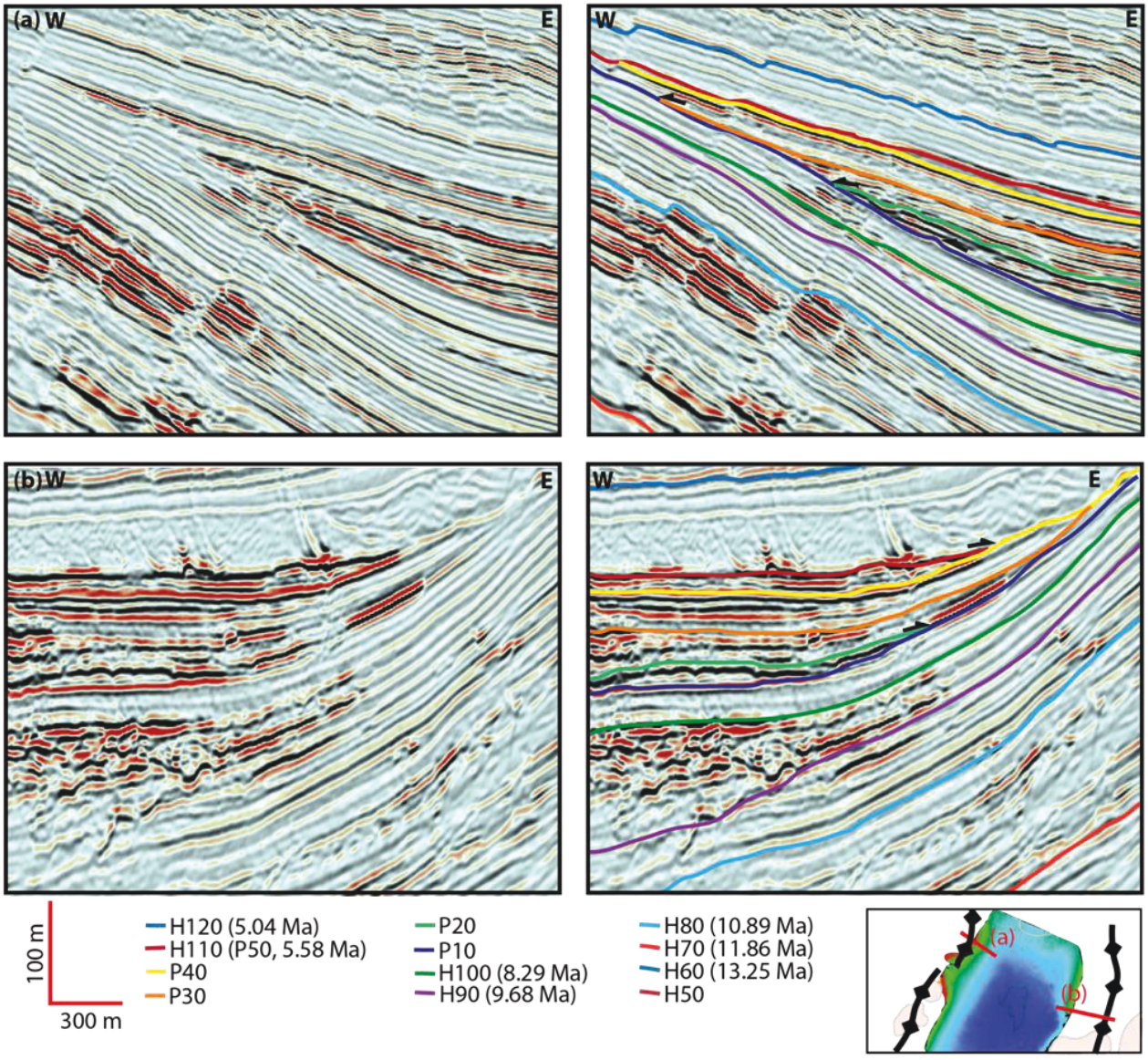


Figure 8.14 Seismic sections along the western (a) and (b) eastern margins of the mini-basin; with black arrows showing some of the onlap that occurs at these locations. Location of these lines also indicated on Figure 8.15.

The P30 horizon marks the top of the next youngest interval and has a significantly different onlap pattern to the P20 horizon (Figure 8.15). The sediment distribution pattern within the basin has changed with the majority of the sediment now entering the mini-basin from the east (Figure 8.12). Overall the beds onlap higher up the structure than the P20 horizon (Figure 8.15). This is particularly apparent along the western edge of the basin where deposition has not been effected by the slump deposits. Towards the northern tip of

Structure 2, Area C the beds are deposited close to the structure terminating parallel to the trend of the anticline. However, towards the southern tip of Structure 2, Area C the P30 horizon appears to overtop the structure, indicating that this did not form a topographic barrier at the time of deposition. In this area the P30 onlap location is approximately 2.5 km closer to the anticline ridge than the P20 horizon (Figure 8.15). This difference is less prominent near Structure 3, Area C where the onlap location of the P30 horizon steps back away from the structure, reducing the difference between the onlap to an average of approximately 1.5 km (Figure 8.15). The P30 onlap pattern varies along the length of this part of the structure; in the north the initial onlap is 0.75 km from the anticline ridge, onlap distance then increases to a maximum of 2 km before decreasing to 1.5 km away from the anticline ridge in the centre of the structure. The onlap location mimics the trend of the anticline between the centre and the southern tip of the Structure 3, Area C with the beds onlapping consistently approximately 2 km away from the anticline ridge.

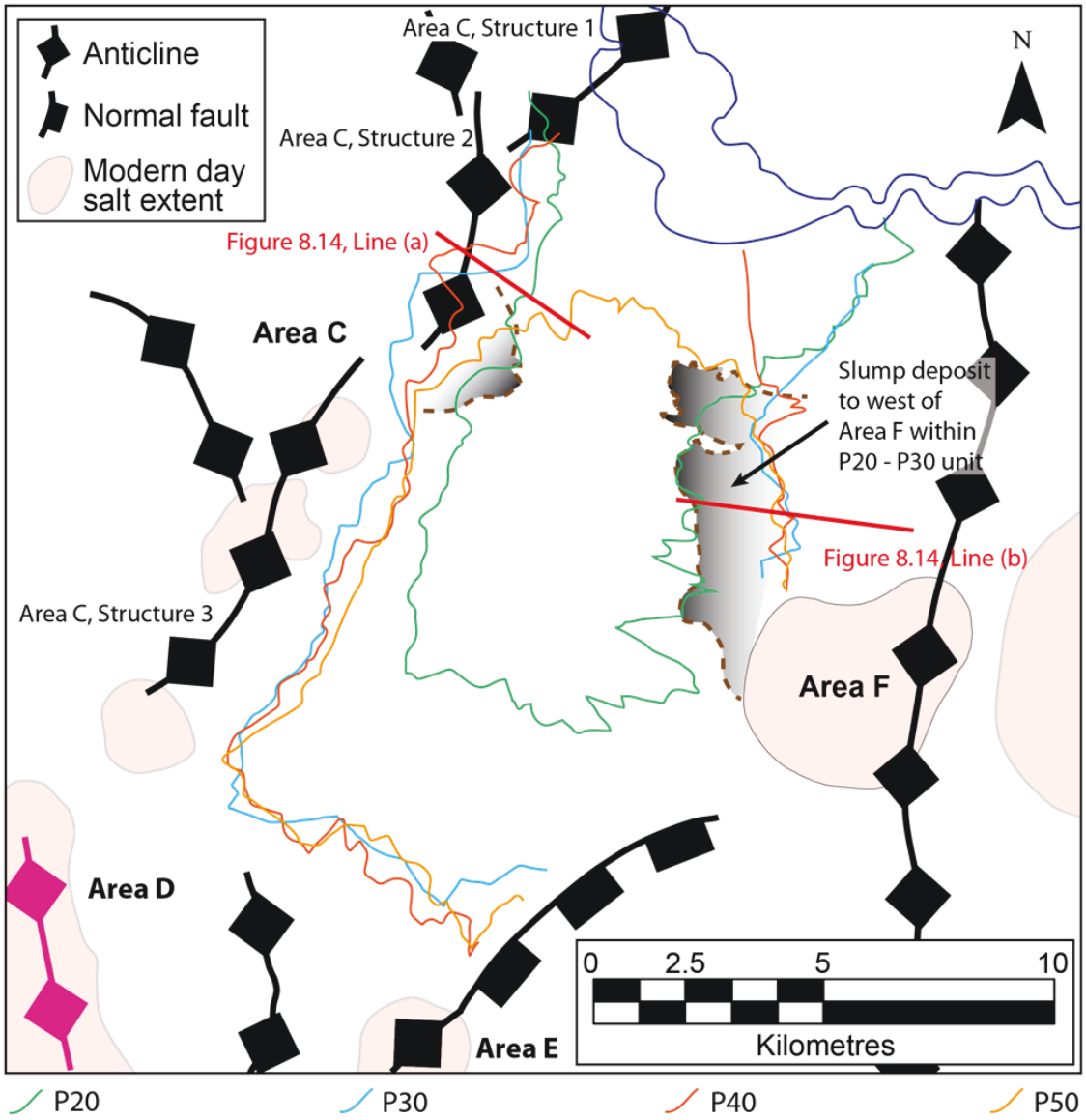


Figure 8.15 Map showing the onlap outline for four mapable boundaries within the ponded package that existed within the basin from 8.98 Ma to 5.58 Ma (H100 – H100) with the oldest P20 horizon outlined to the youngest P50. The maximum outline of the slump deposits are also outlined on the map, the western slump is only active within the P20 – P30 unit. The location of the seismic sections shown in Figure 8.14 are also identified in red.

Due to the change in sediment entry points between the P30 horizon and the P20 horizon the beds extend further south into the basin onlapping the structure in Area D (Figure 8.15). The P30 onlap pattern swings away from the fault in the south of the basin, and may have been responding to growth on anticlines in the north of Area E or tilting of the footwall of the normal fault. On the eastern edge of the basin late canopy salt growth has obscured the location of the onlap. However, to the north of this salt in Area F the P30 and P40 horizons both follow a similar pattern onlapping significantly further down the flank of the anticline within Area F (Figure 8.15). Immediately to the north of the salt the horizons onlap approximately 3 km away from the hinge of the anticline before moving increasingly further away from the anticline axis to a maximum distance of 5 km. Bed length change analysis has found very little difference in the rate of bed length change along this portion of the anticline over this period; therefore it is possible that the ponded sediment is responding to relict topography in the area.

The P40 horizon has a very similar onlap distribution to the P30 horizon (Figures 8.14 and 8.15) but on the western edge of the basin the P30 bed onlaps slightly further away from the structure than the P40 horizon. This is particularly apparent in the northern half of Structure 3, Area C where the onlap is approximately 1 km further away from the structure, indicating either a period of structural growth in this area, or a decrease in the energy of the sediment deposited. The fact that the onlap pattern onto the southern half of the structure mimics that seen in the P30 horizon indicates that the difference may be due to structural growth as opposed to sediment energy (Figure 8.15). The P40 horizon onlaps higher up the flank of the anticline within Area D than the P30 horizon. This could indicate that the structure had less topographic relief during this period.

The youngest horizon, P50, was deposited at the end of the ponded period and has a very different distribution within the basin overall; not extending as far to the north as the other horizons (Figure 8.15). The P50 horizon consistently offlaps the anticlines with the strata terminating further from the axis of the main basin-bounding structures. For example, along the length of Structure 3, Area C the onlap is significantly further away from the anticlinal ridge and closer to the centre of the basin, particularly towards the southern end of the structure where it is approximately 2.5 km from the anticline axis. This could indicate either increased topographic relief on the structures during this period (i.e. a late phase of structural growth) or could be due to the sediments deposited within this package containing less energy than the older sediments or less volume of sediment being deposited within the basin.

8.7.3 Summary Discussion of Ponded Fan Lobe Complexes and their Interactions with Structural Growth

Seismic sections on both flanks of the basin show onlap a long way down from the crest of the structures; this clear onlap demonstrates significant emergent relief on folds at this time, even though the bed length change indicates that the structures had a low growth rate during this interval. In general the oldest unit, represented by the P20 surface, onlaps furthest down flanks of the structures but there is little consistent difference in the younger horizons. Offlap is observed in the P30 to P50 horizons on the western margin of the basin along Structure 3, Area C which corresponds to the area with the highest rate of change of bed

length in the previous 10.89 Ma to 9.68 Ma (H90 to H80) interval. The fan lobe complex deposited between P40 and P50 has the lowest volume of sediment which may also affect the area which the fan is able to cover and extend across. It is also interesting to note that a variety of relationships can be observed in the linkage area between Structure 2 and Structure 3, Area C, suggesting that this area had a lower rate of growth and hence lower bathymetry than the surrounding structures.

However, in general, the stratal relationships (Figure 8.14) and the spatial distribution of the lobes and channels in relation to the structures with the highest growth rates (Figure 8.11) both suggest that the ponded sediment was simply infilling the relict bathymetry generated earlier in the growth history of the mini-basin. Therefore, this highlights that the pre-existing relief within a mini-basin is as important as contemporaneous growth in governing or controlling depositional relationships; although very low growth rates are observed in ponded fan interval itself, fans are infilling topography generated in preceding time intervals when growth was faster.

8.8 Responses of Deepwater Slope Sedimentary Systems to Seabed Topography

The systems examined in the mini-basin respond in different ways to the structures they encounter within the mini-basin. This response appears to be driven, in the most part, by the system (i.e. the volume of sediment entering the mini-basin and the energy carried within that system), as opposed to the rate of growth of the structures. The lower energy systems, the toe-end of the regional MTCs and the ponded fan lobe complexes, respond in a more passive sense to the pre-existing topography and infill the basin whereas the higher energy channel systems respond more actively to subtle changes in rate of change of bed length of the structures. Overall, three main findings can be summarised as follows:

1. channel systems demonstrate that there is a clear link between high rate of change of bed length, high growth rate (i.e. the generation of bathymetry), and relatively high sediment supply, with the channels responding to active changes in bathymetry by altering their flow pathways,
2. relict seafloor topography from previous periods of high growth can have a large impact, particularly in under-filled basins where the spatial distribution of ponded sediments is greatly influenced by the bathymetry, and
3. local MTCS are much less predictable; intuitively it would be expected that they form during the highest growth rates, however the analysis suggests that they form after high growth rate periods when the flanks of the structures are emergent on the seafloor. Thus indicating that prolonged exposure at the seabed may be responsible for generating seafloor instabilities, as opposed to growth rate.

It is clear that high rates of bed length change, and hence inferred high rates of structural growth, which generate emergent topography have a large impact on the sedimentological features within the study area. This interaction can result in different characteristics depending on the sediment type entering the basin at that particular time, as highlighted through a series of conceptual models in Figure 8.16. These responses to

the growth can broadly be grouped into two types; active responses whereby the systems and processes actively respond to the structures in an area (for example by changing their flow pathway or being generated by the growth) and passive responses where the sedimentary systems simply continue to behave with the same characteristics and infill the mini-basin.

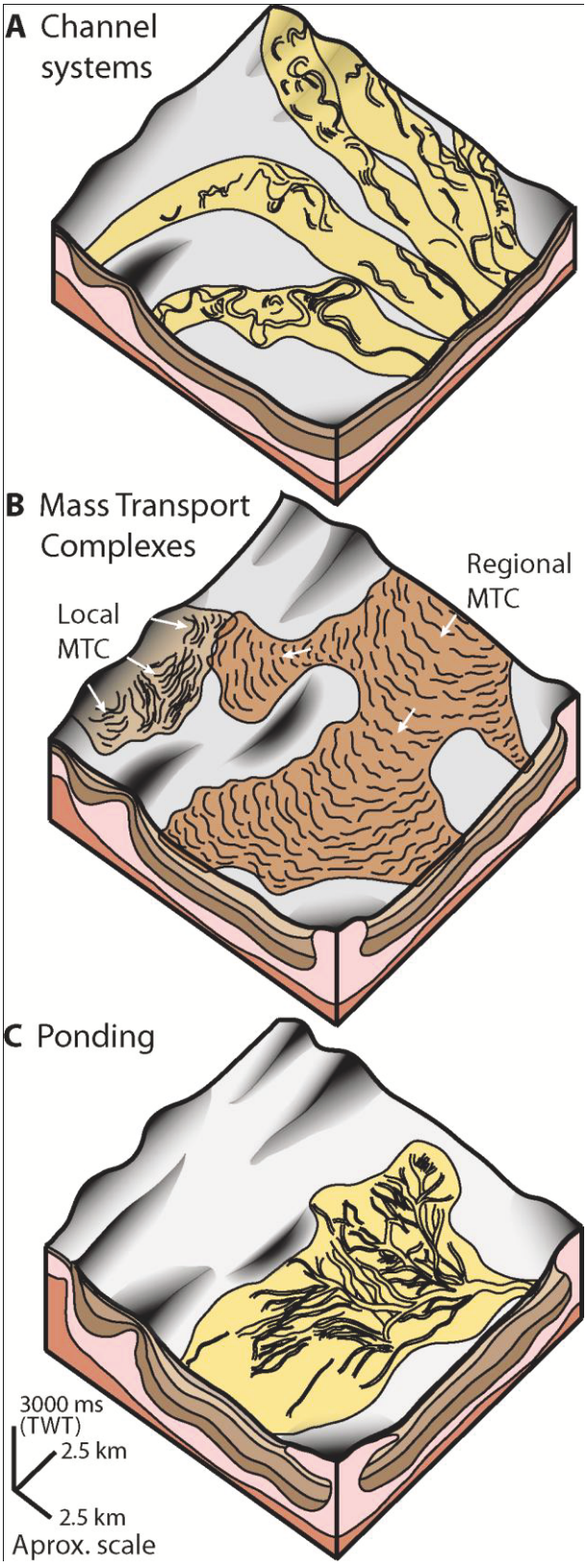


Figure 8.16 Series of conceptual models showing the response of (a) channel complexes, (b) regional MTCs (dark brown), local MTCs (light brown), and (c) ponded fan lobe complexes to the growth of the salt-cored structures in the area.

Recognising the impact that active growth structures have on sediment distribution and facies development is invaluable in the exploration and production of oil and gas. When developing fields such as those currently being developed within this study area, it is important to understand how the sediments interact with actively growing structures as it can impact on channel facies and architecture which in turn affects the reservoir quality. In a similar way likelihood of encountering ancient MTC deposits and knowledge of their characteristics is useful when producing development plans as they could have an adverse effect on fluid flow through a reservoir, and more recent local MTCs could form potential geohazards when siting platforms and subsea tie-backs.

8.8.1 Active Responses to Structural Growth

Channel complex systems (Figure 8.4) react in often dramatic ways to the presence of pre-existing or contemporaneously developing sea-floor topography as indicated by bed length change analysis and observations from the stratal growth geometries. In the study area, the channel complex systems show a wide range of responses, reacting to topography created during earlier periods of growth and contemporaneous growth by taking long diversions around structures orientated perpendicular to depositional slope. In other cases, depending on the balance between the rate of structural growth, as inferred through the bed length change measurements, and the erosional power of the channels, channels divert around small structures, show progressive off-set stacking or are able to continue incising through the growing structure.

This work has demonstrated that the magnitude of bed length change, which is used here as a proxy for growth rate and hence vertical uplift, can be used to explain the response of some of the channel systems within the study area. By integrating the bed length change results with the observations from the stratal relationships it is possible to conclude that:

- structures which have the highest horizontal bed length change rates (i.e. those with rates of change of bed length of >30 mMa^{-1}) clearly form the most significant topographic barriers,
- areas of high to medium growth cause channels to deflect away from the growing structures from which it is possible to infer that these structures have generated positive seafloor topography. This occurs regularly at rates greater that c. 15 mMa^{-1} in this particular study area,
- in a few isolated cases channels are able to make it across structures with moderate growth rates of between c. 10 mMa^{-1} and c.15 mMa^{-1};
- low growth rate structures are more frequently crossed and regularly also have stratigraphy that overtops the structure, which in turn indicates that they had little or no bathymetric expression;
- In a few cases channels are deflected by the low growth-rate structures which may be due to the presence of relict seafloor topography formed during previous intervals of higher growth, and

- antecedent channels located in well-established positions may incise into the structures and keep pace with structural growth, providing that the channel system has enough erosive power.

Therefore, two end-member responses of the channel systems have been observed: when the structures formed a topographic barrier to the flow of sediment down-dip, high rates of change of bed length and extensive onlap are recorded, this causes channels to deflect away from the topographic barrier; whereas when the structural growth is low, overtopping of the sediment is observed and the channels are able to continue to flow across the structure. However, exceptions to these scenarios are common. As discussed in Mayall et al. (2010), in many cases there is a very subtle interplay of timing and rate of structural growth and channel erosional power which determines whether a channel can cut through a growing structure, is off-set laterally with stacking geometries on the flanks of a growing structure or is deflected around it. The sedimentation rate also has an impact on the amount of bathymetry generated by a certain growth rate, with high sedimentation rates able to blanket a structure and prevent the structure from being visible to the channel on the seafloor. As discussed in the vicinity of Area C, earlier relict topography can also impact on the flow pathways, providing additional barriers during periods when bed length change rates, and hence bathymetric growth rates, are low. The final exception to the study occurs due to the resolution of the observations that are able to be made in the study area; rate of change of bed length may not be constant over the time spans they are averaged over and hence periods when growth has slowed may have allowed channels to overtop a fold and then incise and keep pace with the subsequent growth of a structure.

Local MTCs (Figure 8.10) are also classified as having formed as active responses to the structural growth of the mini-basin. These deposits are less predictable in their spatial distribution and do not encounter topography but rather are initiated from unstable structures on the edge of the basins. In general these structures have been subjected to high growth rates and then exposed on the seafloor due to relative sediment starvation of the basin. They commonly move down structures counter to the regional dip of the slope and have been mostly observed on the higher-growth rate western margin of the mini-basin.

Analysis of the stratal relationships of the packages surrounding the local MTC deposits suggests that they were deposited before, during and after the deposition of the ponded fan lobe complexes within the mini-basin during a period when the basin was under-filled. Although the spatial distribution of the deposits does not, in the most part, correlate to the location of structures which had higher growth rates the onlap patterns do suggest that the sediments are sourced from flanks of structures which were exposed and emergent at the time of the initiation of mass movement. This exposure is postulated to have generated gravitational instability. An alternative mechanism for the generation of the MTC deposits is triggering due to the pulsing of salt as opposed to steady growth. Therefore it is not possible to use the bed length change rate measurement to directly infer the likely location of local MTC deposition. However, it would be possible to infer which structures were more likely to source MTCs during an under-filled period by noting which structures had higher growth rates in the preceding periods.

8.8.2 Passive Responses to Structural Growth

Regional MTCs (Figure 8.8) containing shelfal biofacies are focused by, and terminate downslope against, structural highs. The MTCs can be mapped terminating someway downdip on the structures suggesting that the flows were halted by quite low sea-floor dips. The regional MTCs have different distributions within the basin depending on the interplay between the relative growth of the structures and the energy within the MTC deposit; the thicker MTC deposit is able to overtop the structures whilst the thinner deposits are more easily deflected by the high growth rate structures and resulting positive topographic relief.

The regional MTCs observed here are located approximately 100 km west of their source area, however the bathymetry within the basin still impacts the locus of the debris flow deposition as the sediments appear to passively infill the topography within the mini-basin. The rate of change of bed length analysis is less useful in this instance as it was measured over such a large interval. However both the regional MTCs studied here terminate against structures which had rates of change of bed length of >30 mMa^{-1}.

Ponded sediments (Figure 8.12) formed during periods of low structural growth, but infill the bathymetric lows generated during periods of earlier high growth. They are fed by feeder channels which have switched in location from north to south, either in response to structural changes outside the mini-basin or an avulsion of the feeder channel further up-dip. The ponded sheets are formed from stacking of very well-imaged multiple small channels which fan outwards from the entry point and terminate against growing structures.

The onlap patterns within the ponded sediments clearly demonstrate that the folds which bound the basin were emergent at the time the ponded sediments were deposited within the mini-basin, even though the bed length change analysis indicates that the structures were growing very slowly during this interval. Overall, the ponded sediments onlap progressively higher up the structures during this period indicating that they were infilling the mini-basin. The exception to this is on the western margin of the basin on Structure 3, Area C where the rates of change of bed length are slightly higher and some offlapping of the sediment packages can be observed. However, the resolution of the data and the knowledge of the sedimentary systems are not sufficient to be able to decide whether this is due to continued growth, or a pulsing of growth on this structure, or due to less sediment entering the basin during that interval.

Therefore, it is possible to conclude that the ponded sediments passively infill the basins, responding in a similar manor to the lower energy regional MTC deposits by terminating part way up the flanks of the structures and against relict topography generated in the previous intervals of high growth. This highlights the fact that pre-existing topography is as important as evolving topography in determining the spatial distribution of the sediments entering the mini-basin.

8.9 Conclusions

Changes in bathymetry driven by structural growth within and bounding the mini-basin can have an affect on the development of sedimentary systems as they are deposited within the basin. These bathymetric changes are driven by the growth of structures on the seafloor, in this case due to salt movement and bed length

change. The affect that the growth of a structure has on a sedimentary system depends on the amount of bathymetric relief generated as well as the type of sediment entering the basin; the volume of sediment, and the erosive energy of the flow carrying the sediment.

This chapter has examined the responses of channel complex systems, regional and local MTC deposits and ponded fan lobe complexes. Two end-member responses have been observed: active responses whereby sedimentary systems are either actively generated by, or actively evolve away from areas of growth and passive responses where sedimentary systems passively infill the resulting topography. Active responses have primarily been observed within the channel complex systems where rate of change of bed lengths of c. 15 mMa^{-1} and greater have led to the deflection, incision and diversion of channels. The generation of local MTCs is also classed as an active response to the structural growth as this occurs in areas where previous periods of high bed length change has resulted in emergent topography which has become unstable. This prolonged exposure on the seafloor results in mechanical failure and hence this process can also be classified as an active response to structural growth, albeit delayed in its initiation.

Passive responses can occur in response to growth on structures as well as in response to relict topography. Where a passive response is recognised the sedimentary systems tend to be less erosive in character and infill areas of low bathymetry within the mini-basin. These lows can either be formed through the active growth of positive topography on the margins of the basin, as in the case of the regional MTCs, or relict topography generated in preceding periods with high structural growth such as in the interval when the ponded sediments were deposited.

Broad-scale bed length analysis and the more detailed analysis of the stratal relationships complement each other; rate of change of bed length provides a good indication of the relative amount of growth on a structure during a specific interval, whilst the stratal relationships reveal whether this growth has been translated into bathymetric relief or whether the sedimentation rate has been high enough to effectively blanket the emergent topography. An understanding of both is required in order to understand, and ultimately predict, the reaction of sedimentary systems to structural growth.

9 Conclusions

The response of deepwater sedimentary systems to active growth of structures within and bounding a mini-basin located within the contractional domain of the Lower Congo Basin on the Angolan passive margin has been investigated. Structural analysis has been carried out from the Oligocene to present day and the resulting rates of bed length change have been used as a proxy for the growth rate of structures with a range of different responses observed within the three sedimentary systems investigated. Additionally the development of a series of ponded fan lobe complexes has been studied in detail, as have the internal characteristics and distribution of both regional and local mass transport complexes (MTCs) deposited within the mini-basin. This chapter presents a synthesis of the main conclusions and novel results from this study as;

1. a summary of the main project outcomes (Section 9.1),
2. some further discussion of key findings (Section 9.2), and
3. recommendations for future work (Section 9.3).

9.1 Key Conclusions

1. Three sedimentary systems active at four different periods in the history of the basin were investigated: third-order channel complexes deposited between 25 Ma and 18.26 Ma (Chapter 8, Section 8.5); regional mass transport complex (MTC) deposits which were mainly deposited between 18.26 Ma and 13.25 Ma (Chapter 8, Section 8.6.1); local MTC deposits which occurred as discrete slides between 13.25 Ma and 8.29 Ma (Chapter 8, Section 8.6.2) and ponded fan lobe complexes which have been studied within the mini-basin between 8.29 Ma and 5.58 Ma (Chapter 8, Section 8.7). This study has found that high growth rate structures (i.e. those with a rate of change of bed length >30 mMa^{-1}) consistently impact the facies and spatial development of sedimentary systems (particularly the channel systems), whilst medium (10 mMa^{-1} to 30 mMa^{-1}) and low (<10 mMa^{-1}) growth rate structures often have a more subtle impact on sediment distribution. Observations of the interactions between these sedimentary systems and the structures within the study area led to the classification of active and passive sediment responses to structural growth whereby active responses are those where the systems evolve in response to actively forming bathymetry they encounter whereas systems with a passive response respond to previously formed bathymetry and simply infill the bathymetric lows (Chapter 8, Section 8.8).
2. In all the studies of the sedimentary systems responses to structural growth (i.e. MTCs, lobe complexes and channel complexes) there are finer scale responses to the growth that cannot be resolved through bed length change analysis. Whilst basin-wide bed length change analysis can indicate broad-scale growth patterns within a mini-basin, analysis of the basin at

a more detailed stratigraphic resolution is required to understand the finer details of this structural movement. Examination of stratal relationships (e.g. onlapping and overlapping geometries) compliment the bed length change analysis, revealing whether the periods of high growth rate of structures is translated into bathymetric relief within the mini-basin and hence whether the response of the sedimentary systems is related to relict topography generated in previous periods of high growth (Chapter 5, Section 5.11.2). This is particularly relevant in assessing the spatial distribution of the succession of ponded fan lobe complexes during a low-growth rate phase of the mini-basin (see Chapter 8, Section 8.7).

3. Bed length analysis provides a useful, relatively quick way to investigate the structural history of an area and allows results to be mapped spatially; increasing the broad understanding of the development of a basin, including when structures were growing, and how this varies from structure to structure within an area.

4. Two main periods of elevated structural growth on salt-cored folds and salt structures within the mini-basin have been recognised between the start of the Oligocene (33.9 Ma) and present day. The first event can be correlated to the start of uplift and tilting of the passive margin driven by a plume event beneath the African continent. This also triggered high sediment denudation and a correspondingly high sediment flux to the Congo (Zaire) Fan which has continued to present day. However, within this continuum of relatively high growth rates a second phase of mini-basin wide high growth is recognised between 18.26 Ma and 13.25 Ma. This has been tentatively linked to increased growth on a series of extensional listric faults up-dip of the study area (Chapter 5, Section 5.11.1). The high growth rate phases of structural development within the mini-basin appear to record regional-scale shortening driven by up-dip extension in a gravity driven setting as opposed to local sediment loading.

5. Two types of MTC occur within the mini-basin which formed at different times and have distinctly different characteristics (Chapter 6, Section 6.9.1); regional debris flows and local slides. The regional MTC deposits are most concentrated within the period from 18.26 Ma until 13.25 Ma when the some of the highest growth rates were also recorded in the mini-basin. These regional debris flows are sourced near the shelf of the continental margin, at least 100 km east of the study area, and are comprised of chaotic material which becomes more organised and develops into imbricate thrust faults upon interaction with structures that have growth rates higher than 30 mMa^{-1} (Chapter 6, Section 6.8). The timing of initiation of local MTCs is harder to predict and they occur throughout the period from 13.25 Ma to 5.58 Ma, the same time interval as when the ponded sediments were deposited within the mini-basin. They have more organised internal features than the regional MTCs with clear extensional and compressional domains, and can clearly be linked back to headwall scarps on the flanks of structures which bound the mini-basin (Chapter 6, Section 6.6 and 6.7).

6. Contrary to expectations, the occurrence of local slides on the flanks of structures does not correlate to periods of high structural growth on the structures they are sourced from, within the resolution of the bed length change analysis. Instead, they are observed to occur mostly in periods when growth rates were relatively low, but following periods of high growth, when the mini-basin was relatively under-filled. This would suggest that either pulsing of the salt structures occurred at a resolution beneath the bed length change analysis, or that longer periods of emergence of the seafloor along the flanks of the structures (i.e. during the under-filled period) generated slopes that were more prone to gravitational instabilities and hence slope failure (Chapter 6, Section 6.9.2).

7. Four fan lobe complexes have been imaged in exceptional detail at approximately 850 m beneath the seabed. This allows the variations in the orientation of the fan lobe complexes and the geomorphological characteristics of the channels and lobes that make up the lobe complexes to be observed as the system evolves through time. The response of the fan lobe complexes to growth of the structures within and bounding the mini-basin and to bathymetric variations resulting from inherited seabed relief generated by previous lobe growth is observed. The most noticeable variation is a change in the shape and orientation of the lobe complexes through time, with a gradual north to south movement of the main feeder channel and a change in the main sediment flow direction from broadly north to south to channels being more dispersed within the basin and a group of these flowing from south to north, which has been attributed to growth of the basin-bounding salt structures (Chapter 7, Section 7.10.1). Smaller-scale changes are also observed within the lobes in response to both increased bathymetry along the margin of the mini-basin and inherited seafloor relief. In areas where bathymetric relief is highest the lobes and channels which make up these tend to become more elongated in shape and divert away from the bathymetric highs (for example along the edge of the mini-basin and on the downthrown side of the normal fault; Chapter 7, Section 7.10.1). Within the mini-basin compensational stacking is also observed where lobes appear to avulse and preferentially develop in bathymetric lows on the seafloor between older lobe deposits.

8. Lobe complexes imaged in unprecedented detail through the generation of amplitude extraction maps reveal details of the lobe elements and the fringes around the lobes that have never before been imaged in the subsurface. These unparalleled images bridge a gap in current knowledge between outcrop studies and conventional resolution seismic data, with features observed in this high-resolution seismic dataset linked to those seen in outcrops such as the Karoo Basin, South Africa and the Ross Formation of the County Clare Basin, Ireland (Chapter 7, Sections 7.9 and 7.10.2). This work indicates that lobes and lobe elements are fringed by sandy sediments which are thought to be equivalent to amalgamated and layered sheet sands observed in outcrop sections, but never before in the subsurface.

9.1.1 Effect of Structural Growth Rate on Sedimentary Systems

The growth of structures within the mini-basin impacted the sediment distribution to differing degrees depending on the type of sedimentary system active within the basin and the amount of growth on the structures. Two end-member responses have been defined relating to these factors; active responses where medium to high rates of structural growth cause channels to deviate from their pre-planned pathways and trigger local MTC deposits, and passive responses where ponded sediments and regional MTC deposits infill the bathymetric lows within the mini-basin which formed in response to medium and low rates of structural growth or relict bathymetry from previous periods of high growth.

The clearest active responses to growth of the structures within the mini-basin are observed within the third-order channel complexes where the systems are observed to deflect, divert or offset stack in response to recorded rates of bed length change greater than 15 mMa^{-1}. Structures with high growth rates (i.e. rate of change of bed length >30 mMa^{-1}) consistently impact the spatial development of the third-order channel systems causing them to divert away from the actively growing structures and often resulting in long diversions away from the active structures (for example, Channels 1.3 and 2.1; Chapter 8, Sections 8.5.1 and 8.5.1 respectively). In contrast to this low (<10 mMa^{-1}) growth rate structures do not generate as much of an active response from the channel systems with the majority able to incise through these and continue along their previously defined pathways (for example Channels 1.4 and 2.2; Chapter 8, Sections 8.5.1 and 8.5.1 respectively). Medium rates of growth (here defined as rates of bed length change between 10 mMa^{-1} to 30 mMa^{-1}) on structures normally results in the deflection of channel systems away from the actively growing structures, but in the majority of cases not in a full diversion being triggered (for example Channel 2.2 deflecting away from the northern tip of the anticline within Area E).

The generation of local MTCs (slides) is also considered to be an active response to high structural growth. Whilst these do not occur concurrently to high growth periods of the structures, this growth does cause the flanks of the structures to become exposed on the seafloor, which in turn triggers the development of the local slide deposits.

In contrast to these active responses, the sediments which respond to the structural growth in a passive manner simply infill the basin, responding more to the amount of positive seafloor bathymetry as opposed to the amount and rate of the structural growth. This is an important distinction as it means that the sediments such as the ponded fans react to emergent bathymetry generated during previous periods of high growth. The regional MTCs are also considered to show a passive response to the structures active within the mini-basin as, in the most part, they do not appear to change in character in response to the growth. One exception to this is in their response to structures with high structural growth where imbricate thrust faults develop where the debris flows approach structures which have a rate of change of bed length greater than 30 mMa^{-1}.

9.1.2 How Useful is Bed Length Change Analysis?

Whilst bed length change analysis gives a good, broad overview of the structural activity within the basin during a specific time interval, assessing how the structural growth rate converts into bathymetric relief is more important in understanding the impact that a structure has on sediments entering the basin. As discussed in Chapter 4 and 5 (Sections 4.2.12 and 5.11.2) high rates of bed length change do not necessarily equate to high topographic relief, as increased sedimentation rates can compensate for this growth. Using the stratal relationships associated with the structure can help calibrate the response, where onlap indicates positive relief on the seabed and overlap indicates that the structure has no bathymetric expression. Additionally, examining stratal relationships alongside the bed length analysis is useful because it can yield information at a higher resolution, than that afforded by the rate of bed length change; intervals containing predominantly high cumulative bed length change on the structures within the mini-basin can be identified and then the stratal relationships investigated to reveal whether this growth was steady or episodic. For example, the bed length change analysis for the period between 18.26 Ma and 13.25 Ma indicates predominantly medium and high rates of bed length change along the western margin of the basin. However, the spatial distribution of two regional MTC deposits active in the basin during this interval differs in response the structures in the north of Area C. Analysis of the onlap patterns within this interval suggested that there was more topographic relief on these structures towards the start of the interval, suggesting that the episodic nature of this growth was averaged out in the rate of change of bed length analysis (Chapter 8, Section 8.6.2).

This bed length change rate is also averaged over a time interval, and hence the resolution of the bed length change analysis is dependent upon the level of detail of the biostratigraphy in an area. In this study the intervals range between 0.5 Ma and nearly 9 Ma making individual changes in the channel orientation during the Oligocene (i.e. 33.9 Ma to 25 Ma), for example, very difficult to ascertain and link back to specific structures. As discussed above, examination of growth strata can help provide increased resolution. Therefore, whilst the bed length change analysis gives a good broad overview of structural development of the basin, and evolution of individual structures, it is important to be aware that these measurements are time-averaged and as such may be masking some of the detail of the structural movement, and they will always be at a lower resolution than it time it takes for an individual debris flow to be deposited, or a channel complex to form.

Alongside a quantification of growth rate, it is also important to use the changes observed in the facies, such as changes in the location of the individual lobes within the fan lobe complexes and the deflection, and continued incision of channels, or systematic offlap of channels on the flanks of a structure to calibrate results, and to detect responses that may reflect variations in structural growth at finer temporal resolution. Responses that appear anomalous, such as channels that cross a growing structure may in fact be responding to subtle variations in growth rate versus sediment supply beneath the resolution of the bed length change analysis or the seismic data. While the structure was buried, perhaps because growth slowed, a channel may

have been able to cross the fold and then as growth increased the erosive power of the sediment gravity flows within the channel allowed it to keep pace with continued structural growth.

This thesis has found that rates of bed length change provide a good first order control for the structures which are active in the basin at a certain period, and therefore most likely to affect depositional systems, but greater resolution of rate of change of bed length measurements is needed in order to resolve the details of the structural growth. It is also acknowledged that there will always be responses that are unlikely to have structural control, for example changes in sinuosity within channel systems, channels that change pathways due to avulsions up-dip of the direct area of study, and changes in fan lobe location due to compensational stacking where the seabed bathymetry is due to depositional processes.

9.1.3 Main Structural Drivers in the Mini-Basin Formation

The aim of the structural section of work carried out as part of this research was to aid in understanding the structural history of the mini-basin in terms of the rate at which the structures developed and the spatial distribution of the structures with the highest growth rates through time. This was achieved and the results were used to aid the understanding of the reactions of the sedimentary systems to the growth of the structures. However, a secondary conclusion emerged from this work; that although the main structures that define the mini-basin area started to grow in Oligocene times and that some have continued to be active until the present day, two periods of higher growth rate can be identified on the main structures in the basin. These two periods of basin-wide high structural growth occurred in the Oligocene from 33.9 Ma until 25 Ma and in the Miocene between 18.26 Ma and 13.25 Ma.

The onset of deformation in the Oligocene (at 33.9 Ma) correlates to a well-documented uplift event along the African margin (Burke, 1996, Al-Hajri et al., 2009, Roberts and White, 2010, Green et al., 2014, Paul et al., 2014, White and Hoggard, 2014). This is thought to have caused tilting on the passive margin as well as providing an increased sediment supply in the Congo (Zaire) River, which resulted in increased sediment entering the Lower Congo Basin. This increased sediment load and tilting along the passive margin is thought to be responsible for the period of high structural growth recorded during the interval from 33.9 Ma to 25 Ma. However, it would also have generated high sediment influx into the Lower Congo Basin which would have continued until present day due to the longer response time of the continental river systems. Therefore, given the fairly constantly high sediment flux from the Congo River to the basin after the uplift event between 33.9 Ma and 25 Ma (Paul et al. 2014), it is unexpected to observed a second the period of elevated structural growth within the continuum of high growth driven by this regional sediment loading.

The second period of extensive, elevated rates of structural growth within the mini-basin from 18.26 Ma to 13.25 Ma does not relate to any published information on separate regional tectonic or uplift events nor do there appear to be any documented pulses of increased sediment supply through the Congo (Zaire) River during this time. However, this period of growth does correlate to the deposition of extensive regional MTC deposits within the mini-basin which are thought to have formed due to movement on large-scale listric normal faults within the extensional domain of the passive margin. A provisional look at a series of

confidential regional seismic lines showed that thicker growth packages formed on the extensional faults up-dip of the study area during this time. Given current understanding of the margin this would suggest a period of renewed growth on these faults which drove the down-dip movement of the salt and hence increased shortening during this interval. This down-dip movement could have generated coupled salt tectonic features manifesting in salt-cored anticlines, diapirs, salt walls and extrusive salt bodies within the study area. However, a more rigorous study of the timing of movement on the up-dip extensional faults would be required to fully test this hypothesis.

9.1.4 Bed Length Change is a Useful Method to Assess Structural Evolution

The bed length change analysis presented in this research takes a novel approach by quantitatively assessing the structural activity within the mini-basin then plotting the results spatially, thus enabling interactions with the various types of sedimentary systems to be investigated. It is time-consuming to carry out structural restorations within an area, and therefore these are usually performed on a few widely spaced two-dimensional lines. This novel approach of measuring the line lengths of the main sediment packages which interact with the structures then plotting the results onto maps can provide a quick and easy analysis of how the structures are behaving through time. As well as allowing many structures to be analysed, this also reduces the need to rely solely upon more time-consuming structural restorations for this type of analysis.

The results from this bed length change analysis can be mapped onto the structures to create maps highlighting areas within the basin where more or less growth occurred through time. This is particularly useful in areas underlain by a mobile substrate, in this case salt, where the locus of growth can vary significantly through time and simply restoring a few sections does not give a clear picture of the deformation history. Once made, these maps aid in predicting the location and reactions of the sedimentary systems to the bathymetric variations which often occur alongside structural growth within an area.

This research found that the responses of third-order channel systems could be predicted according to the rate of change of bed length of a structure, for example shortening rates on a structure greater than 15 mMa^{-1} caused channels to deflect away from the actively growing structural highs (Chapter 8, Section 8.5.3). Therefore combining this with a knowledge that channel systems occur at a specific time interval can aid in predicting the location of third-order channel complexes, and hence aid in understanding the location of key reservoir rocks. In this sense, a bed length change analysis, such as that performed in this study might be particularly useful in areas where the resolution of the seismic data is less than that used in this study. Knowledge of the biostratigraphy of an area, coupled with a few mapped horizons could allow structural growth rate maps to be produced and facies predictions made with greater confidence.

9.1.5 New Details on Lobe Complex Development

Exceptionally detailed amplitude extraction maps generated from high-resolution three-dimensional seismic data has meant that the facies that make up a fan lobe complex can be imaged in the subsurface in unprecedented detail. These detailed images have been used to prove that lobes and the channels within the

lobe complexes respond to both bathymetry internal to the basin, through compensational stacking and lateral migration, and changes external to the basin causing the feeder channel to avulse and the direction of sediment flow to change.

The unprecedented level of detail at which these features have been imaged has meant that the observations of the changes in facies within these fans can be used to bridge the gap between current research using conventional seismic data and the detail observed within outcrop data. Prior to this study, the level of detail seen within the lobe elements and lobe fringes in this study had only been observed in outcrop data and on the seafloor, but were postulated to occur in the subsurface. The observations from this research confirm that features such as lobes and lobe elements which had previously only been described as 'sheet sands' in the subsurface are in fact composed of narrow individual channels often fringed by high amplitude sands. These sands which are seen fringing the lobes and individual lobe elements are thought to represent amalgamated and layered sheet sands which have been frequently observed in outcrop studies, but never before in the subsurface.

9.1.6 Implications for Petroleum Geology

Whilst this work has led to a series of interesting academic conclusions, the results and observations presented in this thesis can also be applied to the petroleum industry. The response of third-order channel systems to the growth of structures is particularly relevant as interactions such as those observed here between channel complexes and salt structures often lead to the development of important oil and gas plays in the subsurface (for example in the Lower Congo Basin, Angola and in the Gulf of Mexico). In areas with lower resolution seismic data, mapping the bed length change rates of structures within a mini-basin may aid in predicting the response of sedimentary systems to growing structures in the subsurface; for example if structures are observed to have been moving at high shortening rates (in this part of the Lower Congo basin greater than 15 mMa^{-1}), it would be logical to assume that any channels approaching these structures were deflected or diverted by the growth. These ideas can be applied to other areas and used to help predict the most likely location of sediment fairways.

This work has also examined variations in the facies which make up the MTC deposits and the ponded fan lobe complexes in the subsurface, details of which could be important in understanding these systems within the context of a petroleum system. Resolving variations in the extent of the sandy fringes which surround the lobes and lobes elements within the fan lobe complexes as well as the thicker, sandy amalgamated fan package on the downthrown side of the normal fault can aid understanding of reservoir heterogeneities. In a similar way, a greater understanding of the likely distribution of the erosive local MTCs could help predict the likelihood of traps in the area being eroded by the activity of local slides which have been observed to scour into the underlying stratigraphy by up to 300 m in the study area. The large, discrete, undeformed blocks within the extensional and compressional domains of the local MTCs also have the potential to form effective traps for oil and gas, with ponded sediments deposited in the depressions on top of both local and regional MTC deposits also potentially forming effective reservoirs.

9.2 Future Work

Extending the study to seismic datasets to east and west, or along strike on the Angolan margin would test the robustness of the results derived in this study. It would also allow the response of the channel systems to structural growth to be assessed on similar salt-cored anticlines and using channels which had similar, if not the same, properties in terms of sediment type and the volume of sediment entrained within the system. One way to assess the variations in bed length change rate regionally would be to investigate variations in bed length change rate along a regional transect through the extensional and compressional domains, inboard and outboard of the study area, as well as along a strike section parallel to the continental margin and in line with the study area. It would be useful to assess the variations in bulk sediment supply across the Lower Congo Basin through time, using a series of regional isopach maps to assess changes in the locus of the main sediment depocentres. These studies could be used to test whether the predictions relating to the interaction between rate of change of bed length and sedimentary systems can be applied to areas in a similar environment, before being applied elsewhere in the world.

Once the validity of the results from the Angolan passive margin has been assessed further work is required in order to test whether the relationships observed between the sedimentary systems and structural growth here can be applied to similar basins elsewhere in the world. For example comparisons between bed length change measurements and channel systems could be conducted within a similar tectonic setting such as the Gulf of Mexico. It would be interesting to test whether the cut-off value of a shortening rate of 15 mMa^{-1} for active channel diversion is generally applicable for salt related folding or whether different bed length change rates apply in other basins. It would also be interesting to compare the observations drawn here to gravitational deepwater fold and thrust belts formed on a mobile shale substrate such as the Niger Delta.

Within this study there are parts of the stratigraphy which have less robust age controls, particularly the older sediment packages deposited between 33.9 Ma and 13.25 Ma. Increased biostratigraphic resolution, with more data points, would allow for a much improved temporal resolution which would in turn refine the rates of structural growth. There may be other areas on the Angolan margin that have better biostratigraphy in these key sections and further work could be carried out to locate these area and either perform a similar study within the corresponding mini-basins or to extend the horizon interpretations within the current study area.

It would be interesting to expand the study of bed length change rates along the Angolan passive margin, focussing specifically on the second, previously unidentified, period of high growth between 18.26 Ma and 13.25 Ma. This study would particularly focus on assessing whether the event observed within the mini-basin represents a regional change in bed length change rate that might be linked to changes in rates of extension inboard of the study area, or whether it is a more localised phenomena. In order to do this, bed length change rates could be calculated both inboard and along strike of the mini-basin. The bed length change analysis would need to be coupled with a regional study of variations in sediment loading during this period which would help assess whether the study area formed a locus for sediment loading during this

interval, hence justifying a more local explanation for the period of elevated deformation. A rigorous assessment of the thick growth packages formed on the extensional listric faults is also required and it would be useful to carry out an assessment of the growth rate history of these faults. This analysis could help identify whether the growth in this mini-basin during this period was linked to growth on the normal faults and hence that a more regional explanation for the growth is justified.

Given the exceptional resolution and imaging of the ponded sediments, the study of the fan lobe complexes could be expanded to include a more detailed geomorphological study; examining changes of the geomorphic characteristics of the lobes within the lobe complex systems. A discussion of the lobe dimensions, length to width ratios and variations in the surface area of the fan lobe complexes could be carried out and compared to examples elsewhere in the literature, in a similar manner to Prelat et al. (2010). A second package of ponded sediment occurs within the mini-basin almost immediately below the interval studied in this thesis which was deposited between 9.68 Ma and 8.29 Ma (H90 to H100). It is also observed to thicken south of the normal fault and hence would merit further study; it would be interesting to compare the characteristics of the channels south of the normal fault with those observed in the two youngest packages in this study. This would allow the validity of the assumption that the change from a more dispersed fan-like pattern north of the fault to a series of amalgamated, braided channels south of the fault was driven by the elongate depression formed on the hanging wall of the fault to be thoroughly tested.

References

Adeogba, A.A., 2005, Transient fan architecture and depositional controls from near-surface 3-D seismic data, Niger Delta continental slope: AAPG Bulletin, v. 89, p. 627-643.

Al-Hajri, Y., White, N., and Fishwick, S., 2009, Scales of transient convective support beneath Africa: Geology, v. 37, p. 883-886.

Al Ja'Aidi, O.S., McCaffrey, W.D., and Kneller, B.C., 2004, Factors influencing the deposit geometry of experimental turbidity currents: implications for sand-body architecture in confined basins: Geological Society, London, Special Publications, v. 222, p. 45-58.

Albertz, M., and Lingrey, S., 2012, Critical state finite element models of contractional fault-related folding: Part 1. Structural analysis: Tectonophysics, v. 576–577, p. 133-149.

Allen, P.A., and Allen, J.R., 2009, Basin Analysis, Wiley-Blackwell.

Alves, T.M., and Cartwright, J.A., 2010, The effect of mass-transport deposits on the younger slope morphology, offshore Brazil: Marine and Petroleum Geology, v. 27, p. 2027-2036.

Anderson, A.V., Sickafoose, D.K., Fahrer, T.R., and Gottschalk, R.R., 2012, Interaction of Oligocene–Miocene deep-water depositional systems with actively evolving structures: The Lower Congo Basin, offshore Angola, *in* Gao, D., ed., Tectonics and sedimentation: Implications for Petroleum Systems, AAPG Memoir, v. 100, p. 291-313.

Anderson, J.E., Cartwright, J., Drysdall, S.J., and Vivian, N., 2000, Controls on turbidite sand deposition during gravity-driven extension of a passive margin: examples from Miocene sediments in Block 4, Angola: Marine and Petroleum Geology, v. 17, p. 1165-1203.

Anka, Z., Seranne, M., Lopez, M., Scheck-Wenderoth, M., and Savoye, B., 2009, The long-term evolution of the Congo deep-sea fan: a basin-wide view of the interaction between a giant submarine fan and a mature passive margin (ZaiAngo project): Tectonophysics, v. 470, p. 42-56.

Ardill, J., Huang, T.C., and McLaughlin, O., 2003, The stratigraphy and reservoir architecture of the Oligocene to Miocene Malembo Formation of the Lower Congo Basin, offshore Angola; Houston Geological Society Bulletin, v. 8, p. 21.

Arkhanguelsky, D.A., 1933, Slides of sediments on the Black-Sea bottom and the importance of this phenomenon for geology: Bulletin of the Society of Naturalists, Moscow-Sc: Geology, v. 38, p. 38–80.

Armitage, D.A., Piper, D.J.W., McGee, D.T., and Morris, W.R., 2010, Turbidite deposition on the glacially influenced, canyon-dominated Southwest Grand Banks Slope, Canada: Sedimentology, v. 57, p. 1387-1408.

Baas, J.H., Van Kesteren, W., and Postma, G., 2004, Deposits of depletive high-density turbidity currents: a flume analogue of bed geometry, structure and texture: Sedimentology, v. 51, p. 1053-1088.

Babonneau, N., Savoye, B., Cremer, M., and Klein, B., 2002, Morphology and architecture of the present canyon and channel system of the Zaire deep-sea fan: Marine and Petroleum Geology, v. 19, p. 445-467.

Badalini, G., Kneller, B., and Winker, C.D., 2000, Architecture and processes in the late Pleistocene Brazos-Trinity turbidite system, Gulf of Mexico continental slope, *in*, Weimer, P., Slatt, R. M., Coleman, J., Rosen, N. C., Nelson, H., Bouma, A. H., Styzen, M. J. & Lawrence, D. T., eds., Deep-Water Reservoirs of the World: GCSSEPM Foundation 20th Annual Research Conference, p. 16-34.

Bahroudi, A., and Koyi, H., 2003, Effect of spatial distribution of Hormuz salt on deformation style in the Zagros fold and thrust belt: an analogue modelling approach: Journal of the Geological Society, v. 160, p. 719-733.

Bakare, O., 2007, Influence of mass transport deposits on stratigraphic evolution, channel morphology, and turbidite reservoir preservation and architecture, Niger Delta, West Africa: 2007 AAPG Annual Convention and Exhibition.

Baldwin, B., and Butler, C.O., 1985, Compaction curves: AAPG Bulletin, v. 69, p. 622.

Bally, A.W., Gordy, P.L., and Stewart, G.A., 1966, Structure, seismic data, and orogenic evolution of southern Canadian Rocky Mountains: Bulletin of Canadian Petroleum Geology, v. 14, p. 337.

Barker, S.P., Haughton, P.D.W., McCaffrey, W.D., Archer, S.G., and Hakes, B., 2008, Development of rheological heterogeneity in clay-rich high-density turbidity currents: Aptian Britannia Sandstone Member, U.K. Continental Shelf: Journal of Sedimentary Research, v. 78, p. 45-68.

Barley, B., 1999, Deepwater problems around the world: The Leading Edge, v. 18, p. 488-493.

Bartek, L.R., Vail, P.R., Anderson, J.B., Emmet, P.A., and Wu, S., 1991, Effect of Cenozoic ice-sheet fluctuations in Antarctica on the stratigraphic signature of the Neogene: Journal of Geophysical Research-Solid Earth and Planets, v. 96, p. 6753-6778.

Baumgartner, T.R., and van Andel, T.H., 1971, Diapirs of continental margin of Angola, Africa: Geological Society of America Bulletin, v. 82, p. 793-802.

Beaubouef, R., Abreu, V., and Van Wagoner, J., 2003, Basin 4 of the Brazos–Trinity slope system, western Gulf of Mexico: the terminal portion of a late Pleistocene lowstand systems tract, shelf margin deltas and linked down slope petroleum systems, *in,* Roberts, H.H., Rosen, N.C., Fillon, R.H. and Anderson, J.B., eds., Shelf Margin Deltas and Linked Down Slope Petroleum Systems: Global Significance and Future Exploration Potential: GCSSEPM 23rd Annual Research Conference, p. 45-66.

Beaubouef, R.T., and Friedmann, S.J., 2000, High resolution seismic/sequence stratigraphic framework for the evolution of Pleistocene intra slope basins, western Gulf of Mexico: depositional models and reservoir analogs, *in*, Weimer, P., Slatt, R. M., Coleman, J., Rosen, N. C., Nelson, H., Bouma, A. H., Styzen, M. J. & Lawrence, D. T., eds., Deep-Water Reservoirs of the World: GCSSEPM Foundation 20th Annual Research Conference, v. 20, p. 40-60.

Belderson, R., Kenyon, N., Stride, A., and Pelton, C., 1984, A 'braided' distributary system on the Orinoco deep-sea fan: Marine Geology, v. 56, p. 195-206.

Berggren, W.A., Kent, D.V., Swisher, III, C.C. & Aubry, M-P., 1995a, A revised Cenozoic geochronology and chronostratigraphy, *in*: Berggren, W.A., Kent, D.V., Aubry, M-P. and Hardenbol, J., eds, Geochronology, Time Scales And Stratigraphic Correlation: Framework For An Historical Geology. Society for Economic Palaeontologists and Mineralogists Special Publication, v. 54, p. 129-212.

Berggren, W.A., Hilgen, F.J., Langereis, C.G., Kent, D.V., Obradovich, J.D., Raffi, I., Raymo, M.E. and Shackleton, N.J., 1995b., Late Neogene chronology: New perspectives in high-resolution stratigraphy: Geological Society of America Bulletin, v. 107, p. 1272-1287.

Beydoun, W., Kerdraon, Y., Lefeuvre, F., Bancelin, J., Medina, S., and Bleines, B., 2002, Benefits of a 3DHR survey for Girassol Field appraisal and development, Angola: The Leading Edge, v. 21, p. 1152-1155.

Biscontin, G., Pestana, J., and Nadim, F., 2004, Seismic triggering of submarine slides in soft cohesive soil deposits: Marine Geology, v. 203, p. 341-354.

Bolli, H.M., Ryan, W.B.F., McKnight, B.K., Kagami, H., Melguen, M., Siesser, W.G., Longoria, J.F., Decima, F.P., Foresman, J.B., Hottman, W.E., and Natland, J.H., 1978, Initial reports of the Deep Sea Drilling Project; covering Leg 40 of the cruises of the drilling vessel Glomar Challenger; Cape Town, South Africa to Abidjan, Ivory Coast, December 1974-February 1975: Texas A & M University, Ocean Drilling Program, v. 40, p. 1079.

Bolt, B.A., Horn, W.L., Macdonald, G.A., and Scott, R.F., 1977, Geological Hazards: New York, Springer-Verlag.

Bond, G., 1978, Evidence for Late Tertiary uplift of Africa relative to North-America, South-America, Australia and Europe: Journal of Geology, v. 86, p. 47-65.

Bond, G.C., and Kominz, M.A., 1984, Construction of tectonic subsidence curves for the early Paleozoic miogeocline, southern Canadian Rocky Mountains: Implications for subsidence mechanisms, age of breakup, and crustal thinning: Geological Society of America Bulletin, v. 95, p. 155-173.

Bondevik, S., Mangerud, J., Dawson, S., Dawson, A., and Lohne, Ø., 2003, Record-breaking height for 8000-year-old tsunami in the North Atlantic: Eos, Transactions American Geophysical Union, v. 84, p. 289-293.

Booth, J., DuVernay III, A., Pfeiffer, D., and Styzen, M., 2000, Sequence stratigraphic framework, depositional models, and stacking patterns of ponded and slope fan systems in the Auger Basin: Central Gulf of Mexico slope, *in*, Weimer, P., Slatt, R. M., Coleman, J., Rosen, N. C., Nelson, H., Bouma, A. H., Styzen, M. J. & Lawrence, D. T., eds., Deep-Water Reservoirs of the World: GCSSEPM Foundation 20th Annual Research Conference, p. 82-103.

Booth, J.R., Dean, M.C., DuVernay III, A.E., and Styzen, M.J., 2003, Paleo-bathymetric controls on the stratigraphic architecture and reservoir development of confined fans in the Auger Basin: central Gulf of Mexico slope: Marine and Petroleum Geology, v. 20, p. 563-586.

Bornhauser, M., 1969, Geology of Day dome (Madison county, Texas); a study of salt emplacement: AAPG Bulletin, v. 53, p. 1411-1420.

Brami, T.R., Tenney, C.M., Pirmez, C., Holman, K.L., Archie, C., Heeralal, S., and Hannah, R., 2000, Late Pleistocene deep-water stratigraphy and depositional processes, offshore Trinidad and Tobago, *in*, Weimer, P., Slatt, R. M., Coleman, J., Rosen, N. C., Nelson, H., Bouma, A. H., Styzen, M. J. & Lawrence, D. T., eds., Deep-Water Reservoirs of the World: GCSSEPM Foundation 20th Annual Research Conference, p. 402–421.

Braun, J., and Sambridge, M., 1994, Dynamical Lagrangian Remeshing (DLR): A new algorithm for solving large strain deformation problems and its application to fault-propagation folding: Earth and Planetary Science Letters, v. 124, p. 211-220.

Brice, S.E., Cochran, M.D., Pardo, G., and Edwards, A.D., 1982, Tectonics and sedimentation of the South Atlantic Rift Sequence: Cabinda, Angola: AAPG Memoir, v. 34, p. 5-18.

Brognon, G.P., and Verrier, G.R., 1966, Oil and geology in Cuanza basin of Angola: AAPG Bulletin, v. 50, p. 108-158.

Broucke, O., Temple, F., Rouby, D., Robin, C., Calassou, S., Nalpas, T., and Guillocheau, F., 2004, The role of deformation processes on the geometry of mud-dominated turbiditic systems, Oligocene and Lower-Middle Miocene of the Lower Congo basin (West African Margin): Marine and Petroleum Geology, v. 21, p. 327-348.

Brown, A.R., 1999, Interpretation of three-dimensional seismic data, AAPG Memoir 42, SEG Investigations in Geophysics no. 9.

Brunsden, D., and Prior, D.B., 1984, Slope instability: Wiley & Sons Limited.

Brunt, R.L., McAffrey, W.D., and Kneller, B.C., 2004, Experimental modeling of the spatial distribution of grain size developed in a fill-and-spill mini-basin setting: Journal of Sedimentary Research, v. 74, p. 438-446.

Bugge, T., Belderson, R., and Kenyon, N., 1988, The storegga slide: Philosophical Transactions of the Royal Society of London. Series A, v. 325, p. 357-388.

Bull, S., Cartwright, J., and Huuse, M., 2009, A review of kinematic indicators from mass-transport complexes using 3D seismic data: Marine and Petroleum Geology, v. 26, p. 1132-1151.

Burbank, D., Meigs, A., and Brozović, N., 1996, Interactions of growing folds and coeval depositional systems: Basin Research, v. 8, p. 199-223.

Burbank, D.W., and Vergés, J., 1994, Reconstruction of topography and related depositional systems during active thrusting: Journal of Geophysical Research, v. 99, p. 20281-20297.

Burke, K., 1975, Atlantic evaporites formed by evaporation of water spilled from Pacific, Tethyan, and Southern oceans: Geology, v. 3, p. 613-616.

Burke, K., 1996, The African plate: South African Journal of Geology, v. 99, p. 341-409.

Burke, K., Dessauvagie, T., and Whiteman, A., 1971, Opening of the Gulf of Guinea and geological history of the Benue depression and Niger delta: Nature, v. 233, p. 51-55.

Burke, K., Macgregor, D.S., and Cameron, N.R., 2003, Africa's petroleum systems: four tectonic 'Aces' in the past 600 million years, *in* Authur, T.J., MacGregor, D.S., and Cameron, N.R., eds., Petroleum Geology of Africa: New themes and developing technologies: Geological Society, London, Special Publication, v. 207, p. 21-60.

Burollet, P., 1975, Tectonique en radeaux en Angola: Bulletin De La Societe Geologique De France, p. 503-504.

Butler, R., and Turner, J., 2010, Gravitational collapse at continental margins: products and processes; an introduction: Journal of the Geological Society, v. 167, p. 569-570.

Buxtorf, A., 1916, Prognosen und Befunde beim Hauensteinbasis-und Grenchenbergtunnel und die Bedeutung der letztern für die Geologie des Juragebirges, E. Birkhäuser.

Callec, Y., Deville, E., Desaubliaux, G., Griboulard, R., Huyghe, P., Mascle, A., Mascle, G., Noble, M., de Carillo, C.P., and Schmitz, J., 2010, The Orinoco turbidite system: Tectonic controls on sea-floor morphology and sedimentation: AAPG Bulletin, v. 94, p. 869-887.

Cantelli, A., Pirmez, C., Johnson, S., and Parker, G., 2011, Morphodynamic and stratigraphic evolution of self-channelized subaqueous fans emplaced by turbidity currents: Journal of Sedimentary Research, v. 81, p. 233-247.

Carr, M., and Gardner, M., 2000, Portrait of a basin-floor fan for sandy deepwater systems, Permian Lower Brushy Canyon Formation, West Texas, *in* Bouma, A.H. and Stone, C.G., eds. Fine-grained turbidite systems: AAPG Memoir, v. 72 and SEPM Special Publication, v. 68, p. 215-232.

Carter, R., 1975, A discussion and classification of subaqueous mass-transport with particular application to grain-flow, slurry-flow, and fluxoturbidites: Earth-Science Reviews, v. 11, p. 145-177.

Chamberlin, R.T., 1910, The Appalachian folds of central Pennsylvania: The Journal of Geology, v. 18, p. 228.

Chopra, S., and Marfurt, K., 2005, Seismic attributes — A historical perspective: Geophysics, v. 70, p. 3-28.

Chopra, S., and Marfurt, K., 2008, Emerging and future trends in seismic attributes: The Leading Edge, v. 27, p. 298-318.

Clark, I.R., and Cartwright, J.A., 2009, Interactions between submarine channel systems and deformation in deepwater fold belts: Examples from the Levant Basin, Eastern Mediterranean sea: Marine and Petroleum Geology, v. 26, p. 1465-1482.

Clark, I.R., and Cartwright, J.A., 2011, Key controls on submarine channel development in structurally active settings: Marine and Petroleum Geology, v. 28, p. 1333-1349.

Clark, J.D., and Pickering, K.T., 1996a, Architectural elements and growth patterns of submarine channels: Application to hydrocarbon exploration: AAPG Bulletin, v. 80, p. 194-221.

Clark, J.D., and Pickering, K.T., 1996b, Submarine channels: processes & architecture, Vallis.

Costa, E., and Vendeville, B., 2002, Experimental insights on the geometry and kinematics of fold-and-thrust belts above weak, viscous evaporitic décollement: Journal of Structural Geology, v. 24, p. 1729-1739.

Covault, J.A., and Romans, B.W., 2009, Growth patterns of deep-sea fans revisited: Turbidite-system morphology in confined basins, examples from the California Borderland: Marine Geology, v. 265, p. 51-66.

Coward, M.P., Purdy, E.G., Ries, A.C., and Smith, D.G., 1999, The distribution of petroleum reserves in basins of the South Atlantic margins, *in* Cameron, N.R., Bate, R.H., and Clure, V.S., eds., The oil and Gas Habits of the South Atlantic: Geological Society, London, Special Publication, v. 153, p. 110-131.

Cramez, C., and Jackson, M., 2000, Superposed deformation straddling the continental-oceanic transition in deep-water Angola: Marine and Petroleum Geology, v. 17, p. 1095-1109.

Cronin, B.T., 1995, Structurally-controlled deep sea channel courses: examples from the Miocene of southeast Spain and the Alboran Sea, southwest Mediterranean, *in* Hartley, A.J., and Prosser, D.J., eds., Charactorisation of Deep Marine Clastic Systems: Geological Society Special Publication No. 94, p. 115 - 135.

Cronin, B.T., Kenyon, N.H., Woodside, J.M., Ivanov, M., den Bezemer, T., Millington, J., van der Wal, A., and Limonov, A., 1994, Views of the Andarax submarine canyon: a meandering system on an active tectonic margin, *in* Pickering, K.T., Hiscott, R.N., Kenyon, N.H., Ricci Lucchi, F., and Smith, R.D.A., eds., Atlas of Deepwater Environments; Architectural Style in Turbidite Systems: London, Chapman & Hall.

Cross, N.E., Cunningham, A., Cook, R.J., Taha, A., Esmaie, E., and El Swidan, N., 2009, Three-dimensional seismic geomorphology of a deep-water slope-channel system: The Sequoia field, offshore west Nile Delta, Egypt: AAPG Bulletin, v. 93, p. 1063-1086.

Dahlstrom, C.D., 1990, Geometric constraints derived from the law of conservation of volume and applied to evolutionary models for detachment folding: AAPG Bulletin, v. 74, p. 336-344.

Dahlstrom, C.D.A., 1969, Balanced cross sections: Canadian Journal of Earth Sciences, v. 6, p. 743.

Dahlstrom, C.D.A., 1970, Structural geology in the eastern margin of the Canadian Rocky Mountains: Bulletin of Canadian Petroleum Geology, v. 18, p. 332.

Dalley, R., Gevers, E., Stampfli, G., Davies, D., Gastaldi, C., Ruitjenberg, P., and Vermeer, G., 1989, Dip and azimuth displays for 3D seismic interpretation: First Break, v. 7, p. 86-95.

Damuth, J.E., and Embley, R.W., 1981, Mass-transport processes on Amazon Cone: western equatorial Atlantic: AAPG Bulletin, v. 65, p. 629-643.

Davies, R.J., Posamentier, H.W., Wood, L.J., and Cartwright, J.A., 2007, Seismic geomorphology: Applications to hydrocarbon exploration and production: Geological Society of London Special Publications, v. 227.

Davies, R.J., and Stewart, S.A., 2005, Emplacement of giant mud volcanoes in the South Caspian Basin: 3D seismic reflection imaging of their root zones: Journal of the Geological Society, v. 162, p. 1-4.

Davison, I., 1999, Tectonics and hydrocarbon distribution along the Brazilian and South Atlantic margin, *in* Cameron, N.R., Bate, R.H., and Clure, V.S., eds., The Oil and Gas Habits of the South Atlantic: Geological Society, London, Special Publication, v. 153, p. 133-151.

Davison, I., 2007, Geology and tectonics of the South Atlantic Brazilian salt basins: Geological Society, London, Special Publications, v. 272, p. 345-359.

Davison, I., Alsop, I., and Blundell, D., 1996, Salt tectonics: some aspects of deformation mechanics: Geological Society, London, Special Publications, v. 100, p. 1-10.

Davison, I., Anderson, L., and Nuttall, P., 2012, Salt deposition, loading and gravity drainage in the Campos and Santos salt basins: Geological Society, London, Special Publications, v. 363, p. 159-174.

Dawson, A., Long, D., and Smith, D., 1988, The Storegga slides: evidence from eastern Scotland for a possible tsunami: Marine Geology, v. 82, p. 271-276.

de Matos, R.M.D., 1999, History of the northeast Brazilian rift system: kinematic implications for the break-up between Brazil and West Africa: Geological Society, London, Special Publications, v. 153, p. 55-73.

de Sitter, L.U., 1958, Boudins and parasitic folds in relation to cleavage and folding: Geol. en Mijnb., v. 20, p. 277 - 286.

Decker, J., Teas, P.A., Schneider, R.D., Saller, A.H., and Orange, D.L., 2004, Modern deep sea sedimentation in the Makassar Strait: insights from high-resolution multibeam bathymetry and backscatter, sub-bottom profiles, and USBL-navigated cores: Proceedings of the 29th Annual Indonesian Petroleum Association Convention, Jakarta Indonesia, December 2004, v. 1, p. 377–387

Demyttenaere, R., Tromp, J.P., Ibrahim, A., Allman-Ward, P., and Meckel, T., 2000, Brunei deep water exploration: From sea floor images and shallow seismic analogues to depositional models in a slope turbidite setting, *in*, Weimer, P., Slatt, R. M., Coleman, J., Rosen, N. C., Nelson, H., Bouma, A. H., Styzen, M. J. & Lawrence, D. T., eds., Deep-Water Reservoirs of the World: GCSSEPM Foundation 20th Annual Research Conference, p. 304-317.

Deptuck, M., Sylvester, Z., Pirmez, C., and Obyrne, C., 2007, Migration–aggradation history and 3-D seismic geomorphology of submarine channels in the Pleistocene Benin-major Canyon, western Niger Delta slope: Marine and Petroleum Geology, v. 24, p. 406-433.

Deptuck, M.E., Piper, D.J.W., Savoye, B., and Gervais, A., 2008, Dimensions and architecture of late Pleistocene submarine lobes off the northern margin of East Corsica: East Corsica submarine lobes: Sedimentology, v. 55, p. 869-898.

Deptuck, M.E., Steffens, G.S., Barton, M., and Pirmez, C., 2003, Architecture and evolution of upper fan channel-belts on the Niger Delta slope and in the Arabian Sea: Marine and Petroleum Geology, v. 20, p. 649-676.

Deramond, J., Souquet, P., Fondecave-Wallez, M.-J., and Specht, M., 1993, Relationships between thrust tectonics and sequence stratigraphy surfaces in foredeeps: model and examples from the Pyrenees (Cretaceous-Eocene, France, Spain): Geological Society, London, Special Publications, v. 71, p. 193-219.

Diegel, F.A., Karlo, J.F., Schuster, D.C., Shoup, R.C., and Tauvers, P.R., 1995, Cenozoic structural evolution and tectono-stratigraphic framework of the northern Gulf Coast continental margin., *in* Jackson, M.P.A., Roberts, D.G., and Snelson, S., eds., Salt Tectonics: a Global Perspective., AAPG Memoir, v. 65, p. 109-151.

Dominey, J.R., and Wiffe, S., 1998, Salt tectonics and sedimentation: an integrated interpretation ultra deep water area, Lower Congo Basin, offshore Angola (abs.): AAPG International Conference and Exhibition, Rio de Janeiro.

Dott Jr, R., 1963, Dynamics of subaqueous gravity depositional processes: AAPG Bulletin, v. 47, p. 104-128.

Drinkwater, N., and Pickering, K., 2001, Architectural elements in a high-continuity sand-prone turbidite system, late Precambrian Kongsfjord Formation, northern Norway: Application to hydrocarbon reservoir characterization: AAPG Bulletin, v. 85, p. 1731-1757.

Driscoll, N.W., Weissel, J.K., and Goff, J.A., 2000, Potential for large-scale submarine slope failure and tsunami generation along the US mid-Atlantic coast: Geology, v. 28, p. 407-410.

Droz, L., Rigaut, F., Cochonat, P., and Tofani, R., 1996, Morphology and recent evolution of the Zaire turbidite system (Gulf of Guinea): Geological Society of America Bulletin, v. 108, p. 253-269.

Dugan, B., and Flemings, P.B., 2000, Overpressure and fluid flow in the New Jersey continental slope: Implications for slope failure and cold seeps: Science, v. 289, p. 288-291.

Dupré, S., Bertotti, G., and Cloetingh, S., 2007, Tectonic history along the South Gabon Basin: Anomalous early post-rift subsidence: Marine and Petroleum Geology, v. 24, p. 151-172.

Duval, B., Cramez, C., and Jackson, M.P.A., 1992, Raft Tectonics in the Kwanza Basin, Angola: Marine and Petroleum Geology, v. 9, p. 389-404.

Eggenhuisen, J.T., McCaffrey, W.D., Haughton, P.D., and Butler, R.W., 2010, Small-scale spatial variability in turbidity-current flow controlled by roughness resulting from substrate erosion: field evidence for a feedback mechanism: Journal of Sedimentary Research, v. 80, p. 129-136.

Eichenseer, H.T., Walgenwitz, F.R., and Biondi, P.J., 1999, Stratigraphic control on facies and diagenesis of dolomitized oolitic siliciclastic ramp sequences (Pinda Group, Albian, offshore Angola): AAPG Bulletin, v. 83, p. 1729-1758.

Embley, R.W., 1976, New evidence for occurrence of debris flow deposits in the deep sea: Geology, v. 4, p. 371-374.

Enachescu, M.E., 1993, Amplitude interpretation of 3-D reflection data: The Leading Edge, v. 12, p. 678-685.

Ercilla, G., Alonso, B., Baraza, J., Casas, D., Chiocci, F.L., Estrada, F., Farrán, M., Gonthier, E., Pérez-Belzuz, F., Pirmez, C., Reeder, M., Torres, J., and Urgeles, R., 1998, New high-resolution acoustic data from the `braided system' of the Orinoco deep-sea fan: Marine Geology, v. 146, p. 243-250.

Farrell, S., 1984, A dislocation model applied to slump structures, Ainsa Basin, South Central Pyrenees: Journal of Structural Geology, v. 6, p. 727-736.

Ferry, J.N., Mulder, T., Parize, O., and Raillard, S., 2005a, Concept of equilibrium profile in deep-water turbidite systems; effects of local physiographic changes on the nature of sedimentary process and the geometries of deposits, *in* Hodgson, D.M., and Flint, S.S., eds., Submarine Slope Systems; Processes and Products, Geological Society Special Publications v. 244, p. 181-193.

Ferry, J.N., Parize, O., Mulder, T., and Raillard, S., 2005b, Sedimentary architecture and growth pattern of turbidite systems in distal part of a median fan; example of the Upper Miocene sedimentary sequence of the Lower Congo basin: Geodinamica Acta, v. 18, p. 145-152.

Fildani, A., and Normark, W.R., 2004, Late Quaternary evolution of channel and lobe complexes of Monterey Fan: Marine Geology, v. 206, p. 199-223.

Fisher, R.V., and Smith, G.A., 1991, Sedimentation in volcanic settings, *in*: Kokelaar, B.P., Howells, M.F., Marginal Basin Geology: Volcanic and Associated Processes in Modern and Ancient Basins: Geological Society of London Special Publication, v. 16, p. 5–27.

Fonck, J.-M., Cramez, C., and Jackson, M.P.A., 1998, Role of the subaerial volcanic rocks and major unconformities in the creation of South Atlantic margins: AAPG. International Conference Extended Abstracts Volume: Rio de Janeiro, Brazil, p. 38-39.

Fonnesu, F., 2003, 3D seismic images of a low-sinuosity slope channel and related depositional lobe (West Africa deep-offshore): Marine and Petroleum Geology, v. 20, p. 615-629.

Ford, M., Williams, E.A., Artoni, A., Vergés, J., and Hardy, S., 1997, Progressive evolution of a fault-related fold pair from growth strata geometries, Sant Llorenç de Morunys, SE Pyrenees: Journal of Structural Geology, v. 19, p. 413-441.

Frey-Martinez, J., Cartwright, J., and James, D., 2006, Frontally confined versus frontally emergent submarine landslides: a 3D seismic characterisation.: Marine and Petroleum Geology, v. 23, p. 585-604.

Frey-Martinez, J., Cartwright, J., and Hall, B., 2005, 3D seismic interpretation of slump complexes: examples from the continental margin of Israel: Basin Research, v. 17, p. 83-108.

Gamberi, F., and Rovere, M., 2011, Architecture of a modern transient slope fan (Villafranca fan, Gioia basin–Southeastern Tyrrhenian Sea): Sedimentary Geology, v. 236, p. 211-225.

Garcia, M.H., 1994, Depositional turbidity currents laden with poorly sorted sediment: Journal of hydraulic engineering, v. 120, p. 1240-1263.

Gardner, M.H., and Borer, J.M., 2000, Submarine channel architecture along a slope to basin profile, Brushy Canyon Formation, west Texas., *in* Bouma, A.H., and Stone, C.G., eds., Fine-grained turbidite systems: AAPG Memoir 72 and SEPM Special Publication, v. 68, p. 195–214.

Gardner, M.H., Borer, J.M., Melick, J.J., Mavilla, N., Dechesne, M., and Wagerle, R.N., 2003, Stratigraphic process-response model for submarine channels and related features from studies of Permian Brushy Canyon outcrops, West Texas: Marine and Petroleum Geology, v. 20, p. 757-787.

Gaullier, V., Brun, J., and Lecanu, H., 1993, Raft tectonics: the effects of residual topography below a salt decollement: Tectonophysics, v. 228, p. 363-381.

Gawthorpe, R., and Leeder, M., 2000, Tectono-sedimentary evolution of active extensional basins: Basin Research, v. 12, p. 195-218.

Gawthorpe, R.L., and Clemmey, H., 1985, Geometry of submarine slides in the Bowland Basin (Dinantian) and their relation to debris flows: Journal of Geological Society of London, v. 142, p. 555-565.

Gee, M., and Gawthorpe, R., 2006, Submarine channels controlled by salt tectonics: Examples from 3D seismic data offshore Angola: Marine and Petroleum Geology, v. 23, p. 443-458.

Gee, M., Gawthorpe, R., and Friedmann, S., 2006, Triggering and evolution of a giant submarine landslide, offshore Angola, revealed by 3D seismic stratigraphy and geomorphology: Journal of Sedimentary Research, v. 76, p. 9-19.

Gee, M., Masson, D., Watts, A., and Allen, P., 1999, The Saharan debris flow: an insight into the mechanics of long runout submarine debris flows: Sedimentology, v. 46, p. 317-335.

Gee, M.J., Masson, D.G., Watts, A.B., and Mitchell, N.C., 2001, Passage of debris flows and turbidity currents through a topographic constriction: seafloor erosion and deflection of flow pathways: Sedimentology, v. 48, p. 1389-1409.

Gee, M.J.R., Gawthorpe, R.L., Bakke, K., and Friedmann, S.J., 2007, Seismic Geomorphology and Evolution of Submarine Channels from the Angolan Continental Margin: Journal of Sedimentary Research, v. 77, p. 433-446.

Gervais, A., Savoye, B., Mulder, T., and Gonthier, E., 2006, Sandy modern turbidite lobes: A new insight from high resolution seismic data: Marine and Petroleum Geology, v. 23, p. 485-502.

Giles, K.A., and Lawton, T.F., 2002, Halokinetic sequence stratigraphy adjacent to the El Papalote diapir, northeastern Mexico: AAPG Bulletin, v. 86, p. 823-840.

Giles, K.A., and Rowan, M.G., 2012, Concepts in halokinetic-sequence deformation and stratigraphy: Geological Society, London, Special Publications, v. 363, p. 7-31.

Giles, M.R., 1997, Diagenesis: a quantitative perspective, Kluwer Academic Publishers Dordrecht.

Gorsline, D.S., and Emery, K., 1959, Turbidity-current deposits in San Pedro and Santa Monica basins off southern California: Geological Society of America Bulletin, v. 70, p. 279-290.

Gradstein, F. M., Ogg, J. G., Schmitz, M. D. and Ogg, G. M., 2012, The Geologic Time Scale, Elsevier, p. 1083 – 1127.

Green, P., Groger, H., and Machado, V., 2014, The tectonic development of the Onshore Namibe Margin of Angola: Petroleum Geoscience of the West African Margin Conference Abstract, The Geological Society, London.

Groenenberg, R.M., Hodgson, D.M., Prélat, A., Luthi, S.M., and Flint, S.S., 2010, Flow–deposit interaction in submarine lobes: insights from outcrop observations and realizations of a process-based numerical model: Journal of Sedimentary Research, v. 80, p. 252-267.

Haflidason, H., Sejrup, H.P., Nygård, A., Mienert, J., Bryn, P., Lien, R., Forsberg, C.F., Berg, K., and Masson, D., 2004, The Storegga Slide: architecture, geometry and slide development: Marine Geology, v. 213, p. 201-234.

Hampton, M.A., Lee, H.J., and Locat, J., 1996, Submarine landslides: Reviews of Geophysics, v. 34, p. 33-59.

Haner, B.E., 1971, Morphology and sediments of Redondo submarine fan, southern California: Geological Society of America Bulletin, v. 82, p. 2413-2432.

Haq, B.U., Hardenbol, J., and Vail, P.R., 1988 Mesozoic and Cenozoic chronostratigraphy and cycles of sea-level change, *in* Wilgus, C.K., Hastings, B.S., Kendall, C.G.S.C., Posamentier, H.W., Ross, C.A., and Van Wagoner, J.C., eds., Sea-level changes: An Integrated Approach, SEPM Special Publication, v. 42, p. 71-108.

Harders, R., Kutterolf, S., Hensen, C., Moerz, T., and Brueckmann, W., 2010, Tephra layers: A controlling factor on submarine translational sliding?: Geochemistry, Geophysics, Geosystems, v. 11, p. 1-18.

Hardy, S., and Finch, E., 2007, Mechanical stratigraphy and the transition from trishear to kink-band fault-propagation fold forms above blind basement thrust faults: A discrete-element study: Marine and Petroleum Geology, v. 24, p. 75-90.

Hardy, S., and Poblet, J., 1994, Geometric and numerical model of progressive limb rotation in detachment folds: Geology, v. 22, p. 371-374.

Hardy, S., and Poblet, J., 1995, The velocity description of deformation. paper 2: sediment geometries associated with fault-bend and fault-propagation folds: Marine and Petroleum Geology, v. 12, p. 165-176.

Hardy, S., Poblet, J., McClay, K., and Waltham, D., 1996, Mathematical modelling of growth strata associated with fault-related fold structures: Geological Society, London, Special Publications, v. 99, p. 265-282.

Hart, B.S., 1999, Definition of subsurface stratigraphy, structure and rock properties from 3-D seismic data: Earth-Science Reviews, v. 47, p. 189-218.

Hartman, D.A., Swanson, W.A., Smith, P.R., Goulding, F.J., and Kelly, C., 1998, Structural development of the continental margin of Congo and northern Angola (abs.): AAPG Bulletin, v. 82, p. 1923.

Haughton, P., Davis, C., McCaffrey, W., and Barker, S., 2009, Hybrid sediment gravity flow deposits – classification, origin and significance: Marine and Petroleum Geology, v. 26, p. 1900-1918.

Haughton, P.D., 2000, Evolving turbidite systems on a deforming basin floor, Tabernas, SE Spain: Sedimentology, v. 47, p. 497-518.

Haughton, P.D.W., Barker, S.P., and McCaffrey, W.D., 2003, 'Linked' debrites in sand-rich turbidite systems – origin and significance: Sedimentology, v. 50, p. 459-482.

Hay, D.C., 2012, Stratigraphic evolution of a tortuous corridor from the stepped slope of Angola, *in* Application of the principles of seismic geomorphology to continental-slope and base-of-slope systems: Case Studies from Seafloor and Near-Seafloor Analogues, SEPM Special Publication, v. 99, p. 163-180.

Heezen, B.C., and Ewing, W.M., 1952, Turbidity currents and submarine slumps, and the 1929 Grand Banks [Newfoundland] earthquake: American Journal of Science, v. 250, p. 849-873.

Heinio, P., and Davies, R., 2007, Knickpoint migration in submarine channels in response to fold growth, western Niger Delta: Marine and Petroleum Geology, v. 24, p. 434-449.

Hempton, M., Rosen, M., Coughlin, R., Scardina, A., Hagen, E., and Nordstrom, D., 1990, The geology of west Africa—a regional review: AAPG Bulletin, v. 75, p. 583.

Hesse, R., Klaucke, I., Khodabakhsh, S., Piper, D.J., and Ryan, W.B., 2001, Sandy submarine braid plains: Potential deep-water reservoirs: AAPG Bulletin, v. 85, p. 1499-1521.

Higgins, S., Clarke, B., Davies, R.J., and Cartwright, J., 2009, Internal geometry and growth history of a thrust-related anticline in a deep water fold belt: Journal of Structural Geology, v. 31, p. 1597-1611.

Hjelstuen, B.O., Eldholm, O., and Faleide, J.I., 2007, Recurrent Pleistocene mega-failures on the SW Barents Sea margin: Earth and Planetary Science Letters, v. 258, p. 605-618.

Hodgson, D.M., 2006, Stratigraphic evolution of fine-grained submarine fan systems, Tanqua depocentre, Karoo Basin, South Africa: Journal of Sedimentary Research, v. 76, p. 20-40.

Hodgson, D.M., 2009, Distribution and origin of hybrid beds in sand-rich submarine fans of the Tanqua depocentre, Karoo Basin, South Africa: Marine and Petroleum Geology, v. 26, p. 1940-1956.

Hodgson, D.M., and Haughton, P.D., 2004, Impact of syndepositional faulting on gravity current behaviour and deep-water stratigraphy: Tabernas-Sorbas Basin, SE Spain: Geological Society, London, Special Publications, v. 222, p. 135-158.

Holmes, A., 1965, Principles of Physical Geology: Nelson, London.

Hossack, J.R., 1979, The use of balanced cross-sections in the calculation of orogenic contraction: a review: Journal of the Geological Society, v. 136, p. 705.

Hossack, J.R., 1995, Geometrical rules of section balancing of salt structures, *in* Jackson, M.P.A., Roberts, D.G., and Snelson, S., eds., Salt Tectonics: A Global Perspective., AAPG Memoir, v.65 , p. 29-40.

Hovius, N., Stark, C.P., and Allen, P.A., 1997, Sediment flux from a mountain belt derived by landslide mapping: Geology, v. 25, p. 231-234.

Hudec, M., and Jackson, M., 2007, Terra infirma: Understanding salt tectonics: Earth-Science Reviews, v. 82, p. 1-28.

Hudec, M.R., and Jackson, M.P., 2004a, Regional restoration across the Kwanza Basin, Angola: Salt tectonics triggered by repeated uplift of a metastable passive margin: AAPG Bulletin, v. 88, p. 971-990.

Hudec, M.R., Jackson, M.P.A., and Schttltz-Ela, D.D., 2009, The paradox of minibasin subsidence into salt: Clues to the evolution of crustal basins: Geological Society of America Bulletin, v. 121, p. 201-221.

Huvenne, V.A., Croker, P.F., and Henriet, J.P., 2002, A refreshing 3D view of an ancient sediment collapse and slope failure: Terra Nova, v. 14, p. 33-40.

Huyghe, P., Foata, M., Deville, E., Mascle, G., and Grp, C.W., 2004, Channel profiles through the active thrust front of the southern Barbados prism: Geology, v. 32, p. 429-432.

Jacka, A., Beck, R., Germain, L.S., and Harrison, S., 1968, Permian deep-sea fans of the Delaware Mountain Group (Guadalupian), Delaware basin: SEPM Permian Basin Section Publications, v. 68, p. 49-90.

Jackson, M.P.A., and Cramez, C., 2000, Superposed deformation straddling the continental-oceanic transition in deep-water Angola: Marine and Petroleum Geology, v. 17, p. 1095-1109.

Jackson, M.P.A., Cramez, C., and Fonck, J.M., 2000, Role of subaerial volcanic rocks and mantle plumes in creation of South Atlantic margins: implications for salt tectonics and source rocks: Marine and Petroleum Geology, v. 17, p. 477-498.

Jackson, M.P.A., Cramez, C., and Mohriak, W.U., 1998, Salt tectonics provinces across the continental-oceanic boundary in the Lower Congo and Campos basins of the South Atlantic margins, *in* Mello, M.R., and Yilmaz, P.O., eds., AAPG International Conference, Extended Abstracts Volume: Rio de Janeiro, Brazil, p. 40-41.

Jackson, M.P.A., and Talbot, C.J., 1986, External shapes, strain rates, and dynamics of salt structures: Geological Society of America Bulletin, v. 97, p. 305.

Jegou, I., 2008, Channel-mouth lobe complex of the recent Amazon fan: The missing piece: Marine Geology, v. 252, p. 62-77.

Jenyon, M.K., 1984, Seismic response to collapse structures in the Southern North Sea: Marine and Petroleum Geology, v. 1, p. 27-36.

Joanne, C., Lamarche, G., and Collot, J.Y., 2013, Dynamics of giant mass transport in deep submarine environments: the Matakaoa Debris Flow, New Zealand: Basin Research, v. 25, p. 471-488.

Johnson, H.A., and Bredeson, D., 1971, Structural development of some shallow salt domes in Louisiana Miocene productive belt: AAPG Bulletin, v. 55, p. 204-226.

Johnson, S.D., Flint, S., Hinds, D., and De Ville Wickens, H., 2001, Anatomy, geometry and sequence stratigraphy of basin floor to slope turbidite systems, Tanqua Karoo, South Africa: Sedimentology, v. 48, p. 987-1023.

Jones, G., Mayall, M., and Lonergan, L., 2012, Contrasting depositional styles on a slope system and their control by salt tectonics: through-going channels, ponded fans, and mass transport complexes, *in*, Rosen, N.C. Weimer, P., dos Anjos, S.M.C., Henrickson, S., Marques, E., Mayall, M., Fillon, R, D'Agostino, T, Saller, A., Campion, K., Huang, T., Sarg, R. and Schroeder, F., eds, New Understanding of the Petroleum Systems of Continental Margins of the World, 32nd Annual GCSSEPM Foundation Bob. F. Perkins Conference, p. 503-533.

Kane, I.A., Catterall, V., McCaffrey, W.D., and Martinsen, O.J., 2010, Submarine channel response to intrabasinal tectonics: The influence of lateral tilt: AAPG Bulletin, v. 94, p. 189-219.

Kane, I.A., and Pontén, A.S.M., 2012, Submarine transitional flow deposits in the Paleogene Gulf of Mexico: Geology, v. 40, p. 1119-1122.

Karner, G.D., and Driscoll, N.W., 1999, Tectonic and stratigraphic development of the West African and eastern Brazilian Margins: insights from quantitative basin modelling: Geological Society, London, Special Publications, v. 153, p. 11-40.

Karner, G.D., Driscoll, N.W., McGinnis, J.P., Brumbaugh, W.D., and Cameron, N.R., 1997, Tectonic significance of syn-rift sediment packages across the Gabon-Cabinda continental margin: Marine and Petroleum Geology, v. 14, p. 973-1000.

Kenyon, N.H, and Millington, J., 1995, Contrasting deep-sea depositional systems in the Bering Sea: *in* Pickering, K.T., Hiscott, R.N., Kenyon, N.H., Ricci Lucchi, F., and Smith, R.D.A., eds., Atlas of Deepwater Environments; Architectural Style in Turbidite Systems: London, Chapman & Hall, p. 89–93.

Kenyon, N.H., Klaucke, I., Millington, J., and Ivanov, M.K., 2002, Sandy submarine canyon-mouth lobes on the western margin of Corsica and Sardinia, Mediterranean Sea: Marine Geology, v. 184, p. 69-84.

King, R.C., and Backé, G., 2010, A balanced 2D structural model of the Hammerhead Delta–deepwater fold-thrust belt, Bight Basin, Australia: Australian Journal of Earth Sciences, v. 57, p. 1005-1012.

Klaucke, I., and Hesse, R., 1996, Fluvial features in the deep-sea: new insights from the glacigenic submarine drainage system of the Northwest Atlantic Mid-Ocean Channel in the Labrador Sea: Sedimentary Geology, v. 106, p. 223-234.

Kligfield, R., Hunziker, J., Dallmeyer, R., and Schamel, S., 1986, Dating of deformation phases using K-Ar and $^{40}Ar/^{39}Ar$ technique: result from the Northern Apennines: Jounal of Structural Geology, v. 8, p. 781-798.

Kneller, B., and Buckee, C., 2000, The structure and fluid mechanics of turbidity currents: a review of some recent studies and their geological implications: Sedimentology, v. 47, p. 62-94.

Kneller, B., and McCaffrey, W., 1999, Depositional effects of flow nonuniformity and stratification within turbidity currents approaching a bounding slope; deflection, reflection, and facies variation: Journal of Sedimentary Research, v. 69, p. 980-991.

Kolla, V., 2007, A review of sinuous channel avulsion patterns in some major deep-sea fans and factors controlling them: Marine and Petroleum Geology, v. 24, p. 450-469.

Kolla, V., Bourges, P., Urruty, J.M., and Safa, P., 2001, Evolution of deep-water Tertiary sinuous channels offshore Angola (west Africa) and implications for reservoir architecture: AAPG Bulletin, v. 85, p. 1373-1405.

Kolla, V., and Coumes, F., 1987, Morphology, internal structure, seismic stratigraphy, and sedimentation of Indus Fan: AAPG Bulletin, v. 71, p. 650-677.

Kowsmann, R., Machado, L., Viana, A., Almeida Jr, W., and Vicalvi, M., 2002, Controls on mass-wasting in deep water of the Campos Basin, Offshore Technology Conference Abstract.

Koyi, H.A., Sans, M., Teixell, A., Cotton, J., and Zeyen, H., 2004, The significance of penetrative strain in the restoration of shortened layers: insights from sand models and the Spanish Pyrenees., *in* McClay, K.R., ed., Thrust tectonics and hydrocarbon systems: AAPG Memoir, v. 82, p. 207-222.

Kubo, Y.S., 2004, Experimental and numerical study of topographic effects on deposition from two-dimensional, particle-driven density currents: Sedimentary Geology, v. 164, p. 311-326.

Kuenen, P.H., 1952, Estimated size of the Grand Banks [Newfoundland] turbidity current: American Journal of Science, v. 250, p. 874-884.

Lourens, L., Hilgen, F., Shackleton, N.J., and Wilson, D., 2004, The Neogene Period, *in* Gradstein, F., Ogg, J.G. and Smith, A.G., Geologic Time Scale, Cambridge University Press, pp. 409-440.

Lavier, L.L., Steckler, M.S., and Brigaud, F., 2000, An improved method for reconstructing the stratigraphy and bathymetry of continental margins: Application to the Cenozoic tectonic and sedimentary history of the Congo margin: AAPG Bulletin, v. 84, p. 923-939.

Lee, C., Nott, J.A., Keller, F.B., and Parrish, A.R., 2004, Seismic expression of the Cenozoic mass transport complexes deepwater Tarfaya-Agadir Basin offshore Morocco, Offshore Technology Conference Abstracts.

Lemon, N., 1985, Physical modeling of sedimentation adjacent to diapirs and comparison with late Precambrian Oratunga breccia body in central Flinders Ranges, South Australia: AAPG Bulliten, v. 69, p. 1327-1338.

Leyden, R., 1976, South Atlantic diapiric structures: AAPG Bulletin, v. 60, p. 196.

Liner, C., Li, C.-F., Gersztenkorn, A., and Smythe, J., 2004, SPICE: A new general seismic attribute, 72nd Annual International Meeting, SEG, Expanded Abstracts, p. 433-436..

Liro, L.M., and Dawson, W.C., 2000, Reservoir systems of selected basins of the South Atlantic, *in* Mello, M.R., and Katz, B.J., eds., Petroleum Systems of south Atlantic margins: AAPG Memoir, v. 73, p. 77-92.

Liu, J., and Marfurt, K.J., 2007, Instantaneous spectral attributes to detect channels: Geophysics, v. 72, p. 23-31.

Locat, J., and Lee, H.J., 2002, Submarine landslides: advances and challenges: Canadian Geotechnical Journal, v. 39, p. 193-212.

Lohmann, H.H., 1972, Salt dissolution in subsurface of British North Sea as interpreted from seismograms: AAPG Bulletin, v. 56, p. 472-479.

Lowe, D.R., 1979, Sediment gravity flows: their classification and some problems of application to natural flows and deposits: SEPM Special Publication, v. 27, p. 27-82.

Lunde, G., Aubert, K., Lauritzen, O., and Lorange, E., 1992, Tertiary uplift of the Kwanza Basin in Angola, *in* Curneller, R. ed., Geologie Africaine-Compte Rendu des colloques de Geologie de Libreville, Bulletin Centre Recherche Exploration Production, Elf Aquitaine, v. 13, p. 6-8.

Lundin, E.R., 1992, Thin-skinned extensional tectonics on a salt detachment, northern Kwanza Basin, Angola: Marine and Petroleum Geology, v. 9, p. 405-411.

Macdonald, D., Moncrieff, A., and Butterworth, P., 1993, Giant slide deposits from a Mesozoic fore-arc basin, Alexander Island, Antarctica: Geology, v. 21, p. 1047-1050.

Macdonald, D., Gomez-Perez, I., Franzese, J., Spalletti, L., Lawver, L., Gahagan, L., Dalziel, I., Thomas, C., Trewin, N., Hole, M., and Paton, D., 2003, Mesozoic break-up of SW Gondwana: implications for regional hydrocarbon potential of the southern South Atlantic: Marine and Petroleum Geology, v. 20, p. 287-308.

Maerten, L., and Maerten, F., 2006, Chronologic modeling of faulted and fractured reservoirs using geomechanically based restoration: Technique and industry applications: AAPG Bulletin, v. 90, p. 1201-1226.

Magara, K., 1980, Comparison of porosity-depth relationships of shale and sandstone: Journal of Petroleum Geology, v. 3, p. 175-185.

Marfurt, K.J., Kirlin, R.L., Farmer, S.L., and Bahorich, M.S., 1998, 3-D seismic attributes using a semblance-based coherency algorithm: Geophysics, v. 63, p. 1150-1165.

Marr, J.G., Harff, P.A., Shanmugam, G., and Parker, G., 2001, Experiments on subaqueous sandy gravity flows: the role of clay and water content in flow dynamics and depositional structures: Geological Society of America Bulletin, v. 113, p. 1377-1386.

Martinsen, O., 1989, Styles of soft-sediment deformation on a Namurian (Carboniferous) delta slope, Western Irish Namurian Basin, Ireland: Geological Society, London, Special Publications, v. 41, p. 167-177.

Martinsen, O., 1994, Mass movements, *in* Maltman, A., ed., The Geological Deformation of Sediments, Springer Netherlands, p. 127-165.

Martinsen, O.J., and Bakken, B., 1990, Extensional and compressional zones in slumps and slides in the Namurian of County Clare, Ireland: Journal of the Geological Society, v. 147, p. 153-164.

Martinsen, O.J., Lien, T., Walker, R.G., and Collinson, J.D., 2003, Facies and sequential organisation of a mudstone-dominated slope and basin floor succession: the Gull Island Formation, Shannon Basin, Western Ireland: Marine and Petroleum Geology, v. 20, p. 789-807.

Marton, L.G., Tari, G.C., and Lehmann, C.T., 2000, Evolution of the Angolan passive margin, West Africa, with emphasis on post-salt structural styles, *in* Moriak W., Talwani M., eds., Atlantic Rifts and Continental Margins, American Geophysical Union, Washington, DC, p. 129–149.

Masaferro, J.L., Poblet, J., Bulnes, M., Eberli, G.P., Dixon, T.H., and McClay, K., 1999, Palaeogene-Neogene/present day(?) growth folding in the Bahamian foreland of the Cuban fold and thrust belt: Journal of the Geological Society, v. 156, p. 617-631.

Maslin, M., Owen, M., Day, S., and Long, D., 2004, Linking continental-slope failures and climate change: Testing the clathrate gun hypothesis: Geology, v. 32, p. 53-56.

Masson, D., Canals, M., Alonso, B., Urgeles, R., and Huhnerbach, V., 1998, The Canary debris flow: source area morphology and failure mechanisms: Sedimentology, v. 45, p. 411-432.

Masson, D., Harbitz, C., Wynn, R., Pedersen, G., and Løvholt, F., 2006, Submarine landslides: processes, triggers and hazard prediction: Philosophical Transactions of the Royal Society A, v. 364, p. 2009-2039.

Masson, D., Huggett, Q., and Brunsden, D., 1993, The surface texture of the Saharan Debris Flow deposit and some speculations on submarine debris flow processes: Sedimentology, v. 40, p. 583-598.

Masson, D., Van Niel, B., and Weaver, P., 1997, Flow processes and sediment deformation in the Canary debris flow on the NW African continental rise: Sedimentary Geology, v. 110, p. 163-179.

Masson, D., Wynn, R., and Talling, P., 2010, Large landslides on passive continental margins: processes, hypotheses and outstanding questions: Submarine Mass Movements and Their Consequences, Springer, p. 153-165.

Mayall, M., Jones, E., and Casey, M., 2006, Turbidite channel reservoirs—Key elements in facies prediction and effective development: Marine and Petroleum Geology, v. 23, p. 821-841.

Mayall, M., Lonergan, L., Bowman, A., James, S., Mills, K., Primmer, T., Pope, D., Rogers, L., and Skeene, R., 2010, The response of turbidite slope channels to growth-induced seabed topography: AAPG Bulletin, v. 94, p. 1011-1030.

Mayall, M., and O'Byrne, C., 2002, Reservoir prediction and development challenges in turbidite slope channels, Offshore Technology Conference.

Mayall, M., and Stewart, I., 2000, The architecture of turbidite slope channels, *in*, Weimer, P., Slatt, R. M., Coleman, J., Rosen, N. C., Nelson, H., Bouma, A. H., Styzen, M. J. & Lawrence, D. T., eds., Deep-Water Reservoirs of the World: GCSSEPM Foundation 20th Annual Research Conference, p. 578-586.

McArdle, N., and Ackers, M., 2012, Understanding seismic thin-bed responses using frequency decomposition and RGB blending: First Break, v. 30, p. 57-65.

McGilvery, T.A., and Cook, D.L., 2003, The influence of local gradients on accommodation space and linked depositional elements across a stepped slope profile, offshore Brunei, *in,* Roberts, H.H., Rosen, N.C., Fillon, R.H. and Anderson, J.B., eds., Shelf Margin Deltas and Linked Down Slope Petroleum Systems: Global Significance and Future Exploration Potential: GCSSEPM 23rd Annual Research Conference, p. 387–419.

Menard, H., 1960, Possible pre-Pleistocene deep-sea fans off central California: Geological Society of America Bulletin, v. 71, p. 1271-1278.

Middleton, G.V., 1967, Experiments on density and turbidity currents: III. Deposition of sediment: Canadian Journal of Earth Sciences, v. 4, p. 475-505.

Middleton, G.V., 1993, Sediment deposition from turbidity currents: Annual Review of Earth and Planetary Sciences, v. 21, p. 89-114.

Mitra, G., 1994, Strain variation in thrust sheets across the Sevier fold-and-thrust belt (Idaho-Utah-Wyoming): Implications for section restoration and wedge taper evolution: Journal of Structural Geology, v. 16, p. 585-602.

Mohrig, D., Ellis, C., Parker, G., Whipple, K.X., and Hondzo, M., 1998, Hydroplaning of subaqueous debris flows: Geological Society of America Bulletin, v. 110, p. 387-394.

Moore, G.T., 1988, Atlantic Marginal Basins of Africa: AAPG Bulletin, v. 72, p. 224-225.

Moore, J.C., Moore, G.F., Cochrane, G.R., and Tobin, H.J., 1995, Negative-polarity seismic reflections along faults of the Oregon accretionary prism: Indicators of overpressuring: Journal of Geophysical Research, v. 100, p. 12895-12906.

Moretti, I., and Callot, J.P., 2012, Area, length and thickness conservation: Dogma or reality?: Journal of Structural Geology, v. 41, p. 64-75.

Moretti, I., Lepage, F., and Guiton, M., 2006, KINE3D: a new 3D restoration method based on a mixed approach linking geometry and geomechanics: Oil & Gas Science and Technology, v. 61, p. 277-289.

Morgan, R., 2004, Structural controls on the positioning of submarine channels on the lower slopes of the Niger Delta: Geological Society, London, Memoirs, v. 29, p. 45-52.

Moscardelli, L., and Wood, L., 2008, New classification system for mass transport complexes in offshore Trinidad: Basin Research, v. 20, p. 73-98.

Moscardelli, L., Wood, L., and Mann, P., 2006, Mass-transport complexes and associated processes in the offshore area of Trinidad and Venezuela: AAPG Bulletin, v. 90, p. 1059-1088.

Mosher, D.C., Moscardelli, L., Shipp, R.C., Chaytor, J.D., Baxter, C.D., Lee, H.J., and Urgeles, R., 2010, Submarine Mass Movements and their Consequences, Springer.

Muck, M.T., and Underwood, M.B., 1990, Upslope flow of turbidity currents: a comparison among field observations, theory, and laboratory models: Geology, v. 18, p. 54-57.

Mulder, T., and Cochonat, P., 1996, Classification of offshore mass movements: Journal of Sedimentary Research, v. 66, p. 43-57.

Mutti, E., and Normark, W.R., 1987, Comparing examples of modern and ancient turbidite systems: problems and concepts, Marine clastic sedimentology, Springer, p. 1-38.

Mutti, E., and Normark, W.R., 1991, An integrated approach to the study of turbidite systems, *in* Weimer, P., and Link, M.H., eds., Seismic facies and sedimentary processes of submarine fans and turbidite systems, New York, Springer-Verlag, p. 75-106.

Mutti, E., and Ricci Lucchi, F., 1972, Le torbiditi dell'Appennino settentrionale: introduzione all'analisi di facies: Memorie Societa Geologica Italiana, v. 11, p. 161-199.

Nardin, T.R., Hein, F.J., Gorsline, D.S., Edwards, B.D., 1979, A review of mass movement processes, sediment and acoustic characteristics, and contrasts in slope and base-of-slope systems versus canyon-fan-basin floor systems. *in*: Doyle L.J., Pilkey O.H. eds Geology of Continental Slopes, SEPM Special Publication, v. 27, p. 61–73.

Navarre, J.C., 2002, Deepwater turbidite system analysis, West Africa: Sedimentary model and implications for reservoir model construction: The Leading Edge, v. 21, p. 1132.

Nelson, C.H., 1992, Upper Pleistocene turbidite sand beds and chaotic silt beds in the channelized, distal, outer-fan lobes of the Mississippi fan: Geology, v. 20, p. 693-696.

Nemec, W., 1990, Aspects of sediment movement on steep delta slopes: Coarse-Grained Deltas, Blackwell Publishing Ltd., p. 29-73.

Nemec, W., 2009, Aspects of Sediment Movement on Steep Delta Slopes, Coarse-Grained Deltas, Blackwell Publishing Ltd., p. 29-73.

Newton, C., Shipp, R., Mosher, D., and Wach, G., 2004, Importance of mass transport complexes in the Quaternary development of the Nile fan Egypt, Offshore Technology Conference.

Nissen, S.E., Haskell, N.L., Steiner, C.T., and Coterill, K.L., 1999, Debris flow outrunner blocks, glide tracks, and pressure ridges identified on the Nigerian continental slope using 3-D seismic coherency: The Leading Edge, v. 18, p. 595-599.

Norem, H., Locat, J., and Schieldrop, B., 1990, An approach to the physics and the modeling of submarine flowslides: Marine Georesources and Geotechnology, v. 9, p. 93-111.

Normark, W.R., 1970, Growth patterns of deep-sea fans: AAPG Bulletin, v. 54, p. 2170-2195.

Normark, W.R., and Piper, D.J.W., 1991, Initiation processes and flow evolution of turbidity currents: implications for the depositional record, *in* Osborne, R.H., ed., From Shoreline to Abyss, SEPM Special Publication, v. 46, p. 207-230.

Nunns, A.G., 1991, Structural restoration of seismic and geologic sections in extensional regimes (1): AAPG Bulletin, v. 75, p. 278-297.

Ori, G., and Friend, P., 1984, Sedimentary basins formed and carried piggyback on active thrust sheets: Geology, v. 12, p. 475-478.

Owen, M., Day, S., and Maslin, M., 2007, Late Pleistocene submarine mass movements: occurrence and causes: Quaternary Science Reviews, v. 26, p. 958-978.

Parsons, J.D., Schweller, W.J., Stelting, C.W., Southard, J.B., Lyons, W.J., and Grotzinger, J.P., 2002, A preliminary experimental study of turbidite fan deposits: Journal of Sedimentary Research, v. 72, p. 619-628.

Paul, J.D., Roberts, G.G., and White, N., 2014, The African landscape through space and time: Tectonics, v. 32, p. 1-38

Peyton, L., Bottjer, R., and Partyka, G., 1998, Interpretation of incised valleys using new 3-D seismic techniques: A case history using spectral decomposition and coherency: The Leading Edge, v. 17, p. 1294-1298.

Pfiffner, O., and Ramsay, J., 1982, Constraints on geological strain rates: arguments from finite strain states of naturally deformed rocks: Journal of Geophysical Research, v. 87, p. 311-321.

Pickering, K.T., and Corregidor, J., 2005, Mass-transport complexes (MTCs) and tectonic control on basin-floor submarine fans, middle Eocene, south Spanish Pyrenees: Journal of Sedimentary Research, v. 75, p. 761-783.

Piper, D.J.W., and Aksu, A.E., 1987, The source and origin of the 1929 Grand Banks turbidity-current inferred from sediment budgets: Geo-Marine Letters, v. 7, p. 177-182.

Piper, D., Pirmez, C., Manley, P., Long, D., Flood, R., Normark, W., and Showers, W., 1997, Mass-transport deposits of the Amazon Fan, Proceedings of the Ocean Drilling Program. Scientific Results, v. 155, p. 109-146.

Piper, D., Hiscott, R. and Normark, W. 1999, Outcrop-scale acoustic facies analysis and latest Quaternary development of Hueneme and Dume submarine fans, offshore California: Sedimentology, v. 46, p. 47-78.

Piper, D.J.W., and Normark, W.R., 2009, Processes that nitiate turbidity currents and their influence on turbidites: a marine geology perspective: Journal of Sedimentary Research, v. 79, p. 347-362.

Pirmez, C., and Flood, R.D., 1995, Morphology and structure of Amazon Channel: Proceedings of the Ocean Drilling Program. Scientific Results, v. 155, p. 23.

Pirmez, C., Hiscott, R.N., and Kronen Jr., J.D., 1997, Sandy turbidite succession at the base of the channel-levee systems of the Amazon Fan revealed by FMS and cores: unraveling the facies architecture of

large submarine fans.: Proceedings of the Ocean Drilling Program, Scientific Results, v. 155, p. 1-33.

Poblet, J., Bulnes, M., McClay, K., and Hardy, S., 2004, Plots of crestal structural relief and fold area versus shortening: a graphical technique to unravel the kinematics of thrust-related folds, *in* McClay, K., ed., Thrust Tectonics and Hydrocarbon Systems, AAPG Memoir, v. 82, p. 372-399.

Poblet, J., and Hardy, S., 1995, Reverse modelling of detachment folds; application to the Pico del Aguila anticline in the South Central Pyrenees (Spain): Journal of Structural Geology, v. 17, p. 1707-1724.

Poblet, J., McClay, K., Storti, F., and Muñoz, J.A., 1997, Geometries of syntectonic sediments associated with single-layer detachment folds: Journal of Structural Geology, v. 19, p. 369-381.

Porter, M., Sprague, A., Sullivan, M., Jennette, D., Beaubouef, R., Garfield, T., Rossen, C., Sickafoose, D., Jensen, G., and Friedmann, S., 2006, Stratigraphic organization and predictability of mixed coarse- and fine-grained lithofacies successions in a Lower Miocene deep-water slope-channel system, Angola Block15, *in* Harris, P. M. and Weber, L. J., eds., Giant Hydrocarbon Reservoirs of the World: From Rocks to Reservoir Characterization and Modeling: AAPG Memoir 88/SEPM Special Publication, p. 281-305.

Posamentier, H., Jervey, M., and Vail, P., 1988, Eustatic controls on clastic deposition I—conceptual framework: Sea-Level Changes: An Integrated Approach: SEPM Special Publication, v. 42, p. 109-124.

Posamentier, H., and Vail, P., 1988, Eustatic controls on clastic deposition II—sequence and systems tract models: Sea-level changes: An integrated approach: SEPM Special Publication, v. 42, p. 125-154.

Posamentier, H.W., and Kolla, V., 2003, Seismic geomorphology and stratigraphy of depositional elements in deep-water settings: Journal of Sedimentary Research, v. 73, p. 367-388.

Posamentier, H.W., and Martinsen, O.J., 2011, The character and genesis of submarine mass-transport deposits: insight from outcrop and 3D seismic data, *in*: Shipp, R.C., Weimer, P., Posamentier, H., eds, Mass Transport Deposits in Deepwater Settings, SEPM Special Publication, v. 96, p. 7–38.

Posamentier, H.W., and Walker, R.G., 2006, Deep-water turbidites and submarine fans: SEPM Special Publication, v. 84, p. 339-520.

Posamentier, H.W., Wisman, P.S., and Plawman, T., 2000, Deep water depositional systems - ultra deep Makassar Strait, Indonesia, *in*, Weimer, P., Slatt, R. M., Coleman, J., Rosen, N. C., Nelson, H., Bouma, A. H., Styzen, M. J. & Lawrence, D. T., eds., Deep-Water Reservoirs of the World: GCSSEPM Foundation 20th Annual Research Conference, pp. 806–816.

Prather, B.E., 2003, Controls on reservoir distribution, architecture and stratigraphic trapping in slope settings: Marine and Petroleum Geology, v. 20, p. 529-545.

Prather, B.E., Booth, J.R., Steffens, G.S., and Craig, P.A., 1998, Classification, lithologic calibration, and stratigraphic succession of seismic facies of intraslope basins, deep-water Gulf of Mexico: AAPG Bulletin, v. 82, p. 701-728.

Prather, B.E., Pirmez, C., Sylvester, Z., and Prather, D., 2012, Stratigraphic response to evolving geomorphology in a submarine apron perched on the Upper Niger Delta slope, *in* Prather, B.E., Deptuck, M.E., Mohrig, D., Van Hoorn, B., and Wynn, R.B., eds., Application of the Principles of Seismic Geomorphology to Continental Slope and Base-of-slope Systems: Case Studies from Seafloor and Near-seafloor Analogues, SEPM Special Publication, v. 99, p. 145-161.

Prelat, A., Covault, J.A., Hodgson, D.M., Fildani, A., and Flint, S.S., 2010, Intrinsic controls on the range of volumes, morphologies, and dimensions of submarine lobes: Sedimentary Geology, v. 232, p. 66-76.

Prelat, A., Hodgson, D.M., and Flint, S.S., 2009, Evolution, architecture and hierarchy of distributary deep-water deposits: a high-resolution outcrop investigation from the Permian Karoo Basin, South Africa: Sedimentology, v. 56, p. 2132-2154.

Price, N.J., and Cosgrove, J.W., 1990, Analysis of geological structures, Cambridge University Press.

Prior, D.B., Bornhold, B.D., and Johns, M., 1984, Depositional characteristics of a submarine debris flow: The Journal of Geology, v. 92, p. 707-727.

Prior, D.B., and Coleman, J.M., 1982, Active slides and flows in underconsolidated marine sediments on the slopes of the Mississippi delta, *in,* Saxov, S. and Nieuwenhuis, J.K., eds, Marine Slides and Other Mass Movements, v. 6, p. 21-49.

Quirk, D.G., Schødt, N., Lassen, B., Ings, S.J., Hsu, D., Hirsch, K.K., and Von Nicolai, C., 2012, Salt tectonics on passive margins: examples from Santos, Campos and Kwanza basins: Geological Society, London, Special Publications, v. 363, p. 207-244.

Ramsay, J.G., and Huber, M., 1983, The Techniques of Modern Structural Geology.: Strain Analysis, v. 1, London: Academic Press.

Ramsay, J.G., and Huber, M.I., 1987, The Techniques of Modern Structural Geology, Academic Press Limited, 700 p.

Reading, H.G., and Richards, M., 1994a, Turbidite systems in deep-water basin margins classified by grain-size and feeder system: AAPG Bulletin, v. 78, p. 792-822.

Reading, H.G., and Richards, M., 1994b, Turbidite systems in deep-water basin margins classified by grain size and feeder system: AAPG Bulletin, v. 78, p. 792-822.

Remacha, E., 2003, High-resolution correlation patterns in the turbidite systems of the Hecho Group (South-Central Pyrenees, Spain): Marine and Petroleum Geology, v. 20, p. 711-726.

Reyre, D., 1984, Petroleum characteristics and geological evolution of a passive margin: Example of the lower Congo–Gabon Basin: Bulletin du Centre Recherche Exploration Production ELF Aquitaine, v. 8, p. 303-332.

Richards, M., and Bowman, M., 1998, Submarine fans and related depositional systems II: variability in reservoir architecture and wireline log character: Marine and Petroleum Geology, v. 15, p. 821-839.

Richards, M., Bowman, M., and Reading, H., 1998, Submarine-fan systems I: characterization and stratigraphic prediction: Marine and Petroleum Geology, v. 15, p. 689-717.

Richardson, S.E., Davies, R.J., Allen, M.B., and Grant, S.F., 2011, Structure and evolution of mass transport deposits in the South Caspian Basin, Azerbaijan: Basin Research, v. 23, p. 702-719.

Roberts, D.G., 1975, Evaporite deposition in the Aptian south Atlantic Ocean: Marine Geology, v. 18, p. 65-72

Roberts, G.G., and White, N., 2010, Estimating uplift rate histories from river profiles using African examples: Journal of Geophysical Research, v. 115, p. 1-24.

Rottman, J.W., Simpson, J.E., Hunt, J., and Britter, R., 1985, Unsteady gravity current flows over obstacles: some observations and analysis related to the Phase II trials: Journal of Hazardous Materials, v. 11, p. 325-340.

Roure, F., Swennen, R., Schneider, F., Faure, J., Ferket, H., Guilhaumou, N., Osadetz, K., Robion, P., and Vandeginste, V., 2005, Incidence and importance of tectonics and natural fluid migration on reservoir evolution in foreland fold-and-thrust belts: Oil & Gas Science and Technology, v. 60, p. 67-106.

Rowan, M.G., 1993a, Structural geometry of the Wildhorn Nappe between the Aar Massif and the Brienzer See: Eclogae Geologicae Helvetiae, v. 86, p. 87-119.

Rowan, M.G., 1993b, A systematic technique for the sequential restoration of salt structures: Tectonophysics, v. 228, p. 331.

Rowan, M.G., 1996, Benefits and limitations of section restoration in areas of extensional salt tectonics: an example from offshore Louisiana: Geological Society, London, Special Publications, v. 99, p. 147-161.

Rowan, M.G., 2002, Salt-related accommodation in the Gulf of Mexico deepwater: Withdrawal or inflation, autochthonous or allochthonous?: Gulf Coast Association of Geological Societies Transactions, v. 52, p. 861–869.

Rowan, M.G., 2006, Getting started in Salt Tectonics: A Compendium of Influential Papers, AAPG.

Rowan, M.G., and Klingfield, R., 1989, Cross section restoration and balancing as aid to seismic interpretation in extensional terranes: AAPG Bulletin, v. 73, p. 955.

Rowan, M.G., Lawton, T.F., Giles, K.A., and Ratliff, R.A., 2003, Near-salt deformation in La Popa basin, Mexico, and the northern Gulf of Mexico: A general model for passive diapirism: AAPG Bulletin, v. 87, p. 733-756.

Rowan, M.G., Peel, F.J., and Vendeville, B.C., 2004, Gravity-driven fold belts on passive margins, *in*,: McClay, K.R., ed, Thrust Tectonics and Hydrocarbon Systems, AAPG Memoir, v. 82, p. 157–182.

Rowan, M.G., and Ratliff, R.A., 2012, Cross-section restoration of salt-related deformation: Best practices and potential pitfalls: Journal of Structural Geology, v. 41, p. 24-37.

Rowan, M.G., and Vendeville, B., 2006, Foldbelts with early salt withdrawal and diapirism: Physical model and examples from the northern Gulf of Mexico and the Flinders Ranges, Australia: Marine and Petroleum Geology, v. 23, p. 871-891.

Rowan, M.G., and Weimer, P., 1998, Salt-sediment interaction, northern Green Canyon and Ewing Bank (offshore Louisiana), northern Gulf of Mexico: AAPG Bulletin, v. 82, p. 1055-1082.

Sahagian, D., 1988, Epeirogenic motions of Africa as inferred from Cretaceous shoreline deposits: Tectonics, v. 7, p. 125-138.

Saller, A.H., Noah, J.T., Ruzuar, A.P., and Schneider, R., 2004, Linked lowstand delta to basin floor fan deposition, offshore Indonesia: An analog for deep-water reservoir systems: AAPG Bulletin, v. 88, p. 21-46.

Saller, A.H, 2008, Characteristics of Pleistocene deep-water fan lobes and their application to an upper Miocene reservoir model, offshore East Kalimantan, Indonesia: AAPG Bulletin, v. 92, p. 919-949.

Samuel, A., Kneller, B., Raslan, S., Sharp, A., and Parsons, C., 2003, Prolific deep-marine slope channels of the Nile Delta, Egypt: AAPG Bulletin, v. 87, p. 541-560.

Sarg, J., and Skjold, L., 1982, Stratigraphic traps in Paleocene sands in the Balder area, North Sea: The deliberate search for the subtle trap: AAPG Memoir, v. 32, p. 197-206.

Satterfield, W.M., and Behrens, E.W., 1990, A Late Quaternary canyon channel system, northwest Gulf of Mexico continental-slope: Marine Geology, v. 92, p. 51-67.

Sawyer, D.E., Flemings, P.B., Shipp, R.C., and Winker, C.D., 2007, Seismic geomorphology, lithology, and evolution of the late Pleistocene Mars-Ursa turbidite region, Mississippi Canyon area, northern Gulf of Mexico: AAPG Bulletin, v. 91, p. 215-234.

Scheidegger, A.E., and Potter, P.E., 1971, Downcurrent decline of grain size and thickness of single turbidite beds: A semi-quantative analysis: Sedimentology, v. 17, p. 41-49.

Schlische, R.W., 1992, Structural and stratigraphic development of the Newark extensional basin, eastern North America: Evidence for the growth of the basin and its bounding structures: Geological Society of America Bulletin, v. 104, p. 1246-1263.

Schlische, R.W., 1995, Geometry and origin of fault-related folds in extensional settings: AAPG Bulletin, v. 79, p. 1661-1678.

Schneider, C.L., Hummon, C., Yeats, R.S., and Huftile, G.L., 1996, Structural evolution of the northern Los Angeles basin, California, based on growth strata: Tectonics, v. 15, p. 341-355.

Schultz-Ela, D.D., 2003, Origin of drag folds bordering salt diapirs: AAPG Bulletin, v. 87, p. 757-780.

Schultz-Ela, D.D., Jackson, M.P., and Vendeville, B.C., 1993, Mechanics of active salt diapirism: Tectonophysics, v. 228, p. 275-312.

Schultz Ela, D.D., 1992, Restoration of cross-sections to constrain deformation processes of extensional terranes: Marine and Petroleum Geology, v. 9, p. 372.

Schumm, S.A., Mosley, M.P., and Weaver, W., 1987, Experimental Fluvial Geomorphology, Wiley, New York.

Sclater, J.G., and Christie, P.A.F., 1980, Continental stretching: an explanation of the post-mid-Cretaceous subsidence of the central North Sea basin: Journal of Geophysical Research, v. 85, p. 3711.

Scotese, C.R., 2008, The PALEOMAP Project PaleoAtlas for ArcGIS, PALEOMAP Project, Arlington, Texas, v. 2.

Seni, S.J., and Jackson, M.P., 1984, Sedimentary record of Cretaceous and Tertiary salt movement, East Texas Basin: Times, rates, and volumes of salt flow and their implications for nuclear waste isolation and petroleum exploration, Report of Investigation No. 139, Bureau of Economic Geology, University of Texas at Austin.

Seranne, M., and Anka, Z., 2005, South Atlantic continental margins of Africa: A comparison of the tectonic vs climate interplay on the evolution of equatorial west Africa and SW Africa margins: Journal of African Earth Sciences, v. 43, p. 283-300.

Shanmugam, G., 1996, High-density turbidity currents: Are they sandy debris flows?: PERSPECTIVES: Journal of Sedimentary Research, v. 66, p. 2-10.

Shanmugam, G., 2000, 50 years of the turbidite paradigm (1950s—1990s): deep-water processes and facies models—a critical perspective: Marine and Petroleum Geology, v. 17, p. 285-342.

Shanmugam, G., 2002, Ten turbidite myths: Earth-Science Reviews, v. 58, p. 311-341.

Shaw, J.H., Connors, C.D., and Suppe, J., 2005, Seismic interpretation of contractional fault-related folds: An AAPG seismic atlas, AAPG Studies in Geology.

Shaw, J.H., Novoa, E., and Connors, C.D., 2004, Structural controls on growth stratigraphy in contractional fault-related folds, *in,* McClay, K.R. ed., Thrust Tectonics and Hydrocarbon Systems, AAPG Memoir, v. 82, p. 400–412.

Shepard, F.P., 1955, Delta-front valleys bordering the Mississippi distributaries: Geological Society of America Bulletin, v. 66, p. 1489-1498.

Shepard, F.P., 1965, Types of Submarine Valleys: Geological notes: AAPG Bulletin, v. 49, p. 304-310.

Shipp, R.C., Nott, J.A., and Newlin, J.A., 2004, Physical characteristics and impact of mass transport complexes on deepwater jetted conductors and suction anchor piles, Offshore Technology Conference.

Sinclair, H., and Tomasso, M., 2002, Depositional evolution of confined turbidite basins: Journal of Sedimentary Research, v. 72, p. 451-456.

Smart, K.J., Ferrill, D.A., Morris, A.P., Bichon, B.J., Riha, D.S., and Huyse, L., 2010, Geomechanical modeling of an extensional fault-propagation fold: Big Brushy Canyon monocline, Sierra Del Carmen, Texas: AAPG Bulletin, v. 94, p. 221-240.

Smith, R., 2004, Turbidite systems influenced by structurally induced topography in the multi-sourced Welsh Basin: Geological Society, London, Special Publications, v. 222, p. 209-228.

Sohn, Y.K., 2000, Depositional processes of submarine debris flows in the Miocene fan deltas, Pohang Basin, SE Korea with special reference to flow transformation: Journal of Sedimentary Research, v. 70, p. 491-503.

Solheim, A., Berg, K., Forsberg, C., and Bryn, P., 2005a, The Storegga Slide complex: repetitive large scale sliding with similar cause and development: Marine and Petroleum Geology, v. 22, p. 97-107.

Solheim, A., Bryn, P., Sejrup, H., Mienert, J., and Berg, K., 2005b, Ormen Lange—an integrated study for the safe development of a deep-water gas field within the Storegga Slide Complex, NE Atlantic continental margin; executive summary: Marine and Petroleum Geology, v. 22, p. 1-9.

Spathopoulos, F., 1996, An insight on salt tectonics in the Angola Basin, South Atlantic: Geological Society, London, Special Publications, v. 100, p. 153-174.

Sprague, A., Garfield, T., Goulding, F., Beaubouef, R., Sullivan, M., Rossen, C., Campion, K., Sickafoose, D., Abreu, V., Schellpeper, M., Jensen, G.N., Jennette, D.C., Pirmez, C., Dixon, B.T., Ying, D., Ardill, J., Mohrig, D.C., Porter, M.L., Farrell, M.E., Mellere, D. 2005, Integrated slope channel depositional models: the key to successful prediction of reservoir presence and quality in offshore West Africa: CIPM, cuarto E-Exitep, Veracruz, Mexico, p. 1-13.

Steffens, G.S., Biegert, E.K., Scott Sumner, H., and Bird, D., 2003, Quantitative bathymetric analyses of selected deepwater siliciclastic margins: receiving basin configurations for deepwater fan systems: Marine and Petroleum Geology, v. 20, p. 547-561.

Steiner, R.J., 1976, Grand Isle Block 16 field, offshore Louisiana: AAPGeology Memoir, v. 24, p. 229-238.

Storti, F., and Poblet, J., 1997, Growth stratal architectures associated to decollement folds and fault-propagation folds. Inferences on fold kinematics: Tectonophysics, v. 282, p. 353-373.

Stouthamer, E., and Berendsen, H.J., 2007, Avulsion: the relative roles of autogenic and allogenic processes: Sedimentary Geology, v. 198, p. 309-325.

Sullivan, M., Jensen, G., Goulding, F., Jennette, D., Foreman, L., and Stern, D., 2000, Architectural analysis of deep-water outcrops: Implications for exploration and development of the Diana sub-basin, western Gulf of Mexico, *in*, Weimer, P., Slatt, R. M., Coleman, J., Rosen, N. C., Nelson, H., Bouma, A. H., Styzen, M. J. & Lawrence, D. T., eds., Deep-Water Reservoirs of the World: GCSSEPM Foundation 20th Annual Research Conference, p. 928-939.

Sullivan, M.D., Foreman, J.L., Jennette, D.C., Stern, D., Jensen, G.N., and Goulding, F.J., 2004, An integrated approach to characterization and modeling deep-water reservoirs, Diana Field, Western Gulf of Mexico, an integration of outcrop and modern analogs in reservoirs modeling. AAPG Memoir, v. 80, p. 215–234.

Sultan, N., Cattaneo, A., Sibuet, J.-C., and Schneider, J.-L., 2009, Deep sea in situ excess pore pressure and sediment deformation off NW Sumatra and its relation with the December 26, 2004 Great Sumatra-Andaman earthquake: International Journal of Earth Sciences, v. 98, p. 823-837.

Suppe, J., 1983, Geometry and kinematics of fault-bend folding: American Journal of Science, v. 283, p. 684-721.

Suppe, J., Chou, G.T., and Hook, S.C., 1992, Rates of folding and faulting determined from growth strata, Thrust Tectonics, Springer, p. 105-121.

Talling, P., Wynn, R., Masson, D., Frenz, M., Cronin, B., Schiebel, R., Akhmetzhanov, A., Dallmeier-Tiessen, S., Benetti, S., and Weaver, P., 2007, Onset of submarine debris flow deposition far from original giant landslide: Nature, v. 450, p. 541-544.

Talling, P.J., 2012, Subaqueous sediment density flows: Depositional processes and deposit types: Sedimentology, v. 59, p. 1937.

Talling, P.J., 2013, Hybrid submarine flows comprising turbidity current and cohesive debris flow: Deposits, theoretical and experimental analyses, and generalized models: Geosphere, v. 9, p. 460-488.

Taner, M.T., Schuelke, J.S., O'Doherty, R., and Baysal, E., 1994, Seismic attributes revisited, SEG 64th Annual International Meeting, Expanded Abstracts, p. 1104–1106.

Twichell, D.C., Schwab, W.C., Nelson, C.H., Kenyon, N.H., and Lee, H.J., 1992, Characteristics of a sandy depositional lobe on the outer Mississippi fan from SeaMARC IA sidescan sonar images: Geology, v. 20, p. 689-692.

Uchupi, E., 1992, Angola Basin: geohistory and construction of the Continental Rise, *in* Poag, C., and De Graciansky, P.C., eds., Geologic Evolution of Atlantic Continental Rifts, New York: Van Nostrand Reinhold., p. 77-99.

Vail, P.R., Mitchum, R.M., and Thompson, S.I., 1977, Seismic stratigraphy and global changes of sea-level, part 4: global cycles of relative changes of sea-level, *in* Payton, C.E., ed., Seismic Stratigraphy - Applications to Hydrocarbon Exploration, Ammerican Association of Petroleum Geology Memoirs, v. 26, p. 83-97.

Valle, P.J., Gjelberg, J.G., and Helland-Hansen, W., 2001, Tectonostratigraphic development in the eastern Lower Congo Basin, offshore Angola, West Africa: Marine and Petroleum Geology, v. 18, p. 909-927.

Varnes, D.J., 1978, Slope movements, type and processes. *in,* Schuster, R.L., Krizek, R.J., eds, Landslide Analysis and Control, Transportation Research Board, National Academy Sciences, Washington, DC, Special report 176. p. 11–33.

Voight, B., 1978, Rockslides and Avalanches, 1: Natural Phenomena, Elsevier, p. 833.

Volpi, V., Camerlenghi, A., Hillenbrand, C.D., Rebesco, M., and Ivaldi, R., 2003, Effects of biogenic silica on sediment compaction and slope stability on the Pacific margin of the Antarctic Peninsula: Basin Research, v. 15, p. 339-363.

Wach, G.D., Bouma, A.H., Lukas, T., Wickens, H.D., and Goldhammer, R., 2003, Transition from shelf margin delta to slope fan—Outcrop examples from the Tanqua Karoo, South Africa, Shelf margin deltas and linked down slope petroleum systems, *in,* Roberts, H.H., Rosen, N.C., Fillon, R.H. and Anderson, J.B., eds., Shelf Margin Deltas and Linked Down Slope Petroleum Systems: Global Significance and Future Exploration Potential: GCSSEPM 23rd Annual Research Conference, p. 849-861.

Walgenwitz, F., Pagel, M., Meyer, A., Maluski, H., and Monie, P., 1990, Thermo-chronological approach to reservoir diagenesis in the offshore Angola Basin: a fluid inclusion,Ar^{40} – Ar^{39} and K-Ar Investigation (1): AAPG Bulletin, v. 74, p. 547-563.

Walker, R.G., 1966, Shale Grit and Grindslow Shales: transition from turbidite to shallow water sediments in the Upper Carboniferous of northern England: Journal of Sedimentary Research, v. 36, p. 90-114.

Walker, R.G., 1978, Deep-water sandstone facies and ancient submarine fans: models for exploration and stratigraphic traps: AAPG Bulletin, v. 62, p. 932-966.

Wardlaw, N.C., and Nicholls, D.G., 1972, Cretaceous evaporites of Brazil and West Africa, International Geological Conference, v. 24, p. 43-58.

Weijermars, R., Jackson, M., and Vendeville, B., 1993, Rheological and tectonic modeling of salt provinces: Tectonophysics, v. 217, p. 143-174.

Weimer, P., 1990, Sequence stratigraphy, facies geometries, and depositional history of the Mississippi Fan, Gulf of Mexico (1): AAPG Bulletin, v. 74, p. 425-453.

Weimer, P., and Shipp, C., 2004, Mass transport complex: musing on past uses and suggestions for future directions, Offshore Technology Conference.

Weimer, P., Slatt, R.M., and Course, D.I.S., 2004, Petroleum Systems of Deepwater Settings, SEG EAGE Distinguished Instructor Series No. 7.

White, N., and Hoggard, M., 2014, Causes and consequences of long wavelength vertical movements along the Angolan margin, Petroleum Geoscience of the West African Margin Conference Absract: The Geological Society, Burlington House, London.

Winker, C., 1996, High-resolution seismic stratigraphy of a late Pleistocene submarine fan ponded by salt-withdrawal mini-basins on the Gulf of Mexico continental slope, Offshore Technology Conference.

Winker, C.D., and Booth, J.R., 2000, Sedimentary dynamics of the saltdominated continental slope, Gulf of Mexico: integration of observations from the seafloor, near-surface and deep subsurface, *in*, Weimer, P., Slatt, R. M., Coleman, J., Rosen, N. C., Nelson, H., Bouma, A. H., Styzen, M. J. & Lawrence, D. T., eds., Deep-Water Reservoirs of the World: GCSSEPM Foundation 20th Annual Research Conference p. 1059-1086.

Wood, L.J., and Mize-Spansky, K.L., 2009, Quantitative seismic geomorphology of a Quaternary leveed-channel system, offshore eastern Trinidad and Tobago, northeastern South America: AAPG Bulletin, v. 93, p. 101-125.

Woodward, N.B., Boyer, E. And Suppe, J., 1989, Balanced Geological Cross-Sections: An Essential Technique in Geological Research and Exploration, AGU Short Course in Geology, v. 6..

Woodward, N.B., Boyer, S.E., and Suppe, J., 1985 An Outline of Balanced Cross-Sections: Knoxville University of Tennessee, Deptment of Geological Sciences, Studies in Geology, v. 11, p.170.

Wuellner, D.E., and James, W., 1989, Braided and meandering submarine fan channel deposits, Tesnus Formation, Marathon basin, West Texas: Sedimentary Geology, v. 62, p. 27-45.

Wynn, R., Cronin, B., and Peakall, J., 2007, Sinuous deep-water channels: Genesis, geometry and architecture: Marine and Petroleum Geology, v. 24, p. 341-387.

Wynn, R.B., Talling, P.J., Masson, D.G., Stevenson, C.J., Cronin, B.T., and Le Bas, T.P., 2010, Investigating the timing, processes and deposits of one of the world's largest submarine gravity flows: The 'Bed 5 event' off northwest Africa, *in* Mosher, D.C., Shipp, R.C., Moscardelli, L., Chaytor, J.D. Baxter, C.D.P., Lee, H.J. and Urgeles., R. eds., Submarine Mass Movements and their Consequences, Elsevier, Amsterdam, v. 28, p. 463-474.

Zoetemeijer, R., Cloetingh, S., Sassi, W., and Roure, F., 1993, Modelling of piggyback-basin stratigraphy: Record of tectonic evolution: Tectonophysics, v. 226, p. 253-269.